GEOMATRIX

Final Report

SEISMIC GROUND MOTION STUDY FOR HUMBOLDT BAY BRIDGES ON ROUTE 255

Humboldt County, California
Contract No. 59N772

Prepared for

CALTRANS, Division of Structures
Sacramento, California

March 1994
Project No. 2016G

Prepared by
Geomatrix Consultants
in cooperation with
International Civil Engineering Consultants, Inc.

100 Pine Street, 10th Floor
San Francisco, CA 94111
(415) 434-9400 • FAX (415) 434-1365

GEOMATRIX

March 11, 1994
Project 2016G

Mr. Richard C. Wilhelms
Caltrans-Translab
P.O. Box 19128
Sacramento, California 95819

Subject: Seismic Ground Motion Study
for Humboldt Bridges on Route 255
Contract 59N772
Seismic Ground Motion Studies
for Major Bridges in Northern California

Dear Mr. Wilhelms:

We are pleased to submit the enclosed final seismic ground motion study report for the Humboldt Bay bridges on Route 255. The report presents response spectra and acceleration time histories of rock motions for use in the seismic evaluation of the bridge.

This study was conducted as part of an overall study to develop seismic ground motions on rock for five major bridges in the San Francisco Bay Area and three major bridges in the Humboldt Bay Area. The study has been conducted principally by Geomatrix Consultants in association with International Civil Engineering Consultants (CEC).

It has been a pleasure to be of service to Caltrans on this study. Please contact us if you have any questions on the enclosed report.

REGISTERED PROFESSIONAL ENGINEER
MAURICE S. POWER
No. 17174
CIVIL
STATE OF CALIFORNIA

Sincerely,

Maurice S. Power, C.E., G.E.
Project Manager

cc: Drs. J. Penzien, and W.S. Tseng, CEC
Consultants, (Drs. A.H.S. Ang, N. Abrahamson, B.A. Bolt, G.A. Carver, L.S. Cluff, C.A. Cornell, I.M. Idriss)

GEOMATRIX

NOTICE

The contents of this report reflect the views of the author who is responsible for the facts and accuracy of the data presented herein. The contents do not necessarily reflect the official views or the policies of the State of California or the Federal Highway Administration. This report does not constitute a standard, specification, or regulation.

GEOMATRIX

TABLE OF CONTENTS

TABLE OF CONTENTS (continued)

TABLE OF CONTENTS (continued)

LIST OF TABLES

LIST OF FIGURES

TABLE OF CONTENTS (continued)

LIST OF FIGURES (continued)

TABLE OF CONTENTS (continued)

LIST OF FIGURES (continued)

TABLE OF CONTENTS (continued)

LIST OF FIGURES (continued)

TABLE OF CONTENTS (continued)

LIST OF FIGURES (continued)

TABLE OF CONTENTS (continued)

LIST OF FIGURES (continued)

TABLE OF CONTENTS (continued)

LIST OF FIGURES (continued)

SEISMIC GROUND MOTION STUDY FOR HUMBOLDT BAY BRIDGES ON ROUTE 255 HUMBOLDT COUNTY, CALIFORNIA

SUMMARY

Summarized herein is a seismic ground motion study conducted for three existing Humboldt Bay bridges on Route 255. These bridges are the Eureka, Middle and Samoa channel crossings located on Route 255 crossing Humboldt Bay between Eureka and Samoa. The overall objective of this study is to develop response spectra and response-spectrum-compatible acceleration time histories of rock motions for use in the seismic analysis of the bridges.

The scope of studies described in this report includes: seismic source characterization; rock motion attenuation characterization; probabilistic ground motion estimation and development of equal hazard response spectra; deterministic ground motion estimation and development of deterministic response spectra; development of response-spectrum-compatible acceleration time histories; and summary of subsurface conditions at the bridge site. These studies are briefly summarized below.

SEISMIC SOURCE CHARACTERIZATION

A comprehensive model of seismic sources in the Humboldt Bay region was developed for this study. The seismic source model, which was used for both deterministic and probabilistic ground motion assessments for the bridges, is based on analysis of geologic and seismicity data and includes characterizations of maximum earthquake magnitude, source geometry, source segmentation, and earthquake recurrence for the various seismic sources in the region. For this study, the earthquake sources that might affect the ground motions at the site were divided into two basic types: 1) crustal sources lying within the North American plate, and 2) sources associated with the Cascadia subduction zone. Subduction-zone sources were divided into sources that lie within the subducting Gorda plate ("intraslab" sources) and the plate "interface" between the North American and Gorda plates.

ROCK MOTION ATTENUATION CHARACTERIZATION

For shallow crustal earthquakes, an updated rock motion attenuation model was developed with particular emphasis on long-period motions. Numerical ground motion modeling techniques were used to supplement available empirical data in the modeling of long-period ground motions. For subduction zone earthquakes, a set of rock-motion attenuation relationships were selected. These relationships were recently developed by combining regression analysis of recorded ground motion data and numerical ground motion modeling studies and distinguish between interface and intraslab earthquakes. The selected attenuation models were used in both deterministic and probabilistic ground motion assessments. Alternative attenuation models were also selected for use in the probabilistic ground motion analysis.

PROBABILISTIC GROUND MOTION ESTIMATION

Using the seismic source and attenuation models, probabilistic seismic hazard analyses (PSHA) were carried out and equal-hazard response spectra of rock motions were developed for return periods of 100, 300, 500, 1,000 and 2,000 years. Because the Humboldt Bay bridges are oriented essentially parallel to the dominant seismic sources, the seismic hazard is expected to be uniform along the bridges. Therefore, the ground motion hazard was computed for a location at the midpoint of the three bridge spans. The Little Salmon fault, if assumed to act as a separate seismic source, was found to be the dominant seismic source over a wide range of ground motions. If the Little Salmon fault is assumed to slip synchronously with the Gorda plate interface, the Gorda plate and North American crustal sources were found to dominate seismic hazard at the site. The contributions to, uncertainty in, and sensitivity of the seismic hazard results were analyzed in detail. The largest contributors to uncertainty in the hazard were found to be the form of the magnitude distribution (exponential or characteristic), the method for estimating earthquake recurrence (moment rate or paleoseismic), earthquake frequency, and the type of slip on the Little Salmon fault.

DETERMINISTIC GROUND MOTION ESTIMATION

Deterministic estimates of free-field rock motions were prepared at the site for the maximum credible earthquake (MCE) on the Little Salmon fault (moment magnitude M_w 7.5 occurring at closest distance of 5 km), for the MCE associated with the intraslab event in the subducting Gorda Plate (M_w 7.5 at 20 km), and for the MCE associated with the interface event on the

Gorda Plate (M_w 8.5 - 9.0 at 15 km). Deterministic estimates included median and 84th percentile response spectra and median estimates of the duration of strong shaking. The Little Salmon fault event was found to govern by a substantial margin the response spectral values for all periods examined. Based on comparisons of the probabilistic and deterministic results, the design earthquake was selected by Caltrans to be the M_w 7.5 earthquake on the Little Salmon fault and the corresponding target response spectra for acceleration time history development was selected to be at the 84th percentile level. At this level, the response spectral values have return periods in the range of approximately 500 - 1500 years, with the return period increasing with period of vibration (see Figure 5-11 and Table 5-1). At periods of vibration equal to or greater than 1.0 second, the return period is approximately 1500 years.

The Humboldt Bay bridges are located at a closest distance of about 5 km from the Little Salmon fault which is a reverse fault dipping northeast towards the bridges. As discussed in Section 5.5, additional adjustments were made to the response spectra to incorporate near-source effects on long-period ground motions. The adjustments consisted of increasing the response spectrum for the long-period component of ground motion in the transverse direction of the bridges by 15 percent. Specifically, the response spectrum for the transverse component has the same spectral values as the longitudinal component for periods less than 0.4 seconds and has spectral values 15 percent higher than the longitudinal component for periods equal to or greater than 2 seconds. The resulting response spectra for horizontal components are shown in Figure 5-12. The response spectrum for the vertical component is shown in Figure 5-13.

DEVELOPMENT OF ACCELERATION TIME HISTORIES

Three-component (two horizontal and one vertical) acceleration time histories of rock motion were developed to match the target response spectra. The approach used involved selecting natural time histories and then spectrally modifying them. The modification of the time histories to be response-spectrum-compatible was made using an analytical procedure that preserves the basic time domain character of the motions. The resulting acceleration time histories and the corresponding velocity and displacement time histories are shown in Figures 6-7, 6-8, and 6-9, respectively. Comparisons of the response spectra of the time histories and the target response spectra are shown in Figures 6-10, 6-11, and 6-12.

COMPILATION OF SUBSURFACE INFORMATION

Information on the surface soil conditions at the bridge sites (Eureka, Middle, and Samoa Channels) was compiled. An idealized soil profile along each bridge was prepared. Figure 7-3 shows the soil profile along the Eureka Channel bridge, Figure 7-4 shows the soil profile along the Middle Channel bridge, and Figure 7-5 shows the soil profile along the Samoa Channel bridge.

At the Eureka Channel bridge site, the surficial soils generally consist of fill and/or soft clays or silts. Beneath the surficial soils, the soils typically consist of compact to very dense sands overlying compact to very stiff silty clays and clayey silts which are in turn underlain by dense to very dense sands and gravelly sands extending to the bottom of the deepest boring at a depth of approximately 250 feet below the ground surface. The surficial soils at the Middle Channel bridge site generally consist of soft or very loose organic silts and sandy silts. Beneath the surficial soils, the soils typically consist of slightly compact to very dense sands and silty sands overlying slightly compact to compact silts and sandy silts extending to the bottom of the deepest boring at a depth of approximately 100 feet below the ground surface. At the Samoa Channel bridge site, the surficial soils generally consist of relatively thin layers of interbedded very loose to loose sands and organic sands, very soft organic silts and clays, and slightly compact to compact silts and sands. Beneath this upper zone, the soils typically consist of dense to very dense sands with interbedded thin lenses of organics and shell fragments extending to the bottom of the deepest boring at a depth of approximately 230 feet below the ground surface.

1. INTRODUCTION

This report describes a seismic ground motion study conducted for three existing Humboldt Bay Bridges on Route 255. These bridges are the Eureka, Middle, and Samoa channel crossings located on Route 255 crossing Humboldt Bay between Eureka and Samoa (Figure 1-1). This study was conducted as part of an overall study to develop seismic ground motions on rock for five major bridges in the San Francisco Bay Area (including the West San Francisco Bay Bridge, San Mateo-Hayward Bridge, Dumbarton Bridge, San Joaquin River-Antioch Bridge, and the Richmond-San Rafael Bridge) and the aforementioned three major bridges in the Humboldt Bay Area. Separate reports are presented for each San Francisco Bay Area Bridge and one report for the three Humboldt Bay Bridges.

The primary objective of this study is to develop earthquake ground motions on rock for use in the seismic analysis of the Humboldt Bay bridges. The rock motions developed in this study will require appropriate modifications for local site response effects as part of the seismic analysis for the bridge. A secondary objective of this study is to compile available subsurface information in the vicinity of the bridges. Such information can then be used in characterizing the soils at the bridge sites during the seismic analysis studies for the bridges.

The scope of work for this study includes the following items:

1. Characterizing seismic sources in the Humboldt Bay region that are significant in terms of their potential to produce earthquakes and strong ground shaking at the bridge sites. Seismic sources are to be characterized in terms of their location, geometry, maximum earthquake magnitude, and earthquake recurrence.

2. Characterizing rock motion attenuation to estimate free field rock outcrop motions at the bridge sites as a function of earthquake magnitude and distance. Attenuation relationships include those for response spectral values (5 percent damping) as well as peak ground acceleration.

3. Carrying out probabilistic seismic hazard analyses and developing hazard curves (ground motion amplitude versus frequency of exceedance curves) for peak ground

acceleration and response spectral values for the bridges. Mean hazard curves as well as characterization of uncertainty in the hazard curves are to be presented.

4. Developing equal-hazard (equal return period or equal probability of exceedance) rock response spectra for the bridges for several selected return periods or probability levels. Return periods or probability levels are to be selected in consultation with Caltrans.

5. Developing deterministic estimates of response spectra of rock motions for at least two selected earthquakes for the bridges. Earthquakes are to be selected in consultation with Caltrans.

6. Developing three-component (two horizontal and one vertical) acceleration time histories to match target response spectra selected by Caltrans from the deterministic and probabilistic analysis results. One set of time histories is to be developed for the bridge.

7. Compiling available subsurface information pertinent to the bridges including boring logs and test results. Soil profiles are to be constructed for the bridges. A profile of the deeper soil/rock stratigraphy (to the depth of hard rock) is also to be constructed based on available geologic and geophysical data.

8. Documenting the study findings in an engineering report.

This report presents the results of the preceding scope of work.

The remainder of this report is organized as follows. Sections 2 and 3 describe the characterization of seismic sources and of rock motion attenuation, respectively. Section 4 presents the probabilistic estimates of rock motions, including hazard curves and equal-hazard response spectra for the bridges. Deterministic estimates of rock motions are presented in Section 5. Acceleration time histories are presented in Section 6. Subsurface information at the bridge sites is described in Section 7.

1.1 PROJECT TEAM

This project has been conducted by the firms of Geomatrix Consultants (Geomatrix) and International Civil Engineering Consultants (CEC). The firm of Geo/Resource Consultants (GRC) participated in the compilation of subsurface information at the bridge sites. Several project consultants provided expert advice and review during the study. Key project participants are listed below.

Working Project Team

Project Director - J. Penzien (CEC)

Project Manager - M.S. Power (Geomatrix)

Earthquake Source Characterization - K.J. Coppersmith (lead), R.R. Youngs, L. DiSilvestro, N.T. Hall, and M. Angell (Geomatrix)

Attenuation Characterization and Deterministic Ground Motion Estimation - K. Sadigh (lead), R.R. Youngs, C.-Y. Chang, and D. Rosidi (Geomatrix); N. Abrahamson (consultant)

Probabilistic Ground Motion Estimation - R.R. Youngs (lead) and D. Rosidi (Geomatrix)

Acceleration Time History Development - W.S. Tseng (lead), K. Lilhanand, and D. Hamasaki (CEC); C.-Y. Chang and S.-J. Chiou (Geomatrix)

Compilation of Subsurface Information - C.-Y. Chang (lead) and C.L. Taylor (Geomatrix); D.G. Kennedy and E.S. Ng (GRC)

Project Consultants

Professor A.H.S. Ang, University of California, Irvine

Professor B.A. Bolt, University of California, Berkeley

Professor G.A. Carver, Humboldt State University

Dr. L.S. Cluff, Pacific Gas and Electric Company

Professor C.A. Cornell, Stanford University

We appreciate the cooperation and advice provided by Caltrans and their consultants: Mr. R.C. Wilhelms, project manager, Mr. J.H. Gates, Dr. L. Mualchin, and Mr. A.F. Goldschmidt of Caltrans; and Professor I.M. Idriss, University of California, Davis (consultant to Caltrans).

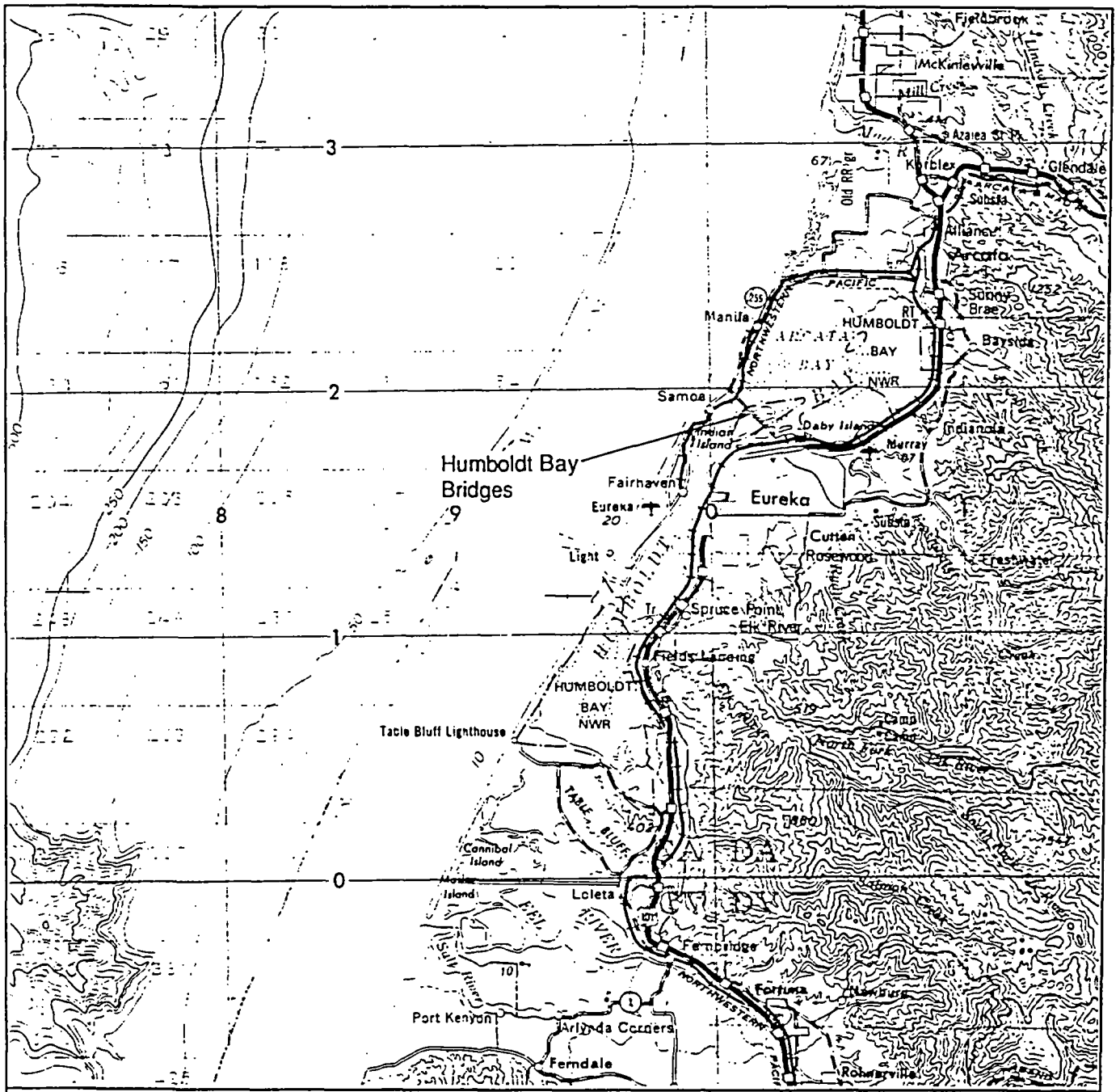

GEOMATRIX

LOCATION MAP
Seismic Ground Motion Studies for Humboldt Bay Bridges
Humboldt County, California

Figure
1-1

Project No.
2016G

2. SEISMIC SOURCE CHARACTERIZATION

This section of the report summarizes the characterization of the seismic sources included in the deterministic and probabilistic ground motions assessments for the Humboldt Bay bridges. In general, source characterization refers to the assessment of source locations, maximum earthquake magnitudes, and recurrence rates. The methods used to characterize earthquake sources for the probabilistic analysis are described in detail in Appendix A and the methods for assessing maximum credible earthquakes are described in Appendix B. The general tectonic elements of the region are shown in Figure 2-1.

The Humboldt Bay region lies in an area of complex tectonic interaction among the Gorda, North American, and Pacific plates. For simplicity in this report, the earthquake sources that might affect the ground motions at the bridge sites are divided into two basic types: 1) sources associated with the Cascadia subduction zone, and 2) crustal sources lying within the North American plate. Subduction-zone sources are further divided into sources that lie within the subducting Gorda plate ("intraslab" sources) and the plate "interface" between the North American and Gorda plates. The rates of observed seismicity during the historical and instrumental record in the Humboldt region have been relatively high. Nearly all of these events have occurred within the Gorda slab or, to a lesser extent, within the North American crust. With the possible exception of the April, 1992 Cape Mendocino earthquake, no moderate-to-large earthquakes have occurred historically along the plate interface, either along the southern part of the Cascadia subduction zone, or to the north in Oregon and Washington. To characterize the plate interface source, characteristics of the 1992 Cape Mendocino earthquake are considered and paleoseismic geologic data are incorporated.

In this section, we first summarize the regional seismicity data set for the Humboldt Bay region, including a summary of the 1992 Cape Mendocino earthquake, then Cascadia subduction zone sources are characterized, followed by a characterization of crustal sources.

2.1 REGIONAL SEISMICITY

Figure 2-2 shows the locations of recorded earthquakes in the Humboldt Bay region superimposed on the features shown in Figure 2-1. The data presented in Figure 2-2 represent all earthquakes above magnitude M_L 3.0 that have been recorded in the time period of 1800 to July 1, 1991. The sources of the data are the DNAG catalog (Engdahl and Rinehart, 1992) for the period 1800 to 1969, the US Geological Survey, Menlo Park for the period 1969 to July 1, 1991, and the PGandE Humboldt Bay temporary seismic network catalog for the period 1974 through 1984 (TERA Corporation, 1974-1984).

The mathematical formulation used in this (and most) hazard analysis is based on an assessment of the frequency of occurrence of independent earthquakes. It has been shown that the inclusion of dependent events (e.g., foreshocks and aftershocks) in the analysis results in only a minor increase in the computed hazard (Mertz and Cornell, 1973; Veneziano and Van Dyke, 1985). For this study, dependent events in the earthquake catalog were identified using empirical criteria for foreshock-aftershock sequence size developed by Arabasz and Robinson (1976), Gardner and Knopoff (1974), and Uhrhammer (1986). These three criteria (shown in Figure 2-3) have been found to perform satisfactorily in identifying dependent events in regional catalogs (Youngs et al., 1987). Earthquakes in the catalog were identified as dependent events (foreshocks or aftershocks) if they were flagged by two or more of the empirical criteria. In applying the criteria to aftershock sequences for the largest earthquakes in the data set, only events lying in a zone approximately parallel with the fault rupture where considered as potential aftershocks. Figure 2-4 shows the spatial distribution of the resulting catalog of independent earthquakes.

Estimation of earthquake recurrence frequencies requires specification of the time periods over which independent events of various magnitudes can be considered completely reported in the catalog. These time periods were estimated by plotting the observed frequency of occurrence of independent events in different magnitude intervals as a function of time before July 1, 1991, with the observed frequency equal to the number of events observed in the last T years divided by T. Assuming the earthquake occurrence rate on a regional scale is stationary in time, the time when the observed frequency begins to steadily decrease with increasing time represents

the date before which the catalog cannot be considered complete. This approach to evaluating catalog completeness is similar to the method proposed by Stepp (1972).

Figure 2-5 presents a plot of the frequency of independent earthquakes as a function of time for earthquakes within the region outlined in Figure 2-4. Separate analyses were conducted for the inner region immediately surrounding Humboldt Bay and the area outboard of the inner region (see Figure 2-4) to evaluate possible differences in catalog coverage due to the temporal and spatial distributions of seismographic stations. It was found that the completeness intervals are generally similar over the entire region shown in Figure 2-4. Some of the estimated completeness intervals are slightly shorter in the outer portion of the study region. The estimated completeness periods for the larger magnitudes extend well into the pre-instrumental period. Although the accuracy of the location and magnitude estimates for the earlier events are not as reliable as those of the modern instrumental period, many of the major events have been the subject of special studies (e.g., Woodward-Clyde, 1982; Toppozada and others, 1981; Toppozada and Park, 1982) and they represent events significant to hazard assessment. The selected periods of completeness shown in Figure 2-5 are:

Complete Period of Catalog Reporting for:

Magnitude	Inner Area	Magnitude	Outer Area
≥3	1973	≥3.0	1981
≥3.5	1950	≥3.5	1977
≥4.0	1846	≥4.5	1964
≥4.5	1831	≥5.5	1931
≥6.0	1805		

The distribution of seismicity shown on Figures 2-2 and 2-4 shows a variety of patterns. There is a clear association of seismicity with the Mendocino transform fault extending westward from the coastline. Within the Gorda plate, the density of seismicity increases toward the Mendocino triple junction, with several northeast trending patterns evident. Within the North American plate (and the underlying subducting Gorda plate) seismicity is also concentrated near the triple junction, decreasing dramatically as one moves north into Oregon. Two northwest trends of seismicity are evident east of and subparallel to the San Andreas fault. The mapped location of

the San Andreas fault itself shows little expression in the recorded seismicity, characteristic of its behavior in regions of large historical and prehistorical ruptures.

As indicated earlier, the seismicity in the region can be separated into two distinct populations, the events occurring within the Gorda plate (and along the Mendocino transform fault) and the events occurring within the North American plate. Figures 2-10 and 2-11 show the spatial distribution of earthquakes in these two groups. Separate regional earthquake recurrence rate estimates were made for the two populations of earthquakes using the maximum likelihood formulation developed by Weichert (1980). Figure 2-12 shows cumulative recurrence rates for the central Humboldt Bay region based on the data for periods of complete reporting. (The central Humboldt Bay region is defined as the region shown on Figure 2-4.) The error bars represent 5^{th} to 95^{th}-percentile cumulative rates computed using the formulation given by Weichert (1980). As described in Appendix A, the relative frequency of different size earthquakes on a regional basis is described by the *b*-value of the exponential magnitude distribution. The regional *b*-value was calculated to be 0.545 for the Gorda Plate and 0.834 for the North America Plate.

The definition of specific sources within these two regions and the development of the source seismicity parameters is discussed below in Section 2-2. In developing recurrence estimates for each of the sources three recurrence models or magnitude distribution models were used, the truncated exponential distribution, the characteristic earthquake distribution, and the maximum moment distribution. The first two distributions are discussed in Appendix A. The maximum moment distribution (Wesnousky and others, 1983) represents a modified form of the characteristic magnitude distribution in which it is assumed that the source generates only one size of independent earthquake, the maximum or characteristic earthquake, with all other events occurring as foreshocks or aftershocks. When these models are used to estimate earthquake recurrence using slip rate, the slip rate was translated into seismic moment rate using the source geometry to derive a fault area and assuming a rigidity of $3 \cdot 10^{11}$ dyne-cm. The moment rates were then converted into recurrence relationships using the formulation of Anderson (1979) for the truncated exponential and Youngs and Coppersmith (1985b) for the characteristic and maximum moment models (the later obtained by excluding the exponential portion of the generalized characteristic model), and using the moment-magnitude relationship of Hanks and

Kanamori (1979). In applying Youngs and Coppersmith's (1985b) characteristic magnitude distribution, the maximum magnitude assessed for the fault, m_{max}, is taken to be the expected magnitude for the characteristic size event, with individual events uniformly distributed in the range of $m_{max} \pm ¼$ magnitude units. The cumulative frequency for earthquakes of magnitude m_{max}-¼ is then set equal to the annual frequency of maximum events assessed for the fault and the upper bound magnitude in the hazard integration is equal to m_{max}+¼. To provide a consistent interpretation for the exponential model, the standard truncated exponential distribution (Cornell and Van Marke, 1969) was modified to treat the upper bound magnitude in the density function as uniformly distributed over the range of $m_{max} \pm ¼$ magnitude units. The effect is to smear out the upper boundary of the magnitude distribution without altering the general shape of the recurrence relationship. The cumulative frequency for earthquakes of magnitude m_{max}-¼ is again set equal to the annual frequency of maximum events assessed for the fault and the upper bound magnitude for hazard integration is equal to m_{max}+¼. In this modified form the distribution of events in the range $m_{max} \pm ¼$ remains nearly exponential. Figure 2-13 compares the shape of the exponential, modified exponential, characteristic, and maximum moment magnitude distributions. As can be seen, the modified exponential distribution is essentially equal to the exponential distribution except at the upper bound. The characteristic magnitude distribution results in about a factor of 10 reduction in the frequency of small magnitude events compared to the exponential model when the total rate of seismicity is fixed by the rate of moment release.

2.1.1 1992 Cape Mendocino Earthquake

The 1992 Cape Mendocino earthquake occurred on April 25 near the town of Petrolia, California. The magnitude of the earthquake was M_S 7.1, its focal depth was 10.5 km, and its focal mechanism indicated nearly pure thrust faulting (Oppenheimer and others, 1993). Because this event may have implications to the seismic source characterization for the Humboldt Bay Bridges, the current interpretations of the earthquake are summarized here. The places where the characteristics of the event have importance to this analysis are identified throughout this section of the report.

The location of the 1992 Cape Mendocino earthquake and its focal mechanism are shown in Figure 2-6. The mainshock as followed the next day by two aftershocks, both having M_S 6.6,

located offshore to the west of the mainshock. Unlike the April 25 event, the two large aftershocks had strike-slip focal mechanisms suggesting, along with their location and depth, that they occurred within the Gorda plate. The right lateral plane in the focal mechanisms for both events strikes northwest. The first event was associated with too few aftershocks to identify the rupture plane. The second event was associated with aftershocks that appear to be consistent with a northwest-striking plane (Oppenheimer and others, 1993). Because these two events occurred within the Gorda plate with different focal mechanisms than the mainshock, it appears that they occurred on different faults than the mainshock. Oppenheimer and others, (1993), have modeled the stress changes between an east-west-trending Mendocino fault, a northeast-trending fault related to the first large aftershock, and a northwest-trending fault associated with the second aftershock. Their results suggest that the mainshock rupture brings both the Mendocino fault and the northwest fault closer to failure, and the rupture of the northwest fault would be sufficient to trigger the northeast-trending fault.

In addition to aftershocks in the Gorda plate, a number of small magnitude earthquakes occurred along the Mendocino fault zone and its landward projection, as well as within the shallow parts of the North American crust. The temporal linkage of elevated seismicity within these diverse zones suggests that the zones are mechanically coupled and responding to complex plate interactions.

Important effects of the earthquake include coseismic uplift along the coast and a tsunami. By documenting the vertical extent of mortality of intertidal organisms, Carver and others (in review) identified a 25 km-long zone of uplift along the coast from 3 km south of Punta Gorda north to Cape Mendocino. The maximum uplift inferred from the biota mortality was 1.4 $\pm$ 0.2 m, which occurred near the center of the uplifted area (Carver and others, in review). Reoccupation of the Global Position System (GPS) stations showed maximum subsidence at a position about 5 km northeast of the epicenter (Oppenheimer and others, 1993). Displacement modeling of both the coastal uplift and GPS data, result in a displacement of about 2.7 m along a thrust surface shown in Figure 2-7. A small tsunami was generated by the mainshock and was recorded by tide gauges along the California, southern Oregon, and Hawaiian coastlines.

A potentially important aspect of the 1992 Cape Mendocino earthquake concerns whether or not the event occurred along the plate interface between the Gorda and North American plates. At present the issue has not been resolved within the earth science community and various arguments are being presented. The thrust mechanism for the event would argue against the event having occurred within the Gorda plate, which has historically been associated with high-angle strike slip earthquakes and normal faulting in the region to the east (McPherson, 1989; 1992; Smith and others, in press). The thrust mechanism suggests that the event occurred either on the plate interface or within the North American plate. Oppenheimer and others (1993) argue that the Cape Mendocino mainshock was a plate interface earthquake based on the following assessment. If the shallowly-east-dipping focal plane is extrapolated updip to the west, it projects to the sea floor within 5 km of the location of the seaward edge of the Cascadia deformation front (Oppenheimer and others, 1993). This interpretation is shown in Figure 2-6. In this interpretation, the mainshock would extrapolate *above* the pattern of aftershocks, as shown in cross section A-A' in Figure 2-6. Also, the mainshock is interpreted as having occurred about 7 km above the upper boundary of the pre-mainshock seismicity zone. Oppenheimer and others (1993) note that if the upper boundary of the pre-mainshock seismicity zone is extrapolated to the west, it would intersect the surface well west of the deformation front, thus arguing against this surface representing the plate interface.

The arguments favoring the mainshock having occurred within the North American plate several kilometers above the plate interface concern interpretations of the thickness of the North American crust. Wang and Rogers (in review) have conducted thermal modeling to explain the distinctive double seismic layers observed at depths of 15-25 km beneath the region (Figure 2-8. They conclude that the upper layer is the upper crust of the Gorda slab and the lower layer is the upper mantle. The plate interface, then, would be expected to lie at a depth of about 15 to 20 km at the longitude of the site (124° 13.7' on Figure 2-8), which is 5 to 10 km below the mainshock depth. Verdonck and Zandt (in press) used seismic tomography to invert for three-dimensional velocity structure in the region. Their results suggest that velocities typical of Gorda crust lie at depths of at 15-20 km, well below the hypocenter for the mainshock (Figure 2-9).

Although the issue of whether or not the 1992 Cape Mendocino earthquake occurred on the plate interface has not yet been resolved, there is ample evidence to support the conclusion that the mainshock and its aftershock reflect the relative interaction of the three tectonic plates in this region and, because all three plates experienced stress release, the earthquake sequence showed that the plates are mechanically coupled in terms of stresses.

Throughout the following discussion of seismic source characterization, we will assume that the origin of the Cape Mendocino earthquake is an open issue and we will evaluate the potential implications to the hazard analysis as if the event in fact occurred on the plate interface.

2.2 CASCADIA SUBDUCTION ZONE SOURCES

The Cascadia subduction zone is the convergent boundary extending over 1,000 km from north of Vancouver Island to northern California (Figure 2-1). Most of the Cascadia subduction zone marks the boundary between the subducting Juan de Fuca plate and the North American plate. However, to the north, the plate boundary separates the Explorer plate from the North American plate and, to the south, the Gorda plate is subducting beneath the North American plate. Wilson (1989) notes that the so-called "Gorda plate" is, in fact, not a separate plate from the Juan de Fuca plate. Deferring to common usage, we shall use the term Gorda plate in this discussion. The levels of seismicity within the offshore Gorda plate are markedly higher than those within the Juan de Fuca plate, reflecting the internal deformation occurring within the Gorda plate. The direction of relative plate convergence is to the northeast and averages about 20-40 mm/yr along the margin (e.g., Nishimura and others, 1984; Engebretson and others, 1985; DeMets and others, 1990).

The Humboldt Bay bridges are located in the vicinity of the southern Cascadia subduction zone. This part of the subduction zone is characterized by relatively high levels of Gorda plate seismicity both within the slab offshore and beneath the continent (Figure 2-10). Several moderate-to-large earthquakes have occurred within the Gorda plate historically, such as the M_S 7.2 1980 earthquake and the M_S 6.6 earthquakes that occurred on April 26, 1992. The larger instrumentally-recorded earthquakes have been strike-slip events and appear to be occurring along northeast- and northwest-trending strike-slip faults. These faults are likely accommodating

north-south compression in the southeastern corner of the Gorda plate due to converging Mendocino and San Andreas transforms (Wilson, 1989; McPherson, 1992; Smith and others, in press).

Studies of subduction zones worldwide have shown that subduction zone earthquakes are related to two separate and distinct processes: stresses within the subducting slab (usually downdip-tension due to slab-pull forces), and compressional stresses at the interface between the two plates. Experience has shown that these two domains act as independent seismic sources from the standpoint of source locations, maximum magnitudes, and earthquake recurrence. We therefore treat these two subduction zone-related sources separately, as discussed below.

2.2.1 Plate Interface Source

In typical subduction zones, the plate interface is the locus of plate boundary coseismic deformation and is the location of the largest earthquakes observed worldwide. Plate interface earthquakes are usually thrust events occurring on relatively shallow-dipping faults, typically at depths of less than about 45 km (Tichelaar and Ruff, 1993). A common method for distinguishing plate interface events from intraslab earthquakes in worldwide catalogs is to identify shallow thrust events. Intraslab events, in contrast, are typically deeper and have normal-faulting mechanisms. In the case of the Gorda slab, strike slip focal mechanisms also are observed. Based on these criteria, it has been noted by several researchers that the Cascadia plate interface has been markedly quiescent, both in southern Cascadia (Smith and others, in press) and along the northern part of the margin (e.g., Taber and Smith, 1985; Heaton and Hartzell, 1987; Rogers, 1988). In addition to the absence of larger earthquakes, the plate interface has been apparently devoid of even small-magnitude events, which is highly unusual for any subduction zone. Whereas thrust-faulting earthquakes have not been observed at any magnitude level in the region monitored by the Washington state network (e.g., Crosson and Owens, 1987), in the Gorda plate area small-magnitude thrust-faulting earthquakes have been recorded. However, the thrust-faulting earthquakes are not localized along the plate interface, instead they appear to be scattered throughout the same volume as intraslab earthquakes having normal-faulting and strike slip mechanisms. Smith and others (in press) note: "There is no hint of their concentration along what could be the plate boundary." The 1992 Cape Mendocino

earthquake could represent the first historical occurrence of a large-magnitude earthquake occurring on the plate interface (Oppenheimer and others, 1993).

The Cape Mendocino earthquake as well as other more indirect lines of evidence are used to interpret the earthquake potential of the plate interface source. The various components of the logic tree for characterizing the plate interface as a seismic source are shown in Figure 2-14.

Probability of Activity. With the possible exception of the 1992 Cape Mendocino earthquake, the absence of moderate-to-large plate interface earthquakes in the historical record along the Cascadia subduction zone raises the question of whether or not the interface is capable of generating large-magnitude earthquakes. The historical quiescence can be interpreted as either a quiet period between the occurrence(s) of large earthquakes, or as diagnostic of the long-term behavior of the margin. The seismogenic potential of the Cascadia plate interface has been the subject of considerable controversy and scientific study in the past few years. To reflect the present uncertainties, we include an expression of the probability of activity in the characterization of the plate interface (Figure 2-14). "Activity" in this context is defined as being capable of generating moderate-to-large earthquakes.

We provide here a brief summary of some of the technical arguments that have been made for and against the Cascadia plate interface being active.

Arguments Favoring Activity

- Geologic evidence for episodic, sudden, and synchronous coastal subsidence at several locations along the Cascadia margin from the northern Olympic Peninsula to Humboldt County, California.
- Stratigraphic evidence at multiple localities for tsunami following subsidence.
- Geologic evidence for multiple turbidities in the offshore Cascadia basin that may have been triggered by large earthquakes.
- Offshore deformation, geodetic data, and volcanism all confirm that interplate convergence is an ongoing process, albeit at low rates.

- Modeling of geodetic data indicates a locked plate interface in the offshore region.
- Analogy to other seismogenic subduction zones.
- Likelihood that the 1992 Cape Mendocino earthquake occurred on the plate interface

Arguments Against Activity

- Marked seismic quiescence of the plate interface during the historical and instrumental record (assuming Cape Mendocino earthquake occurred within North American plate).
- Young slab age, low convergence rate, quiescence may suggest that analogies to other subduction zones may be inappropriate.
- Thermal modeling suggests very narrow to non-existent seismogenic interface.
- At least some of the locations of coastal subsidence may be explained by local crustal folding.

As summarized above, the most compelling evidence for the activity of the plate interface comes from the geologic record, rather than the seismicity record. In particular, the evidence for rapid coastal subsidence has become pervasive at several locations along the coast and is consistent with the pattern of coseismic deformation expected along a seismogenic plate interface. Further, the evidence for the synchroneity of subsidence at several locations is difficult to explain by local mechanisms such as crustal folding (e.g., Atwater, 1992). Although uncertainty still remains, many would conclude that the Cape Mendocino earthquake was a plate interface event. In light of the present data and interpretations, including those data specifically related to the southern Cascadia zone, we judge that the likelihood that the Cascadia plate interface is seismogenic is very high (0.95). To provide in the hazard analysis for some uncertainty on this scientific issue, we assign the probability that the interface is not seismogenic a very low probability (0.05).

Geometry of Plate Boundary. The geometry of the subduction plate boundary is important to assessments of the distances of the intraslab and plate interface to the bridge sites. The geometry of the subducted Gorda plate is interpreted from seismicity data, as observed along several cross-sections across the margin (Figures 2-16a through 2-16d). As discussed

previously, the plate interface is not distinguished by thrust-type earthquakes. However, we can discern the uppermost part of the oceanic slab on the basis of strong concentrations of earthquakes that appear to be distinct from seismicity occurring within the North American plate. The interpretation of the cross-sectional geometry of the subduction zone that we use in this analysis is shown in Figures 2-17 and 2-18 and is discussed below. This geometry defines the closest distance from the site to the interface source to be about 15 km.

Because they are well-expressed in the instrumental seismicity data, the locations of the intraslab seismicity and the North American crustal seismicity are readily interpreted. The interpreted boundary between the subducted slab and the North American plate is the general location of the plate interface. However, the location of the seismogenic plate interface is not imaged from thrust-faulting seismicity. Therefore, other means must be used to locate the likely updip and downdip extent of the seismogenic interface.

Downdip Seismogenic Width. The downdip width of the seismogenic plate interface is important because it places a constraint on the dimensions of coseismic rupture (and thereby estimates of maximum earthquake magnitude). It also is important to estimates of seismic moment rate (and thereby recurrence rates) inasmuch as the fault area is constrained by the downdip width.

In general, the methodology that we use to estimate the width of the interface follows the general concept that competent rocks must be present on both sides of the plate interface for it to generate earthquakes. Along the shallowest parts of the plate interface, young poorly consolidated sediments are juxtaposed with the subducting slab, leading to aseismic deformation of the accretionary sediments (Byrne and others, 1988; Marone and Scholz, 1988). At some point downdip of the seismogenic interface, the plate interface will separate competent oceanic crust with quasi-plastic continental crust beneath the seismogenic zone of the North American plate. This point marks the downdip location of the seismogenic interface. In this analysis, we essentially endorse the interpretations of the interface given for the southern Cascadia subduction zone by Clarke and Carver (1992). We also incorporate information from the northern part of the subduction zone and from analogies to other subduction zones (e.g., Pacheco and others, 1993).

As shown in Figure 2-15, the fold and thrust belt that defines the accretionary wedge along the Cascadia subduction zone comes onshore in the Humboldt Bay region. Folds and thrust faults represent the generally west-southwest vergence of deformation related to interplate compression. The seawardmost tapered wedge tip of the accretionary fold and thrust belt is marked by a deformation front. In this region near the deformation front, the accretionary wedge is thin and the deformation is occurring aseismically within relatively young, weak sediments. About 20 km landward of the deformation front (less at the southern end), a structural discontinuity is identified (Figure 2-15) at which the trend of folds and faults changes to a more easterly orientation landward of the discontinuity (Clarke and Carver, 1992). The orientation of the structures to the east of the discontinuity is normal to the interplate convergence direction and suggests that interplate compression is propagated across the interface into the overlying North American plate. The accretionary wedge is thicker landward of the discontinuity and seismicity in the North American plate confirms that the rocks in this area are sufficiently strong to accumulate seismic strain energy. We therefore interpret the structural discontinuity to mark the surface projection of the updip extent of the seismogenic interface. Our interpretation of the location of this boundary in map view is shown in Figure 2-17, and in cross section in Figure 2-18.

The interpretation of the location of the updip location of the interface at a depth of about 6 km is consistent with the possible updip extension of the Cape Mendocino earthquake and with observations at other subduction zones. Pacheco and others (1993) studied the seismogenic widths of 19 subduction zones. Their studies indicate that the depth to the updip location of the seismogenic interface varies from 5 to 25 km with an average depth of about 10 km. Pacheco and others (1993) note that the greater depths to the seismogenic interface are typically associated with zones having very thick accretionary prisms. The accretionary wedge associated with the Cascadia subduction zone is quite thick, reflecting the high sedimentation rates as well as the low rates of plate convergence. As a result, there is no topographic trench associated with the zone.

The location of the downdip extent of the seismogenic interface is defined primarily by the point of intersection of the base of the seismogenic North American crust with the interface. As shown in Figure 2-18, earthquakes are occurring in the North American plate down to depths

of about 25 km. Several researchers (e.g., Sibson, 1982; Scholz, 1988) have suggested that the "brittle-ductile" transition in continental crust is marked as the depth above which most (90%) of the seismicity occurs. The depth of this lower stability transition is believed to be controlled principally by temperature (Sibson, 1982). Below this depth, the continental crust is interpreted to deform by plastic, aseismic mechanisms. Therefore, the juxtaposition of these rocks with oceanic crust across the plate interface will also occur aseismically. This point on the interface also marks the approximate point where the Juan de Fuca increases in dip from about 9°-13° to about 15°-20° (Clarke and Carver, 1992).

In addition to following the lines of reasoning presented above for defining the downdip width of the seismogenic interface, we also have considered possible thermal-mechanical constraints on the width of the interface. Hyndman and Wang (1993) have used thermal modeling to assess the downdip seismogenic width of the southern Vancouver-to-northern Oregon portion of the Cascadia subduction. They conclude that the downdip width at their profile in northern Oregon is about 70 km. The thermal arguments, which are related to the extremely young age of the Juan de Fuca plate, are likely also appropriate for the Gorda plate (Wang and Rogers, in review). Byrne and others (1988) offered a clear definition of the seismogenic width and possible physical constraints. Pacheco and others (1993) systematically defined the seismogenic widths of 19 subduction zones and attempted unsuccessfully to correlate width to other subduction zone parameters such as age of oceanic lithosphere, plate convergence rates, and seismic coupling. They conclude that seismogenic width is most likely controlled by rock and sediment composition, fluid pressure, and the thermal regime. Pacheco and others (1993) speculate that the large amount of young sediments offshore along the Cascadia subduction zone and the high temperatures related to the presence of very young oceanic lithosphere could lead to a very small or no seismogenic width along the Cascadia interface or portions of it.

The above constraints and their uncertainties lead to the following assessments of the downdip seismogenic width of the plate interface and their associated weights: 60 km (0.1), 70 km (0.3), 80 km (0.3), 90 km (0.2), 100 km (0.1). These widths are generally consistent with estimates made for locations to the north in southern Vancouver Island, Washington, and Oregon (e.g., Savage and Lisowski, 1991; Wang and Hyndman, 1992; Mitchell and others, 1992; Hyndman and Wang, 1993) based on geodetic data and thermal modeling.

As shown in Figure 2-18, this interpretation of the location of the seismogenic interface suggests that the closest approach of the seismogenic interface to the site is about 15 km. This distance is used in the deterministic assessment of ground motions due to the plate interface source.

Rupture Segmentation. The maximum length of ruptures along the plate interface, together with the downdip seismogenic width, defines the rupture area along the interface. Rupture area is in turn related to magnitude and seismic moment. Potential interface rupture segments are usually defined along subduction zones based on the extent and pattern of large-magnitude earthquakes and ongoing small-magnitude thrust earthquakes. However, with the possible exception of the 1992 Cape Mendocino earthquake, we have not observed any moderate-to-large earthquakes along the Cascadia zone historically, and small-magnitude thrust earthquakes (observed only in southern Cascadia) do not appear to be unequivocally associated with the plate interface. If we assume that the Cape Mendocino earthquake occurred on the plate interface, it is considered unlikely that the rupture length and width associated with this event would define a maximum event for the interface. For example, Carver and others (in review) have identified late Holocene terraces similar to those developed during the 1992 event but broader, more continuous, and extending both north and south of the 1992 zone of uplift. This suggests that larger ruptures have occurred over this part of the subduction zone (Carver and others, in review). We therefore base our estimates of the length of plate interface ruptures on geologic data regarding the timing of prehistoric earthquakes, structural features along the plate boundary, and analogies to other subduction zones.

Considerable effort has been expended in identifying evidence for prehistorical coastal subsidence (or uplift) and dating individual episodes along the Cascadia margin. In ideal circumstances, the knowledge that a large prehistorical earthquake occurred at several coastal localities at the same time would provide compelling evidence for the extent of the rupture. Also, the knowledge that earthquakes had occurred at different times along the margin would lead to interpretations that separate ruptures had occurred in the past. Actual circumstances are, of course, less than ideal. We have uncertainties related to the identification of prehistorical earthquakes, to the actual timing of each event, and to the correlation of individual earthquakes from location to location. For example, several investigators (summarized in Atwater, 1992) have identified evidence for rapid coastal subsidence along the Cascadia margin in the past 2,000

years (Figure 2-19). Locations showing subsidence stretch from the Strait of Juan de Fuca to Alsea Bay in central Oregon. Some sites to the south of Alsea Bay also show subsidence (e.g., Coos Bay and Humboldt Bay), but other sites either show no subsidence or evidence for uplift. Further, the sites in the Humboldt Bay area show both subsidence and uplift (Clarke and Carver, 1992). These observations have alternative explanations and lead to different conclusions regarding the coseismic behavior of the margin.

The most recent earthquake at several sites along the margin has been dated at about 300 years ago, suggesting that a single earthquake rupture occurred along these sites (Atwater, 1992). The precision of conventional radiocarbon dating at these has uncertainties of about 100 yrs for any given age-date. Dendrochronologic calibration at several sites has improved precision of some age-dates to about 10-15 years (Carver. pers. comm.). The similarities in the timing of the most recent event at several localities along the margin supports the interpretation that at least a large part of the margin ruptured during a single event. However, because of the imprecision of the age-dating, the apparent synchroneity does not prove that the margin ruptured at one time ("at one time" in this context means during a single earthquake, as opposed to two earthquakes separated by, say, several weeks). For example, earthquake sequences along subduction zones in the Nankai trough, Japan, southern Chile, Columbia, and Mexico experienced the independent rupture of adjacent segments of the subduction zone during a time period of less than 20 years. The rupture of adjacent segments closely spaced in time would be indistinguishable using paleostratigraphic evidence and age-dating. On the other hand, the observation that several locations experienced coseismic deformation at approximately the same time is difficult to reconcile with a model in which the margin consists of several independent segments that each have their own recurrence behavior.

For this analysis, we consider four rupture segment scenarios for the plate interface. In the first scenario, a 125-km-long rupture segment is based on observed aspect ratios of plate interface earthquakes. This rupture length corresponds with the expected rupture rupture length associated with a downdip width of about 70 km. Because the scenario is based on aspect ratios rather than segmentation, it is assumed to occur randomly along the plate. In the second scenario, the plate interface along the Gorda plate is assumed to rupture along a 240-km-long segment. The assumed northern limit of this rupture segment would be at the projection of the Blanco fracture

zone with the plate interface (Figure 2-1). This segmentation model is supported by the observation that the Gorda plate appears to be distinct seismically from the adjacent Juan de Fuca plate. Whereas the Juan de Fuca plate is markedly quiescent, the Gorda plate is characterized by elevated levels of seismicity. The presence of historical large-magnitude strike slip earthquakes also distinguishes the Gorda plate from the Juan de Fuca plate. The third rupture segment model assumes that a 450 km-long rupture could occur that would include the Gorda plate margin and could extend as far north as about Alsea Bay, Oregon (Figure 2-19). As summarized in Atwater (1992), sites from Alsea Bay to the north show evidence of coseismic subsidence in the past 2,000 years. Conversely, Nelson and Personius (1991) report that at the Siuslaw River there is evidence against coseismic subsidence in the past 2,000 years. Likewise, possible evidence for uplift has been reported for the Cape Blanco area (Kelsey, 1990). The third rupture segment model allows for the possibility that these differences are due to differences in the nature or timing of ruptures along the margin. Nelson and Personius (1991) have also suggested a possible segmentation point in this vicinity. A secondary line of evidence is the presence of three large left-lateral faults along the offshore continental margin in central coastal Oregon that appear to displace both the oceanic crust and the North American crust (Goldfinger and others, 1992). A fourth rupture segment model assumes that the entire 1000 km-long margin can rupture in a single plate interface earthquake. The primary support for this model is the apparent synchroneity of at least some of the deformation events at various points along 700 km of the margin from the Strait of Juan de Fuca to Humboldt Bay (Figure 2-19). Such a rupture of the entire length of a subducting margin would be unusual worldwide (Spence, 1989).

Each of the four rupture segment scenarios have lines of evidence that support or contradict them. We give higher weight to the third model, which has some support in the coastal subsidence data as well as structural evidence of segmentation. The plate interface rupture lengths and their associated weights are: 125 km (0.1), 240 km (0.3), 450 km (0.5), and 1000 km (0.1).

Maximum Earthquake Magnitude. Maximum magnitude is estimated for the plate interface by combining the estimates of downdip seismogenic width with the estimates of rupture length to arrive at rupture areas and by using rupture length directly. We use the empirical correlations

between rupture area and moment magnitude developed for subduction zones by Abe (1981; 1984), which is M = Log A + 3.99, where A is the rupture area; and by Geomatrix (1993), which is M = 0.81 Log A + 4.7. We also use a relationship between rupture length and moment magnitude developed for interface ruptures: M = 1.39 Log RL + 4.94 (Geomatrix, 1993).

The combinations of rupture widths, rupture lengths, and their associated weights yields the following maximum magnitude distribution for the plate interface: 7.8 (0.01), 7.9 (0.06), 8.0 (0.03), 8.1 (0.12), 8.2 (0.18), 8.3 (0.20), 8.4 (0.25), 8.5 (0.05), 8.6 (0.04), 8.7 (0.05), 8.8 (0.01). The broad range of this distribution reflects the considerable uncertainties in estimating the rupture dimensions of the plate interface, given the available data.

For the deterministic analysis, a maximum credible earthquake magnitude must be assessed. Because of the present uncertainties, a range of magnitude from moment magnitude 8 to 9 are possible given the present uncertainties. A central value of 8 1/2 is appropriate for ground motion evaluation at the present time, if a single magnitude is required.

Earthquake Recurrence Methodology. As discussed previously, with the possible exception of the 1992 Cape Mendocino earthquake, the plate interface has been seismically quiescent during the historical period, thereby precluding the use of seismicity data to constrain the recurrence rate. Even if the Cape Mendocino event is assumed with certainty to be a plate interface event, the occurrence of a single event does little to constrain the recurrence rate on the plate interface source. Consequently, we use two alternative approaches to estimate recurrence: geologic evidence for recurrence intervals and the seismic moment rate approach. Geologic recurrence intervals are estimated from evidence for coastal subsidence/uplift in the Humboldt Bay region and elsewhere along the margin. The seismic moment rate approach uses the rate of plate convergence and estimates of the degree of seismic coupling across the interface. We assign these methods equal weight of 0.5.

Geologic Recurrence Intervals. Geologic evidence for multiple episodes of rapid coastal subsidence are recorded by buried marsh peats and fossil forests and uplifted late Holocene marine terraces in the Humboldt Bay area (Clarke and Carver, 1992; Vick, 1988; Valentine and

others, 1990; Carver, 1992; Carver and Aalto, 1992; Li and Carver, 1992). At least some of these events appear to be synchronous with displacement events on the Little Salmon fault, suggesting that plate interface events may be accompanied by faulting in the overlying accretionary wedge (see later section on the Little Salmon fault for a detailed discussion). Paleoseismic investigation sites at the Mad River Slough, Arcata Bay, South Humboldt Bay, and the Eel River all show geologic evidence for sudden submergence of intertidal marsh deposits; the synchroneity of at least the most recent event at about 300 years ago leads to the interpretation that these sites underwent coseismic subsidence (Carver, 1992). These sites lie within the axes of the Freshwater, South Bay, and Eel River synclines (Figure 2-20). At Clam Beach to the north of Humboldt Bay, marine terrace cover sediments on the Clam beach platform are interpreted to record two sudden uplift events occurring at about 300 years ago and 1100 years ago (Clarke and Carver, 1992).

Figure 2-21 from Clarke and Carver (1992) presents a recent interpretation of the timing of subsidence and uplift events in the Humboldt Bay area. Additional paleoseismic investigations are underway and additional efforts are being made to better resolve and age-date individual events. However, for purposes of recurrence analysis, the available data provide a meaningful constraint on the average recurrence intervals for large plate interface earthquakes. To allow for the present uncertainties in these data, we shall include a fairly broad distribution of recurrence intervals. Clarke and Carver's (1992) "most probable" estimates of recurrence intervals are the following: 304 years (open interval), 561 years, 325 years, 92 years, and 304 years. (Note that some age estimates based on radiocarbon dating are sometimes given in years "bp"; bp refers to before present, with "present" being defined as the calendar year 1950). The open interval is the time period from the most recent event to the present. Assuming a log-normal distribution, the statistics for the four closed intervals results in a median recurrence interval T_{med} = 267 years with σ_{lnT} = 0.76 and $\sigma_{ln(Tmed)}$ = 0.38. The statistics for five intervals are T_{med} = 274 years with σ_{lnT} = 0.66 and $\sigma_{ln(Tmed)}$ = 0.30.

Based on the recurrence interval data and considering the uncertainties, we arrive at the following distribution of median recurrence intervals for large plate interface earthquakes in the Humboldt Bay area: 125 yrs (0.1), 200 yrs (0.2), 270 yrs (0.4), 400 yrs (0.2), 560 yrs (0.1).

In order to use the above recurrence intervals in a recurrence relationship for the seismic hazard analysis, we must consider what magnitudes they might be related to. We do so by considering the synchroneity of the timing of these events recorded in the Humboldt Bay area with those events recorded in the paleoseismic record to the north in Washington and northern Oregon. We postulate that those events that appear to be synchronous in the north and south might represent larger earthquakes than those events that are recorded in the south only or in the north only. First, a distinction should be made between the physical mechanisms leading to the subsidence observed in the Humboldt Bay area and that observed in coastal Washington and northern Oregon. At the northern sites the subsidence appears to occurring as a result of regional processes. Studies of land elevation changes following large plate interface earthquakes along other subduction zones shows that the typical pattern of deformation is one of uplift just landward of the trench and subsidence further landward (e.g., West and McCrumb, 1988). Typically, the zero isobase separating uplift from subsidence marks the surface projection of the downdip extent of the seismogenic interface. Depending on the trench-coastline distance, then, the coastal area along a subduction zone may show evidence of either coseismic uplift or subsidence (West and McCrumb, 1988). It has also been observed that the uplift and subsidence that occurred coseismically can recover partially or completely in the years and decades following the earthquake (Carver, pers. comm.). Assuming that the geologic evidence for subsidence in Washington and northern Oregon is recording coseismic subsidence (minus some unknown amount of post-earthquake recovery), then we would expect the subsidence to be regional and for a zone of uplift to have occurred farther seaward.

As we move to the south toward Humboldt Bay, the trench-coastline distance decreases ("trench" in this case is not a topographic feature but is marked by the seaward-most location of the accretionary wedge tip). In the Humboldt Bay area the young, deforming parts of the accretionary wedge complex that lie offshore of Washington and Oregon come into the nearshore and onshore regions. Late Pleistocene and older marine terraces record the long-term uplift in the region, which is probably related to large-scale accretion of sediments and growth of the wedge complex. However, the dominant regional coseismic process, which would be expected to be uplift, is somewhat obscured by the local deformation occurring along faults and folds of the accretionary wedge (Carver, 1992). Therefore, the observations of episodic subsidence in the Humboldt Bay area are observed to occur in the axes of young synclines. Uplift, such as

that observed at Clam Beach, is occurring in conjunction with the hanging wall of thrust faults. This further explains why individual surface faulting events on the Little Salmon fault, which bounds the Freshwater syncline, appear to synchronous with subsidence. Given this model for the Humboldt Bay area, any given observation of subsidence or uplift could be related solely to displacement on nearby faults and not necessarily to plate interface earthquakes. It is the observation of synchronous events at multiple sites that lends support to the conclusion that the observed deformation is related to seismogenic plate interface.

Bearing in mind the differences in the mechanisms for coastal subsidence in the northern and southern parts of the Cascadia margin, we next examine the timing of individual episodes in coastal Washington and Humboldt Bay. The general timing of individual events is summarized below (Atwater, 1992; Clarke and Carver, 1992; Carver, unpub. data).

Approx. Date (yrs ago)	Humboldt	Washington
300	X	X
800	X	
1100	X,X	X*
1600	X	X,X

* Event expressed by uplift in the southern Puget Sound region and landslides in Lake Washington; weak to no evidence for coastal subsidence

The X's above represent individual subsidence events. Two X's represent a "couplet" or two distinct events geologically (e.g., two distinct buried marsh surfaces) that have indistinguishable ages. Based on these data, we can speculate on the lateral extent of ruptures that might have occurred on the plate interface. It appears that the episode 300 years ago affected both sites; one of the events 1100 years ago and one of the events 1600 years ago appears to also have affected both sites. Conversely, the event 800 years ago and one of the events 1100 years ago appears to have been a southern Cascadia event; one of the events 1600 years ago appears to have been a northern Cascadia event.

Assuming that the above arguments are reasonable, we have evidence for three "large" events that we assume ruptured from northern Washington to southern Cascadia and two recurrence intervals that are about 800 and 500 years. Considering the uncertainties, we arrive at the following distribution for median recurrence intervals: 400 yrs (0.2), 650 yrs (0.6), 900 yrs (0.2). Based on our model for the extent of ruptures and associated recurrence intervals, we conclude that the distribution of recurrence intervals presented previously based on southern Cascadia data only is appropriate for M > 8 earthquakes (i.e. both southern Cascadia and longer ruptures), and the distribution given immediately above is appropriate for M > 8.5 earthquakes (i.e. longer ruptures only).

Seismic Moment Rate. The seismic moment rate approach to estimating recurrence is based on the premise that the slip rate on a fault represents the average rate of seismic energy release (e.g., Anderson, 1979). The product of the slip rate and the area of the fault surface directly constrains the seismic moment rate for the fault (see Appendix A). To use this approach for the plate interface, we consider the rate of interplate convergence, defining the slip rate, and the amount of seismic coupling across the interface. Several studies of worldwide subduction zones have shown that there is a discrepancy between slip rates determined from global plate models and seismic slip rates determined from observed seismicity (e.g., Kanamori, 1971, 1977; McNally and Minster, 1981; Sykes and Quittmeyer, 1981; Peterson and Seno, 1984; Anderson and others, 1989). This discrepancy is explained by a certain percentage of the plate convergence occurring aseismically. The ratio of the seismic slip rate to the plate convergence rate determined from plate models is termed the seismic coupling coefficient, α (e.g., Peterson and Seno, 1984; Pacheco and others, 1993). To estimate recurrence, then, for the Cascadia subduction zone we must consider estimates of plate convergence rates and seismic coupling.

Rates of relative plate convergence across the Cascadia subduction zone are based primarily on plate reconstruction models. Rates that appear to be appropriate for southern Cascadia range from about 20 to 40 mm/yr (e.g., Nishimura and others, 1984; Engebretson and others, 1985; DeMets and others, 1990). Uncertainties are related to the fact that convergence rates have significantly decreased over the past 70 my (e.g., Verplanck and Duncan, 1987) and the most recent paleomagnetic evidence for rate is the time of the last magnetic reversal at 750,000 yrs. Also, it is not clear whether the internal deformation of the Gorda plate, represented by large-

magnitude strike-slip earthquakes, might be accommodating some component of the interplate convergence. Shortening of the forearc region by lateral faulting and folding of the upper plate may accommodate a significant amount of plate convergence (Goldfinger and others, 1992). Given the available interpretations and uncertainties, we arrive at the following distribution on plate convergence rate: 20 mm/yr (0.3), 30 mm/yr (0.4), 40 mm/yr (0.3).

The estimate of the seismic coupling coefficient α for the Cascadia margin is highly uncertain. The observed α during the historical period is zero, which is highly unusual for subduction zones. Pacheco and others (1993) calculate α for a 90 year period for 19 subduction zones. The average value of α for their data set is about 0.3 and they conclude that a sizable percentage of the slip at subduction plate boundaries occurs aseismically, that is, as stable sliding frictional behavior. Their results show that even margins having relatively small values of α such as Mexico (α = 0.26), Solomon Islands (α = 0.13), and Japan (α = 0.18) are characterized by the relatively frequent occurrence of moderate magnitude thrust earthquakes on the interface. The absence of these events along Cascadia may argue for a very low value of α. As discussed previously, quantitative and qualitative thermal modeling of the Cascadia margin suggests that the width of the Cascadia seismogenic interface may be very small or nonexistent, thus allowing plate convergence to be accommodated by aseismic stable sliding (Byrne and others, 1988; Pacheco and others, 1993). Such behavior would likely result in very low values of seismic coupling.

On the other hand, arguments can be presented that suggest the seismic coupling across the interface might be high. Clarke and Carver (1992), Carver (1992), and Clarke (1992) develop and compile estimates of 15 to 20 mm/yr of shortening across the folds and faults that comprise the onshore expression of the shortening in the overriding North American plate. They conclude the shortening is a substantial portion of the plate convergence rate and is evidence for strong coupling across the plate interface. Goldfinger and others (1992) provide evidence for large strike slip faults off the Oregon coast that appear to displace both oceanic and North American rocks, leading them to conclude that there is strong coupling across the plate interface. It should be noted that "coupling" in this context refers to the transmission of stresses across the interface such that relative motions at the plate boundary are propagated into the overriding continental plate. It is not clear that such "coupling" is necessarily the same as seismic coupling. Stable

sliding behavior, although not seismogenic, is still frictional behavior and to some degree stresses are transmitted across a lubricated boundary. Further work to examine the degree of shortening in the overriding plates at subduction zones having better-constrained estimates of α would shed light on this issue.

If it is assumed that all or most the 15 to 20 mm/yr of horizontal shortening noted by Clarke and Carver (1992) is the direct result of interplate convergence, then we develop a relationship between seismic coupling and plate convergence rate, which is shown in Figure 2-14. For lower convergence rates, the assessed rates of coupling are higher; and vice versa. The resulting α values are multiplied by the relative plate convergence rates to arrive at seismic moment rates for the plate interface.

Magnitude Distribution Model. A magnitude distribution model defines how the seismic moment rate is partitioned into earthquakes of various magnitude. Alternative magnitude distribution models are the exponential, characteristic earthquake, and maximum moment models (see Section 2.1 and Appendix A for discussion). We give highest weight to the characteristic earthquake model (0.6) because it appears to be appropriate for other subduction zones (Youngs and Coppersmith, 1985b). The exponential model is given lowest weight because it does not provide for the observation that the recurrence behavior of subduction zones appears to be dominated by the occurrence of earthquakes having a relatively narrow range of magnitudes and because of the relative paucity of moderate magnitude thrust events occurring on the interface. The maximum moment model incorporates this concept but does not provide for the occurrence of smaller magnitude events. If the Cape Mendocino earthquake were a plate interface event, the maximum moment model would not readily accommodate the recurrence of such an event.

The resulting recurrence relationships for the plate interface source are shown in Figure 2-22. Two plots are shown, one assuming that the Gorda plate is a separate segment, and one assuming that the Cascadia margin is unsegmented. The curves labeled 5^{th}%, mean, and 95^{th}% show the range of predicted recurrence rates using the full distribution for convergence rate, α, *b*-value and magnitude distribution, assuming the slip-rate approach for recurrence estimation. These are compared to the rates for larger magnitude events based on paleoseismic data (dashed boxes). The results indicate a wider distribution for recurrence rates based on slip rate than on

paleoseismic rates. (Note that the paleoseismic rates are extrapolated back to smaller magnitudes using the same three magnitude distributions, and thus would have a similar broad distribution for the frequency of events greater than magnitude 5.) The slip-rate and paleoseismic estimates of recurrence for the largest events are generally comparable.

2.2.2 Intraslab Source

The intraslab seismic source is represented by the earthquakes occurring within the Gorda plate offshore and beneath the continental margin (Figure 2-10). The relatively high rates of seismicity within the Gorda plate and the historical occurrence of moderate-to-large earthquakes, such as the M_S 7.2 1980 earthquake and the M_S 6.6 April 1992 earthquakes, attest to the activity of this source. The geometry of the oceanic slab is assessed on the basis of multiple hypocentral cross-sections across the margin (Figures 2-16a through 2-16d). Based on hypocenter locations using their velocity model, McPherson (1992) and Smith and others (in press) interpret the Gorda plate seismicity to show a double seismogenic layer. Relocations using another hypocenter location scheme (Houston and Vidale, unpub. report) do not result in the double layer. The presence or absence of a double seismogenic layer within the Gorda plate does not have a significant effect on source characterization for this seismic hazard analysis.

Studies of the focal mechanisms of earthquakes within the Gorda plate show that in the offshore region the earthquakes are predominantly strike slip (McPherson, 1989, 1992; Smith and others, in press). Alignments of epicenters and the pattern of aftershocks for the 1980 earthquake show northeasterly trends, leading to the selection of the northeasterly-trending left-lateral focal planes in the focal mechanisms. The second aftershock of the April 1992 earthquake sequence appears to have occurred on a right-lateral northwest-trending fault (Oppenheimer and others, 1993). It is suggested that a series of these strike slip faults are accommodating north-south shortening within the Gorda plate as it is buttressed against the Pacific plate to the south (Wilson, 1989; Smith and others, in press). This strike slip activity within the Gorda plate is unusual for oceanic slabs (away from oceanic transforms) in general, and is not present elsewhere along the Cascadia subduction zone to the north.

Beneath the continental margin the seismicity defining the oceanic slab gradually deepens reflecting the increase in dip. In the deeper parts of the slab, the focal mechanisms reflect

predominantly normal- and normal-oblique-faulting along north-south trends (McPherson, 1992). The mechanisms and orientation are consistent with downdip tension within the slab, which is commonly observed in the northern part of the Cascadia margin and along other subduction zones. The change in focal mechanisms within the slab from the offshore to the eastern area probably reflects the relative dominance of compressional stresses offshore to extensional stresses related to gravitational forces (slab-pull) in the eastern portion of the slab. The location of the transition between the strike slip regime and the normal-faulting regime is uncertain and may occur over a broad region. McPherson (1992) suggests that it occurs at the approximate longitude of the Mendocino triple junction at 124.15°.

For this seismic hazard study, we divide the intraslab source into two separate sources: the strike slip intraslab source and the normal-faulting intraslab source. The approximate boundary between the two sources we take to be the beginning (most westerly location) of the bend in the slab beneath the continental margin (Figure 2-18). To account for the uncertainty in the location of this boundary, we use two alternative locations shown in Figure 2-10. A third source associated with the Gorda plate is the zone of concentrated seismicity along the Mendocino transform fault (Figure 2-10). Earthquakes within this zone are predominately strike slip, reflecting relative motion between the Gorda and Pacific plates.

Maximum Earthquake Magnitude. We do not have detailed information on the locations and dimensions of faults that are present within the Gorda plate, so we are unable to use their dimensions directly to constrain maximum magnitudes. The occurrence of the M_B 7.0 1949 and the M_B 6.5 1965 earthquakes in the Puget Sound area attests to the potential for large intraslab events along the Cascadia subduction zone. The maximum size of earthquakes occurring within oceanic plates is constrained by the thickness of oceanic crust because faults occurring within oceanic plates are typically high-angle normal faults (and strike slip in the case of the Gorda plate). Further, the thickness of oceanic crust is a function of its age--younger plates have thinner oceanic crust. Compilations of intraslab earthquakes show that the largest events have been about M 7½ (Isacks and Molnar, 1971; Fujita and Kanamori, 1981).

Based on a consideration of the observed seismicity as well as observations of other zones, we arrive at the following maximum magnitude distribution for both the strike slip and normal-

faulting intraslab sources: 7.00 (0.33), 7.25 (0.34), 7.50 (0.33). For purposes of the deterministic analysis, we select a maximum credible earthquake MCE of 7½ for the intraslab source. The closest distance from the site to the source is about 15 km (Figure 2-18). For the Mendocino transform zone, it is assumed that larger earthquakes are somewhat more likely due to the continuous nature of this zone and the assessed maximum magnitude distribution is 7.25 (0.1), 7.5 (0.7), 7.75 (0.2).

Earthquake Recurrence. The earthquake recurrence rates for the intraslab sources are estimated from the observed seismicity directly. The boundary between the strike slip and normal-faulting intraslab sources is discussed above. The geometries of these sources is shown in Figure 2-10. The recurrence rates that are developed for the two sources are shown in Figure 2-23. Uncertainty in the cumulative frequency of events greater than M 5 and the *b*-value were defined by taking a range of values and computing their relative likelihoods using the formulation of Weichert (1980). These relative likelihoods were then normalized into a distribution for the recurrence parameters.

2.2.3 Little Salmon Fault

The Little Salmon fault (Figure 2-15) is the closest and most active fault in the vicinity of the Humboldt Bay bridges. Recent paleoseismic studies have provided information regarding its near-surface geometry, slip rate, displacement per event, and recurrence intervals (Clarke and Carver, 1992; Carver, 1992). As discussed previously in the context of the plate interface source (Section 2.2.1), the Little Salmon fault may be important not only as an independent seismic source but may represent the synchronous occurrence of plate interface earthquakes and deformation within the overriding accretionary wedge. We include these possibilities in modeling the Little Salmon fault as a seismic source.

Relationship of Little Salmon Fault to Plate Interface. Studies of the timing of individual displacement events on the Little Salmon fault and comparisons with episodes of subsidence and uplift elsewhere along the Humboldt coastal region have led Clarke and Carver (1992) to postulate that the Little Salmon fault may undergo slip in conjunction with the plate interface. The available data on the timing of events are not sufficiently well-resolved to prove this conclusion nor is it clear that the two always occur synchronously. However, we include models

for the interaction of the Little Salmon fault with the plate interface to express the range of interpretations that presently exist as well as to assess the importance of these models to the hazard analysis.

Two models are considered (Figure 2-24) that define the Little Salmon fault and its relationship with the plate interface:

1. Separate: The Little Salmon fault is independent from the plate interface as aseismic source. Fault-specific data define the earthquake behavior for the Little Salmon fault under this model. Little Salmon earthquakes could occur, by chance, at roughly the same time as plate interface events.

2. Synchronous: The Little Salmon fault moves synchronously with the plate interface. For the ground motion assessment we assume either that the Little Salmon generates its own earthquake at the same time as the interface or that the fault acts to propagate plate interface seismic energy to the surface. For this model, the recurrence rates developed for the plate interface are assumed to be appropriate for the Little Salmon fault as well.

The following relative weights are assigned to the three models: separate (0.2), and synchronous (0.8). The separate model appears to be credible because it represents, for hazard analysis purposes, a traditional method for characterizing seismic sources and relies on fault-specific slip rates, recurrence intervals, etc. to define future earthquake behavior. Support for this model comes from the lack of reported cases along other subduction zones where seismogenic slip has occurred on faults within the accretionary wedge at the same time as the plate interface. The synchronous model is supported by the apparent synchroneity of slip events on the fault with subsidence/uplift events recorded in the coastal stratigraphy (Figure 2-21).

We have also considered the possibility that the Little Salmon fault slips aseismically in a manner that is analogous to the sympathetic, aseismic slip that occurred on shallow-seated thrust faults of the accretionary wedge during the 1964 Alaska earthquake (e.g., the Patton Bay fault). However we have rejected this model because seismic reflection studies of the Little Salmon fault offshore suggest that the fault extends to a depth of about 14 - 15 km, which is within about 4 km of the plate interface (Clarke, 1992). Such depths are within the seismogenic

continental crust, hence, we find it difficult to imagine a fault that penetrates to these depths slipping aseismically.

Dip and Downdip Width. The downdip seismogenic width of the Little Salmon fault is defined by its average dip and the thickness of the seismogenic crust.

Exploratory trenches dug across two traces of the Little Salmon fault at the confluence of the Salmon and Little Salmon Creeks (Figure 2-20) indicate an average dip of about 25° (Carver and Aalto, 1992). This relatively low dip persists to at least two kilometers depth based on the depth of intersection of a borehole with the fault in the Tompkins Hill gas field area (presented in Carver and Aalto, 1992). Clarke's (1992) interpretation of seismic reflection profiles across the Little Salmon and other faults in the Eel River basin suggests dips that are commonly 20° to 30°. Based on these data, we arrive at the following estimates for the dip of the Little Salmon fault: 20° (0.2), 25° (0.6), 30° (0.2).

The thickness of the seismogenic North American crust varies along the length of the fault, as shown by the hypocentral cross sections (Figures 2-16a through 2-16d). At its seaward end, the depth of the seismogenic crust is about 5 km; it gradually increases to 25 km at the eastern end of the Little Salmon fault in the vicinity of the Freshwater fault (Figure 2-8). The average seismogenic depth along the entire length of the fault, then, is about 15 km. Using a 15 km depth and the dips described above, we arrive at the following distribution on the downdip seismogenic width of the fault: 30 km (0.2), 35 km (0.6), 44 km (0.2).

Maximum Earthquake Magnitude. Under the condition that the Little Salmon fault is an independent source, estimates of the maximum magnitude for the fault are based on estimates of rupture area and from paleoseismic data on displacement per event. Given the available data on the Little Salmon fault, both of these approaches result in estimates that have a similar degree of uncertainty, so we assign them an equal weight of 0.5. To calculate moment magnitude from rupture area, A, we use the empirical regression of Wells and Coppersmith (in press), which is $M=\text{Log}A+4.02$. For moment magnitude estimates from displacement per event, D, we use the empirical regression of Wells and Coppersmith (in press) for maximum displacement per event, which is $M=0.79\text{Log}D+6.69$.

The assessment of rupture lengths on the Little Salmon fault is difficult because studies of its segmentation have not been made and the fault goes in the offshore region where information on its recent behavior cannot be readily determined. The total length of the fault is assessed to be about 96 km, which is the length from its intersection with a more northerly fault zone in the west to its projected intersection with the Freshwater fault to the east (Figure 2-25). Studies of historical surface ruptures indicate that it is highly unlikely that a long fault (> 50 km) will rupture its entire length during a single earthquake (e.g., Schwartz and Coppersmith, 1986; Knuepfer, 1989; Coppersmith, 1991). Following the methodology proposed by Mualchin and Jones (1989), we would postulate that a fault longer than 50 km would rupture about one-half its length, or 48 km. Examining the mapped Little Salmon fault (Figure 2-25), we would postulate a potential 50 km-long rupture segment that extends from a right stepover in the mapped trace about 9 km offshore to a point where displacement is transferred over to the Yager fault (at about the "YF" in Figure 2-25). We assign highest weight to the 50 km scenario (0.6), lesser weight to the half-length estimate (0.3), and least weight to the total length scenario (0.1).

Geologic investigations along the Little Salmon fault provide information on the amount of slip that was associated with individual surface faulting events. At the Little Salmon River exploration site the fault consists of two traces. Displacement per event is estimated in exploratory trenches by interpreting the Holocene floodplain stratigraphy and unravelling the components of folding and faulting that have occurred (Clarke and Carver, 1992; Carver, 1992; Carver and Aalto, 1992). Three events in the past 1700 years are identified along the western trace with displacements of about 3.6 to 4.5 m per event. Displacements of 1 to 2 m are identified along the eastern trace, which lies a few hundred meters from the western trace. The displacement events on the two traces may or may not have been synchronous. Considering these data and their associated uncertainties, we arrive at the following distribution of the displacement per event on the Little Salmon fault: 4.5 m (0.2), 5.6 m (0.3), 6.5 m (0.3), and 8 m (0.2).

Incorporating the parameters and their associated weights leading to rupture area estimates and to displacement per event estimates, and then combining the magnitude values that come from these two approaches, the following maximum moment magnitude values and their associated weights are calculated: 7.2 (0.28), 7.3 (0.51), 7.4 (0.16), 7.5 (0.04), 7.6 (0.01). For the

deterministic analysis, we select a maximum credible earthquake MCE of 7½ for the Little Salmon fault.

For the case of synchronous slip, the "equivalent" earthquake on the Little Salmon fault is evaluated by considering the fraction of total slip on the interface that propagates up the Little Salmon fault. We consider a range of from 1/2 to 3/4 of the total interface slip that propagates up the Little Salmon, with equal weights (Figure 2-24). In other words, when the interface is assumed to undergo a 10 meter slip event, 5 to 7 meters are assumed to be transferred updip onto the Little Salmon fault. To determine the magnitude of this event for the hazard analysis, the "equivalent" earthquake magnitude is obtained by estimating the average interface slip based on the moment and rupture area for the interface event, then using the assigned fraction of slip and the fault area of the Little Salmon to obtain an "equivalent" moment and moment magnitude. The "equivalent" event is typically ½ to 1 magnitude unit below the interface event.

Earthquake Recurrence. As discussed previously, we incorporate alternative models for the interaction between the Little Salmon fault with the plate interface (Figure 2-24). In the synchronous model, we assume that the fault will have the earthquake recurrence rate developed for the plate interface. In the aseismic model, the fault is not considered. In the separate model, fault-specific data are used to express the recurrence rate, as discussed here. Two methods are used to estimate the recurrence rate for the Little Salmon fault: recurrence intervals from paleoseismic data and seismic moment rate (see Appendix A for a discussion of these approaches). We assign the approaches equal weights of 0.5.

Paleoseismic investigations have placed constraints on the approximate timing of individual surface-faulting events on two traces of the Little Salmon fault (Carver, 1992; Clarke and Carver, 1992). Radiocarbon ages for events on the western trace suggest that faulting occurred about 300, 800, and 1600 years ago (Figure 2-21). The actual timing of events on the eastern trace is not known but they may have been synchronous with those on the western trace. Allowing for the uncertainties in the timing of events and their synchroneity, we arrive at the following distribution of average recurrence intervals for the Little Salmon fault: 150 yrs (0.1), 300 yrs (0.4), 550 yrs (0.4), 700 yrs (0.1).

Estimates of the Holocene (past approximately 6,000 years) slip rate on the Little Salmon fault based on trenching studies is reported to be about 6 to 12 mm/yr (Carver, 1987; Clarke and Carver, 1992). To check if there is evidence for a change in this rate over longer time periods, we examine the amount of cumulative displacement of older geologic units. The total vertical displacement of the contact between the Pliocene Wildcat Group and the Eocene Yager is about 2,000 m at Tompkins Hill (Wagner, 1980 reported in Clarke, 1992). Assuming the initiation of movement on the Little Salmon fault occurred about 700,000 years ago (Carver, 1987) and assuming a 25 degree dip, a late Quaternary slip rate of about 7 mm/yr is calculated. The general agreement of the longer term rate with the late Holocene rates suggests that the late Holocene slip rates are representative of the longer term behavior of the Little Salmon fault and are appropriate for our purposes in this analysis. We therefore arrive at the following distribution of slip rates for the Little Salmon fault: 6 mm/yr (0.2), 8 mm/yr (0.6), 12 mm/yr (0.2).

To translate these slip rates into recurrence rates, we consider two earthquake size distribution models: the exponential model and the characteristic earthquake model (see Section 2.1 and Appendix A). We give highest weight (0.9) to the characteristic earthquake model because it has been shown to be most appropriate in describing the recurrence behavior of individual faults (Youngs and Coppersmith, 1985b; Coppersmith, 1991; Youngs and others, 1992).

The recurrence relationships developed for the Little Salmon fault on the basis of slip rates are compared in Figure 2-26 with the observed rate of small magnitude seismicity and with the rate inferred from paleoseismic data. Similarly to Figure 2-22, the curves labeled 5th%, mean, and 95th% show the range of predicted recurrence rates assuming the slip-rate approach for recurrence estimation and the dashed box shows the rate for larger magnitude events based on paleoseismic data. As can be seen, the slip rate and paleoseismic estimates of the frequency of large magnitude events are similar. The predicted seismicity rates somewhat over predict the observed frequency of moderate magnitude earthquakes, although there is large uncertainty in estimating the latter due to the limited recording history.

For the cases where the Little Salmon River fault zone is considered to move synchronously with the interface or to move aseismically, it is assumed that the North American plate background zone (Figure 2-11) encompasses the area defined as the Little Salmon zone in Figure 2-11.

2.2.4 Mad River Fault Zone

Because of its greater distance to the site relative to the Little Salmon fault and the Cascadia subduction zone sources, we characterize the Mad River fault zone as an areal seismic source zone and do not characterize individual faults within the zone. The Mad River fault zone (Figure 2-25) is a zone up to 10 km wide of at least five major northwest-trending, northeast-dipping imbricate thrust faults. Field studies focusing on displacement of marine and fluvial terraces have shown them to have a history of late Quaternary slip (e.g., Carver, 1987, 1992; Kelsey and Carver, 1988). Recent preliminary studies have identified a fault, called the Greenwood Heights fault, that intersects the northernmost tip of Humboldt Bay and we interpret this fault to mark the southern boundary of the Mad River seismic source zone (Figure 2-11). The northwestern extent of the zone is defined by where the zone dies out based on seismic reflection data (Clarke, 1992). The southeastern limit of the zone is difficult to identify because of a lack of Quaternary data and investigations. We extend the zone to the approximate location of a cluster of seismicity at the latitude of about 40.5°N that appears to crosscut the Mad River trend (Figure 2-11).

Maximum Earthquake Magnitude. We estimate the maximum earthquake magnitude for the Mad River zone by comparing it to the Little Salmon fault zone. Individual faults within the Mad River are not as continuous as the Little Salmon fault zone, nor is their total length as great. We arrive at the following distribution for the Mad River fault zone: 7.0 (0.2), 7.25 (0.6), 7.5 (0.2).

Slip Rate. Estimates of the late Quaternary slip rates for most of the faults within the Mad River fault zone have been estimated (Carver, 1987; 1992). In general, individual faults have slip rates of about 1 - 2 mm/yr. Summing the slip rates across the zone we estimate the following: 5 mm/yr (0.2), 7 mm/yr (0.6), 9 mm/yr (0.2).

To develop moment rate estimates for the Mad River zone, it is assumed that the dips of individual faults are the same as the Little Salmon fault and that the average depth of the seismogenic crust is about 20 km. The estimated recurrence rates for the Mad River fault zone are compared with the observed seismicity rate in Figure 2-26. As was the case for the Little Salmon River source, the predicted seismicity rates somewhat over predict the observed frequency of moderate magnitude earthquakes.

2.2.5 Other Seismic Sources

In addition to the seismic sources discussed above, other seismic source zones are identified that reflect major tectonic elements or seismicity patterns. These zones are the North American plate zone, the northern San Andreas fault zone, and two zones south of the Mendocino triple junction. These seismic source zones are shown in Figure 2-11. The recurrence rates for these sources are defined by the observed seismicity directly with the exception of the San Andreas, which incorporates the paleoseismic information developed along the fault farther to the south. The maximum magnitude distributions for the source zones are assumed to be similar to that of the Mad River, except for the San Andreas, where it is assessed to be M 7.8 (0.3) to 8.0 (0.7).

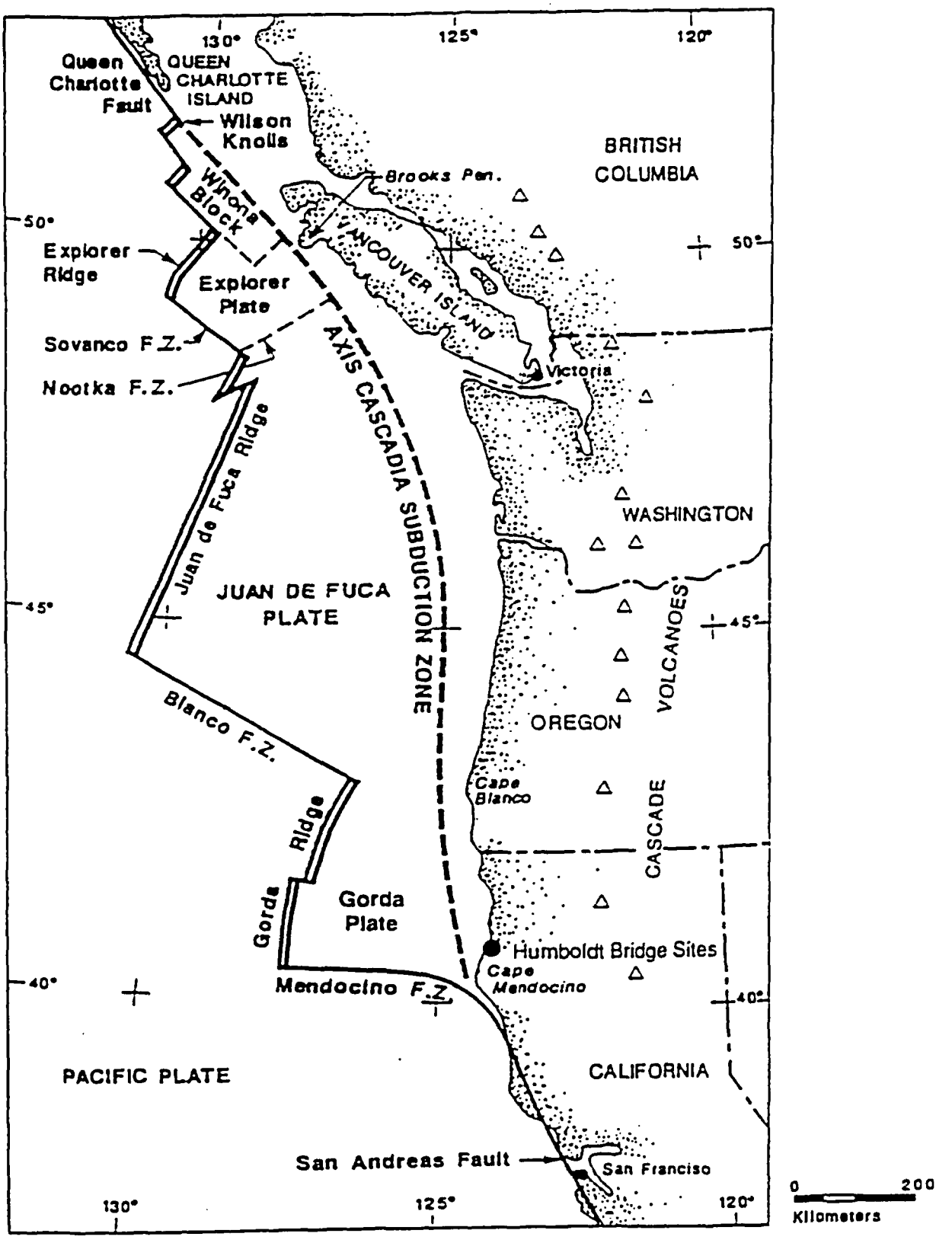

Figure 2-1 Regional map of the Cascadia subduction zone.

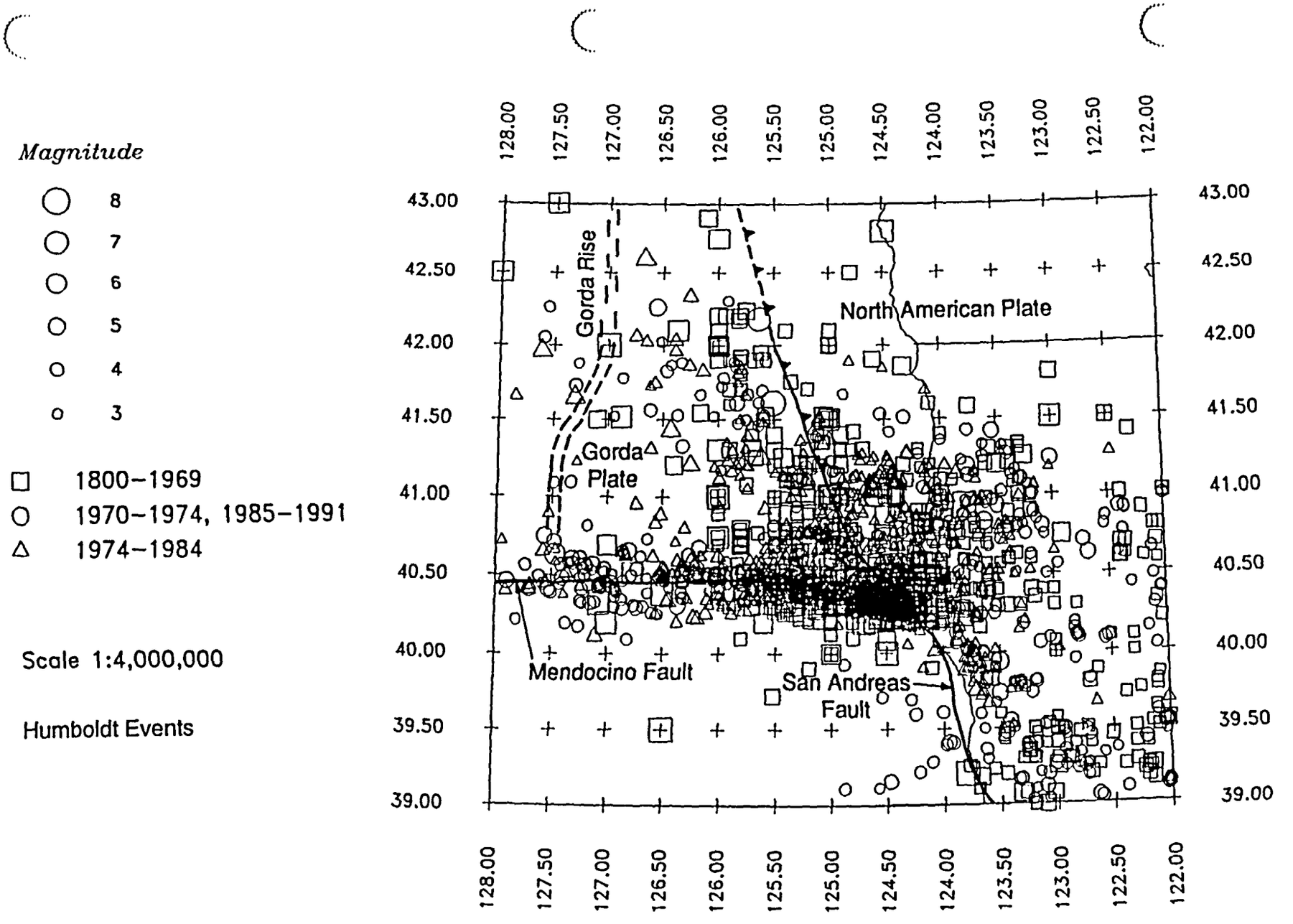

Figure 2-2 Regional seismicity of Humboldt Bay region. Also shown are the major tectonic features of the region.

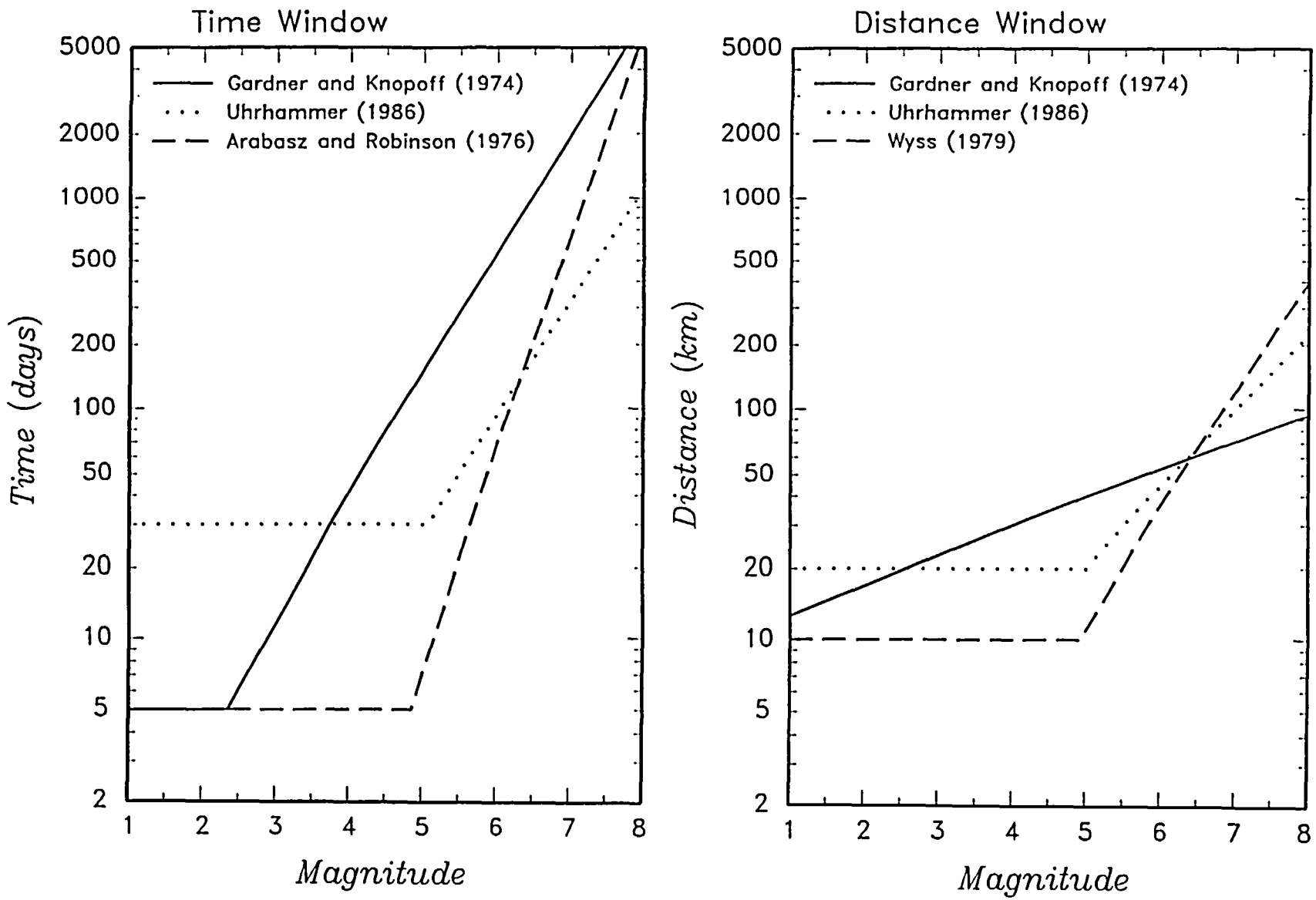

Figure 2-3 Time and distance windows used to identify dependent earthquakes (foreshocks and aftershocks).

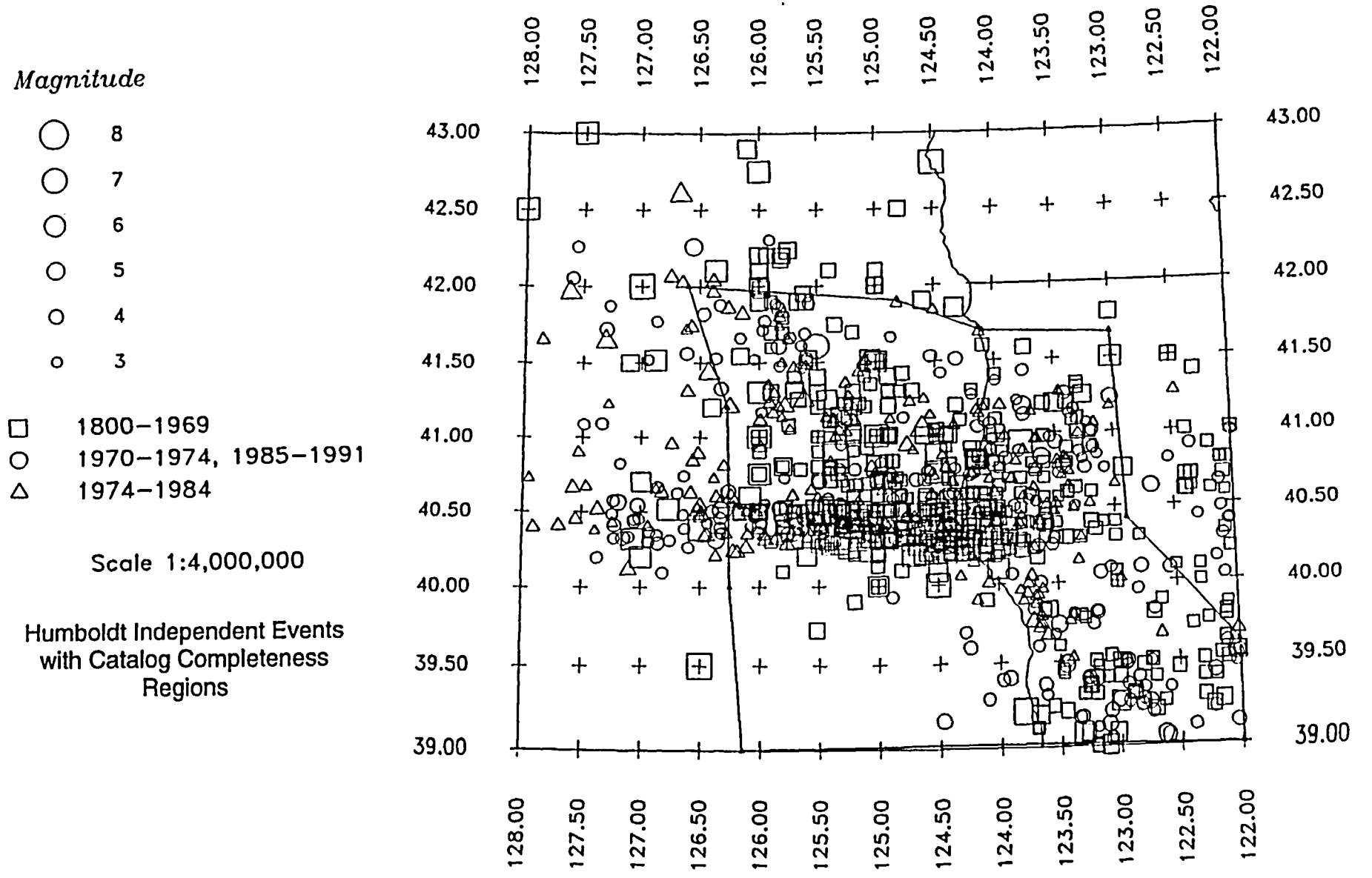

Figure 2-4 Regional seismicity of Humboldt Bay region showing only independent events. Also shown are the two catalog completeness regions defined for the study area.

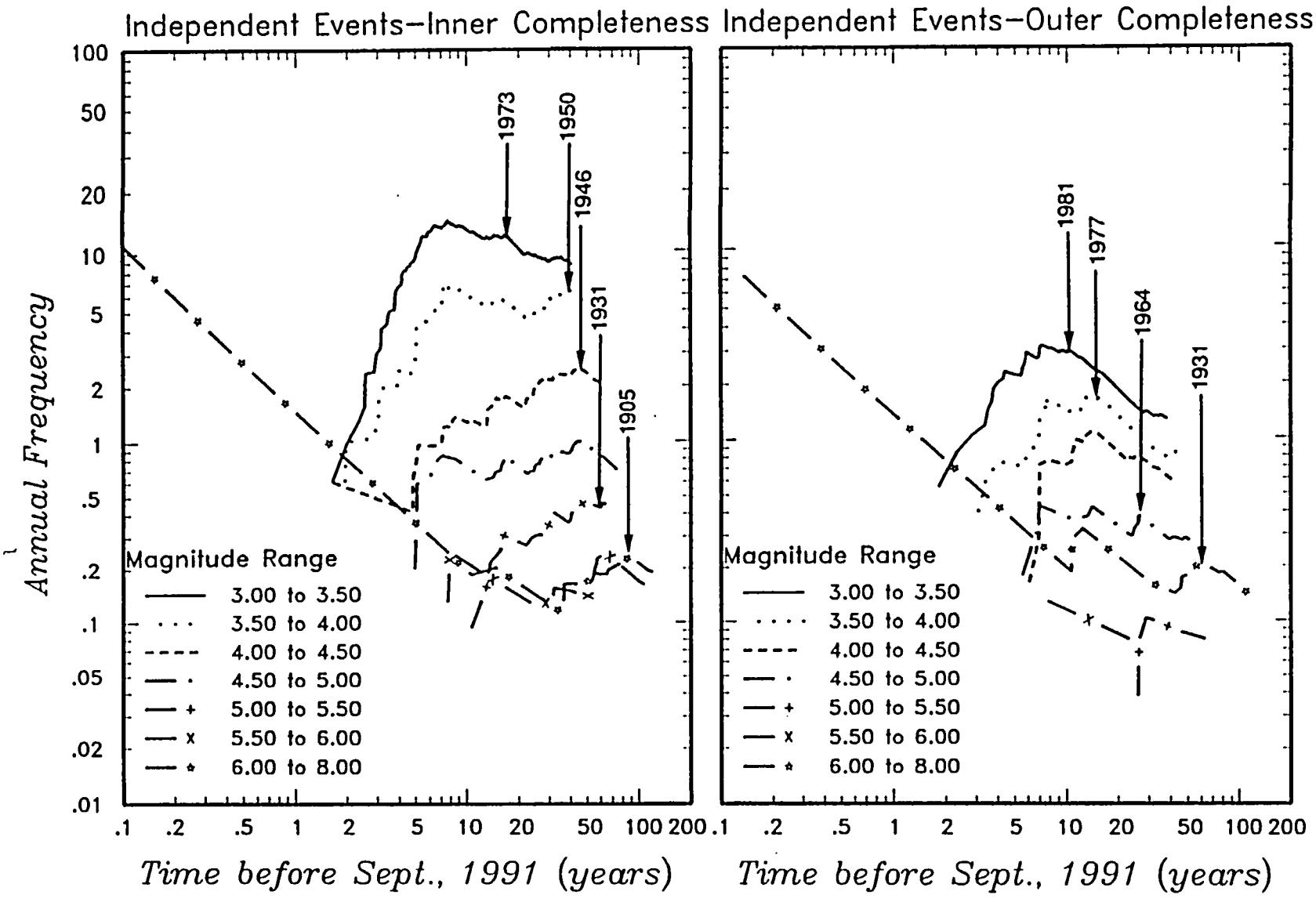

Figure 2-5 Plot of annual frequency of earthquake occurrence as a function of time before the present for the two completeness regions defined in Figure 2-4.

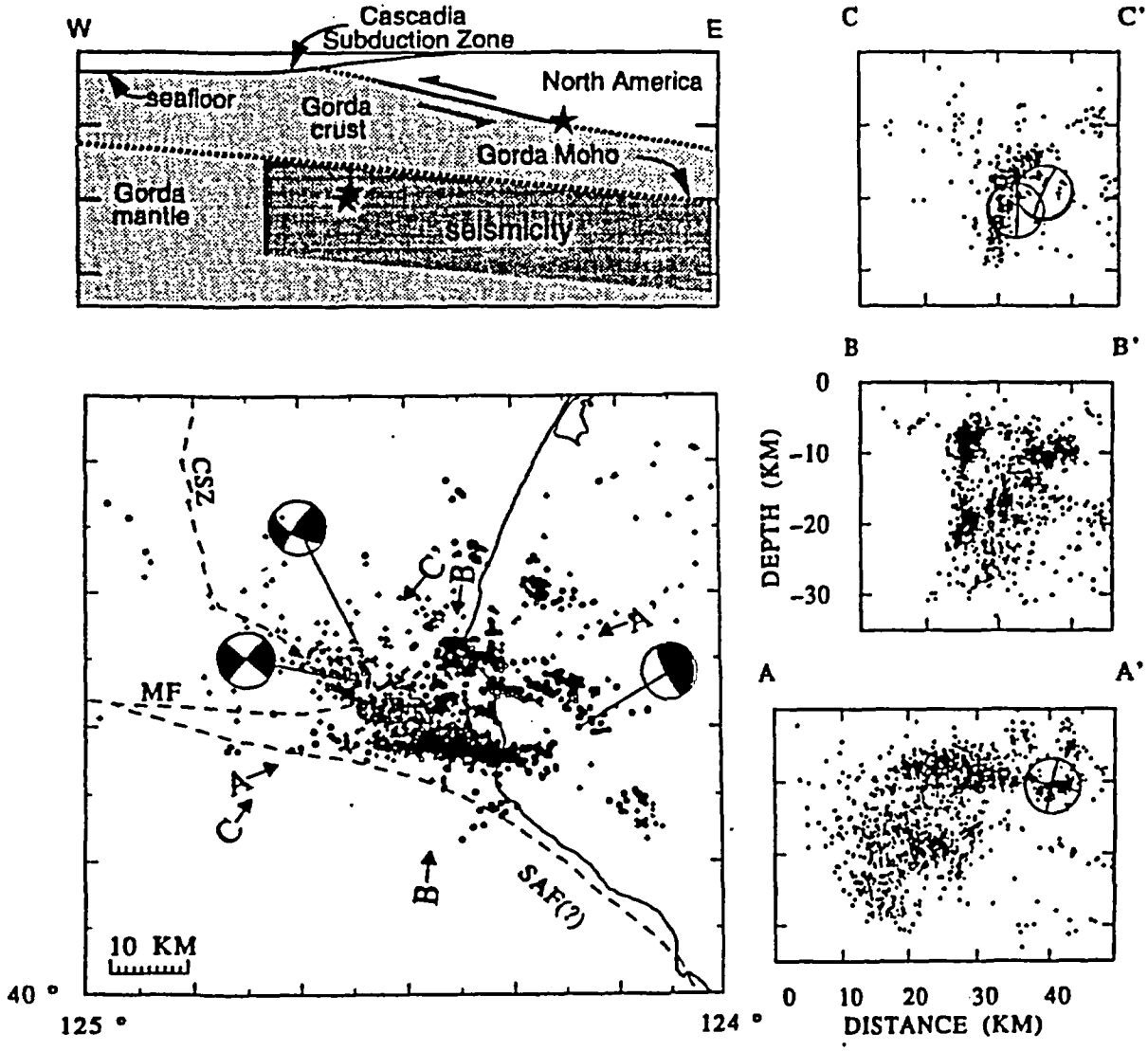

Figure 2-6 (Lower left) focal mechanisms of the mainshock and two large aftershocks at their epicentral locations, aftershocks for the period 4/25/92 - 9/30/92, and cross sections. Aftershocks in map view are shown as open circles for foci less than 12 km and plus symbols for deeper foci. Cross section width is ±20 km for sections A-A' (perpendicular to mainshock strike) and B-B' (perpendicular to Mendocino fault), ±9 km for C-C' (perpendicular to strike of M_S 6.6 aftershocks). Focal mechanisms are lower hemisphere projections; the compressional quadrant is black in map view and marked by a "T" in cross sections. EW-cross section (upper left) depicts location of mainshock rupture plane (solid line), hypocenters (stars), and pre-mainshock seismicity with respect to plausible interpretation of Gorda-North America plate geometry. (From Oppenheimer and others 1993.)

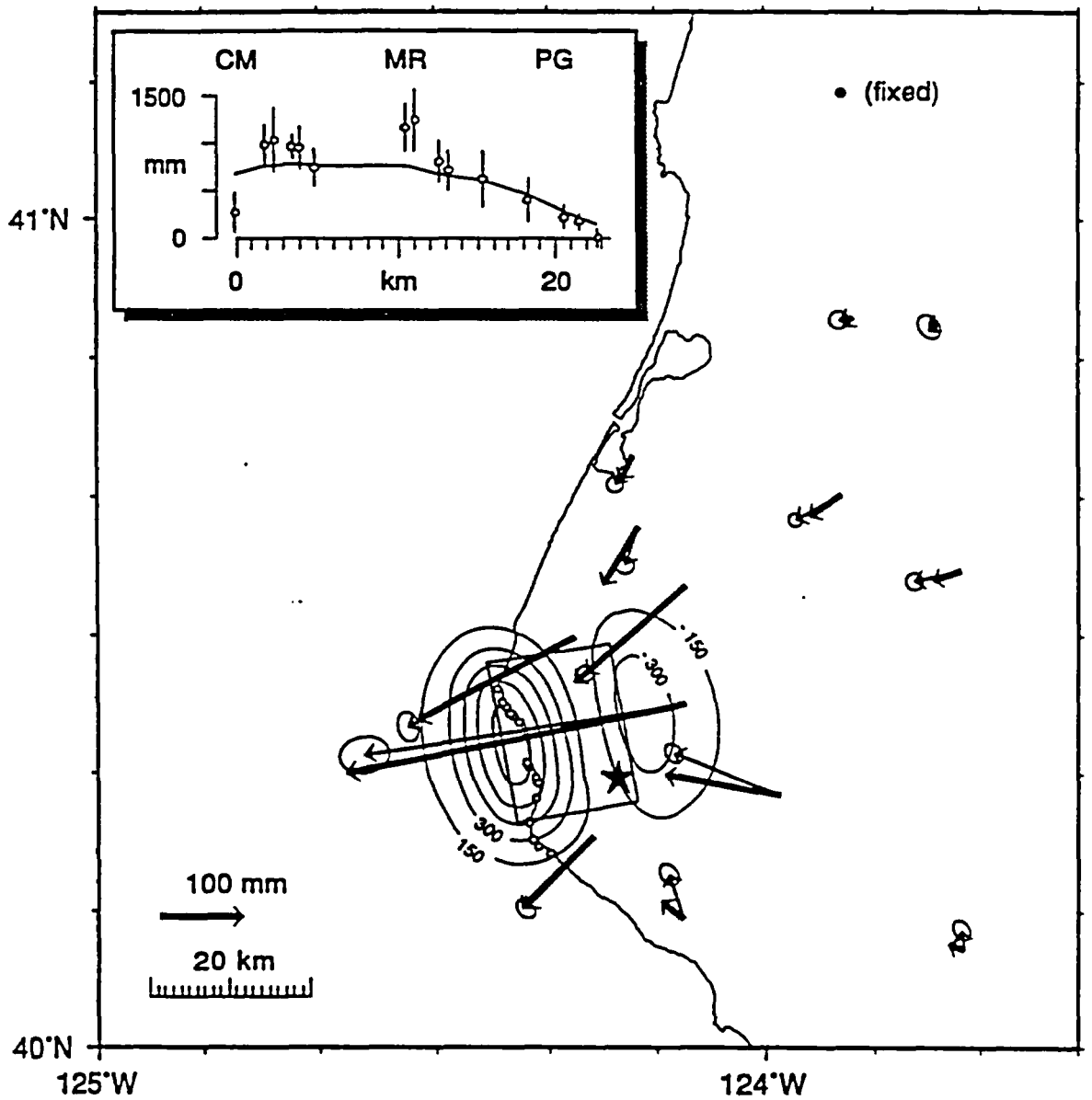

Figure 2-7 Horizontal and vertical coseismic displacements for the Cape Mendocino mainshock. Light vectors with 95% confidence region ellipses are horizontal displacements measured with GPS relative to the northernmost site in figure. Bold vectors are predicted displacements based on model of uniform slip on the rectangular fault plane indicated by its surface projection. Star denotes mainshock epicenter. The 150 mm contours denote predicted elevation change; the zero contour is omitted. Graph in the upper left corner shows uplift (open circles) observed from the die-off of marine organisms at coastal sites projected onto a plane with N10°W strike. Vertical bars depict 1 standard deviation about the mean, and solid line is the predicted elevation change. CM - Cape Mendocino, MR - Mussel Rock, PG - Punta Gorda. (From Oppenheimer and others, 1993.)

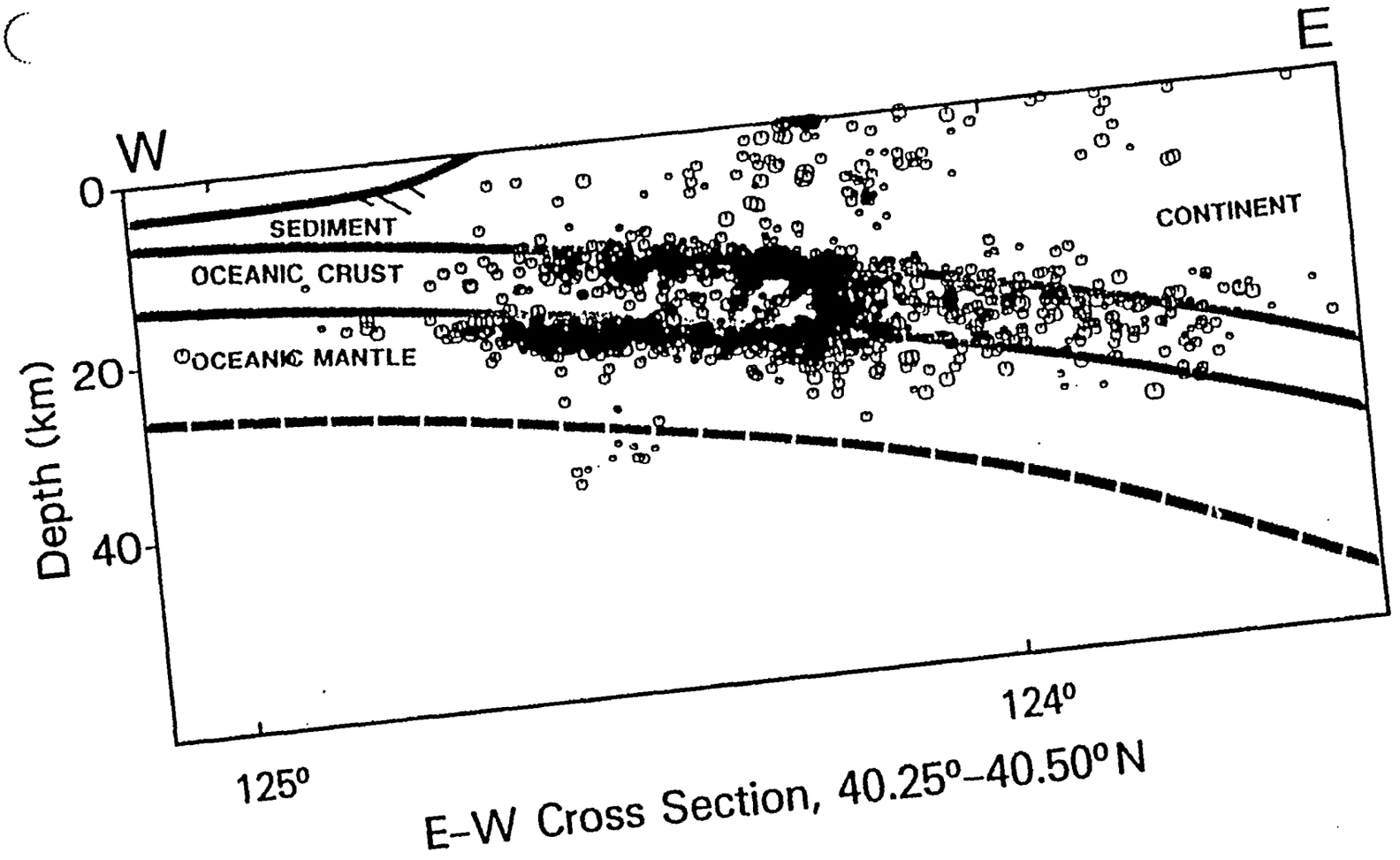

Figure 2-8 Cross section showing seismicity (adapted from Fig. 8b of Smith and others, 1992). The geological structures, inferred from seismicity using the rheological model for the double seismic layers, agree well with the body wave velocity model of Smith and others (1992). (From Wang and Rogers, 1993.)

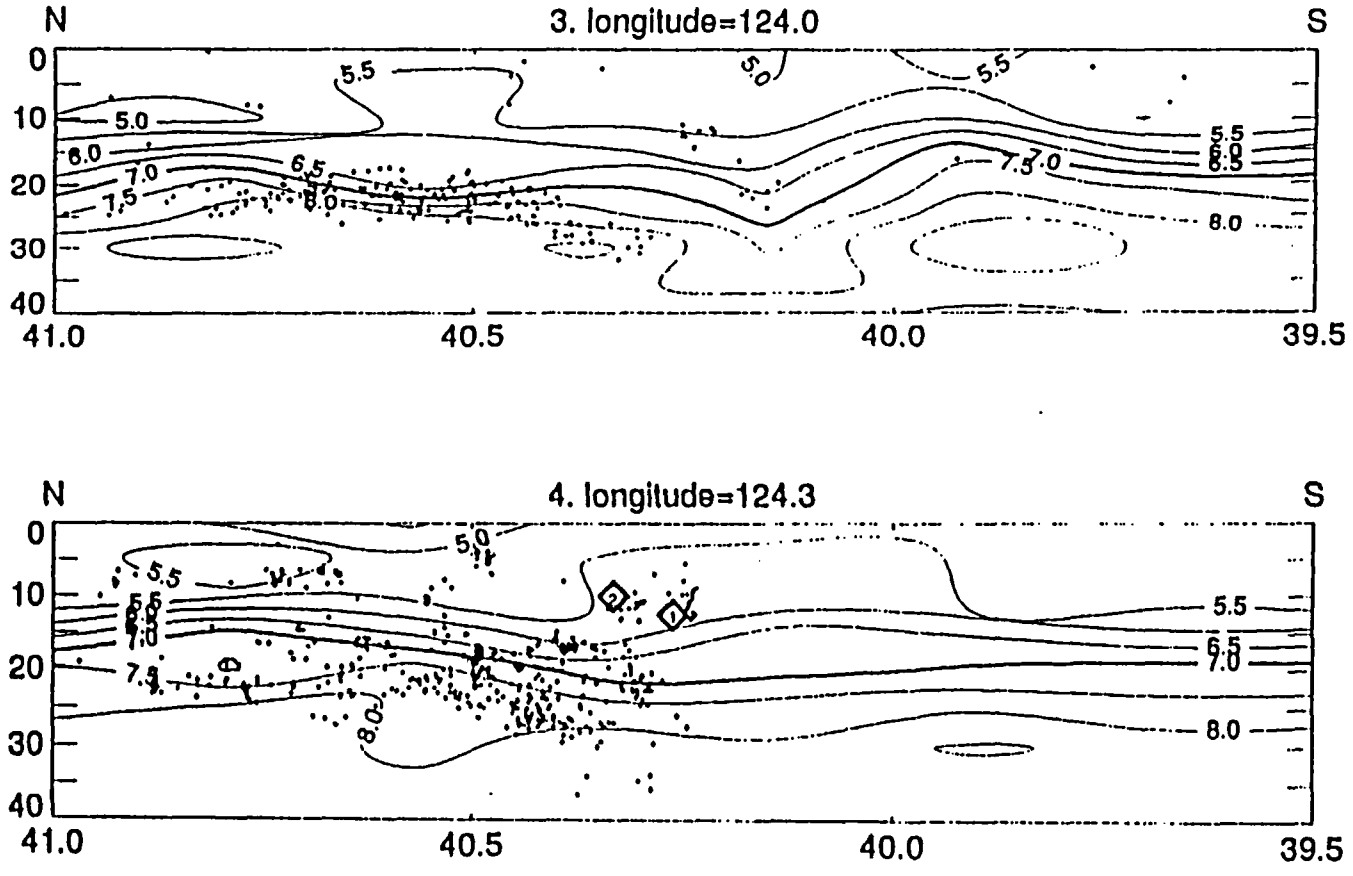

Figure 2-9 Contours of the P-wave velocity along north-south cross sections. The contour interval is 0.5 km/s. The diamonds are locations for events within 12.5 km of the profile projecterd onto the plane of the cross section. The large bold diamonds show the hypocenters of the Honeydew (M = 6.2, August 17, 1991) and Petrolia (M = 7.1, April 25, 1992) earthquakes, labeled 1 and 2, respectively. (From Verdonk and Zandt, 1993.)

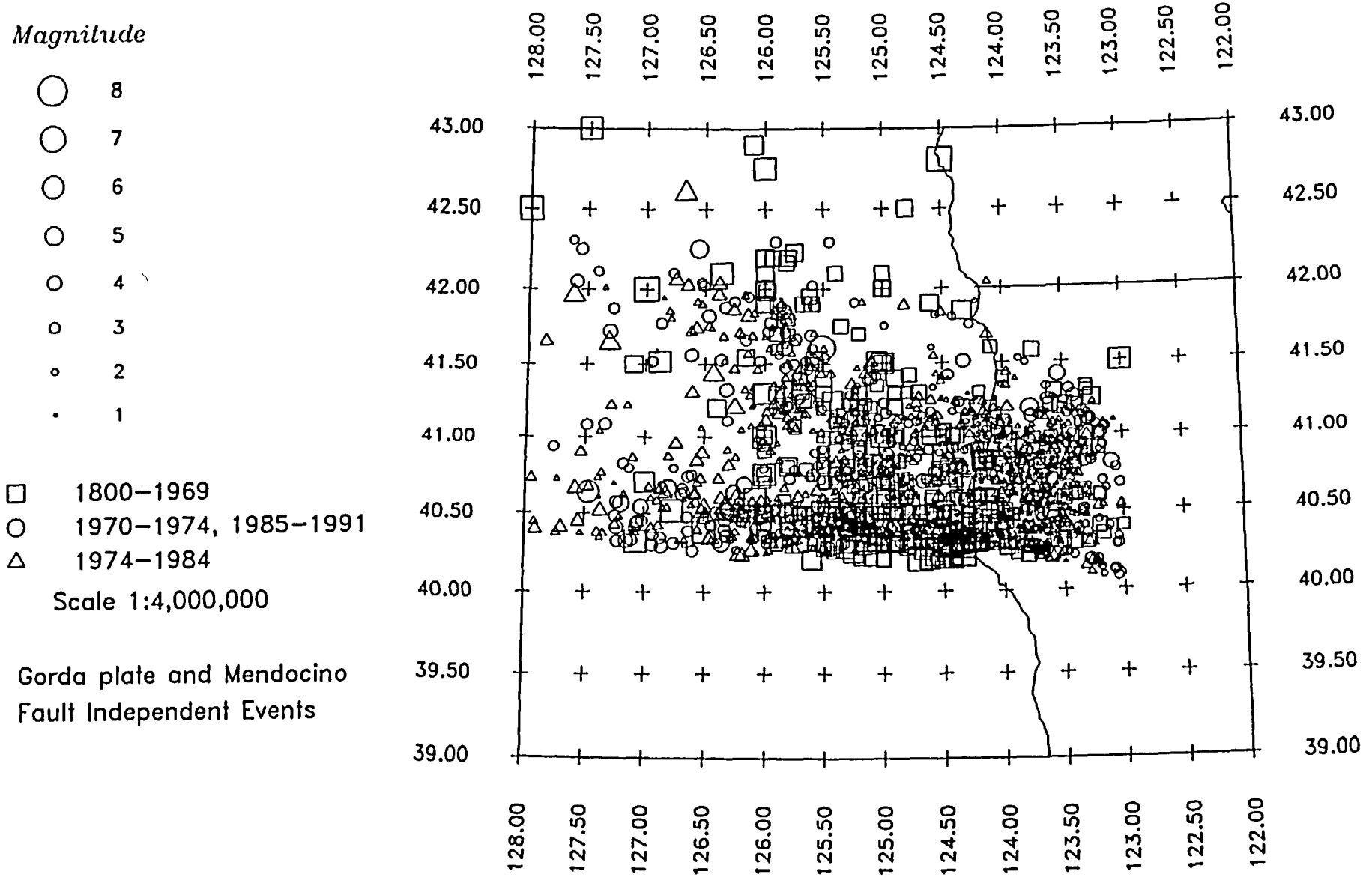

Figure 2-10 Spatial distribution of seismicity inferred to be occurring within the Gorda plate or at the boundary with the Pacific plate. Shown are independent events.

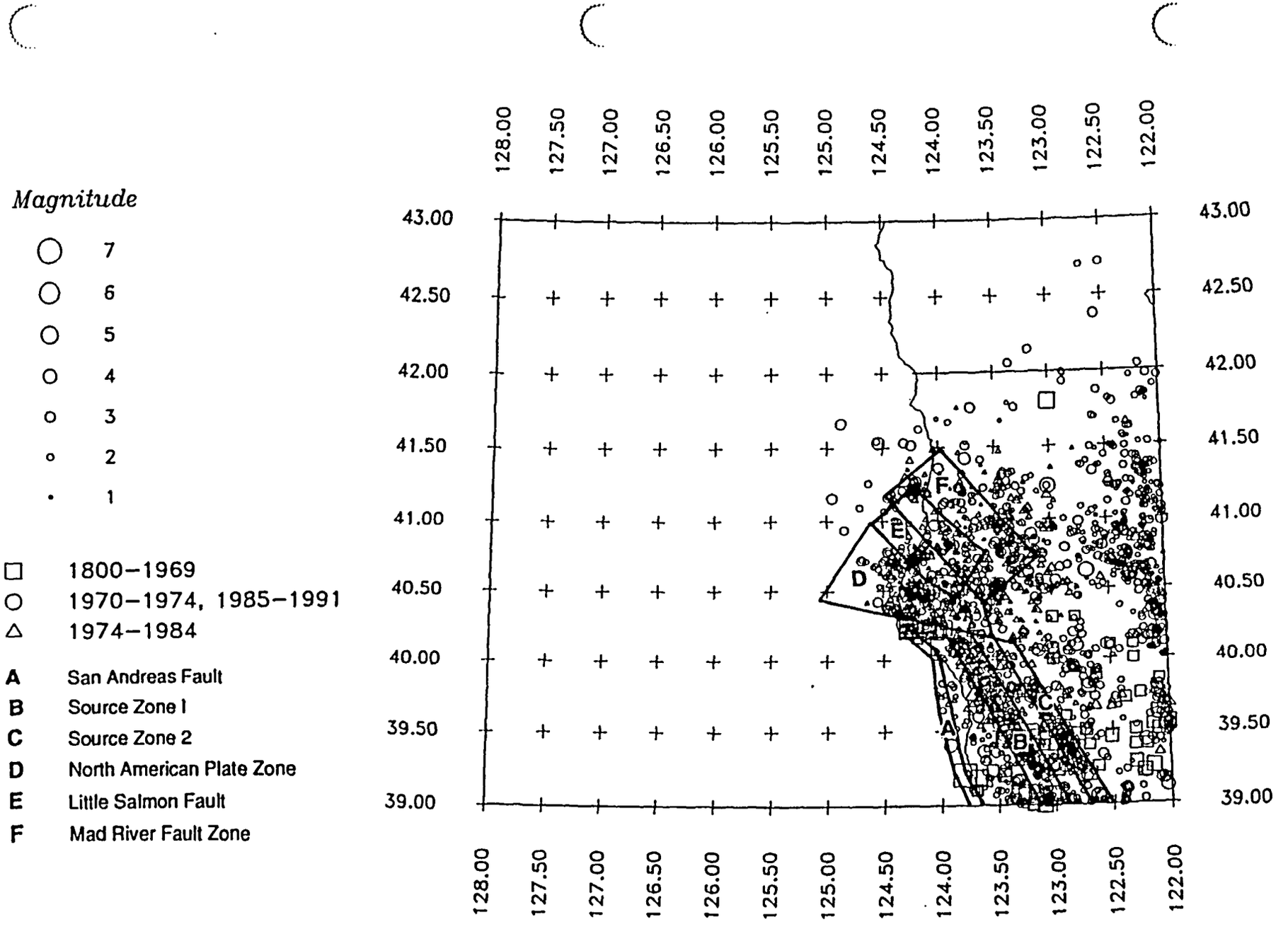

Figure 2-11 Spatial distribution of seismicity inferred to be occurring within the North American plate. Shown are independent events.

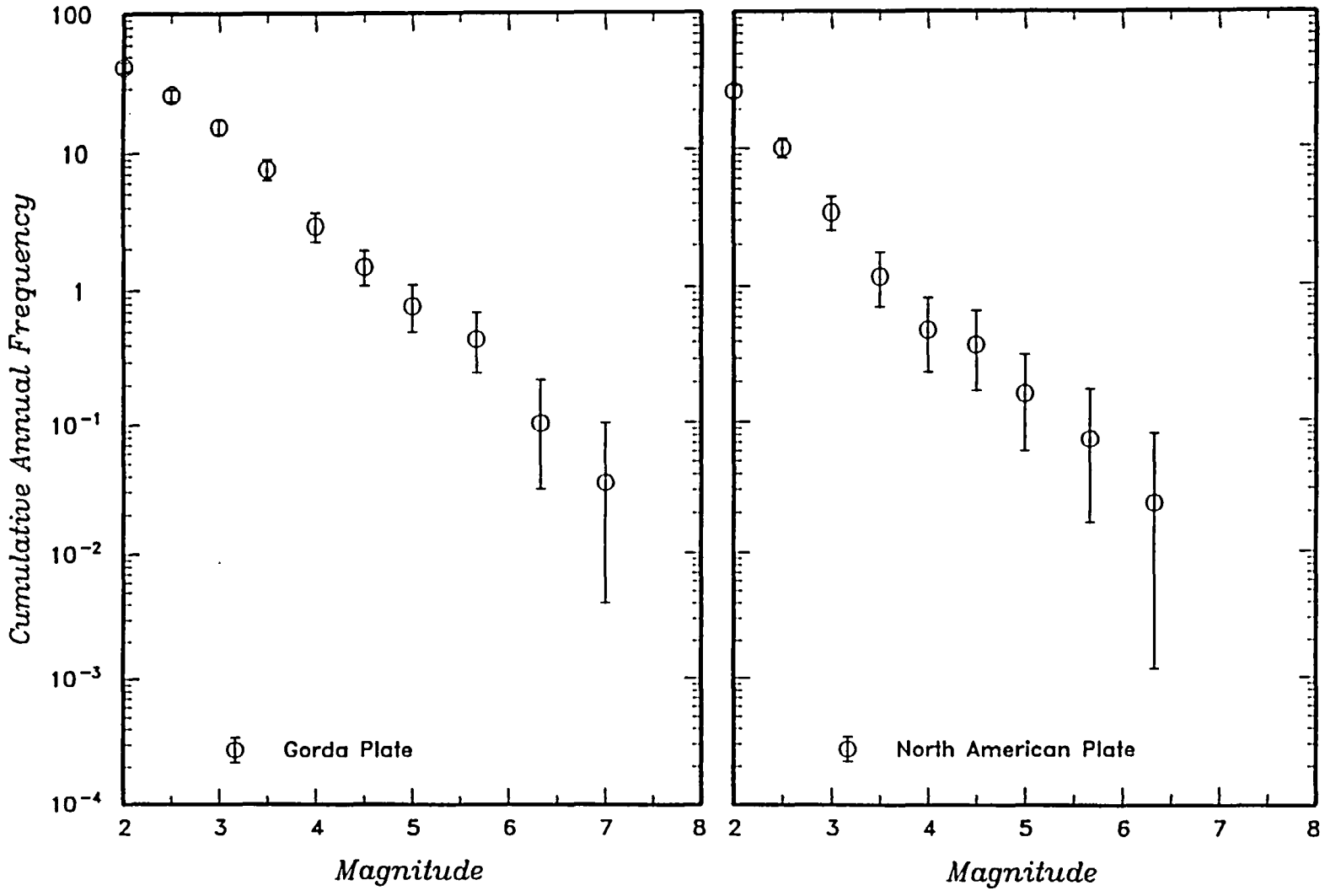

Figure 2-12 Regional seismicity rates for Gorda plate (Figure 2-10) and North American plate (Figure 2-11) seismicity.

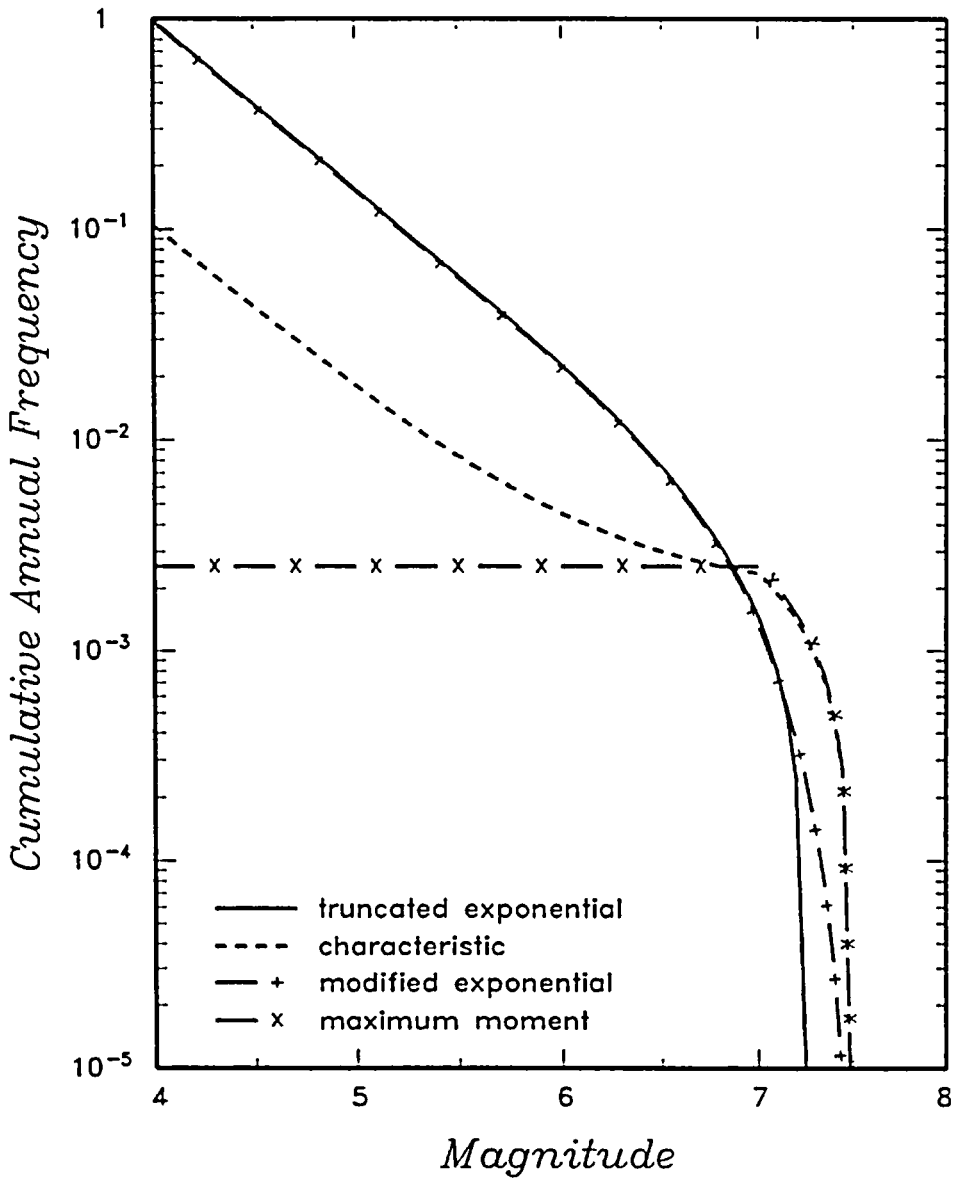

Figure 2-13 Recurrence models used in the hazard analysis.

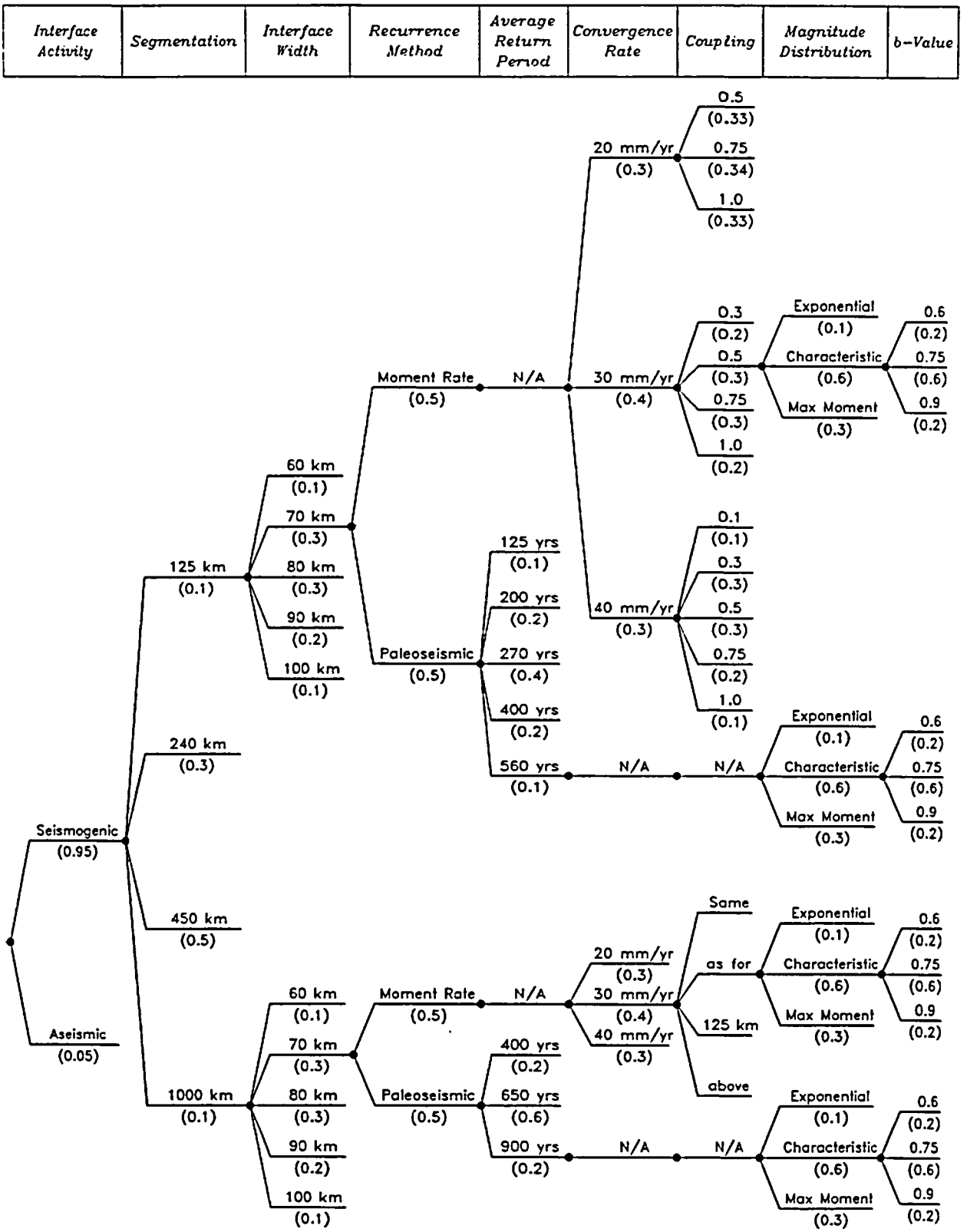

Figure 2-14 Logic tree for the plate interface source.

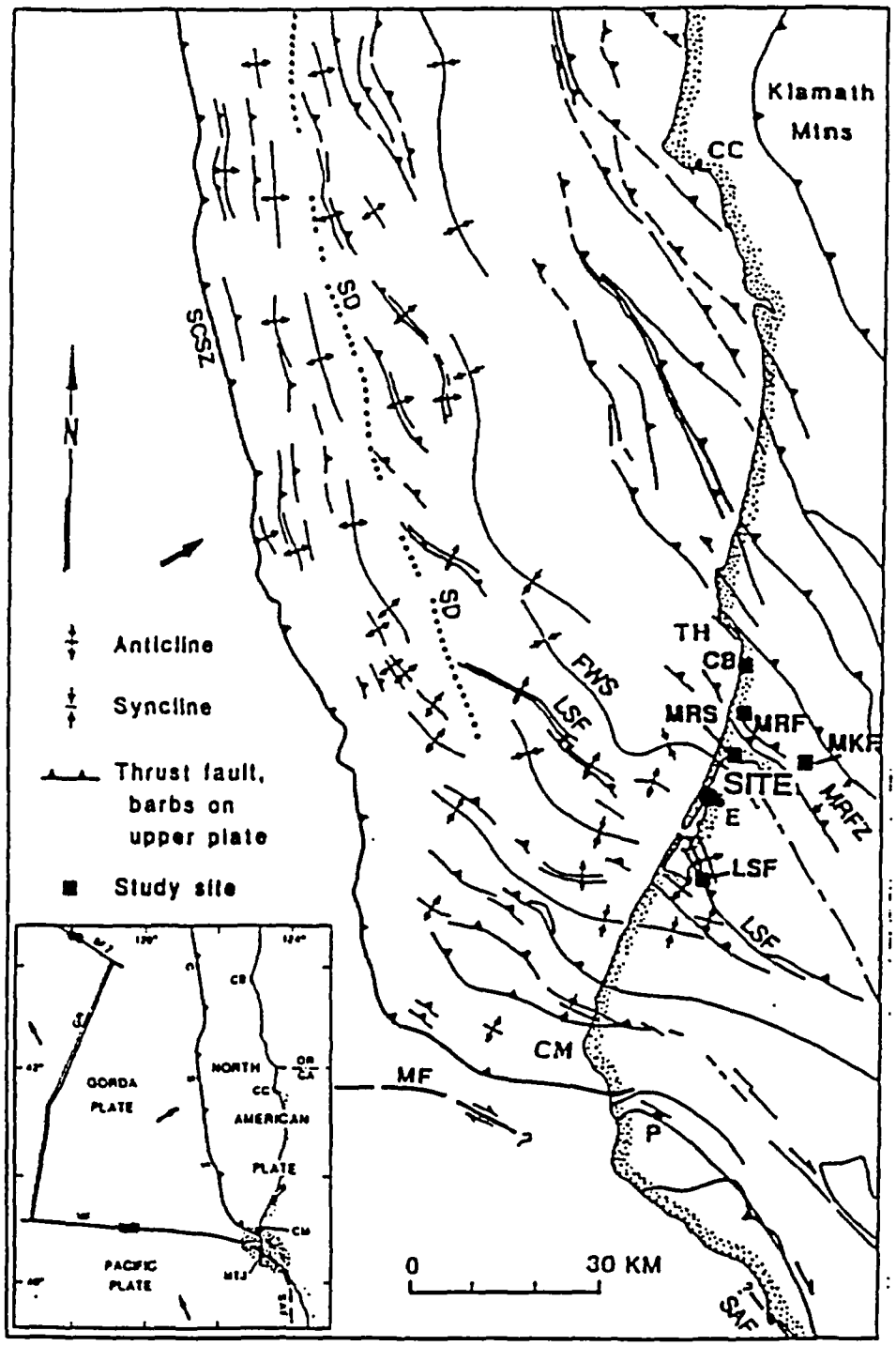

Figure 2-15 Plate tectonic setting of the northwestern California continental margin. Arrows indicate oceanic-plate motions relative to North American plate. Barbed line shows the base of the continental slope. Half arrows on inset map indicate relative motions along the Blanco fracture zone and the Mendocino fault. Abbreviations are as follows: Locations, CB, Cape Blanco; CC, Crescent City, CM, Cape Mendocino; E, Eureka; P, petrolia; TH, Trinidad Head; Structural features, BFZ, Blanco fracture zone, CSZ, Cascadia subduction zone; GR, Gorda Ridge; LSF, Little Salmon fault; MF, Mendocino fault; MRFZ, Mad River fault zone; MRJ, area of Mendocino triple junction; SAF, San Andreas fault; SCSZ, southern Cascadia subduction zone; SD, structural discontinuity mentioned in text; Study sites, CB, Clam Beach; LSF, Little Salmon fault; MKF, McKinleyville fault; MRF, Mad River fault; MRS, Mad River Slough. (from Clarke and Carver, 1992).

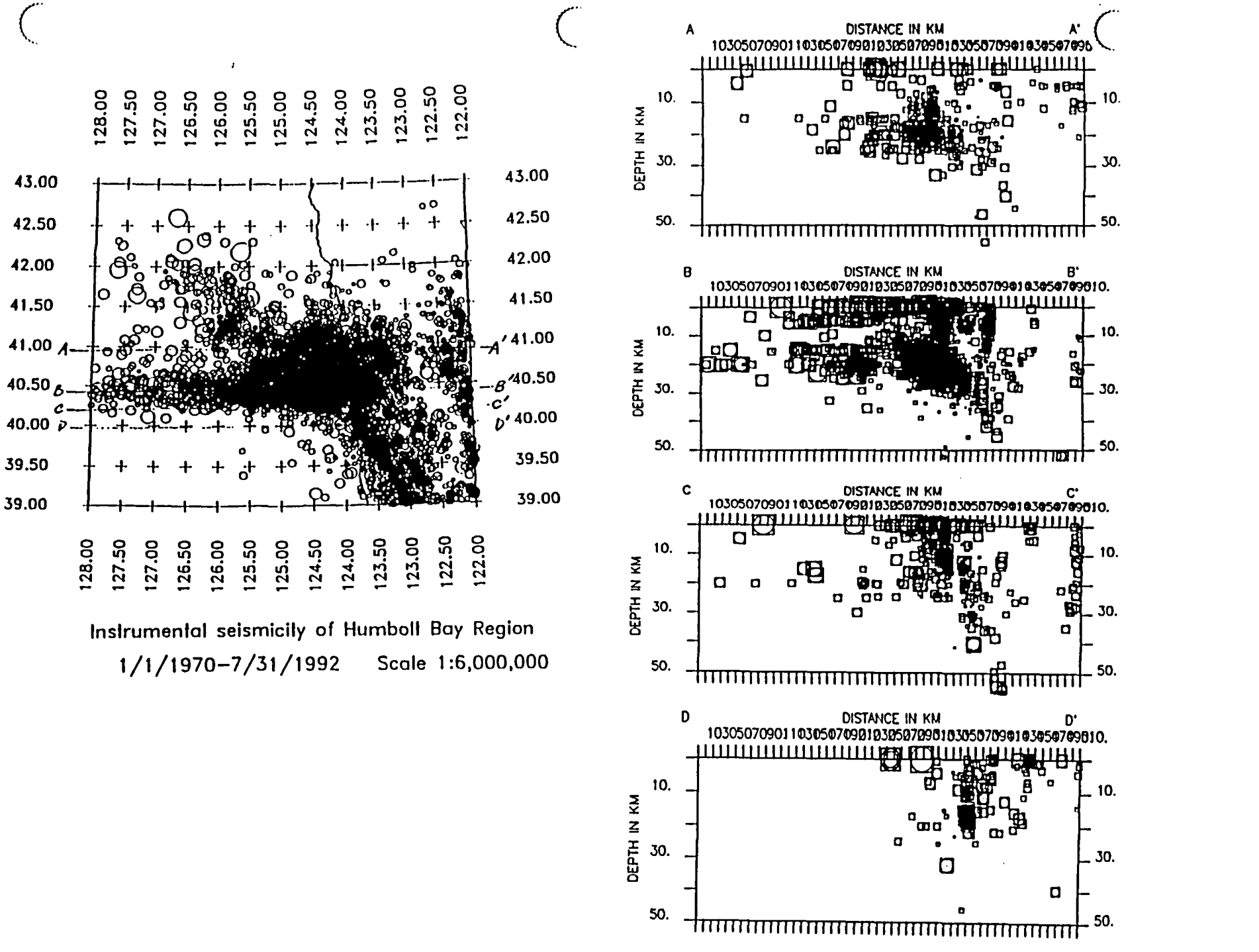

Figure 2-16 East-west cross sections through Gorda plate at 4:1 vertical exaggeration.

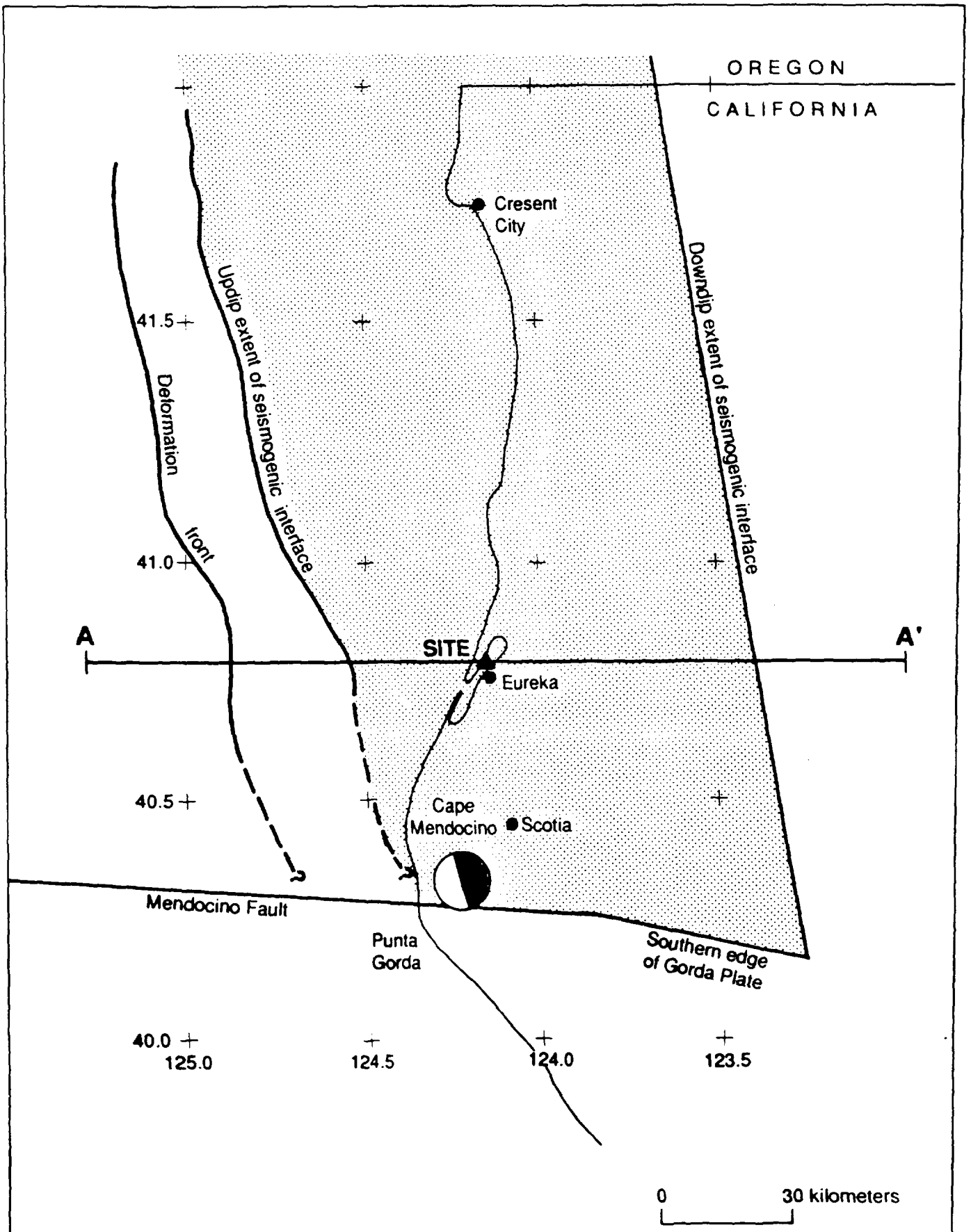

Figure 2-17 Map view of inferred interface source.

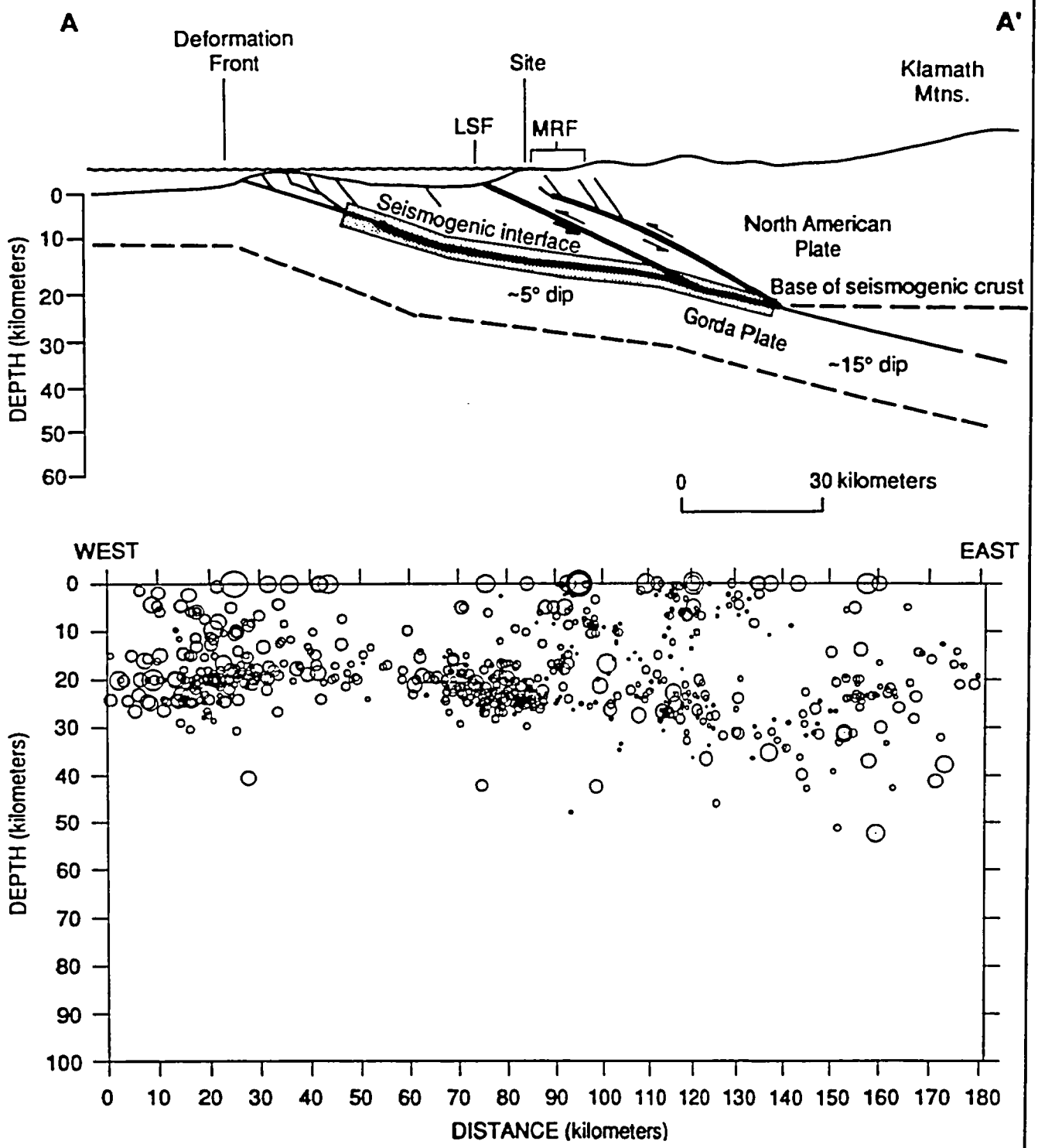

Figure 2-18 a. Schematic E-W cross section of subduction zone beneath the site (see Figure 2-17 for location), showing seismogenic interface. LSF - Little Salmon fault, MRF - Mad River fault zone.

b. Cross section of earthquake hypercenters within 10 km wide corridor centered on cross section A-A'. No vertical exaggeration. Events with squares are aftershocks on the 4/25/92 Mendocino earthquake.

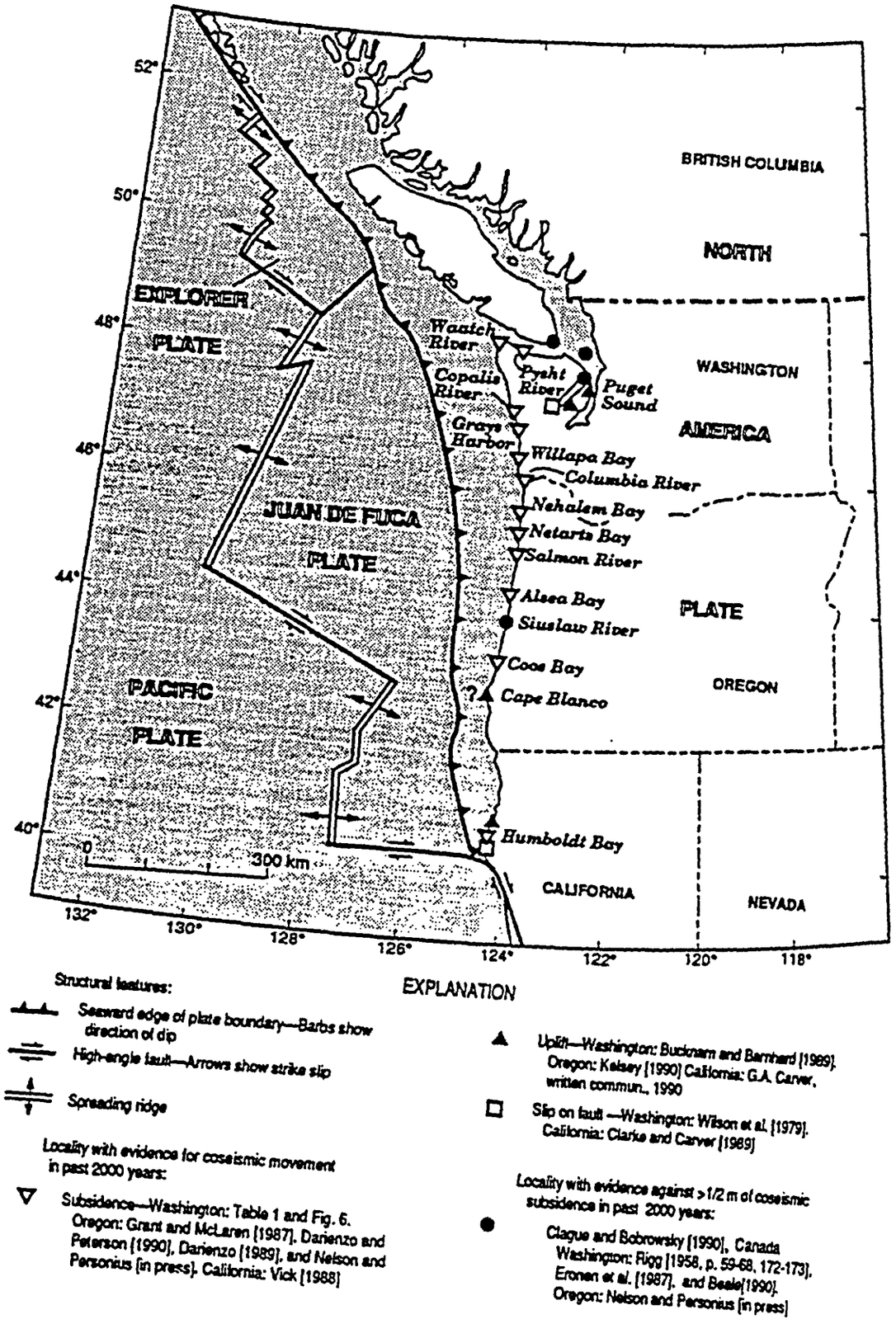

Figure 2-19 Exploration localities along the Cascadia subduction zone (from Atwater, 1992).

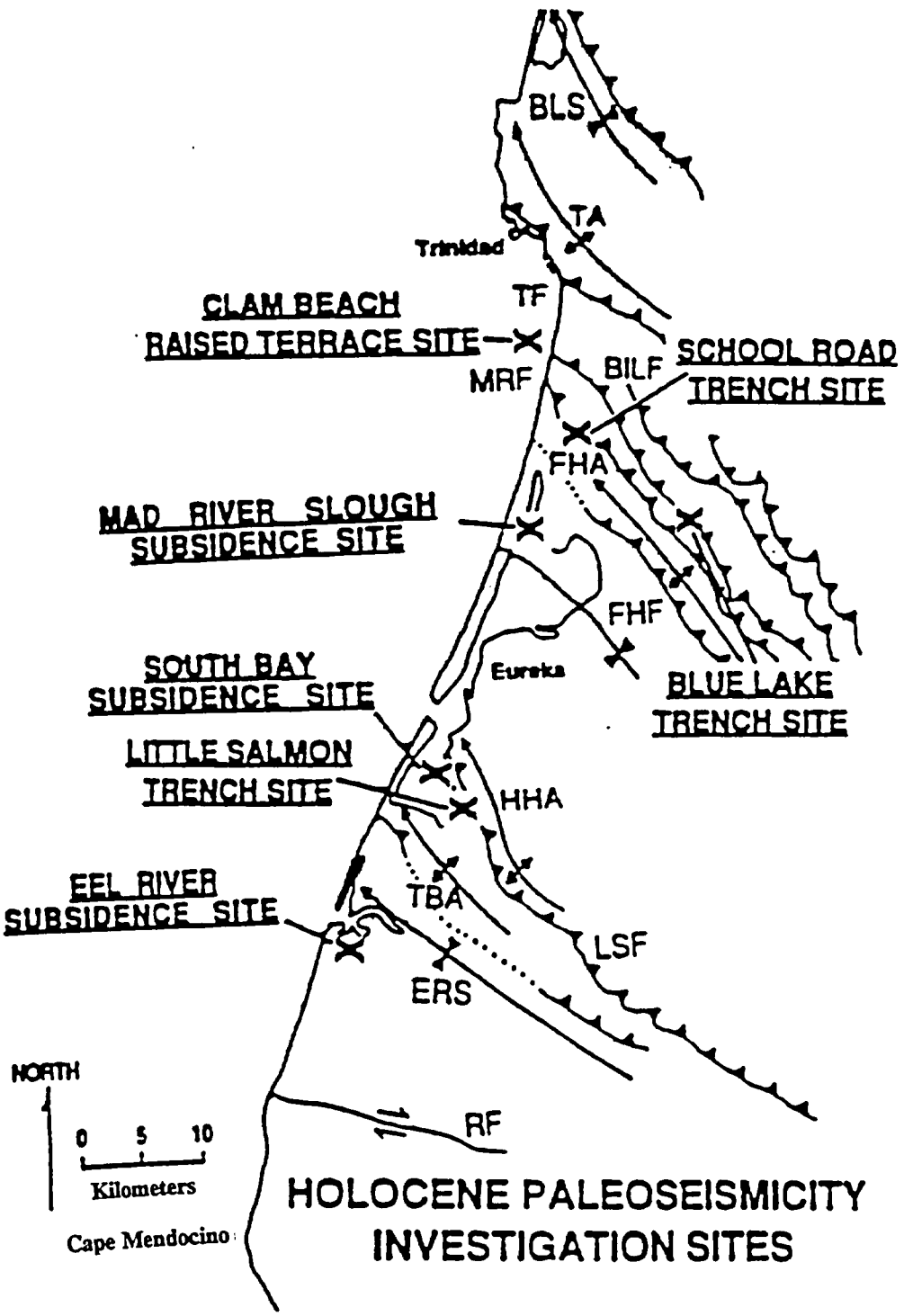

Figure 2-20 Locations of late Holocene paleoseismic investigation sites in the Humboldt Bay region (from Carver, 1992).

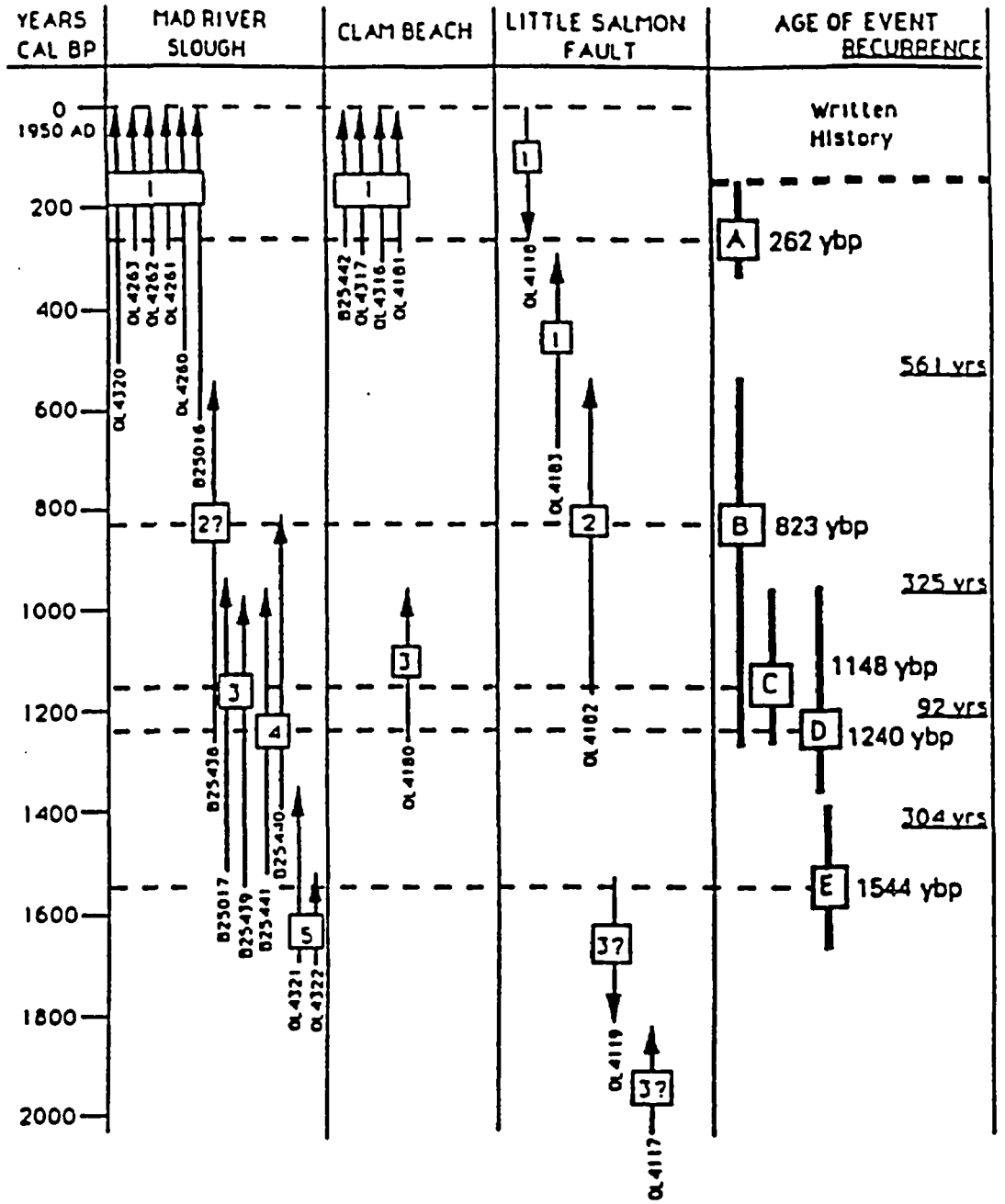

Figure 2-21 Summary chart showing age estimates and recurrence intervals for late Holocene paleoseismic events from the Humboldt Bay region. Dashed lines show averages of the most probable calibrated ages of individual paleoseismic events. Lengths of arrows indicate ranges of 2 sigma calibrated age determinations for individual events. Upward directed arrows are maximum limiting ages. Downward directed arrows are minimum limiting ages. Numbered boxes refer to the stratigraphic positions of paleoseismic horizons at the localities specified. ^{14}C age estimates for paleoseismic events at the three sites discussed provide a preliminary chronology for five large earthquakes (A through E) during the past 1690 years bp, with recurrence intervals ranging from 92 to 561 years. The most recent event occurred about 150 to 277 years bp, with the most probable age about 260 years bp. (from Clarke and Carver, 1992).

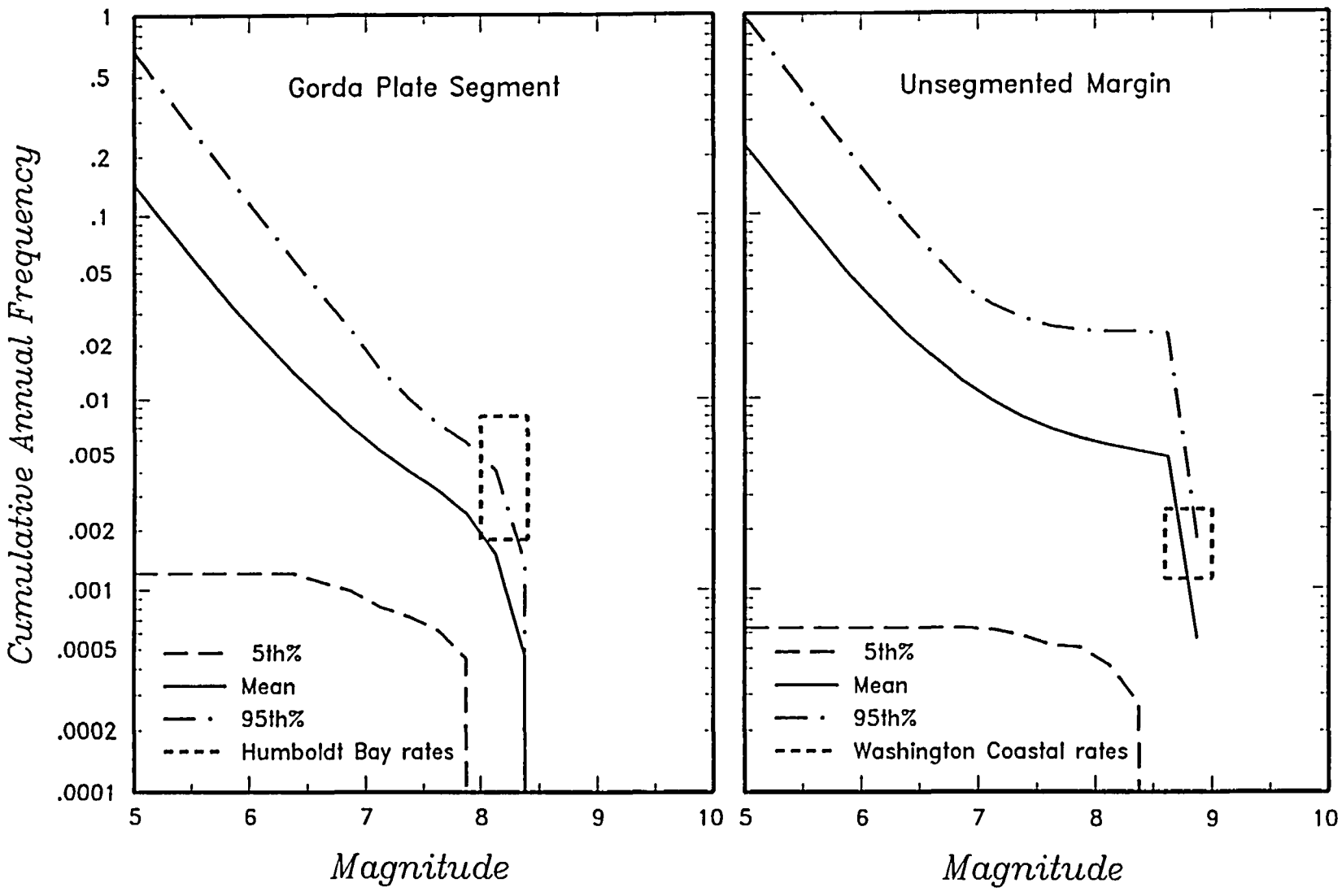

Figure 2-22 Comparison of slip-rate based and paleoseismic based recurrence relationships for interface source.

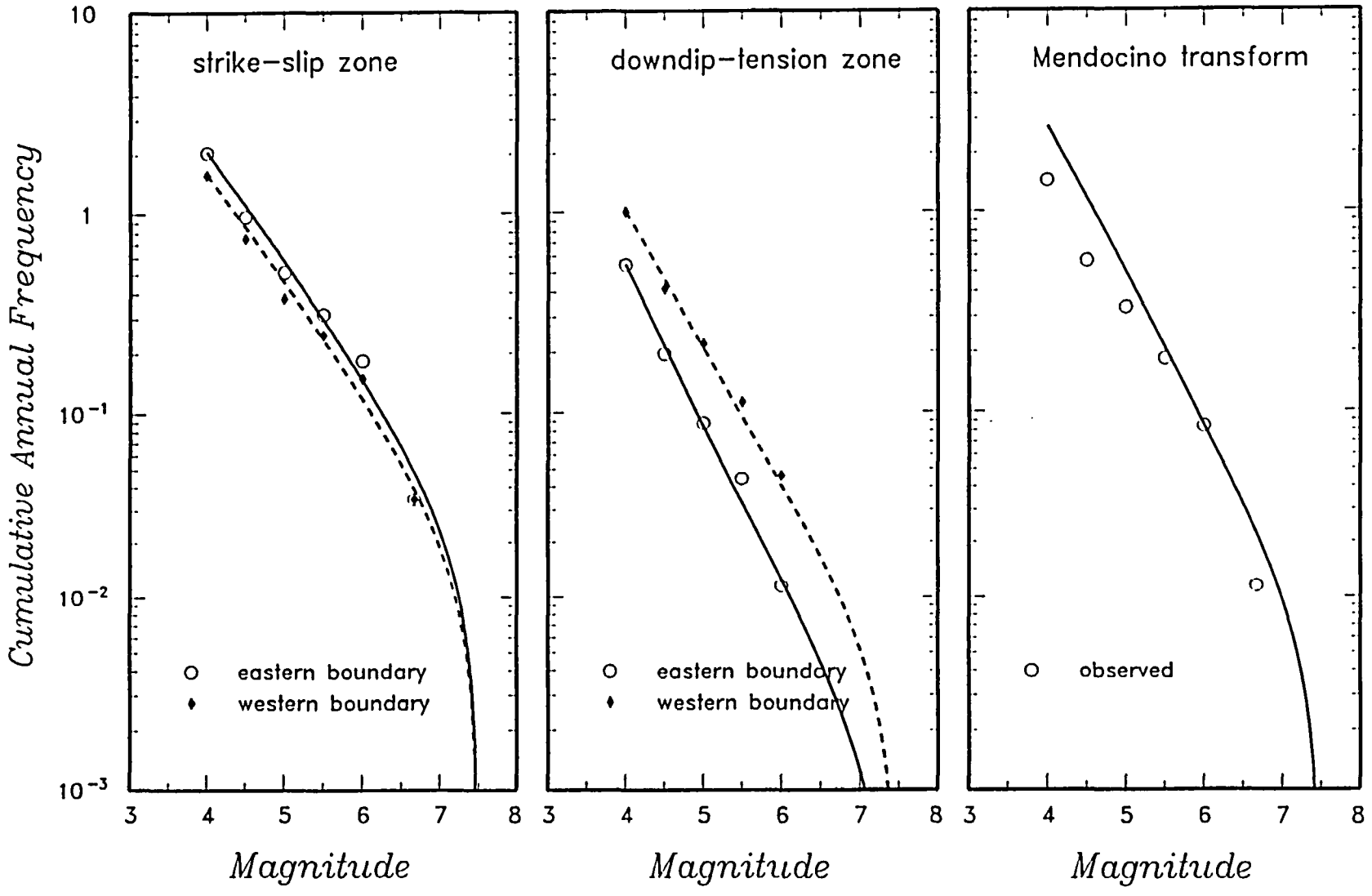

Figure 2-23 Earthquake recurrence relationships for the Gorda plate sources.

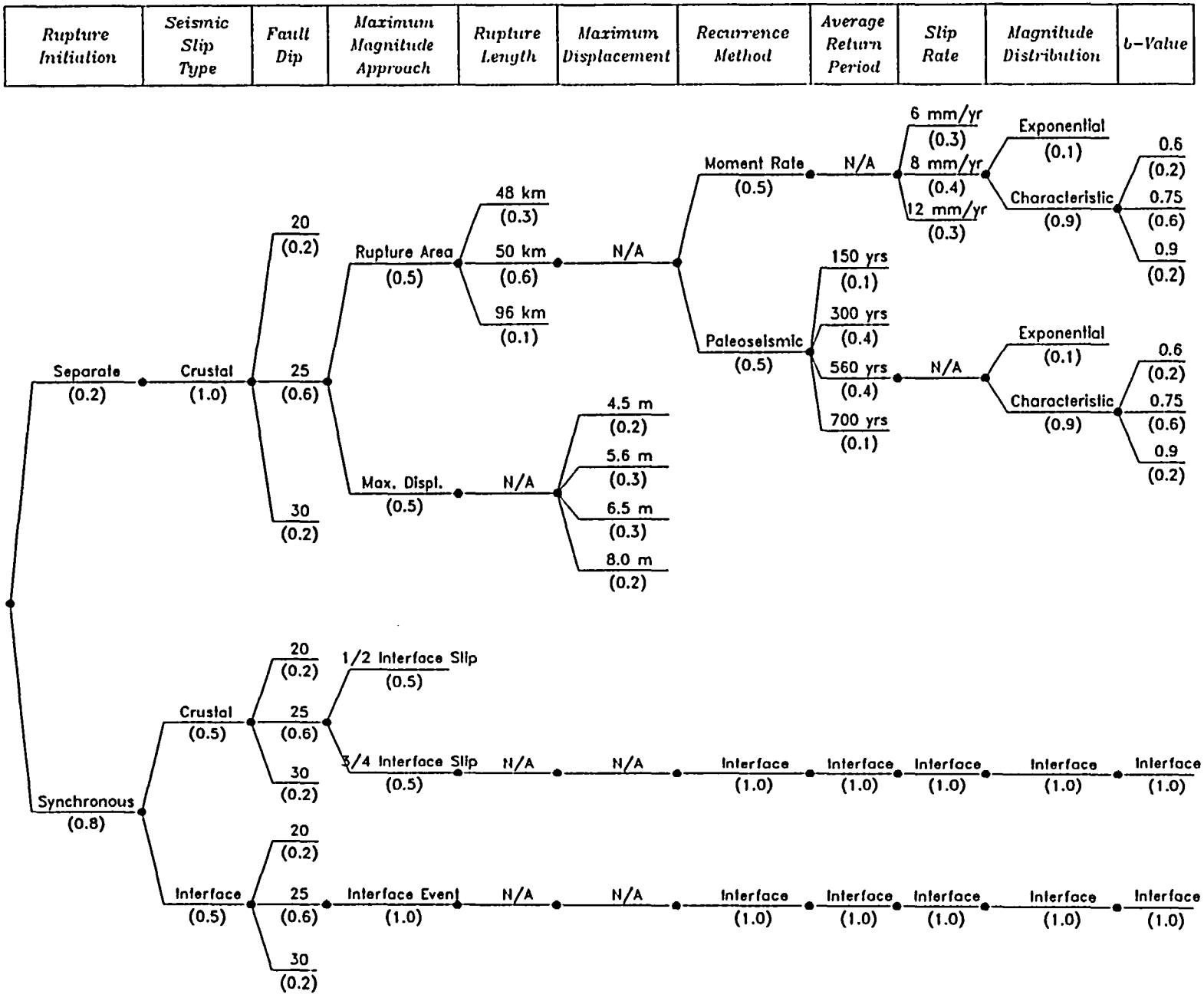

Figure 2-24 Logic tree for the Little Salmon fault.

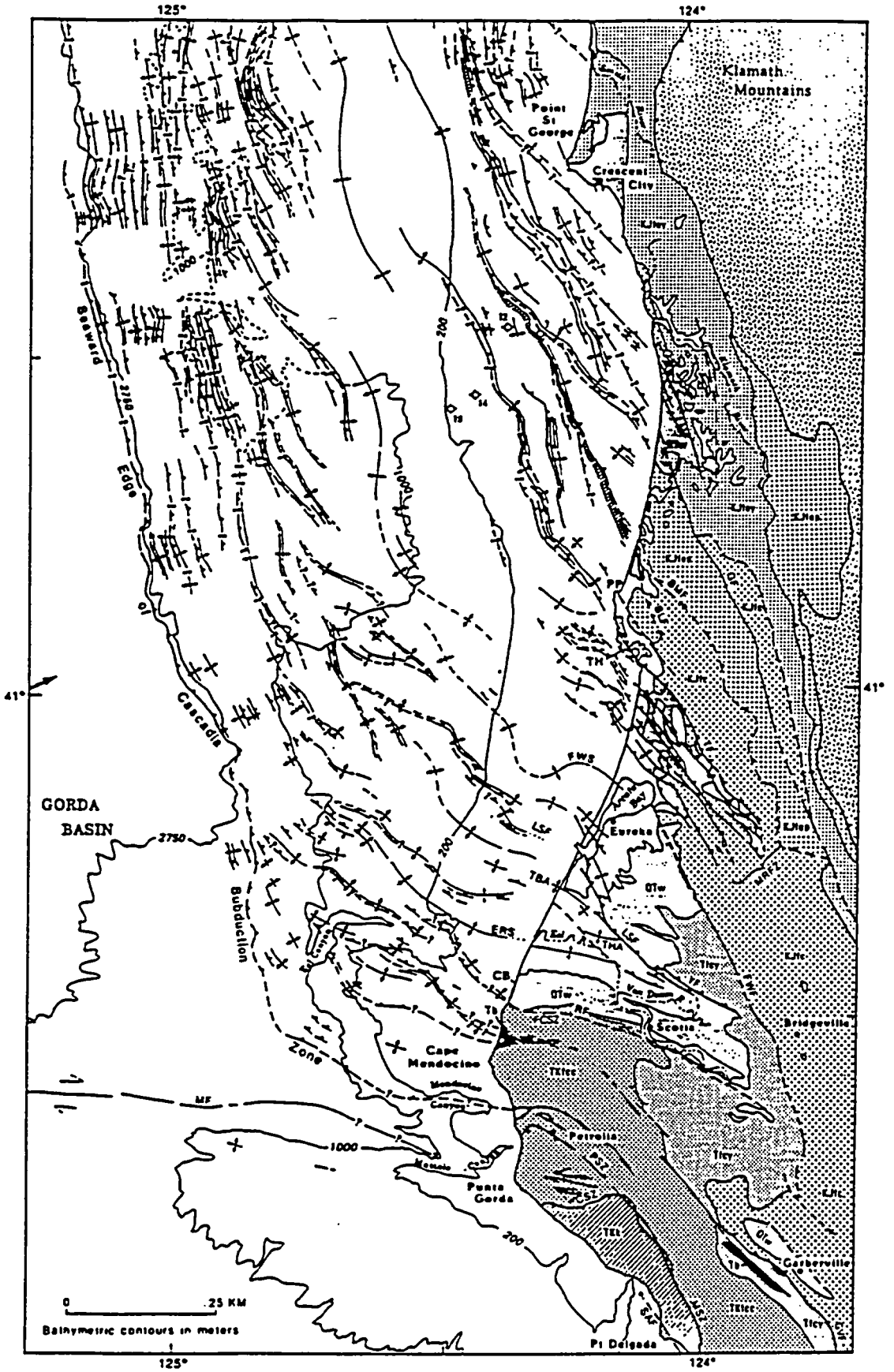

Figure 2-25 Geologic and structural map of the Eel River basin and adjacent region. MRFZ, Mad River fault zone; FWS, Freshwater syncline; LSF, Little Salmon fault; FWF, Freshwater fault; YF, Yager fault. (from Clarke, 1992).

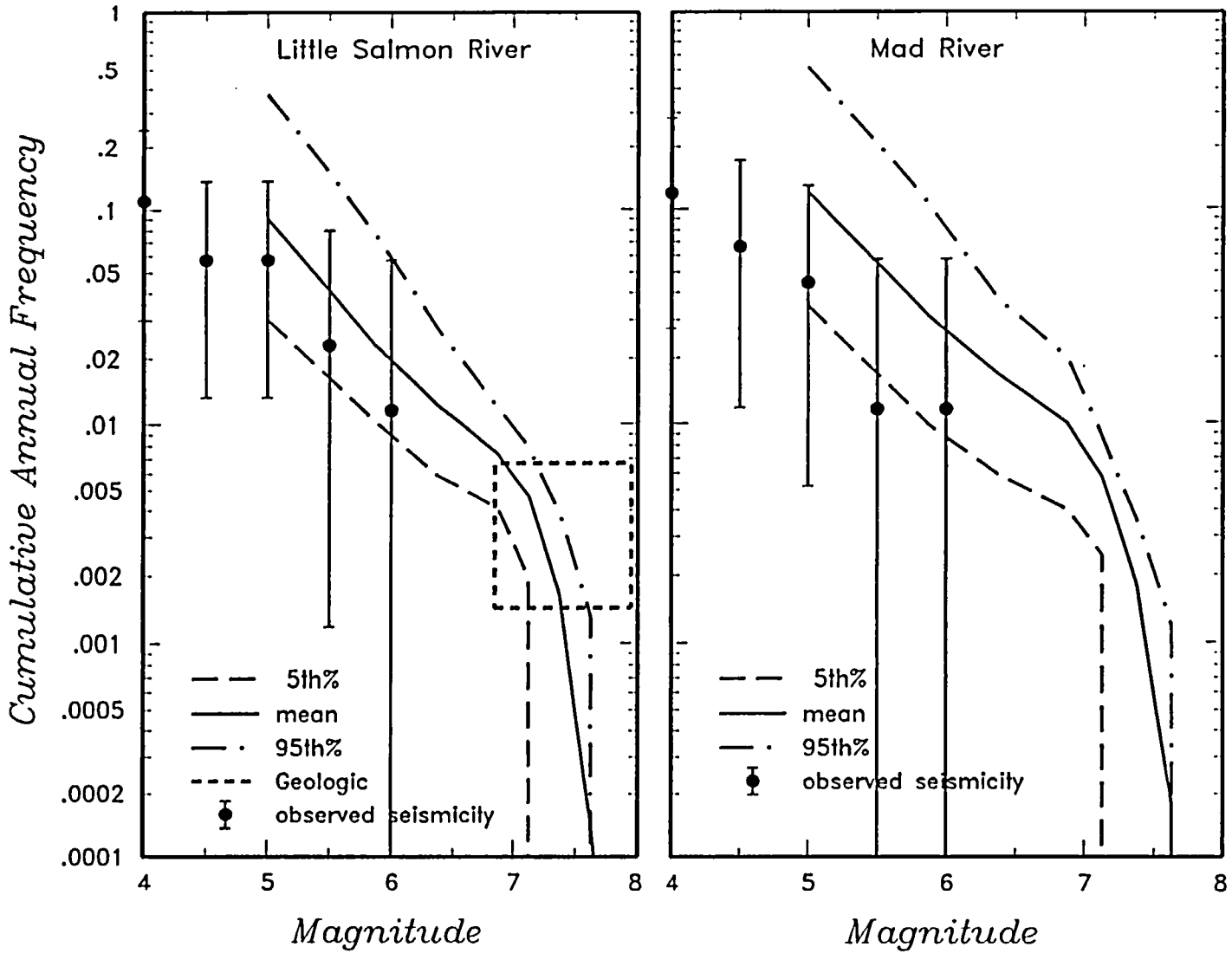

Figure 2-26 Comparison of predicted and observed seismicity rates for the Little Salmon River and Mad River fault zones.

3. ROCK MOTION ATTENUATION CHARACTERIZATION

Earthquake ground motions were characterized in terms of attenuation relationships for use in making probabilistic as well as deterministic estimates of free-field rock motions at the Humboldt Bay bridges. The result of the evaluations dealing with earthquake source characterization presented in Section 2 indicates the need for the following ground motion relationships in estimating site ground motions:

1) Attenuation relationships are required for shallow crustal earthquakes having magnitudes up to 7½ and source-to-site distances as close as about 3 to 5 kilometers.

2) Attenuation relationships are required for subduction zone earthquakes. For intraslab-type events these relationships should be specialized to provide estimates of ground motion for earthquakes having magnitudes up to 7½ and source-to-site distances as close as 20 kilometers. For interface-type events these relationships should be specialized to provide estimates of ground motions for earthquakes having magnitudes up to 9 and source-to-site distances as close as 15 kilometers.

Furthermore, the relationships should be applicable to rock-site conditions.

The following relationships were selected/developed for rock motions:

1) Attenuation relationships for median horizontal peak ground acceleration, PGA

2) Attenuation relationships for median horizontal response spectral acceleration, Sa, (5-percent damped) for periods up to seven seconds

3) Associated dispersion relationships for horizontal PGA and Sa

4) Attenuation relationships for median vertical peak ground acceleration, PVA

5) Attenuation relationships for vertical response spectral acceleration, Sa (5% damped) for periods up to three seconds

6) Associated dispersion relationships for vertical PVA and Sa

The relationships selected for this study are summarized below. The approach and basic considerations involved in selecting/developing attenuation relationships are described in Appendix C for shallow crustal earthquakes and Appendix F for subduction zone earthquakes.

3.1 ATTENUATION RELATIONSHIPS FOR HORIZONTAL MOTIONS: CRUSTAL EARTHQUAKES

Three sets of ground motion attenuation relationships were used in the present study to represent ground motions from shallow crustal earthquakes: the relationship developed in Geomatrix (1992), termed the Caltrans (1991) relationship; the relationship developed by Idriss (1991), and a modified form of the relationship developed by Campbell (1991). Descriptions of these relationships are provided in this section of the report and in Appendices C and D. The three selected ground motion relationships represent the latest efforts to model strong ground motions on rock sites for the western U.S.

The three relationships selected provide attenuation relationships for horizontal peak ground acceleration and horizontal response spectral ordinates. All three relationships were used in the probabilistic ground motion (seismic hazard) analyses to represent ground motion modeling uncertainty.

The deterministic estimates of rock motion at the Humboldt Bridge site were based on the Caltrans (1991) relationships because: (1) these relationships were developed using the most complete and up-to-date data base of rock recordings, (2) attenuation relationships were developed for both horizontal and vertical PGA and response spectral ordinates, and (3) dispersion relationships associated with the horizontal and vertical ground motion attenuation relationships represent the most comprehensive study conducted to-date to model ground motion uncertainty.

A description of Caltrans (1991) attenuation relationships is provided in Sections 3.1.1 through 3.2.2. Descriptions of attenuation relationships by Idriss (1991) and modified Campbell (1991) are contained in Appendix D. Comparison of the above three attenuation relationships is provided in Section 3.5

3.1.1 Horizontal Peak Ground Acceleration

The attenuation relationships selected for the horizontal peak ground acceleration (PGA) and designated herein as Caltrans (1991) PGA relationships are those by Sadigh et al (1989). For ease of reference, descriptions of the data base, methodology, and basic assumptions used in deriving these relationships are provided in Appendix C.

The selected relationships are presented below.

- For strike-slip faulting:
  - For magnitudes equal to or greater than 6.5:
    $\ln PGA = -1.274 + 1.1\ M - 2.1 \ln [R + \exp (-0.4845 + 0.524\ M)]$
  - For magnitudes less than 6.5:
    $\ln PGA = -0.624 + 1.0\ M - 2.1 \ln [R + \exp (1.2965 + 0.250\ M)]$

- For reverse/thrust faulting:
  - For magnitudes equal to or greater than 6.5:
    $\ln PGA = -1.092 + 1.1\ M - 2.1 \ln [R + \exp (-0.4845 + 0.524\ M)]$
  - For magnitudes less than 6.5:
    $\ln PGA = -0.442 + 1.0\ M - 2.1 \ln [R + \exp (1.2965 + 0.250\ M)]$

In the above equations, PGA is peak horizontal ground acceleration in g's, M is moment magnitude, and R is the closest source-to-site distance in kilometers.

The above relationships provide median (50th percentile) estimates of peak horizontal ground acceleration. Other percentile levels can be computed from the following dispersion relationships (expressed in terms of standard deviation, σ), which are associated with the above attenuation equations.

- For magnitudes equal to or greater than 7¼
  σ (ln PGA) = 0.38

- For magnitudes less than 7¼
  σ (ln PGA) = 1.39 - 0.14 M

3.1.2 Horizontal Acceleration Response Spectra

The available response spectral attenuation relationships were reviewed and judged to require updating and extension for use in the present project. The most relevant relationships were those developed in connection with the PGandE, Diablo Canyon Power Plant, Long Term Seismic Program (LTSP) studies (see Sadigh et al., 1989). These relationships provide the basis for the modified and extended relationships that were developed by Sadigh and Chang (1990) and those developed for the present study; therefore, the approach used in developing the LTSP relationships is reviewed in Appendix C.

The studies summarized by Sadigh et al. (1989) were conducted before the 1989 Loma Prieta earthquake. In a follow-up study, conducted by Sadigh and Chang (1990), response spectral ordinate attenuation relationships were revised by including the available recordings from the 1989 Loma Prieta earthquake. The studies by Sadigh and Chang (1990) extended the attenuation relationships to periods longer than 1 second and allowed the spectral shape to be a function of distance. The attenuation relationships developed by Sadigh and Chang (1990) were further modified for this study by making the following changes:

(1) including additional rock recording from the 1989 Loma Prieta earthquake

(2) extending the relationships to periods as long as 7.5 seconds

(3) refining the form of the attenuation relationships

(4) enriching the long-period spectral relationships during the smoothing process.

The above modified Sadigh and Chang (1990) relationships are designated herein as Caltrans (1991) horizontal response spectral relationships.

The final median attenuation relationships selected for this study are presented in Table 3-1 for PGA and S_a for twenty one (21) spectral periods in the range 0.04 to 7.5 seconds. The

frequency-dependent dispersion relationships associated with these relationships are presented in Table 3-2 for the corresponding 21 periods.

3.2 ATTENUATION RELATIONSHIPS FOR VERTICAL MOTIONS: CRUSTAL EARTHQUAKES

3.2.1 Vertical Peak Ground Acceleration

The attenuation relationships selected for vertical peak ground acceleration (PVA), and designated herein Caltrans (1991) PVA relationships, are those developed by Sadigh and Chang (1990). These are described in Appendix C and summarized below.

- For strike-slip faulting:
  - For magnitudes equal to or greater than 6.5:
    $\ln PVA = -1.08 + 1.1\ M - 2.3 \ln [R + \exp (-0.3524 + 0.478\ M)]$
  - For magnitudes less than 6.5:
    $\ln PVA = -0.430 + 1.0\ M - 2.3 \ln [R + \exp (1.2726 + 0.228\ M)]$
- For reverse/thrust faulting:
  - For magnitudes equal to or greater than 6.5:
    $\ln PVA = -0.98 + 1.1\ M - 2.3 \ln [R + \exp (-0.3524 + 0.478\ M)]$
  - For magnitudes less than 6.5:
    $\ln PVA = -0.330 + 1.0\ M - 2.3 \ln [R + \exp (1.2726 + 0.228\ M)]$

In the above equations, PVA is peak vertical ground acceleration in g's, M is moment magnitude, and R is the closest source-to-site distance in kilometers.

The above relationships provide median (50^{th} percentile) estimates of vertical peak ground acceleration. Other percentile values can be computed using the following dispersion relationships:

$\sigma (\ln PVA) = 0.48$ for $M \geq 6.5$

$\sigma (\ln PVA) = 3.08 - 0.40\ M$ for $6.0 < M < 6.5$

σ (ln PVA) = 0.68 for M $\leq$ 6.0

3.2.2 Vertical Acceleration Response Spectra

Attenuation relationship were developed by Sadigh and Chang (1990) for 5-percent-damped response spectral acceleration as a function of magnitude and distance for periods up to 1 second. The study by Sadigh and Chang (1990) used data for rock sites from shallow crustal earthquakes of magnitude 4.7 to 7.4, including the recordings available at the time from the 1989 Loma Prieta earthquake. The steps involved in deriving these relationships are described in Appendix C. The relationships developed by Sadigh and Chang were selected for this study and extended to a period of 3 seconds and designated as Caltrans (1991) vertical response spectral relationships.

The attenuation relationships for vertical response spectral acceleration (5 percent damping) corresponding to median values and strike-slip and reverse/thrust faulting mechanisms are presented in Table 3-3. The relationships shown provide spectral ordinate relationships for periods up to 3 seconds.

The following relationships were selected for the total standard error, σ (ln S_a); these relationships are applicable for periods 0.05 to 3 seconds:

σ (ln S_a) = 0.57 for M $\geq$ 6.5
σ (ln S_a) = 2.91 - 0.36 M for 6.0 < M < 6.5
σ (ln S_a) = 0.75 for M $\leq$ 6.0

3.3 ATTENUATION RELATIONSHIPS FOR HORIZONTAL MOTIONS: SUBDUCTION ZONE EARTHQUAKES

The existing published attenuation relationships for ground motions from subduction zone earthquakes (Iwasaki and others, 1978; Sadigh, 1979; NOAA, 1982; Mori and others, 1984; Vyas and others, 1984; Kawashima and others, 1984; Krinitzky and others, 1987; Crouse and others, 1988) typically indicate that at distances greater than 50 km from the earthquake rupture, ground motions from subduction zone earthquakes are substantially larger than those from shallow crustal earthquakes. Use of the published relationships for estimation of near

field motions that might result from large interface thrust earthquakes requires extrapolation beyond the empirical data base used for these relationships, which consists of recordings at distances greater than 50 km primarily from events of magnitude ≤ 7.5. These extrapolations require assessment of the appropriate form of near field distance and magnitude scaling which requires considerable judgment. In addition, the published relationships have been derived largely on the basis of soil-site, rather than rock-site, recordings.

The occurrence of magnitude 8 earthquakes in Chile and Mexico during 1985 provided a significant extension of the existing strong motion data base. The recordings from these earthquakes significantly expanded the data base for large magnitude, near field strong motion recordings on rock. These data have provided a reasonable basis for estimating near field motions for moderate to large magnitude subduction zone earthquakes.

Youngs and others (1988) developed attenuation relationships for estimating peak horizontal accelerations and 5 percent damped horizontal spectral velocities on rock sites from subduction zone earthquakes. Their attenuation relationships were developed from regression analysis of recorded ground motions and numerical simulations of ground motions for large earthquakes. The empirical data base consisted of the available recordings obtained on rock from 60 earthquakes including the 1985 events in Chile and Mexico. Youngs and others (1988) grouped subduction zone earthquakes into two basic types of events: low angle thrust earthquakes occurring on plate interfaces (interface events) and predominantly normal faulting earthquakes occurring within the downgoing plate (intraslab events).

The Youngs and others (1988) relationships have been recently updated (Geomatrix, 1993; Youngs and others, 1993) through: evaluation of additional strong motion data, including the recordings of the mainshock of the 1992 Cape Mendocino earthquake; use of improved regression techniques that allow for a separation of distance and magnitude scaling; and use of numerical modeling studies that provided guidance in evaluation of the empirical data and extrapolation to larger magnitudes and small source-to-site distances. Appendix F presents the description of the development of the attenuation relationships abstracted from Geomatrix (1993). The revised empirical attenuation relationships are similar to those of Youngs and others (1988) and predict ground motion levels over the distance range of 50 to 500 km that are similar to those resulting from numerical modeling studies. Figure 3-1 compares the peak

accelerations predicted by the empirical attenuation relationship developed in Geomatrix (1993) with the peak accelerations predicted by numerical modeling (Youngs and others, 1993) for magnitude 8 and 8.5 events.

As indicated on Figure 3-1, the ground motions predicted by the two methods are similar, except at distances less than about 50 km. At these smaller distances, where the recording sites lie above the rupture surface, the two methods give significantly different results. The empirical model predicts relatively low ground motion levels at small distances, following the trend of the relationships developed over a large distance range. These predictions are influenced heavily by the recordings from the Guerrero array in Mexico, which recorded relatively low levels of motions on rock sites during the 1985 Michaocan earthquake sequence. The relatively low rock motions are also consistent with the limited rock site data from the 1985 M 8 Valpariaso, Chile earthquake. On the other hand, the numerical modeling results show a change in the rate of attenuation with distance in the near field, and indicate that at close source-to-site distances the attenuation is similar to that for crustal earthquakes. This is indicated on Figure 3-1 by peak accelerations predicted by the crustal earthquake attenuation relationship described in Section 3.1 extrapolated to magnitude M 8 and 8.5 events. If one considers that the 1992 Cape Mendocino main shock was an interface event, then the ground motions resulting from this earthquake are also consistent with near field attenuation characteristics that are similar to those of crustal earthquakes. Accordingly, the crustal attenuation relationship described above was also used to evaluate ground motions from the Cascadia interface events at small source-to-site distances.

The attenuation relationship developed by Geomatrix (1993) for horizontal peak ground acceleration are:

$$\ln PGA = 0.3633 + 1.414M - 2.553 \ln [R + 1.782\exp(0.554M)]$$

for interface events with focal depths of 20 km and

$$\ln PGA = 0.8694 + 1.414M - 2.553 \ln [R + 1.782\exp(0.554M)]$$

for intraslab events with focal depths of 40 km

The above relationships provide median (50th percentile) estimates of peak ground acceleration. Other percentile levels can be computed from the dispersion relationships associated with this median attenuation equation:

- For magnitude less than or equal to 8.0

$$\sigma \text{ (ln PGA)} = 1.45 - 0.1\ M$$

- For magnitudes greater than 8.0

$$\sigma \text{ (ln PGA)} = 0.65$$

Table 3-4 presents the relationships used to estimate 5 percent damped horizontal spectral velocities. These relationships were developed from the relationships published by Youngs and others (1988) and Geomatrix (1993).

3.4 ATTENUATION RELATIONSHIPS FOR VERTICAL MOTIONS: SUBDUCTION ZONE EARTHQUAKES

Geomatrix (1993) did not update the attenuation relationship for vertical peak ground acceleration (PVA) on rock developed by Youngs and others (1988). However, because the attenuation relationships for horizontal motions of Youngs and others (1988) and Geomatrix (1993) are very similar, the vertical peak ground acceleration relationships of Youngs and others (1988) should be appropriate. The median attenuation equations are:

$$\ln PGA = 18.67 + 1.045M - 4.738 \ln [R + C(M)] + 0.54Z$$

$$C(M) = 205.5 \exp (0.0968M) \qquad \text{for } M \leq 8.0$$

$$C(M) = 154.7 \exp (0.1323M) \qquad \text{for } M > 8.0$$

$Z = 0$ for interface events and 1 for intraslab events

The dispersion relationships associated with the above median attenuation equation are as follows:

- For magnitudes less than or equal to 8.0

$$\sigma \text{ (ln PVA)} = 1.55 - 0.125M$$

- For magnitudes greater than 8.0

$$\sigma \text{ (ln PVA)} = 0.55$$

Youngs and others (see Geomatrix Consultants, 1988) also developed attenuation relationships for 5 percent-damped vertical spectral velocity on rock; these relationships are summarized in Table 3-5. The dispersion relationships associated with these median relationships are as follows for periods 0.04 to 3 seconds:

- For magnitudes less than or equal to 8.0

$$\sigma \text{ (ln PSRV)} = 1.55 - 0.125\ M$$

- For magnitudes greater than 8.0

$$\sigma \text{ (ln PSRV)} = 0.55$$

These attenuation relationships were selected for use in the present study to provide estimates of vertical ground motions at the bridge site from the postulated subduction zone events.

3.5 TREATMENT OF UNCERTAINTY IN ATTENUATION FOR PROBABILISTIC ANALYSIS

The relationships presented in the previous sections represent the preferred relationships for estimating ground motions at the site of the Humboldt Bay bridges. As the seismic characteristics of the region present a somewhat unusual setting for ground motion estimation compared with that typically found for both crustal and subduction zone interface sources, uncertainty in specifying the attenuation relationships was explicitly included in the probabilistic seismic hazard analysis. The uncertainty treated included uncertainty in specifying the relationships for crustal earthquakes, uncertainty in specifying the attenuation relationships for the interface source at close distances, and uncertainty in specifying the relationships for intraslab earthquakes.

The ground motion attenuation relationships presented (Caltrans, 1991) represent our best effort to model strong ground motions on rock sites from western U.S. earthquakes. Others have developed attenuation relationships for rock conditions utilizing somewhat different functional forms and ground motion data sets. Two recent relationships are those developed by Idriss (1991) and the modification by Abrahamson (1992) of the soil site relationships developed by Campbell (1991). These relationships are listed in Appendix D. Both of these sets of relationships are intended for estimating rock site ground motions in the western U.S. Figures 3-2 through 3-4 compare these two sets of attenuation relationships with those developed for this study (labeled Caltrans, 1991). Figure 3-2 compares the peak horizontal accelerations estimated by the three sets of relationships for magnitude 5 to 8 earthquakes. The relationships by Idriss (1991) and modified Campbell (1991) tend to predict lower ground motions at small source-to-site distances than the values given by the Caltrans (1991) relationship. Figure 3-3 compares the response spectra predicted by the three sets of relationships for magnitude 5 to 8 earthquakes at a distance of 15 km. All three sets of relationships predict similar estimates of long-period ground motion. At short periods, the modified Campbell (1991) relationships give significantly lower estimates of spectral acceleration than those predicted by the Idriss (1991) and Caltrans (1991) relationships. Figure 3-4 compares the estimates of standard error in log spectral acceleration specified by the three sets of relationships. As indicated on the figure, the modified Campbell (1991) relationships have a much lower estimate of standard error than do those given by Caltrans (1991) and Idriss (1991).

The Caltrans (1991), Idriss (1991), and modified Campbell (1991) attenuation relationships were used in the probabilistic ground motion (hazard) analysis to represent the uncertainty in modeling ground motion. The seismic hazard model logic trees presented in Section 2 were extended to include a node for attenuation relationships. The Caltrans (1991) relationships were given a weight of 0.5 because they are judged to be the most comprehensive effort to model rock site ground motions in the western U.S. The Idriss (1991) and modified Campbell (1991) relationships were given weights of 0.35 and 0.15, respectively. The Idriss (1991) relationships are preferred over those of Campbell (1991) because Idriss (1991) considered a larger rock motion data base than did the Campbell (1991) study on which the modified Campbell relationships are based, and because we judged that the estimates of standard error associated with the modified Campbell (1991) relationships are low in comparison to the observed scatter in recorded ground motions.

As discussed above in Section 3.3, there is uncertainty about the attenuation characteristics of subduction zone interface earthquake ground motions at small source-to-site distances. The data from large interface earthquakes suggest relatively low ground motion levels in the near source region while the results of the numerical modeling studies presented in Youngs and others (1993) as well as earlier modeling work presented by Cohee and others (1991) indicate the attenuation characteristics are similar to those of crustal earthquakes at distances less than approximately 50 km. The data from the 1992 Cape Mendocino earthquake, if interpreted to be an interface earthquake, also suggest that the near source attenuation characteristics are similar to those of crustal earthquakes. Accordingly, both the interface attenuation relationships developed by Geomatrix (1993) and the crustal attenuation relationship presented in Section 3.1 were used to compute the hazard from the interface source. Figure 3-1 presented a comparison of the peak acceleration attenuation relationships for interface and shallow crustal attenuation relationships. Figure 3-5 compares the response spectra associated with the two attenuation relationships. As indicated, the shallow crustal attenuation relationships predict significantly more long period motion than do the interface attenuation relationships. The two attenuation relationships were given equal weight because the limited near source data do not provide a clear choice between them.

The intraslab earthquake attenuation relationships developed by Youngs et al. (1988) were specified for downdip tension earthquakes, such as those that would occur in the Gorda plate as it subducts beneath the North American plate. It is uncertain whether these relationships also apply to the Gorda plate in the offshore strike slip zone or along the Mendocino transform, or instead, that crustal attenuation relationships, such as those described in Section 3.1 should apply. The empirical data from offshore Gorda plate earthquakes, including the aftershocks of the 1992 Cape Mendocino earthquakes, contain significant scatter and either relationship might be appropriate. Accordingly, both relationships were used for these two zones in the probabilistic analysis and they were given equal weight.

There is some uncertainty in specifying the appropriate attenuation relationship for estimating ground motions associated with the Little Salmon River fault when it is assumed to move synchronous with the interface during large shallow thrust earthquakes. However, because the data from the Cape Mendocino earthquake main shock display characteristics similar to those

for crustal earthquakes, the crustal attenuation relationship developed in Section 3.2 was used in the analysis.

3.6 PRELIMINARY EVALUATION OF BASIN EFFECT

A preliminary evaluation analysis of the significance of large basins on earthquake ground motions at the site of the Humboldt Bay bridges was conducted (see Appendix G). The intent was not to determine the basin effect, but rather to determine if the basin effect is likely to significantly increase the ground motion at the site of the bridges. The results of this study indicated that the 2-D basin effects at the site of the Humboldt Bay bridges are not likely to produce significant anomalously large motions at the bridge sites.

TABLE 3-1a

ATTENUATION RELATIONSHIPS OF HORIZONTAL ROCK MOTION (PEAK GROUND ACCELERATION AND RESPONSE SPECTRAL ACCELERATIONS, 5% DAMPING FOR STRIKE-SLIP FAULTING)

M_w = or < 6½

Period(s)	C_1	C_2	C_3	C_4	C_5	C_6	C_7
PGA	-0.624	1.0	0.000	-2.100	1.29649	0.250	0.0
0.05	-0.090	1.0	0.006	-2.128	1.29649	0.250	-0.082
0.07	0.110	1.0	0.006	-2.128	1.29649	0.250	-0.082
0.09	0.212	1.0	0.006	-2.140	1.29649	0.250	-0.052
0.10	0.275	1.0	0.006	-2.148	1.29649	0.250	-0.041
0.12	0.348	1.0	0.005	-2.162	1.29649	0.250	-0.014
0.14	0.307	1.0	0.004	-2.144	1.29649	0.250	0.0
0.15	0.285	1.0	0.002	-2.130	1.29649	0.250	0.0
0.17	0.239	1.0	0.0	-2.110	1.29649	0.250	0.0
0.20	0.153	1.0	-0.004	-2.080	1.29649	0.250	0.0
0.24	0.060	1.0	-0.011	-2.053	1.29649	0.250	0.0
0.30	-0.057	1.0	-0.017	-2.028	1.29649	0.250	0.0
0.40	-0.298	1.0	-0.028	-1.990	1.29649	0.250	0.0
0.50	-0.588	1.0	-0.040	-1.945	1.29649	0.250	0.0
0.75	-1.208	1.0	-0.050	-1.865	1.29649	0.250	0.0
1.00	-1.705	1.0	-0.055	-1.800	1.29649	0.250	0.0
1.50	-2.407	1.0	-0.065	-1.725	1.29649	0.250	0.0
2.00	-2.945	1.0	-0.070	-1.670	1.29649	0.250	0.0
3.00	-3.700	1.0	-0.080	-1.615	1.29649	0.250	0.0
4.00	-4.230	1.0	-0.100	-1.570	1.29649	0.250	0.0
5.00	-4.714	1.0	-0.100	-1.540	1.29649	0.250	0.0
7.50	-5.530	1.0	-0.110	-1.510	1.29649	0.250	0.0

Notes: Relationships for reverse/thrust faulting are obtained by multiplying the strike-slip amplitudes by 1.2. Relationships for oblique faulting are obtained by multiplying the strike-slip amplitudes by 1.09.

Attenuation relationships:

$$\ln(y) = C_1+C_2*M+C_3*(8.5-M)^{2.5}+C_4*\ln(R+\exp(C_5+C_6*M))+C_7*\ln(R+2)$$

TABLE 3-1b

ATTENUATION RELATIONSHIPS OF HORIZONTAL ROCK MOTION (PEAK GROUND ACCELERATION AND RESPONSE SPECTRAL ACCELERATIONS, 5% DAMPING FOR STRIKE-SLIP FAULTING)

M_w = or > 6½

Period(s)	C_1	C_2	C_3	C_4	C_5	C_6	C_7
PGA	-1.274	1.1	0.000	-2.100	-0.48451	0.524	0.0
0.05	-0.740	1.1	0.006	-2.128	-0.48451	0.524	-0.082
0.07	-0.540	1.1	0.006	-2.128	-0.48451	0.524	-0.082
0.09	-0.438	1.1	0.006	-2.140	-0.48451	0.524	-0.052
0.10	-0.375	1.1	0.006	-2.148	-0.48451	0.524	-0.041
0.12	-0.302	1.1	0.005	-2.162	-0.48451	0.524	-0.014
0.14	-0.343	1.1	0.004	-2.144	-0.48451	0.524	0.0
0.15	-0.365	1.1	0.002	-2.130	-0.48451	0.524	0.0
0.17	-0.411	1.1	0.0	-2.110	-0.48451	0.524	0.0
0.20	-0.497	1.1	-0.004	-2.080	-0.48451	0.524	0.0
0.24	-0.590	1.1	-0.011	-2.053	-0.48451	0.524	0.0
0.30	-0.707	1.1	-0.017	-2.028	-0.48451	0.524	0.0
0.40	-0.948	1.1	-0.028	-1.990	-0.48451	0.524	0.0
0.50	-1.238	1.1	-0.040	-1.945	-0.48451	0.524	0.0
0.75	-1.858	1.1	-0.050	-1.865	-0.48451	0.524	0.0
1.00	-2.355	1.1	-0.055	-1.800	-0.48451	0.524	0.0
1.50	-3.057	1.1	-0.065	-1.725	-0.48451	0.524	0.0
2.00	-3.595	1.1	-0.070	-1.670	-0.48451	0.524	0.0
3.00	-4.350	1.1	-0.080	-1.610	-0.48451	0.524	0.0
4.00	-4.880	1.1	-0.100	-1.570	-0.48451	0.524	0.0
5.00	-5.364	1.1	-0.100	-1.540	-0.48451	0.524	0.0
7.50	-6.180	1.1	-0.110	-1.510	-0.48451	0.524	0.0

Notes: Relationships for reverse/thrust faulting are obtained by multiplying the strike-slip amplitudes by 1.2. Relationships for oblique faulting are obtained by multiplying the strike-slip amplitudes by 1.09.

Attenuation relationships:

$$\ln(y) = C_1+C_2*M+C_3*(8.5-M)\hat{}2.5+C_4*\ln(R+\exp(C_5+C_6*M))+C_7*\ln(R+2)$$

TABLE 3-2

DISPERSION RELATIONSHIPS FOR HORIZONTAL ROCK MOTION

Ground Motion Parameter	Period	Sigma (lny)
Peak Ground Acceleration	--	1.39 - 0.14*M; 0.38 for M> = 7.25
Response Spectra Accel.	0.05	1.39 - 0.14*M; 0.38 for M> = 7.25
Response Spectra Accel.	0.07	1.40 - 0.14*M; 0.39 for M> = 7.25
Response Spectra Accel.	0.09	1.40 - 0.14*M; 0.39 for M> = 7.25
Response Spectra Accel.	0.10	1.41 - 0.14*M; 0.40 for M> = 7.25
Response Spectra Accel.	0.12	1.41 - 0.14*M; 0.40 for M> = 7.25
Response Spectra Accel.	0.14	1.42 - 0.14*M; 0.41 for M> = 7.25
Response Spectra Accel.	0.15	1.42 - 0.14*M; 0.41 for M> = 7.25
Response Spectra Accel.	0.17	1.42 - 0.14*M; 0.41 for M> = 7.25
Response Spectra Accel.	0.20	1.43 - 0.14*M; 0.42 for M> = 7.25
Response Spectra Accel.	0.24	1.44 - 0.14*M; 0.43 for M> = 7.25
Response Spectra Accel.	0.30	1.45 - 0.14*M; 0.44 for M> = 7.25
Response Spectra Accel.	0.40	1.48 - 0.14*M; 0.47 for M> = 7.25
Response Spectra Accel.	0.50	1.50 - 0.14*M; 0.49 for M> = 7.25
Response Spectra Accel.	0.75	1.52 - 0.14*M; 0.51 for M> = 7.25
Response Spectra Accel.	1.00	1.53 - 0.14*M; 0.52 for M> = 7.25
	>1.00	1.53 - 0.14*M; 0.52 for M> = 7.25

TABLE 3-3a

ATTENUATION RELATIONSHIPS OF VERTICAL ROCK MOTION
(PEAK GROUND ACCELERATION AND RESPONSE SPECTRAL
ACCELERATIONS, 5% DAMPING FOR STRIKE-SLIP FAULTING)

M_w = or < 6½

Period(s)	C_1	C_2	C_3	C_4	C_5	C_6
PGA	-0.430	1.0	0.000	-2.300	1.2726	0.228
0.04	0.3379	1.0	0.000	-2.450	1.2726	0.228
0.05	0.5041	1.0	0.000	-2.450	1.2726	0.228
0.06	0.6095	1.0	0.000	-2.450	1.2726	0.228
0.07	0.6896	1.0	0.000	-2.450	1.2726	0.228
0.09	0.6718	1.0	-0.00330	-2.420	1.2726	0.228
0.10	0.6252	1.0	-0.00468	-2.400	1.2726	0.228
0.12	0.5535	1.0	-0.00707	-2.380	1.2726	0.228
0.14	0.3813	1.0	-0.00909	-2.333	1.2726	0.228
0.15	0.2524	1.0	-0.01000	-2.300	1.2726	0.228
0.17	0.0122	1.0	-0.01462	-2.241	1.2726	0.228
0.20	-0.3005	1.0	-0.02061	-2.164	1.2726	0.228
0.24	-0.6678	1.0	-0.02734	-2.077	1.2726	0.228
0.30	-1.1392	1.0	-0.03558	-1.971	1.2726	0.228
0.40	-1.7656	1.0	-0.04619	-1.835	1.2726	0.228
0.50	-2.2748	1.0	-0.05442	-1.729	1.2726	0.228
0.75	-3.2062	1.0	-0.06939	-1.536	1.2726	0.228
1.00	-3.8818	1.0	-0.08000	-1.400	1.2726	0.228
1.50	-4.2618	1.0	-0.08554	-1.400	1.2726	0.228
2.00	-4.5719	1.0	-0.08946	-1.400	1.2726	0.228
2.50	-4.8167	1.0	-0.09251	-1.400	1.2726	0.228
3.00	-5.0364	1.0	-0.09500	-1.400	1.2726	0.228

Notes: Relationships for reverse/thrust faulting are obtained by multiplying the strike-slip amplitudes by 1.1. Relationships for oblique faulting are obtained by multiplying the strike-slip amplitudes by 1.048.

Attenuation relationships:

$$\ln(y) = C_1+C_2*M+C_3*(8.5-M)^{2.5}+C_4*\ln(R+\exp(C_5+C_6*M))$$

TABLE 3-3b

ATTENUATION RELATIONSHIPS OF VERTICAL ROCK MOTION (PEAK GROUND ACCELERATION AND RESPONSE SPECTRAL ACCELERATIONS, 5% DAMPING FOR STRIKE-SLIP FAULTING)

M_w = or > 6½

Period(s)	C_1	C_2	C_3	C_4	C_5	C_6
PGA	-1.080	1.1	0.000	-2.300	-0.3524	0.478
0.04	-0.3121	1.1	0.000	-2.450	-0.3524	0.478
0.05	-0.1459	1.1	0.000	-2.450	-0.3524	0.478
0.06	-0.0405	1.1	0.000	-2.450	-0.3524	0.478
0.07	0.03956	1.1	0.000	-2.450	-0.3524	0.478
0.09	0.0218	1.1	-0.00330	-2.420	-0.3524	0.478
0.10	-0.0248	1.1	-0.00468	-2.400	-0.3524	0.478
0.12	-0.0965	1.1	-0.00707	-2.380	-0.3524	0.478
0.14	-0.2687	1.1	-0.00909	-2.333	-0.3524	0.478
0.15	-0.3976	1.1	-0.01000	-2.300	-0.3524	0.478
0.17	-0.6378	1.1	-0.01462	-2.241	-0.3524	0.478
0.20	-0.9505	1.1	-0.02061	-2.164	-0.3524	0.478
0.24	-1.3178	1.1	-0.02734	-2.077	-0.3524	0.478
0.30	-1.7893	1.1	-0.03558	-1.971	-0.3524	0.478
0.40	-2.4157	1.1	-0.04619	-1.835	-0.3524	0.478
0.50	-2.9248	1.1	-0.05442	-1.729	-0.3524	0.478
0.75	-3.8562	1.1	-0.06939	-1.536	-0.3524	0.478
1.00	-4.5318	1.1	-0.08000	-1.400	-0.3524	0.478
1.50	-4.9118	1.1	-0.08554	-1.400	-0.3524	0.478
2.00	-5.2219	1.1	-0.08946	-1.400	-0.3524	0.478
2.50	-5.4667	1.1	-0.09251	-1.400	-0.3524	0.478
3.00	-5.6864	1.1	-0.09500	-1.400	-0.3524	0.478

Notes: Relationships for reverse/thrust faulting are obtained by multiplying the strike-slip amplitudes by 1.1. Relationships for oblique faulting are obtained by multiplying the strike-slip amplitudes by 1.048.

Attenuation relationships:

$\ln(y) = C_1+C_2*M+C_3*(8.5-M)\text{^}2.5+C_4*\ln(R+\exp(C_5+C_6*M))$

TABLE 3-4

HORIZONTAL SPECTRAL VELOCITIES FOR SUBDUCTION ZONE EARTHQUAKES

T = 0.04 sec	$\ln(S_v/a_{max})$	= 1.960
T = 0.07 sec	$\ln(S_v/a_{max})$	= 2.845
T = 0.1 sec	$\ln(S_v/a_{max})$	= 3.431
T = 0.15 sec	$\ln(S_v/a_{max})$	= $3.985 - 0.0026(10 - M_w)^3$
T = 0.2 sec	$\ln(S_v/a_{max})$	= $4.278 - 0.0044(10 - M_w)^3$
T = 0.3 sec	$\ln(S_v/a_{max})$	= $4.652 - 0.0069(10 - M_w)^3$
T = 0.4 sec	$\ln(S_v/a_{max})$	= $4.906 - 0.0087(10 - M_w)^3$
T = 0.5 sec	$\ln(S_v/a_{max})$	= $5.076 - 0.0101(10 - M_w)^3$
T = 0.7 sec	$\ln(S_v/a_{max})$	= $5.154 - 0.0123(10 - M_w)^3$
T = 0.8 sec	$\ln(S_v/a_{max})$	= $5.164 - 0.0131(10 - M_w)^3$
T = 0.9 sec	$\ln(S_v/a_{max})$	= $5.167 - 0.0138(10 - M_w)^3$
T = 1.0 sec	$\ln(S_v/a_{max})$	= $5.140 - 0.0145(10 - M_w)^3$
T = 1.5 sec	$\ln(S_v/a_{max})$	= $5.059 - 0.0170(10 - M_w)^3$
T = 2.0 sec	$\ln(S_v/a_{max})$	= $4.960 - 0.0189(10 - M_w)^3$
T = 3.0 sec	$\ln(S_v/a_{max})$	= $4.725 - 0.0214(10 - M_w)^3$

The units of S_v/a_{max} are cm/sec/g.

TABLE 3-5

VERTICAL SPECTRAL VELOCITIES FOR SUBDUCTION ZONE EARTHQUAKES

T = 0.04 sec	$\ln(S_v/a_{max})$	=	2.103
T = 0.05 sec	$\ln(S_v/a_{max})$	=	3.033
T = 0.1 sec	$\ln(S_v/a_{max})$	=	3.506
T = 0.15 sec	$\ln(S_v/a_{max})$	=	$3.967 - 0.0026(10 - M_w)^3$
T = 0.2 sec	$\ln(S_v/a_{max})$	=	$4.303 - 0.0044(10 - M_w)^3$
T = 0.3 sec	$\ln(S_v/a_{max})$	=	$4.683 - 0.0069(10 - M_w)^3$
T = 0.4 sec	$\ln(S_v/a_{max})$	=	$4.791 - 0.0087(10 - M_w)^3$
T = 0.5 sec	$\ln(S_v/a_{max})$	=	$4.767 - 0.0101(10 - M_w)^3$
T = 0.7 sec	$\ln(S_v/a_{max})$	=	$4.850 - 0.0123(10 - M_w)^3$
T = 0.8 sec	$\ln(S_v/a_{max})$	=	$4.866 - 0.0131(10 - M_w)^3$
T = 0.9 sec	$\ln(S_v/a_{max})$	=	$4.874 - 0.0138(10 - M_w)^3$
T = 1.0 sec	$\ln(S_v/a_{max})$	=	$4.882 - 0.0145(10 - M_w)^3$
T = 1.5 sec	$\ln(S_v/a_{max})$	=	$4.937 - 0.0170(10 - M_w)^3$
T = 2.0 sec	$\ln(S_v/a_{max})$	=	$5.015 - 0.0189(10 - M_w)^3$
T = 3.0 sec	$\ln(S_v/a_{max})$	=	$5.017 - 0.0214(10 - M_w)^3$

The units of S_v/a_{max} are cm/sec/g.

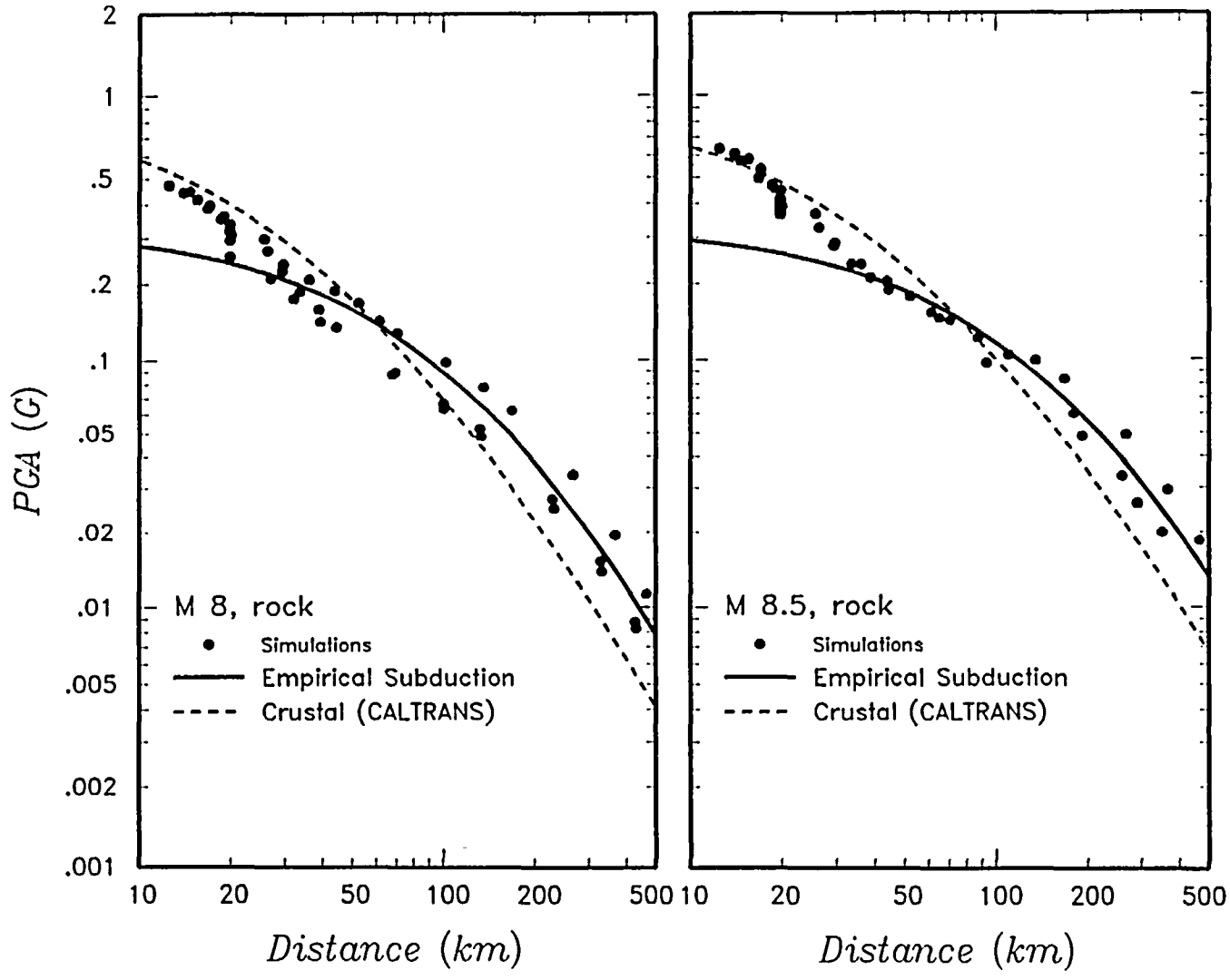

Figure 3-1 Comparison of numerical simulations of interface earthquake ground motions with empirical models based on subduction zone and crustal earthquake ground motions.

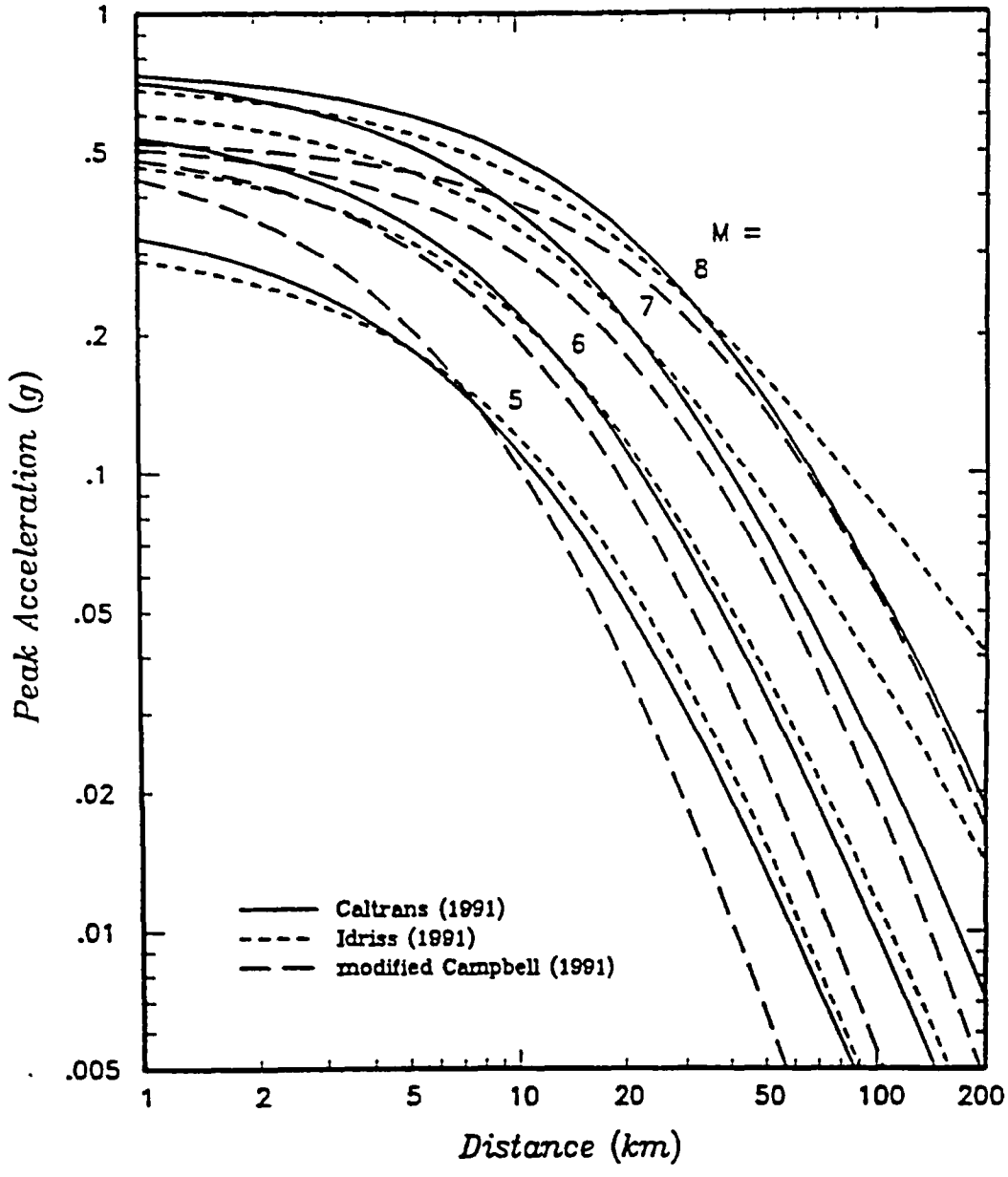

Figure 3-2 Recently developed peak acceleration attenuation relationships for estimating ground motions at rock sites in the western United States compared with the relationship developed for this study.

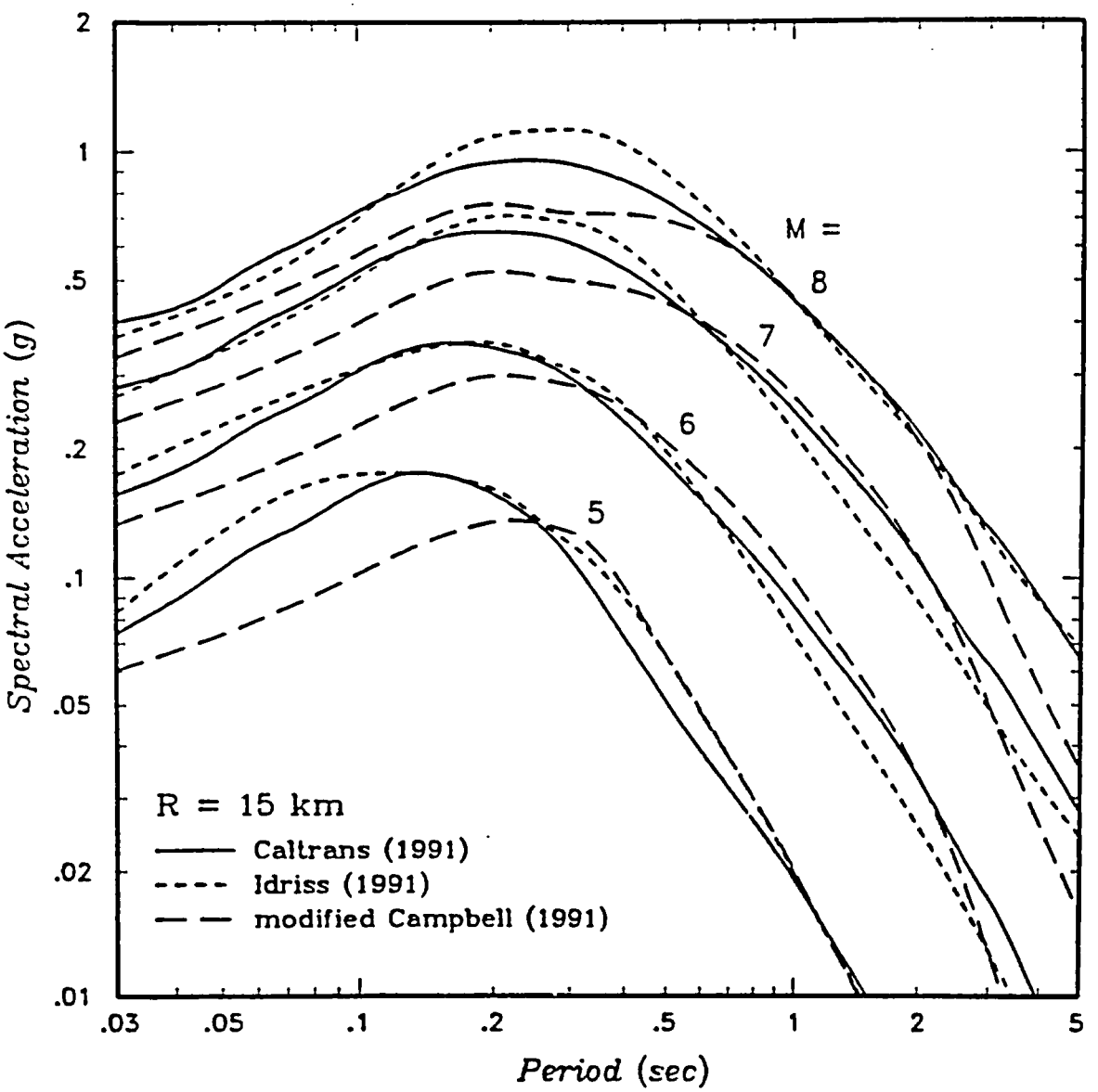

Figure 3-3 Five-percent damped response spectra predicted using two recently developed rock site attenuation relationships compared with those predicted by the relationships developed for this study.

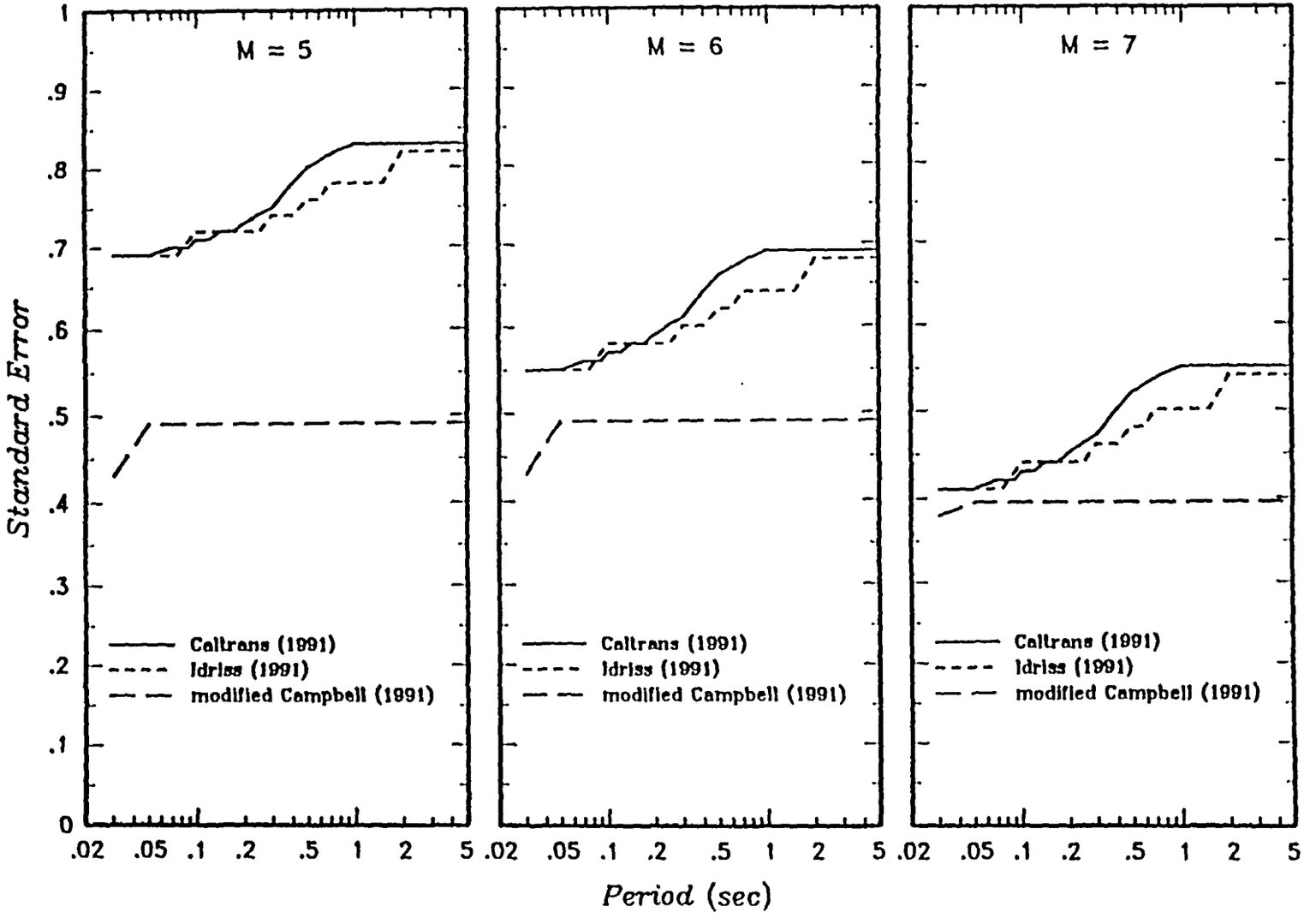

Figure 3-4 Standard errors in the natural log of peak ground motion amplitude for the attenuation relationships compared in Figures 3-1 and 3-2.

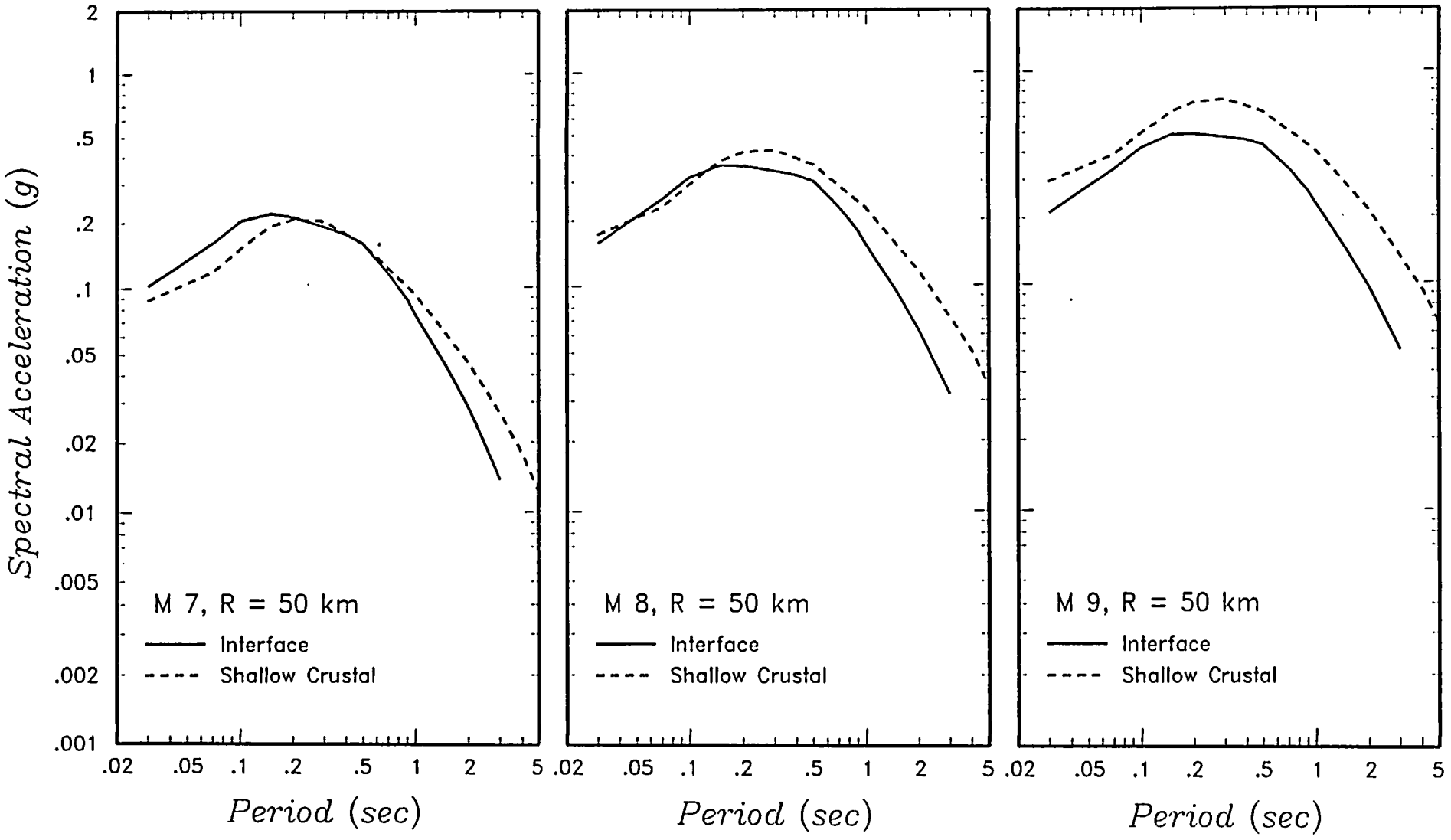

Figure 3-5 Comparison of subduction zone interface and shallow crustal response spectra.

4.0 PROBABILISTIC SEISMIC HAZARD ANALYSIS

4.1 INTRODUCTION

This section describes results of the probabilistic seismic hazard analysis (PSHA) conducted for the Humboldt Bay bridges. A PSHA provides an evaluation of the annual frequency or return periods of exceedance of various levels of rock motion at the bridge site. (Note that the return period for exceedance, in years, is equal to the reciprocal of the annual frequency of exceedance.) The PSHA is carried out by developing a probabilistic model of seismic hazards in the site region that consists of two basic components: (1) a model of the sources of potential future earthquakes, in terms of location and frequency of occurrence of various size events, and (2) a model of the effects at the site in terms of expected ground motion levels and their variability. The methodology employed in this analysis evaluates these elements within a probabilistic framework that addresses both the randomness of the earthquake process and the uncertainty in modeling the process. The methodology for performing the PSHA is summarized below in Section 4.2; the analysis procedure and the basic formulations used to model the occurrence of earthquakes and their resulting ground motions are detailed in Appendix A.

4.2 METHODOLOGY

4.2.1 Approach

The methodology used to conduct a PSHA was developed by Cornell (1968). Current practice is described in detail in several publications, such as by the National Research Council (1988) and Earthquake Engineering Research Institute (1989). The basic formulation involves computing the frequency at which a ground motion parameter, Z, exceeds a specified level, z. The mathematical expression for computing the frequency of exceedance, $\nu(z)$, is given in Equation 2 of Appendix A, and involves assessing four parameters: (1) the frequency of earthquake occurrence, (2) given an earthquake occurrence, the distribution of possible earthquake sizes (magnitudes), (3) given an earthquake of a particular size, the distribution of the possible distances from the site to the rupture, and (4) given an earthquake of a particular size and location, the distribution of possible ground motions at the site. Items (1) and (2) are specified by the earthquake recurrence relationships developed for the seismic sources; item (3) is specified by the locations and geometries of the seismic sources relative to the site; and item (4) is specified by the attenuation relationships for seismic waves. The detailed

characterization of seismic sources in terms of items (1) through (3) is described in Section 2. Section 3 presents the attenuation relationships used to describe ground motions as a function of magnitude and source-to-site distance.

The PSHA formulation outlined above attempts to evaluate the likelihood that various levels of seismic loading will affect a structure by using a set of probability models to model the randomness of the physical process of earthquake generation and seismic wave propagation. Any evaluation will involve uncertainty in defining the models and model parameters that are most appropriate for performing the analysis. In the methodology used in this study, these uncertainties are modeled directly within the analytical framework. The uncertainty in characterizing the seismic sources and characterizing attenuation was modeled using logic trees (see Appendix A for a discussion of logic trees), which provide a simple probabilistic model to define distributions for input models and model parameters on the basis of the present state of scientific uncertainty. Section 2 describes the development of the distributions for seismic source parameters and documents the basis for the assigned probability distributions. Section 3 describes the treatment of uncertainty in modeling ground motions. These distributions are convolved in the analysis to provide a computed distribution for the frequency of exceedance, $\nu(z)$ (see Equations 4, 5, and 6 of Appendix A). The resulting distribution provides a quantitative assessment of the uncertainty in assessed seismic hazard.

4.2.2 Analysis Procedure

The seismic hazard at the Humboldt Bay bridges was computed using the seismic sources shown on Figures 2-10 (Gorda plate), 2-11 (crustal source zones), 2-17 (Interface), and 2-20 (crustal faults). Individual faults were modeled as segmented planar features; earthquake rupture surfaces were located randomly on the fault plane, distributed uniformly along the fault length, and distributed in depth accordingly to the observed hypocentral depth pattern. Within distributed seismicity zones, earthquakes were assumed to occur randomly following a uniform distribution in map view and the empirically observed focal depth distribution. The size of an individual earthquake rupture was computed using an empirical relationship between earthquake magnitude and rupture area derived from empirical data (Wells and Coppersmith, in press). The specific relationship used was $ln(A) = 2*M - 7.12$.

The seismic hazard was computed considering the contributions from events of magnitude M 5.0 and larger because smaller events were not considered to pose a significant hazard to well engineered structures. Hazard computations were made for peak horizontal ground acceleration and 5%-damped spectral accelerations at periods of 0.1, 0.2, 0.3, 0.5, 1.0, and 3.0 seconds. Calculations were made for the parameter sets defined by each end branch of the seismic hazard model logic trees discussed in Section 2. The hazard was computed for a location at the mid point of the three bridge spans. Because the bridges are roughly parallel with the Little Salmon River and Mad River fault zones, the hazard should not vary significantly spatially along the bridges.

4.3 ANALYSIS RESULTS AND SENSITIVITY

Figure 4-1 presents the computed hazard curves for the Humboldt Bay bridges site for peak ground acceleration and spectral acceleration at a period of 1.0 second. Shown are the computed mean hazard curves and the 5^{th}- 15^{th}-, 50^{th}-, 85^{th}-, and 95^{th}-percentiles of the distributions for the frequency of exceeding various levels of ground motion computed from the defined uncertainty in the seismic hazard model parameters. The uncertainty in the computed hazard increases slightly as the spectral period increases from peak ground acceleration (equivalent to spectral acceleration at a period of 0.03 sec) to 1.0 seconds. The uncertainty in the computed hazard increases with increasing ground motion level.

Figure 4-2 shows the contributions of events in various magnitude intervals to the computed hazard at return periods of 100 and 1,000 years (annual frequencies of exceedance of 10^{-2} and 10^{-3}). For higher frequency ground motions (spectral periods less than about 0.3 seconds) the hazard at the Humboldt Bay bridges results from events over a wide range of magnitudes. At longer periods the hazard is dominated by events in the magnitude range of 7 to 7.5 occurring on the Little Salmon River fault.

Figure 4-3 shows the contributions of the various sources to the total hazard at the Humboldt Bay bridges site, assuming that the Little Salmon River fault acts as a separate seismic source. The results indicate that the Little Salmon River fault and the Gorda plate are the dominant source over a wide range of ground motions. Figure 4-4 shows the contributions of the various sources assuming that the Little Salmon River fault slips synchronously with the plate interface.

In this scenario the Gorda plate and North American crustal sources are the dominant sources of the hazard. The combined Little Salmon/interface source has a contribution to hazard similar to that for the interface alone in the separate model (Figure 4-3) because the recurrence rate and attenuation models for the interface source define the hazard from this combined source.

Figure 4-5 compares the total hazard at the bridge sites obtained using the two alternative representations of the Little Salmon River fault (see Figure 2-24). As can be seen, considering the Little Salmon as a separate source results in higher hazard. The higher hazard in this case occurs because the Little Salmon fault is considered to produce earthquakes in addition to those occurring on the plate interface, and is thus an additive source of seismic hazard.

Figure 4-6 shows the distribution in hazard from the interface source based on the source characterization logic tree shown in Figure 2-14 assuming that it slips separately from the Little Salmon River fault. As can be seen, the uncertainty in the hazard from this source is significantly broader than that for the total hazard. Figures 4-7 and 4-8 show the effect of choice of attenuation relationship and magnitude distribution, respectively, on the computed hazard from the interface. The choice of attenuation relationship has opposite effects at short and long periods of vibration. At short periods, the use of the interface relationship results in higher hazard because of the larger ground motion variance and the contribution from distant events. At longer periods, the use of the shallow crustal attenuation relationships results in higher hazard because these relationships predict larger long period motion than do the interface relationships for the same magnitude event (see Figure 3-5). The choice of magnitude distribution has the greatest impact at low ground motion levels and shorter period motions where the hazard is dominated by moderate magnitude earthquakes (Figure 4-2) and the various recurrence models predict vastly different recurrence rates for these events.

Overall, the distribution in the computed hazard shown in Figure 4-1 results from the defined uncertainty in the seismic hazard model logic tree (Section 2). Examination of the results indicates that the largest contributions to uncertainty are in assessment of the form of the magnitude distribution, the method for estimating earthquake recurrence, earthquake frequency, and the type of slip on the Little Salmon fault. At longer periods of ground motion the effect

of uncertainty in magnitude distribution diminishes due to the reduced contribution of moderate magnitude events.

4.4 EQUAL-HAZARD SPECTRA

Equal-hazard spectra for the Humboldt Bay bridges site were developed by obtaining the ground motion levels at each of the 7 spectral periods analyzed corresponding to specified frequencies of exceedance and constructing a smooth spectral shape through these spectral ordinates. Figure 4-9 presents 5%-damped equal-hazard pseudo velocity response spectra developed for return periods of 100, 300, 500, 1,000, and 2,000 years (annual exceedance frequencies of 0.01, 0.0033, 0.002, 0.001, 0.0005). These spectra show a relative increase in the long period content of the ground motions (i.e., a broadening of the spectra) as the return period increases, reflecting an increase in the contributions of larger magnitude earthquakes to the long period hazard (Figure 4-2).

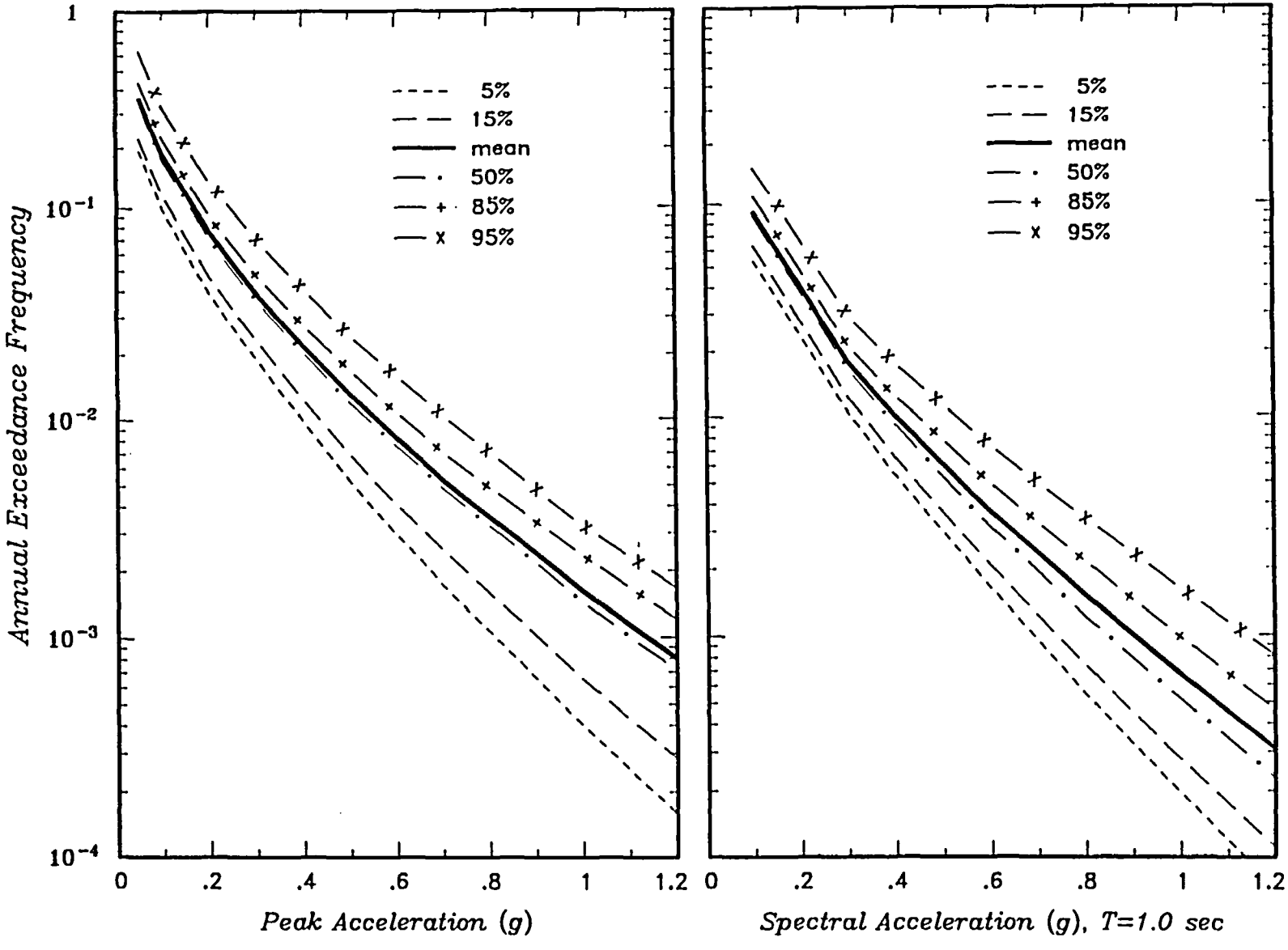

Figure 4-1 Computed hazard for Humboldt Bay bridges. Shown are the computed 5th- to 95th-percentiles of the distribution in frequency of exceedance.

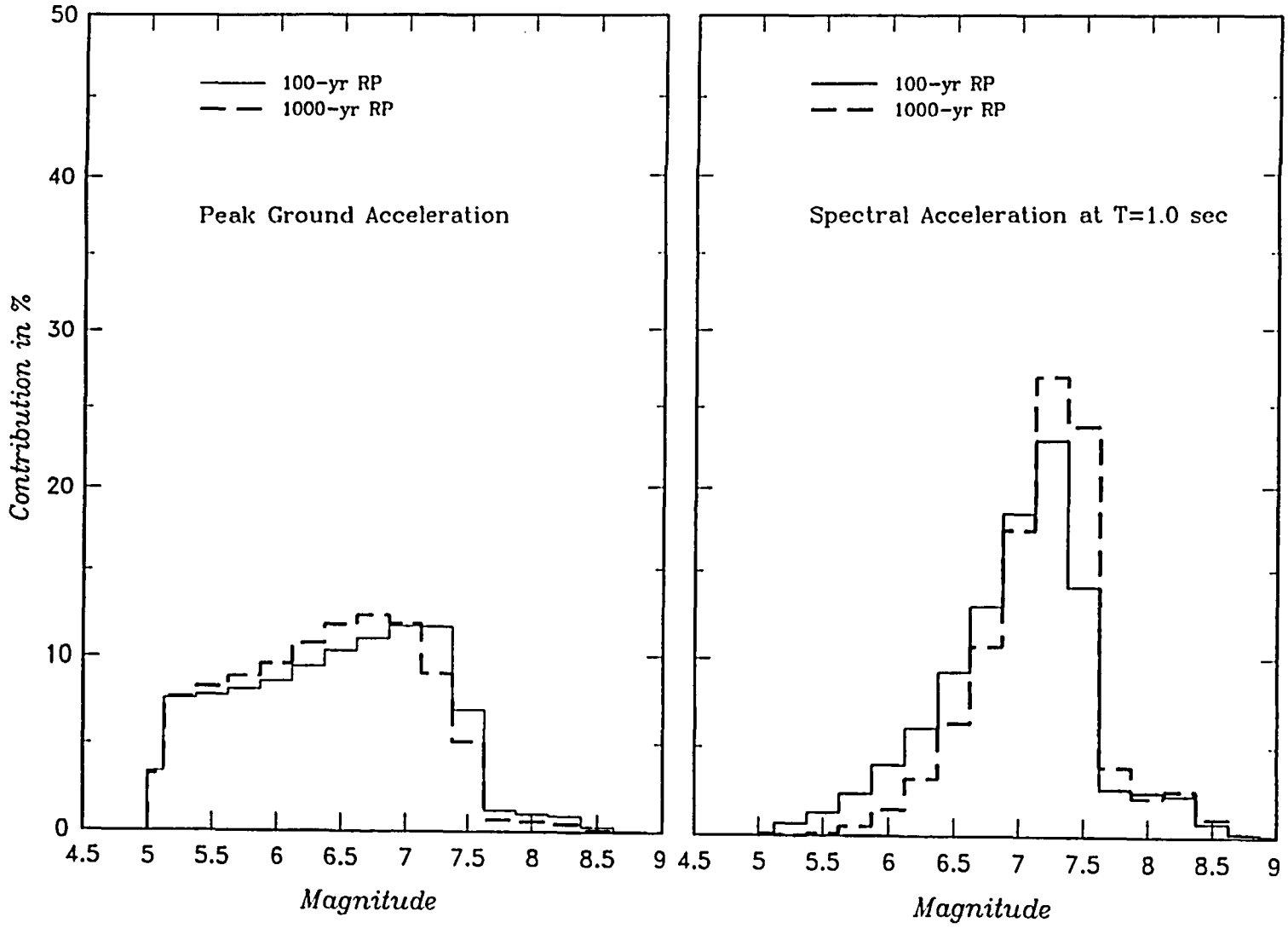

Figure 4-2 Contributions of events of various magnitudes to the total hazard for the Humboldt Bay bridges.

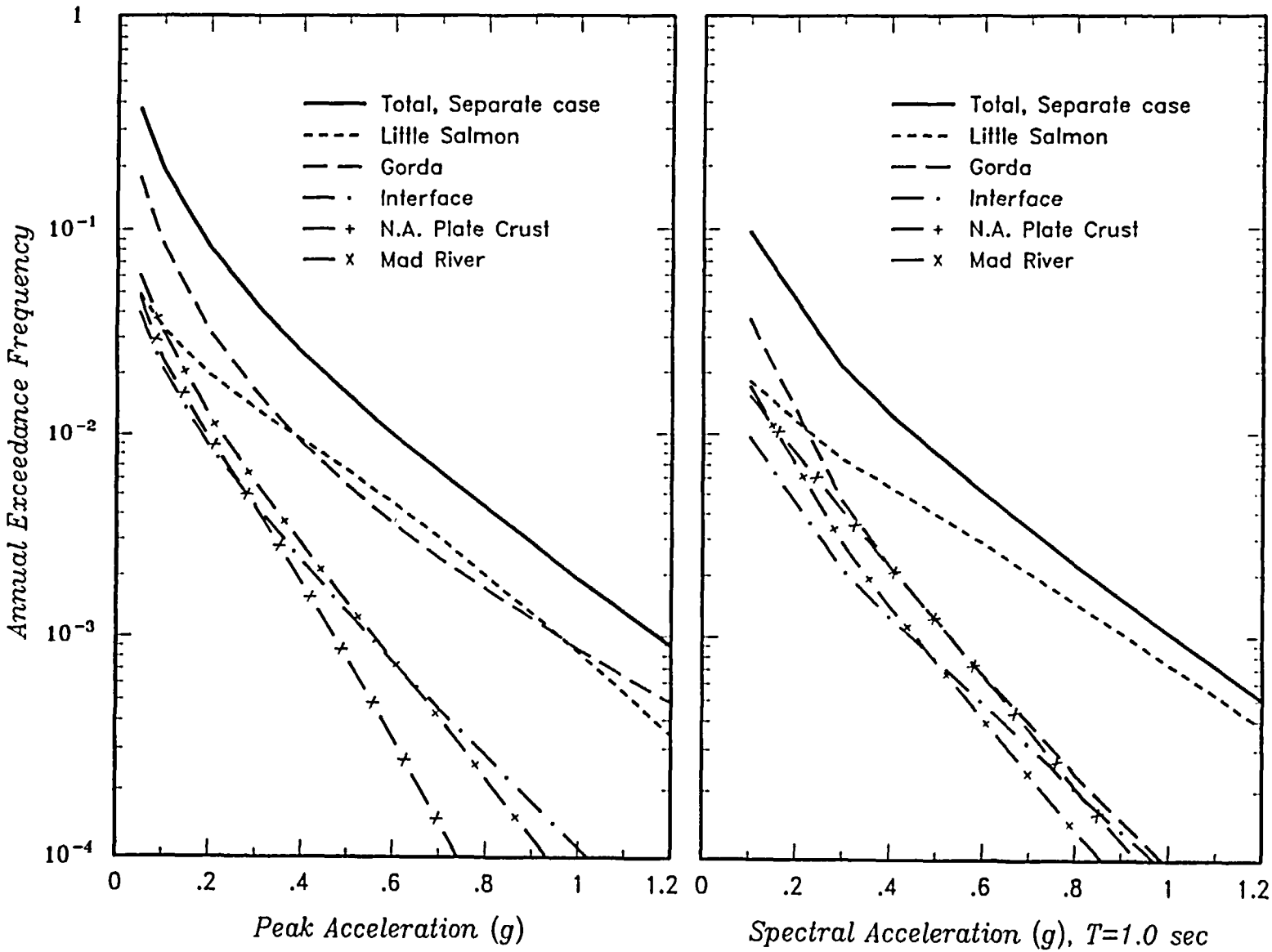

Figure 4-3 Contributions of various sources to the total hazard for the Humboldt Bay bridges assuming the Little Salmon acts as a separate source.

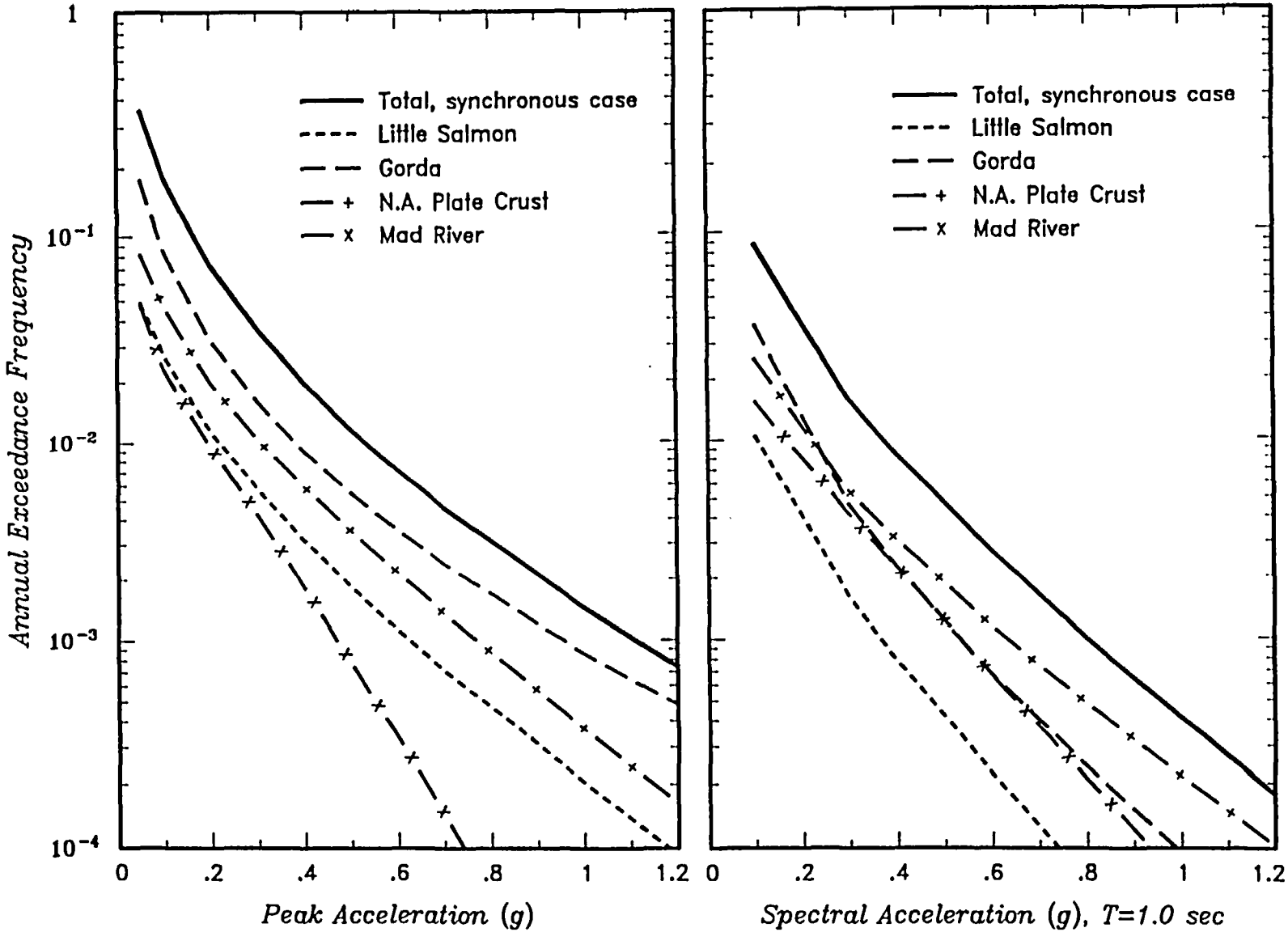

Figure 4-4 Contributions of various sources to the total hazard for the Humboldt Bay bridges assuming the Little Salmon slips synchronously with the interface.

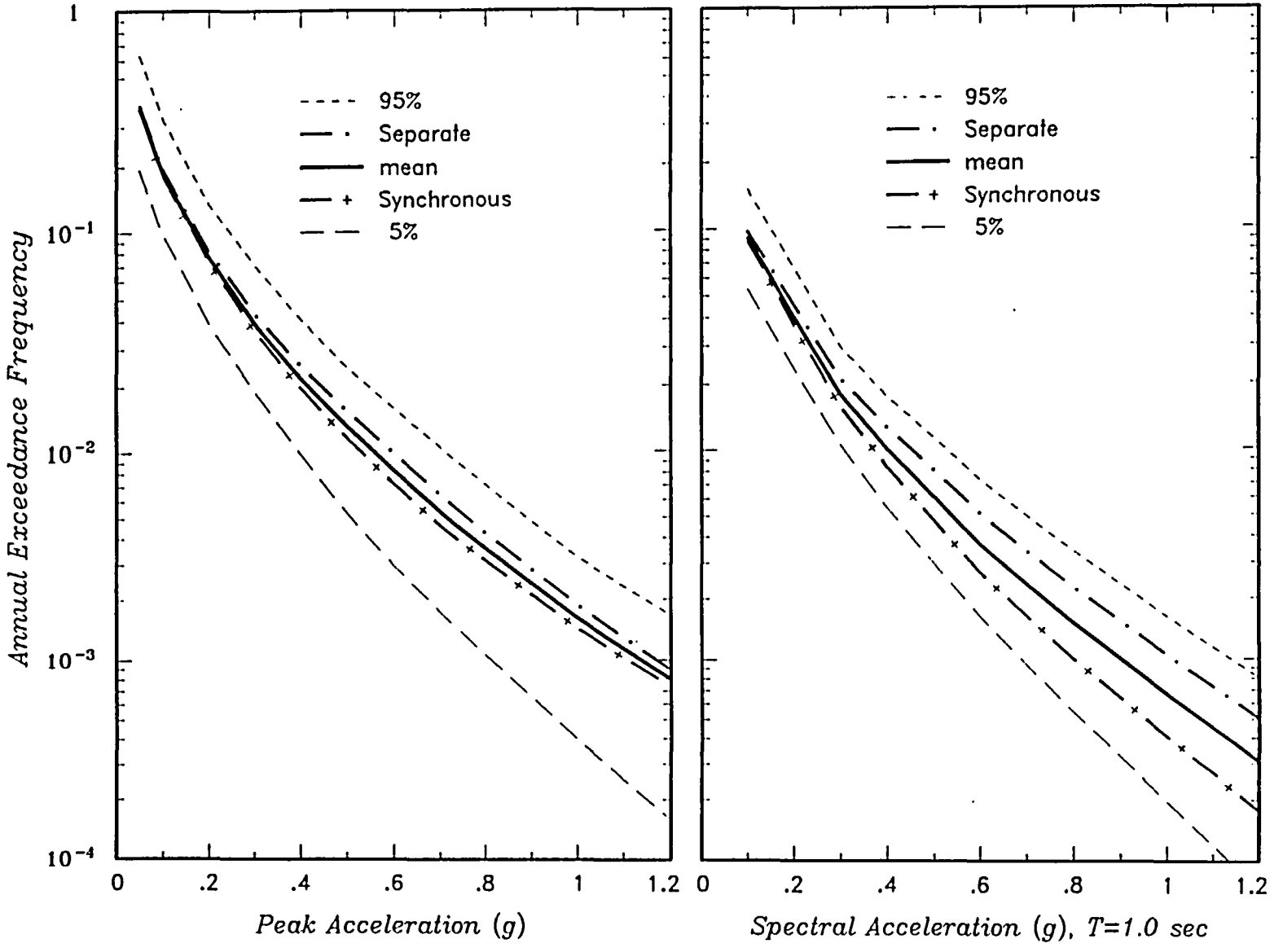

Figure 4-5 Effect of choice of slip model for Little Salmon River fault slip on total hazard.

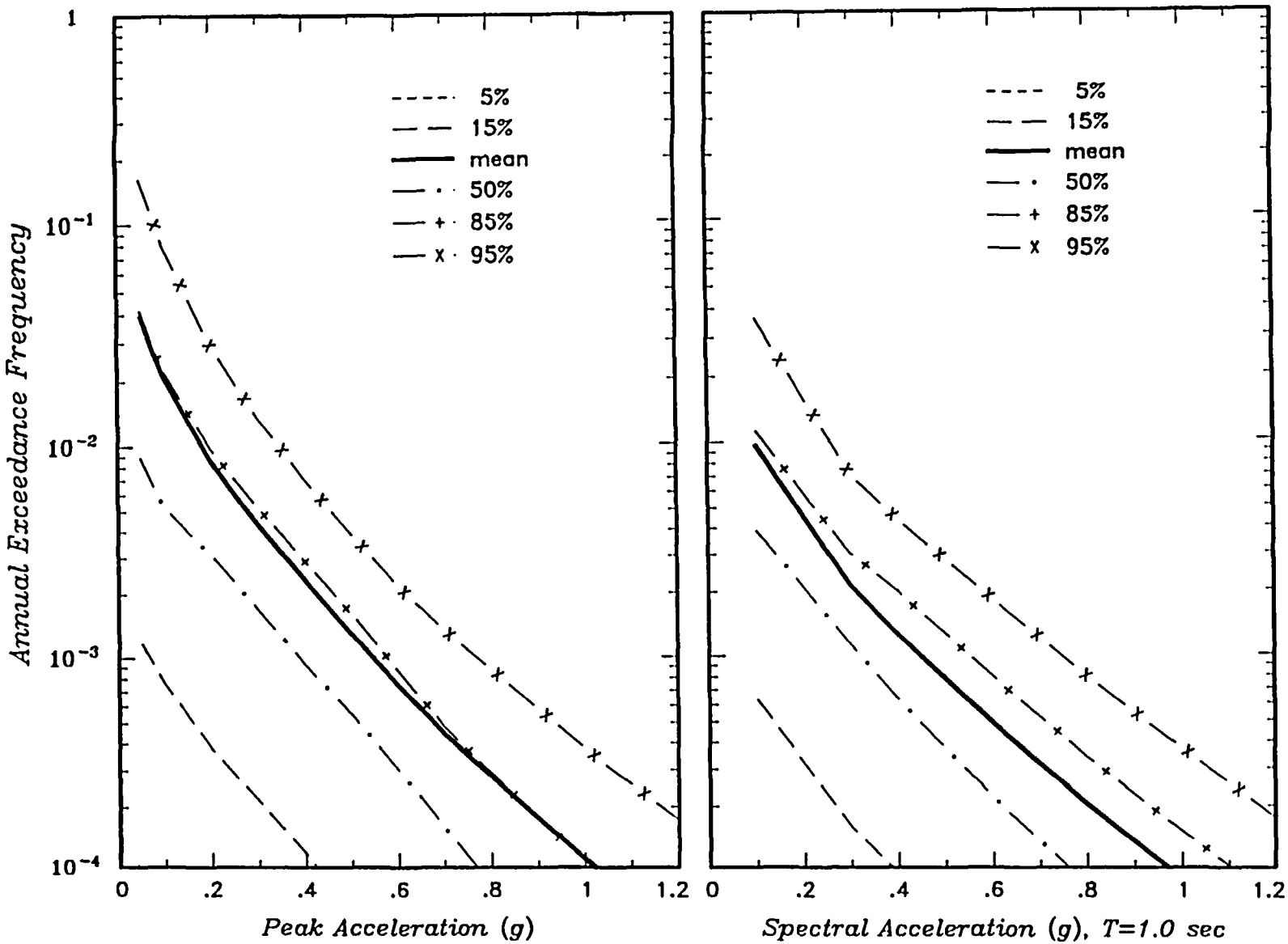

Figure 4-6 Computed hazard at the Humboldt Bay bridges from the interface source acting as a separate source. Shown are the computed 5th- to 95th-percentiles of the distribution in frequency of exceedance. (Note the 5th-percentile is not visible as the frequency of exceedance is zero.)

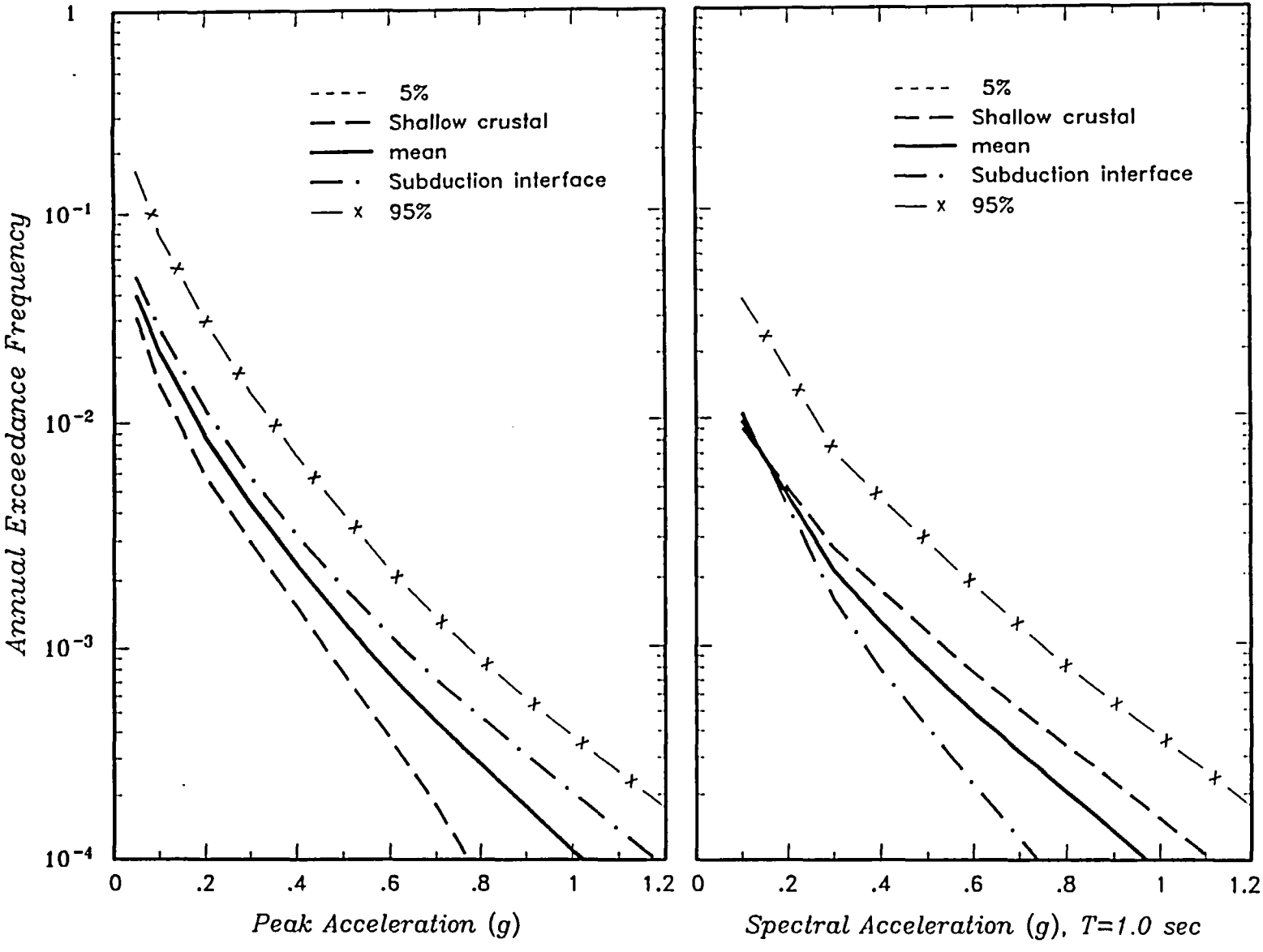

Figure 4-7 Effect of choice of attenuation relationship on computed hazard from the interface source.

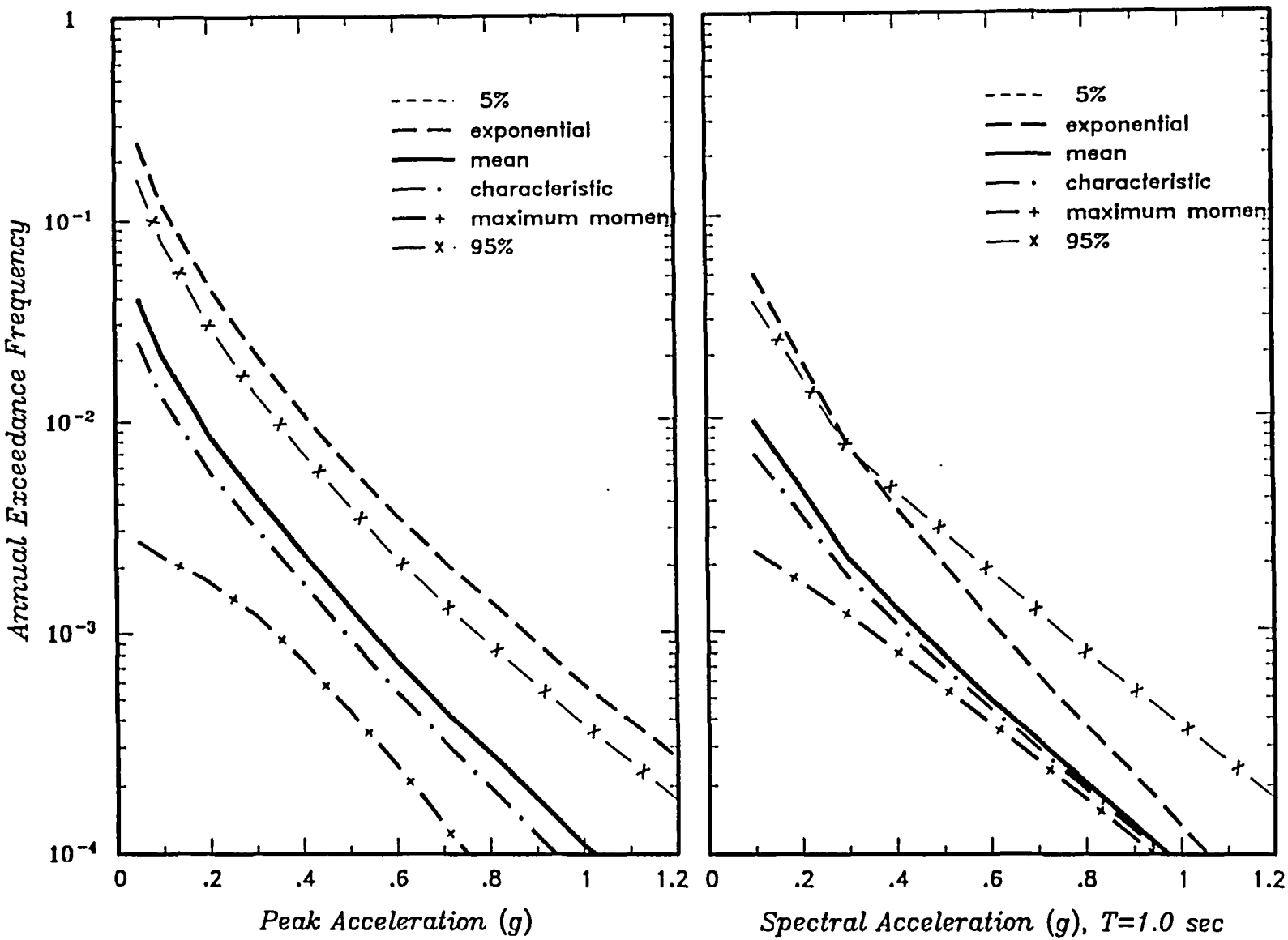

Figure 4-8 Effect of choice of magnitude distribution on computed hazard from the interface source.

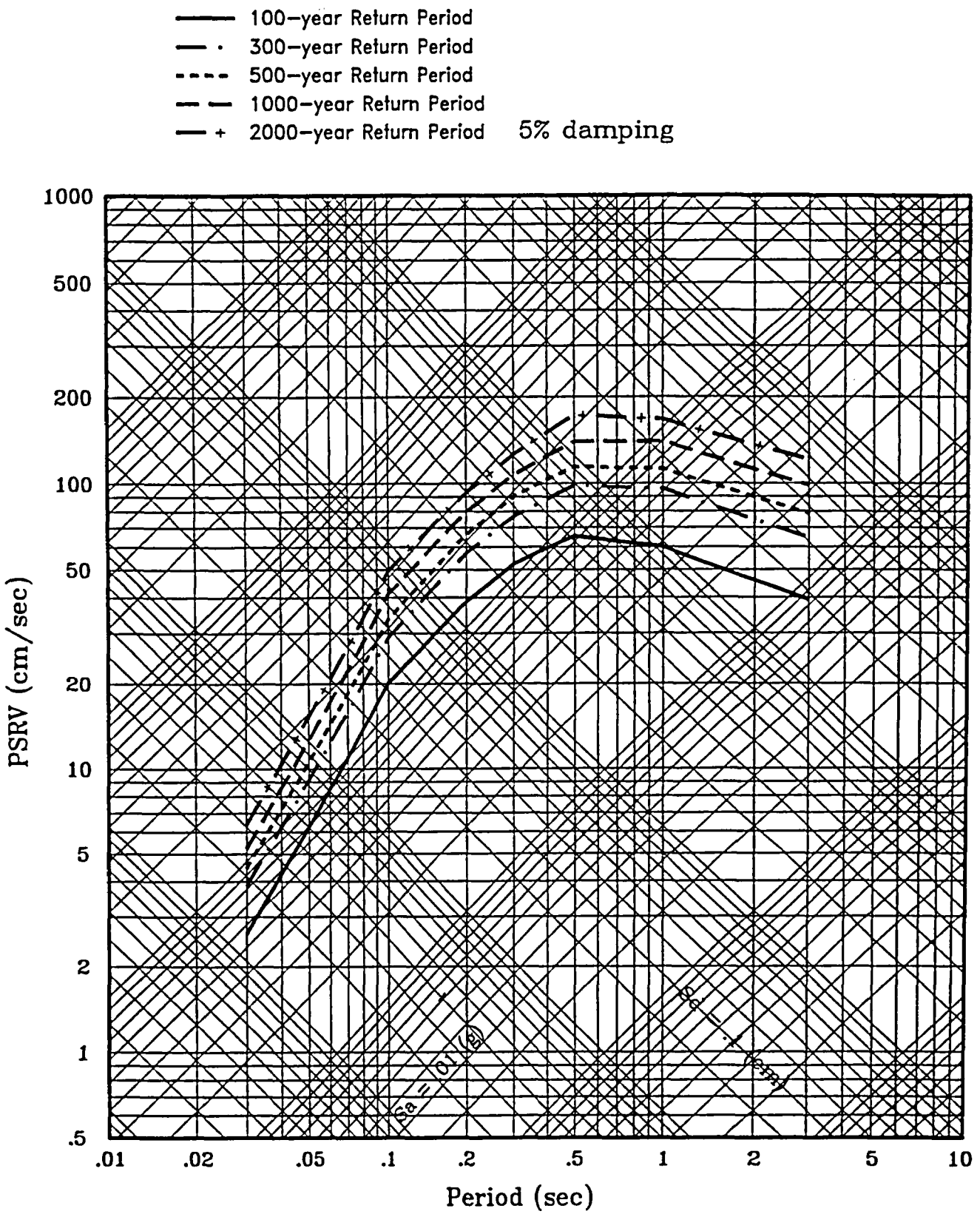

Figure 4-9 Equal-hazard spectra for Humboldt Bay bridges.

5. DETERMINISTIC ESTIMATES OF ROCK MOTIONS

5.1 SELECTED EARTHQUAKES

Deterministic ground motion estimates at the Humboldt Bay bridges have been developed for those maximum credible earthquakes (MCE's) that would produce the strongest ground shaking at the bridge site in terms of horizontal and vertical peak ground acceleration, horizontal and vertical response spectra (5 percent damping), and duration of strong shaking. The following are the selected MCE's:

Selected MCE's: Humboldt Bay Bridges

Source	MCE (Mw)	Closest Distance (km)
Little Salmon Fault (Shallow Crustal)	7.5	5
Subducting Gorda Plate (Intraslab)	7.5	20
Subducting Gorda Plate (Interface)	8.5 - 9.0	15

5.2 ESTIMATED GROUND MOTIONS FOR THE SELECTED EARTHQUAKES

Using the preferred attenuation relationships for shallow crustal earthquakes (see Sections 3.1.1 and 3.2.1), and for subduction zone earthquakes (see Section 3.3 and 3.4) the estimated median PGA's are the following:

	Estimated Median Peak Ground Acceleration (g's)	
Source/MCE/Distance (km)	Horizontal PGA	Vertical PGA
Little Salmon Fault, M_w 7.5, 5 km	0.68	0.56
Gorda Plate (Intraslab Event) M_w 7.5, 20 km	0.35	0.16

Gorda Plate (Interface Event) M 8.5, 15 km	0.27	0.16
Gorda Plate (Interface Event) M 9.0, 15 km	0.29	0.20

Using the attenuation relationships for horizontal response spectral acceleration (see relationships in Table 3-1 for shallow crustal earthquakes and in Table 3-4 for subduction zone earthquakes), the median and 84th percentile response spectra were computed at the bridge site for the selected earthquakes on the Little Salmon Fault and the intraslab and interface earthquakes on the subducting Gorda plate. These spectra are shown in Figures 5-1 through 5-4. The median response spectra shown in Figures 5-1 through 5-4 are compared in Figure 5-5. As can be noted in this figure, the response spectral values corresponding to the MCE on the Little Salmon Fault substantially exceed (by about a factor of 2 to 3) the spectral values corresponding to the subduction zone events for all periods examined.

The corresponding vertical median and 84th percentile response spectra for the selected earthquakes (computed using the attenuation relationships for the vertical response spectral acceleration given in Tables 3-3 and 3-5) are shown in Figures 5-6 through 5-9, respectively. The median response spectra are compared in Figure 5-10.

5.3 DURATION OF STRONG SHAKING

The duration of strong shaking for the postulated MCE events are defined herein in terms of (1) "bracketed duration" as originally defined by Bolt (1973), specifically as the length of time between the first and last accelerations of the accelerogram exceeding 0.05 g, and (2) "significant duration" of shaking defined as the time required to build up from 5 to 95 percent of the energy of an accelerogram as originally proposed by Trifunac and Brady (1975).

Chang and Krinitzky (1977) developed empirical relationships for the "bracketed duration" for rock and soil site conditions as a function of magnitude and distance. Dobry and others (1978) provide estimates of "significant duration" for rock and soil conditions as a function of magnitude. Using the relationships for rock site conditions provided by Chang and Krinitzky

(1977) and Dobry and others (1978), estimates of the duration of strong shaking for the potentially dominant events are as follows:

Source/MCE/Distance (km)	Duration of Strong Shaking (seconds) "Bracketed"	"Significant"
Little Salmon Fault, M_w 7.5, 5 km	26 - 27	26
Gorda Plate (Intraslab Event), M_w 7.5, 20 km	20	26
Gorda Plate (Interface Event), M_w 8.5 - 9.0, 15 km	≥40	≥40

5.4 COMPARISON OF PROBABILISTIC AND DETERMINISTIC ROCK MOTIONS

The results of the probabilistic seismic hazard analyses conducted for the Humboldt Bay bridges are presented in Section 4. For this bridge 5%-damped equal-hazard response spectra were developed for return periods of 100, 300, 500, 1000, and 2000 years (annual exceedance frequencies of 0.01, 0.0033, 0.002, 0.001, and 0.0005). The equal-hazard spectra are compared to the deterministically-estimated response spectra for the MCE on the Little Salmon fault in Figure 5-11. The return periods associated with the median and 84th percentile deterministic response spectra for the selected earthquakes are summarized in Table 5-1.

5.5 SELECTION OF DESIGN EVENTS AND ASSOCIATED ROCK MOTIONS AND TARGET SPECTRA

The probabilistic and deterministic estimates of rock motions at the site of the Humboldt Bay bridges were evaluated jointly with Caltrans. Based on these evaluations, the design earthquake was selected to be the MCE on the Little Salmon fault (M_w 7.5). The corresponding target response spectra for acceleration time history development were selected to be at the 84th percentile level. At this level, the response spectral values have return periods in the range of about 500 to 1500 years, with the return period increasing with period

of vibration (see Figure 5-11 and Table 5-1). At periods of vibration equal to or greater than 1.0 second, the return period is approximately 1500 years.

The 84th percentile peak rock motion parameters (PGA, PGV, and PGD) and median values for strong motion duration for this design event are summarized in Table 5-2. Note that the PGV and PGD values are given as a range to be used as guideline values when developing spectrum-compatible acceleration time histories. The PGV and PGD values were estimated using the relationships by Sadigh and Akky (1989).

The Humboldt Bay bridges are located at a closet distance of about 5 km from the Little Salmon fault which is a reverse fault dipping northeast towards the bridges. Examination of the alignment of the bridges relative to the orientation of the Little Salmon fault indicates that the transverse direction of each bridge is approximately perpendicular and the longitudinal direction of each bridge is approximately parallel to the fault strike.

As noted in Appendix E, for periods greater than 2 seconds, the horizontal component of motion perpendicular to the fault strike is found to be significantly larger than the component parallel to the fault strike for ground motions associated with nearby, large vertical strike-slip earthquakes. The fault movement on the Little Salmon fault is expected to be dominantly thrust with some component of strike-slip movement. It is expected that for thrust earthquakes the stronger component for the long-period motions will also be in the direction perpendicular to the fault strike.

Although the studies in Appendix E address strike-slip earthquakes, we have assumed that the ground motion differences between the horizontal components will be similar for thrust earthquakes. Therefore, it was decided to increase the response spectrum for the long-period component of ground motion in the transverse bridge direction by 15 percent. The resulting target spectra for the longitudinal and transverse components of the design event on the Little Salmon fault are shown in Figure 5-12. The corresponding vertical target spectrum is presented in Figure 5-13. Note that the target spectrum for the transverse component has the same spectral values as the longitudinal component for periods up to 0.4 seconds, and is 15 percent higher for periods equal to or greater than 2 seconds.

TABLE 5-1

RETURN PERIODS ASSOCIATED WITH THE MEDIAN AND 84th PERCENTILE DETERMINISTIC RESPONSE SPECTRA FOR THE DOMINANT EARTHQUAKES

HUMBOLDT BAY BRIDGES

	Return Period (yrs) in the Structural Period Range:		
Source / MCE / Level	0.05 to 0.2 sec	0.2 to 1.0 sec	1.0 to 7.5 sec
Little Salmon Fault / M 7.5 at 5 km / median	100 - 200	200 - 300	300±
Little Salmon Fault / M 7.5 at 5 km / 84th%	300 - 700	700 - 1300	1300- 1600

TABLE 5-2

PEAK GROUND ACCELERATION, VELOCITY, AND DISPLACEMENT AND DURATION OF STRONG SHAKING ASSOCIATED WITH THE SELECTED DESIGN EVENT

HUMBOLDT BAY BRIDGES

Selected Design Event	Component	PGA (g)	PGV (cm/sec)	PGD (cm)	Duration (sec) (1) (2)
Little Salmon Event	Longitudinal[3]	0.99	108 - 132	51 - 63	27 26
M_w = 7.5, R = 5 km	Transverse[3]	0.99	121 - 149	59 - 73	27 26
	Vertical	0.90	65 - 79	38 - 46	27 26

Notes:

(1) "Bracketed duration", as originally defined by Bolt (1973), is the length of time between the first and last accelerations of the accelerogram exceeding 0.05g.

(2) "Significant duration" defined as the time between 5 to 95 percent of energy measure by $\int a^2(t)dt$.

(3) Longitudinal refers to direction parallel to the alignment of the bridge. Transverse refers to direction perpendicular to the alignment of the bridge.

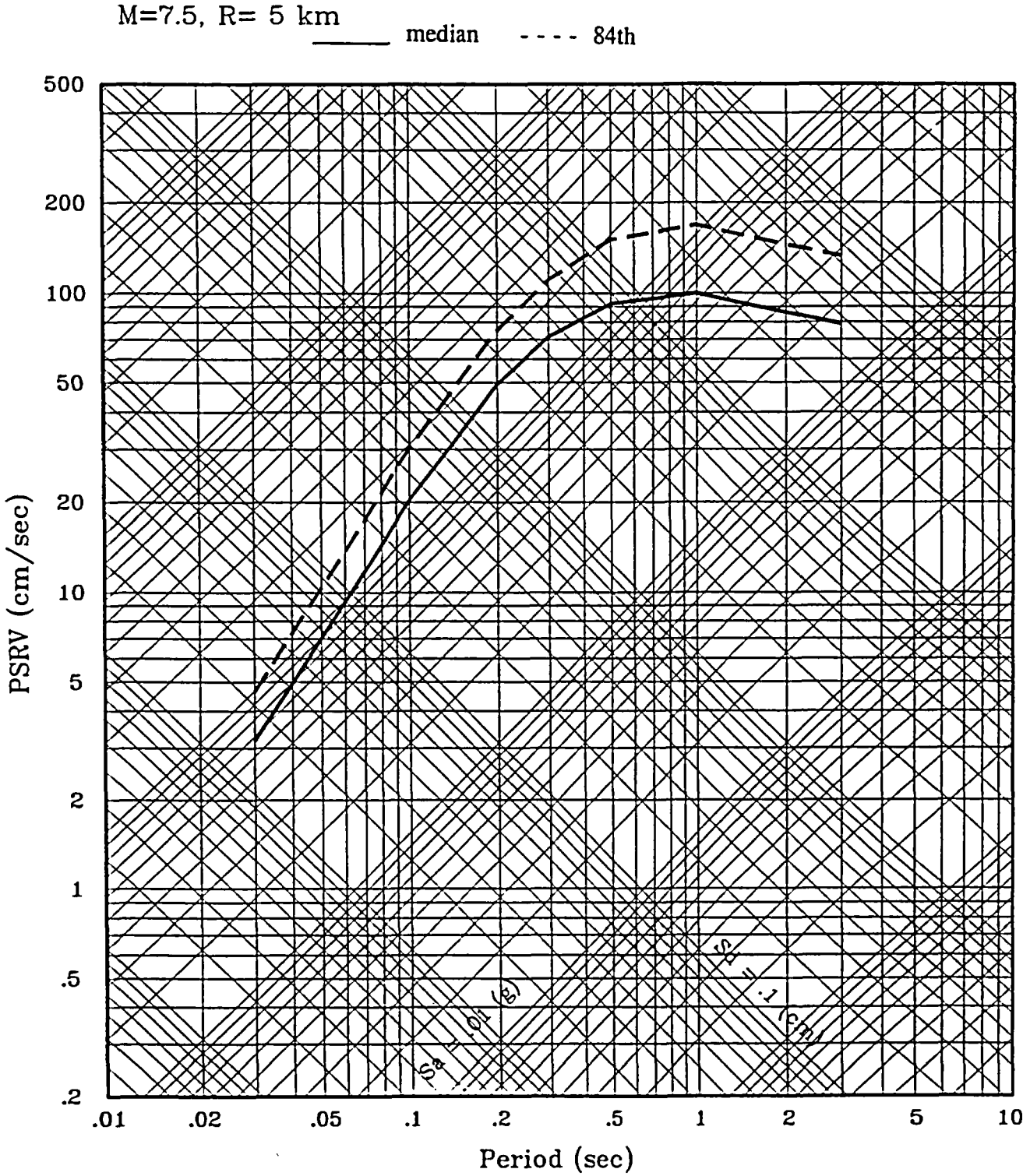

Figure 5-1 Humboldt Bay Crossing, MCE on Little Salmon Fault (horizontal motions)

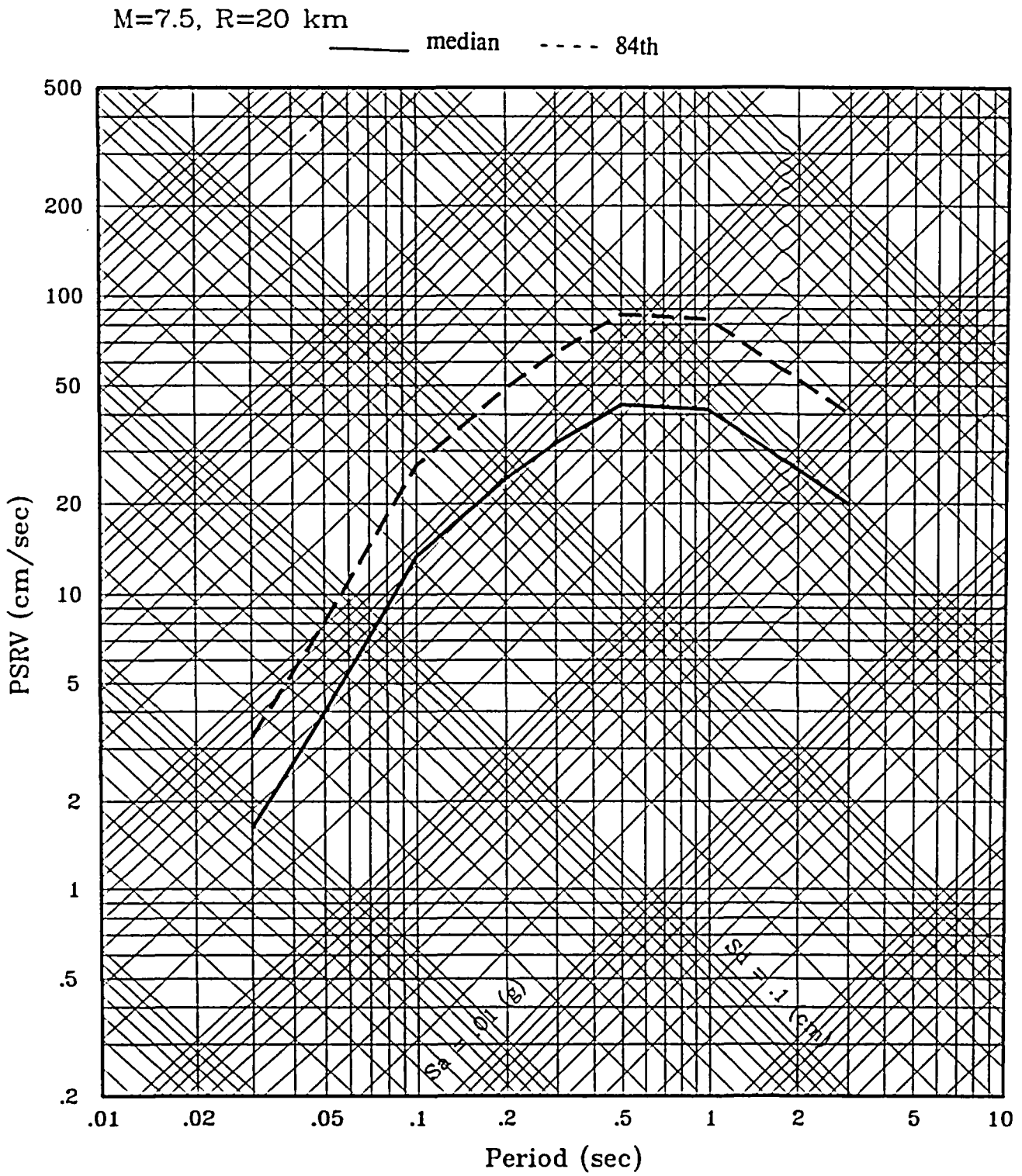

Figure 5-2 Humboldt Bay Crossing, Intraslab Event (horizontal motions)

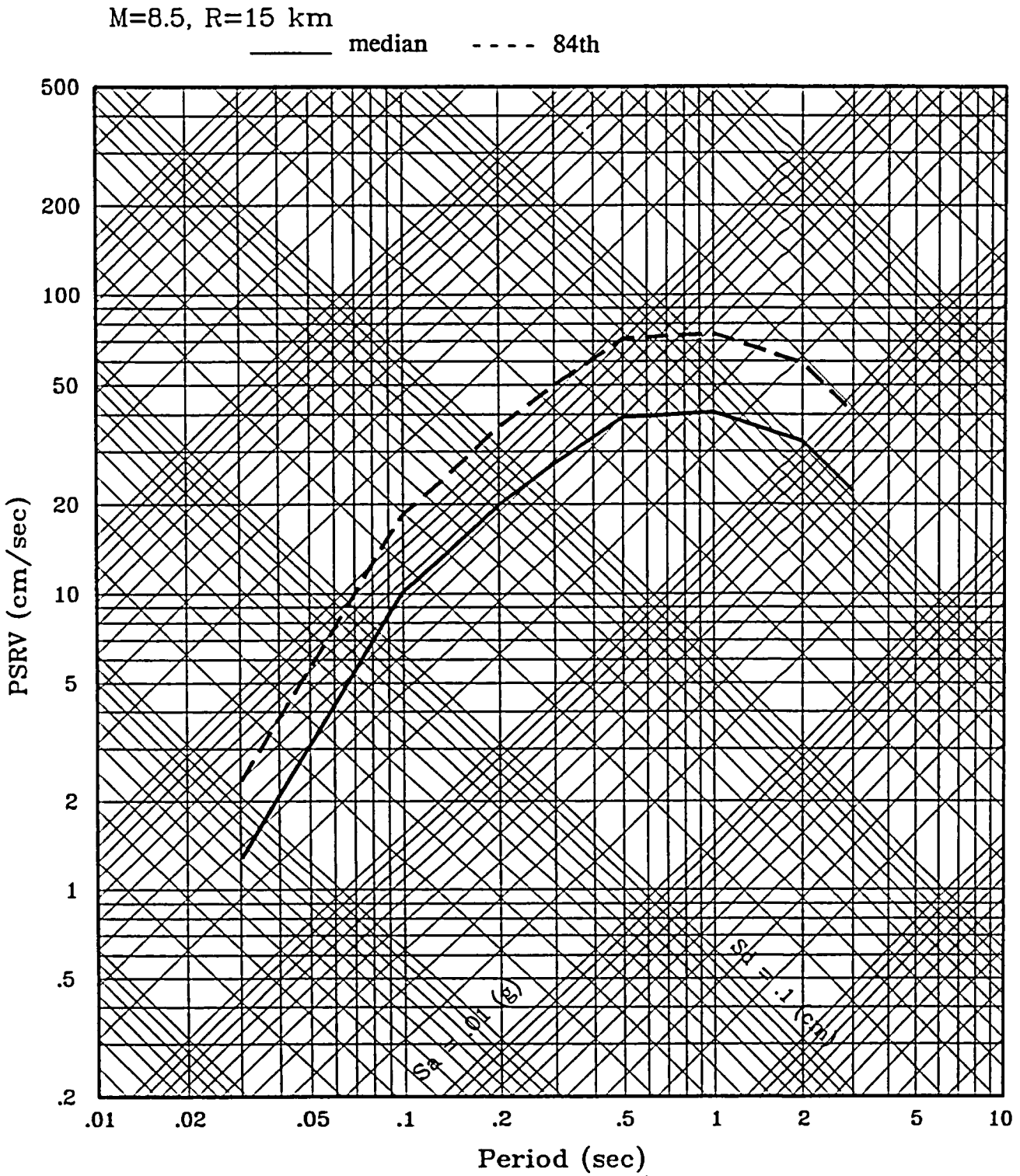

Figure 5-3 Humboldt Bay Crossing, Interface Event (horizontal motions)

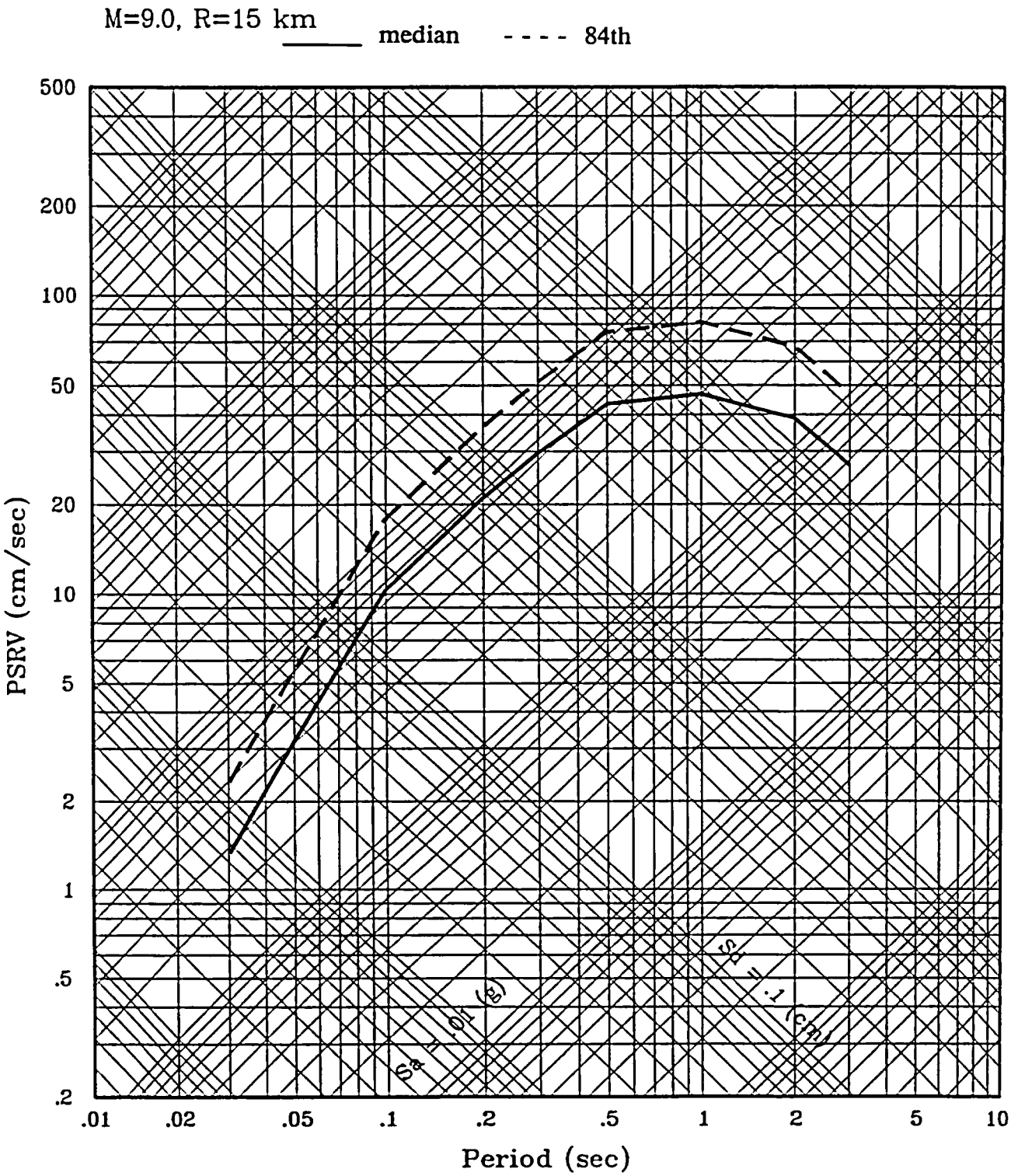

Figure 5-4 Humboldt Bay Crossing, Interface Event (horizontal motions)

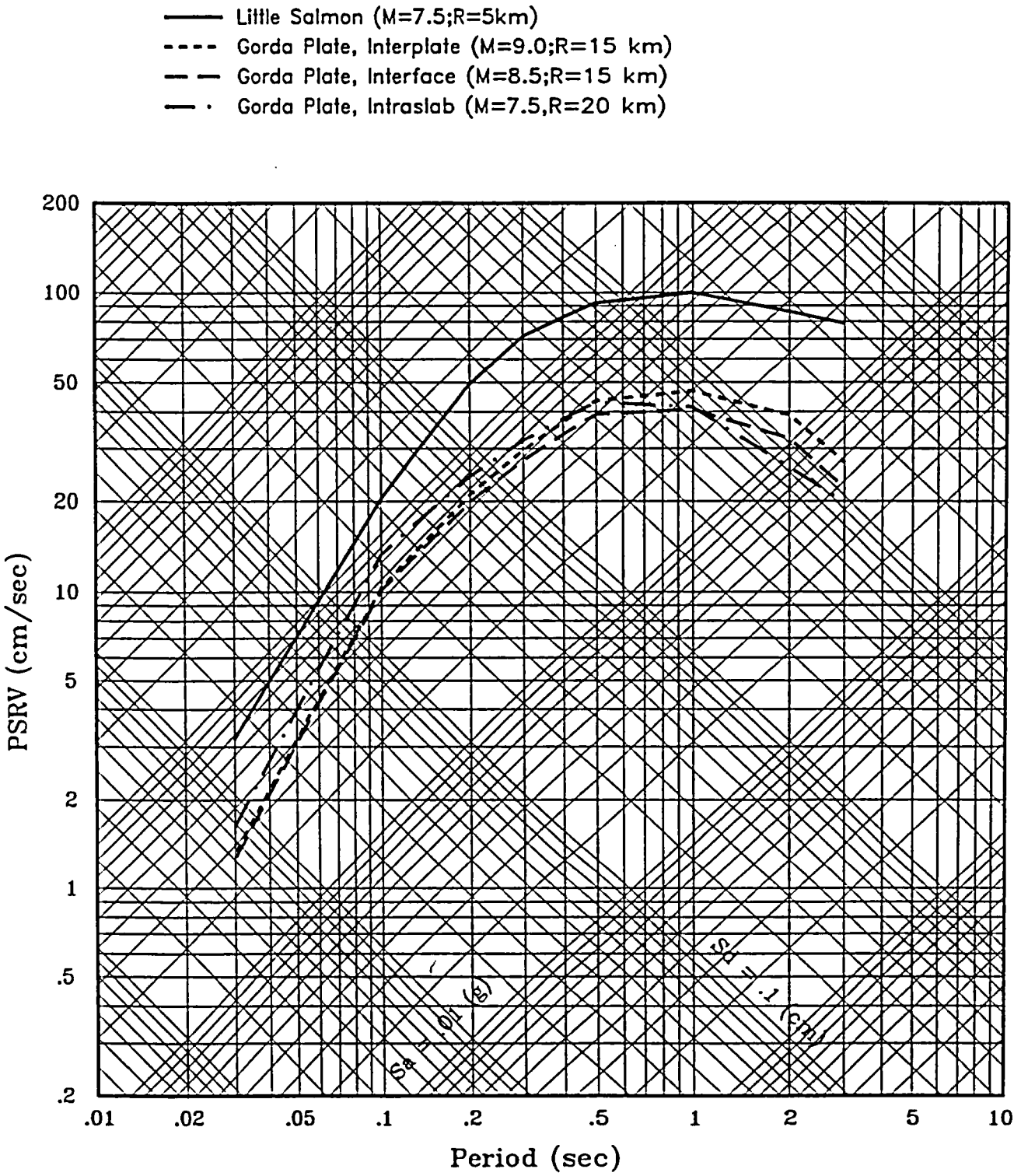

Figure 5-5 Humboldt Bay Crossing, Comparison between different sources (horizontal motions)

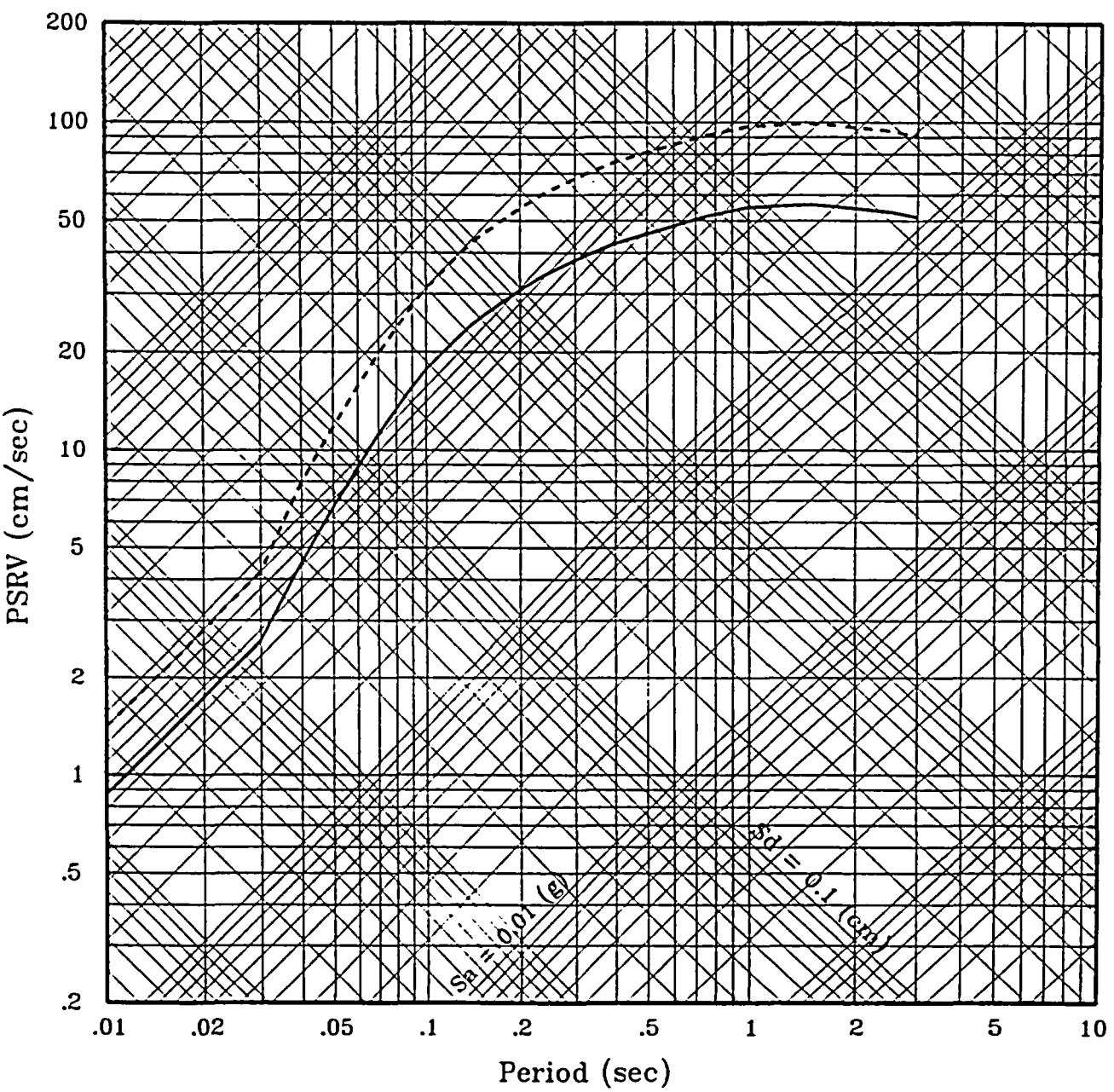

Figure 5-6 Humboldt Bay Crossing, MCE on Little Salmon Fault (vertical motions)

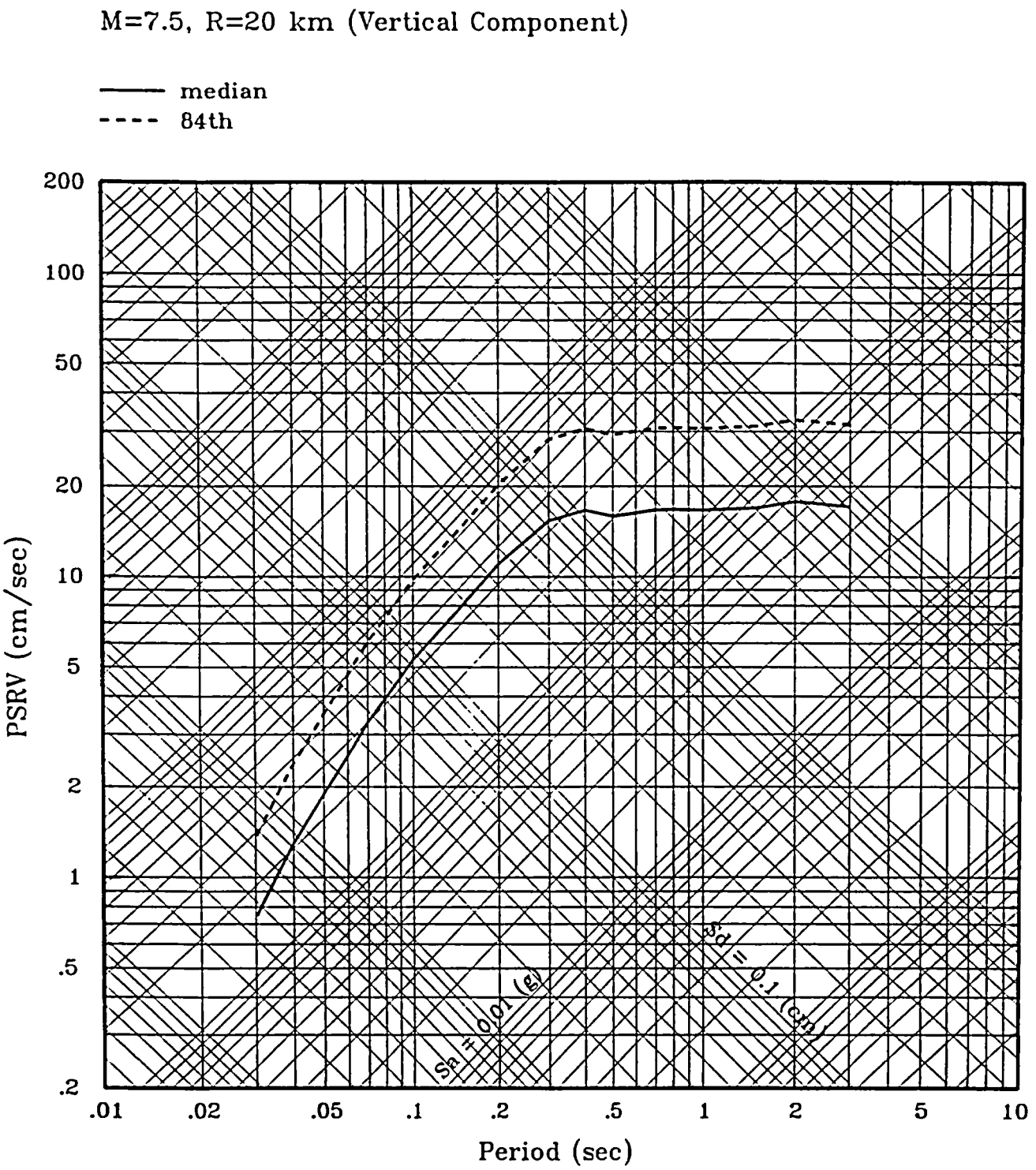

Figure 5-7 Humboldt Bay Crossing, Intraslab Event (vertical motions)

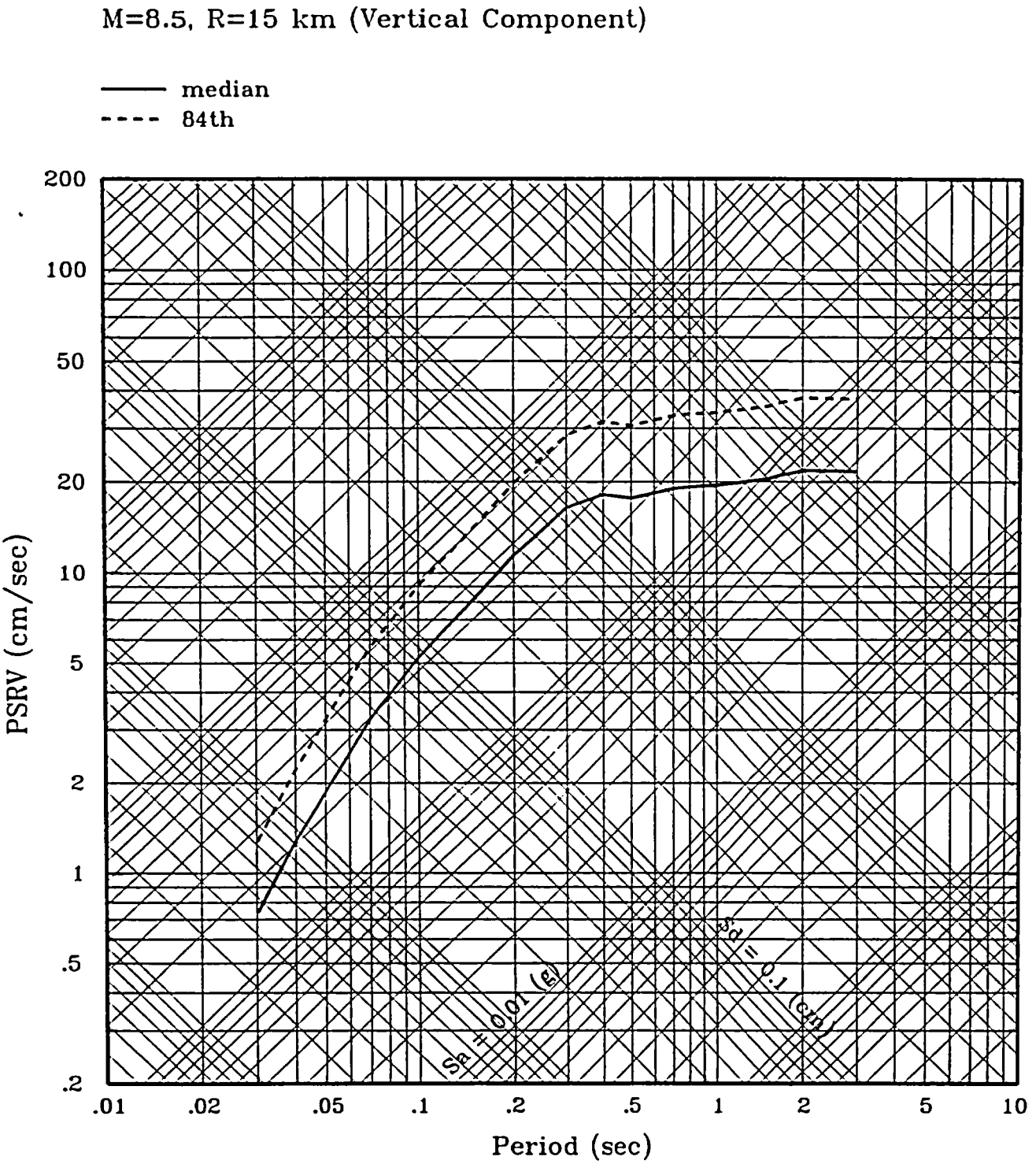

Figure 5-8 Humboldt Bay Crossing, Interface Event (vertical motions)

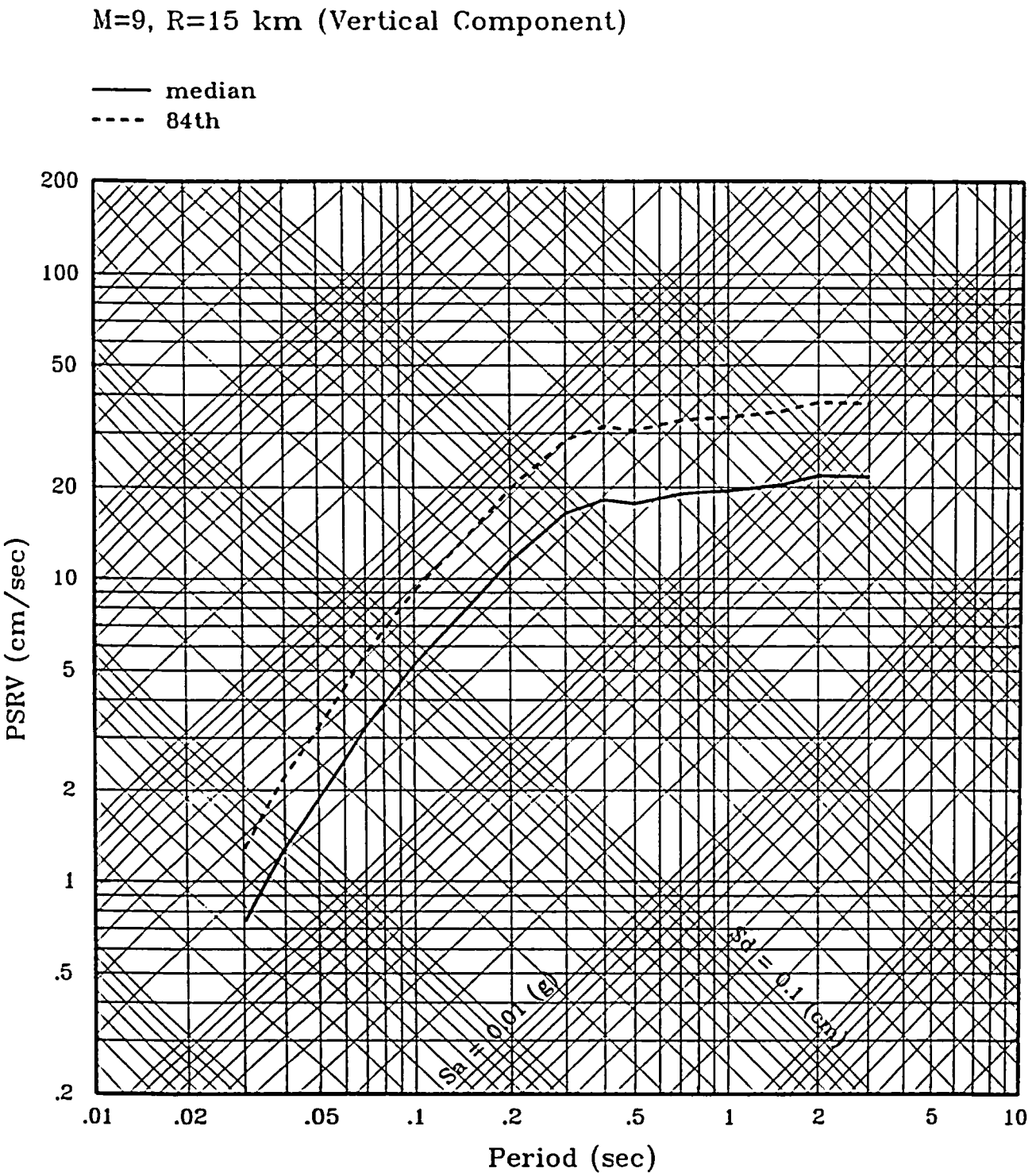

Figure 5-9 Humboldt Bay Crossing, Interface Event (vertical motions)

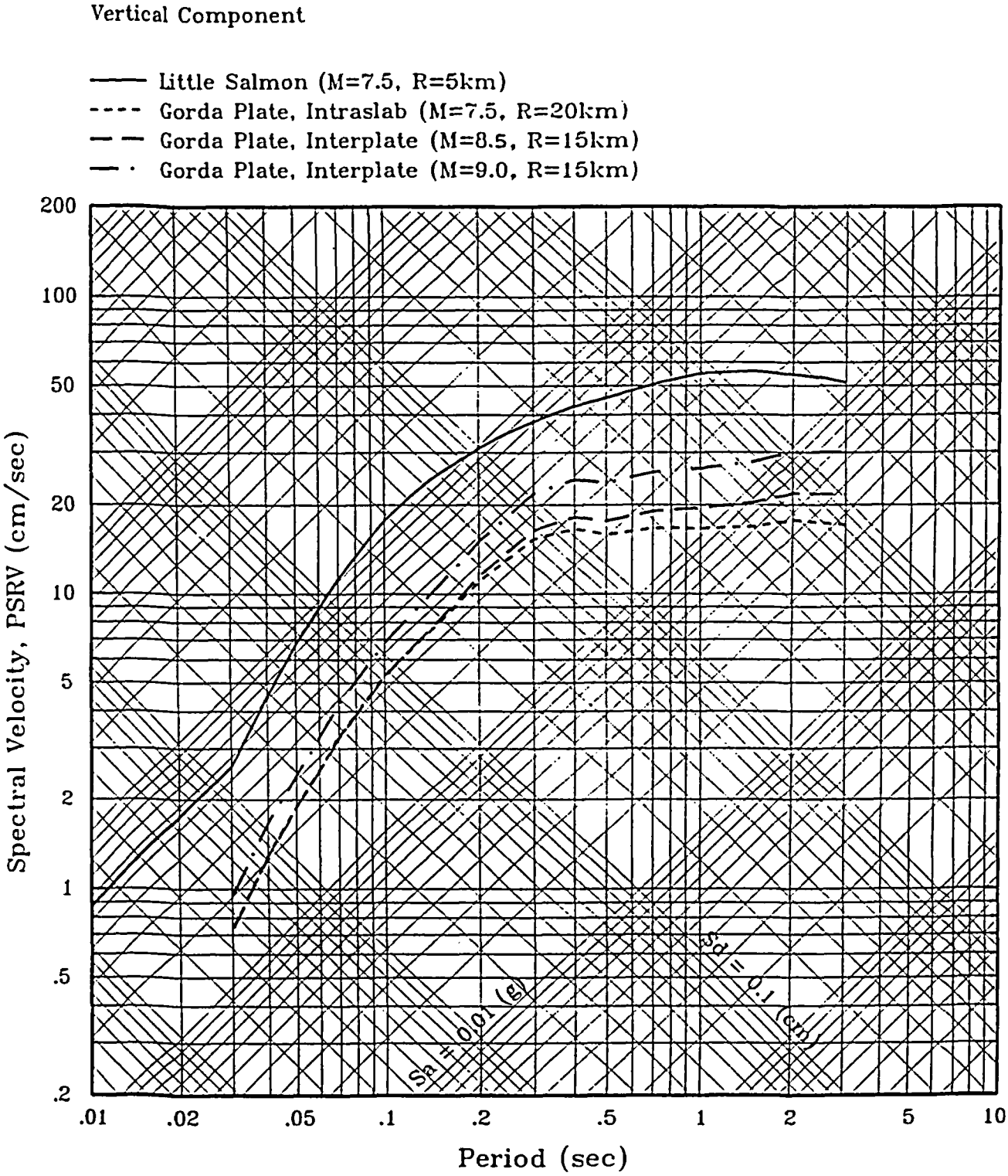

Figure 5-10 Humboldt Bay Crossing, Comparison between different sources (vertical motions)

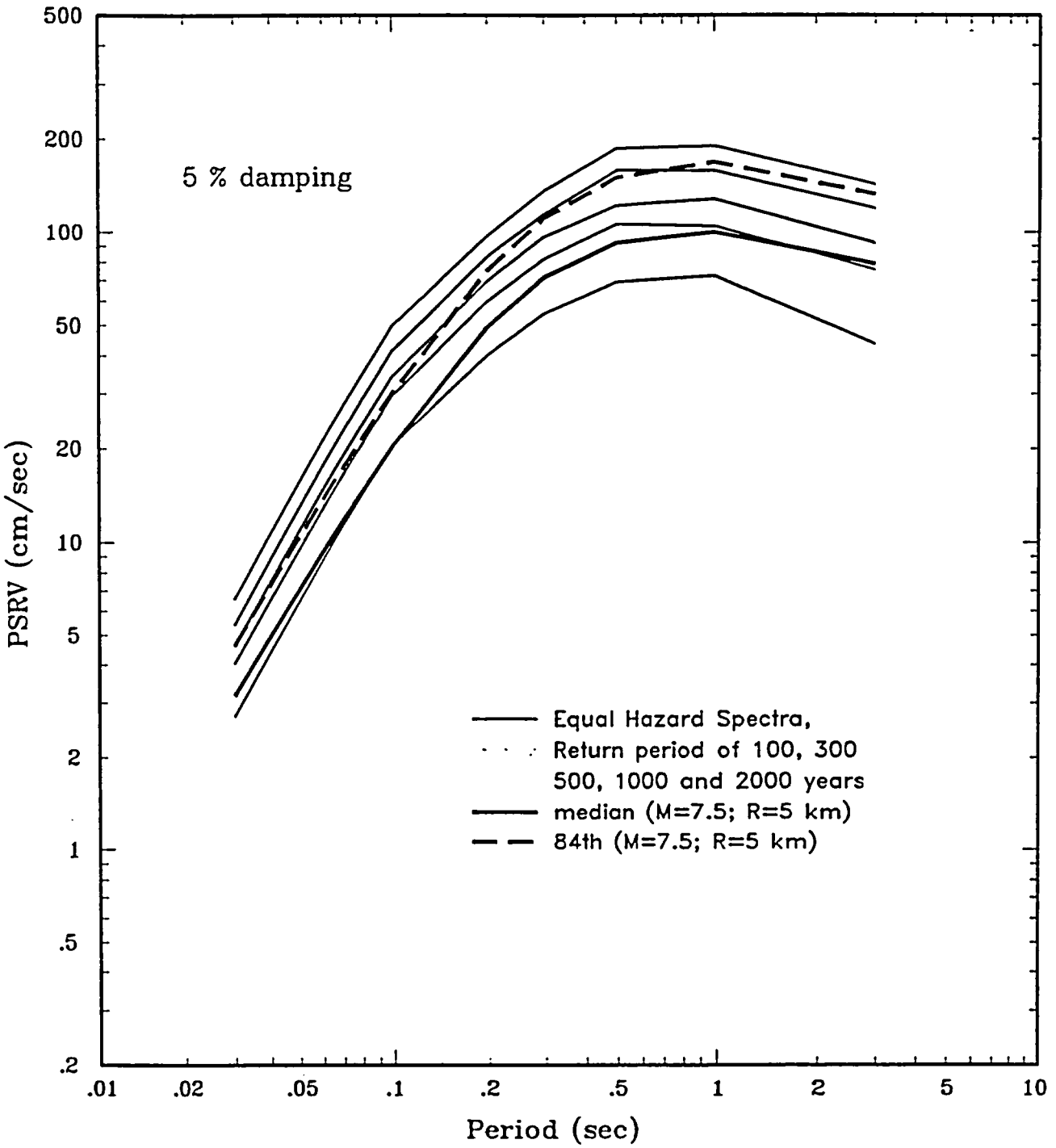

Figure 5-11 Humboldt Bay Crossing, Comparison of the deterministic response spectra with equal-hazard response spectra

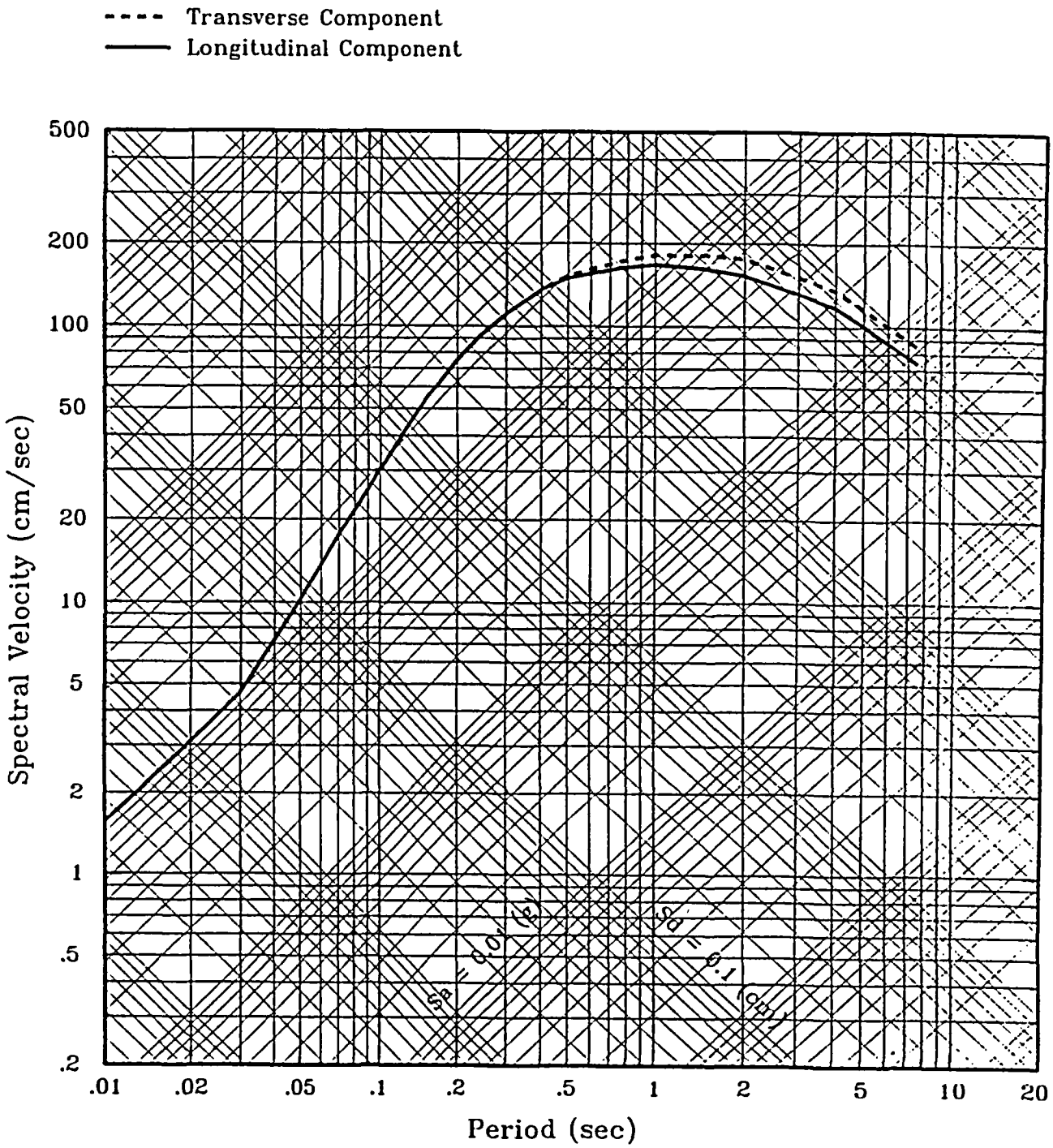

Figure 5-12 Target response spectra (5% damped) for the longitudinal and transverse components associated with the Little Salmon fault event, Humboldt Bay bridges.

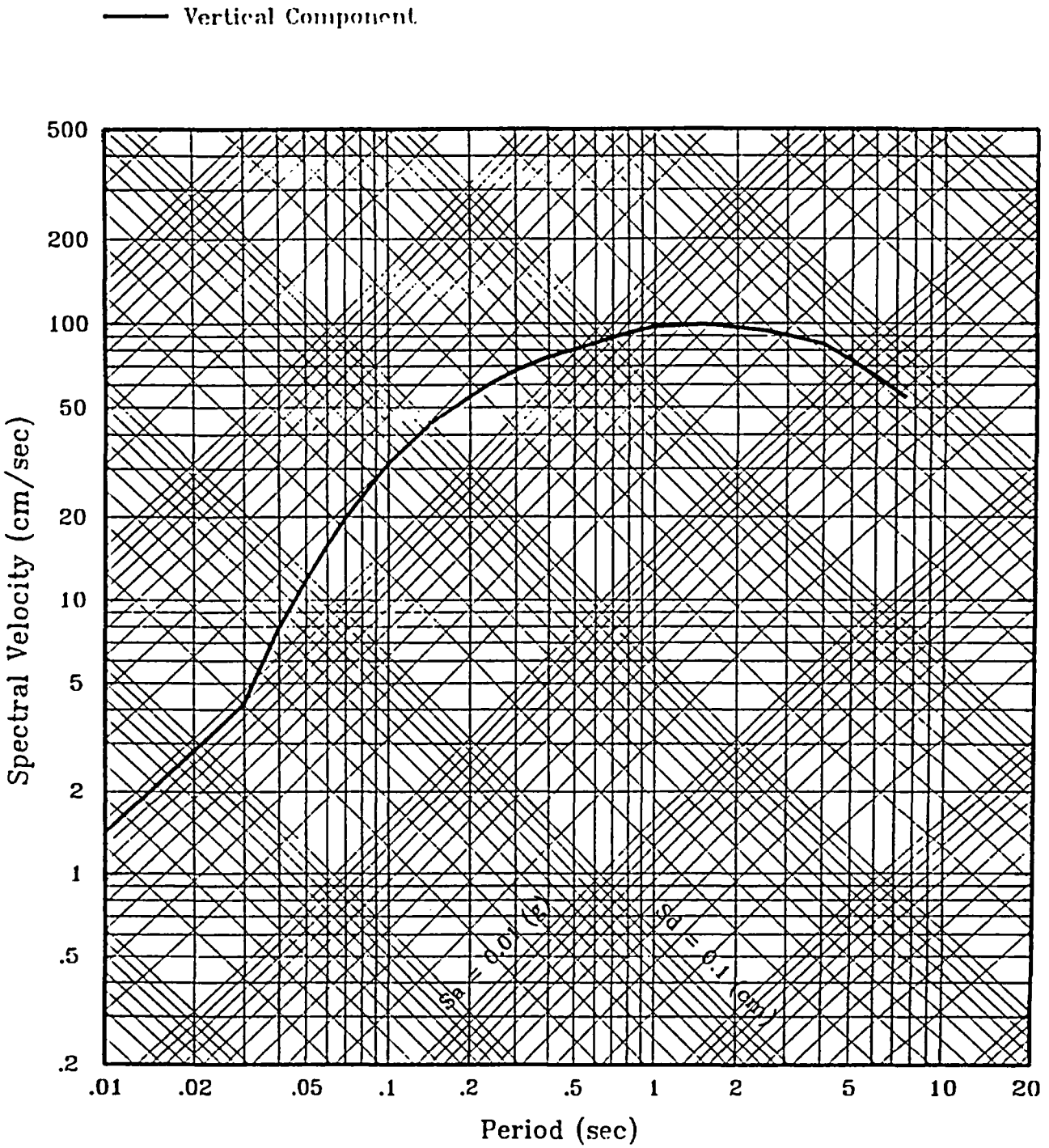

Figure 5-13 Target response spectra (5% damped) for the vertical component associated with the Little Salmon fault event, Humboldt Bay bridges.

6. ACCELERATION TIME HISTORIES

6.1 INTRODUCTION

This section describes the selection and development of acceleration time histories of rock motion to be compatible with the target response spectra presented in Section 5. The objective is to develop acceleration time histories that provide a reasonable match to the target response spectra, have reasonable values of peak ground acceleration, velocity, and displacement, and have an appropriate duration of strong shaking (see Section 5). The approach used is to select recorded natural time histories (three-component ground motions) and then spectrally modify them. In selecting natural time histories, consideration was given to the earthquake magnitude, source-to-site distance, and overall characteristics (level of shaking, frequency content, duration, and phasing) of the ground motion.

For the Humboldt Bay bridges, the maximum credible earthquake Little Salmon fault (M_w 7.5, closest source-to-site distance R = 5 km) on the was selected as the design earthquake (see Section 5.5). The Tabas records from the 1978 Tabas, Iran earthquake were selected and used as initial time histories to develop spectrum-compatible time histories representative of the selected design earthquake.

6.2 MODIFYING SELECTED EARTHQUAKE ACCELEROGRAMS TO BE RESPONSE-SPECTRUM COMPATIBLE

6.2.1 Analytical Procedure

The response spectra of the accelerograms selected as described in Section 6.1 have peaks and valleys which deviate substantially from the site-specific response spectrum developed for the bridge site; thus, it is necessary to modify these motions to improve their response-spectrum compatibility. This modification should be made, however, in a manner which minimizes the resulting changes which occur to the general characteristics of the selected recorded motions. To achieve this objective, the method developed by Lilhanand and Tseng (1988) for generating realistic synthetic time histories of motion having response spectra closely matching a set of

target design response spectra representing multiple damping ratios has been used. This method is a time-domain procedure that recognizes the inherent definition of a response spectrum and adjusts each time history of motion in the neighborhoods of those times when the spectral values for the specified discrete frequencies and damping values occur. Each adjustment, which is made by adding a small perturbation, $\delta a(t)$, to the selected initial acceleration time history $a(t)$, is carried out in an iterative manner such that, for each iteration, i, a modified time history, $a_i(t)$, is obtained from the time history of the previous iteration, $a_{(i-1)}(t)$, using the relation

$$a_i(t) = a_{(i-1)}(t) + \delta a_i(t) \tag{6-1}$$

The small local adjustment, $\delta a_i(t)$, is determined by solving the following integral equation:

$$\delta R_i(\omega_j, \beta_k) = \int_0^{t_{jk}} \delta a_i(\tau) h_{jk}(t_{jk} - \tau) d\tau \tag{6-2}$$

which expresses the small change in the acceleration response value, $\delta R_i(\omega_j, \beta_k)$, for frequency ω_j, and damping, β_k, resulting from the local time-history adjustment, $\delta a_i(t)$. This equation makes use of the acceleration unit-impulse response function, $h_{jk}(t)$, for a single-degree-of-freedom oscillator having a natural frequency, ω_j, and a damping ratio, β_k. Quantity, t_{jk}, in the integral represents the time its corresponding spectral value occurs, and τ is a time lag.

By expressing $\delta a_i(t)$ as a linear combination of impulse response functions with unknown coefficients, the above integral equation can be transformed into a system of linear algebraic equations that can be easily solved for the unknown coefficients. Since the unit-impulse response functions decay rapidly due to damping, they produce only localized perturbations on the acceleration time history. By repeatedly applying the above adjustment, the desired degree of matching between the response spectra of the modified motions and the corresponding target spectra is achieved, while, in doing so, the general characteristics of the original recorded accelerograms are preserved.

6.2.2 Modifications of Time Histories for Spectrum Compatibility

The acceleration time histories selected as described in Section 6.1 represent horizontal components of motion at the Samoa Channel Bridge in directions parallel (approximately N47°W) and normal (approximately N43°E) to the Little Salmon fault. The acceleration time histories for the horizontal components N74°E and N16°W and associated vertical motion recorded at Tabas, Iran during the earthquake of September 16, 1978 were used to represent the longitudinal, transverse, and vertical components of the initial motions requiring modification to make them response-spectrum compatible. The acceleration, velocity, and displacement time histories of the initial motions are shown in Figures 6-1, 6-2, and 6-3, respectively. The 5%-damped pseudo-velocity response spectra for these initial components of motion are shown in Figures 6-4, 6-5, and 6-6, where they can be compared with the corresponding target response spectra. It is seen that the spectrum curves for the initial motions have peaks and valleys which deviate substantially from the corresponding target response-spectrum curves.

Using the analytical procedure described in Section 6.2.1, the initial time histories were repeatedly adjusted until their response spectra closely matched the corresponding target response spectra. The resulting modified spectrum-compatible acceleration time histories are shown in Figure 6-7 and their corresponding velocity and displacement time histories are shown in Figures 6-8 and 6-9, respectively. Values of peak acceleration, velocity, and displacement of the modified time histories of motion are shown in Table 6-1. Guideline values of these parameters, estimated as described in Section 5, are also summarized in Table 6-1. The 5%-damped pseudo-velocity response spectra for the final modified time histories of motion in the longitudinal, transverse, and vertical directions are shown in Figures 6-10, 6-11, and 6-12, respectively, where they can be compared with the corresponding target response spectra. It is seen that the response spectra for the final modified motions closely match and generally envelop the corresponding target spectra. From Table 6-1, it is seen that values of peak ground acceleration, velocity, and displacement are in reasonable correspondence with guideline values. Also, comparing Figure 6-7 with Figure 6-1, Figure 6-8 with Figure 6-2, and Figure 6-9 with Figure 6-3, it is apparent that the general characteristics of the modified acceleration, velocity, and displacement time histories closely resemble those of the unmodified initial time histories.

To check the statistical independency of the generated acceleration time histories, the cross-correlation coefficients among the longitudinal, transverse, and vertical components of the generated acceleration time histories were computed and the results are shown in Table 6-2. Since the generated acceleration time histories have values of cross-correlation coefficients all less than 0.15, they can be considered to be mutually independent from one another. In addition to checking the mutual independence of generated acceleration time histories, the cross-correlation coefficients among the three components of integrated velocity and displacement time histories associated with the generated acceleration time histories were also separately computed and their results are also shown in Table 6-2. As shown in Table 6-2, the values of cross-correlation coefficients for the integrated velocity and displacement time histories are less than or equal to 0.20 and 0.40, respectively.

TABLE 6-1

PEAK ACCELERATION, VELOCITY, AND DISPLACEMENT OF MODIFIED TIME HISTORIES

HUMBOLDT BAY BRIDGES

Component	Peak Accel. (g's)	Peak Velocity (cm/sec)	Peak Displ. (cm)	Guideline Values		
				Accel. (g's)	Velocity (cm/sec)	Displ. (cm)
Longitudinal	1.00	129.7	62.9	0.99	108-132	51-63
Transverse	1.00	125.2	64.8	0.99	121-149	59-73
Vertical	0.91	73.7	43.2	0.90	65-79	38-46

TABLE 6-2

SUMMARY OF CROSS-CORRELATION COEFFICIENTS LITTLE SALMON EVENT

HUMBOLDT BAY BRIDGES

Direction	Cross-Correlation Coefficient*		
	Acceleration	Velocity	Displacement
Long/Tran	0.08	0.18	0.39
Tran/Vert	0.05	0.12	0.31
Vert/Long	0.03	0.08	0.38

*Cross-correlation coefficient = $\rho_{ij} = |R_{ij}(0)| / \sqrt{R_{ii}(0)R_{jj}(0)}$, where $R_{ij}(0)$ is the cross-correlation function at zero time lag between a pair of time histories x_i and x_j, and $R_{ii}(0)$ and $R_{jj}(0)$ are the auto-correlation functions at zero time lag for x_i and x_j, respectively.

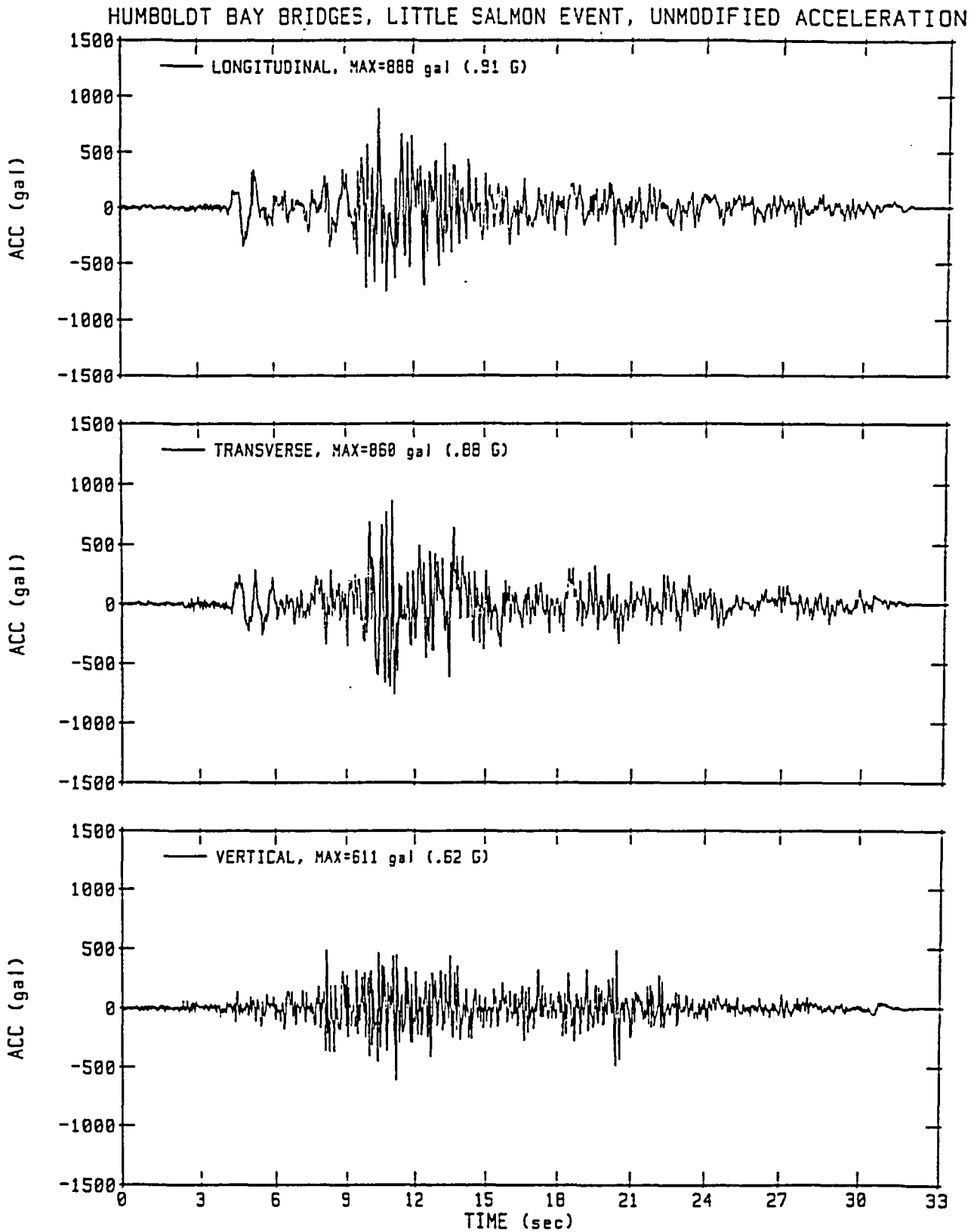

Figure 6-1 Selected Acceleration Time Histories of Rock Motions (Little Salmon Event)

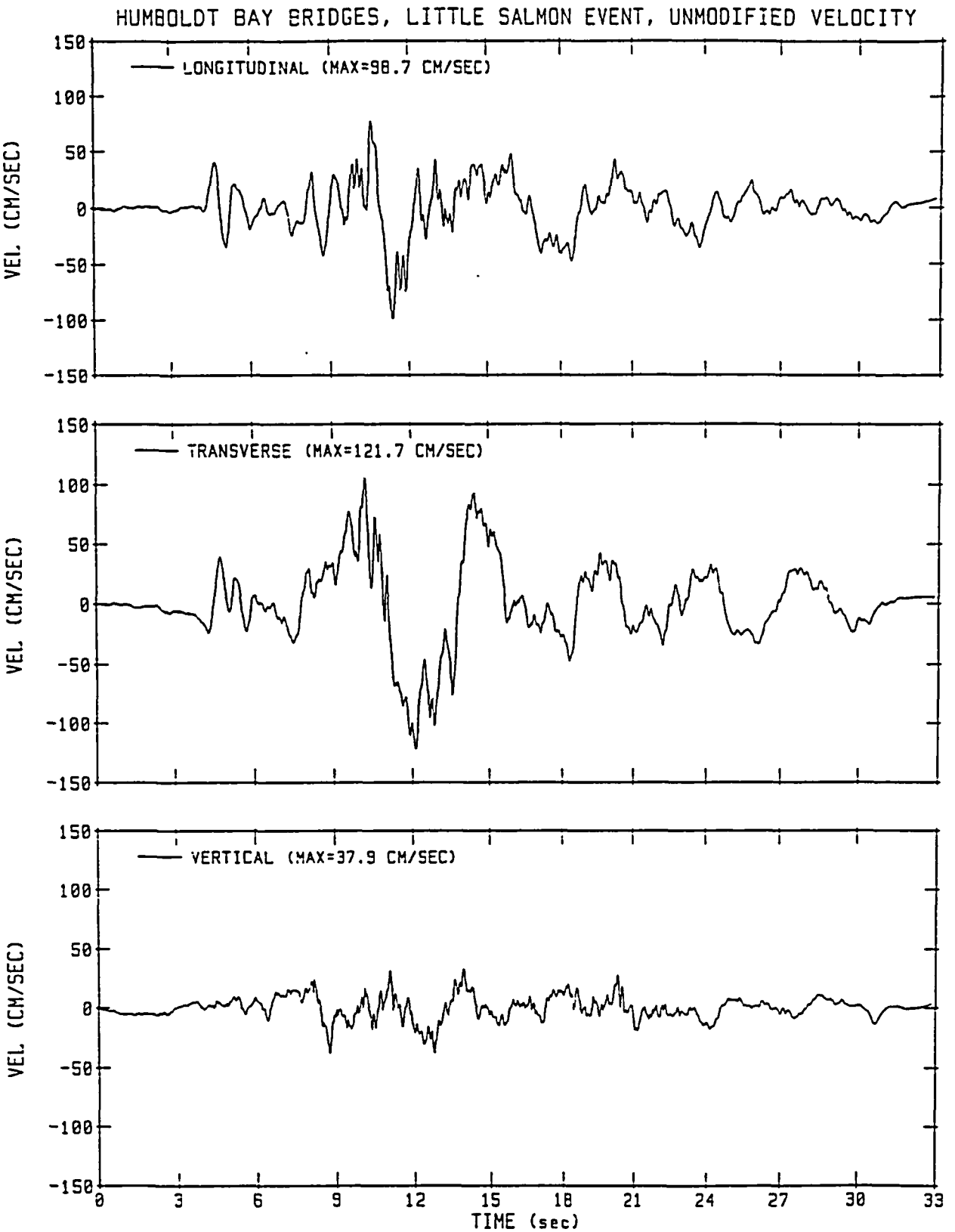

Figure 6-2 Integrated Velocity Time Histories of the Selected Acceleration Time Histories (Little Salmon Event)

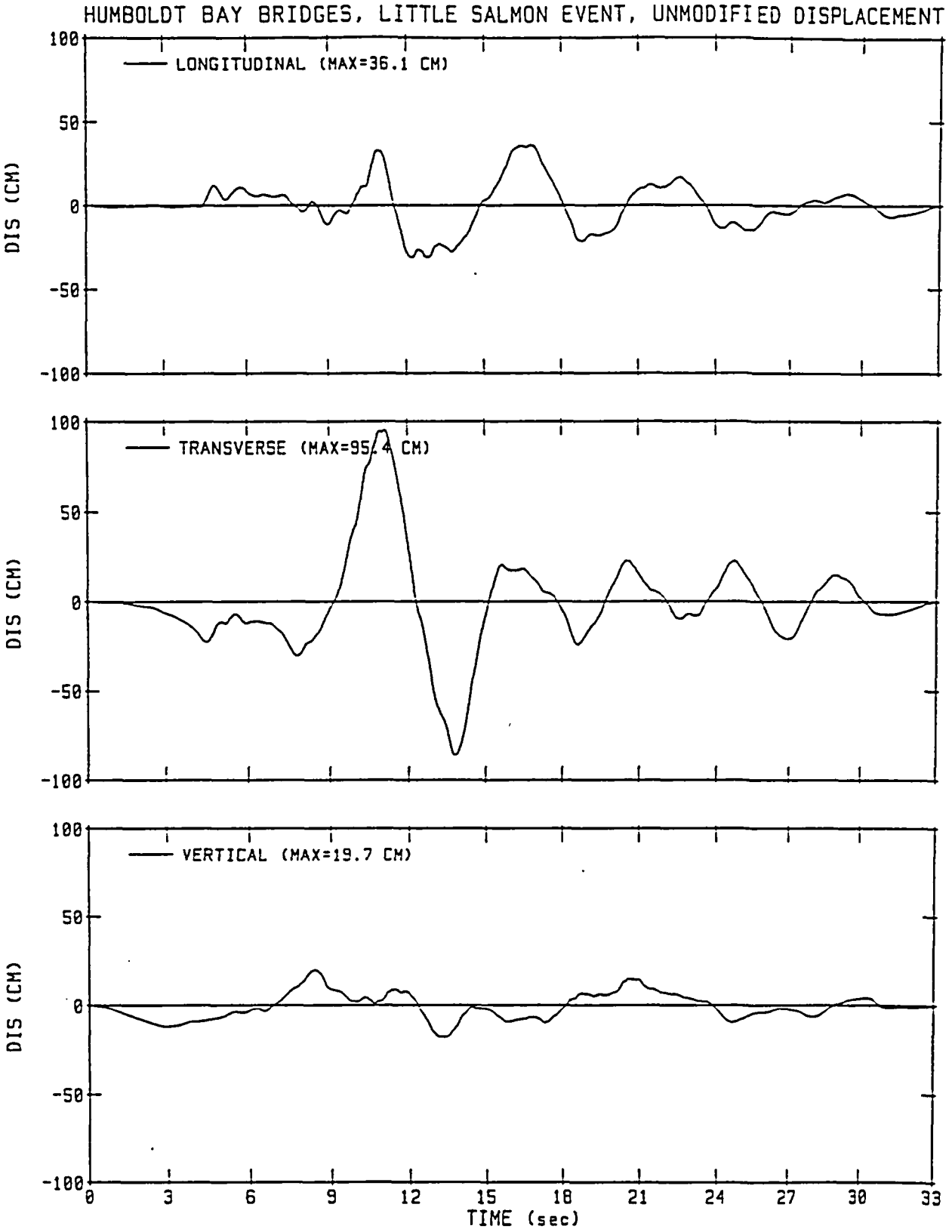

Figure 6-3 Integrated Displacement Time Histories of the Selected Acceleration Time Histories (Little Salmon Event)

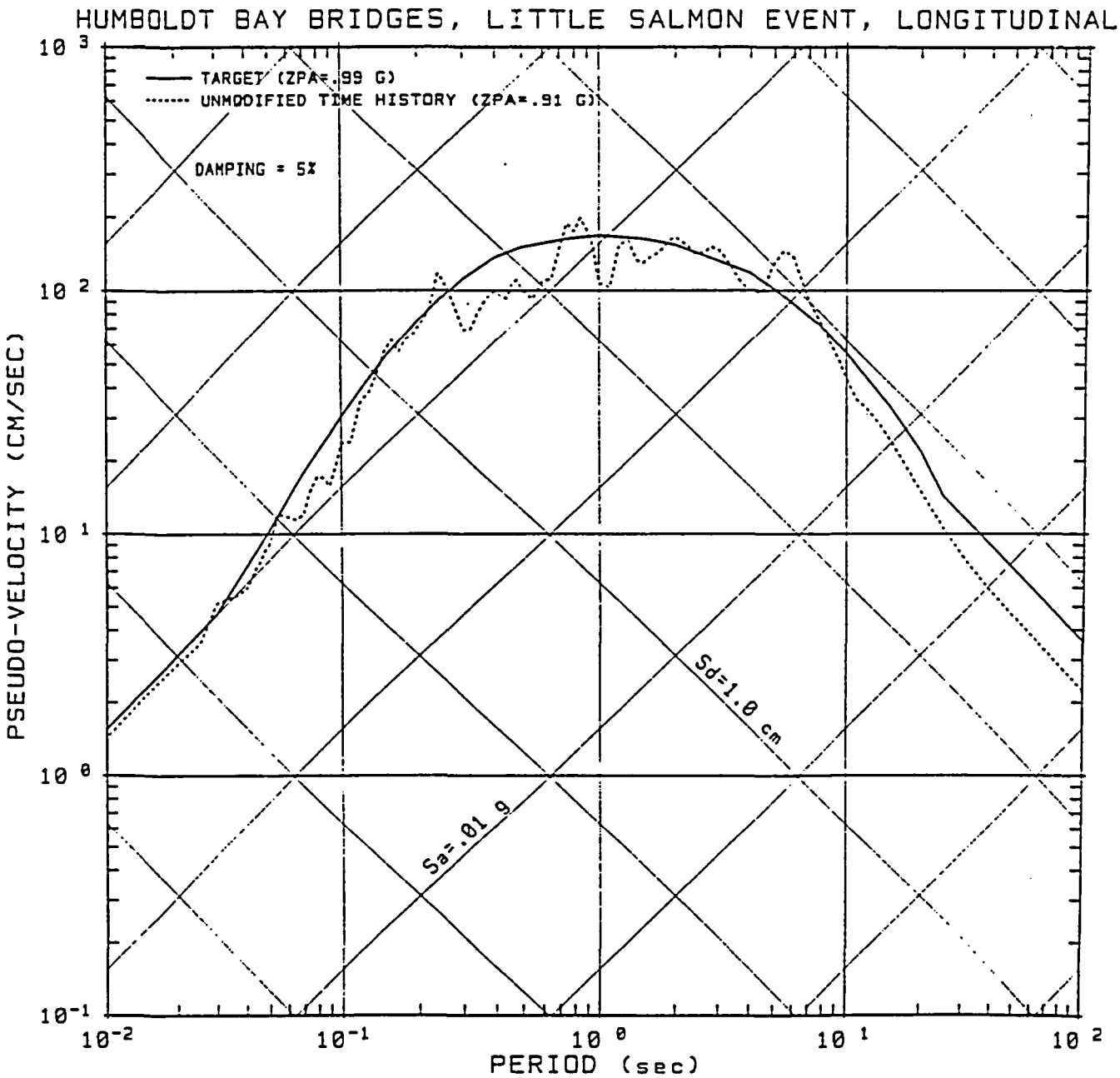

Figure 6-4 Comparison of Target Spectrum and Initial Unmodified Time-History Spectrum (Little Salmon Event)

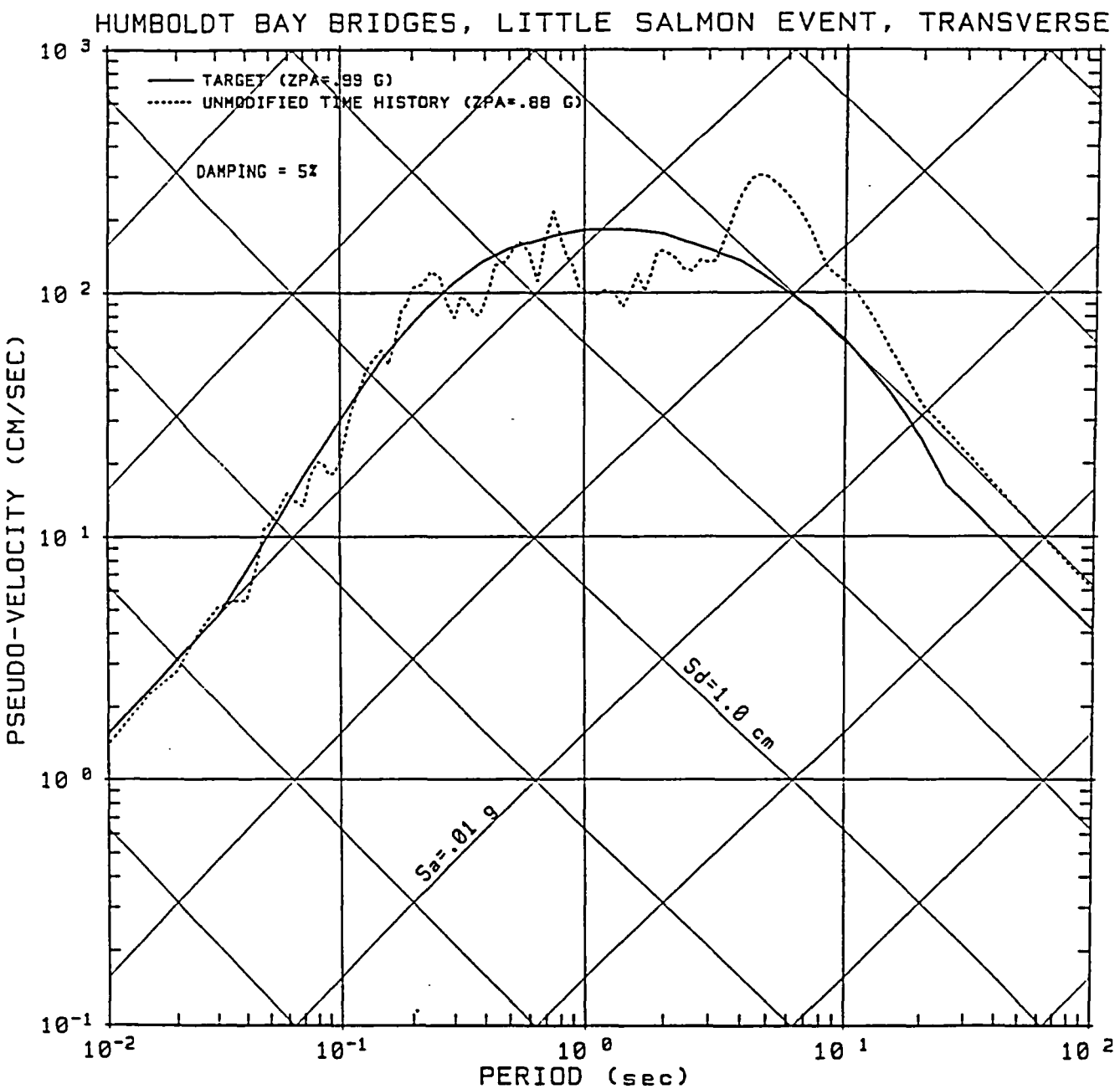

Figure 6-5 Comparison of Target Spectrum and Initial Unmodified Time-History Spectrum - Transverse Component (Little Salmon Event)

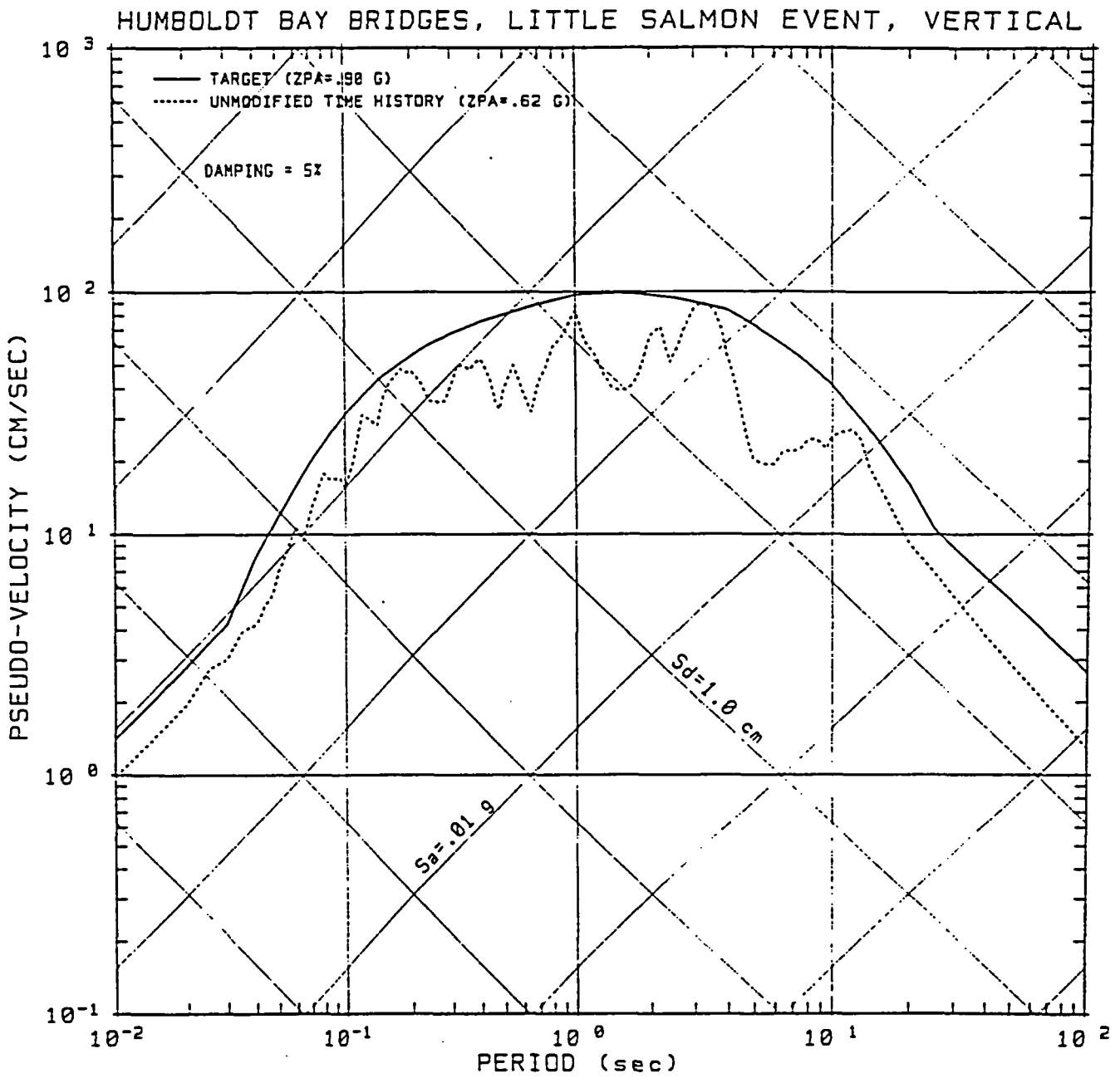

Figure 6-6 Comparison of Target Spectrum and Initial Unmodified Time-History Spectrum - Vertical Component (Little Salmon Event)

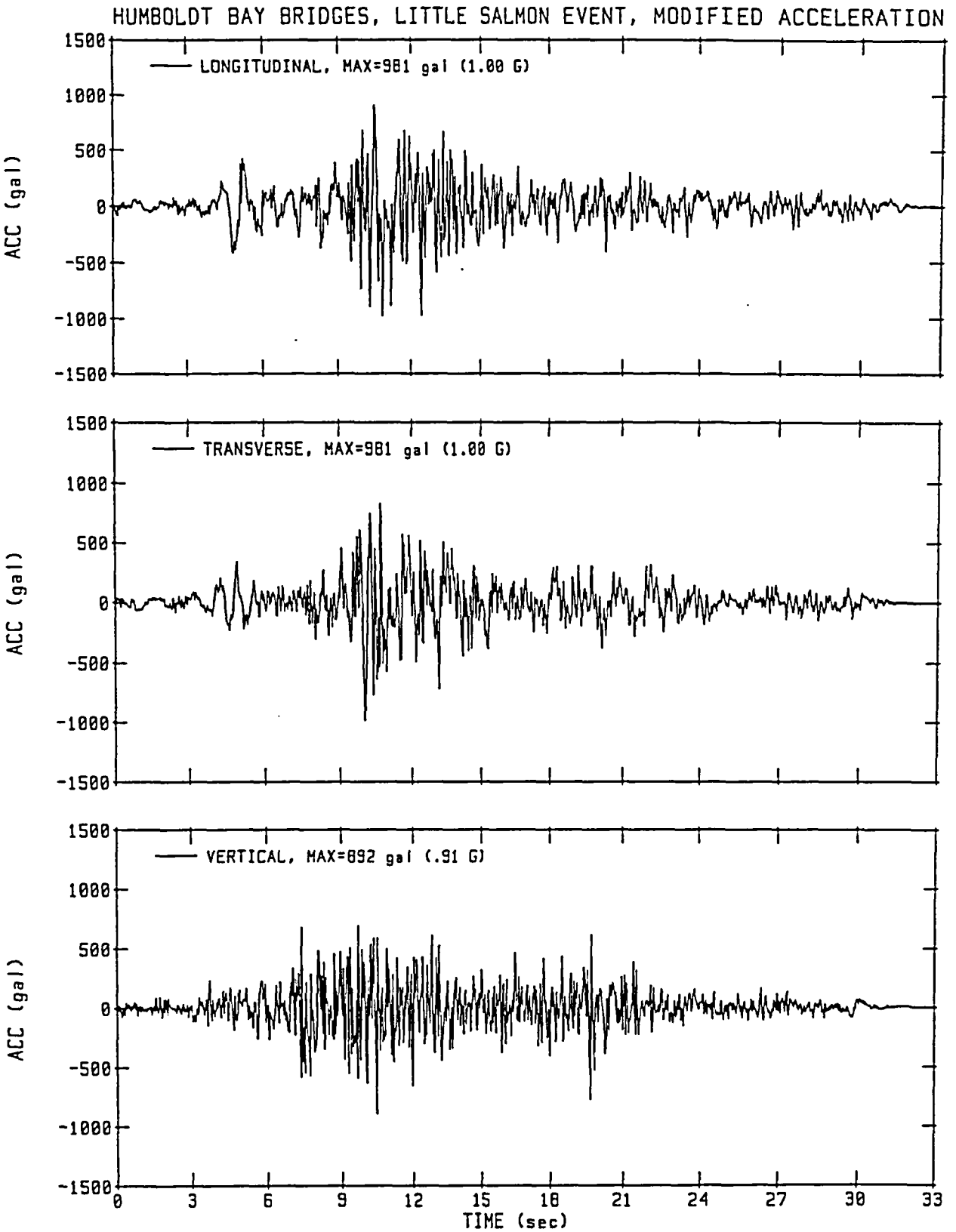

Figure 6-7 Generated Spectrum-Compatible Acceleration Time Histories (Little Salmon Event)

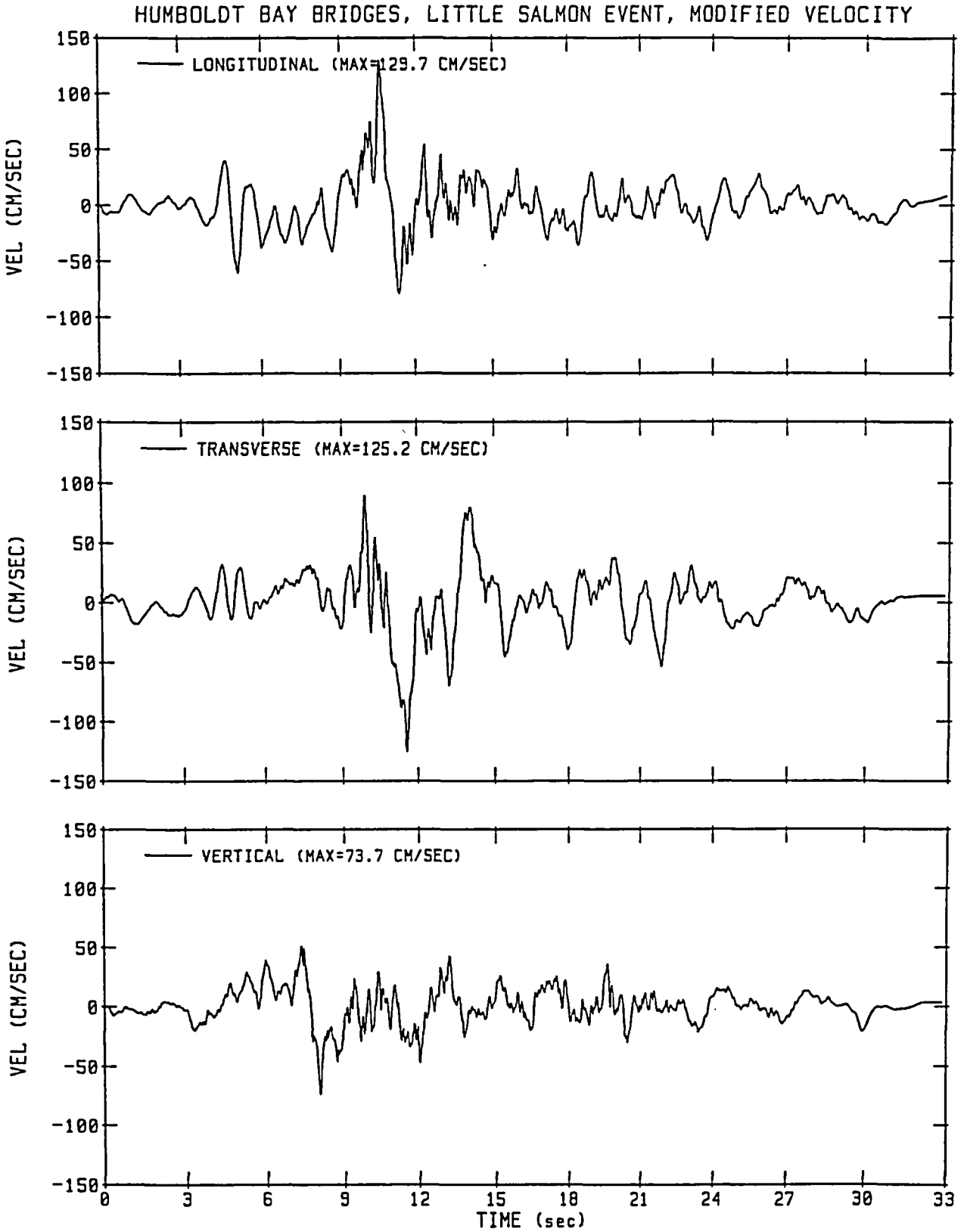

Figure 6-8 Integrated Velocity Time Histories of the Generated Spectrum-Compatible Motions (Little Salmon Event)

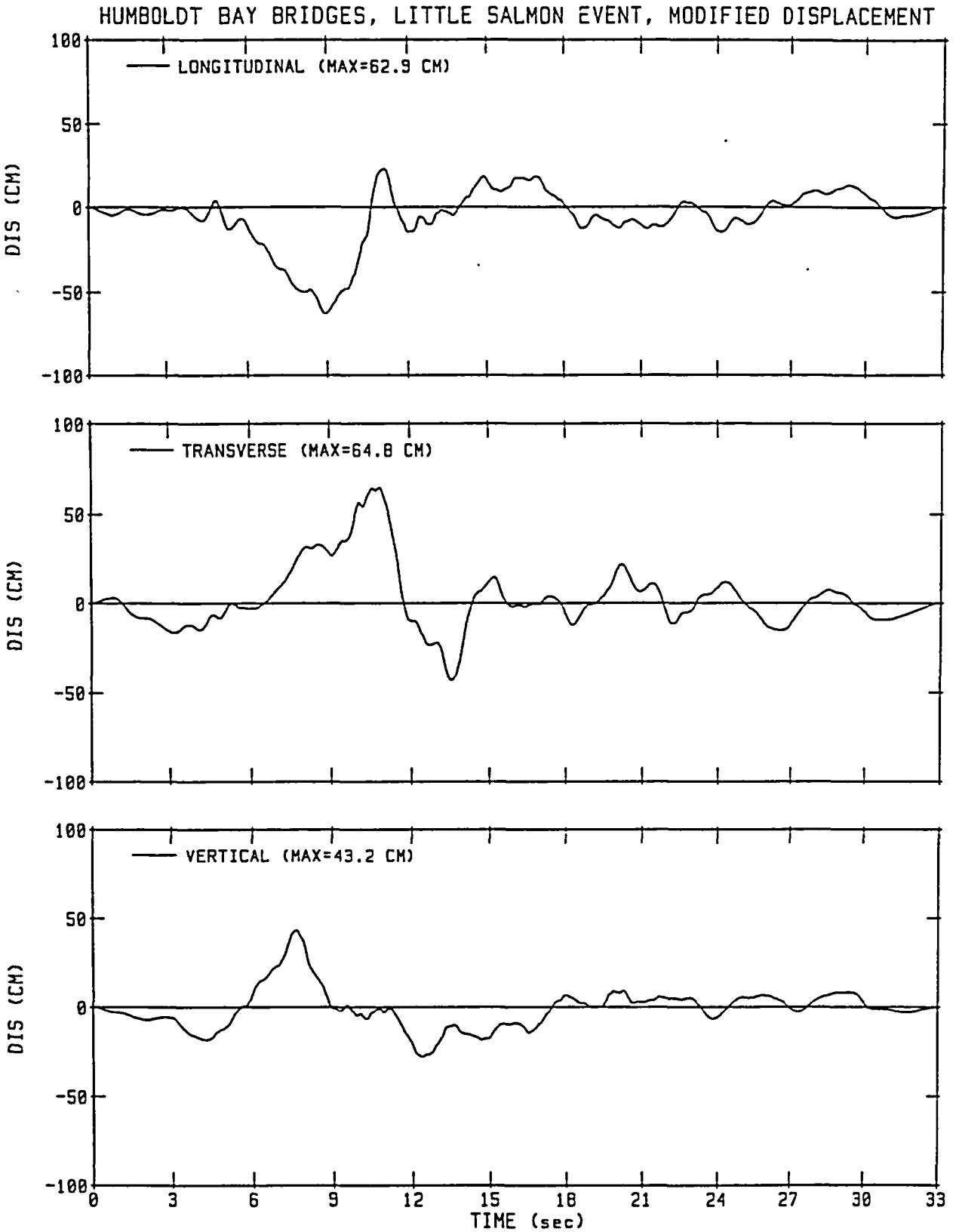

Figure 6-9 Integrated Displacement Time Histories of the Generated Spectrum-Compatible Motions (Little Salmon Event)

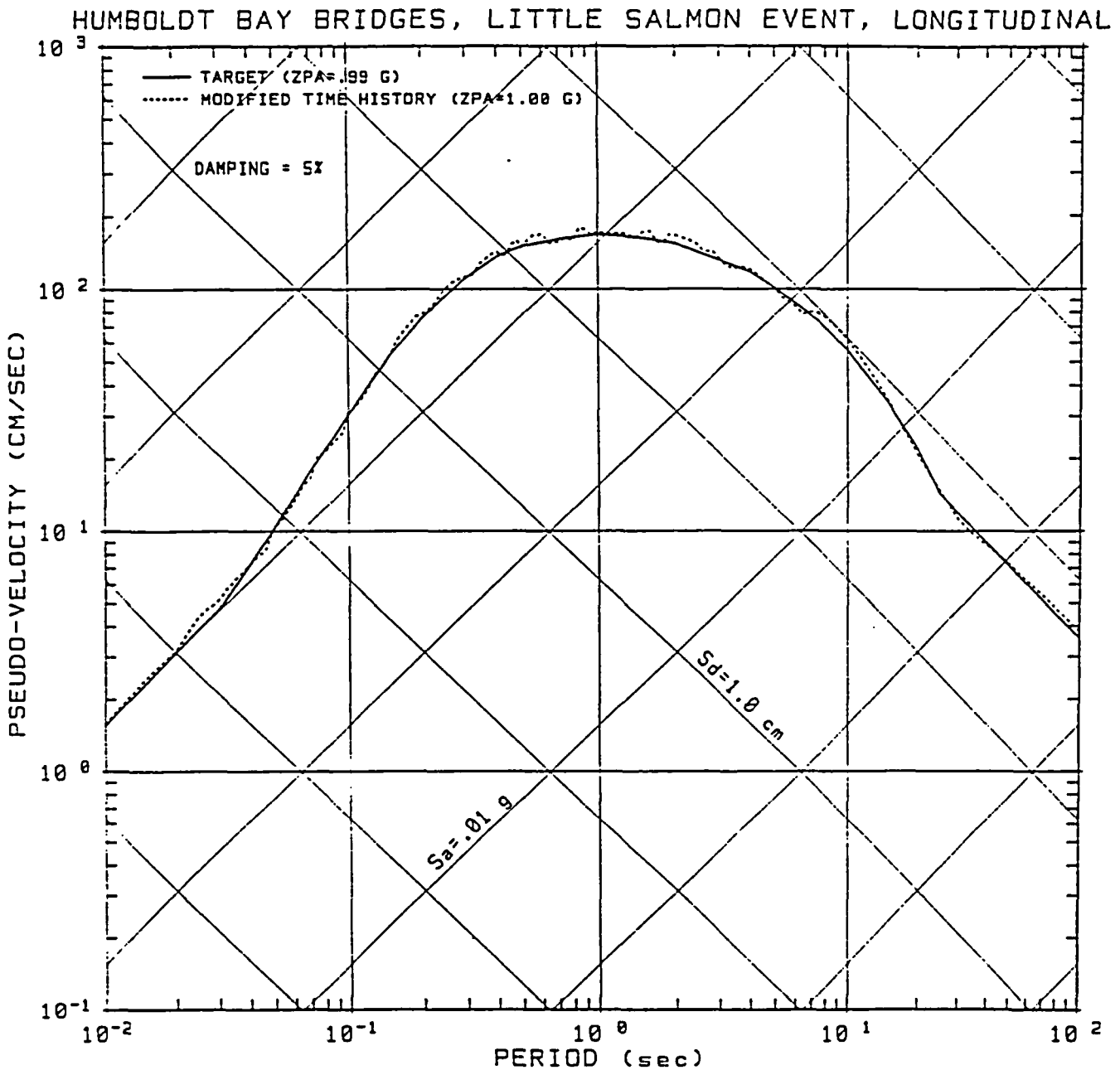

Figure 6-10 Comparisons of Target Spectrum and Spectrum-Compatible Time-History Response Spectrum - Longitudinal Component (Little Salmon Event)

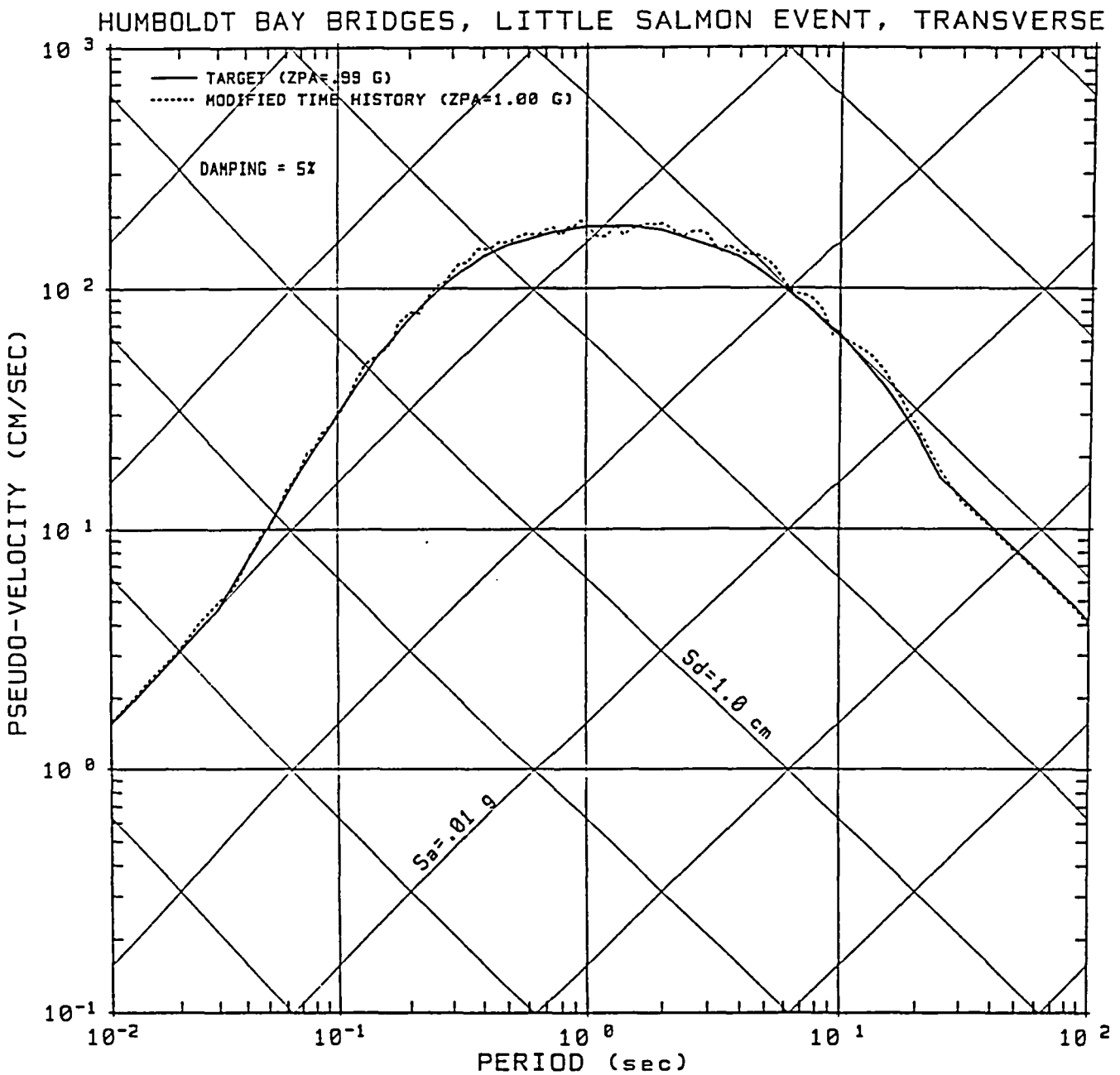

Figure 6-11 Comparison of Target Spectrum and Spectrum-Compatible Time-History Response Spectrum - Transverse Component (Little Salmon Event)

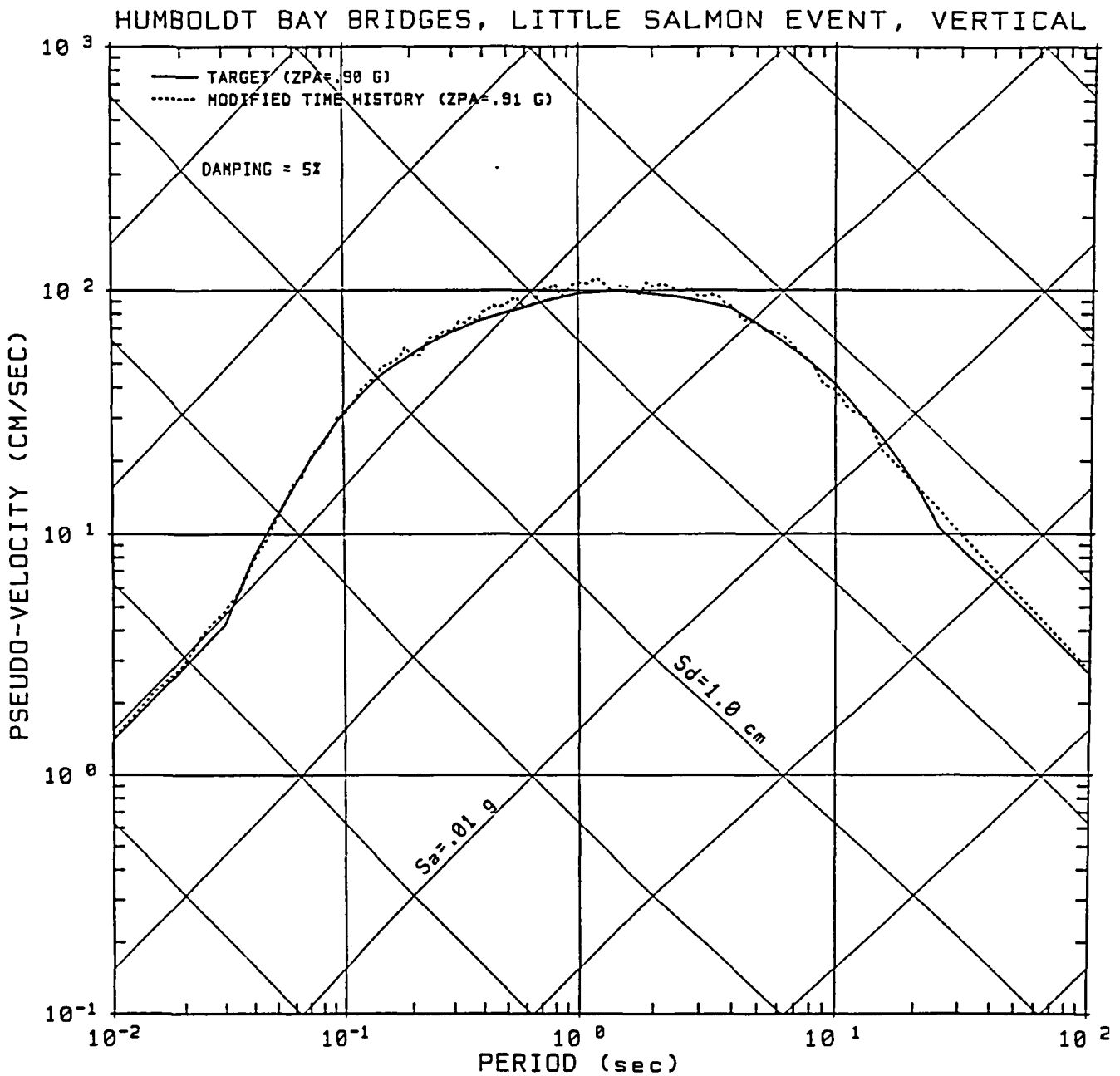

Figure 6-12 Comparisons of Target Spectrum and Spectrum-Compatible Time-History Response Spectrum - Vertical Component (Little Salmon Event)

7. SUBSURFACE CONDITIONS AT BRIDGE SITES

7.1 GENERAL SUBSURFACE GEOLOGY AT HUMBOLDT BAY BRIDGES AND VICINITY

The geology of the area has been described by Ogle (1953), Evenson (1959), Clarke (1987), and Nilsen and Clarke (1987). The geology of the Humboldt Bay bridges consists of relatively young surface materials over older bedrock. These materials are shown on an east-west geologic cross section. The location of the cross section is shown in Figure 7-1, and the geologic cross section is shown in Figure 7-2. As shown in Figure 7-2, the Humboldt Bay area is a gentle down warp. Sediments are deposited in this small basin which is being down warped. The basin is bounded by the Freshwater fault on the east as shown in Figure 7-2.

The Eureka-Humboldt Bay area is the location of relatively young deposition and deep subsurface deformation. The late Oligocene through Pleistocene Eel River basin represents a deformed basin within a zone of continental underthrusting north of the Mendocino triple junction (Ingle, 1987). This deformation has continued to the present (Clarke, 1987). From early Pliocene or late Miocene to the middle Pleistocene the basin has been progressively shallowing from depths of about 6,000 feet to shallow marine and nonmarine near shore conditions (Clarke, 1987).

The surface materials over most of the area are Holocene alluvium consisting of sand, silt, clay, gravel, and bay mud. Some dune sand is also present. The total thickness of these unconsolidated Holocene materials ranges from a few feet to 350 feet thick (Evenson, 1959). Below this alluvium is the Holocene to late Pleistocene Hookton Formation of gravel, sand, and silt predominantly of fluvial origin. This poorly consolidated formation may be up to 400 feet thick. In some areas this formation interfingers with marine sediments. Below the Hookton Formation is the late Pleistocene (Ingle, 1987) continental Carlotta Formation. This poorly consolidated formation may be on the order of 500 to 3,500 feet thick and consists of clay, sand, and gravel of predominantly fluvial origin (Evenson, 1959). Within the Eureka-Humboldt Bay area, the Carlotta Formation was deposited in the littoral-inner shelf and interfingers with marine sediments (Ingle, 1987).

Poorly indurated/semiconsolidated early Pleistocene to Miocene age marine sediments are located below the above continental deposits. These sediments consist of the early Pleistocene to late Pliocene (Ingle, 1987) Rio Dell Formation of massive, friable, fine-grained sandstone, and the Pliocene Eel River Formation of mudstone, siltstone, and sandstone. Sediments of the Rio Dell Formation were deposited on the outer continental shelf, outer continental slope, and as a marine fan (Ingle, 1987). Eel River sediments were deposited as a marine fan, on the floor of the basin, and directly on the Yager or Franciscan Formations (Ingle, 1987). The combined thickness of these formations is up to 6,000 or 11,000 feet (Evenson, 1959; Ingle, 1987). The top of the semiconsolidated marine bedrock formations (Eel River and River Dell) is estimated to be on the order of 1,500 to 2,000 feet deep at the Humboldt Bridges site.

Consolidated bedrock in the area consists of the Franciscan and Yager formation of sandstone, shale, chert, graywacke, and conglomerate. The Franciscan Formation is generally located inland of Humboldt Bay. Rocks of the Yager Formation are generally found west of the Franciscan Formation. Consolidated Yager/Franciscan bedrock is estimated to be on the order of 4,000 feet deep below the bridge.

7.2 SOIL PROFILE AT BRIDGE SITES

Information on the subsurface soil conditions at the bridge sites (Eureka, Middle, and Samoa Channels) is available from the borings made by the Division of Highways, Department of Public Works in 1967 and 1968 and by the California Department of Transportation in 1990. The logs of these borings are shown on the following Caltrans Drawings:

Eureka Channel:

Drawing No. 2929 (sheet 5 of 7), 1967
Drawing No. 04230-40 and 04230-41, 1968
Log of Test Borings for Single Column Retrofit, Project 58, 1990

Middle Channel:

Drawing No. 04224-42, 1968
Log of Test Borings, 1990

Samoa Channel:

Drawing No. 2929 (sheet 6 of 7), 1967
Drawing No. 04228-43 through 04228-46, 1968
Log of Test Borings for Single Column Retrofit, Project 58, 1990

The locations of the original borings along with an idealized soil profile along each bridge are shown in Figures 7-3 (Eureka Channel bridge), 7-4 (Middle Channel bridge), and 7-5 (Samoa Channel bridge).

At the Eureka Channel bridge site, the surficial soils generally consist of fill and/or soft clays or silts extending to a maximum depth of approximately 20 feet at the boring locations. Beneath the fill and soft clays or silts, the soils typically consist of compact to very dense sands overlying compact to very stiff silty clays and clayey silts. The silty clays and clayey silts are in turn underlain generally by dense to very dense sands and gravelly sands extending to the bottom of the deepest boring at a depth of approximately 250 feet below the ground surface.

The surficial soils at the Middle Channel bridge site generally consist of soft or very loose organic silts and sandy silts varying in thickness from less than 5 feet to approximately 60 feet at the boring locations. Beneath the organic silts and sandy silts, the soils typically consist of slightly compact to very dense sands and silty sands overlying slightly compact to compact silts and sandy silts extending to the bottom of the borings along the bridge alignment. The maximum depth of the borings along the bridge is approximately 100 feet below the ground surface.

At the Samoa Channel bridge site, the surficial soils generally consist of relatively thin layers, generally less than 20 feet thick, of interbedded very loose to loose sands and organic sands, very soft organic silts and clays, and slightly compact to compact silts and sands. The thickness of this upper zone of surficial soil generally varies from less than 5 feet to approximately 70 feet at the boring locations. Beneath this upper zone, the soils typically consist of dense to very dense sands with interbedded thin lenses of organics and shell fragments extending to the bottom of the deepest boring at a depth of approximately 230 feet below the ground surface.

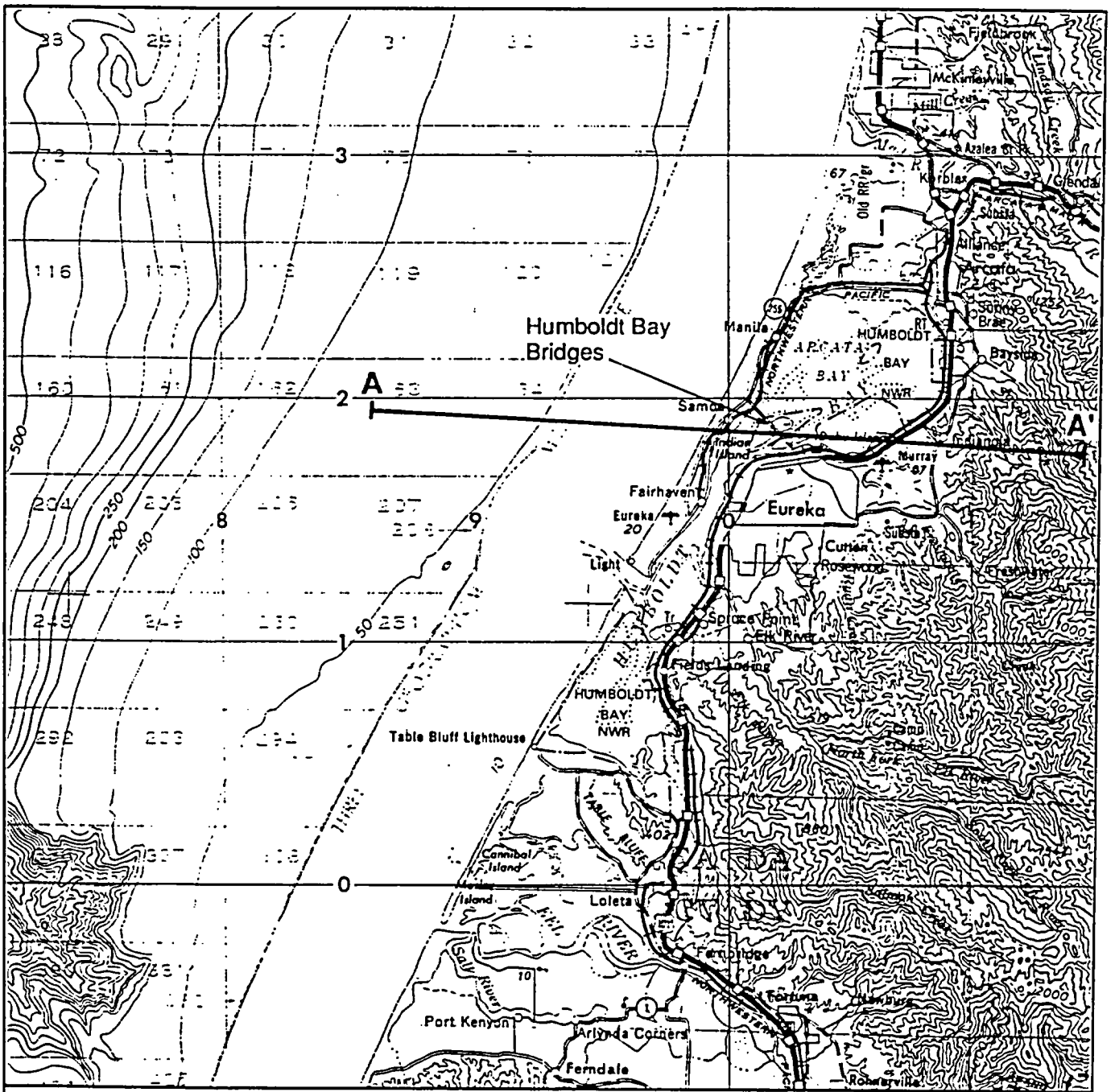

GEOMATRIX

LOCATION OF GEOLOGIC CROSS SECTION A-A'
Seismic Ground Motion Studies for Humboldt Bay Bridges
Humboldt County, California

Figure
7-1

Project No.
2016G

GEOMATRIX

GEOLOGIC CROSS SECTION A-A'
Seismic Ground Motion Studies for Humboldt Bay Bridges
Humboldt County, California

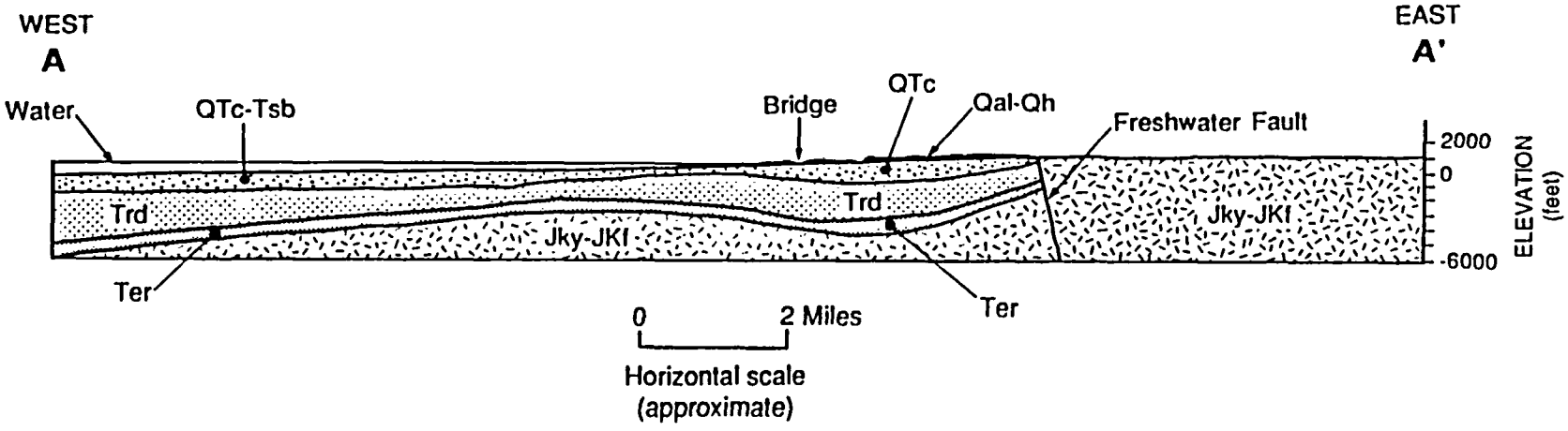

EXPLANATION

Formation and Description

JKf – Franciscan Formation; sandstone, shale, and chert

JKy – Yager Formation; indurated mudstone, shale, graywacke, and conglomerate

Ter – Eel River Formation; mudstone, siltstone, and sandstone

Trd – Rio Dell Formation; massive mudstone and thin sandstone layers

Tsb – Scotia Bluff Sandstone; massive, friable, fine-grained sandstone

QTc – Carlotta Formation; conglomerate, sandstone, and claystone

Qh – Hookton Formation; gravel, sand, and silt

Qal – Recent alluvium; gravel, sand, silt, clay, and bay mud

Sources: Ogle, B. A., 1953; Evenson, R. E.,1959; Strand, R. G., 1962; and Schymiczek, H. and Suchsland, R., 1987.

Figure 7-2

Project No. 2016G

THIS PAGE IS AN OVERSIZED DRAWING OR FIGURE,

THAT CAN BE VIEWED AT THE RECORD TITLED:

"SOIL PROFILE ALONG BRIDGE ALIGNMENT SEISMIC GROUND MOTION STUDIES FOR EUREKA CHANNEL BRIDGE HUMBOLDT COUNTY, CALIFORNIA."

WITHIN THIS PACKAGE..

D-01

THIS PAGE IS AN OVERSIZED DRAWING OR FIGURE,

THAT CAN BE VIEWED AT THE RECORD TITLED:

"SOIL PROFILE ALONG BRIDGE ALIGNMENT SEISMIC GROUND MOTION STUDIES FOR MIDDLE CHANNEL BRIDGE HUMBOLDT COUNTY, CALIFORNIA."

WITHIN THIS PACKAGE..

D-02

THIS PAGE IS AN OVERSIZED DRAWING OR FIGURE,

THAT CAN BE VIEWED AT THE RECORD TITLED:

"SOIL PROFILE ALONG BRIDGE ALIGNMENT SEISMIC GROUND MOTION STUDIES FOR SAMOA CHANNEL BRIDGE HUMBOLDT COUNTY, CALIFORNIA."

WITHIN THIS PACKAGE..

D-03

REFERENCES

Abe, K., 1981, Magnitudes of large shallow earthquakes from 1904 to 1980: Physics of the Earth and Planetary Interiors, v. 34, p. 72-92.

Abe, K., 1984, Complements to "Magnitude of large shallow earthquakes from 1904-1980": Physics of the Earth and Planetary Interiors, v. 34, p. 17-23.

Abe, K., and Noguchi, S., 1983a, Determination of magnitudes for large shallow earthquakes, 1898-1917: Physics of the Earth and Planetary Interiors, v. 32, p. 45-59.

Abe, K., and Noguchi, S., 1983b, Revision of magnitudes of large shallow earthquakes, 1897-1912: Physics of the Earth and Planetary Interiors, v. 33, p. 1-11.

Aki, K., and Richards, P.G., 1980, Quantitative Seismology Theory and Methods 1: W.H. Freeman and Company, 557 p.

Anderson, J.G., 1979, Estimating the seismicity from geological structure for seismic risk studies: Bulletin of the Seismological Society of America, v. 69, no. 1, p. 135-158.

Anderson, J., Singh, S., Espinola, J., and Yamamoto, J., 1989, Seismic strain release in the Mexican subduction thrust: Physics of the Earth and Planetary Interiors, v. 58, p. 307-332.

Anima, R.J., Williams, P.L., and McCarthy, J., 1992, Galehouse, J.S., ed., High-resolution marine seismic reflection profiles across East Bay faults (abs): Program with Abstracts, Second Conference on Earthquake Hazards in the Eastern San Francisco Bay Area, p. 4.

Arabasz, W.J., and Robinson, R., 1976, Microseismicity and geologic structure in the northern South Island, New Zealand: New Zealand Journal of Geology and Geophysics, v. 19, no. 2, p. 561-601.

Archuleta, R.J., 1984, A faulting model for the 1979 Imperial Valley earthquake: Journal of Geophysical Research, v. 89, p. 4459-4585.

Atwater, B.F., 1992, Geologic evidence for earthquakes during the past 2000 years along the Copalis River, southern coastal Washington: Journal of Geophysical Research, v. 97, p. 1901-1919.

Atwater, B.F., Hedel, C.W., and Helley, E.J., 1977, Late Quaternary depositional history, Holocene sea-level changes, and vertical crustal movement, Southern San Francisco Bay, California: U.S. Geological Survey Professional Paper 1014.

Bailey, T.L., 1930, The geology of the Potrero Hills and Vacaville region, Solano County, California: University of California Publications in Geological Sciences, v. 19, p. 321-334.

Bartow, J.A., 1991, The Cenozoic evolution of the San Joaquin Valley, California: U.S. Geological Survey Professional Paper 1501.

Ben-Menahem, A., 1978, Source mechanism of the 1906 San Francisco earthquake: Physics of the Earth and Planetary Interiors, v. 17, p. 163-181.

Blair, M.L., and Spangle, W., 1979, Seismic safety and land-use planning -- selected examples from California: U.S. Geological Survey Professional Paper 941-B.

Bolt, B.A., 1968, The focus of the 1906 California earthquake: Bulletin of the Seismological Society of America, v. 50, no. 1, p. 457-471.

Bolt, B.A., 1973, Duration of strong ground shaking: Proceedings, Fifth World Conference on Earthquake Engineering, Rome, Italy, v. I, p. 1304-1313.

Bolt, B.A., McEvilly, T.V., and Uhrhammer, R.A., 1981, The Livermore Valley, California, sequence of January 1980: Bulletin of the Seismological Society of America, v. 71, p. 451-463.

Bolt, B.A., and Miller, R.D., 1975, Catalogue of earthquakes in northern California and adjoining areas, in Seismographic Stations: University of California Press, Berkeley, p. 7-18.

Bolt, B.A., and Uhrhammer, R.A., 1986, Report on the March 31, 1986 Mt. Lewis, California, earthquake (east of Fremont)--seismology aspects: Earthquake Engineering Research Institute Special Earthquake Report, University of California, Berkeley, 3 p.

Bonilla, M.G., and Buchanon, J.M., 1970, Interim report on worldwide historic surface faulting: U.S. Geological Survey Open-File Report 70-34, 32 p.

Bonilla, M.G., Mark, R.K., and Lienkaemper, J.J., 1984, Statistical relations among earthquake magnitude, surface rupture length, and surface fault displacement: Bulletin of the Seismological Society of America, v. 74, p. 2379-2411.

Boore, D.B., and Joyner, W.B., 1982, The empirical prediction of ground motion: Bulletin of the Seismological Society of America, v. 72, no. 6, p. S43-S60.

Bortugno, E.J., McJunkin, R.D., and Wagner, D.L., 1991, Map showing recency of faulting, San Francisco-San Jose quadrangles, California, scale 1:250,000: California Division of Mines and Geology, RGM-5A.

Bouchon, M., 1982, The rupture mechanism of the Coyote Lake earthquake of 6 August 1979 inferred from near-field data: Bulletin of the Seismological Society of America, v. 72, p. 745-757.

Brillinger, D.R., and Preisler, H.K., 1984, An exploratory analysis of the Joyner-Boore attenuation data: Bulletin of the Seismological Society of America, v. 74, p. 1441-1450.

Bryant, W.A., 1982, West Napa fault zone; Soda Creek fault (East Napa fault): California Division of Mines and Geology Fault Evaluation Report FER-129, 9 p.

Budding, K.E., Schwartz, D.P., and Oppenheimer, D.H., 1991, Slip rate, earthquake recurrence, and seismogenic potential of the Rodgers Creek fault zone, northern California: initial results: Geophysical Research Letters, v. 18, p. 447-450.

Burger, R.W., Somerville, P.G., Barker, J.S., Herrmann, R.B., and Helmberger, D.V., 1987, The effect of crustal structure on strong ground motion attenuation relations in eastern North America: Bulletin of the Seismological Society of America, v. 77, p. 420-439.

Burke, D.B., and Helley, E.J., 1973, Map showing evidence for recent fault activity in the vicinity of Antioch, Contra Costa County, California: U.S. Geological Survey Miscellaneous Field Studies Map MF-533, scale 1:24,000.

Byrne, D., Davies, D., and Sykes, L., 1988, Loci and maximum size of thrust earthquakes and the mechanics of the shallow region of subduction zones: Tectonics, v. 7, p. 833-857.

California Division of Mines and Geology, 1975, Recommended guidelines for determining the maximum credible and the maximum probable earthquakes: California Division of Mines and Geology Note 43, State of California.

Campbell, K.W., 1989, Empirical prediction of near-source ground motion for the Diablo Canyon Power Plant site, San Luis Obispo County, California: U.S. Geological Survey Open-File Report 89-484.

Campbell, K.W., 1990, Reanalysis of strong-motion recordings; empirical prediction of near-source ground motion for the Diablo Canyon Power Plant site, San Luis Obispo County, California: Report to the U.S. Nuclear Regulatory Commission.

Campbell, K.W., 1991, A random-effects analysis of near-source ground motion for the Diablo Canyon Power Plant site, San Luis Obispo County, California, California: Dames & Moore, Evergreen, Colorado, Prepared for Lawrence Livermore National Laboratory.

Carver, G.A., 1987, Late Cenozoic tectonics of the Eel River basin region, coastal northern California, in Schymiczek, H., and Suchland, R., eds., Tectonics, Sedimentation, and Evolution of the Eel River and Other Coastal Basins of Northern California: San Joaquin Geological Society Miscellaneous Publication 37, p. 61-72.

Carver, G.A., 1992, Late Cenozoic tectonics of coastal northern California: AAPG-SEPM Field Trip Guidebook, May.

Carver, G.A., and Aalto, K.R., 1992, Late Cenozoic subduction tectonics and sedimentation, northern coastal California: trip stop guide: AAPG-SEPM Field Trip Guidebook, May.

Carver, G.A., Jayco, A.S., Valentine, D.W., Li, W.H., and Foss, A., in review, Coastal uplift associated with the 1992 Petrolia earthquakes, Northern California.

Cerveny, V., 1985, Ray synthetic seismograms for complex two-dimensional and three-dimensional structures: Journal of Geophysics, v. 58, p. 2-26.

Chang, C.-Y., Mok, C.M., Power, M.S., Tang, Y.K., Tang, T.H., and Stepp, J.C., 1990, Equivalent linear versus nonlinear ground response analyses at Lotung seismic experiment site, Proceedings of the Fourth U.S. National Conference on Earthquake Engineering, Palm Springs, California.

Chang, F.K., and Krinitzsky, E.L., 1977, Duration, spectral content, and predominant period of strong motion earthquake records from western United States, in State-of-the-Art for Assessing Earthquake Hazards in the United States: U.S. Army Engineers Waterways Experiment Station Miscellaneous Paper S-73-1, Report 8, Vicksburg, Mississippi.

Clark, D.H., Hall, N.T., Hamilton, D.H., and Heck, R.G., 1991, Structural analysis of late Neogene deformation in the central offshore Santa Maria Basin, California: Journal of Geophysical Research, v. 96, no. B4, p. 6435-6457.

Clarke, S.H. Jr., 1992, Geology of the Eel River Basin and adjacent region: implications for late Cenozoic tectonics of the southern Cascadia subduction zone and Mendocino triple junction: American Association of Petroleum Geologists Bulletin (expected publication early-1992).

Clarke, S.H. Jr., and Carver, G.A., 1992, Late Holocene tectonics and paleoseismicity, southern Cascadia subduction zone: Science, v. 255, 188-192.

Cloud, W.K., Hill, D.M., Huffman, M.E., Jennings, C.W., McEvilly, T.V., Nason, R.D., Steinbrugge, K.V., Tocher, D., Unger, J.D., and Youd, T.L., 1970, The Santa Rosa earthquakes of October, 1969: California Division of Mines and Geology Mineral Information Service, v. 23, no. 3, p. 43-63.

Cohee, B.P., Somerville, P.G., and Abrahamson, N.A., 1991, Simulated ground motions for hypothesized M_W = 8 subduction earthquakes in Washington and Oregon: Bulletin of the Seismological Society of America, v. 81, no. 1, p. 28-56.

Coppersmith, K.J., 1979, Activity assessment of the Zayante-Vergeles fault, central San Andreas fault system, California: Ph.D. thesis, University of California, Santa Cruz, 216 p.

Coppersmith, K.J., 1991, Seismic source characterization for engineering seismic hazard analyses: Proceedings Fourth International Conference on Seismic Zonation, v. 1, p. 3-60.

Cornell, C.A., 1968, Engineering seismic risk analysis: Bulletin of the Seismological Society of America, v. 58, p. 1583-1606.

Cornell, C.A., and Van Marke, E.H., 1969, The major influences on seismic risk: Proceedings of the Third World Conference on Earthquake Engineering, Santiago Chile, v. A-1, p. 69-93.

Cox, A., and Engebretson, D., 1985, Change in motion of Pacific plate at 5 Myr BP: Nature, v. 313, p. 472-272.

Crosson, R.S., and Owens, T.J., 1987, Slab geometry of the Cascadia subduction zone beneath Washington from earthquake hypocenters and teleseismic converted waves: Geophysical Research Letters, v. 14, p. 824-827.

Crouse, C.B., Vyas, Y.K., and Schell, B.A., 1988, Ground motions from subduction-zone earthquakes: Bulletin of the Seismological Society of America, v. 78, no. 1, p. 1-25.

Davis, J.F., Bennett, J.H., Borchardt, G.G., Kahle, J.E., Rice, S.T., and Silva, M.A., 1982, Earthquake planning scenario for a magnitude 8.3 earthquake on the San Andreas fault in the San Francisco Bay Area: California Division of Mines and Geology Special Publication 61.

DeMets, C., Gordon, R.G., Argus, D.F., and Stein, S., 1990, Current plate motions: Geophysical Journal International, v. 101, p. 425-478.

DeMets, C., Gordon, R.G., Stein, S., and Argus, D.F., 1987, A revised estimate of Pacific-North America motion and implications for western North America plate boundary zone tectonics: Geophysical Research Letters, v. 14, no. 9, p. 911-914.

Dibblee, T.W. Jr., 1980a, Preliminary geologic map of the Walnut Creek quadrangle, Contra Costa County, California: U.S. Geological Survey Open-File Report 80-351.

Dibblee, T.W. Jr., 1980b, Preliminary geologic map of the Benicia quadrangle, Contra Costa and Solano counties, California: U.S. Geological Survey Open-File Report 80-400.

Dibblee, T.W. Jr., 1980c, Preliminary geologic map of the Briones Valley quadrangle, Alameda and Contra Costa counties, California: U.S. Geological Survey Open-File Report 80-539.

Dibblee, T.W. Jr., 1980d, Preliminary geologic map of the Antioch South quadrangle, Contra Costa County, California: U.S. Geological Survey Open-File Report.

Dibblee, T.W. Jr., 1981, Preliminary geologic map of the Port Chicago quadrangle, Solano and Contra Costa counties: California, U.S. Geological Survey Open-File Report 81-106.

Dibblee T.W. Jr., and Darrow, R.L., 1981, Guidebook to the regional geology of the East Bay Hills and the Northern Diablo Range - Livermore Valley area, Society of Economic Paleontologists and Mineralogists: in Frizzell, V., ed., Geology of the Central and Northern Diablo Range, California.

Dieterich, J.H., and others, 1990, Probabilities of large earthquakes occurring in the San Francisco Bay Region, California: Working Group on California Earthquake Probabilities, U.S. Geological Survey Circular 1053.

Dobry, R., Idriss, I.M., and Ng, E., 1978, Duration characteristics of horizontal components of strong motion earthquake records: Bulletin of the Seismological Society of America, v. 68, no. 5, p. 1487-1520.

Dobry, R., and Vucetic, M., 1987, State-of-the-art report: dynamic properties and response of soft clay deposits: Proceedings, International Symposium on Geotechnical Engineering of Soft Soils, v. 2, 51-87.

Du, Y., and Aydin, A., 1992, Northward progression of slip and stress transfer during three sequential moderate earthquakes along the central Calaveras fault, in Galehouse, J.S., ed., Program and Abstracts, Second Conference on Earthquake Hazards in the Eastern San Francisco Bay Area: California State University, Hayward, p. 19.

Earthquake Engineering Research Institute, 1989, The basics of seismic risk analysis: Earthquake Spectra, v. 5, p. 675-702.

Earth Sciences Associates, 1973, Preliminary report on the geology and seismicity of the southwestern Montezuma Hills and vicinity: Consultant's Report for Pacific Gas and Electric.

Earth Sciences Associates, 1982, Seismotectonic study of Contra Loma Dam and vicinity: Consultant's Report for the U.S. Bureau of Reclamation.

Earth Sciences Associates, 1983, Seismotectonic study of Martinez Dam and vicinity: Consultant's Report for the U.S. Bureau of Reclamation.

Eaton, J.P., 1986, Tectonic environment of the 1892 Vacaville/Winters earthquake and the potential for large earthquakes along the western edge of the Sacramento Valley: U.S. Geological Survey Open-File Report 86-370, 11 p.

Eaton, J.P., 1990, The earthquake and its aftershocks from May 2 through September 30, 1983: U.S. Geological Survey Professional Paper 1487, p. 113-117.

Eberhart-Phillips, D., and Reasenberg, P.A., 1990, Complex faulting structure inferred from local seismic observations of $M \leq 1.0$ aftershocks, May 2-June 30, 1983, in Rymer, M.J.. and Ellsworth W.L., ed., The Coalinga, California, Earthquake of May 2, 1983: U.S. Geological Survey Professional Paper 1487.

Ekström, G., Stein, R.S., Eaton, J.P., and Eberhart-Phillips, D., in review, Seismicity and geometry of a 110-km-long blind fault, the 1985 Kettleman Hills, California, earthquake: Submitted to Journal of Geophysical Research.

Ellsworth, W.L., 1975, Bear Valley, California, earthquake sequence of February - March, 1972: Bulletin of the Seismological Society of America, v. 65, no. 2, p. 483-506.

Ellsworth, W.L., Olson, J.A., Shijo, L.N., and Marks, S.M., 1982, Seismicity and active faults in the eastern San Francisco Bay region, in Hart, E.W., Hirschfeld, S.E., and Schulz. S.S., eds., Proceedings of the Conference on Earthquake Hazards in the Eastern San Francisco Bay Area: California Department of Conservation, Division of Mines and Geology Special Publication 62, p. 83-92.

Engdahl, E.R., and Rinehart, W.A., 1992, Seismicity map of North America, in Slemmons D.B., Engdahl, E.R., Blackwell, D., and Schwartz, D., Neotectonics of North America: Geological Society of America, Boulder, Colorado, CSMV-1.

Engebretson. D.C., Cox, A., and Gordon, R.G., 1985, Relative motions between oceanic and continental plates in the Pacific basin: Geological Society of America Special Paper 206, 59 p.

Evans, D.G., and McEvilly, T.V., 1982, A note on relocating the 1963 Watsonville earthquakes: Bulletin of the Seismological Society of America, v. 72, no. 4, p. 1309-1316.

Finn, W.D.L., Lee, K.W., and Martin, G.R., 1977, An effective stress model for liquefaction: Journal of Geotechnical Engineering Division, ASCE, v. GT6.

Fox, K.F. Jr., 1983, Tectonic setting of Late Miocene, Pliocene, and Pleistocene rocks in part of the Coast Ranges north of San Francisco, California: U.S. Geological Survey Professional Paper 1239.

Fox, K.F. Jr., Sims, J.D., Bartow, J.A., and Helley, E.J., 1973, Preliminary geologic map of eastern Sonoma County and western Napa County, California: U.S. Geological Survey Miscellaneous Field Studies Map MF-483.

Frizzell, V.A. Jr., and Brown, R.D. Jr., 1976, Map showing recently active breaks along the Green Valley fault, Napa and Solano counties, California: U.S. Geological Survey Miscellaneous Field Studies Map MF-743.

Fuis, G.S., and Mooney, W.D., 1990, Lithospheric structure and tectonics from seismic-refraction and other data, in Wallace, R.E., ed., The San Andreas Fault System, California: U.S. Geological Survey Professional Paper 1515, p. 207-236.

Fujita, K., and Kanamori, H., 1981, Double seismic zones and stresses of intermediate depth earthquakes: Geophysical Journal of the Royal Astronomical Society of London, v. 66, p. 131-156.

Gardner, J.K., and Knopoff, L., 1974, Is the sequence of earthquakes in Southern California, with aftershocks removed, Poissonian: Bulletin of the Seismological Society of America, v. 64, no. 5, p. 1363-1367.

Geomatrix Consultants, 1986, Geological assessment of the seismic potential of the Bartlett Springs shear zone for Scott Dam, Lake County, California: Consultant's Report for Pacific Gas and Electric Company.

Geomatrix Consultants, 1988, Cascadia subduction zone: An evaluation of the earthquake potential and implications to WNP-3: Unpublished report for Washington Public Power Supply, Response to NRC Questions 230.1 and 230.2., 136 p.

Geomatrix Consultants, 1993, Seismic margin earthquake for the Trojan Nuclear Power Plant: Report prepared for General Electric Company, Portland, May.

Goldfinger C., Kulm, L.D., Yeats, R.S., Applegate, B., MacKay, M.E., Moore, G.F., 1992, Transverse structural trends along the Oregon convergent margin: Geology, v. 20, p. 141-144.

Goldman, H.B., 1969, Geology of San Francisco, in Goldman, H.B., ed., Geologic and Engineering Aspects of San Francisco Bay Fill: California Division of Mines and Geology Special Report 97.

Goter, S.K., 1988, Seismicity of California 1808-1987: National Earthquake Information Center Open-File Report 88-286.

Gutenberg, B., and Richter, C.F., 1954, Seismicity of the earth and associated phenomena: 2nd ed., Princeton University Press, Princeton, New Jersey, 310 p.

Gutenberg, B., and Richter, C.F., 1956, Earthquake magnitude, intensity, energy, and acceleration: Bulletin of the Seismological Society of America, v. 46, p. 105-145.

Hall, N.T., Lettis, W.R., de Wit, M.W., and Angell, M., 1991, Late Quaternary uplift along the Pajaro River, southern Santa Cruz Mountains, California: Unpublished Technical Report prepared for U.S. Geological Survey, Contract no. 14-08-0001-G1828.

Hanks, T.C., and Kanamori, H., 1979, A moment-magnitude scale: Journal of Geophysical Research, v. 84, no. B5, p. 2348-2350.

Hanson, K.L., and Lettis, W.R., in press, Estimated Pleistocene slip rate for the San Simeon fault zone, south-central coastal California: Geological Society of America Memoir on the Santa Maria Basin.

Harbert, W., 1991, Late Neogene relative motions of the Pacific and North American plates: Tectonics, v. 10, p. 1-16.

Harris, R.A., 1992, Dynamic interaction of parallel strike-slip fault segments: some implications for the San Francisco Bay area (abs.): Program and Abstracts, Second Conference on Earthquake Hazards in the Eastern San Francisco Bay Area, p. 29.

Harsh, P.W., and Burford, R.O., 1982, Alignment array measurements of fault slip in the eastern San Francisco Bay Area, California: Proceedings, Conference on Earthquake Hazards in the Eastern San Francisco Bay Area, p. 251-260.

Hart, E.W., 1988, Fault-ruptured hazard zones in California, Alquist-Priolo Special Studies Zones act of 1972 with index to special studies zones maps: California Division of Mines and Geology Special Publication 42, revised 1988.

Hazelwood, R.M., 1974, Preliminary report of seismic refraction survey along the east side of San Francisco Bay, Alameda County, California: U.S. Geological Survey Open-File Report.

Heaton, T.H., and Hartzell, S.H., 1987, Earthquake hazards on the Cascadia subduction zone: Science, v. 236, p. 162-168.

Helley, E.J., Lajoie, K.R., Spangle, W.E., and Blair, M.L., 1979, Flatland deposits of the San Francisco Bay Region, California - their geology and engineering properties, and their importance to comprehensive planning: U.S. Geological Survey Professional Paper 943.

Herd, D.G., 1978, Neotectonic framework of central coastal California and its implications to microzonation of the San Francisco Bay Region: Proceedings, Second International Conference on Microzonation, v. 21, p. 232-240.

Herd, D.G., 1979, The San Joaquin fault zone--evidence for late Quaternary faulting along the west side of the northern San Joaquin Valley, California: Geological Society of America Abstracts with Programs, v. 11, no. 3, p. 83.

Hill, D.P., Eaton, J.P, and Jones, L.M., 1990, Seismicity, 1980-86, in Wallace, R.E., ed., The San Andreas Fault System, California: U.S. Geological Survey Professional Paper 1515, p. 115-151.

Hoose, S.N., 1987, The Morgan Hill earthquake: an overview, in Hoose, S.W., ed., The Morgan Hill, California Earthquake of April 24, 1984: U.S. Geological Survey Bulletin 1639.

Houston, H., and Vidale, J.E., unpub. report, Report on relocated seismicity in the vicinity of Cape Mendocino using QUAKE3D, consulting report to Geomatrix Consultants, 1992 4p.

Hyndman, R.D., and Wang, K., 1993, Thermal constraints on the zone of major thrust earthquake failure: the Cascadia subduction zone: Journal of Geophysical Research, v. 98, p. 2039-2060.

Idriss, I.M., 1987, Earthquake ground motions, Lecture notes, Course on Strong Ground Motion: Earthquake Engineering Research Institute, Pasadena, California, April 10-11.

Idriss, I.M., 1991, Selection of earthquake ground motions at rock sites: Report Prepared for the Structures Division, Building and Fire Research Laboratory, National Institute of Standards and Technology, Department of Civil Engineering, University of California, Davis, September.

Isacks, B.L, and Molnar, P., 1971, Distribution of stresses in the descending lithosphere from a global survey of focal mechanisms of mantle earthquakes: Rev. Geophys. v. 9, p. 103-174.

Iwasaki, T., Katayama, T., Kawashima, K., and Saeki, M., 1978, Statistical analysis of strong-motion acceleration records obtained in Japan: Proceedings of the Second International Conference on Microzonation for Safer Construction, Research and Application, v. II, p. 705-716.

Jennings, C.W., 1975, Fault map of California: California Geologic Data Map Series, Map No. 1 - Faults, Volcanoes, Thermal Springs and Wells, California Division of Mines and Geology.

Jennings, C.W., 1985, An explanatory text to accompany the 1:750,000-scale fault and geologic maps of California: California Division of Mines and Geology Bulletin 201.

Jennings, C.W., and Burnett, J.L., 1961, San Francisco sheet, geologic map of California (Olaf P. Jenkins Edition): California Division of Mines and Geology.

Johnson, L.R., and McEvilly, T.V., 1974, Near-field observations and source parameters of central California earthquakes: Bulletin of Seismological Society of America, v. 64, no. 6, p. 1855-1886.

Joyner, W.B., and Boore, D.M., 1982, Prediction of earthquake response spectra: U.S. Geological Survey Open-File Report 82-977.

Joyner, W.B., and Boore, D.M., 1988, Measurement, characterization, and prediction of strong ground motion, in Earthquake Engineering and Soil Dynamics II - Recent Advances in Ground Motion Evaluations: ASCE Geotechnical Special Publication 20, p. 43-102.

Joyner, W.B., and Fumal, T.E., 1985, Predictive mapping of earthquake ground motion, in Evaluating Earthquake Hazards in the Los Angeles Region: U.S. Geological Survey Professional Paper 1360, p. 203-220.

Joyner, W.B., Warrick, R.E., and Oliver, A.A. III, 1976, Analysis of seismograms from a downhole array in sediments near San Francisco Bay: Bulletin of the Seismological Society of America, v. 66, p. 937-958.

Kanamori, H., 1971, Great earthquakes at island arcs and the lithosphere: Tectonophysics, v. 12, p. 187-198.

Kanamori, H., 1977, Seismic and aseismic slip along subduction zones and their tectonic implications, in Island Arcs Deep Sea Trenches and Back-Arc Basins, Maurice Ewing Series, American Geophysical Union, v. 4, Talwani, M., and Pitman, W.C., eds., p. 163-174.

Kanamori, H., 1983, Magnitude scale and quantification of earthquakes: Tectonophysics, v. 93, p. 185-199.

Kanamori, H., and Anderson, D.L., 1975, Theoretical basis of some empirical relations in seismology: Bulletin of the Seismological Society of America, v. 65, p. 1073-1096.

Kawashima, K., Aizawa, K., and Takahashi, K., 1984, Attenuation of peak ground motion and absolute acceleration response spectra: Proceedings of the Eighth World Conference on Earthquake Engineering, San Francisco, v. II, p. 257-264.

Keefer, D.L., Bodily, S.E., 1983, Three-point approximations for continuous random variables: Management Science, v. 29, no. 5, p. 595-609.

Kelsey, H.M., 1990, Late Quaternary deformation of marine terraces on the Cascadia subduction zone near Cape Blanco, Oregon: Tectonics, v. 9, p. 983-1014.

Kelsey, H.M., and Carver, G.A., 1988, Late Neogene and Quaternary tectonics associated with the northward growth of the San Andreas transform fault, northern California: Journal of Geophysical Research, v. 93, p. 4797-4819.

King, N.E., Savage, J.C., Lisowski, M., and Prescott, W.H., 1981, Preseismic and coseismic deformation associated with the Coyote Lake, California, earthquake: Journal of Geophysical Research, v. 86, p. 892-898.

Knuepfer, P.L., 1977, Geomorphic investigations of the Vaca and Antioch fault systems, Solano and Contra Costa counties, California: Stanford University, California, unpublished M.S. thesis, 53 p.

Knuepfer, P.L., 1989, Implications of the characteristics of end-points of historical surface fault ruptures for the nature of fault segmentation: Proceedings of the Workshop on Fault Segmentation and Controls of Rupture Initiation and Termination, U.S. Geological Survey Open-File Report 89-315, p.193-228.

Krinitzky, E.L., Chang, F.K., and Nuttli, O.W., referenced in Krinitzky, E.L., 1987, Empirical relationships for earthquake ground motions in Mexico City: Proceedings of the ASCE Conference: The Mexico Earthquake - 1985, Factors Involved and Lessons Learned, held in Mexico City, September 19-20, 1986.

Lajoie, K.R., and Helley, E.J., 1975, Differentiation of sedimentary deposits for purposes of seismiczonation, in Borcherdt, R.D., ed., Studies for Seismic Zonation of the San Francisco Bay Region: U.S. Geological Survey Professional Paper 941-A.

Lawson, A.C., 1908, The California Earthquake of April 18, 1906: The Carnegie Institution of Washington, Reprinted 1969.

Lawson, A.C., 1914, Description of the San Francisco District; Tampalpais, San Francisco, Concord, San Mateo and Hayward quadrangles: U.S. Geological Survey, Geology Atlas San Francisco Folio (no. 193).

Lee, K.W., and Finn, L.W.D., 1985, DESRA-2 computer program: University of British Columbia.

Li, W.H., and Carver, G.A., 1992, Late Holocene subsidence in the Eel River syncline, northern California (abs.): 1992 Geol. Soc. Am. Cord. Section Mtg., Eugene, Oregon.

Li, X.S., Wang, Z.L., and Shen, C.K., 1992, SUMDES--A nonlinear procedure for response analysis of horizontally-layered sites subjected to multi-directional earthquake loading: Department of Civil Engineering, University of California, Davis.

Lienkaemper, J.J., 1984, Comparison of two surface-wave magnitude scales: M of Gutenberg and Richter (1954) and Ms of "preliminary determination of epicenters": Bulletin of the Seismological Society of America, v. 74, p. 2357-2378.

Lienkaemper, J.J., 1989, Field trip guide to the Hayward fault: U.S. Geological Survey Open-File Report 89-500, 23 p.

Lienkaemper, J.J., Borchardt, G., Wilmesher, J.F., and Meier, D., 1989, Holocene slip rate along the Hayward fault, northern California: Eos, Transactions of the American Geophysical Union, v. 70, no. 43, p. 1349.

Lilhanand, K., and Tseng, W.S., 1988, Development and application of realistic earthquake time histories compatible with multiple-damping design spectra: Proceedings, 9th World Conference on Earthquake Engineering, Tokyo-Kyoto, Japan, August.

Lisowski, M., Savage, J.C., and Prescott, W.H., 1991, The velocity field along the San Andreas fault in central and southern California: Journal of Geophysical Research, v. 96, no. B5, p. 8369-8389.

Louderback, G.D., 1947, Central California earthquakes of the 1830's: Bulletin of the Seismological Society of America, v. 37, no. 1, p. 31-74.

Luco, J.E., and D.A. Sotiropoulos, 1980, Local characteristic of free-field ground motion and effects of wave passage: BSSA, 70, p. 2229-2244.

Marone, C., and Scholz, C., 1988, the depth of seismic faulting and the upper transition from stable to unstable slip regimes: Geophysical Research Letters, v. 15, p. 621-624.

Martin, P.P., 1975, Nonlinear methods for dynamic analysis of ground response: Ph.D. Thesis, University of California, Berkeley.

McEvilly, T.V., 1966, The earthquake sequence of November 1964, near Corralitos, California: Bulletin of the Seismological Society of America, v. 56, no. 3, p. 755-773.

McNally, K., and Minster, B., 1981, Nonuniform seismic slip rates along the middle America trench: Journal of Geophysical Research, v. 86, p. 4949-4959.

McPherson, R.C., 1989, Seismicity and focal mechanisms near Cape Mendocino, northern California: 1974-1984, unpub.M.S. thesis, Humboldt State University, Arcata, CA, 75 p.

McPherson, R.C., 1992, Seismicity and stress at the southern end of the Cascadia subduction zone: AAPG-SEPM Field Trip Guidebook, May, 1992, p. 19-29.

Mertz, H.A., and Cornell, C.A., 1973, Aftershocks in engineering seismic risk analysis: M.I.T. Department of Civil Engineering Research Report R73-25, Cambridge, Massachusetts.

Mitchell, C.E., Weldon, R.J., Vincent, P., and Pittock, H.L., 1992, Active uplift of the Pacific Northwest margin (abs.): EOS Transactions, American Geophysical Union, v. 72, p. 314.

Mori, J., Jacob, K.H., and Beavan, J., 1984, Characteristics of strong ground motions from subduction zone earthquakes in Alaska and Japan: Earthquake Notes, v. 55, no. 1, p. 16.

Mualchin, L, and Jones, A.L., 1989, Peak acceleration from maximum credible earthquakes in California (rock and stiff-soil sites) for the design of highway bridges and overpasses, Proposed Map Sheet 42 (Subject to Revision), California Division of Mines and Geology.

Mualchin, L., and Jones, A.L., 1992, Peak acceleration from maximum credible earthquakes in California: California Division of Mines and Geology Open-File Report 92-1.

Namson, J.S., and Davis, T.L., 1988, Seismically active fold and thrust belt in the San Joaquin Valley, California: Geological Society of America Bulletin, v. 100, p. 257-273.

Namson, J.S., and Davis, T.L., 1990, Late Cenozoic fold and thrust belt of the southern Coast Ranges and Santa Maria Basin, California: American Association of Petroleum Geologists Bulletin, v. 74, p. 467-492.

Namson, J.S., Davis, T.L., and Lagoe, M.B., 1990, Tectonic history and thrust-fold deformation style of seismically active structures near Coalinga, in Rymer, M.J., and Ellsworth, W.L., eds., The Coalinga, California, Earthquake of May 2, 1983: U.S. Geological Survey Professional Paper 1487.

National Earthquake Information Service (NEIS), Catalog of earthquakes.

National Research Council, 1988, Probabilistic Seismic Hazard Analysis: National Academy Press.

Nelson, A.R., and Personius, S.F., 1991, The potential for great earthquakes in Oregon and Washington: an overview of recent coastal geologic studies and their bearing on segmentation of Holocent ruptures, central Cascadia subduction zone: U.S. Geological Survey Open-File Report 91-441-A, 29 p.

Niemi, T.M., and Hall, N.T., 1992, Late Holocene slip rate and recurrence of great earthquakes on the San Andreas fault in northern California: Geology, v. 20, p. 195-198.

Nishimura, C., Wilson, D.S., and Hey, R.N., 1984, Pole of rotation analysis of present-day Juan de Fuca plate motion: Journal of Geophysical Research, v. 89, p. 10,283-10,290.

NOAA, 1982, Development and initial application of software for seismic exposure evaluation, report by Woodward-Clyde Consultants, prepared for National Oceanic and Atmospheric Administration, two volumes, May.

Nur, A., Ron, H., Beroza, G., and Alfonsi, L., 1992, A fault is born: the mechanical origin of the Mojave seismic line (abs.): EOS Transactions of the American Geophysical Union, v. 73, p. 362.

Oppenheimer, D.H., Bakun, W.H., and Lindh, A.G., 1990, Slip partitioning of the Calaveras fault, California, and prospects for future earthquakes: Journal of Geophysical Research, v. 95, p. 8483-8498.

Oppenheimer, D., Beroza, G., Carver, G., Dengler, L., Eaton, J., Gee, L., Gonzalez, F., Jayko, A., Li, W.H., Lisowski, M., Magee, M., Marshall, G., Murray, M., McPherson, R., Romanowicz, B., Satake, K., Simpson, R., Somerville, P., Stein, R., Valentine, D., 1993, The Cape Mendocino, California Earthquakes of April 1992: Subduction at the Triple Junction: Science, v. 261, no. 5120, p. 433-438.

Ostenaa, D., LaForge, R., and Wilson, J., 1989, Preliminary seismic risk analysis for the delta water management study: south delta: Geotechnical Engineering and Geology Division, U.S. Bureau of Reclamation, Denver, CO, Seismotectonic Report 89-1.

Pacheco, J.F., Sykes, L.R., and Scholz, C.H., 1993, Nature of seismic coupling along simple plate boundaries of the subduction type: Journal of Geophysical Research, v. 98, no. B8. p. 14133-14160.

Pacific Gas and Electric Company (PG&E), 1988, Final Report of the Diablo Canyon Long Term Seismic Program: U.S. Nuclear Regulatory Commission Docket Nos. 50-275 and 50-323.

Pacific Gas and Electric Company (PG&E), 1990, Response to questions on the Final Report of the Diablo Canyon Long Term Seismic Program: U.S. Nuclear Regulatory Commission Docket Nos. 50-275 and 50-323.

Pampeyan, E.H., 1979, Preliminary map showing recency of faulting in coastal north-central California: U.S. Geological Survey Miscellaneous Field Studies Map MF-1070.

Peterson, E.T., and Seno, T., 1984, Factors affecting seismic moment release rates in subduction zones: Journal of Geophysical Research, v. 89, p. 10,233-10,248.

Radbruch, D.H., 1969, Areal and engineering geology of the Oakland East quadrangle, California: U.S. Geological Survey, Geologic Quadrangle Maps of the United States, MAP GQ-769.

Redpath, B., 1990, Borehole velocity surveys at the Embarcadero in San Francisco and the Cypress structure in Oakland: Report Prepared for California Department of Transportation, August.

Redpath Geophysics, 1991, Seismic velocity logging in the San Francisco Bay Area: Report Prepared for Electric Power Research Institute, Palo Alto, California.

Reiche, P., 1950, Rio Vista, California, fault scarp (abs): Geological Society of America Bulletin, v. 61, p. 1529-1530.

Richter, C.F., 1958, Elementary Seismology: W.H. Freeman and Company, San Francisco and London.

Rockwell, T., Vaughan, P., Bickner, F., and Hanson, K.L., in press, Correlation and age estimates of soils developed in marine terraces across the San Simeon fault zone Central California: Geological Society of America Memoir on the Santa Maria Basin.

Rogers, G.C., 1988, An assessment of the megathrust earthquake potential of the Cascadia subduction zone: Canadian Journal of Earth Sciences, v. 25, p. 844-852.

Rogers, J.D., and Figuers, S.H., 1991, Engineering geologic site characterization of the greater Oakland-Alameda area, Alameda and San Francisco Counties, California: Final Report to the National Science Foundation.

Ron, H., and Nur, A., 1992, Block rotations and the formation of new faults in the San Gabriel and the central Mojave fault domains (abs.): EOS Transactions of the American Geophysical Union, v. 73, p. 381.

Rubin, C.M., and McGill, S.F., 1992, The June 28, 1992 Landers earthquake: slip distribution and variability along a portion of the Emerson fault: Eos, v. 73, no. 43, p. 362.

Rymer, M.J., and Ellsworth, W.L., eds., 1990, The Coalinga, California, earthquake of May 2, 1983: U.S. Geological Survey Professional Paper 1487.

Sadigh, K., 1979, Ground motion characteristics for earthquakes originating in subduction zones and in the western United States: Sixth Pan-American Conference, Lima, Peru.

Sadigh, K., 1983, Considerations in the development of site-specific spectra, in Proceedings of Conference XXII, Site-Specific Effects of Soil and Rock on Ground Motion and the Implications for Earthquake Resistant Design: U.S. Geological Survey Open-File Report 83-845.

Sadigh, K., 1984, Characteristics of strong motion records and their implications for earthquake-resistant design: Earthquake Engineering Research Institute Publication 84-06, v. 12, p. 31-45.

Sadigh, K., and Akky, R., 1989, Relationships for horizontal peak ground velocity and peak ground displacement for shallow crustal earthquakes (abs): Seismological Research Letters, v. 60, no. 1, p. 15.

Sadigh, K., and Chang, C.-Y., 1990, Response spectral relationships for rock, deep-stiff soil and soft soil site conditions: Seismological Research Letters, v. 61, no. 1.

Sadigh, K., Chang, C.-Y., Makdisi, F., and Egan, J.A., 1989, Attenuation relationships for horizontal peak ground acceleration and response spectral acceleration for rock sites (abs.): Seismological Research Letters, v. 60, no. 1, p. 19.

Sadigh, K., Egan, J.A., and Youngs, R.R., 1986, Specification of ground motion for seismic design of long period structures: Earthquake Notes, v. 57, no. 1, p. 13, relationships are tabulated in Joyner and Boore (1988) and Youngs et al. (1987).

Safonov, A., 1962, The challenge of the Sacramento Valley, California, in Bowen, O.E., ed., Geologic Guide to the Gas and Oil Fields of Northern California: California Division of Mines and Geology Bulletin 181, p. 77-97.

Saul, R.B., 1973, Geology and slope stability of the S.W. 1/4 Walnut Creek quadrangle, Contra Costa County, California: California Division of Mines and Geology Map Sheet 16.

Savage, J.C., and Lisowski, M., 1991, Strain measurements and the potential for a great subduction earthquake off the coast of Washington: Science, v. 252, p.101-103.

Schlocker, J., 1974, Geology of the San Francisco North quadrangle, California: U.S. Geological Survey Professional Paper 782.

Schnabel, P.B., Seed, H.B., and Lysmer, J., 1972, SHAKE--A computer program for earthquake response analysis of horizontally layered sites: Report No. EERC 72-12, Earthquake Engineering Research Center, University of California, Berkeley, December 1972.

Schneider, J.F., Abrahamson, N.A., and Stepp, J.C., 1992, The spatial variation of earthquake ground motion and effects of local site conditions: Proceedings of the Tenth World Conference on Earthquake Engineering, II, p. 967-972.

Scholz, C., 1988, The brittle-ductile transition and the depth of seismic faulting: Geol. Runds., v. 77, p. 319-328.

Schwartz, D.P., and Coppersmith, K.J. 1984, Fault behavior and characteristic earthquakes from the Wasatch and San Andreas faults: Journal of Geophysical Research, v. 89, no. B7, p. 5681-5698.

Schwartz, D.P. and Coppersmith, K.J., 1986, Seismic hazards: new trends in analysis using geologic data: Active Tectonics, Academic Press, Washington D.C., p. 215-230.

Schwartz, D.P., Okumura, K., Pantosti, D., Powers, T.J., and Fuentes, J.M.B., 1991, Paleoseismologic constraints on earthquake recurrence, San Andreas fault, Santa Cruz Mountains, California (abs.): Geological Society of America, Abstracts with Programs, 1991 Annual Meeting, p. A98.

Schwartz, D.P., Pantosti, D. Hecker, S., Okumura, K., Budding, K.E., and Powers, T., 1992, the Rodgers Creek fault zone: fault behavior and earthquake potential (abs.): Submitted to East San Francisco Bay Area Seismic Hazards Conference, March 1992.

Schwartz, D.P., Prentice, C.S., and Fumal, T., 1990, Geologic constraints on earthquake recurrence models, Santa Cruz Mountains segment, San Andreas fault zone (abs.): Transactions, American Geophysical Union, v. 71, no. 43, p. 1461.

Scott, N.H., 1970, Felt area and intensity, in Steinbrugge, K.V., Cloud, W.K., and Scott, N.H., eds., The Santa Rosa, California, Earthquakes of October 1, 1969: U.S. Department of Commerce, p. 94-99.

Seed, H.B., and Idriss, I.M., 1970, Soil moduli and damping factors for dynamic response analysis: Report No. UCB/EERC-70/10, University of California, Berkeley, December.

Seed, H.B., and Idriss, I.M., 1982, Ground motions and soil liquefaction during earthquakes, v. 5 of a series titled Engineering Monographs on Earthquake Criteria, Structural Design, and Strong Motion Records: Earthquake Engineering Research Institute.

Seed, H.B., and Schnabel, P., 1980, presented in Ground Motions and Soil Liquefaction During Earthquakes, v. 5 of a series titled Engineering Monographs on Earthquake Criteria, Structural Design, and Strong Motion Records, by Seed, H.B., and I.M. Idriss (1982): Earthquake Engineering Research Institute.

Seed, H.B., Wong, R.T., Idriss, I.M., and Tokimatsu, K., 1984, Moduli and damping factors for dynamic analyses of cohesionless soils: Report No. UCB/EERC-84/14, University of California, Berkeley, September.

Sharp, R.V., 1973, Map showing tectonic movement on the Concord fault, Contra Costa and Solano counties, California: U.S. Geological Survey Miscellaneous Field Studies Map MF-505.

Shedlock, K.M., McGuire, R.K., and Herd, D.G., 1980, Earthquake recurrence in the San Francisco Bay Region, California, from fault slip and seismic moment: U.S. Geological Survey Open-File Report 80-999.

Sibson, R., 1982, Fault zone models, heat flow, and the depth distribution of earthquakes in the continental crust of the United States: Bulletin of the Seismological Society of America, v. 72, p. 151-163.

Sibson, R.H., 1985, Stopping of earthquake ruptures at dilational fault jogs: Nature, v. 316, p. 248-251.

Sims, J.D., Fox, K.F. Jr., Bartow, J.A., and Helley, E.J., 1973, Preliminary geologic map of Solano County and parts of Napa, Contra Costa, Marin, and Yolo counties, California: U.S. Geological Survey Miscellaneous Field Studies Map MF-484.

Slemmons, D.B., 1982, Determination of design earthquake magnitudes for microzonation, in 3rd International Earthquake Microzonation Conference Proceedings, p. 119-130.

Slemmons, D.B., Bodin, P., and Xhang, X., 1988, Determination of earthquake from surface faulting events: Proceedings of the International Seminar and Seismic Zonation, Guangzhou, China, 13 p.

Slemmons, D.B., and Chung, D.H., 1982, Maximum credible earthquake magnitudes for the Calaveras and Hayward fault zones, California, in Proceedings on Earthquake Hazards - Eastern San Francisco Bay Area: California Division of Mines and Geology, Special Publication 62.

Slemmons, R., and Yoshimura, J., 1990, The influence of critical Moho reflections on strong ground motions recorded in San Francisco and Oakland during the 1989 Loma Prieta earthquakes: Geophysical Research Letters, v. 17, p. 1203-1206.

Smith, D.L., and Angell, M.M., 1990, Neogene thrust kinematics in the San Luis Range, south-central California Coast Ranges: balanced cross-sections of basement-involved thrust faults (abs): EOS, v. 71, no. 43, p. 1224.

Smith, S.W., Knapp, J.S., and McPherson, R., in press, Seismicity of the Gorda plate and an eastward jump of the Mendocino triple junction: submitted to Journal of Geophysical Research.

Somerville, P.G., McLaren, J.P., Saikia, C.K. and Helmberger, D.V., 1988, Site-specific estimation of spatial incoherence of strong ground motion: Proceedings, ASCE Specialty Conference on Earthquake Engineering and Soil Dynamics II, Recent Advances in Ground Motion Evaluation, Park City, Utah, p. 188-202.

Spence, W., 1989, Stress origins and earthquake potentials in Cascadia: Journal of Geophysical Research, v. 94, p. 3076-3088.

Steffen, Robertson, and Kirsten, 1983, McLaughlin Project - seismic design criteria: Consultant's Report Prepared for Homestake Mining Company by Steffen, Robertson, and Kirsten and Woodward-Clyde Consultants.

Stein, R.S., and Ekström, G., 1989, Rupture sequence and fault geometry beneath the 100-km-long New Idria-Coalinga-Kettleman Hills segmented fold chain: EOS, v. 70, p. 1378.

Stein, R., and Ekström, G., 1990, Anatomy of a 100-km-long blind thrust fault in central California, from short & long period seismology, geodesy, and seismic reflection profiles (abs.): Seismological Research Letters, v. 61, no. 1, p. 23.

Steinbrugge, K.V., Bennett, J.H., Lagorio, H.J., Davis, J.F., Borchardt, G., and Toppozada, T.R., 1987, Earthquake planning scenario for a magnitude 7.5 earthquake on the Hayward fault in the San Francisco Bay Area: California Division of Mines and Geology Special Publication 78.

Stepp, J.C., 1972, Analysis of completeness of the earthquake sample in the Puget Sound area and its effect on statistical estimates of earthquake hazard: Proceedings of the International Conference on Microzonation, v. 2, p. 897-910.

Sun, J.I., Golesorkhi, R., and Seed, H.B., 1988, Dynamic moduli and damping ratios for cohesive soils: Report No. UCB/EERC-88/15, University of California, August.

Suppe, J., 1985, Principles of Structural Geology: Prentice-Hall, Inc., Englewood Cliffs, New Jersey, 537 p.

Sweeney, J.J., 1982, Magnitudes of slip along the Greenville fault in the Diablo Range and Corral Hollow areas: Proceedings, Conference on Earthquake Hazards in the Eastern San Francisco Bay Area, p. 137-146.

Sykes, L., and Quittmeyer, R., 1981, Repeat times of great earthquakes along simple plate boundaries, in Earthquake Prediction: An International Review, Maurice Ewing Series, American Geophysical Union, Simpson, D., and Richards, P., eds., v. 4, p. 217-247.

Taber, J.J., and Smith, S.W., 1985, Seismicity of focal mechanisms associated with the subduction of the Juan de Fuca plate beneath the Olympic Peninsula, Washington: Bulletin of the Seismological Society of America, v. 75, p. 237-249.

Thatcher, W., 1975, Strain accumulation and release mechanism of the 1906 San Francisco earthquake: Journal of Geophysical Research, v. 80, no. 35, p. 4862-4872.

Tichelaar, B.W., and Ruff, L.J., 1993, Depth of seismic coupling along subduction zones: Journal of Geophysical Research, v. 98, p. 2017-2037.

Tocher, D., 1959, Seismic history of the San Francisco Bay region, in G.B. Oakeshott, ed., San Francisco Earthquake of March 1957: California Division of Mines and Geology Special Report 57.

Toppozada, T.R., 1992, Location and magnitude of the 1898 "Mare Island" earthquake, in Galehouse, J.S., ed., Second Conference on Earthquake Hazards in the Eastern San Francisco Bay Area, Program and Abstracts: California State University Hayward, p. 74.

Toppozada, T., Hallstrom, C., and Ransom D., 1990, $\geq$ 5.5 earthquakes within 100 km of Parkfield, California: Seismological Research Letters, v. 61, p. 42.

Toppozada, T.R., and Parke, D.L., 1982, Areas damaged by California earthquakes, 1900-1949: California Division of Mines and Geology Open File Report 82-17 SAC.

Toppozada, T.R., Real, C.R., and Parke, D.L., 1981, Preparation of isoseismal maps and summaries of reported effects for pre-1990 California earthquakes: California Division of Mines and Geology Open-File Report 81-11.

Trask, P.D., and Rolston, J.W., 1961, Engineering geology of San Francisco Bay, California: Bulletin of the Geological Society of America, v. 62, p. 1079-1110.

Treasher, R.C., 1963, Geology of the sedimentary deposits in San Francisco Bay, California: California Division of Mines and Geology Special Report 82.

Trifunac, M.D., and Brady, A.G., 1975, A study of the duration of strong earthquake ground motions: Bulletin of the Seismological Society of America, v. 65, no. 3, p. 581-626.

Tuttle, M., and Sykes, L., 1992, Re-evaluation of several large earthquakes in the vicinity of Loma Prieta and peninsular segments of the San Andreas fault, California: Bulletin of the Seismological Society of America, v. 82, p. 1802-1820.

U.S. Geological Survey, 1989, The Loma Prieta earthquake of October 17, 1989: Pamphlet by U.S. Geological Survey, November, 1989.

U.S. Geological Survey, 1990, Effects of the Loma Prieta earthquake on the Marina district, San Francisco, California: U.S. Geological Survey Open-File Report 90-253.

U.S. Geological Survey, 1992, Seismic velocities and geologic logs from borehole measurements at seven strong-motion stations that recorded the 1989 Loma Prieta Earthquake: U.S. Geological Survey Open-File Report 92-287.

Uhrhammer, R.A., 1980, Observations of the Coyote Lake, California, earthquake sequence of August 6, 1979: Bulletin of the Seismological Society of America, v. 70, p. 559-570.

Uhrhammer, R.A., 1986, Characteristics of northern and central California seismicity (abs.): Earthquake Notes, v. 57, no. 1, p. 21.

Unruh, J.R., and Moores, E.M., 1992, Quaternary blind thrusting in the southwestern Sacramento Valley, California: Tectonics, v. 11, no. 2, p. 192-203.

Utsu, T., 1969, Aftershocks and earthquake statistics (I), some parameters which characterize an aftershock sequence and their interrelations: Journal of the Faculty of Science, Hokkaido University, Japan, Series VII, v. III, no. 3, p. 129-195.

Valentine, D.W., Carver, G.A., and Shivelle, C., 1990, Late Holocene stratigraphic evidence for rapid episodic subsidence, Humboldt Bay, California (abs.): Geological Society of America Abstracts with Program, v. 23, p. 42.

Veneziano, D., and Van Dyck, J., 1985, Analysis of earthquake catalogs for incompleteness and recurrence rates: Seismic Hazard Methodology for Nuclear Facilities in the Eastern United States, EPRI Research Project No. P101-29, EPRI/SOG Draft 85-1, v. 2, Appendix A-6, April 30.

Verdonck, D. and Zandt, G., in press, Three-dimensional geometry of the Mendocino triple junction: submitted to Journal of Geophysical Research.

Verplanck, E.P., and Duncan, R.A., 1987, Temporal variations in plate convergence and eruption rates in the western Cascades, Oregon: Tectonics, v. 6, p. 197-209.

Vick, G.S., 1988, Late Holocene paleoseismicity and relative sea level changes of the Mad River Slough, northern Humboldt Bay, California: unpub. M.s. thesis, Humboldt State University, Dept. of Geology, Arcata, CA, 87p.

Vidale, J., and Helmberger, D.V., 1988, Elastic finite-difference modeling of the 1971 San Fernando, California, earthquake: Bulletin of the Seismological Society of America, v. 78, p. 122-141.

Vyas, Y.K., Crouse, C.B., and Schell, B.A., 1984, Ground motion attenuation equations for Benioff Zone earthquakes offshore Alaska: Earthquake Notes, v. 55, no. 1, p. 17.

Wagner, D.L., and Bortugno, E.J., 1982, Geologic map of the Santa Rosa quadrangle, California, Sheet 1 of 5, Regional Geologic Map Series, Santa Rosa Quadrangle (Geology): California Division of Mines and Geology - Map No. 2A.

Wagner, D.L., Jennings, C.W., Bedrossian, T.L., and Bortugno, E.J., 1981, Geologic map of the Sacramento quadrangle, regional geologic map series: California Division of Mines and Geology, Map No. 1A (Geology).

Wagner, J.R., 1980, Summary of regional stratigraphy and geologic structure, Appendix A, in Evaluation of the Potential for Resolving the Geologic and Seismic Issues at the Humboldt Bay Power Plant Unit No.3: prepared for the Pacific Gas and Electric Company by Woodward-Clyde Consultants, San Francisco, CA, p. A1-A73.

Wahrhaftig, C., 1989, Geology of San Francisco and vicinity: 28th International Geology Congress, Field Trip Guidebook T105, San Francisco Bay Region, California, July 1-7, 1989, American Geophysical Union, Washington, D.C.

Wakabayashi, J., Hamilton, D.H., and Smith, D.L., 1991, Miller Creek and related faults, eastern San Francisco Bay Area, California: seismotectonic significance (abs): Geological Society of America Abstracts with Programs, p. A84.

Wakabayashi, J., Smith, D.L., and Hamilton, D.H., 1992, Miller Creek and related faults: a potentially active fold and thrust belt, eastern San Francisco Bay Area: Program and Abstracts, 2nd Conference on Earthquake Hazards in the Eastern San Francisco Bay Area, March 25-29, p. 80.

Walter, A.W., 1990, Upper-crustal velocity structure near Coalinga, as determined from seismic-refraction data, in Rymer, M.J., and Ellsworth, W.L., ed., The Coalinga, California, Earthquake of May 2, 1983: U.S. Geological Survey Professional Paper 1487.

Wang, K., and Hyndman, R.D., 1992, Thermal constraints on the zone of possible major thrust earthquake failure on the Cascadia margin (abs.): EOS Transactions, American Geophysical Union, v. 72, p. 314.

Wang, K. and Rogers, G.C., in review, Double seismic layers in the subducted Gorda Plate and their implications on the rheology of oceanic lithosphere.

Wang, Z.L., 1990, Bounding surface hypoplasticity model for granular soils and its applications: Ph.D. Dissertation, University of California, Davis.

Ward, S.N., 1990, Pacific North America plate motions: new results from very long baseline interferometry: Journal of Geophysical Research, v. 95, no. B13, p. 21,965-21,981.

Warrick, R.E., 1974, Seismic investigation of a San Francisco Bay mud site: Seismological Society of America Memoirs 33, v. 64.

Weaver, C.E., 1949, Geology of the Coast Ranges immediately north of the San Francisco Bay Region, California: Geological Society of America Memoirs 35, 242 p.

Weber, G.E., and Cotton, W.R., 1981, Geologic investigation of recurrence intervals and recency of faulting along the San Gregorio fault zone, San Mateo County, California: U.S. Geological Survey Open File Report 81-263, 133 p.

Weber, G.E., and Lajoie, K.R., 1980, Map of Quaternary faulting along the San Gregorio fault zone, San Mateo and Santa Cruz counties, California: U.S. Geological Survey Open File Report, 80-907, scale 1:24,000.

Weber, G.E., Lajoie, K.R., and Griggs, G.B., 1979, Coastal tectonics and coastal geologic hazards in Santa Cruz and San Mateo counties, California: Cordilleran Section of The Geological Society of America 75th Annual Meeting.

Weichert, D.H., 1980, Estimation of the earthquake recurrence parameters for unequal observation periods for different magnitudes: Bulletin of the Seismological Society of America, v. 70, no. 4, p. 1337-1346.

Wells, D.L., and Coppersmith, K.J., 1992, Analysis of empirical relationships among magnitude, rupture length, rupture area, and surface displacement (abs.): Seismological Research Letters, v. 63, no. 1, p. 73.

Wells, D.L., and Coppersmith, K.J., 1994 (in press), Empirical relationships among magnitude, rupture length, rupture width, rupture area, and surface displacement: Bulletin of the Seismological Society of America, v. 84, no. 4.

Wentworth, C.M., Blake, M.C., Jones, D.L. Jr., Walter, A.W., and Zoback, M.D., 1984, Tectonic wedging associated with emplacement of the Franciscan assemblage, California Coast Ranges, in Blake, M.C., ed., Franciscan Geology of Northern California, Pacific Section: Society of Economic Paleontologists and Mineralogists, 43, p. 163-173.

Wentworth, C.M., and Zoback, M.D., 1989, The style of Late Cenozoic deformation at the eastern front of the California Coast Ranges: Tectonics, v. 8, p. 237-246.

Wentworth, C.M., and Zoback, M.D., 1990, Structure of the Coalinga area and thrust origin of the earthquake, in Rymer, M.J., and Ellsworth W.L. (eds.), The Coalinga, California, Earthquake of May 2, 1983: U.S. Geological Survey Professional Paper 1487.

Wesnousky, S.G., Scholz, C.H., Shimazaki, K., and Matsuda, T., 1983, Earthquake frequency distribution and the mechanics of faulting: Journal of Geophysical Research, v. 88, no. B11, p. 9331-9340.

West, D.O., and McCrumb, D.R., 1988, Coastline uplift in Oregon and Washington and the nature of Cascadia subduction-zone tectonics: Geology, v. 16, p. 169-172.

Weston, R.L., Helley, E.J., Lajoie, K.R., and Wentworth, C.M., 1975, Faults and future earthquakes, in Borcherdt, R.D., ed., Studies for Seismic Zonation of the San Francisco Bay Region: U.S. Geological Survey Professional Paper 941-A.

Williams, P.L., Anima, R., and McEvilly, T.V., 1992, High resolution profiling of the East Bay faults in BASIX (Bay Area Seismic Imaging Experiment), 1. Pittsburgh-Antioch area: Proprietary Data, LNL Earth Sciences.

Wills, C.J., 1992, The elusive Antioch fault (abs): Program with Abstracts, Second Conference on Earthquake Hazards in the Eastern San Francisco Bay Area, p. 84.

Wilson, D.S., 1989, Deformation of the so-called Gorda plate: Journal of Geophysical Research, v. 94, p. 3065-3075.

Wong, I.G., 1984, Reevaluation of the 1892 Winters, California earthquakes based upon a comparison with the 1983 Coalinga earthquake (abs): Eos, v. 65, p. 996-997.

Wong, I.G., 1990, Seismotectonics of the Coast Ranges in the vicinity of Lake Berryessa, Northern California: Bulletin of the Seismological Society of America, v. 80, no. 4, p. 935-950.

Wong, I.G., and Biggar, N., 1989, Seismicity of eastern Contra Costa County, San Francisco Bay region, California: Bulletin of the Seismological Society of America, v. 79, no. 4, p. 1270-1278.

Wong, I.G., Ely, R.W., and Kollman, A.C., 1988, Contemporary seismicity and block tectonics of the northern California and central Coast Ranges-Sierran Block boundary zone, California: Journal of Geophysical Research, v. 93, p. 7813-7833.

Woodward-Clyde Consultants, 1977, Final geotechnical studies, Travis Composite Medical Facility, Travis Air Force Base, Fairfield, California: Consultant's Report for Kaplan/McLaughlin Architects/Planners, San Francisco, California.

Woodward-Clyde Consultants, 1982, Evaluation of the seismicity data associated with the November 1980 Trinidad offshore earthquake for the Humboldt Bay Power Plant, Unit No. 3: Report prepared for Pacific Gas and Electric Company, July.

Woodward-Clyde Consultants, 1986, Revision of portions of Contra Costa County Seismic Safety Element: Consultant's Report for Contra Costa County Community Development Department.

Working Group on California Earthquake Probabilities, 1988, Probabilities of large earthquakes occurring in California on the San Andreas fault: U.S. Geological Survey Open-File Report 88-398, 62 p.

Working Group on California Earthquake Probabilities, 1990, Probabilities of large earthquakes in the San Francisco Bay region, California: U.S. Geological Survey Circular 1053, 51 p.

Wright, R.H., Hamilton, D.H., Hunt, T.D., Traubenik, M.L., and Shlemon, R.J., 1982, Character and Activity of the Greenville structural trend, in Proceedings of the Conference on Earthquake Hazards in the Eastern San Francisco Bay Area: California Division of Mines and Geology Special Publication 62.

Wyss, M., 1979, Estimating maximum expectable magnitude of earthquakes from fault dimensions: Geology, v. 7, p. 336-340.

Youngs, R.R., Chiou, S.-J., Silva, W.L., and Humphrey, J.R., 1993, Strong ground motion attenuation relationships for subduction zone earthquakes based on empirical data and numerical modeling (abs.): Seismological Research Letters, v. 64, no. 1, p. 18.

Youngs, R.R., and Coppersmith, K.J., 1985a, Development of a fault-specific recurrence model: Earthquake Notes (abs.), v. 56, no. 1, p. 16.

Youngs, R.R. and Coppersmith, K.J., 1985b, Implications of fault slip rates and earthquake recurrence models to probabilistic seismic hazard estimates: Bulletin of the Seismological Society of America, v. 75, no. 4, p. 939-964.

Youngs, R.R, Coppersmith, K.J., Taylor, C.L., Power, M.S., Di Silvestro, L.A., Angell, M.M., Hall, N.T., Wesling, J.R., and Mualchin, L., in press, A comprehensive seismic hazard model for the San Francisco Bay Region: Proceedings of the Second Conference on Earthquake Hazards in the Eastern San Francisco Bay Area, California Division of Mines and Geology.

Youngs, R.R., Day, S.M., and Stevens, J.B., 1988, Near field motions on rock for large subduction zone earthquakes, in Earthquake Engineering and Soil Dynamics II -- Recent Advances in Ground Motion Evaluation: American Society of Civil Engineers Geotechnical Special Publication 20, p. 445-462.

Youngs, R.R., Makdisi, F., Sadigh, K., and Abrahamson, N.A., 1990, The case for magnitude dependent dispersion in peak ground acceleration (abs.): Seismological Research Letters, v. 61, no. 1, p. 30.

Youngs, R.R., Swan, F.H., Power, M.S., Schwartz, D.P., and Green, R.K., 1987, Probabilistic analysis of earthquake ground shaking hazard along the Wasatch Front, Utah, in Assessment of Regional Earthquake Hazards and Risk Along the Wasatch Front, Utah: U.S. Geological Survey Open-File Report 87-585, v. II, p. M-1-110.

APPENDIX A

PROBABILISTIC SEISMIC HAZARD ANALYSIS METHODOLOGY

APPENDIX A

PROBABILISTIC SEISMIC HAZARD ANALYSIS METHODOLOGY

INTRODUCTION

This appendix describes the approach utilized by Geomatrix Consultants to perform the probabilistic seismic hazard analysis for this study. Seismic hazard is usually defined as the levels of strong ground motion that could occur at the site of a facility during its useful life. The ground motion levels may be represented in terms of peak ground acceleration and/or peak response spectral amplitudes for a range of frequencies of vibration. Probabilistic seismic hazard analysis (PSHA) represents an evaluation of the probability or likelihood that various levels of ground motion will be exceeded during a specified time period. The analysis procedure was originally proposed by Cornell (1968). Since that time there has been significant progress in our understanding of the earthquake process and in the techniques for evaluation of the relevant seismological, geological, and geophysical data. The analysis methodology presented herein incorporates the significant advances that have been made in PSHA. The next section outlines the important considerations involved in selecting the analysis models and input parameters. Following that, the mathematical formulation and analysis products are described.

DEVELOPMENT OF SEISMIC HAZARD MODEL

The seismic hazard at a site is a function of the location and geometry of potential sources of future earthquakes, the frequency of occurrence of various size earthquakes on these sources, and the characteristics of seismic wave propagation in the region. In the methodology described here, these elements are analyzed within a probabilistic framework that addresses both the randomness of the earthquake process and the uncertainty in modeling the process. The seismic hazard model consists of two basic components, a model of the sources of potential future earthquakes and a model of the effects at the site of future earthquakes. Detailed discussion of these two components is given below.

Seismic Source Characterization

A seismic source model provides a description of potential future earthquakes in terms of their spatial distribution, the rate of seismic activity and the relative frequency of various size events. The steps involved in source characterization are (1) definition of regions within the crust that are potential sources of future earthquakes, (2) assessment of the source geometry, (3) assessment of the maximum size of future earthquakes possible on each source, and (4) assessment of recurrence rates for earthquakes of various sizes.

Source Definition - A seismic source represents a region of the earth's crust where the characteristics of earthquake activity are recognized to be different than that of the adjacent crust. Seismic sources are identified on the basis of geological, seismological and geophysical

data. An understanding of the regional tectonics, local Quaternary history, and seismicity of an area leads to the identification of geologic structures that may be seismic sources. To this end, the development of tectonic models for crustal deformation and the assessment of the tectonic role of individual geologic structures is essential for both identifying potential sources and assessing their characteristics. Geologic studies can be used to assess the location, timing, and style of crustal deformation. The association of geologic structures with historic or instrumental seismicity may clarify their role within the present tectonic stress regime. Characteristics of seismic energy release, such as focal depths and source mechanisms, can also aid in identifying potential sources.

Because earthquakes occur as a result of differential slip on faults, modeling of seismic sources as individual faults is the most physically realistic model for seismic hazard analysis. Under favorable conditions, individual faults can be identified and treated as distinct seismic sources. Active faults are usually identified on the basis of geomorphic expression and stratigraphic displacements but can also be identified by lineations of seismicity or by geophysical measurements. For example, the results of marine seismic reflection surveys have been used successfully to identify active faulting. A fault model for individual sources allows the use of geologic data on fault behavior to characterize earthquake activity as the use of seismicity data alone may not be sufficient for source modeling.

Fault models of seismic sources can be used to model seismic hazards in the vicinity of subduction zones. In these environments the interface between the subducting plate and the overriding plate can be modeled as a large thrust fault. The depth and orientation of the fault plane is defined on the basis of seismicity and deep geophysical measurements, such as seismic refraction or magnetotelluric imaging.

An understanding of the local tectonics can provide a basis for identifying seismic sources in areas where individual faults cannot be identified at the surface. Recent earthquakes in California (Coalinga, 1983; Whittier Narrows, 1987) occurred on thrust faults located beneath active folds. Geologic structures that show evidence of active deformation can be identified using similar techniques as those used to identify active faults. Such structures can be identified as seismic sources where the location of the actual fault plane is uncertain. For such structures, quantitative structural geology techniques (e.g. Suppe, 1983) may provide a basis for estimating the location of buried faults.

In areas of low rates of crustal deformation away from plate margins seismic sources are often defined on the basis of the spatial distribution of seismicity. However, an understanding of the local tectonics can also provide the basis for identifying seismic sources. Recent analyses of crustal stress data in stable continental regions has shown that the stress in these regions is usually compressive and is remarkably uniform in orientation (e.g. Zoback et al., 1986; Zoback and Zoback, 1988; Adams, 1989). It is believed that in such regions earthquakes occur as a result of reactivation of geological zones of weakness that are favorably oriented relative to the contemporary regional stress field. Thus identification of geologic structures

suitably oriented in the local stress field can provide a basis for defining potential seismic sources (see, for example, EPRI 1987.)

In regions where no distinguishing geologic features can be identified, seismicity is usually modeled as occurring randomly within large areal background sources. Here again, geologic and tectonic data can be used to identify blocks of the earth's crust that are expected to have fairly homogeneous characteristics. The extent of such regions can serve as the basis for defining the boundaries of regional areal sources of distributed seismicity.

Source Geometry - Description of the geometry of a seismic source is necessary in order to evaluate the distances from the site at which future earthquakes could occur. In addition, source geometry can place physical constraints on the maximum size earthquake that can occur on the source.

Seismic sources defined as faults are modeled in the analysis as segmented planar features. The depth distribution of historical seismicity can be used to define the down dip distribution of earthquake ruptures and evaluation of fault segmentation can be used to specify the distribution of earthquake ruptures along strike. Earthquake ruptures on fault sources are modeled as rupture areas, with the size of rupture defined on the basis of empirical relationships between earthquake magnitude and rupture size (e.g. Wyss, 1979).

For seismic sources defined as geologic structures suspected to contain faults the distribution of earthquakes can be modeled as rupture surfaces occurring on multiple fault planes distributed throughout the source volume if the general trend of such planes is known or can be inferred. Alternatively, earthquake locations can be modeled as random point sources within the source volume if the orientation of potential fault planes is unknown. The spatial distribution of seismicity within large areal sources can be modeled in a similar fashion.

Maximum Earthquake Magnitude - The limiting size earthquake that can occur on each seismic source is an important parameter, especially in evaluating seismic hazards at low probability levels. The maximum magnitude can most easily be estimated when the seismic source is defined on the basis of an identifiable fault. For faults, the maximum earthquake magnitude is related to fault geometry and fault behavior through an assessment of the maximum dimensions of a single rupture. Here fault segmentation plays a key role in identifying the portions of the fault zone likely to represent the largest sizes of coherent rupture (Schwartz and Coppersmith, 1986; Schwartz, 1988). The maximum magnitude is related to the maximum rupture size through empirical relationships (e.g. Slemmons, 1982, Bonilla et al., 1984, Wells and Coppersmith, 1992). Because these relationships are subject to some uncertainty, the use of a number of magnitude estimation techniques can result in more reliable estimates of maximum magnitude than the application of a single relationship. Techniques have been proposed for using the statistics of the individual relationships to arrive at a consensus estimate of maximum magnitude (Youngs and Coppersmith, 1989).

The assessment of maximum magnitude is more difficult when seismic sources are defined on the basis of large scale tectonic features or crustal blocks. Often, the seismicity data form the primary basis with the maximum magnitude estimated to be the maximum historical plus an increment or the magnitude event with a specified return period. The chief weakness of these approaches is the generally short time period of historical observations as compared to the likely return period of a maximum event for an individual source. An alternative approach is to identify analogous features for which the maximum magnitude is better defined or to identify the largest event that has occurred on such features. Recent efforts have been made to use a global earthquake data base to identify the factors that control or limit the maximum size of earthquakes within stable continental regions in order to develop a formal method for estimating maximum magnitude in such regions (Coppersmith et al., 1989).

Earthquake Recurrence - Earthquake recurrence is represented in terms of the rate of seismic activity and the relative frequency of various magnitude earthquakes. Recurrence rates are estimated from historical seismicity, from geological data on rates of fault movement, and from paleoseismic data on the timing of large prehistoric events.

For large areal sources, historical seismicity is usually used to estimate earthquake recurrence rates. In analyzing the earthquake catalog, it is important to translate the data into a common magnitude scale consistent with the magnitude scale used in the ground motion models, and to account for completeness in earthquake reporting as a function of time and location. Once these are established, straight-forward statistical techniques can be used to estimate earthquake recurrence parameters (e.g. Weichert, 1980). For areal sources, the truncated exponential recurrence model (Cornell and Van Marke, 1969) based on Gutenberg and Richter's (1954) recurrence law is usually used. The resulting relationships are then extrapolated out to the maximum magnitude for the seismic source to provide recurrence estimates for the full range of magnitudes considered in the analysis.

For sources defined as individual faults, the available historical seismicity is usually insufficient to characterize the earthquake recurrence. Geologic data can be used to evaluate the rate of fault slip and this, in turn can be used to estimate the rate of seismic energy release, leading to the rate of earthquake recurrence. In addition, paleoseismic studies can lead to dating of large prehistoric events. Predictions of recurrence rates for larger events from fault-specific geologic data have been shown to match well with observed historical rates on a regional basis (Youngs and Coppersmith, 1985b; Youngs et al., 1988a).

The above techniques provide the basis for specifying the recurrence rate of the largest earthquakes on a source. The recurrence rate for small and intermediate size events is estimated by extrapolating from the largest events using a recurrence model. Initially the exponential model was used (e.g. Anderson, 1979). However, recent advances in understanding of the earthquake generation process have indicated that earthquake recurrence on individual faults may not conform to the exponential model developed from regional observations. Instead, individual faults or fault segments may tend to rupture in what have been termed "characteristic" size events at or near the maximum size earthquake (Schwartz and

Coppersmith, 1984). This has led to the development of fault-specific recurrence models such as the characteristic size recurrence model of Youngs and Coppersmith (1985a, 1985b). Figure A-1 compares the characteristic size model with the truncated exponential model, indicating that when anchored to the recurrence rate for the largest events the two models provide significantly different rates for smaller events.

Application of either of the two models requires specification of a *b*-value (slope of the exponential portion of the recurrence curve) in order to define the frequency of smaller magnitude events. In the absence of fault specific data, the *b*-value obtained from analysis of the regional seismicity is usually used. However, when the regional *b*-value is used for fault specific recurrence models, the predicted regional recurrence rate obtained by combining the recurrence estimates for all of the sources will have a somewhat different *b*-value due to the varying maximum magnitudes of the different sources (Youngs and Coppersmith, 1985b). To recover the observed regional *b*-value, a somewhat smaller *b*-value should be used on a fault-specific basis with the truncated exponential model and a somewhat larger *b*-value should be used with the characteristic model.

The basic probability model used in most hazard analyses is that earthquakes occur as a Poisson process in time. While the Poisson model has been shown to match the observed data on a regional basis, it does not conform to the physical process believed to result in earthquakes - one of gradual strain accumulation followed by sudden release. Detailed paleoseismic studies of several faults as well as historical seismicity from very active subduction zones has indicated that the occurrence of the largest events on a source tends to be more cyclic in nature. These observations have led to the use of nonstationary or "real-time" recurrence models that predict the probability of events in the ***next*** time period, rather than any time period. Typically, a simple renewal model is used to evaluate the likelihood of events within specified future time periods (e.g., Working Group on California Earthquake Probabilities, 1988).

Ground Motion Attenuation Relationships

Attenuation relationships define the values of a ground motion parameter, such as peak ground acceleration or response spectral values, as a function of earthquake magnitude and distance in terms of both the expected values and the dispersion about the expected values. Typically attenuation relationships are developed from statistical analysis of strong motion data or from peak ground motion parameters inferred from reported shaking intensities. Joyner and Boore (1988) present a detailed summary of recently developed strong motion relationships.

The important aspects to consider in selecting the appropriate attenuation relationships are source effects, the regional characteristics of seismic wave propagation and local site effects. For example, analysis of recorded ground motion data has indicated that there are significant differences in the rate of attenuation of ground motions from shallow crustal plate-boundary earthquakes and large subduction zone earthquakes (Crouse et al., 1988; Youngs et al., 1988b). Local site conditions have been clearly shown to have a major influence on response spectral shape.

In regions for which there are few applicable data, attenuation relationships may be developed on the basis of theoretical ground motion models that have been shown to model observed data (e.g. Hanks and McGuire, 1981; Boore, 1983, 1986; Boore and Atkinson, 1987). Alternatively, existing empirically-based attenuation relationships can be modified to account for differences in rates of attenuation between the region of interest and the region for which the attenuation relationship was developed. These differences can be inferred from the patterns of shaking intensity, evaluations of crustal wave propagation characteristics, or analogies based on similar geologic and tectonic environments. Theoretical and numerical models of ground motion can also be used to extend empirically-based attenuation relationships to magnitude and distances beyond the range of the data (e.g. Youngs et al., 1988b).

The uncertainties in the level of a ground motion parameter that may be recorded during any single earthquake are of considerable importance to the seismic hazard evaluation. A lognormal probability distribution is typically used to model this uncertainty, with reported values of the standard deviation of the natural log of peak motion varying from 0.3 to over 0.7. Lower values tend to come from the analyses where there have been attempts made to develop uniform data sets. Also, examination of large ground motion data sets indicates that the variability in ground motion tends to decrease as the magnitude of the earthquake increases (Sadigh, 1983; Idriss, 1985; Sadigh et al., 1986; Abrahamson, 1988, Youngs et al., 1990). In using the lognormal model it is important to consider potential upper bounds on the motions near to the fault as significant probabilities could be associated with unrealistically high ground motion levels (Sadigh and Youngs, 1984).

MATHEMATICAL FORMULATION

Basic Analysis Model

In probabilistic terms seismic hazard is defined as the likelihood that various levels of ground motion will be exceeded at a site during a specified time period. It is commonly assumed that the occurrence of individual main shocks can be represented as a Poisson process. Following the approach developed by Cornell (1968), the probability that at a given site a ground motion parameter, Z, will exceed a specified level, z, during a specified time period, T, is given by the expression:

$$P(Z>z)=1.0-e^{-\nu(z)\cdot T} \leq \nu(z)\cdot T \qquad \text{(A-1)}$$

where $\nu(z)$ is the average frequency during time period T at which the level of ground motion parameter Z exceeds z at the site resulting from earthquakes on all sources in the region. The inequality at the right of Equation A-1 is valid regardless of the appropriate probability model for earthquake occurrence, and $\nu(z)\cdot T$ provides an accurate and slightly conservative estimate of the hazard for probabilities of 0.1 or less provided $\nu(z)$ is the appropriate value for the time period of interest.

The frequency of exceedance, $\nu(z)$, is a function of the uncertainty in the time, size and location of future earthquakes and uncertainty in the level of ground motions they may produce at the site. It is computed by the expression:

$$\nu(z)=\sum_{n=1}^{N} \alpha_n\ (m^o) \int_{m=m^o}^{m^u} \int_{r=0}^{\infty} f_n(m) f_n(r|m) \cdot P(Z>z|m,r)\ dr\ dm \qquad \text{(A-2)}$$

where $\alpha_n(m^o)$ is the frequency of earthquakes on source n above a minimum magnitude of engineering significance, m^o; $f_n(m)$ is the probability density function for event size on source n between m^o and a maximum event size for the source, m^u; $f_n(r \mid m)$ is the probability density function for distance to earthquake rupture on source n, which is usually conditional on the earthquake size; and $P(Z>z \mid m,r)$ is the probability that, given a magnitude m earthquake at a distance r from the site, the ground motion exceeds level z. In practice, the double integral in Equation A-2 is replaced by a double summation, with the density functions $f_n(m)$ and $f_n(r \mid m)$ replaced by discretizations of their corresponding cumulative functions.

The three probability functions required to evaluate $\nu(z)$ are described below.

Magnitude Distribution - The relative frequency of various magnitude earthquakes is generally assumed to follow a truncated exponential relationship with the complimentary cumulative form

$$P(M>m|m^o,m^u) = \frac{e^{-\beta(m-m^o)} - e^{-\beta(m^u-m^o)}}{1.0 - e^{-\beta(m^u-m^o)}} \qquad \text{(A-3)}$$

where $\beta = b \cdot \ln(10)$ and b is the b-value of the recurrence relationship. Other forms of Equation A-3, such as that proposed by Youngs and Coppersmith (1985a, 1985b) can be used. Their model combines a truncated exponential distribution for magnitudes below a characteristic size and a uniform distribution for the characteristic magnitudes. The corresponding complimentary cumulative form is shown in Figure A-1.

Conditional Distance Distribution - The conditional probability distribution for distance from the earthquake rupture to the site is usually computed numerically due to the irregular geometry of the seismic sources. For segmented fault planes, the algorithm moves a suitably sized rupture surface incrementally over the entire fault plane. For cases incorporating straight line segments, the analytical relationships presented by Der Kiureghian and Ang (1977) for the cumulative distance distribution are used. Volumetric sources are represented by multiple lines or planes. The distance distribution is obtained as a weighted combination of the distance distributions computed for each line or plane.

Conditional Exceedance Probability Distribution - The amplitude of ground motion parameter Z is treated as a random variable whose expected value is dependent on the magnitude of the earthquake and the source-to-site distance. The actual value of the parameter in any one event is assumed to be lognormally distributed about a mean value of $\ln(Z)$ specified by an attenuation relationship. Several studies have shown that a lognormal distribution is appropriate for modeling the variability of ground motion levels (e.g. Esteva, 1969; Campbell, 1981). The conditional probability that Z exceeds level z is given by the complimentary cumulative function for a lognormally distributed variable. The model used in the analysis incorporates a procedure to truncate the distribution of Z to prevent the occurrence of physically unrealistic ground motion levels at very low probabilities.

Treatment of Modeling and Parameter Uncertainties

The probability functions contained in Equations A-1 through A-3 represent the randomness inherent in the natural phenomena of earthquake generation and seismic wave propagation. It is considered randomness because it is beyond our current understanding of the physical process. In addition, one is usually faced with considerable uncertainty in selecting the appropriate models and model parameters required to apply Equations A-1 through A-3. This uncertainty arises from limited data and/or alternative interpretations of the available data. The approach used in this study explicitly incorporates these additional uncertainties into the analysis to assess their impact on the estimate of the expected level of seismic hazard as well as the uncertainty in that estimate.

The uncertainty in modeling the natural phenomena is addressed through the use of logic trees. The logic tree formulation for seismic hazard analysis (Kulkarni et al., 1984; Youngs et al., 1985; Coppersmith and Youngs, 1986; National Research Council, 1988) involves specifying discrete alternatives for states of nature or parameter values and specifying the relative likelihood that each discrete alternative is the correct value or state of the input parameter. The relative likelihoods of the different parameter values are typically based on subjective judgment because the available data are too limited to allow an objective statistical analysis.

The logic tree structure is shown in Figure A-2. Logic trees are composed of nodes and branches. Each node represents a point at which a choice is possible between alternative states or values of an input parameter. Each branch represents one possible discrete parameter value. (If the variable in question is continuous, it can be discretized at a suitable increment.) Probabilities are assigned to each branch that represent the relative likelihood or degree of belief that a branch is the correct value or state of the input parameter. The nodes of the logic tree are sequenced to provide for the conditional aspects or dependencies among the parameters and to provide a logical progression of assumptions regarding parameter definition.

The example logic tree shown in Figure A-2a might be used to represent the uncertainty in assessing the maximum magnitude for a fault on the basis of a relationship between maximum displacement per event and earthquake magnitude (e.g., Slemmons, 1982). In order to assess the maximum magnitude, two pieces of information are required: the sense of slip (S) of the fault and the maximum displacement in any one event (DE). The logic tree thus contains two

levels of nodes, one for each parameter. In the example, the particular values that might be assigned to the maximum displacement are dependent on the assumed sense of slip (strike-slip earthquakes may tend to produce greater displacements than reverse earthquakes) and are thus most easily assessed given knowledge of the sense of slip. Consequently, the node for maximum displacement per event is located after the node for sense of slip.

At each node the probabilities assigned to each branch are assessed conditional on the assumption that all the branches leading to that node represent the true state of the preceding parameters. The parameter values and their relative likelihoods are based on subjective judgments because the available data are too limited to allow for statistical analysis, and because scientific judgment is needed to weigh alternative interpretations of the available data. The logic tree approach simplifies these subjective assessments because the uncertainty in a single parameter is considered individually with all other parameters assumed to be known with certainty.

The weights assigned to the branches of the logic tree are subjective probabilities and are based on judgment. In most cases, the probabilities are in units of tenths, unless there is a basis for more fine-scale resolution. Usually the weights represent one of two types of probability assessments. In the first, a range or distribution of parameter values is represented by the logic tree branches for that parameter and their associated weights. For example, the slip rate on a fault is usually uncertain because of uncertainties in the amount of displacement of a particular geologic unit across the fault and the age of the unit. The resulting slip rate is usually represented by a preferred value and a range of higher and lower values, similar to a normal or log normal statistical distribution. This type of distribution can be represented by three (or more) branches of a logic tree. For example, Keefer and Bodily (1983) has shown that a normal distribution can be reliably represented by three values: the central estimate (with a weight of 0.6) and a higher and lower value (each with weights of 0.2) that represent the 5^{th} and 95^{th} percentiles (about plus or minus two standard deviations). Although a large number of branches can be included on a logic tree, usually the results are not sensitive to having more than about three branches.

A second type of probability assessment to which logic trees are suited is in indicating a relative preference for, or degree of belief in, alternative hypotheses. For example, the sense of slip on a fault may be uncertain, two possible alternatives might be strike-slip or reverse-slip. Based on the pertinent data, a relative preference for these alternatives can be expressed by the logic tree weights. A strong preference is usually represented by weights such as 0.9 and 0.1 for the two alternatives. If there is no preference for either hypothesis, they are assigned equal weights (0.5 and 0.5 for two hypotheses). Increasing weights from 0.5 to 0.9 reflects an increasing preference for the alternative. Although the logic tree weights are ultimately subjective judgments based on available information, it is important to document the data and interpretations that led to the assessment of parameter values and to assignment of weights.

Two sense of slip models are considered in Figure A-2: strike-slip and reverse. In the example, the assigned weights reflect a slight preference for reverse faulting. The probability that 2 meters is the correct maximum displacement per event is assessed conditionally on which sense of slip is assumed to be correct [that is, the probability of a 2-meter displacement given strike-slip faulting, $P(DE=2 \mid S=strike\ slip)$, is a separate assessment from $P(DE=2 \mid S=reverse)$, and the two probabilities do not have to be equal]. As the branches at each node are intended to represent mutually exclusive and collectively exhaustive states of the input parameter, the sum of the conditional probabilities at each node is unity. In practice, a sufficient number of branches are placed at a given node to adequately represent the uncertainty in the parameter estimation.

The logic tree shown in Figure A-2a defines a discrete distribution for the maximum magnitude computed using the relationship developed by Slemmons (1982). The resulting distribution is shown in Figure A-2b. The probability that the maximum magnitude, $M^u(S,DE)$, will take on any particular value $M^u(s_i,de_j)$ is equal to the joint probability of the set of parameters s_i and de_j being the true parameter values.

$$P[M^u(s_i,de_j)] = P(S=s_i)\cdot P(DE=de_j \mid s_i) \qquad \text{(A-4)}$$

The expected or mean value of $M^u(S,DE)$ given the uncertainty in the input parameters S and DE is given by:

$$E[M^u(S,DE)] = \sum_i \sum_j M^u(s_i,de_j)\cdot P(S=s_i)\cdot P(DE=de_j \mid s_i) \qquad \text{(A-5)}$$

and the variance in $M^u(S,DE)$ is given by:

$$VAR[M^u(S,DE)] = \sum_i \sum_j (M^u(s_i,de_j)-E[M^u(S,DE)])^2\cdot P(S=s_i)\cdot P(DE=de_j \mid s_i) \qquad \text{(A-6)}$$

Figure A-3 displays a logic tree representing a seismic hazard model developed for analysis of the seismic hazard in the North Sea. The logic tree is laid out to provide a logical progression from general aspects/hypotheses regarding the characteristics of seismicity and seismic wave propagation in the region to specific input parameters for individual sources. The rationale for developing the various levels of the logic tree is discussed below. The bases for selecting the parameter values and assigning relative weights are presented in Coppersmith and Youngs (1986).

The first node of the logic tree represents the uncertainty in selecting the appropriate strong ground motion attenuation relationship. Attenuation was placed first in the tree because it is felt that a single relationship (whichever relationship may be "correct") is applicable to all earthquake sources in the region. The second node of the logic tree represents the uncertainty in identifying what are structures and processes giving rise to earthquakes in the region. The fault model assumes the activity is occurring on reactivated normal faults that have been mapped using high resolution seismic refraction and reflection surveys. The source zone model assumes that the sources of earthquakes are unknown except for their general extent as imaged by the historical seismicity. The next node applies to the fault source model only and addresses the question of differences in the rate of activity of the identified faults defined on the basis of differences in the age and amount of recent slip. The following node addresses the uncertainty in specifying the depth distribution of earthquake activity, the details of seismic zonation in the North Sea region, various alternative input parameter values for estimating earthquake recurrence parameters, and the appropriate relationship between earthquake magnitude and rupture size.

All the levels of the logic tree to this point are assumed to apply universally to all sources. The logic tree is now expanded into subtrees to address parameters that vary independently from source to source. These include the sense of slip on individual sources, the dip of fault planes, and individual source maximum magnitudes.

Each end branch of the logic shown in Figure A-3 defines a particular characterization of the seismic hazard at the site for which the rate of exceedance can be computed using Equation A-2. The likelihood that this computation is the "correct" hazard at the site is given by the product of all the conditional probabilities along the path through the logic tree. The end branches thus define a discrete distribution for $\nu(z)$ (see Equations A-4 through A-6).

Analysis Results

The results of the analysis are expressed in terms of a relationship between the level of a ground motion parameter and the frequency with which the level is exceeded. As discussed above, discrete distributions for the frequency of exceedance are computed by calculating hazard for all the possible combinations of parameters represented by the end branches of the seismic hazard model logic tree. Figure A-4 shows an example of such a distribution. Given the distribution, one can then estimate various statistical measures of the frequency of exceedance, such as the mean value and various percentiles of the distribution. Connecting these values for various levels of ground motion yields hazard curves representing the mean hazard and various percentile hazard curves. Figure A-5 shows the resulting mean and 5th-percentile to 95th-percentile hazard curves obtained from the discrete distributions of frequency of exceedance computed at various ground motion levels.

The 5th-percentile and 95th-percentile hazard curves can be considered as bounding a 90-percent confidence band on the computed hazard. The width of this band thus represents the cumulative effect of all levels of parameter uncertainty expressed in the seismic hazard model logic tree. The relative contributions of uncertainties in various components of the model to

the overall uncertainty can be identified readily from the logic tree formulation by computing the hazard holding individual parameters fixed at specific values. For example, the contribution of uncertainty in attenuation relationship can be obtained by computing the mean hazard assuming each of the attenuation relationships is, in turn, the "correct" relationship, with weight of 1.0, and the other has zero weight. Figure A-6 shows the result of this operation for all of the levels of the logic tree shown in Figure A-3. Each plot shows the mean hazard (solid curve) and 5^{th}- and 95^{th}-percentile hazard curves considering all parameter uncertainties (long dashed curve). Each plot also shows the range in mean hazard resulting from variations in the parameter identified in the upper corner of the plot (dotted curves). From such displays one can see which hazard mode parameters contribute the most to the uncertainty in the seismic hazard.

The computed hazard can also be displayed in terms of the relative contributions of various sources, and earthquakes in various magnitude and source-to-site intervals. Figure A-7 presents an example for a site in the northwestern United States where the hazard results from three different types of sources with significantly different contributions to the hazard in terms of earthquake size and source-to-site distance. Such plots provide a basis for selecting appropriate accelerograms for analysis of structural response to selected hazard loading levels.

Equal-hazard response spectra are developed by conducting hazard analyses using the response spectral ordinate attenuation relationships for periods of vibration significant to the seismic response of the facility being evaluated. Given a specified probability level, response spectral ordinates are interpolated from the hazard curves for each period of vibration and a smooth response spectrum is drawn through these points. It is important to realize that an equal-hazard spectrum does not represent the motions of any single earthquake. It is an aggregate of the contributions of earthquakes of different sizes, different distances, and from different sources. The relative contributions of various events to the spectral ordinates also changes with period. As the period of vibration increases, the spectral ordinates increasingly represent the contributions of the larger earthquakes modeled in the seismic hazard analysis.

REFERENCES

Abrahamson, N.A., 1988, Statistical properties of peak ground accelerations recorded by the SMART 1 array: Bulletin of the Seismological Society of America, v. 78, p. 26-41.

Adams, J., 1989, Crustal stresses in eastern Canada: in S. Gregerson and P.N. Basham (eds.), Earthquakes at North-Atlantic Passive Margins: Neotectonics and Postglacial Rebound, Kluwer Academic Publishers, p. 289-297.

Anderson, J.G., 1979, Estimating the seismicity from geological structure for seismic risk studies: Bulletin of the Seismological Society of America, v. 69, p. 135-158.

Bonilla, M.G., Mark, R.K., and Lienkaemper, J.J., 1984, Statistical relations among earthquake magnitude, surface rupture length, and surface fault displacement: Bulletin of the Seismological Society of America, v. 74, pp. 2379-2411.

Boore, D.M., 1983, Stochastic simulation of high-frequency ground motions based on seismological models of the radiated spectra: Bulletin of the Seismological Society of America, v. 73, p. 1865-1894.

Boore, D.M., 1986, Short period P- and S-wave radiation from large earthquakes: Implications for spectral scaling relations: Bulletin of the Seismological Society of America, v. 76, p. 43-64.

Boore, D.M., and Atkinson, G.M., 1987, Stochastic prediction of ground motion and spectral response parameters at hard-rock sites in eastern North America: Bulletin of the Seismological Society of America, v. 77, p. 440-467.

Campbell, K.W., 1981, Near-source attenuation of peak horizontal acceleration: Bulletin of the Seismological Society of America, v. 71, no. 6, p. 2039-2070.

Coppersmith, K.J., and Youngs, R.R., 1986, Capturing uncertainty in probabilistic seismic hazard assessments within intraplate environments: in Proceedings of the 3rd National Conference on Earthquake Engineering, Charleston, South Carolina, August 24-28, v. I, p. 301-312.

Coppersmith, K.J., Youngs, R.R., Johnson, R.J., and Kantor, L.R., 1989, Methods for assessing maximum magnitude in the central and eastern United States: EPRI Research Project 2556-12, Electric Power Research Institute, Palo Alto, California.

Cornell, C.A., 1968, Engineering seismic risk analysis: Bulletin of the Seismological Society of America, v. 58, p. 1583-1606.

Cornell, C.A., and Van Marke, E.H., 1969, The major influences on seismic risk: in Proceedings of the Third World Conference on Earthquake Engineering, Santiago Chile, v. A-1, p. 69-93.

Crouse, C.B., Vyas, Y.K., and Schell, B.A., 1988, Ground motions from subduction-zone earthquakes: Bulletin of the Seismological Society of America, v. 78, p. 1-25.

Der Kiureghian, A., and Ang, A.H., 1977, A fault-rupture model for seismic risk analysis: Bulletin of the Seismological Society of America, vol. 67, p. 1173-1194.

EPRI, 1987, Seismic hazard methodology for the central and eastern United States - Volume 1: Methodology: Report NP-4726, Volume 1, prepared for Seismicity Owners Group and Electric Power Research Institute under research projects P101-38, -45, -46, 2256-14, Revised, February, 1987.

Esteva, L., 1969, Seismicity Prediction: A Bayesian Approach, Proceedings of the Fourth World Conference on Earthquake Engineering, Santiago, Chile, January 13-18, 1969, v. 1, p. Al 172-184.

Gutenberg, B., and Richter, C.F., 1954, Seismicity of the Earth and Associated Phenomena, 2nd ed., Princeton University Press, Princeton, New Jersey, 310 p.

Hanks, T.C., and McGuire, R.K., 1981, The character of high frequency strong ground motion: Bulletin of the Seismological Society of America, v. 71, p. 2071-2095.

Idriss, I.M., 1985, Evaluating seismic risk in engineering practice: Proceedings of the Eleventh International Conference on Soil Mechanics and Foundation Engineering, San Francisco, August 12-16, p. 255-320.

Joyner, W.B., and Boore, D.M., 1988, Measurement, characterization, and prediction of strong ground motion: in Earthquake Engineering and Soil Dynamics II - Recent Advances in Ground Motion Evaluation, ASCE Geotechnical Special Publication 20, p. 43-102.

Keefer, D.L., Bodily, S.E., 1983, Three-point approximations for continuous random variables: Management Science, v. 29, no. 5, p. 595-609.

Kulkarni, R.B., Youngs, R.R., and Coppersmith, K.J., 1984, Assessment of confidence intervals for results of seismic hazard analysis: in Proceedings of the Eight World Conference on Earthquake Engineering, San Francisco, California, v. 1, p. 263-270.

National Research Council, 1988, Probabilistic Seismic Hazard Analysis: National Academy Press, Washington D.C., 97 p.

Sadigh, K., 1983, Considerations in the development of site-specific spectra, in Proceedings of Conference XXII, site-specific effects of soil and rock on ground motion and the implications for earthquake resistant design: U.S. Geological Survey Open File Report 83-845.

Sadigh, K., Egan J.A., and Youngs, R.R., 1986, Specification of ground motion for seismic design of long period structures: Earthquake Notes, v. 57, no. 1, p. 13., relationships are tabulated in Joyner and Boore (1988).

Sadigh, K. and Youngs, R.R., 1984, Specification of upper-bound values of ground motion (abs.): Earthquake Notes, vol. 55, no. 1.

Schwartz, D.P., 1988, Geology and seismic hazards - moving into the 1990's: in Earthquake Engineering and Soil Dynamics II - Recent Advances in Ground Motion Evaluation, ASCE Geotechnical Special Publication 20, p. 1-42.

Schwartz, D.P., and Coppersmith, K.J., 1984, Fault behavior and characteristic earthquakes from the Wasatch and San Andreas faults: Journal of Geophysical Research, v. 89, p. 5681-5698.

Schwartz, D.P., and Coppersmith, K.J., 1986, Seismic hazards: new trends in analysis using geologic data: in Active Tectonics, Academic Press, Washington D.C., pp. 215-230.

Slemmons, D.B., 1982, Determination of design earthquake magnitudes for microzonation: Proceedings of the Third International Microzonation Conference, v. 1, p. 119-130.

Suppe, J., 1983, Geometry and kinematics of fault-bend folding: American Journal of Science, v. 289, p. 684-721.

Weichert, D.H., 1980, Estimation of the earthquake recurrence parameters for unequal observation periods for different magnitudes: Bulletin of the Seismological Society of America, v. 70, p. 1337-1346.

Wells, D., and Coppersmith, K.J., 1992, Analysis of empirical relationships among magnitude, rupture length, rupture area, and surface displacement (abs.): Seismological Research Letters, v. 63, no. 1, p. 73.

Working Group on California Earthquake Probabilities, 1988, Probabilities of large earthquakes occurring in California on the San Andreas fault: U.S. Geological Survey Open-File Report 88-398.

Wyss, M., 1979, Estimating maximum expectable magnitude of earthquakes from fault dimensions: Geology, v. 7, p. 336-340.

Youngs, R.R. and Coppersmith, K.J., 1985a, Development of a fault-specific recurrence model: Earthquake Notes (abs.), vol 56, no. 1, p. 16.

Youngs, R.R. and Coppersmith, K.J., 1985b, Implications of fault slip rates and earthquake recurrence models to probabilistic seismic hazard estimates: Bulletin of the Seismological Society of America, v. 75, p. 939-964.

Youngs, R.R. and Coppersmith, K.J., 1989, Objective estimation of maximum magnitude using multiple assessment techniques (abs.): Seismological Research Letters, v. 60, p. 27.

Youngs, R.R., Coppersmith, K.J., Power, M.S., and Swan, F.H., 1985, Seismic hazard assessment of the Hanford region, eastern Washington State: in Proceedings of the DOE Natural Hazards Phenomena Hazards Mitigation Conference, Las Vegas, Nevada, October 7-11, p. 169-176.

Youngs, R.R., Swan, F.H., and Power, M.S., 1988a, Use of detailed geologic data in regional probabilistic seismic hazard analysis - an example from the Wasatch Front, Utah: in Earthquake Engineering and Soil Dynamics II -Recent Advances in Ground Motion Evaluation, ASCE Geotechnical Special Publication 20, p. 156-172.

Youngs, R.R., Day, S.M., and Stevens, J.P., 1988b, Near field motions on rock for large subduction zone earthquakes: in Earthquake Engineering and Soil Dynamics II - Recent Advances in Ground Motion Evaluation, ASCE Geotechnical Special Publication 20, p. 445-462.

Youngs, R.R., Makdisi, F., Sadigh, K., and Abrahamson, N.A., 1990, The case for magnitude dependent dispersion in peak ground acceleration (abs.): Seismological Research Letters, v. 61, n. 1, p. 30.

Zoback, M.D., and Zoback, M.L., 1988, Tectonic stress field of the continental U.S.: in L. Pakiser and W. Mooney, eds., Geophysical Framework of the Continental United States, Geological Society of America Memoir (in press).

Zoback, M.L., Nishenko, S.P., Richardson, R.M., Hasegawa, H.S., and Zoback, M.D., 1986, Mid-plate stress, deformation, and seismicity: in Vogt, P.R., and Tucholke, B.E., eds., The Geology of North America, v. M, The Western North Atlantic Region, Geological Society of America, Boulder, Colorado, United States of America, p. 297-312.

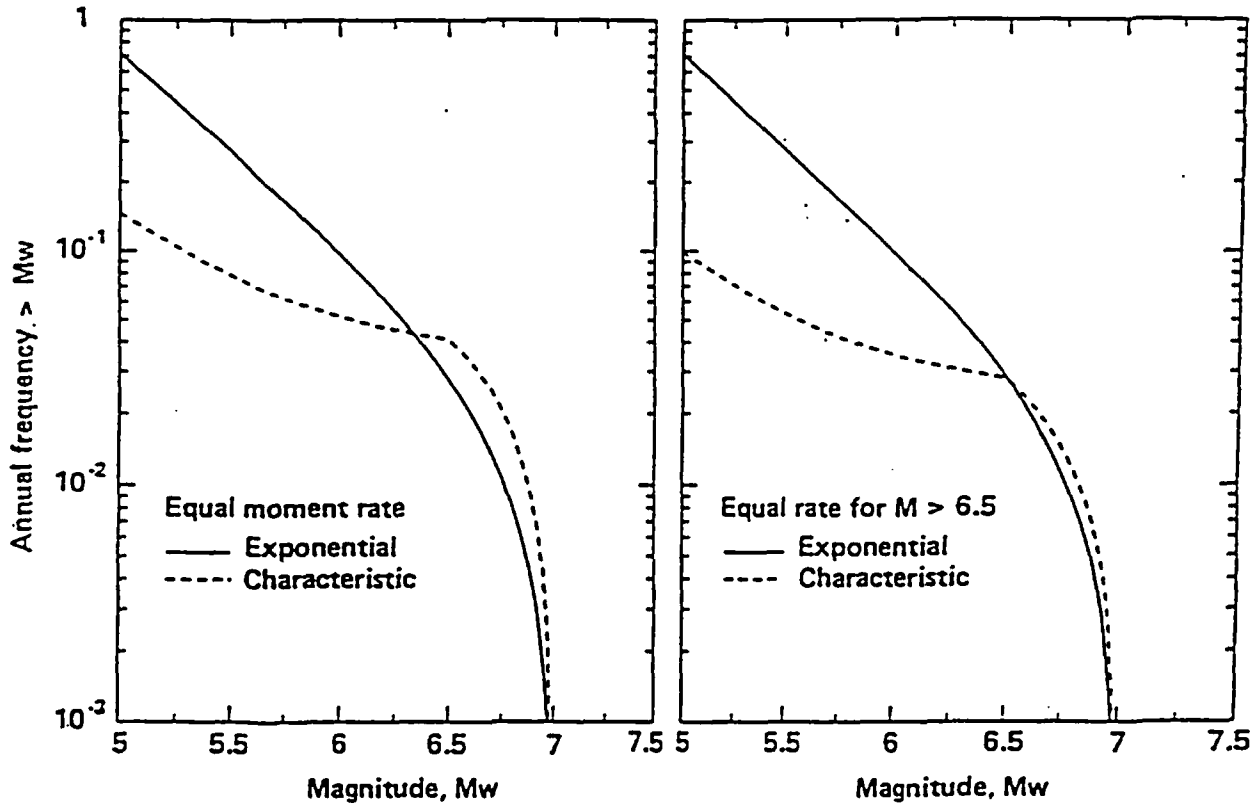

Figure A-1 Comparison of truncated exponential and characteristic earthquake magnitude distributions.

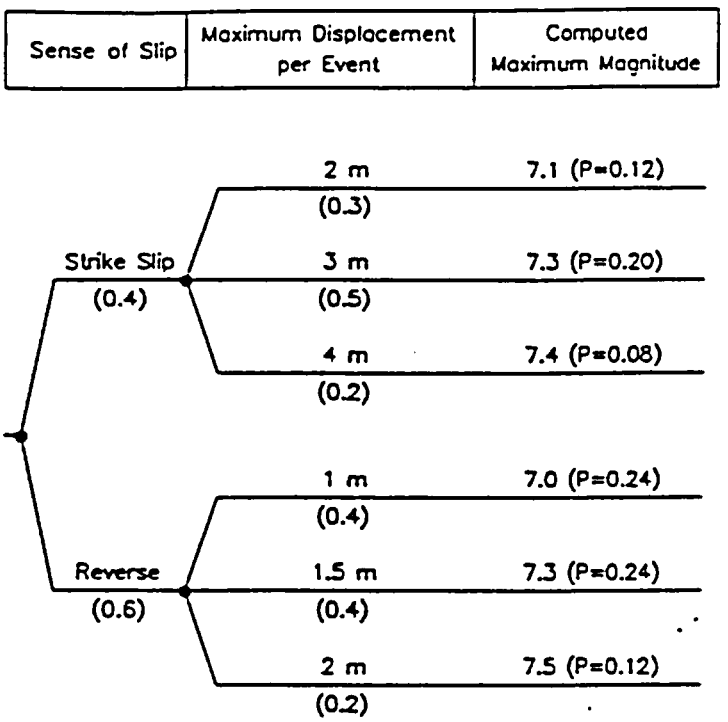

a) Logic Tree for evaluating maximum magnitude

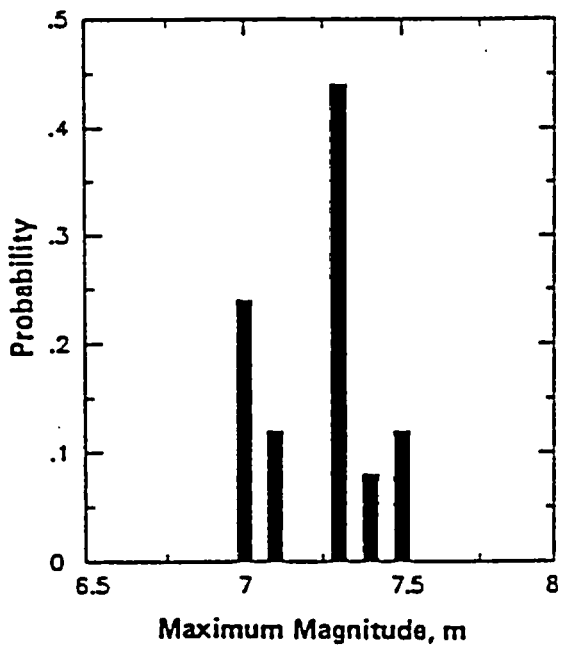

b) Discrete distribution for maximum magnitude

Figure A-2 Example logic tree for evaluating maximum magnitude.

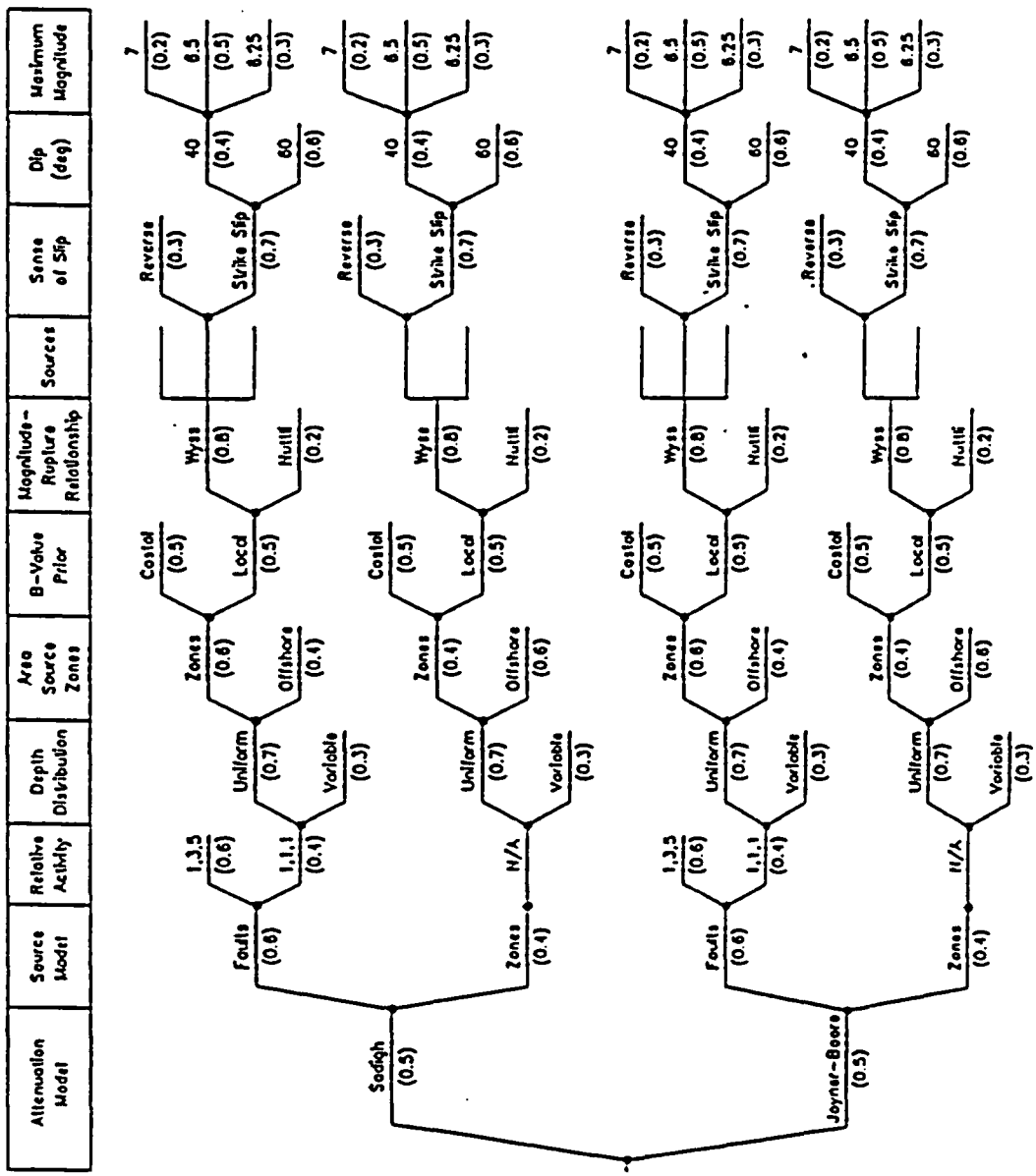

Figure A-3 Seismic hazard model logic tree for North Sea site.

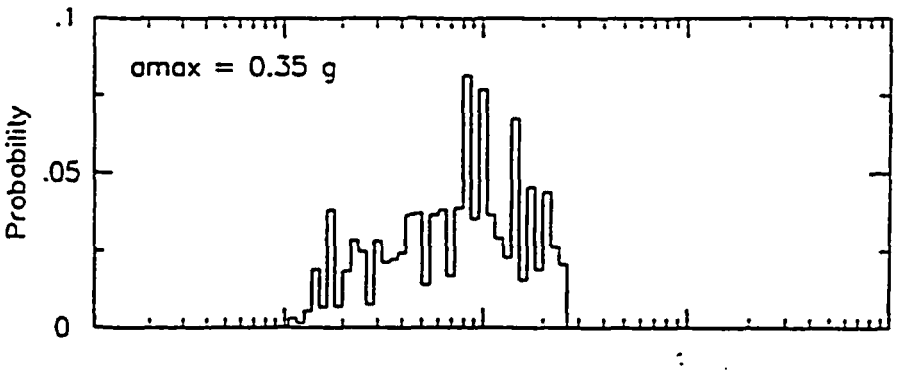

Figure A-4 Computed distribution for exceedance frequency.

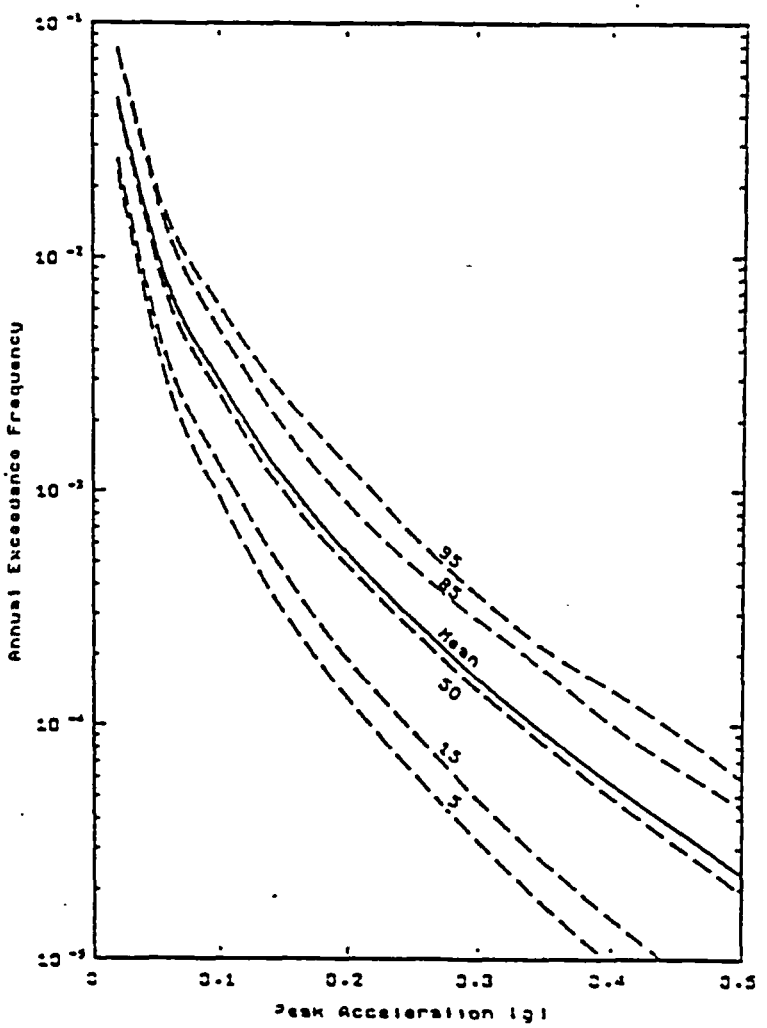

Figure A-5 Hazard curves for peak ground acceleration.

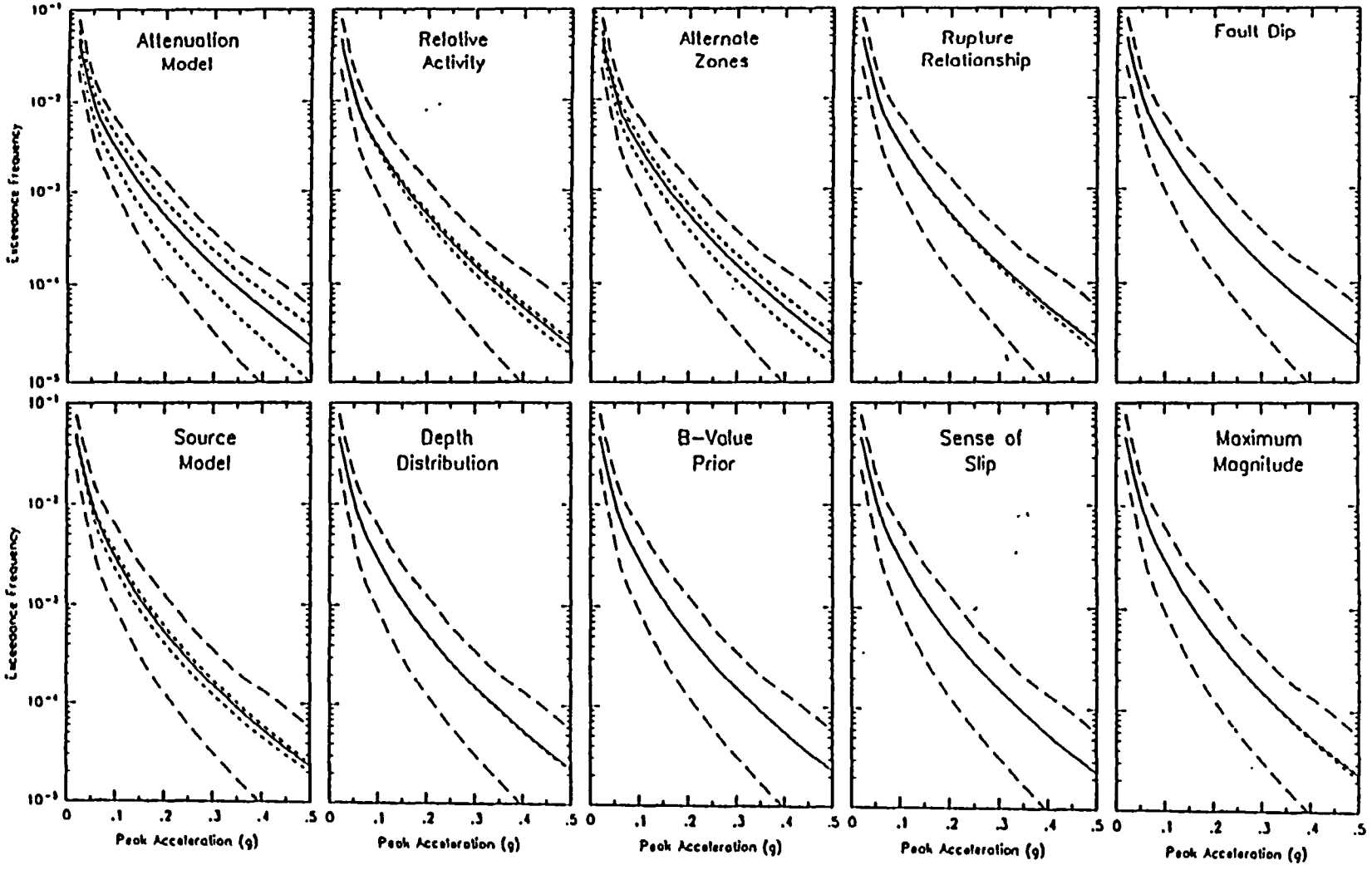

Figure A-6 Contributions to uncertainty in hazard for peak acceleration.

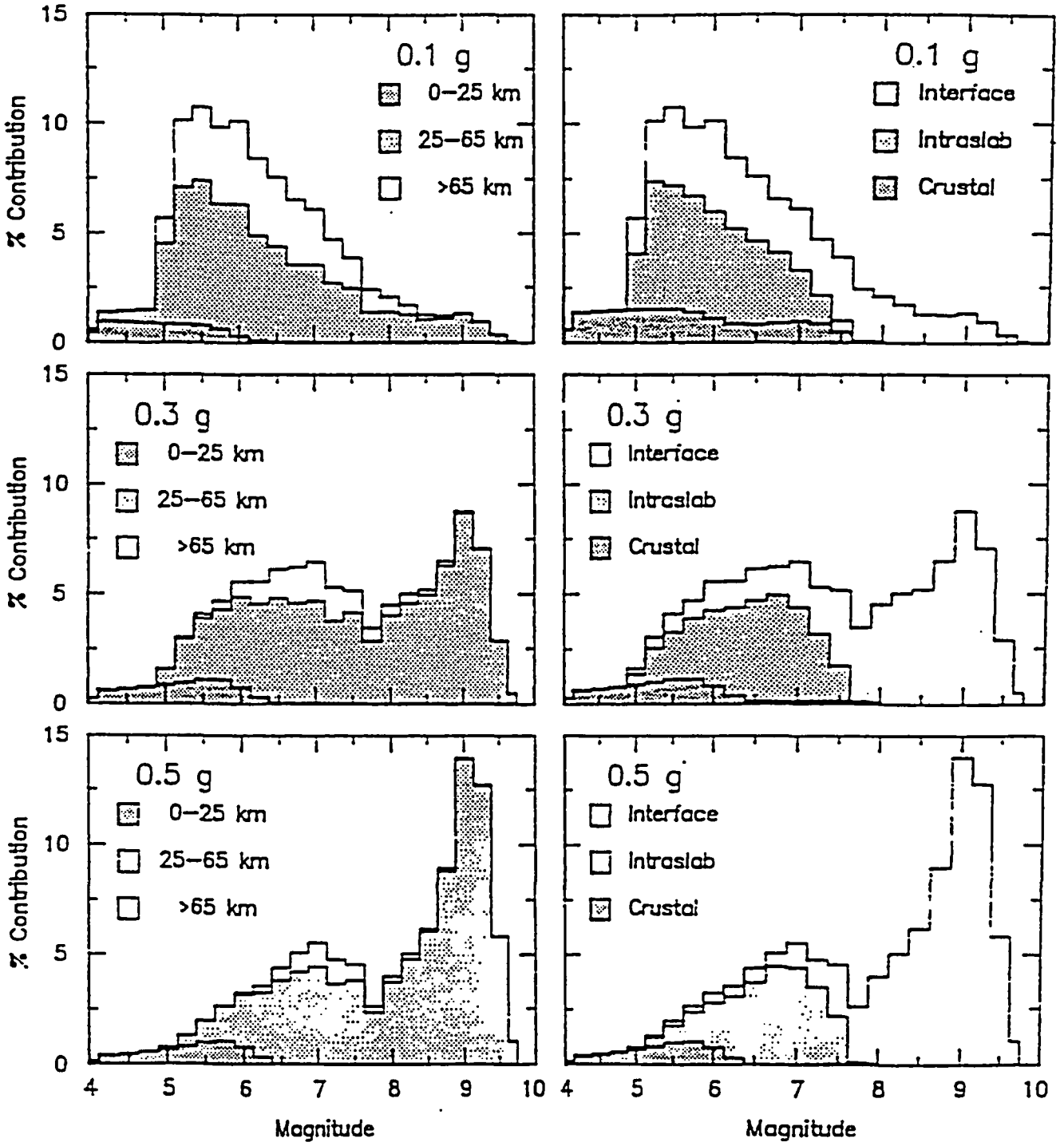

Figure A-7 Magnitude, distance and source contribution to hazard.

APPENDIX B

MAXIMUM CREDIBLE EARTHQUAKE ESTIMATION METHODOLOGY

APPENDIX B

MAXIMUM CREDIBLE EARTHQUAKE ESTIMATION METHODOLOGY

We have estimated the maximum credible earthquake (MCE) for each of the potential earthquake sources as part of the deterministic ground motion assessment. The MCE is defined in guidelines prepared by the California Division of Mines and Geology (1975) as follows:

> "The maximum credible earthquake is the maximum earthquake that appears capable of occurring under the presently known tectonic framework. It is a rational and believable event that is in accord with all known geologic and seismologic facts. In determining the maximum credible earthquake, little regard is given to its probability of occurrence, except that its likelihood of occurring is great enough to be of concern. It is conceivable that the maximum credible earthquake might be approached more frequently in one geologic environment than in another."

The guidelines also indicate that in estimating the MCE, consideration should be given to the seismic history of the vicinity and the geologic province, the length of the significant faults that can affect the site, the types of faults involved, the tectonic and/or structural history, tectonic or regional setting (geologic framework), and the largest historical earthquake to have occurred along a particular fault. It is generally accepted that the magnitude of the maximum credible earthquake will be at least equal to the maximum historical earthquake.

There is no uniquely accepted method for assigning a maximum credible earthquake to a given fault. Assessing maximum earthquake magnitude requires a professional judgement that considers specific fault characteristics, the regional tectonic environment, comparison to other faults of known seismic potential, and data on regional seismicity.

The maximum credible earthquakes estimated for this study are based on: 1) review and consideration of published magnitude estimates, and 2) empirical relationships between fault rupture length, rupture area, and magnitude. The resulting MCE magnitudes are rounded to the nearest quarter magnitude.

Various approaches have been developed to express the empirical relationships between earthquake magnitude and specific fault rupture dimensions.

Worldwide data on historical earthquakes have been compiled to develop linear regressions of earthquake magnitude on length, magnitude on displacement, and magnitude on rupture area for faults in various tectonic settings. These relationships, when used with specific fault characteristics, can provide estimates of ranges of most likely earthquake magnitudes for a given set of conditions.

Our estimates of MCEs are based on empirical fault rupture length/magnitude relationships of the type developed by Bonilla and others (1984), Slemmons (1982), Slemmons and others (1988), and Wells and Coppersmith (1992; in preparation). All four of these relationships provide a surface wave magnitude (M_S). In addition, the relationships by Wells and Coppersmith provide a moment magnitude (M_W). In our opinion the Wells and Coppersmith relationships are based on the most recent and complete data sets available for a strike-slip fault environment similar to the San Francisco Bay Area. Therefore, we have placed greater reliance on these relationships. Specifically, we have relied on the empirical regressions between moment magnitude (M_W) and fault rupture length, and between M_W and rupture area.

Rupture length estimates used in the empirical relationships were selected using two approaches: fractional fault length and fault segmentation. In the fractional fault length approach, a fraction of the total fault length is assumed to rupture according to the following criteria (Mualchin and Jones, 1989): 1) one-half of the total fault length (mapped or reported) was used for faults longer than 50 km; 2) two-thirds of the total fault length was used for faults between 25 and 50 km in length; and 3) the total fault length was used for faults less than 25 km long. When a fault is segmented on the basis of historical rupture (for example, the 1906 earthquake on the San Andreas) or on adjacent segments having different characteristics, the individual fault segments so defined are used to estimate rupture length. Criteria for recognizing fault segmentation are reviewed in Schwartz and Coppersmith (1986) and Coppersmith (1991).

The magnitude of the MCE for a given fault is selected from magnitudes estimated for different fault rupture scenarios. Each scenario is based on different rupture lengths considered for that fault. For each scenario, the rupture length is used with the empirical relationships between moment magnitude and surface length, subsurface length, and rupture area to obtain M_W magnitudes. The magnitudes obtained from the different scenarios for a given fault are then examined, and the MCE magnitude is selected on the basis of a judgement that it is the maximum earthquake that appears capable of occurring under the presently known tectonic framework, and its likelihood of occurring is great enough to be of concern. Note that some scenarios that have a very low probability of being credible will not be considered further in the MCE assessment, but may be part of the probabilistic distribution of maximum magnitudes in the probabilistic assessment.

REFERENCES

Bonilla, M.G., Mark, R.K., and Lienkaemper, J.J., 1984, Statistical relations among earthquake magnitude, surface rupture length, and surface fault displacement, Bulletin Seismological Society of America, v. 74, p. 2379-2411.

California Division of Mines and Geology, 1975, Recommended guidelines for determining the maximum credible and the maximum probable earthquakes, CDMG Note 43, California Division of Mines and Geology, State of California.

Coppersmith, K.J., 1991, Seismic source characterization for engineering seismic hazard anslyses: Proceedings, Fourth International Conference on Seismic Zonationa, v. 1, p. 1-60.

Mualchin, L., and Jones, A.L., 1989, Peak acceleration from maximum credible earthquakes in California (rock and stiff-soil sites) for the design of highway bridges and overpasses, Proposed Map Sheet 42 (Subject to Revision), California Division of Mines and Geology.

Schwartz, D.P. and K.J. Coppersmith, 1986, Seismic hazards: new trends in analysis using geologic data: in Active Tectonics, Academic Press, Washington D.C., p. 215-230.

Slemmons, D.B., 1982, Determination of design earthquake magnitudes for microzonation, in 3rd International Earthquake Microzonation Conference Proceedings, p. 119-130.

Slemmons, D.B., Bodin, P., and Xhang, X., 1988, Determination of earthquake from surface faulting events, Proceedings of the International Seminar and Seismic Zonation, Guangzhou, China, 13 p.

Wells, D.L. and Coppersmith, K.J., (in preparation, 1992), Earthquake source parameters: update empirical relationships among magnitude, rupture length, rupture area, and surface displacement: (to be submitted to Bulletin of the Seismological Society of America).

APPENDIX C

DESCRIPTION OF APPROACH AND BASIC CONSIDERATIONS IN SELECTING ROCK MOTION ATTENUATION RELATIONSHIPS FOR SHALLOW CRUSTAL EARTHQUAKES

APPENDIX C

DESCRIPTION OF APPROACH AND BASIC CONSIDERATIONS IN SELECTING ROCK MOTION ATTENUATION RELATIONSHIPS FOR SHALLOW CRUSTAL EARTHQUAKES

Earthquake ground motions were characterized in terms of attenuation relationships for use in making probabilistic as well as deterministic estimates of free-field rock motions at the bridge site. The approach and basic consideration involved in selecting/developing the relationships are described in this appendix for shallow crustal earthquakes and in Appendix F for subduction zone earthquakes.

The results of the evaluations dealing with earthquake source characterization presented in Section 2 indicate the need for attenuation relationships for shallow crustal earthquakes having magnitudes up to 7½ and source-to-site distances as close as about 3 to 5 kilometers. It should be noted that the occurrence of several significant California earthquakes (e.g., 1979 Imperial Valley; 1983 Coalinga; 1984 Morgan Hill; 1986 North Palm Springs; 1987 Whittier; and 1989 Loma Prieta) has greatly expanded the strong motion data obtained from shallow crustal earthquakes. Several recently developed empirically-derived attenuation relationships include post-1978 earthquake recordings, but few have been updated to include data from the 1989 Loma Prieta earthquake. However, the number of attenuation relationships for vertical peak ground acceleration as well as for response spectral ordinates is very limited.

A summary of recent attenuation relationships developed using primarily California earthquake data is shown in Table C-1. Comparisons of ground motion predictions using these relationships are provided in Section 5 (for PGA) and in a later section of this appendix for response spectra. Examination of the information summarized in Table C-1 shows that only two sets of relationships (Sadigh et al 1989; Sadigh and Chang, 1990; Campbell, 1990) provide attenuation relationships for horizontal and vertical peak ground acceleration as well as for horizontal and vertical response spectral ordinates.

The relationships by Campbell (1990) were developed using a relatively complete and up-to-date data base of soil-site recordings; the data base used does not include recordings from some of the more recent earthquakes, notably the 1989 Loma Prieta earthquake.

The relationships by Sadigh et al. (1989); Sadigh and Chang (1990) were developed using the most up-to-date data base of rock-site recordings including the rock recordings from the 1989 Loma Prieta earthquake. These relationships were considered most appropriate for use in the present study; however, it was judged desirable to refine, extend and specialize these relationships as follows:

1) The attenuation relationships for horizontal response spectral acceleration were refined to allow change in the relative frequency content (spectral shape) with distance.

2) The attenuation relationships for horizontal response spectral acceleration were extended to a period of 7.5 seconds.

3) As an independent check of the empirical attenuation relationships for longer periods (periods greater than 2 seconds), numerical simulation procedures were used to evaluate magnitude-scaling relationships used in extrapolation to magnitudes as large as Mw 8.

4) The dispersion relationships for the horizontal PGA were updated and those for S_a were updated and extended to a period of 7.5 seconds.

5) Supplemental relationships were developed for vertical peak ground acceleration for magnitudes less than 6.5.

6) The attenuation relationships for the vertical response spectra were extended to a period of 3 seconds.

7) The dispersion relationships for vertical PGA were updated and those for S_a were updated and extended to a period of 3 seconds.

C.1 ATTENUATION RELATIONSHIPS FOR HORIZONTAL MOTIONS

C.1.1 Horizontal Peak Ground Acceleration

The attenuation relationships selected for the horizontal peak ground acceleration (PGA) are those which were developed in connection with PGandE, Diablo Canyon Project, Long Term Seismic Program and have been summarized in Sadigh et al (1989). For ease of reference, descriptions of the data base, methodology and basic assumptions used in deriving these relationships are provided below.

It should be noted that the data base used in deriving these relationships did not include the recordings from the 1989 Loma Prieta earthquake. However, following the 1989 Loma Prieta earthquake, the predictions from these relationships were checked against the observed rock-site recording and were found consistent with the Loma Prieta data. Therefore, these relationships were adopted in their original form for use in the present study.

In the studies presented by Sadigh et al. (1989), attenuation relationships for the horizontal PGA were developed by multiple-regression analyses of a data base of rock recordings from shallow-crustal earthquakes of magnitude 4.7 to 7.4.

The approach consisted of conducting the following analyses of the rock-site PGA data:

(1) Single-regression analyses for narrow magnitude bands using the following relationship:

$$\ln PGA = C_1 + C_3 \ln(R + C) + \epsilon$$

(2) Multiple-regression analyses for the magnitude range 6.5 to 7.5 using the following relationship:

$$\ln PGA = C_1 + C_2M + C_3 \ln [R + C(M)] + \epsilon$$

(3) Multiple-regression analyses for the magnitude range 5 to 6.5 using the following relationship:

$$\ln PGA = C_1 + C_2M + C_3 \ln [R + C(M)] + \epsilon$$

$$\text{where } C(M) = C_4 \exp (C_5M)$$

In the above equations, PGA is peak ground acceleration, M is moment magnitude, R is the closest distance to fault rupture surface, and ϵ is a random variable having a mean of zero and a standard deviation of σ, and C_1 through C_5 are constants determined by the regression analysis.

The analyses of step (1) above provided constraints on parameter C_3 (far field slope) and on parameter C(M). Based on regression analysis of magnitude 6.5$\pm$ data, the far field slope of -2.1 was selected. Accordingly, the analyses in steps (2) and (3) above were conducted using C_3 = -2.1. Furthermore, analysis of magnitude 6.5 $\pm$ data having a far field slope of -2.1 resulted in C (distance normalizing parameter) in the range of 18 to 19. A value of 18.5 was selected for C corresponding to magnitude 6.5 in conducting the analyses in steps (2) and (3).

Analysis of reverse/thrust earthquake recordings for the magnitude 6.3 to 7.4 range indicated essentially full magnitude saturation at zero distance. Analysis of recordings in the magnitude range of about 4.5 to 6.5 indicated little of no magnitude saturation at close distances. The median peak ground acceleration attenuation relationships for thrust faulting mechanism were found to be as follows:

- For magnitudes equal to or greater than 6.5:

$$\ln PGA = -1.092 + 1.1\ M - 2.1 \ln [R + \exp (-0.4845 + 0.524\ M)]$$

- For magnitudes less than 6.5:

$$\ln PGA = -0.442 + 1.0\ M - 2.1 \ln [R + \exp (1.2965 + 0.250\ M)]$$

Quantification of the effect of style of faulting on peak ground acceleration was based on (a) literature review, (b) analysis of soil and rock data sets, and (c) numerical modeling results. Based on the above, a scaling factor of 0.833 was selected to convert peak ground acceleration from thrust to strike-slip style of faulting. Using this factor along with peak ground acceleration attenuation relationships for thrust earthquakes, the following attenuation relationships were developed for strike-slip earthquakes.

- For magnitudes equal or greater than 6.5:

$$\ln PGA = -1.274 + 1.10\,M - 2.1 \ln [R + \exp (-0.4845 + 0.524\,M)]$$

- For magnitudes less than 6.5:

$$\ln PGA = -0.624 + 1.0\,M - 2.1 \ln [R + \exp (1.2965 + 0.250\,M)]$$

The above relationships, which correspond to a strike-slip faulting mechanism, were selected for use in the present study; these relationships provide median (50^{th} percentile) estimates of the horizontal peak ground acceleration. Other percentile levels can be readily computed from the dispersion relationships associated with these relationships.

In the present study we have selected magnitude-dependent dispersion relationships presented by Youngs et al. (1990). Magnitude-dependent dispersion relationships for horizontal peak ground acceleration were developed by Youngs et al (1990) employing a regression formulation that models the various random effects in ground motion by independent intra-event (within earthquake) and inter-event (earthquake to earthquake) components in a manner similar to Brillinger and Preisler (1984, 1985). The authors applied the model to a large data set consisting of 800 soil and rock recordings from 124 earthquakes and examined the resulting dependence of the two components of variance on earthquake magnitude. The results showed that both components of variance decrease with increasing magnitude, with the inter-event component becoming nearly insignificant for events of $M_w \geq 6\frac{1}{2}$. There analyses were subsequently repeated by including the 1989 Loma Prieta earthquake data resulting in the following relationships for the total standard error, σ (ln PGA):

- For magnitudes equal or greater than 7.5

$$\sigma (\ln PGA) = 0.38$$

- For magnitudes less than 7.25

$$\sigma (\ln PGA) = 1.39 - 0.14\,M$$

C.1.2 Horizontal Acceleration Response Spectra

The available response spectral attenuation relationships were reviewed in detail and found to require updating and extension for use in the present project. The most relevant relationships were found to be those originally developed in connection with the PG&E, Diablo Canyon Power Plant, Long Term Seismic Program (LTSP) Studies (see Sadigh et al 1989). These relationships provide the basis for the modified and extended relationships that were developed by Sadigh and Chang (1990) and these developed for use in the present study; therefore a brief review of the approach used in developing the LTSP relationships is presented below.

The LTSP attenuation relationships were developed for 5 percent damped response spectral acceleration as a function of magnitude and distance for fourteen periods in the range of 0.04 to 1 second. Attenuation relationships for response spectral acceleration were developed using the three-step procedure originally developed by Sadigh (1983; 1984). Step 1 involves development of attenuation relationships for peak ground acceleration; Step 2 involves development of attenuation relationships for normalized spectra, S_a/a; and Step 3 involves development of attenuation relationships for absolute spectra, S_a, through the synthesis of results of Steps 1 and 2.

Specifically, the spectral values set for rock-site recordings were normalized by their corresponding peak ground acceleration values and analyzed period by period by multiple regression using the following relationship (note that this relationship assumes spectral shape is independent of distance):

$$\ln S_a/a = C'_1 + C'_2 (8.5 - M)^{2.5}$$

$$\ln S_a = C''_1 + C_2 M (8.5 - M)^{2.5} + C_3 \ln [R + C(M)]$$

$$C''_1 = C_1 + C'_1$$

The LTSP studies summarized by Sadigh et al. (1989) were conducted prior to the 1989 Loma Prieta earthquake. In a follow-up study, conducted by Sadigh and Chang (1990), revised response spectral attenuation relationships were developed by including the available recordings from the 1989 Loma Prieta earthquake. The studies by Sadigh and Chang (1990) (1) extended the attenuation relationships to periods beyond 1 second and (2) allowed the spectral shape to be a function of distance. The attenuation relationships developed by Sadigh and Chang (1990) were further updated, refined, and extended to develop relationships for this study; these changes included the following:

(1) Inclusion of additional rock recordings from the 1989 Loma Prieta earthquake

(2) Extensions of the relationships to periods as long as 7.5 seconds

(3) Refinement of the attenuation relationships to the following form:

$$\ln S_a(T) = C_1 + C_2 M + C_3 (8.5-M) + 2.5$$

$$+ C_4 \ln [R + \exp (C_5 + C_6 M)] + C_7 \ln (R + 2)$$

(4) Enrichment of the long-period spectral relationships during the smoothing process

The final median attenuation relationships selected for this study are presented in Table C-2 for PGA and S_a for 21 periods in the range 0.04 to 7.5 seconds. The dispersion relationships associated with these relationships are presented in Table C-3.

C.1.3 Statistical Analysis of Horizontal Response Spectra to Examine Distance-dependence of the Spectra

Statistical analyses were conducted on several sets of horizontal response spectra and spectral shapes from recordings obtained on rock in the distance range of 1 to 100 kilometers from shallow-crustal earthquakes with magnitudes in the range of 6¼ to 7. The two main objectives of these analyses were: (1) to examine the dependence of the spectral shape (relative frequency content) on the source-to-site distance, and (2) to compare the absolute level of spectral ordinates predicted by the attenuation relationships with the corresponding values obtained from statistics of spectra from recordings in narrow magnitude and distance bands.

The results of these statistical analyses were used to refine and adjust the attenuation relationships previously developed by Sadigh et al. (1989) and Sadigh and Chang (1990); specifically, the following refinements and adjustments were made:

1) The attenuation relationships were refined to provide more realistic dependence of high frequency motions with distance by including the term $C_7 \ln (R+2)$ in the spectral attenuation relationships; note that quantification of coefficient C_7 was guided and constrained primarily by the results of the statistical analyses of spectral shapes.

2) Refinement and adjustment of the values for coefficients C_1 and C_3 in the spectral attenuation relationships. Note that refinement and adjustment of coefficient C_3 was strongly influenced by the results of the statistical analyses of spectral shapes, particularly for periods beyond 1 second. Adjustment of coefficient C_1 was primarily based on the results of statistical analyses of absolute spectral values resulting in the enrichment of the long period spectral relationships.

C.1.4 Attenuation Relationships Modified to Incorporate the Influence of Crustal Reflections

Recent studies have suggested that the amplitudes of strong ground motions in the distance range of 50 to 150 km may be affected by critical reflections of seismic waves from the base of the crust (e.g., Burger et al., 1987; Somerville and Yoshimura, 1990). These observations are particularly apparent for ground motions recorded during the 1989 Loma Prieta earthquake (Somerville and Yoshimura, 1990). Figure C-1 compares the recorded peak accelerations at rock sites with the attenuation relationships developed above. As can be seen, the data recorded

in the distance range of 45 to 90 km generally lie well above the developed attenuation relationships and show little attenuation with distance. These effects have not been typically observed in western US strong ground motion data because the typical focal depths of 8 to 12 km result in reflected waves reaching the surface only at large distances (100 km or greater). However, as discussed by Somerville and Yoshimura (1990) the pronounced effect on crustal reflections on the observed ground motion amplitudes of the Loma Prieta data arose because the deeper than usual focal depth of 18 km resulted in reflected waves arriving at the surface at source-to-site distances in the range of 40 to 100 km.

The influence of crustal reflections is not likely to be important in evaluating ground motions at the site except for any deeper than usual crustal earthquakes occurring at distances greater than about 50 km from the site. Because the probabilistic seismic hazard analyses consider the contributions of earthquakes at all source-to-site distances to the likelihood of exceeding various ground motion levels at the site, a set of modified attenuation relationships was developed to allow examination of the influence of potential critically reflected waves on the probabilistic seismic hazard at the site. Figure C-1 shows the modified attenuation relationships which was constructed by assuming than no attenuation occurs in the distance range of 45 to 90 km and that the effective distance beyond 90 km is 45 km less than the actual distance. The variance in peak amplitudes about the median relationships was assumed to be the same as that for the primary attenuation relationship as a similar value of variance was found for the data in the 80 to 90 km distance range.

Examination of the data in Figure C-1 suggests that the presence of critically reflected waves may not occur at all sites. The solid diamonds indicate the data recorded south of the epicenter, while the open circles show the data recorded north of the epicenter. The limited data suggest a normal attenuation of amplitude with distance may have occurred to the south of the earthquake. Accordingly, an alternative model was developed in which it was assumed that critically reflected waves occur randomly at points located beyond 45 km from the source. This effect could be modeled in the probabilistic seismic hazard analysis by increasing the variance in the natural log of peak amplitude by a factor of 0.58^2 for distances greater that 45 km. The influence of crustal reflections on ground motions at the site was judged not to be important; therefore, no formal sensitivity analyses were made in this study using the above alternative models.

C.1.5 Estimates of Long Period Motions using Numerical Simulations

The long period motions in the empirical data base are not as reliable as the high frequency motions. In particular, at periods greater than about 4 seconds, the empirical data is often filtered to remove baseline errors. As a result, the long period motion in the empirical data base may underestimate the true long period ground motions.

As an independent check of the long period empirical attenuation relations, numerical simulation procedures were used to estimate the long period ground motion for nearby magnitude 6.75 event and nearby and distant magnitude 8 events.

The fundamental method used in this study is based on the representation theorem (Aki and Richards, 1980) which described the ground motion from a point source as the convolution of a Green's function and a source function. For high frequency motions, previous studies have generally used either empirical Green's functions or empirical source functions to capture the stochastic nature of the motions. However, for long period motions, previous studies have shown that they can be reasonably well modelled using simple theoretical source functions and Green's functions (e.g., Spudich and Archuleta, 1987).

The method described by Archuleta (1984) was used in this simulation study. This method computes the Green's functions for a 1-D crustal model. The results of these simplified numerical simulations are compared to the predictions from the selected attenuation relationships in Figures C-2 through C-4. These comparisons indicate that the empirical attenuation relationships developed for this study are adequate at long periods.

C.1.6 Comparison of Predicted Ground Motions from Recent Attenuation Relationships

As discussed previously, several attenuation relationships have been developed recently using primarily California earthquake data; a summary description of these relationships is given in Table C-1. Only five of these published relationships (Joyner and Boore, 1982; Idriss, 1987, 1991; Sadigh et al., 1986, 1989, 1990; and Campbell, 1990) provide attenuation relationships for horizontal response spectral ordinates.

For ready reference, predicted response spectra from the relationships developed for this study (designated Caltrans 91) are compared in the following figures with corresponding response spectra predicted using: (1) the rock relationships by Joyner and Boore (1982); (2) the stiff soil/rock relationships by Idriss (1991); (3) the rock relationships by Sadigh et al. (1989) (designated PG&E); and (4) the relationships by Campbell (1990).

Figure	Magnitude, M_w	Source-to-Site Distance (km)
C-5	6½	5
C-6	6½	20
C-7	6½	50
C-8	7¼	5
C-9	7¼	20
C-10	7¼	50
C-11	8	10
C-12	8	20
C-13	8	50

In general, the predicted ground motions from these relationships are in fair to good agreement in particular at moderate distances. Note that the Sadigh et al (1989) relationship designed PG&E is in closest agreement with the relationships selected for this study (designated Caltrans 91); however, as was discussed previously, the Caltrans 91 relationships are minor

refinement of PG&E relationships up to a period of 1 second and have been extended to a period of 7.5 seconds.

The most substantial differences in predicted response spectra from various relationships appear to be for larger magnitude events at distances of 20 to 50 km. In particular, the predicted spectra from Joyner and Boore (1982) relationships substantially differ from the other predictions for periods of about 0.5 second or greater. It should be emphasized that the relationships of Joyner and Boore (1982) were derived without the benefit of strong motion data from several recent significant earthquakes (1983 Coalinga; 1984 Morgan Hill; 1986 North Palm Springs; 1987 Whittier Narrows; and 1989 Loma Prieta) and, therefore, are not as well constrained by data as the more recent relationships.

It is also significant to note that the relationships developed for use in this study predict long-period ground motions in general equal to or higher than other predictions except those from Campbell's relationships at closed to intermediate source-to-site distances. The relationships selected for use in this study are preferred for the following reasons:

(1) The selected relationships use an up-to-date data base of rock recordings including data from the 1989 Loma Prieta earthquake and provide similar predicted ground motions to those derived using rock relationships by Idriss (1987, 1991) and Sadigh et al. (1986, 1989, 1990).

(2) The differences with Joyner and Boore's (1982) predictions appear to be primarily attributable to the much smaller data base of rock recordings available at the time the relationships were developed by Joyner and Boore.

(3) The differences with Campbell's (1990) predictions appear to be primarily attributable to the fact that Campbell's data base is primarily soil-site recordings and does not include recordings from some of the more recent earthquakes, notably the 1989 Loma Prieta earthquake.

(4) Comparison of predicted ground motions using the selected relationships with observed rock recordings conducted by examining residuals (see Section C.1.7) shows very good agreement.

(5) The selected relationships provide attenuation relationships for horizontal and vertical peak acceleration as well as for horizontal and vertical response spectra.

C.1.7 Comparison of Predicted Ground Motions with Observed (Recorded) Ground Motions

The procedure, data base and basic steps used to developed attenuation relationships for use in this study were described previously. It was noted that during the last steps involving the smoothing process, the spectral relationships in particular for long-period motions were enriched

to compensate for the possibility that the long period motion in the empirical data base may underestimate the true long period ground motions.

This section provides comparison of predicted response spectra using the selected attenuation relationships with corresponding spectra for rock recording from earthquakes with magnitudes equal to or greater than 6.3. The comparisons are made most readily in terms of residuals of observed minus predicted values.

Figures C-14 through C-23 present computed residuals as a function of distance for horizontal response spectral ordinates at twenty (20) periods (in the range of 0.05 to 5 seconds).

Examination of the residuals shown in Figures C-14 through C-23 shows that the mean error is in the range of -0.08 to -0.28; in other words, the final selected attenuation relationships are higher than the mean of the data (in the distance and magnitude range shown in the figures) by about 10 to 30 percent. The lower portion of Figure C-24 graphically illustrates the computed mean residual of S_a at the twenty periods shown in Figures C-14 through C-23.

The upper portion of Figure C-24 shows the corresponding mean residuals of S_a if the Coalinga earthquake data are excluded from the data base. The reason for also examining the residuals without Coalinga data is that the Coalinga records are exceptionally rich in longer period motion and deficient in high frequency motions. Therefore, it was judged prudent to envelop the high frequency portion without the Coalinga records and the long-period portion with the Coalinga records.

Examination of the mean residual values shows that the selected relationships provide a reasonable and somewhat conservative estimate of spectral values for all periods in the range of 0.05 to 5 seconds.

C.2 ATTENUATION RELATIONSHIPS FOR VERTICAL MOTIONS

C.2.1 Vertical Peak Ground Acceleration

The attenuation relationships selected for peak ground acceleration are those developed by Sadigh and Chang (1990) and are described in detail below.

The empirical attenuation equation for the vertical peak ground acceleration was selected to have the same form as that for the horizontal:

$$\ln PVA = C_1 + C_2M + C_3 \ln [R + \exp (C_4 + C_5M)] + C_6Z_f$$

In the above equation, PVA is vertical peak ground acceleration, M is moment magnitude, R is the closest distance to the fault rupture surface, Z_f is a dummy variable to account for the style of faulting ($Z_f = 0$) for strike slip and $Z_f = 1$ for reverse), and C_1 through C_6 are constants determined from regression analyses. The data bases used in determining coefficients C_1 through C_6 consisted of: (1) the vertical peak ground acceleration data for rock sites from shallow crustal earthquakes of magnitude 4.7 to 7.4 including the 1989 Loma Prieta earthquake peak ground

acceleration data for rock sites, and (2) the vertical peak ground acceleration associated with the combined rock and soil data to develop the magnitude-dependent dispersion relationships.

Several sets of regression analyses were conducted on the vertical peak ground acceleration data to determine regression coefficients C_1 through C_6 and the magnitude-dependent dispersion. The initial step involved quantification of the coefficient for magnitude, C_2, and the style-of-faulting factor (coefficient C_6) by conducting regression analysis of the combined rock and soil data set. Based on these analyses, the magnitude coefficient, C_2, was estimated to be 1.1 and the style of faulting coefficient, C_6, was estimated to be 0.1. The C_2 and C_6 coefficients were held to these values in all subsequent regression analyses.

The second step involved conducting single-regression analyses of the vertical peak ground acceleration data set for rock for a narrow magnitude band (magnitude 6.5 $\pm$ 0.2) using the following relationship:

$$\ln PVA = C_1 + C_3 \ln (R + C) + 0.1 Z_f$$

The third step involved conducting a weighted multiple-regression analysis of the vertical peak ground acceleration data set for rock, consisting of earthquakes having magnitudes of 6.3 or greater recorded within 50 kilometers.

Based on these regression analyses, the following relationships were developed for median peak ground acceleration corresponding to strike-slip faulting mechanism.

- For magnitudes equal or greater than 6.5:

  $$\ln PVA = -1.08 + 1.1\,M - 2.3 \ln [R + \exp (-0.3524 + 0.478\,M)]$$

- For magnitude less than 6.5:

  $$\ln PVA = -0.430 + 1.0\,M - 2.3 \ln [R + \exp (1.2726 + 0.228\,M)]$$

The fourth and last step involved conducting regression analyses on the combined rock and soil data base using a random-effects model to obtain the standard error as a function of magnitude. A detailed discussion of this topic for the horizontal peak ground acceleration data follow those described for the horizontal motions by Youngs et al (1990). Based on the results of these analyses the following relationships were selected for the total standard error, σ (ln PVA):

$$\sigma (\ln PVA) = 0.48 \text{ for } M \geq 6.5$$

$$\sigma (\ln PVA) = 3.08 - 0.40\,M \text{ for } 6.0 < M < 6.5$$

$$\sigma (\ln PVA) = 0.68 \text{ for } M \leq 6.0$$

C.2.2. Vertical Acceleration Response Spectra

Attenuation relationships were developed by Sadigh and Chang (1990) for 5-percent-damped response spectral acceleration as a function of magnitude and distance for periods up to 1 second. The relationships developed by Sadigh and Chang were selected for this study and extended to a period of 3 seconds. The data base used in the study by Sadigh and Chang (1990) consists of data for rock sites from shallow crustal earthquakes of magnitude 4.7 to 7.4 including the recordings available at the time of study from the 1989 Loma Prieta earthquake.

In the study by Chang and Sadigh (1990) the empirical attenuation equations for the vertical response spectral ordinates were selected to have the following form:

$$\ln S_a(T) = C_1 + C_2 M + C_3 (8.5 - M)^{2.5} + C_4 \ln [R + \exp (C_5 + C_6 M)] + C_7 Z_f$$

In the above equation, $S_a(T)$ is acceleration response spectral ordinate at period T, M is moment magnitude, R is the closest distance to fault rupture surface, Z_f is a dummy variable to account for style of faulting ($Z_f = 0$ for strike-slip and $Z_f = 1$ for reverse), and C_1 through C_7 are regression constants.

The regression coefficients, C_1 through C_7, were obtained for the PVA and S_a/PVA terms. The first step involved analyzing the PVA data to determine coefficients C_2, C_5, C_6, and C_7. The results of this step were presented in the previous section:

The second step involved development of attenuation relationships for S_a/PVA in the form of:

$$\ln S_a/PVA = C'_1 + C_3 (8.5 - M)^{2.5} + C'_4 \ln [R + \exp (C_5 + C_6 M)]$$

To simplify the problem, coefficients C_5 and C_6 were set to the values determined from the PVA regression analysis. Therefore, the final relationship for S_a/PVA was selected to have the following form:

- For magnitudes equal or greater than 6.5:

$$\ln S_a/PVA = C'_1 + C_3 (8.5 - M)^{2.5} + C'_4 \ln [R + \exp (-0.3542 + 0.478M)]$$

- For magnitudes less than 6.5:

$$\ln S_a/PVA = C'_1 + C_3 (8.5 - M)\, 2.5 + C'_4 \ln [R + \exp (1.2726 + 0.228M)]$$

Coefficients C_3 and C'_4 were determined using both variance-weighted regression and random-effects regression with relevance weights. Coefficient C_3 defines the magnitude scaling relationship and was determined from regression analyses of S_a/PVA rock data in the magnitude

range 4.7 to 7.4. Based on these analyses, coefficients C_3 were quantified and used in subsequent analyses to determine coefficient C'_4. The S_a/PVA data base to determine coefficient C'_4 consisted of records in the magnitude range 6.3 to 7.4.

The third step consisted of fixing coefficients C_2 through C_7 and conducting regression analysis to obtain coefficient C_1 and $\sigma_{\ln Sa}$. the resulting smoothed coefficients defining the attenuation relationships for vertical response spectral acceleration corresponding to median values and strike-slip faulting mechanism are presented in Table C-4.

Also, based on the results of these analyses and other studies, the following relationships were selected for the total standard error, σ (ln S_a); these relationships are applicable for periods 0.05 to 3 seconds:

$$\sigma (\ln Sa) = 0.57 \text{ for } M \geq 6.5$$

$$\sigma (\ln Sa) = 2.91 - 0.36\ M \text{ for } 6.0 < M < 6.5$$

$$\sigma (\ln Sa) = 0.75 \text{ for } M \leq 6.0$$

REFERENCES

Aki, K., and Richards, P.G., 1980, Quantitative Seismology Theory and Methods 1: W.H. Freeman and Company, 557 p.

Archuleta, R.J., 1984, A faulting model for the 1979 Imperial Valley earthquake: Journal of Geophysical Research, v. 89, p. 4459-4585.

Brillinger, D.R., and Preisler, H.K., 1985, Further analysis of the Joyner-Boore attenuation data: Bulletin of the Seismological Society of America, v. 75, p. 611-614.

Brillinger, D.R., and Preisler, H.K., 1984, An exploratory analysis of the Joyner-Boore attenuation data: Bulletin of the Seismological Society of America, v. 74, p. 1441-1450.

Burger, R.W., Somerville, P.G., Barker, J.S., Herrmann, R.B., and Helmberger, D.V., 1987, The effect of crustal structure on strong ground motion attenuation relations in eastern North America: Bulletin of the Seismological Society of America, v. 77, p. 420-439.

Campbell, K.W., 1990, Reanalysis of strong-motion recordings; empirical prediction of near-source ground motion for the Diablo Canyon Power Plant site, San Luis Obispo County, California: Report to the U.S. Nuclear Regulatory Commission.

Idriss, I.M., 1987, Earthquake ground motions - lecture notes, course on Strong Ground Motion: Earthquake Engineering Research Institute, Pasadena, California, April 10-11.

Idriss, I.M., 1991, Selection of earthquake ground motions at rock sites: Report Prepared for the Structures Division, Building and Fire Research Laboratory, National Institute of Standards and Technology, Department of Civil Engineering, University of California, Davis, September.

Joyner, W.B., and Boore, D.M., 1982, Prediction of earthquake response spectra: U.S. Geological Survey Open File Report 82-977.

Sadigh, K., 1983, Considerations in the development of site-specific spectra, in Proceedings of Conference XXII, Site-Specific Effects of Soil and Rock on Ground Motion and the Implications for Earthquake Resistant Design: U.S. Geological Survey Open File Report 83-845.

Sadigh, K., 1984, Characteristics of strong .motion records and their implications for earthquake-resistant design: Earthquake Engineering Research Institute Publication 84-06, v. 12, p. 31-45.

Sadigh, K., and Chang, C.-Y., 1990, Response spectral relationships for rock, deep-stiff soil and soft soil site conditions: Seismological Research Letters, v. 61, no. 1.

Sadigh, K., Chang, C.-Y., Makdisi, F., and Egan, J.A., 1989, Attenuation relationships for horizontal peak ground acceleration and response spectral acceleration for rock sites (abs.): Seismological Research Letters, v. 60, no. 1, p. 19.

Sadigh, K., Egan, J.A., and Youngs, R.R., 1986, Specification of ground motion for seismic design of long period structures: Earthquake Notes, v. 57, no. 1, p. 13; relationships are tabulated in Joyner and Boore (1988) and Youngs et al. (1987).

Somerville, P., and Yoshimura, J., 1990, The influence of critical Moho reflections on strong motions recorded in San Francisco and Oakland during the 1989 Loma Prieta earthquake: Geophysic Research Letters v. 17, p. 1203-1206.

Spudich, P., and Archuleta, R.J., 1987, Techniques for earthquake ground motion calculation with application to source parametenization of finite fault: Seismic Strong Motion Synthetics, Bolt, B.A., ed., Academic Press, p. 205-265.

Youngs, R.R., Makdisi, F., Sadigh, K., and Abrahamson, N.A., 1990, The case for magnitude dependent dispersion in peak ground acceleration (abs.): Seismological Research Letters, v. 61, no. 1, p. 30.

TABLE C-1

A SUMMARY OF RECENT ATTENUATION RELATIONSHIPS DEVELOPED USING PRIMARILY CALIFORNIA EARTHQUAKE DATA

Relationship	Peak Ground Acceleration		Response Spectral Ordinate		Comments
	Horizontal	Vertical	Horizontal	Vertical	
Seed and Idriss (1982)	X				Applicable to rock-site conditions (graphical form)
Joyner and Boore (1982)	X		X		Coefficient for rock and soil sites
Sadigh et al. (1986)	X		X		Developed separately for rock and soil sites
Mualchin and Jones (1992)	X				Composite relationship
Idriss (1987, 1991)	X		X		Developed separately for rock and soil sites. 1987 spectral relationships are in graphical form; 1991 updates of these relationships are in equation form
Campbell (1990)	X	X	X	X	Data base of soil site recordings (does not include 1989 Loma Prieta recordings)
Sadigh et al. (1989, 1990)	X	X	X	X	Data base of rock-site recordings (includes 1989 Loma Prieta recordings)

TABLE C-2a

ATTENUATION RELATIONSHIPS OF HORIZONTAL ROCK MOTION (PEAK GROUND ACCELERATION AND RESPONSE SPECTRAL ACCELERATIONS, 5% DAMPING FOR STRIKE-SLIP FAULTING)

M_w = or < 6½

Period(s)	C_1	C_2	C_3	C_4	C_5	C_6	C_7
PGA	-0.624	1.0	0.000	-2.100	1.29649	0.250	0.0
0.05	-0.090	1.0	0.006	-2.128	1.29649	0.250	-0.082
0.07	0.110	1.0	0.006	-2.128	1.29649	0.250	-0.082
0.09	0.212	1.0	0.006	-2.140	1.29649	0.250	-0.052
0.10	0.275	1.0	0.006	-2.148	1.29649	0.250	-0.041
0.12	0.348	1.0	0.005	-2.162	1.29649	0.250	-0.014
0.14	0.307	1.0	0.004	-2.144	1.29649	0.250	0.0
0.15	0.285	1.0	0.002	-2.130	1.29649	0.250	0.0
0.17	0.239	1.0	0.0	-2.110	1.29649	0.250	0.0
0.20	0.153	1.0	-0.004	-2.080	1.29649	0.250	0.0
0.24	0.060	1.0	-0.011	-2.053	1.29649	0.250	0.0
0.30	-0.057	1.0	-0.017	-2.028	1.29649	0.250	0.0
0.40	-0.298	1.0	-0.028	-1.990	1.29649	0.250	0.0
0.50	-0.588	1.0	-0.040	-1.945	1.29649	0.250	0.0
0.75	-1.208	1.0	-0.050	-1.865	1.29649	0.250	0.0
1.00	-1.705	1.0	-0.055	-1.800	1.29649	0.250	0.0
1.50	-2.407	1.0	-0.065	-1.725	1.29649	0.250	0.0
2.00	-2.945	1.0	-0.070	-1.670	1.29649	0.250	0.0
3.00	-3.700	1.0	-0.080	-1.615	1.29649	0.250	0.0
4.00	-4.230	1.0	-0.100	-1.570	1.29649	0.250	0.0
5.00	-4.714	1.0	-0.100	-1.540	1.29649	0.250	0.0
7.50	-5.530	1.0	-0.110	-1.510	1.29649	0.250	0.0

Notes: Relationships for reverse/thrust faulting are obtained by multiplying the strike-slip amplitudes by 1.2. Relationships for oblique faulting are obtained by multiplying the strike-slip amplitudes by 1.09.

Attenuation relationships:

$$\ln(y) = C_1+C_2*M+C_3*(8.5-M)\hat{}2.5+C_4*\ln(R+\exp(C_5+C_6*M))+C_7*\ln(R+2)$$

GEOMATRIX

TABLE C-2b

ATTENUATION RELATIONSHIPS OF HORIZONTAL ROCK MOTION
(PEAK GROUND ACCELERATION AND RESPONSE SPECTRAL
ACCELERATIONS, 5% DAMPING FOR STRIKE-SLIP FAULTING)

M_w = or > 6½

Period(s)	C_1	C_2	C_3	C_4	C_5	C_6	C_7
PGA	-1.274	1.1	0.000	-2.100	-0.48451	0.524	0.0
0.05	-0.740	1.1	0.006	-2.128	-0.48451	0.524	-0.082
0.07	-0.540	1.1	0.006	-2.128	-0.48451	0.524	-0.082
0.09	-0.438	1.1	0.006	-2.140	-0.48451	0.524	-0.052
0.10	-0.375	1.1	0.006	-2.148	-0.48451	0.524	-0.041
0.12	-0.302	1.1	0.005	-2.162	-0.48451	0.524	-0.014
0.14	-0.343	1.1	0.004	-2.144	-0.48451	0.524	0.0
0.15	-0.365	1.1	0.002	-2.130	-0.48451	0.524	0.0
0.17	-0.411	1.1	0.0	-2.110	-0.48451	0.524	0.0
0.20	-0.497	1.1	-0.004	-2.080	-0.48451	0.524	0.0
0.24	-0.590	1.1	-0.011	-2.053	-0.48451	0.524	0.0
0.30	-0.707	1.1	-0.017	-2.028	-0.48451	0.524	0.0
0.40	-0.948	1.1	-0.028	-1.990	-0.48451	0.524	0.0
0.50	-1.238	1.1	-0.040	-1.945	-0.48451	0.524	0.0
0.75	-1.858	1.1	-0.050	-1.865	-0.48451	0.524	0.0
1.00	-2.355	1.1	-0.055	-1.800	-0.48451	0.524	0.0
1.50	-3.057	1.1	-0.065	-1.725	-0.48451	0.524	0.0
2.00	-3.595	1.1	-0.070	-1.670	-0.48451	0.524	0.0
3.00	-4.350	1.1	-0.080	-1.610	-0.48451	0.524	0.0
4.00	-4.880	1.1	-0.100	-1.570	-0.48451	0.524	0.0
5.00	-5.364	1.1	-0.100	-1.540	-0.48451	0.524	0.0
7.50	-6.180	1.1	-0.110	-1.510	-0.48451	0.524	0.0

Notes: Relationships for reverse/thrust faulting are obtained by multiplying the strike-slip amplitudes by 1.2. Relationships for oblique faulting are obtained by multiplying the strike-slip amplitudes by 1.09.

Attenuation relationships:

$$\ln(y) = C_1 + C_2*M + C_3*(8.5-M)^{2.5} + C_4*\ln(R+\exp(C_5+C_6*M)) + C_7*\ln(R+2)$$

GEOMATRIX

TABLE C-3

DISPERSION RELATIONSHIPS FOR HORIZONTAL ROCK MOTION

Ground Motion Parameter	Period	Sigma (lny)
Peak Ground Acceleration	–	1.39 - 0.14*M; 0.38 for M> = 7.25
Response Spectra Accel.	0.05	1.39 - 0.14*M; 0.38 for M> = 7.25
Response Spectra Accel.	0.07	1.40 - 0.14*M; 0.39 for M> = 7.25
Response Spectra Accel.	0.09	1.40 - 0.14*M; 0.39 for M> = 7.25
Response Spectra Accel.	0.10	1.41 - 0.14*M; 0.40 for M> = 7.25
Response Spectra Accel.	0.12	1.41 - 0.14*M; 0.40 for M> = 7.25
Response Spectra Accel.	0.14	1.42 - 0.14*M; 0.41 for M> = 7.25
Response Spectra Accel.	0.15	1.42 - 0.14*M; 0.41 for M> = 7.25
Response Spectra Accel.	0.17	1.42 - 0.14*M; 0.41 for M> = 7.25
Response Spectra Accel.	0.20	1.43 - 0.14*M; 0.42 for M> = 7.25
Response Spectra Accel.	0.24	1.44 - 0.14*M; 0.43 for M> = 7.25
Response Spectra Accel.	0.30	1.45 - 0.14*M; 0.44 for M> = 7.25
Response Spectra Accel.	0.40	1.48 - 0.14*M; 0.47 for M> = 7.25
Response Spectra Accel.	0.50	1.50 - 0.14*M; 0.49 for M> = 7.25
Response Spectra Accel.	0.75	1.52 - 0.14*M; 0.51 for M> = 7.25
Response Spectra Accel.	1.00	1.53 - 0.14*M; 0.52 for M> = 7.25
	>1.00	1.53 - 0.14*M; 0.52 for M> = 7.25

TABLE C-4a

ATTENUATION RELATIONSHIPS OF VERTICAL ROCK MOTION (PEAK GROUND ACCELERATION AND RESPONSE SPECTRAL ACCELERATIONS, 5% DAMPING FOR STRIKE-SLIP FAULTING)

M_w = or < 6½

Period(s)	C_1	C_2	C_3	C_4	C_5	C_6
PGA	-0.430	1.0	0.000	-2.300	1.2726	0.228
0.04	0.3379	1.0	0.000	-2.450	1.2726	0.228
0.05	0.5041	1.0	0.000	-2.450	1.2726	0.228
0.06	0.6095	1.0	0.000	-2.450	1.2726	0.228
0.07	0.6896	1.0	0.000	-2.450	1.2726	0.228
0.09	0.6718	1.0	-0.00330	-2.420	1.2726	0.228
0.10	0.6252	1.0	-0.00468	-2.400	1.2726	0.228
0.12	0.5535	1.0	-0.00707	-2.380	1.2726	0.228
0.14	0.3813	1.0	-0.00909	-2.333	1.2726	0.228
0.15	0.2524	1.0	-0.01000	-2.300	1.2726	0.228
0.17	0.0122	1.0	-0.01462	-2.241	1.2726	0.228
0.20	-0.3005	1.0	-0.02061	-2.164	1.2726	0.228
0.24	-0.6678	1.0	-0.02734	-2.077	1.2726	0.228
0.30	-1.1392	1.0	-0.03558	-1.971	1.2726	0.228
0.40	-1.7656	1.0	-0.04619	-1.835	1.2726	0.228
0.50	-2.2748	1.0	-0.05442	-1.729	1.2726	0.228
0.75	-3.2062	1.0	-0.06939	-1.536	1.2726	0.228
1.00	-3.8818	1.0	-0.08000	-1.400	1.2726	0.228
1.50	-4.2618	1.0	-0.08554	-1.400	1.2726	0.228
2.00	-4.5719	1.0	-0.08946	-1.400	1.2726	0.228
2.50	-4.8167	1.0	-0.09251	-1.400	1.2726	0.228
3.00	-5.0364	1.0	-0.09500	-1.400	1.2726	0.228

Notes: Relationships for reverse/thrust faulting are obtained by multiplying the strike-slip amplitudes by 1.1. Relationships for oblique faulting are obtained by multiplying the strike-slip amplitudes by 1.048.

Attenuation relationships:

$$\ln(y) = C_1+C_2*M+C_3*(8.5-M)\text{^}2.5+C_4*\ln(R+\exp(C_5+C_6*M))$$

TABLE C-4b

ATTENUATION RELATIONSHIPS OF VERTICAL ROCK MOTION (PEAK GROUND ACCELERATION AND RESPONSE SPECTRAL ACCELERATIONS, 5% DAMPING FOR STRIKE-SLIP FAULTING)

M_W = or > 6½

Period(s)	C_1	C_2	C_3	C_4	C_5	C_6
PGA	-1.080	1.1	0.000	-2.300	-0.3524	0.478
0.04	-0.3121	1.1	0.000	-2.450	-0.3524	0.478
0.05	-0.1459	1.1	0.000	-2.450	-0.3524	0.478
0.06	-0.0405	1.1	0.000	-2.450	-0.3524	0.478
0.07	0.03956	1.1	0.000	-2.450	-0.3524	0.478
0.09	0.0218	1.1	-0.00330	-2.420	-0.3524	0.478
0.10	-0.0248	1.1	-0.00468	-2.400	-0.3524	0.478
0.12	-0.0965	1.1	-0.00707	-2.380	-0.3524	0.478
0.14	-0.2687	1.1	-0.00909	-2.333	-0.3524	0.478
0.15	-0.3976	1.1	-0.01000	-2.300	-0.3524	0.478
0.17	-0.6378	1.1	-0.01462	-2.241	-0.3524	0.478
0.20	-0.9505	1.1	-0.02061	-2.164	-0.3524	0.478
0.24	-1.3178	1.1	-0.02734	-2.077	-0.3524	0.478
0.30	-1.7893	1.1	-0.03558	-1.971	-0.3524	0.478
0.40	-2.4157	1.1	-0.04619	-1.835	-0.3524	0.478
0.50	-2.9248	1.1	-0.05442	-1.729	-0.3524	0.478
0.75	-3.8562	1.1	-0.06939	-1.536	-0.3524	0.478
1.00	-4.5318	1.1	-0.08000	-1.400	-0.3524	0.478
1.50	-4.9118	1.1	-0.08554	-1.400	-0.3524	0.478
2.00	-5.2219	1.1	-0.08946	-1.400	-0.3524	0.478
2.50	-5.4667	1.1	-0.09251	-1.400	-0.3524	0.478
3.00	-5.6864	1.1	-0.09500	-1.400	-0.3524	0.478

Notes: Relationships for reverse/thrust faulting are obtained by multiplying the strike-slip amplitudes by 1.1. Relationships for oblique faulting are obtained by multiplying the strike-slip amplitudes by 1.048.

Attenuation relationships:

$$\ln(y) = C_1+C_2*M+C_3*(8.5-M)\text{^}2.5+C_4*\ln(R+\exp(C_5+C_6*M))$$

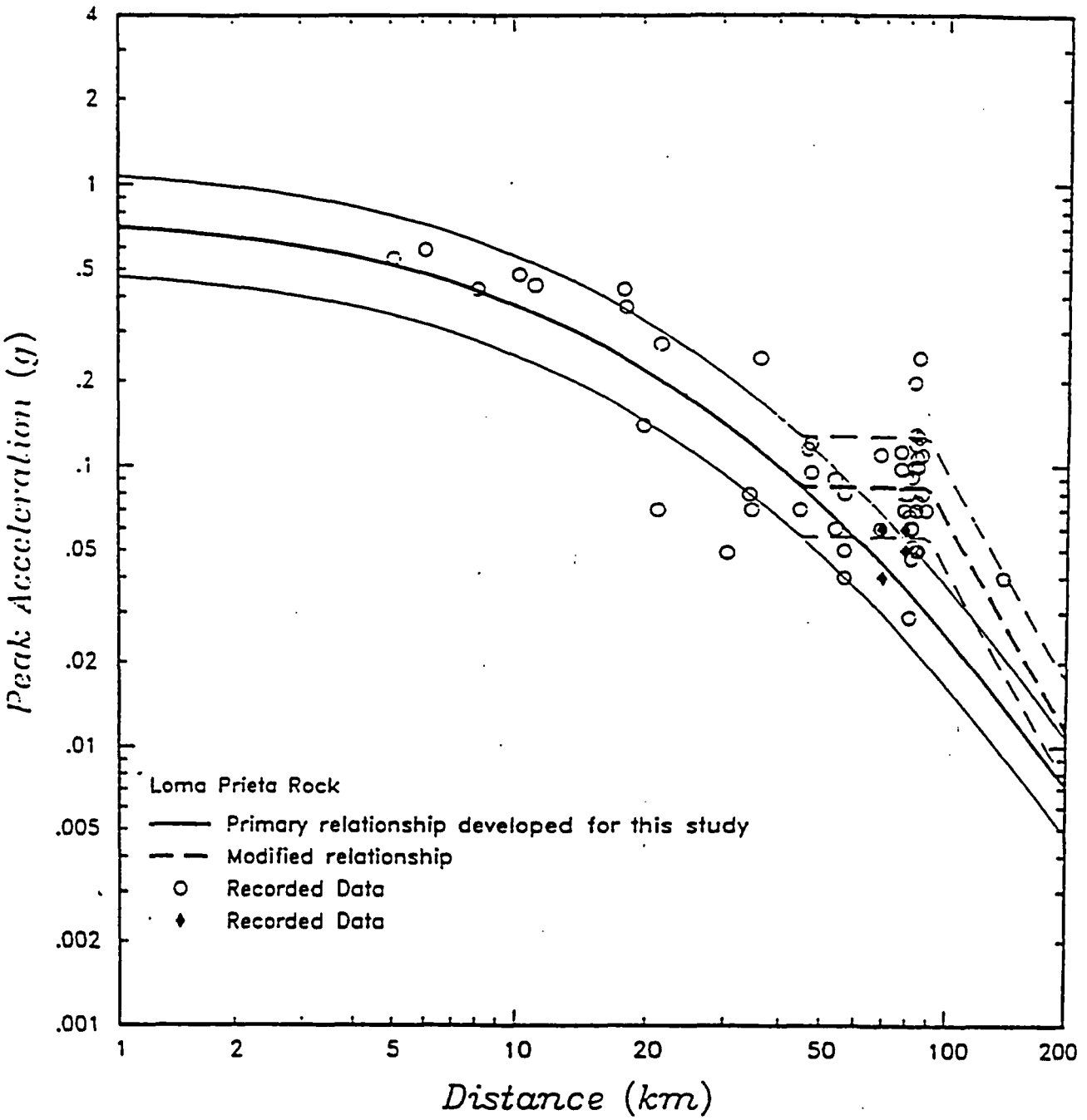

Figure C-1 Comparison of the primary and modified PGA attenuation relationships with the recorded data.

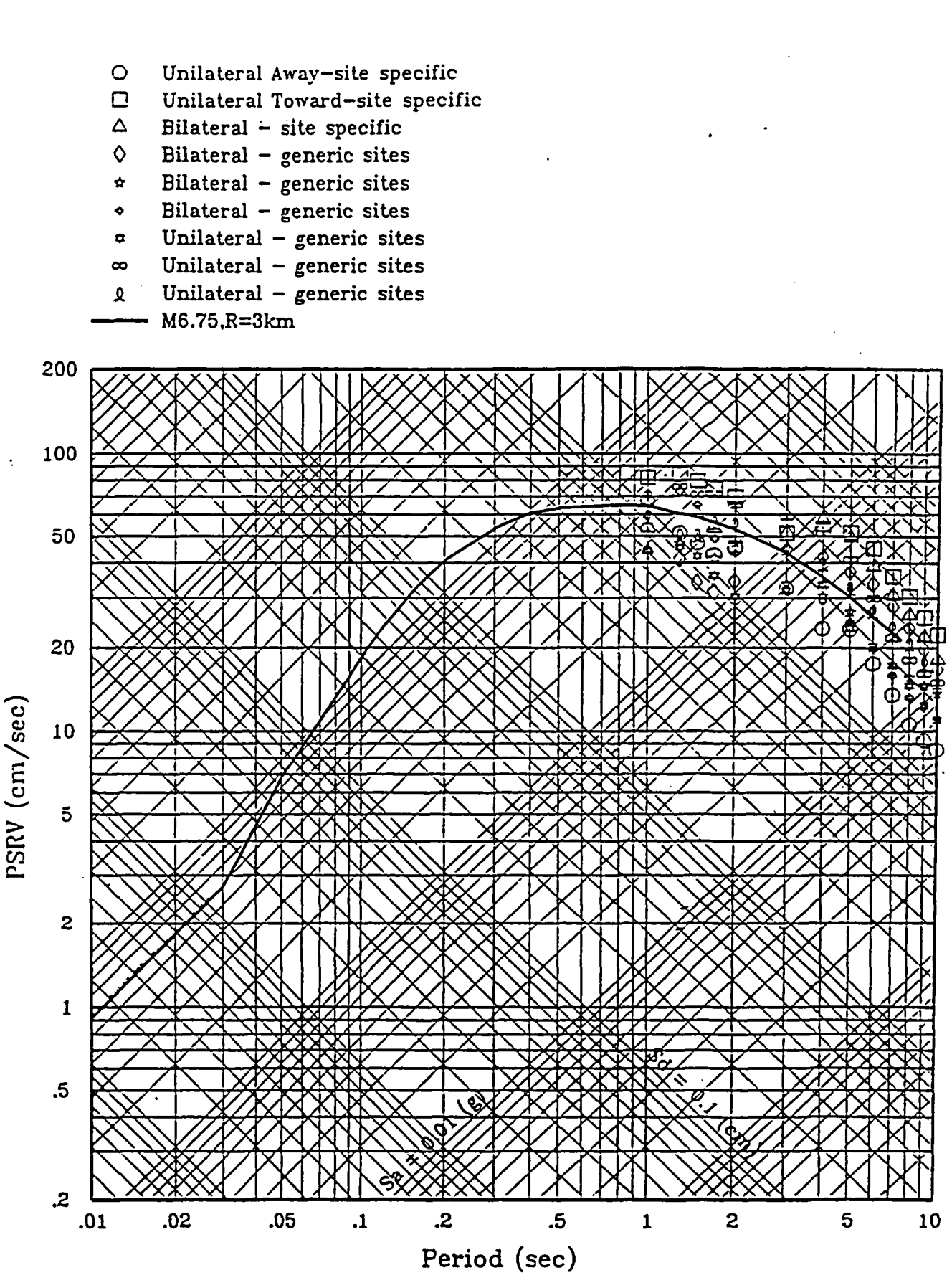

Figure C-2 Comparison of the numerically simulated long period motions with the empirical median spectrum for M 6¾ at R=3 km.

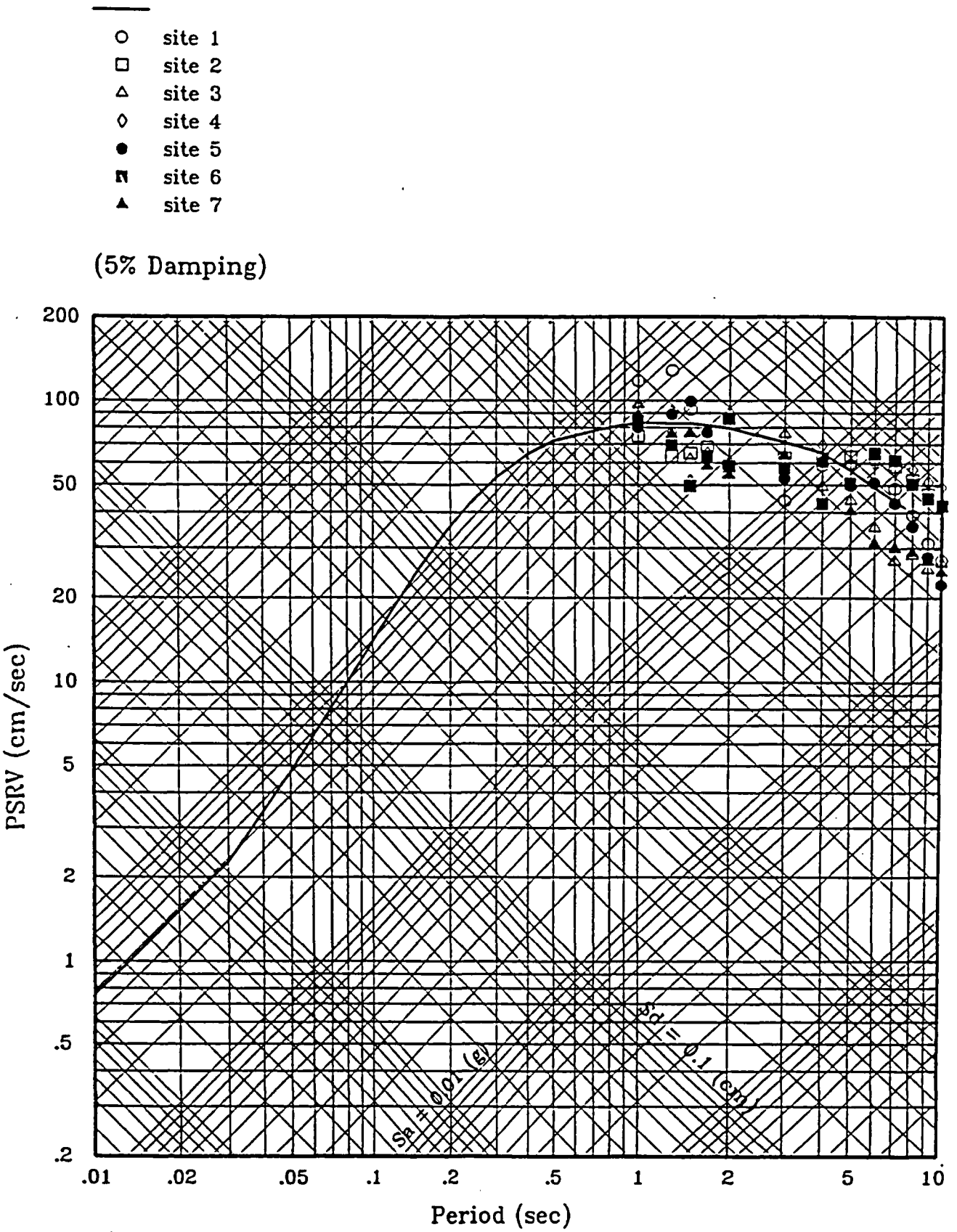

Figure C-3 Comparison of the numerically simulated long period motions with the empirical median spectrum for M 8 at R=10 km.

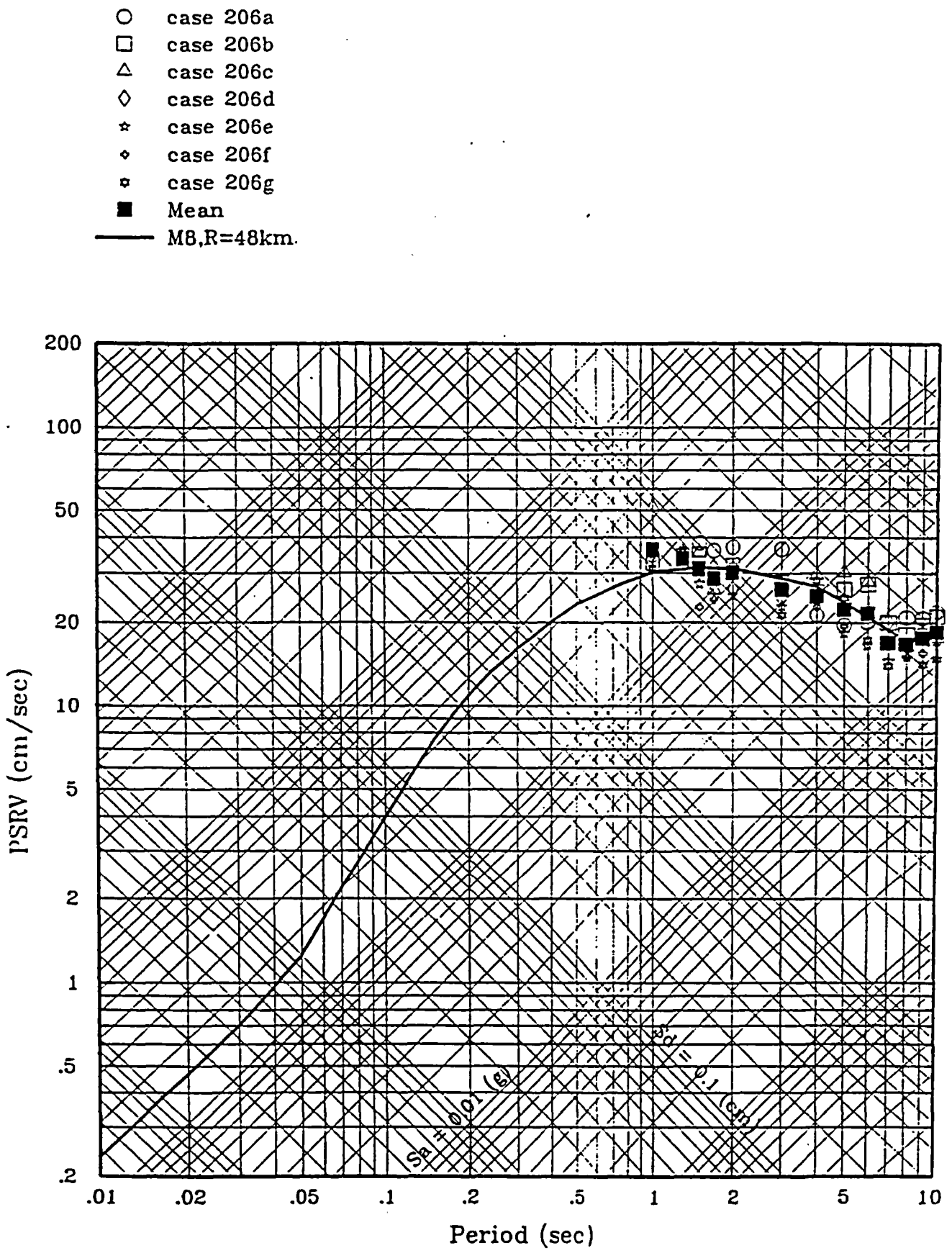

Figure C-4 Comparison of the numerically simulated long period motions with the empirical median spectrum for M 8 at R=48 km.

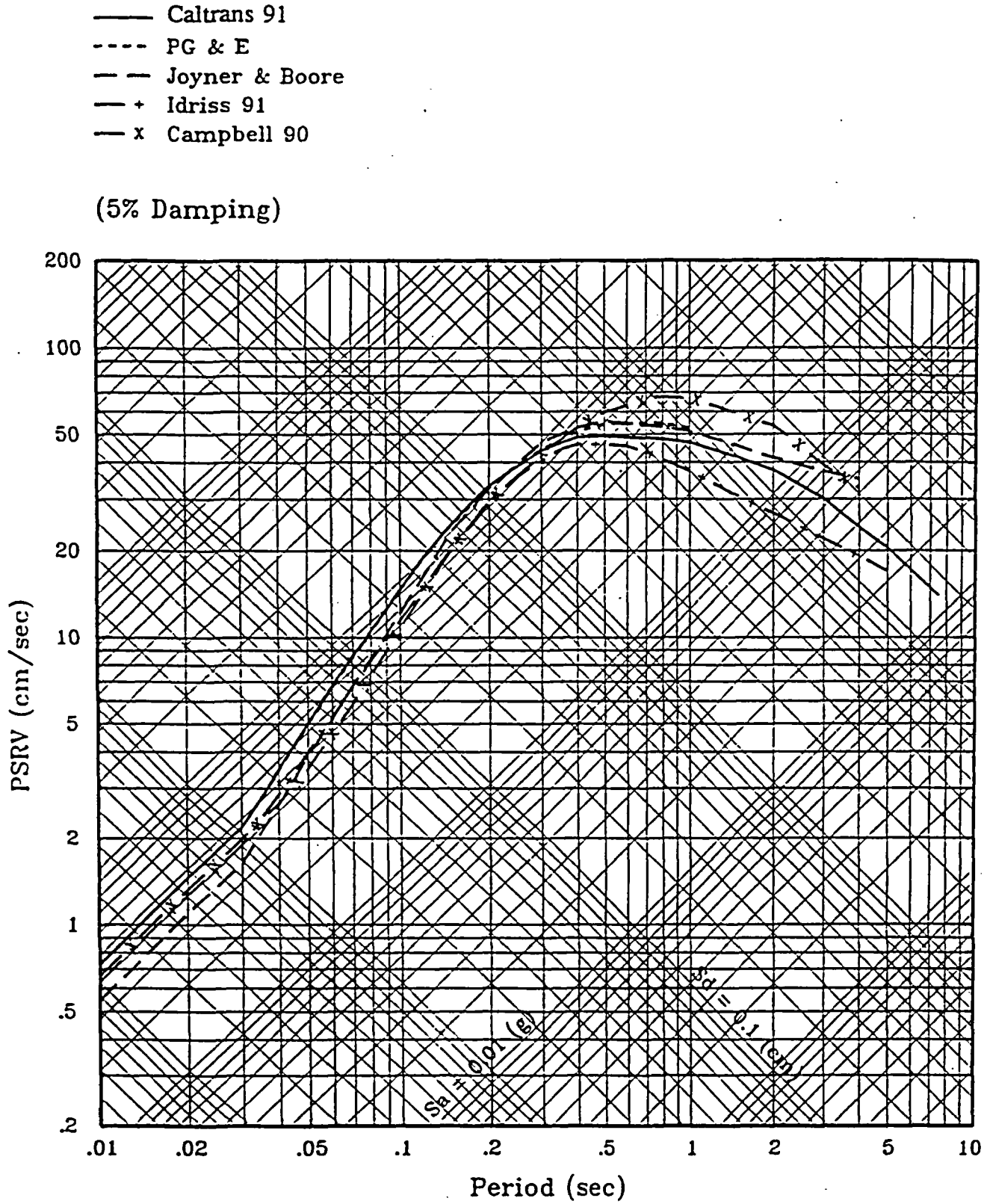

Figure C-5 Comparison of median spectra for M 6½ at R=5 km computed using several recent relationships.

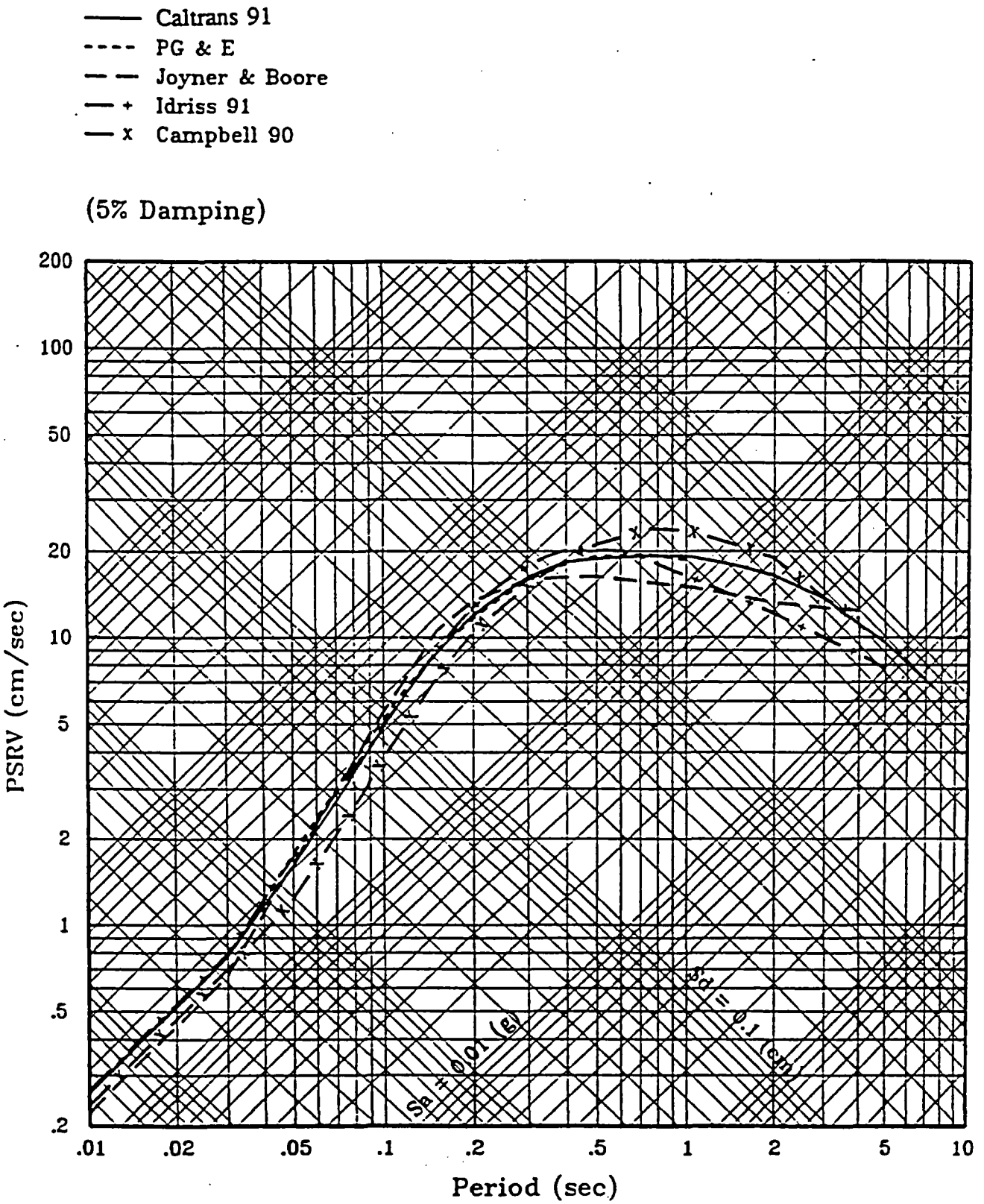

Figure C-6 Comparison of median spectra for M 6½ at R=20 km computed using several recent relationships.

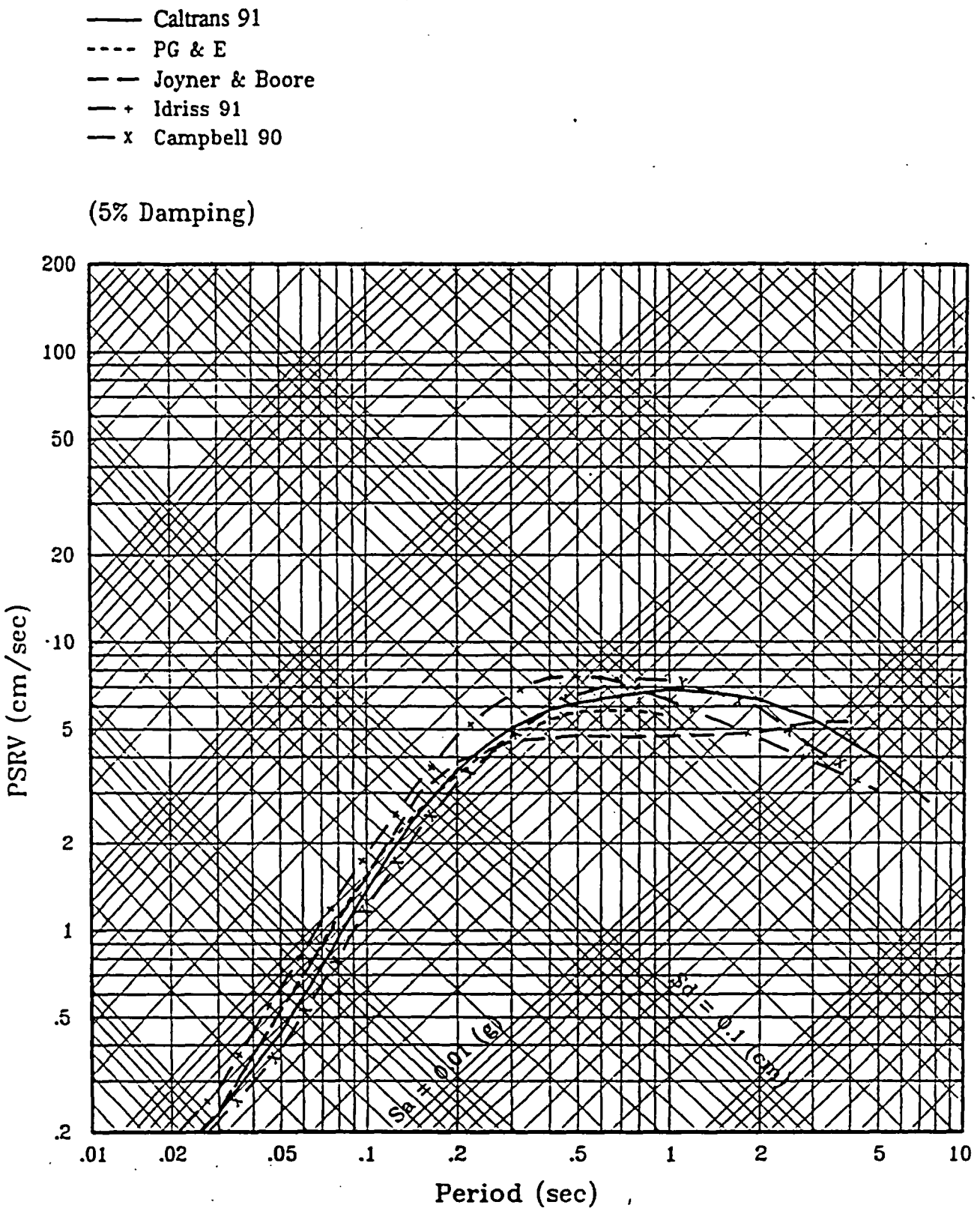

Figure C-7 Comparison of median spectra for M 6½ at R=50 km computed using several recent relationships.

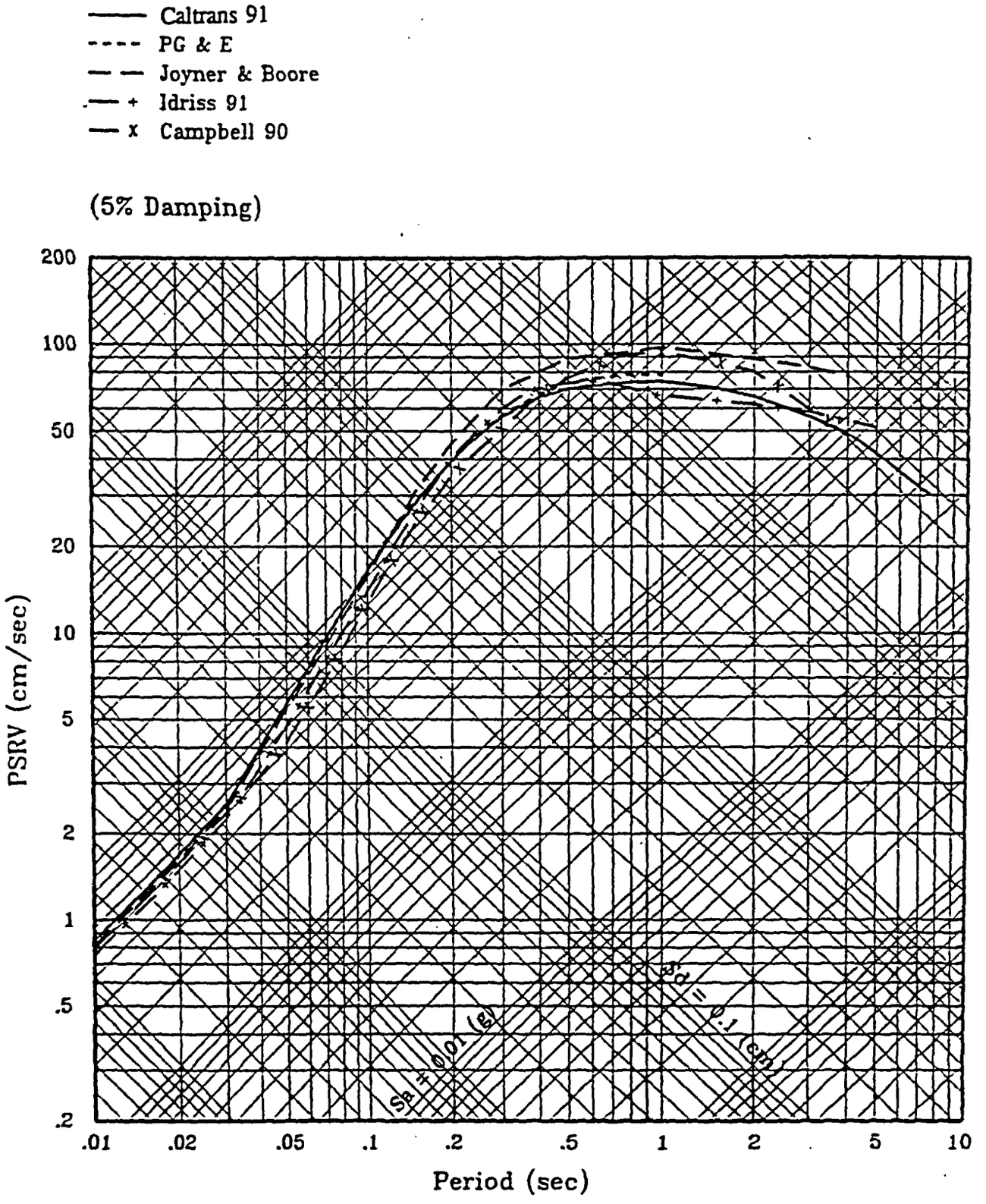

Figure C-8 Comparison of median spectra for M 7¼ at R=5 km computed using several recent relationships.

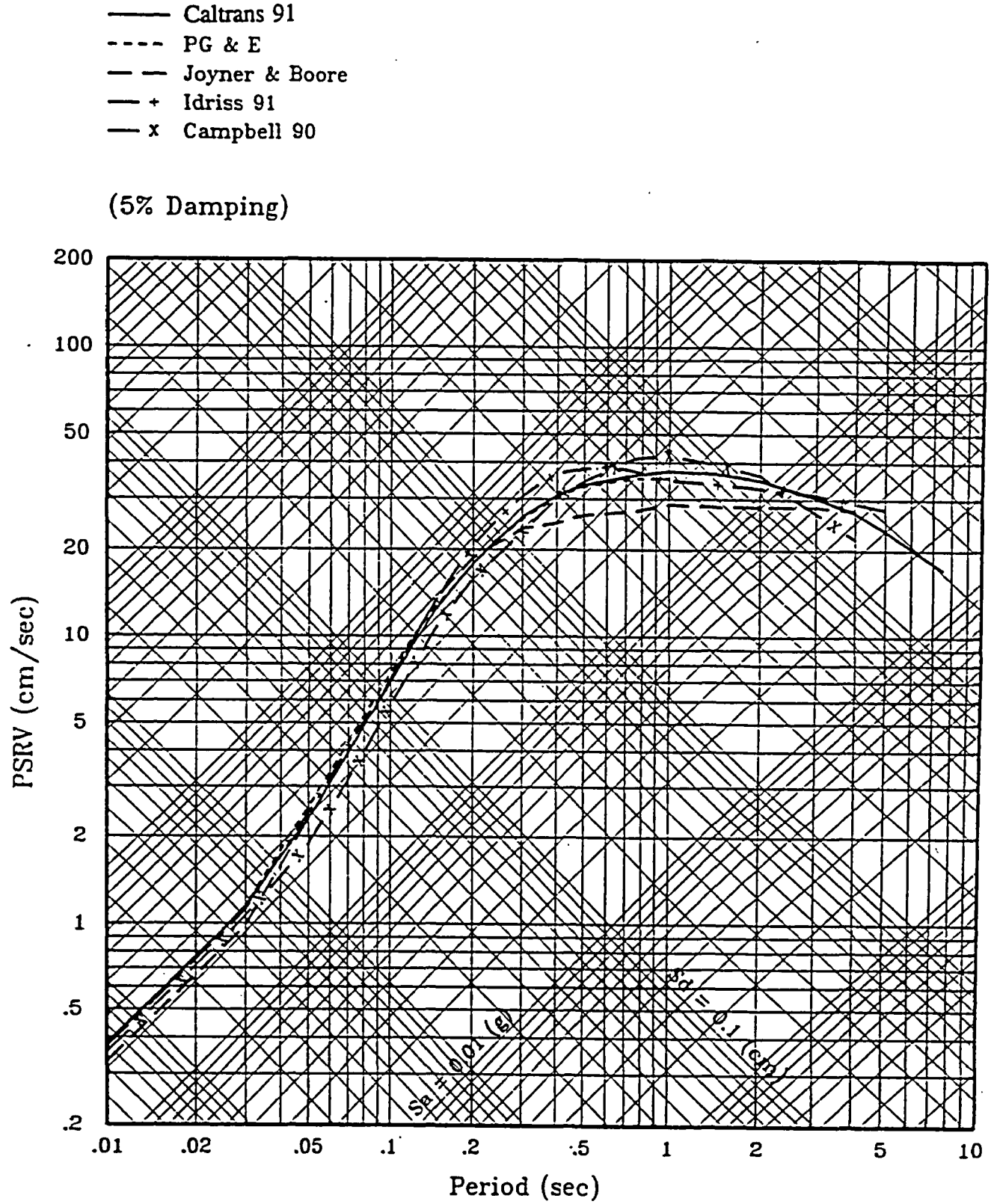

Figure C-9 Comparison of median spectra for M 7¼ at R=20 km computed using several recent relationships.

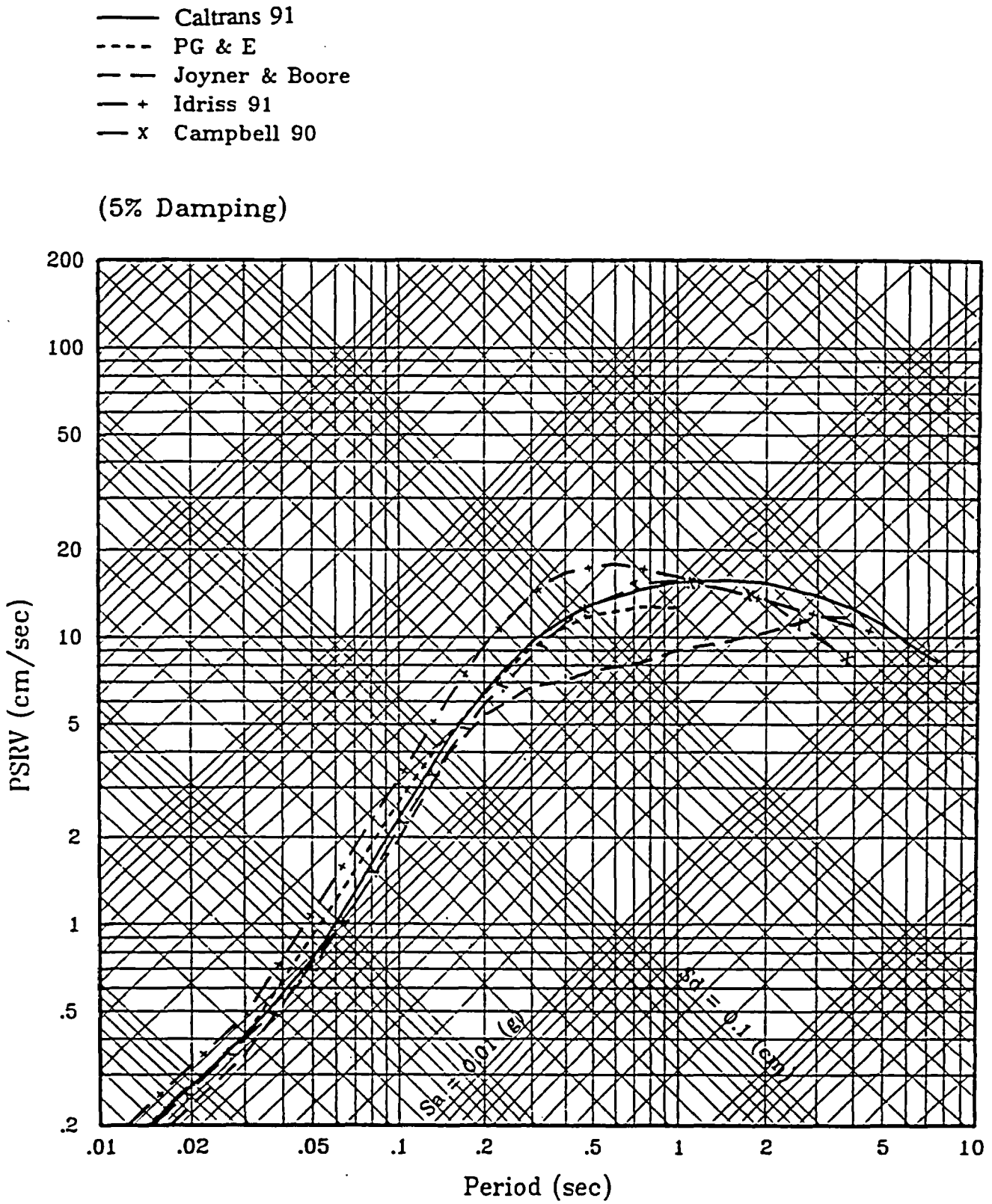

Figure C-10 Comparison of median spectra for M 7¼ at R=50 km computed using several recent relationships.

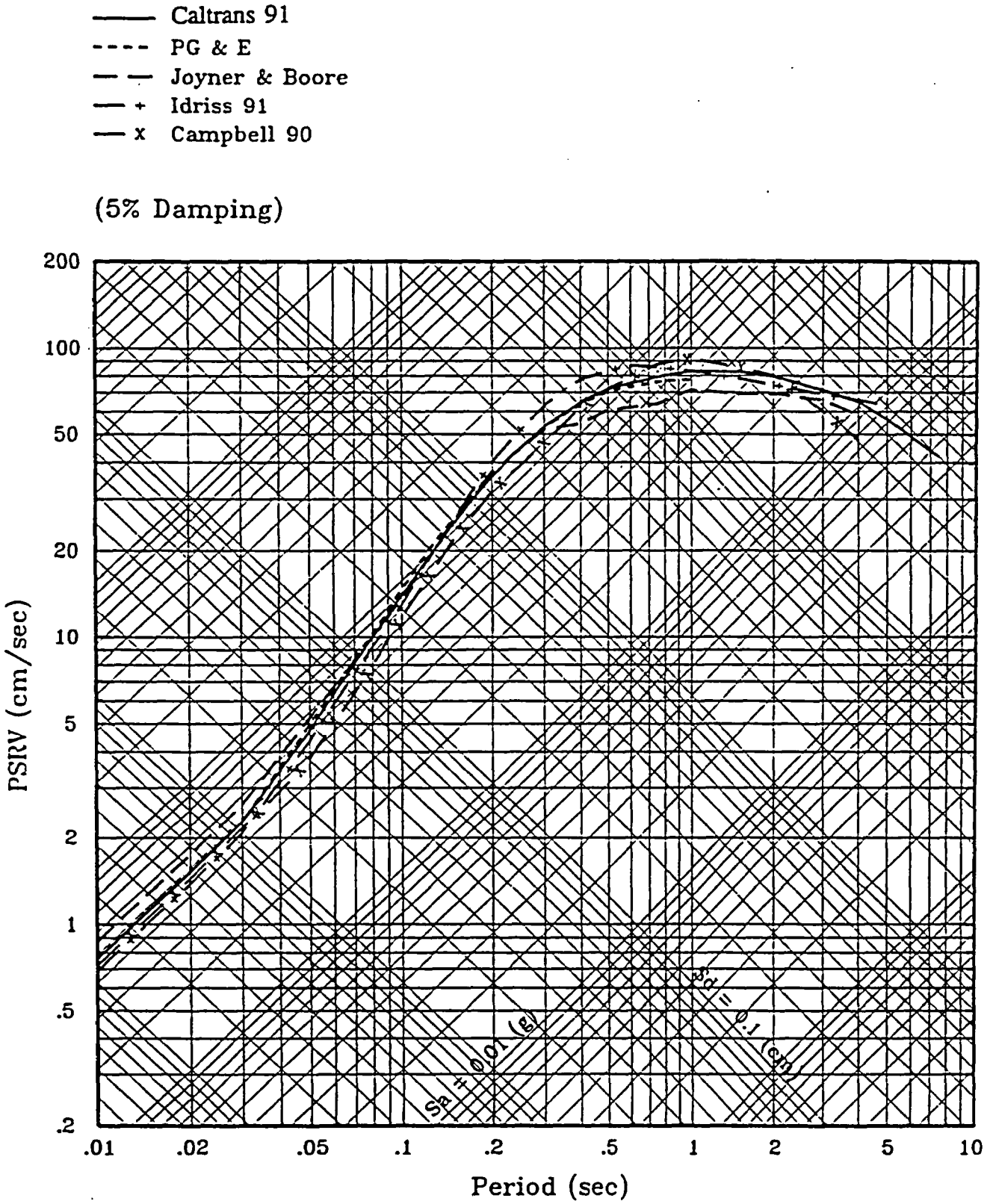

Figure C-11 Comparison of median spectra for M 8 at R=10 km computed using several recent relationships.

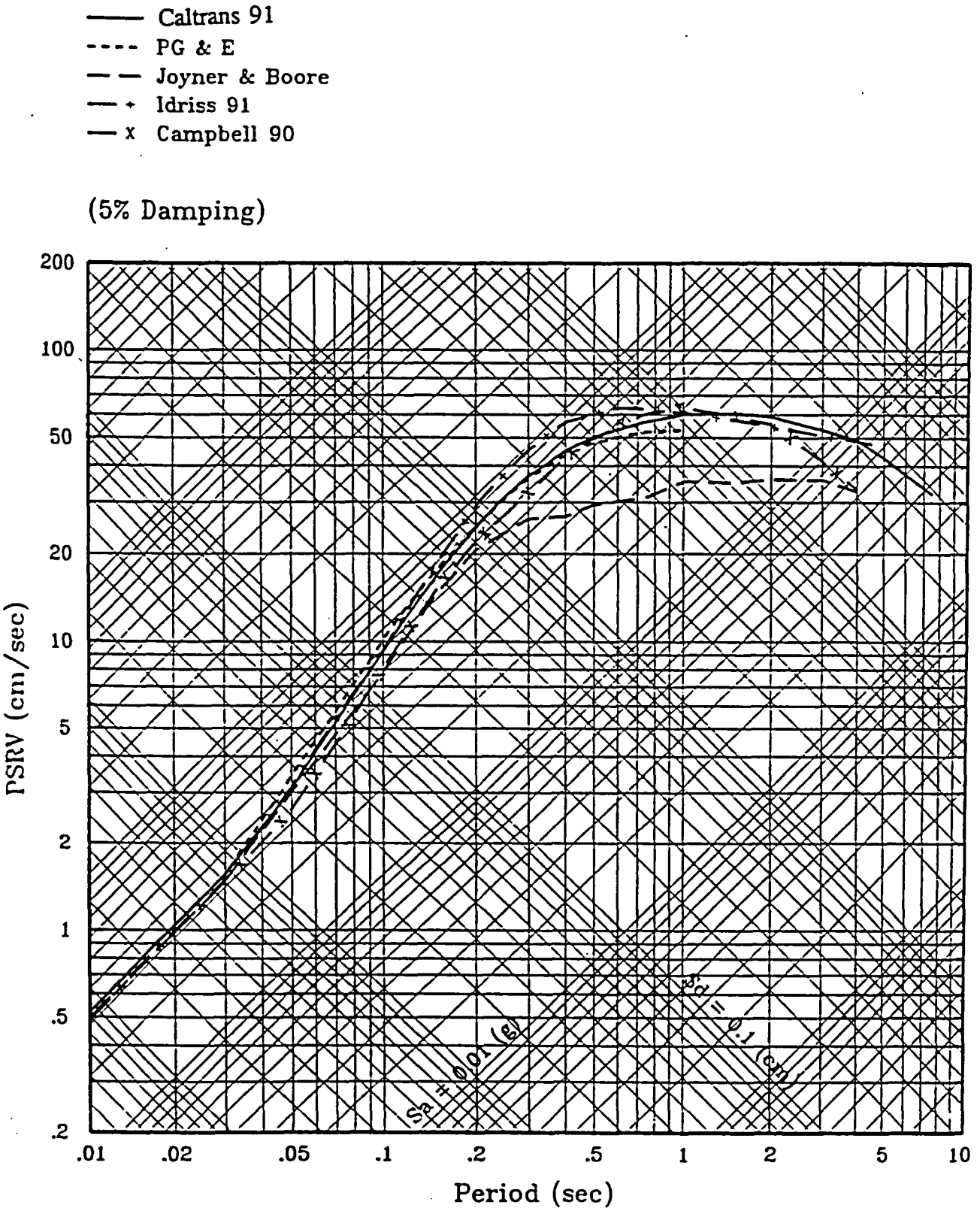

Figure C-12 Comparison of median spectra for M 8 at R=20 km computed using several recent relationships.

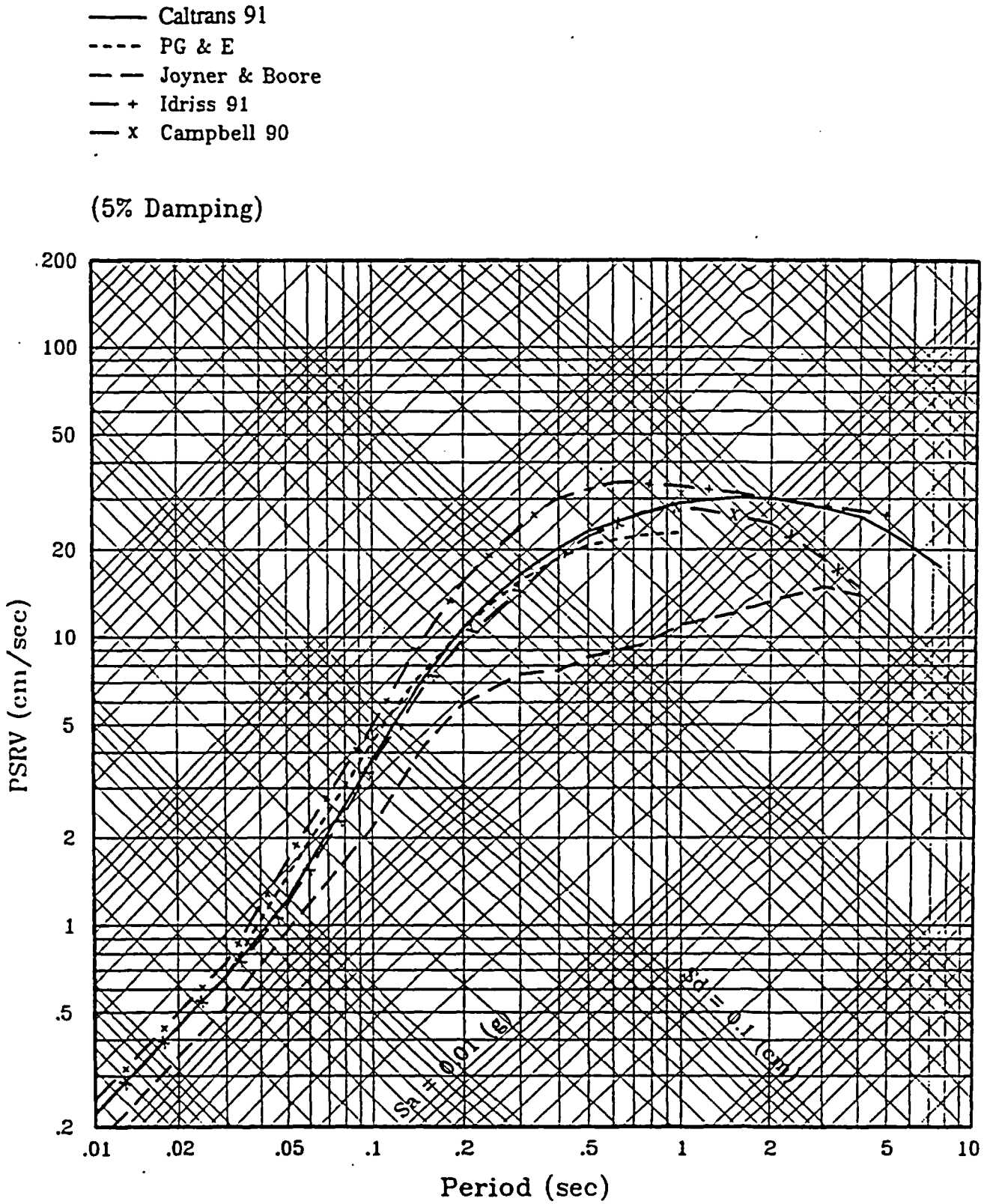

Figure C-13 Comparison of median spectra for M 8 at R=50 km computed using several recent relationships.

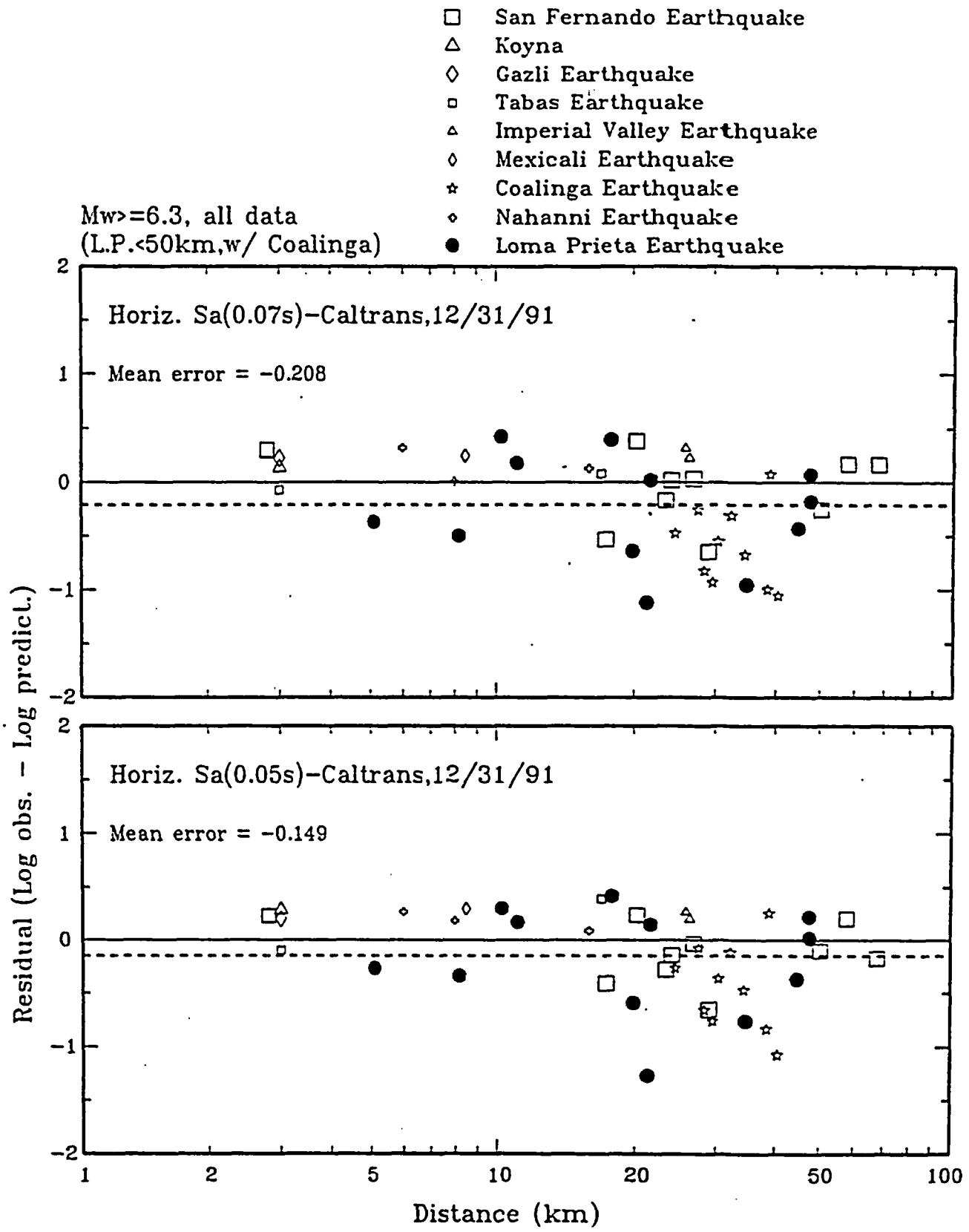

Figure C-14 Residuals of horizontal response acceleration (difference between natural logarithms of the observed and predicted values) versus distance for rock recordings from M ≥ 6.3 earthquakes.

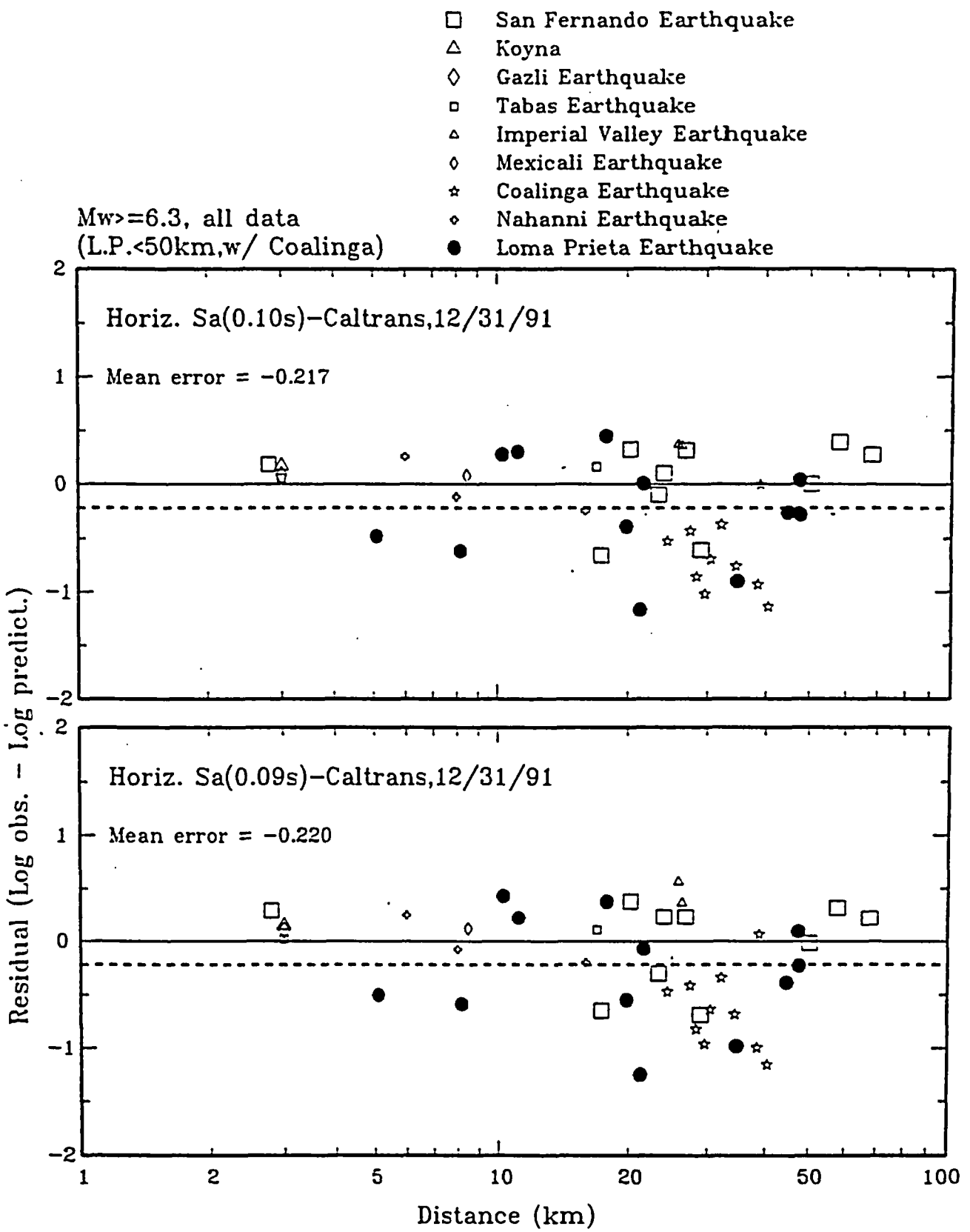

Figure C-15 Residuals of horizontal response acceleration (difference between natural logarithms of the observed and predicted values) versus distance for rock recordings from M ≥ 6.3 earthquakes.

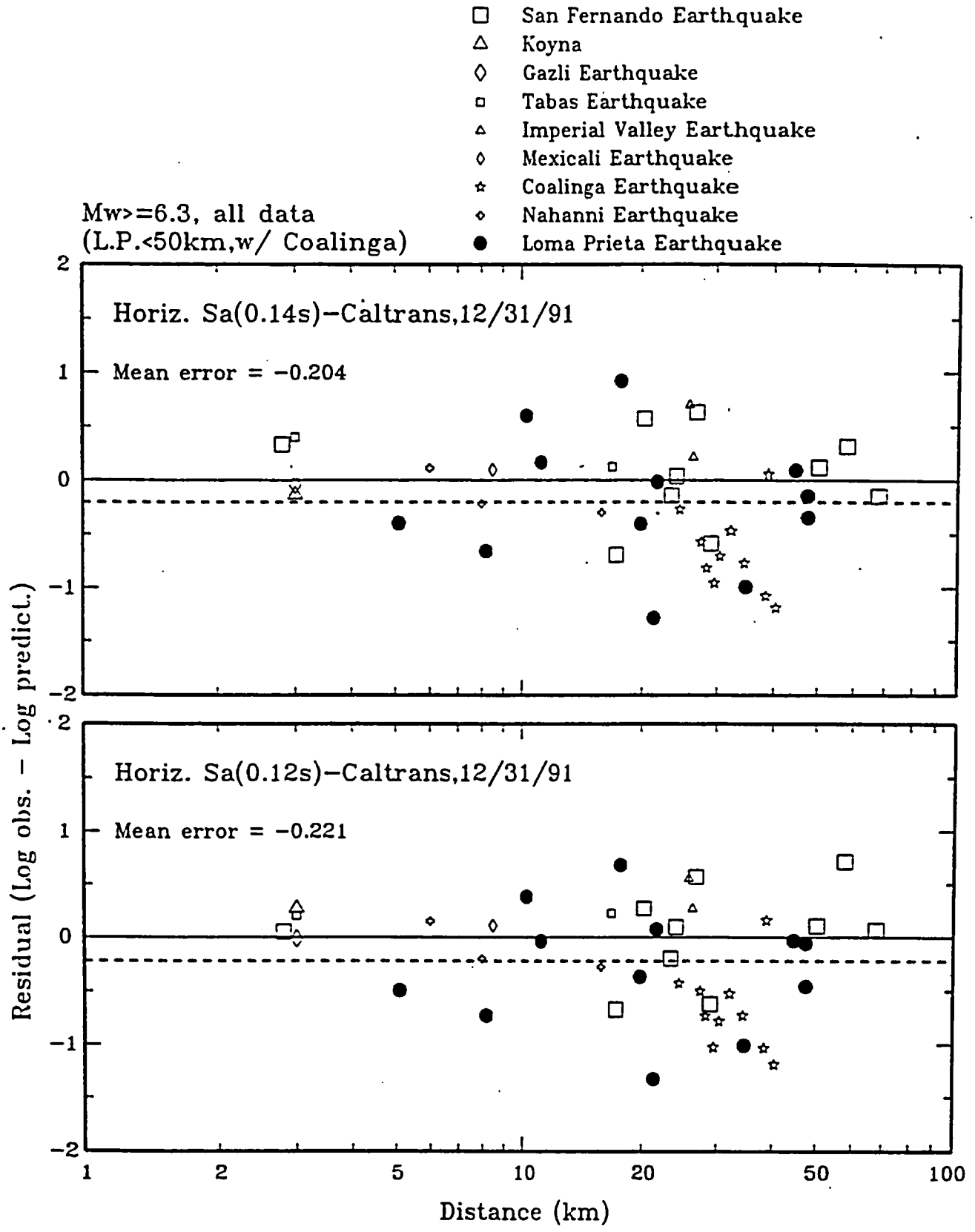

Figure C-16 Residuals of horizontal response acceleration (difference between natural logarithms of the observed and predicted values) versus distance for rock recordings from M ≥ 6.3 earthquakes.

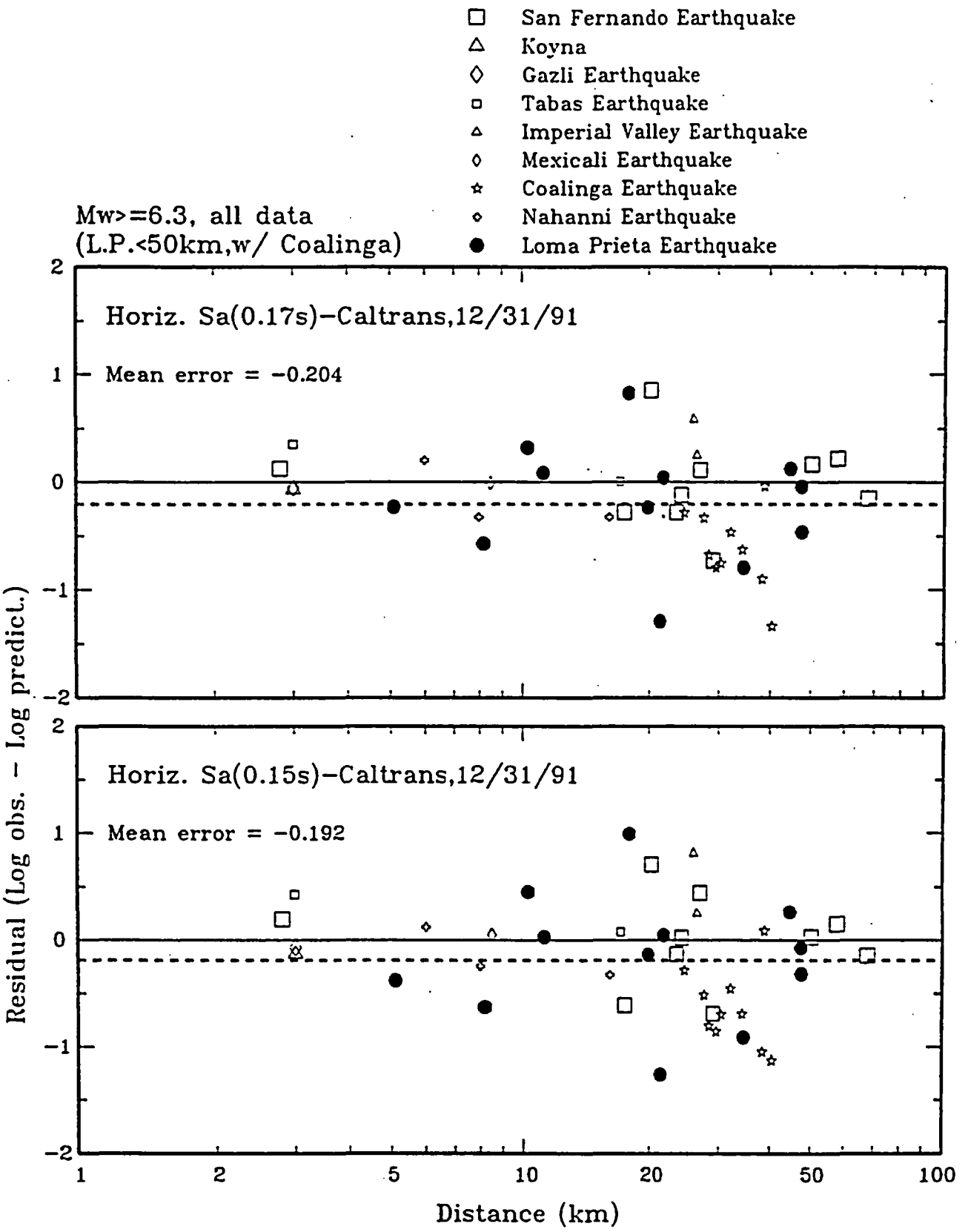

Figure C-17 Residuals of horizontal response acceleration (difference between natural logarithms of the observed and predicted values) versus distance for rock recordings from M ≥ 6.3 earthquakes.

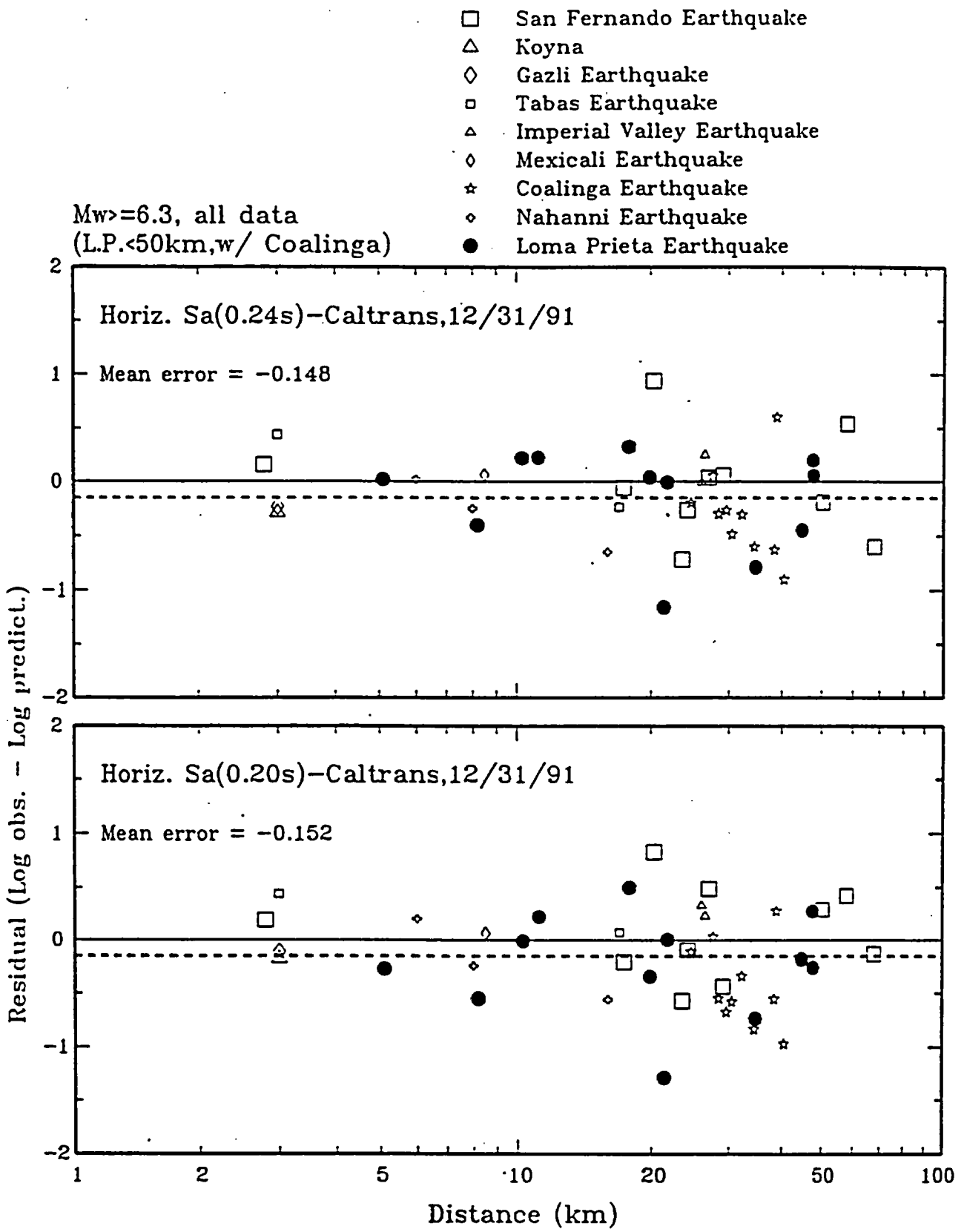

Figure C-18 Residuals of horizontal response acceleration (difference between natural logarithms of the observed and predicted values) versus distance for rock recordings from M ≥ 6.3 earthquakes.

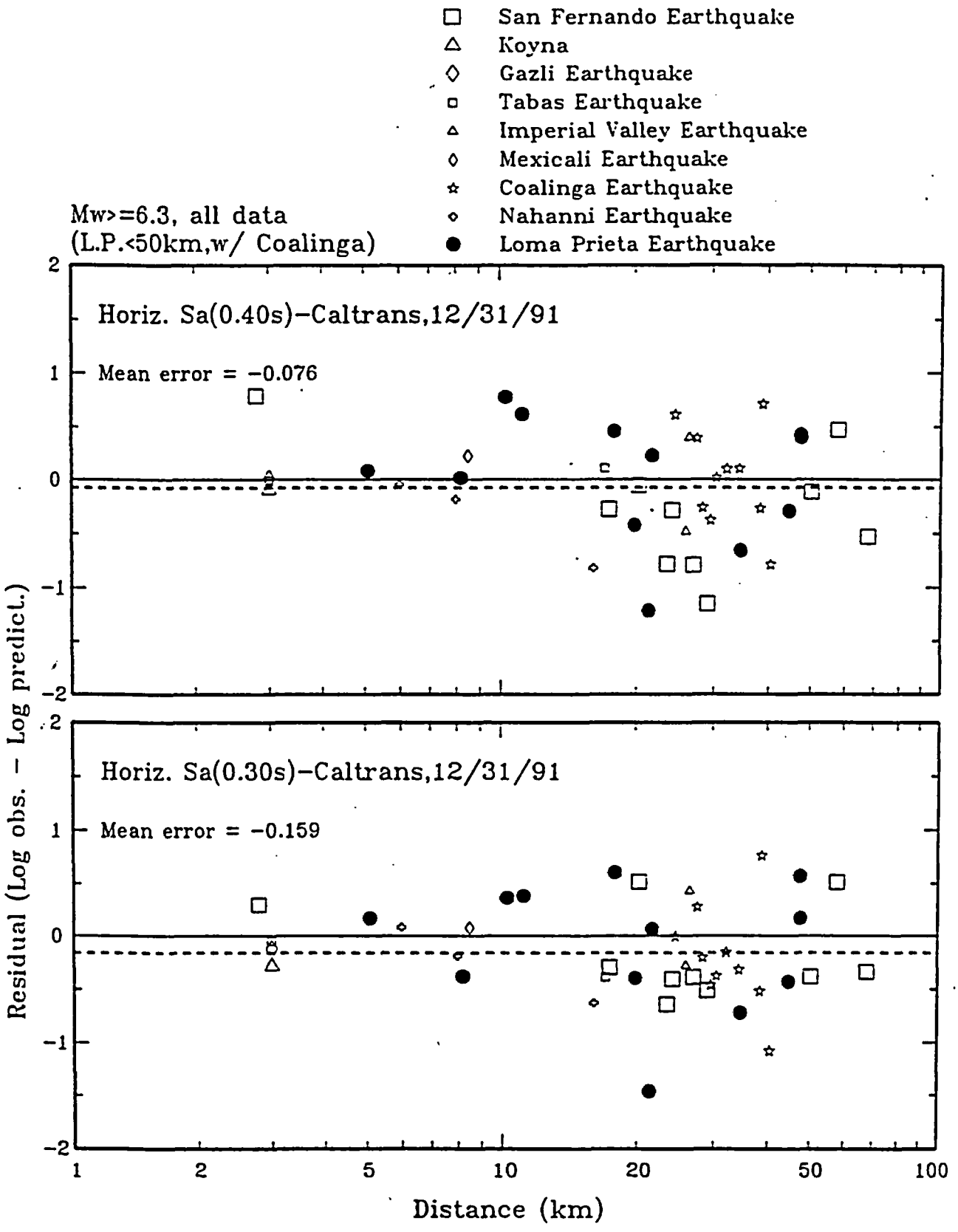

Figure C-19 Residuals of horizontal response acceleration (difference between natural logarithms of the observed and predicted values) versus distance for rock recordings from M ≥ 6.3 earthquakes.

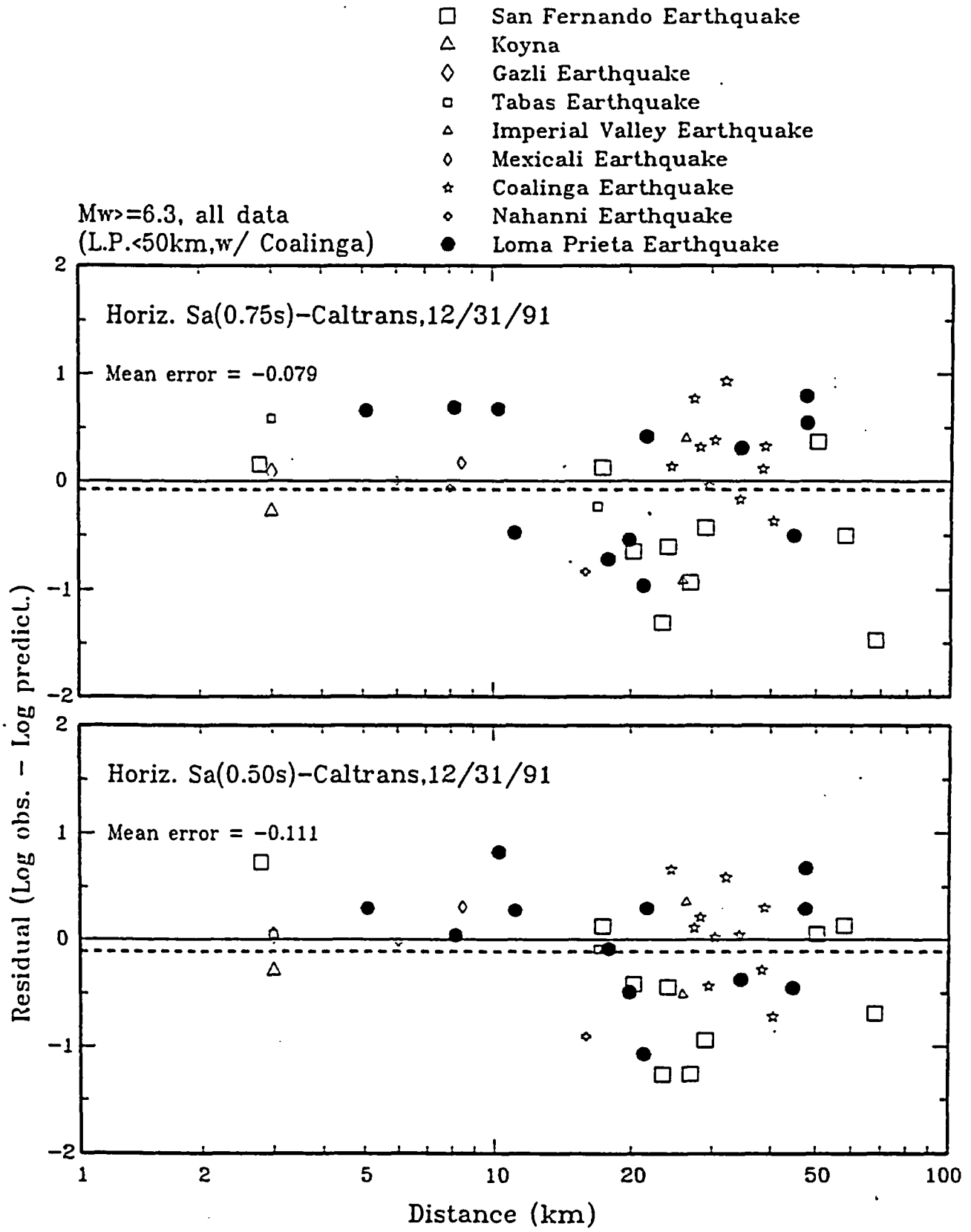

Figure C-20 Residuals of horizontal response acceleration (difference between natural logarithms of the observed and predicted values) versus distance for rock recordings from M ≥ 6.3 earthquakes.

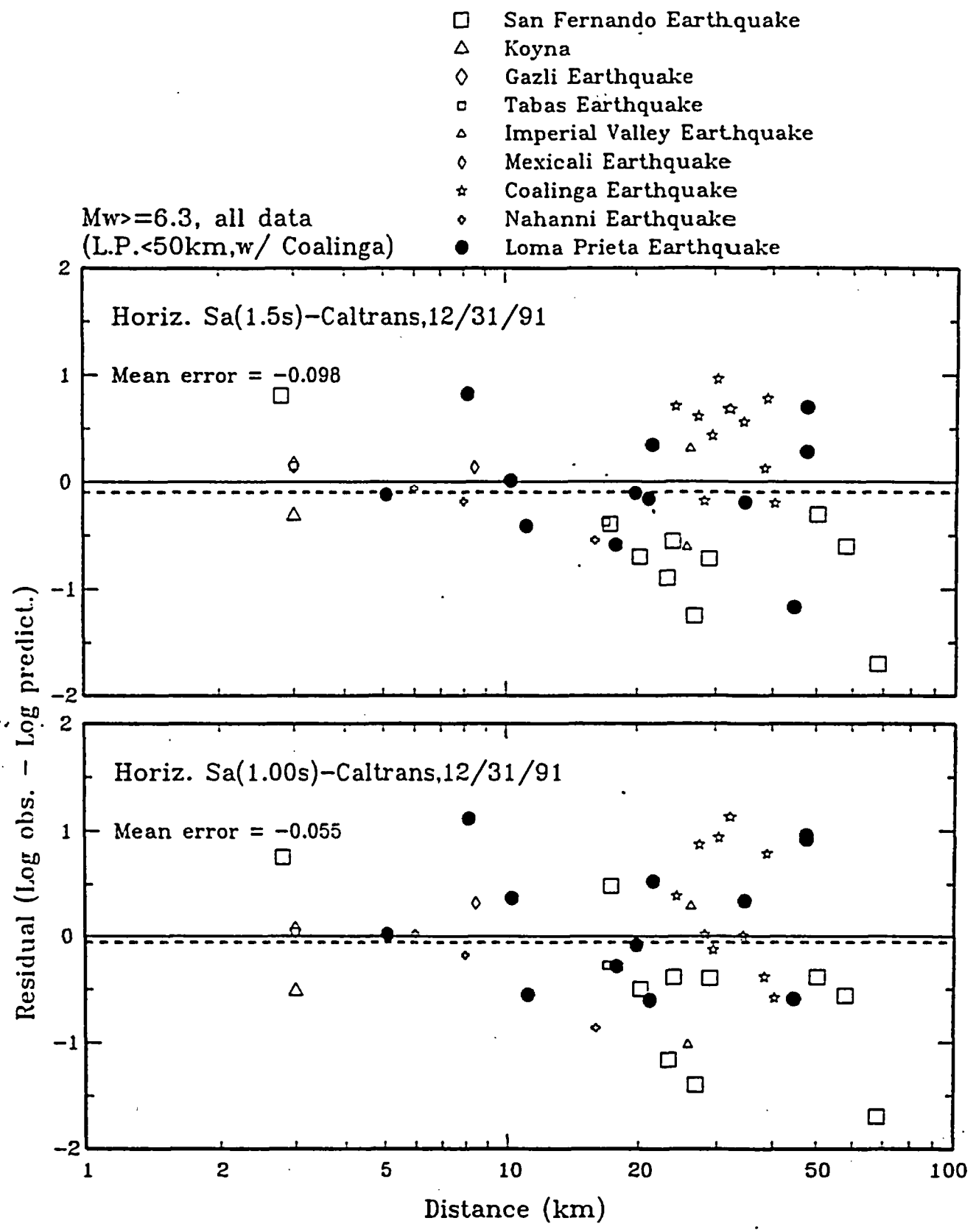

Figure C-21 Residuals of horizontal response acceleration (difference between natural logarithms of the observed and predicted values) versus distance for rock recordings from M ≥ 6.3 earthquakes.

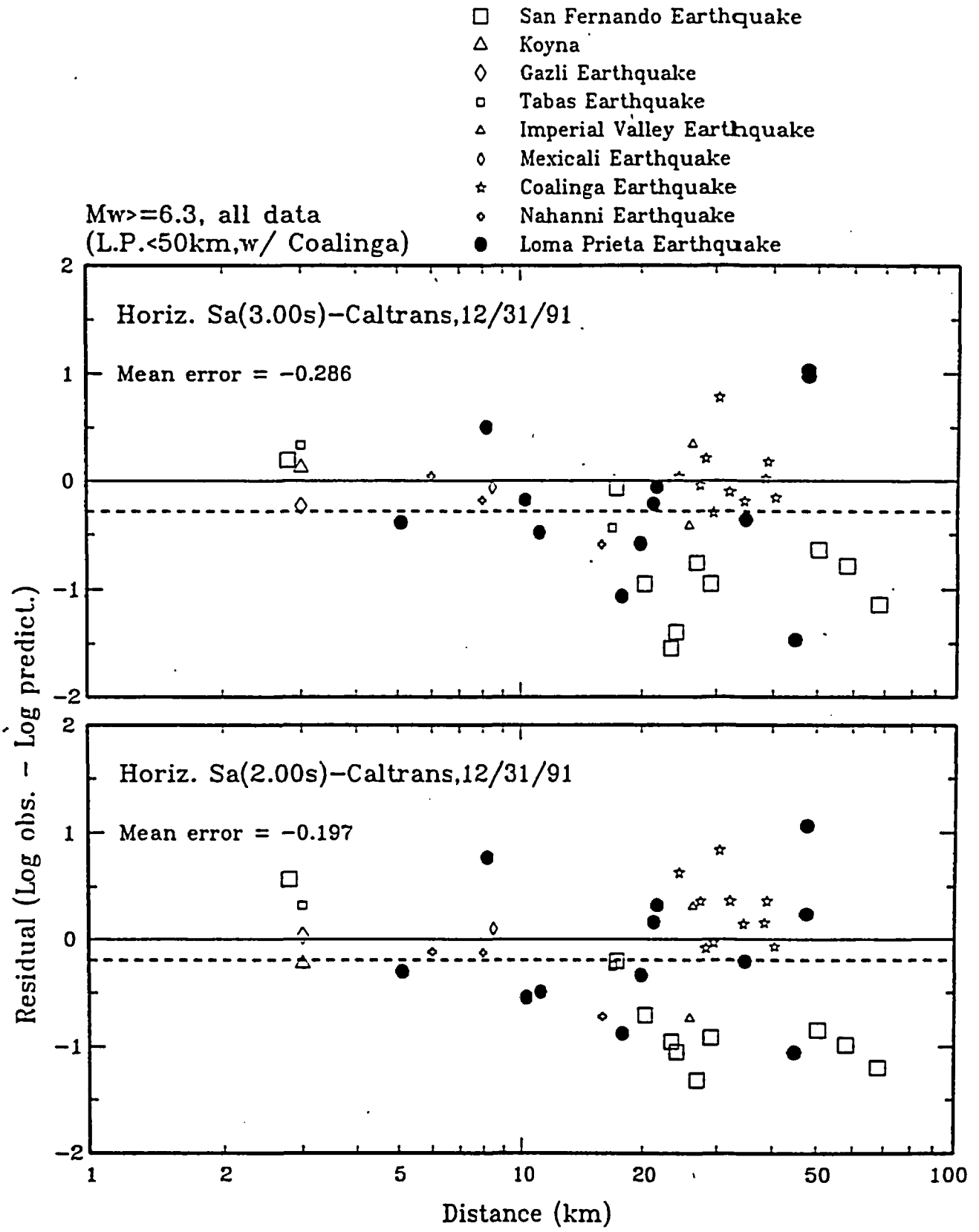

Figure C-22 Residuals of horizontal response acceleration (difference between natural logarithms of the observed and predicted values) versus distance for rock recordings from M ≥ 6.3 earthquakes.

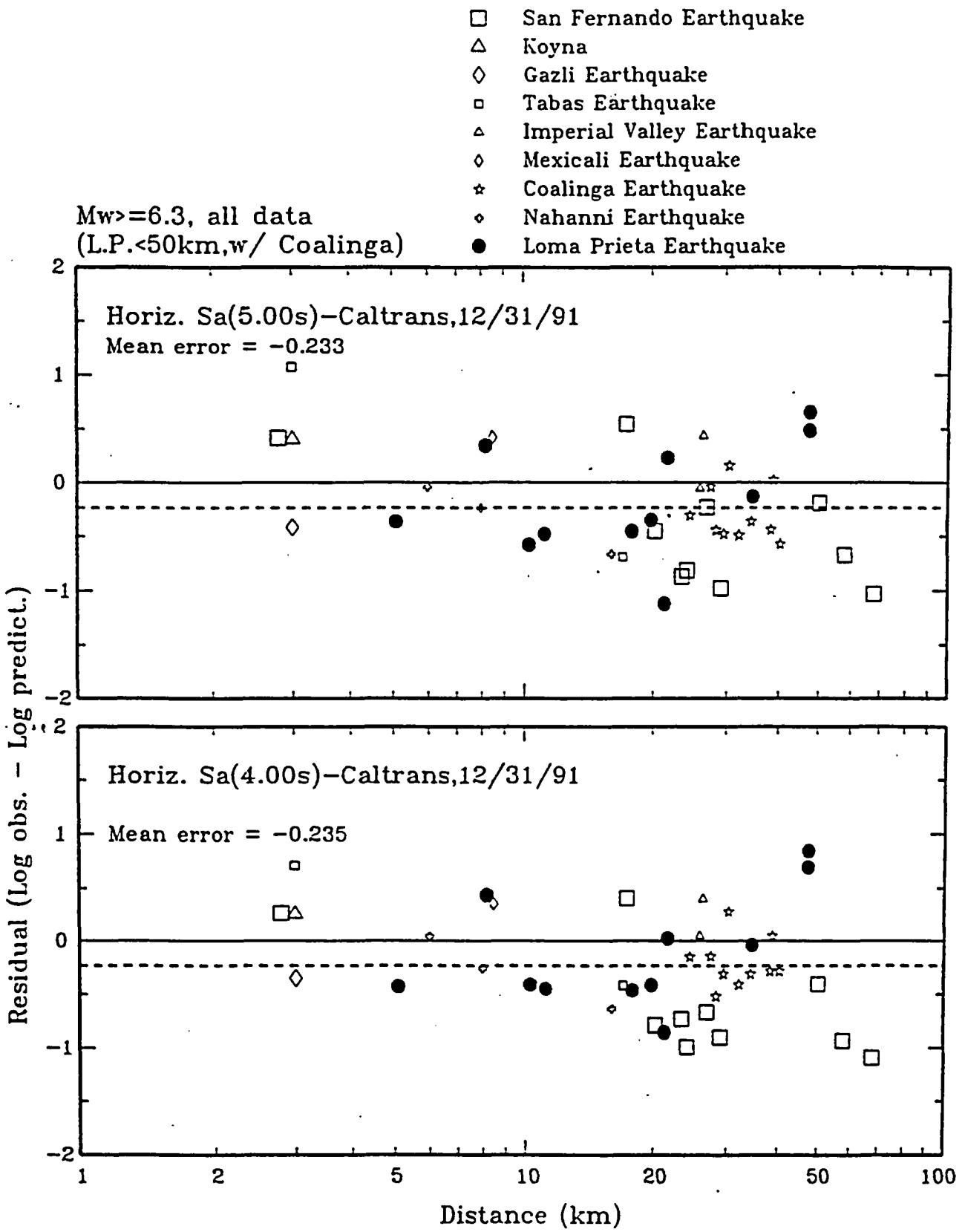

Figure C-23 Residuals of horizontal response acceleration (difference between natural logarithms of the observed and predicted values) versus distance for rock recordings from M ≥ 6.3 earthquakes.

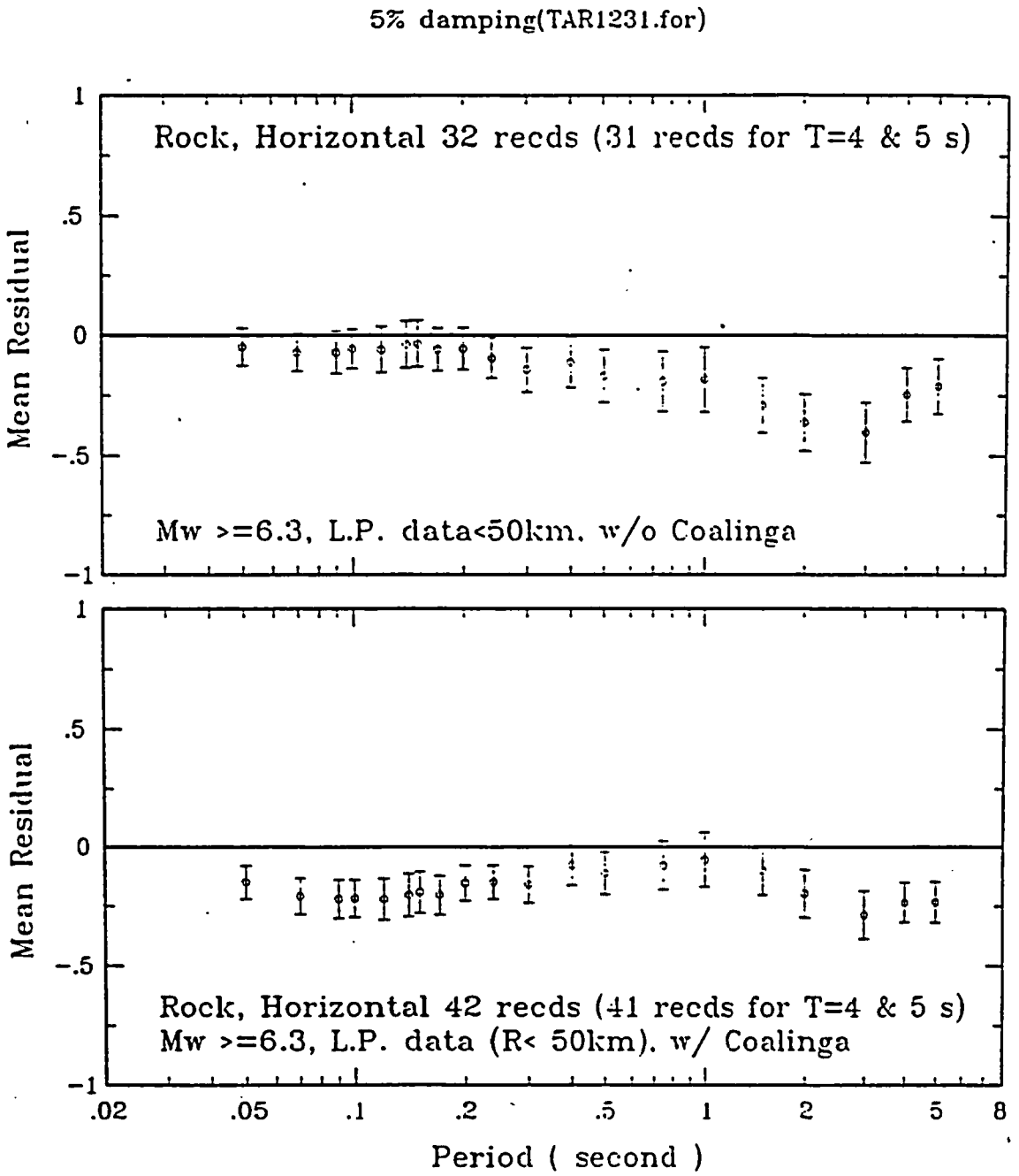

Figure C-24 Mean residuals of horizontal response acceleration (difference between natural logarithms of the observed and predicted values) for rock recordings from M ≥ 6.3 earthquakes.

GEOMATRIX

APPENDIX D

ALTERNATE ATTENUATION RELATIONSHIPS FOR SHALLOW CRUSTAL EARTHQUAKES USED IN PROBABILISTIC SEISMIC HAZARD ANALYSES

APPENDIX D

ALTERNATE ATTENUATION RELATIONSHIPS FOR SHALLOW CRUSTAL EARTHQUAKES USED IN PROBABILISTIC SEISMIC HAZARD ANALYSES

ATTENUATION EQUATIONS BY I. IDRISS (1991)

Equation for horizontal peak ground acceleration (pga) and for spectral accelerations derived for rock sites:

$$Ln(Y) = [\alpha_0 + \exp(\alpha_1 + \alpha_2 * M)] + [\beta_0 - \exp(\beta_1 + \beta_2 * M)] * Ln(R + 20) + 0.2 * F + \varepsilon$$

in which:

- Y = ground motion parameter (peak horizontal acceleration in g's or spectral acceleration in g's).
- M = earthquake magnitude; for M less than 6, local magnitude M_L, is used and for M equal to or greater than 6, surface wave magnitude, M_S, is used. Thus, in essence, M represents moment magnitude, M_W.
- R = closest distance to the source in km; however, for small magnitude earthquakes (say M less than 6), the hypocentral distance is used.
- F = style of faulting factor; F = 0 for a strike slip fault; and F = 1 for a reverse fault.
- ϵ = standard error term.

Ln is the natural logarithm and exp is the exponential function. The coefficients α_0, α_1, α_2, β_0, β_1, and β_2 and the standard error term ϵ are determined from appropriate regression analyses.

These coefficients together with values of ϵ are listed in the Table D-1 for $M \leq 6$ and Table D-2 for $M > 6$.

TABLE D-1

FOR MAGNITUDE M ≤ 6

$\beta_1 = 1.602$ and $\beta_2 = -0.142$

Period sec	α_0	α_1	α_2	β_0	Standard Error Term, ϵ
pga	-0.150	2.261	-0.083	0	1.39 - 0.14*M
0.03	-0.150	2.261	–0.083	0	1.39 - 0.14*M
0.05	-0.278	2.365	-0.092	0.066	1.39 - 0.14*M
0.075	-0.308	2.334	-0.081	0.070	1.39 - 0.14*M
0.10	-0.318	2.319	-0.075	0.072	1.42 - 0.14*M
0.11	-0.328	2.294	-0.070	0.073	1.42 - 0.14*M
0.13	-0.338	2.255	-0.062	0.075	1.42 - 0.14*M
0.15	-0.348	2.219	-0.055	0.076	1.42 - 0.14*M
0.20	-0.358	2.146	-0.042	0.078	1.42 - 0.14*M
0.25	-0.429	2.073	-0.030	0.080	1.42 - 0.14*M
0.30	-0.486	2.010	-0.020	0.082	1.44 - 0.14*M
0.35	-0.535	1.977	-0.016	0.087	1.44 - 0.14*M
0.4	-0.577	1.912	-0.009	0.092	1.44 - 0.14*M
0.5	-0.648	1.818	0.003	0.099	1.46 - 0.14*M
0.6	-0.705	1.704	0.017	0.105	1.46 - 0.14*M1
0.7	-0.754	1.644	0.022	0.111	1.48 - 0.14*M
0.8	-0.796	1.593	0.025	0.115	1.48 - 0.14*M
0.9	-0.834	1.482	0.039	0.119	1.48 - 0.14*M
1	-0.867	1.432	0.043	0.123	1.48 - 0.14*M
1.5	-0.970	1.072	0.084	0.136	1.48 - 0.14*M
2	-1.046	0.762	0.121	0.146	1.52 - 0.14*M
3	-1.143	0.194	0.191	0.160	1.52 - 0.14*M
4	-1.177	-0.466	0.280	0.169	1.52 - 0.14*M
5	-1.214	-1.361	0.410	0.177	1.52 - 0.14*M

Note: For M5, the standard error term is assumed to be equal to that calculated for M = 5.

TABLE D-2

FOR MAGNITUDE M > 6

$\beta_1 = 2.475$ and $\beta_2 = -0.286$

Period sec	α_0	α_1	α_2	β_0	Standard Error Term, ϵ, M < 7¼	Standard Error Term, ϵ, M > 7¼
pga	-0.050	3.477	-0.284	0	1.39 - 0.14*M	0.38
0.03	-0.050	3.477	-0.284	0	1.39 - 0.14*M	0.38
0.05	-0.278	3.426	0.269	0.066	1.39 - 0.14*M	0.38
0.075	-0.308	3.359	-0.252	0.070	1.39 - 0.14*M	0.38
0.10	-0.318	3.327	-0.243	0.072	1.42 - 0.14*M	0.41
0.11	-0.328	3.289	-0.236	0.073	1.42 - 0.14*M	0.41
0.13	-0.338	3.233	-0.225	0.075	1.42 - 0.14*M	0.41
0.15	-0.348	3.185	-0.216	0.076	1.42 - 0.14*M	0.41
0.20	-0.358	3.100	-0.201	0.078	1.42 - 0.14*M	0.41
0.25	-0.429	3.034	-0.190	0.080	1.42 - 0.14*M	0.41
0.30	-0.486	2.982	-0.182	0.082	1.44 - 0.14*M	0.43
0.35	-0.535	2.943	-0.177	0.087	1.44 - 0.14*M	0.43
0.4	-0.577	2.906	-0.173	0.092	1.44 - 0.14*M	0.43
0.5	-0.648	2.850	-0.169	0.099	1.46 - 0.14*M	0.45
0.6	-0.705	2.803	-0.166	0.105	1.46 - 0.14*M1	0.45
0.7	-0.754	2.765	-0.165	0.111	1.48 - 0.14*M	0.47
0.8	-0.796	2.728	-0.164	0.115	1.48 - 0.14*M	0.47
0.9	-0.834	2.694	-0.163	0.119	1.48 - 0.14*M	0.47
1	-0.867	2.662	-0.162	0.123	1.48 - 0.14*M	0.47
1.5	-0.970	2.536	-0.160	0.136	1.48 - 0.14*M	0.47
2	-1.046	2.447	-0.160	0.146	1.52 - 0.14*M	0.51
3	-1.143	2.295	-0.159	0.160	1.52 - 0.14*M	0.51
4	-1.177	2.169	-0.159	0.169	1.52 - 0.14*M	0.51
5	-1.214	2.042	-0.157	0.177	1.52 - 0.14*M	0.51

Presented below are the modifications by N.A. Abrahamson, of the soil site relationships developed by Campbell (1991). Abrahamson reanalyzed the Campbell (1990) data set supplemented with Loma Prieta earthquake data to specialize Campbell's (1991) soil relationships to a condition of soft-rock.

MODIFIED CAMPBELL (1991) ATTENUATION RELATIONSHIPS

Sites include records in Buildings (a building effect is estimated and removed)

$$\ln PGA(g) = a_1 + bM + d \ln(R + c_1 \exp(c_2 M)) + eF$$

$$\ln \left(\frac{PSV(cm/s)}{PGA(g)}\right) = a_2 + f_1 \tanh(f_2(M+f_3)) + g_1 (\tanh(g_2 D) + t_s \ln\left(\frac{T}{T_O}\right) H(T-T_O)$$

D = Depth to basement (km)
R = Closest distance
F = Style-of-faulting factor (0 = SS, 1 = RV)
$H(T_O-T)$ = Heaviside function (o for $T<T_O$, 1 for $T>T_O$)

PGA (soil or soft-rock)

a_1 = -2.245
b = 1.605
c1 = 0.536
c2 = 0.612
d = -2.623
e = 0.297
σ = 0.38 (for M≥6.2)

Note: For M<6.2, magnitude-dependent sigma values developed by Geomatrix (see Appendix C) is used in analyses.

SPECTRAL SHAPE (soft-rock)

t_s = 0.183
T_o = 1.0 second

PERIOD	a2	b	c1	c2	d	e	f1	f2	f3	g1
0.04	1.8255	1.605	0.536	0.61	-2.623	0.297	0	0.54	-4.7	0
0.05	2.1247	1.605	0.536	0.61	-2.623	0.297	0	0.54	-4.7	0
0.075	2.7543	1.605	0.536	0.61	-2.623	0.297	0	0.54	-4.7	0
0.1	3.2622	1.605	0.536	0.61	-2.623	0.297	0	0.54	-4.7	0
0.15	3.8816	1.605	0.536	0.61	-2.623	0.297	0	0.54	-4.7	0
0.2	4.2328	1.605	0.536	0.61	-2.623	0.297	0	0.54	-4.7	0
0.3	4.5908	1.605	0.536	0.61	-2.623	0.297	0	0.54	-4.7	0
0.4	4.3826	1.605	0.536	0.61	-2.623	0.297	0.5455	0.54	-4.7	0
0.5	4.3099	1.605	0.536	0.61	-2.623	0.297	0.7971	0.54	-4.7	0
0.75	4.0296	1.605	0.536	0.61	-2.623	0.297	1.3249	0.54	-4.7	0
1	3.6478	1.605	0.536	0.61	-2.623	0.297	1.7670	0.54	-4.7	0.07
1.5	2.958	1.605	0.536	0.61	-2.623	0.297	2.4637	0.54	-4.7	0.25
2	2.5215	1.605	0.536	0.61	-2.623	0.297	2.8752	0.54	-4.7	0.30
3	1.8284	1.605	0.536	0.61	-2.623	0.297	3.2880	0.54	-4.7	0.62
4	0.988	1.605	0.536	0.61	-2.623	0.297	3.799	0.54	-4.7	0.97
5	0.233	1.605	0.536	0.61	-2.623	0.297	4.287	0.54	-4.7	1.27
7.5	-0.164	1.605	0.536	0.61	-2.623	0.297	4.408	0.54	-4.7	1.27
10	-0.561	1.605	0.536	0.61	-2.623	0.297	4.627	0.54	-4.7	1.27

Note: $g_2 = 0.8$

REFERENCES

Campbell, K.W., 1990, Reanalysis of strong-motion recordings; empirical prediction of near-source ground motion for the Diablo Canyon Power Plant site, San Luis Obispo County, California: Report to the U.S. Nuclear Regulatory Commission.

Campbell, K.W., 1991, A random-effects analysis of near-source ground motion for the Diablo Canyon Power Plant site, San Luis Obispo County, California, California: Dames & Moore, Evergreen, Colorado, Prepared for Lawrence Livermore National Laboratory.

Idriss, I.M., 1991, Selection of earthquake ground motions at rock sites: Report Prepared for the Structures Division, Building and Fire Research Laboratory, National Institute of Standards and Technology, Department of Civil Engineering, University of California, Davis, September.

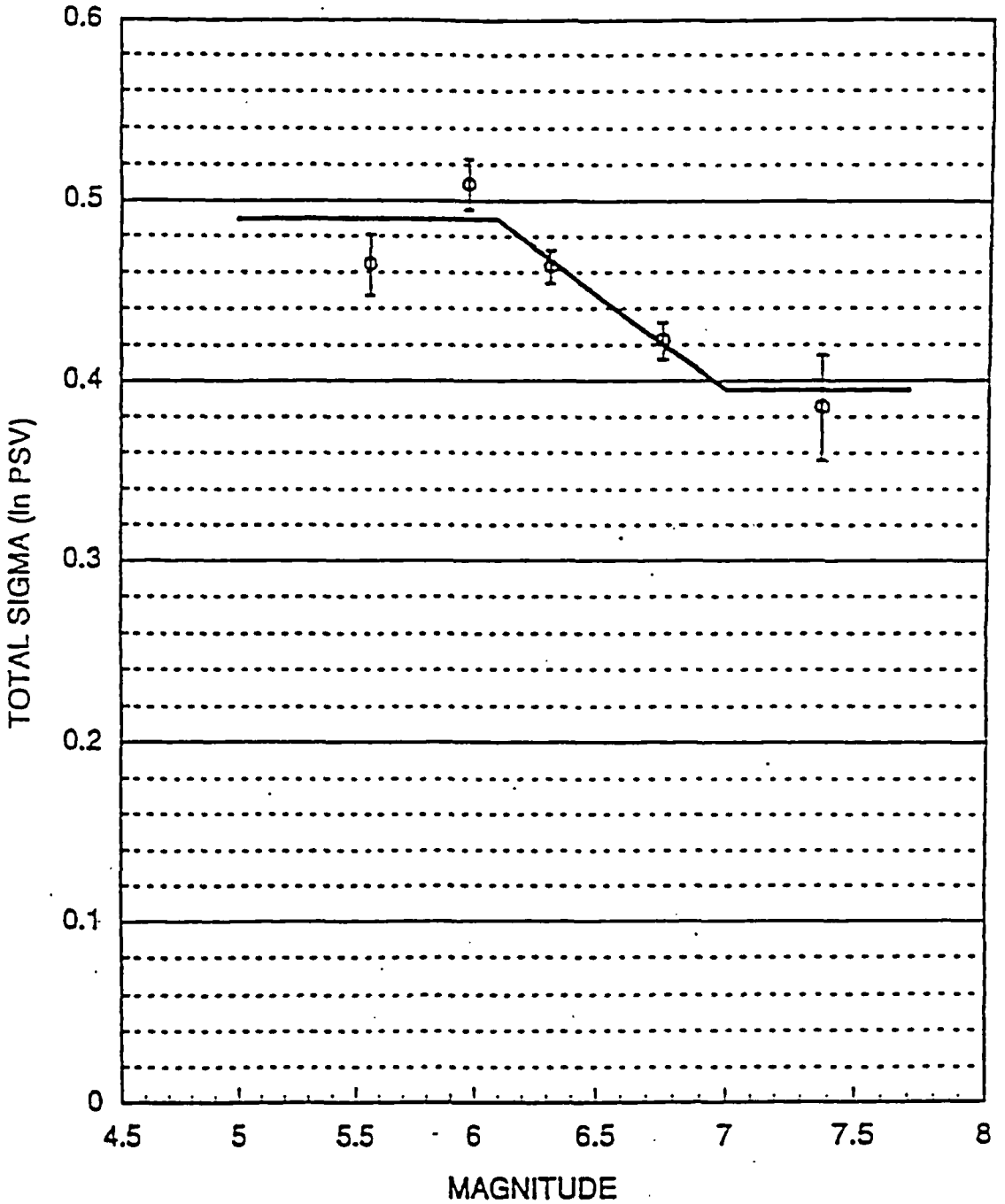

Figure D-1 Magnitude dependent dispersion of the natural log horizontal spectral velocity of Campbell (1990) data set - reanalysis (averaged over all periods: 0.04 sec to 4.0 sec)

APPENDIX E

EXAMINATION OF FAULT-NORMAL AND FAULT-PARALLEL COMPONENTS OF EARTHQUAKE GROUND MOTIONS

APPENDIX E

EXAMINATION OF FAULT-NORMAL AND FAULT-PARALLEL COMPONENTS OF EARTHQUAKE GROUND MOTIONS

The estimation procedure of ground motion at a specific site from earthquakes of a specified magnitude commonly uses the empirically derived predictive relationships for ground motion parameters (see Section 3). The principal parameters included in these predictive equations are the earthquake magnitude, site condition, and distance to the fault. The fault-receiver geometry and the instrument orientation are not explicitly included.

However, an important aspect in characterizing the ground motion from a nearby, large earthquake is that the partitioning of the S wave energy, which produces most of the strong shaking in the near-source region, into a specified orientation is largely determined by the fault-receiver geometry and the faulting mechanism. An extreme condition is a site located near the end of a vertical strike-slip fault in the forward rupture direction, such as the station Gilroy #6 of the 1984 Morgan Hill earthquake (Figure E-1). The level of ground shaking (as indicated by the 5% damped response spectra in Figure E-1) at this site is higher on the fault-normal component than on the fault-parallel component. In such cases, the orientation of the horizontal components relative to the fault strike direction has a significant effect on the horizontal ground motions.

The study presented in this appendix documents and quantifies the difference in the level of ground shaking of the two individual horizontal components in terms of the ratio of 5%-damped response spectra between the fault normal component and the geometrical mean of the fault normal and fault paralell components. Mean correction factors are developed that can be used to modify existing attenuation relations to account for the above-mentioned effects from future earthquakes. Both empirical recordings and synthetic seismograms are used in this analysis.

In this study, the orientation of the two horizontal components are conveniently chosen as components parallel and normal to the fault strike direction. Some justifications for adopting this orientation are given here. The important factor that defines the fault-receiver geometry in most seismological literature is the angle between rupture direction and source-to-receiver direction. However, it is not practical to incorporate the rupture direct as the reference limitation in determining the scaling factor, because location and rupture direction for future earthquakes is not known exactly. On the other hand, fault strike is a more convenient choice since fault strike of potential earthquakes may be more reliably defined. In addition, there are events where the angle between fault strike and the gross rupture direction is more or less constant, such as the earthquakes being examined in this study. For these events, the distinction between the two definitions of fault-receiver geometry is not important.

E.1 RESULTS FROM EMPIRICAL RECORDINGS

Data

We selected four well-recorded California earthquakes (Table E-1): the 1979 Coyote Lake, the 1979 Imperial Valley, 1984 Morgan Hill, and the 1989 Loma Prieta earthquakes. All four earthquakes have roughly strike-slip faulting on a nearly vertical fault plane, except the 1989 Loma Prieta. The available strong motion data are recorded by USGS, CDMG, and U.C. Santa Cruz strong motion instruments. Because it is also interesting to know the maximum distance beyond which the geometrical effect is not significant, strong motions recorded at a distance up to 100 km from the fault surface are used in our study. The two recorded horizontal components are vectorially rotated into components parallel and normal to the fault strike direction before response spectra are computed.

Spectral Ratios

To examine how the ratio varies with distance, spectral ratios at five selected periods from the 1979 Imperial Valley earthquake recorded along the El Centro Array are plotted in Figure E-2. These ratios are roughly symmetrical to the fault trace, except at El Centro 4 where high values are observed. The ratio decreases as the recording site moves away from the fault trace, and small or no amplification on the fault normal component for sites beyond 10 km distance.

The ratios for each event are shown in Figures E-3 through E-9, for stations whose closest distance to fault is less than and greater than 10 km, separately (no stations at distances greater than 10 km are included for the 1979 Coyote Lake event). The arithmatic mean of the log average in the 2 to 5 sec period range is listed in Table E-2, which shows a maximum value of 1.3, i.e., the observed fault normal component in this period range is, on the average, at most 30% higher than the geometrical mean of the two components. The results also suggest that, in the 2 to 5 sec period range, the geometrical effect is stronger at close distances (< 10 km) than at farther distances (> 10 km).

It should be noted that the above observations are from a data set that samples only a small portion of the seismic sources that occur in California. To confirm that the results obtained in this study are not heavily biased due to undersampling, we also used numerical simulations as described in Section E.2.

E.2 RESULTS FROM SYNTHETIC SEISMOGRAMS

Numerical Simulations

The numerical simulations can provide theoretical data at distances, magnitudes, and geometries not well represented in the selected empirical data base. For example, large ($M_w > 7$) strike-slip events are completely absent in the selected data base so for large magnitudes, numerical simulations are needed to estimate the value of the scale factor.

Numerical simulations based on theoretical Green's functions have been successfully used to model long period ($T > 2$ seconds) ground motions using simple source and velocity models

(e.g., Spudich and Archuleta, 1987). The fundamental method used in this study is based on the representation theorem (Aki and Richards, 1980) which describes the ground motion from a point source as the convolution of a Green's function with a source function. The Green's function is the impulse response of the earth's crust to a point source dislocation. The source function describes the slip time history at a point on the fault. The total ground motion from an extended source is found by discritizing the fault and summing the motions from each fault element (assumming linear site response).

There are several alternative numerical methods for computing the Green's functions; however, we have found that the specification of the seismic source parameters is more important than the particular numerical procedure used to compute the Green's functions. We use the method described by Bouchon (1981) and modified by Hermann. This method computes the Green's function for a 1-D velocity model that includes both near-field and far-field terms and surface waves as well as body waves. This method is appropriate for use in predicting strong ground motions at both small and large distance.

Some of the key input source parameters for the prediction of ground motion are the slip distribution (asperity size and depth), the rise-time, and the rake angle. In order to use the method for predicting ground motions of future earthquakes, it is important to use simple descriptions of the seismic source.

The slip distribution is developed based on a model of the 2-D wave number spectrum of the slip (EPRI, in press). An example of the slip for a magnitude 7.0 event is shown in Figure E-10. This procedure leads to asperities.

The rise-time is computed by first specifying a source time function. In particular, the slip-velocity time function is modeled as a combination of the commonly used rectangle and triangle functions. The first half of the velocity source function is modeled by a rectangle and the second half is modeled by a triangle. The result is that the slip at a point on the fault starts abruptly, but stops more smoothly. The duration of the source functions (e.g., rise-time) is given by the quotient of the slip over the slip-velocity and varies along the fault.

For this study, the 1-D crustal model developed by Wald et al. (1991) for the Loma Prieta earthquake is used. This model is listed in Table E-3. The velocity model represents a rock site condition.

Magnitudes of hypothetical earthquakes are 6.5, 7.0 and 8.0. A vertical strike-slip fault is used. The source parameters are listed in Table E-4. The ground motions are computed at distances of 1 to 30 km from the fault at 7 evenly spaced locations along the fault shown by the triangles in Figure E-11. Numerical simulations are computed for 10 different hypocenters for each magnitude shown by the stars in Figure E-11. The ratios of the fault normal to average horizontal response spectrum are plotted in Figures E-12 and E-13 for periods of 2 and 5 seconds, respectively.

As with the empirical data, the increase in the fault normal component at long periods is greatest at distances less than 10 km. The average fault normal to average horizontal ratios for distances less than 10 km are summarized in Table E-5.

E-3. RECOMMENDED MODIFICATIONS

Based on the empirical and numerical studies, the fault normal component is taken to be 20% larger than the average horizontal component in the period range of 2 to 5 seconds and at distances less than 10 km.

REFERENCES

Aki, K., and Richards, P.G., 1980, Quantitative Seismology Theory and Methods 1: W.H. Freeman and Company, 557 p.

Bouchon, M., 1981, A simple method to calculate Green's functions for elastic layered media: Bulletin of the Seismological Society of America, v. 71, p. 959-971.

Spudich, P., and Archuleta, R.J., 1987, Techniques for earthquake ground motion calculation with application to source parametenization of finite fault: Seismic Strong Motion Synthetics, Bolt, B.A., ed. Academic Press, p. 205-265.

Wald, D.J., Helmberger, D.V., and Heaton, T.H., 1991, Rupture model of the 1989 Loma Prieta earthquake from the inversion of strong motion and broadband teleseismic data: Bulletin of the Seismological Society of America, v. 81, p. 1540-1572.

TABLE E-1

STUDIED EARTHQUAKES

Earthquake	M_w	Strike (Degrees)	Dip (Degrees)
1979 Coyote	5.7	150.0	90.0
1979 Imperial Valley	6.6	140.0	90.0
1984 Morgan Hill	6.2	150.0	90.0
1989 Loma Prieta	6.9	130.0	70.0

TABLE E-2

ARITHMATIC MEAN OF THE
LOG AVERAGE RATIO BETWEEN 2 AND 5 SEC PERIOD

Event	1979 Coyote	1984 Morgan Hill	1979 Imperial	1989 Loma Prieta
Mw	5.7	6.2	6.5	6.9
Distance < 10 km	1.06	?	1.30	1.24
Distance > 10 km	?	1.20	0.95	1.12

? - Not Enough Recordings.

TABLE E-3

VELOCITY MODEL USED FOR NUMERICAL SIMULATIONS

Layer Thickness (km)	Vp (km/s)	Vs (km/s)	ρ (gm/cm3)
0.1	1.73	1.00	2.16
0.4	3.38	1.95	2.00
0.5	4.29	2.48	2.00
2.0	4.80	2.77	2.00
2.0	5.37	3.10	2.05
2.0	5.74	3.31	2.26
2.0	6.15	3.55	2.45
4.0	6.25	3.61	2.48
5.0	6.27	3.62	2.62
7.0	6.67	3.82	2.63
∞	8.0-	4.62	2.77

TABLE E-4

SOURCE PARAMETER VALUES

Magnitude	M = 6.5	M = 7.0	M = 8.0
Fault Length (km)	36	72	600
Fault Width (km)	9	15	15
Slip Velocity (cm/s)	100	100	100
Rake (deg)	5	5	5
Dip (deg)	5	85	85
Rake Variability (deg)	±40	±40	±40
Rupture Velocity (km/s)	2.5	2.5	2.5

TABLE E-5

RATIO OF FAULT NORMAL TO AVERAGE HORIZONTAL BASED ON NUMERICAL SIMULATIONS

Distance (km)	M = 6.5 to 7.0 FN/Ave (2 - 5 sec)
3	20 to 40%
10	3 to 30%
20	-5 to 20%

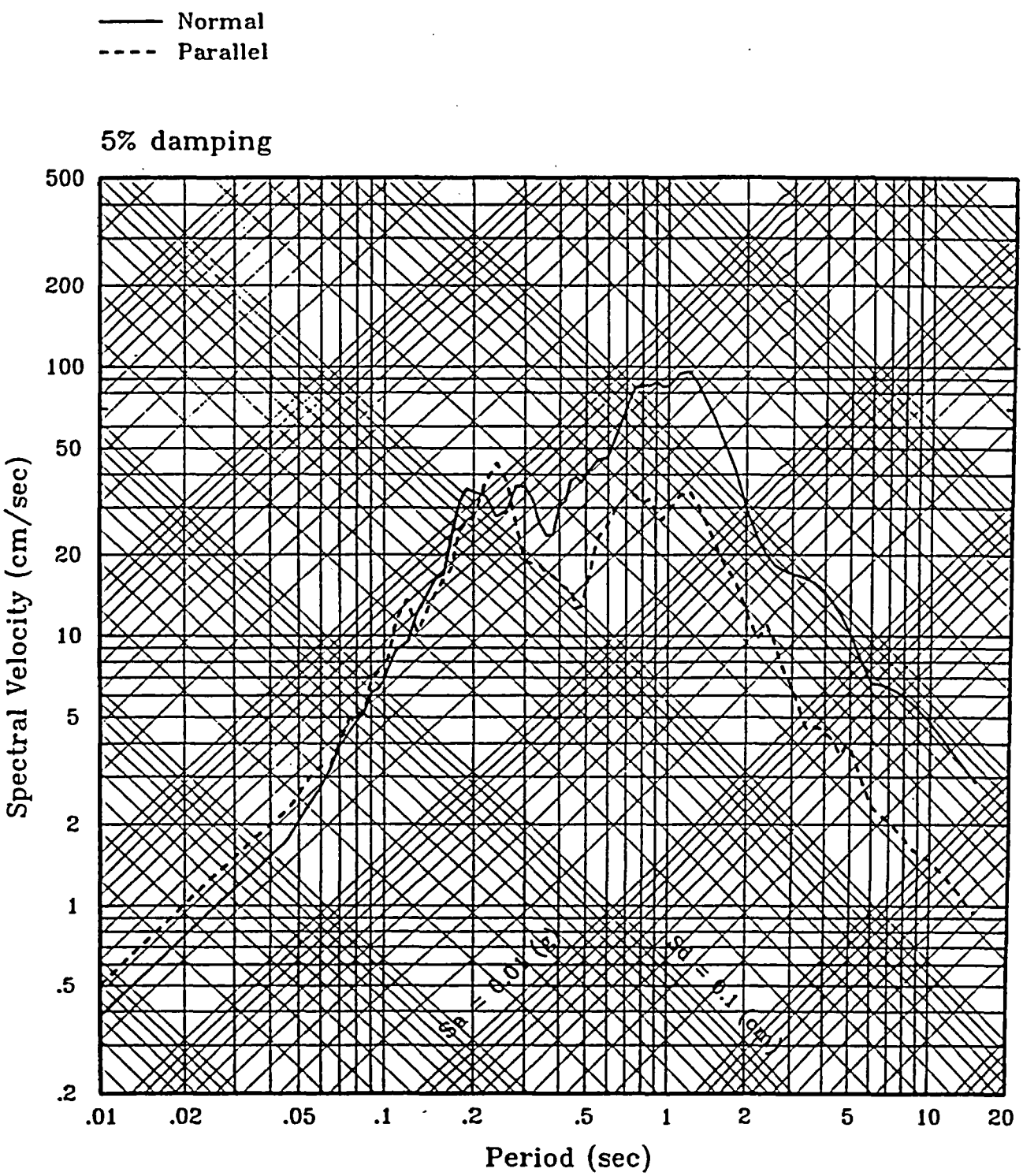

Morgan Hill, 1984, @st Gilroy Sta 6

Figure E-1

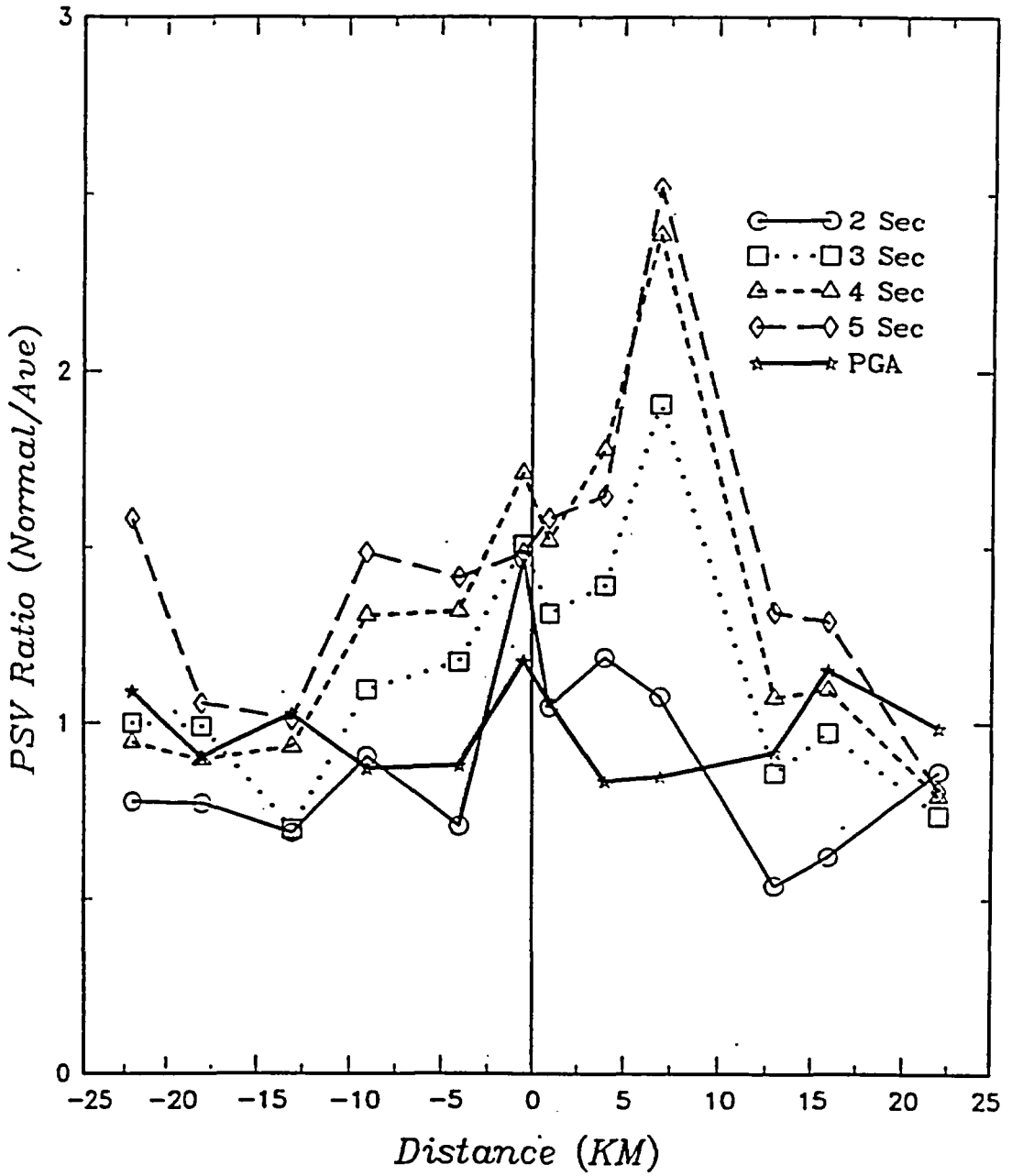

Imperial Valley, 1979

Figure E-2

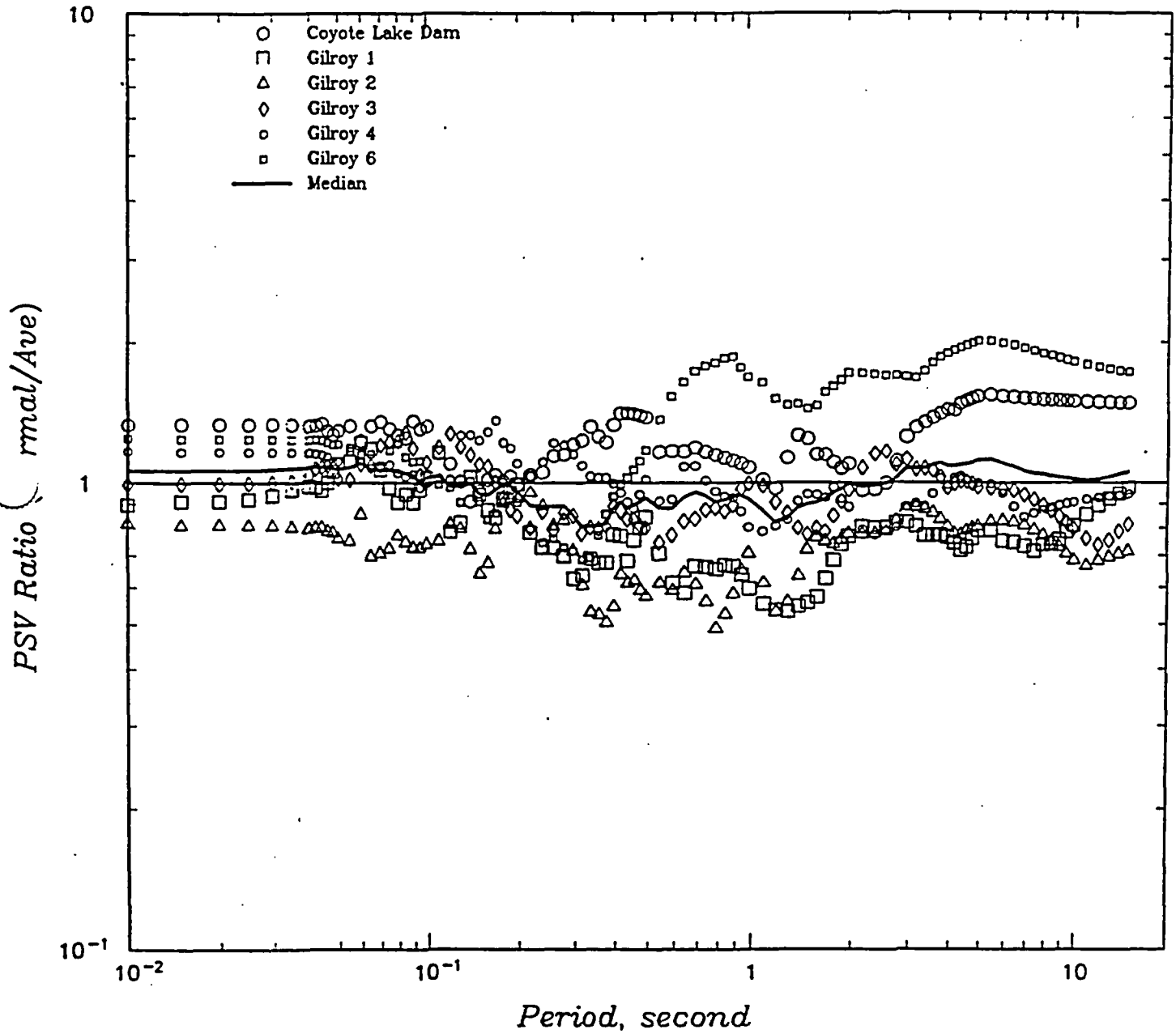

Coyote Lake. 1979; Distance to Fault Less Than 10 KM

Figure E-3

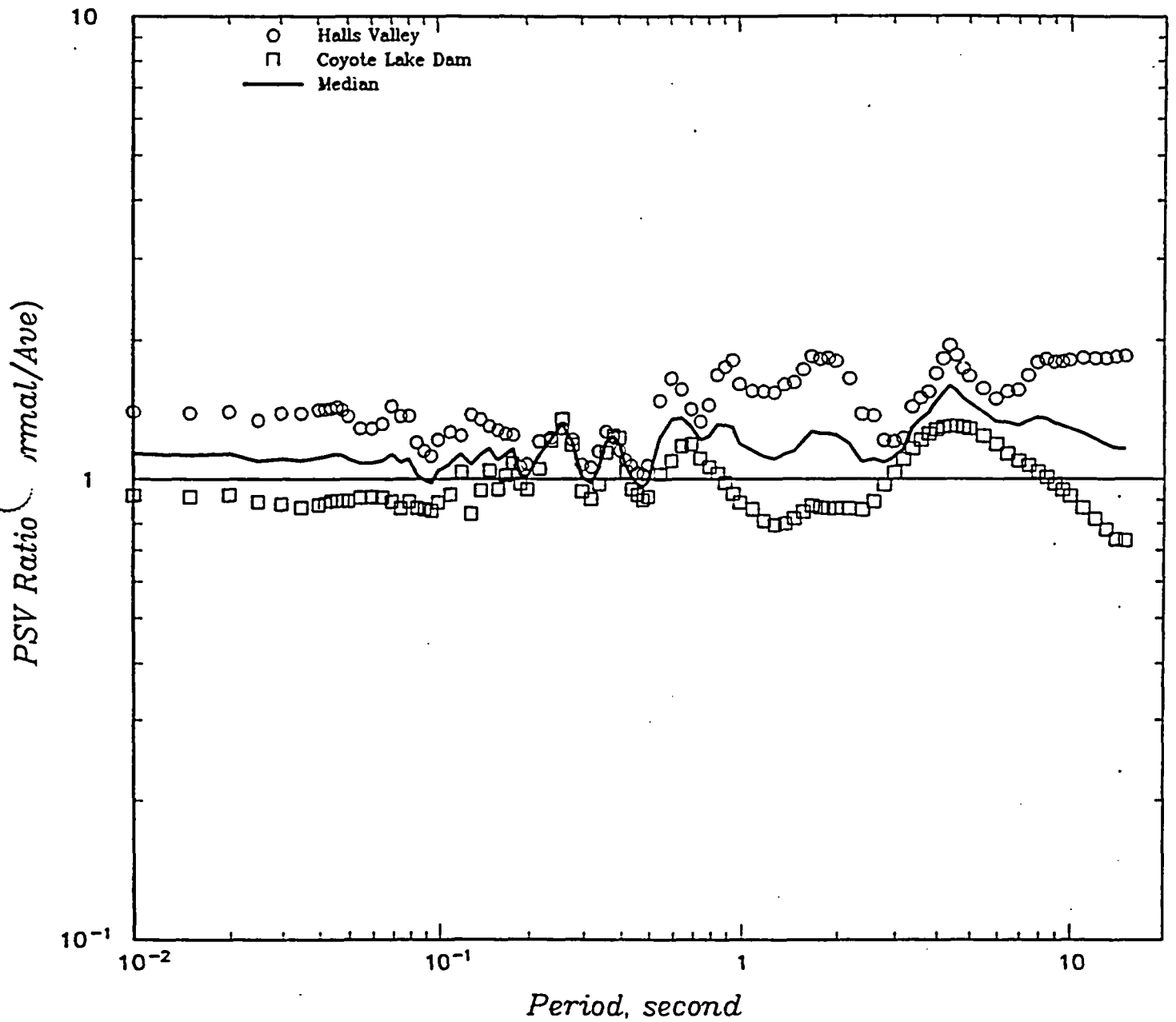

Morgan Hill, 1984; Distance to Fault Less Than 10 KM

Figure E-4

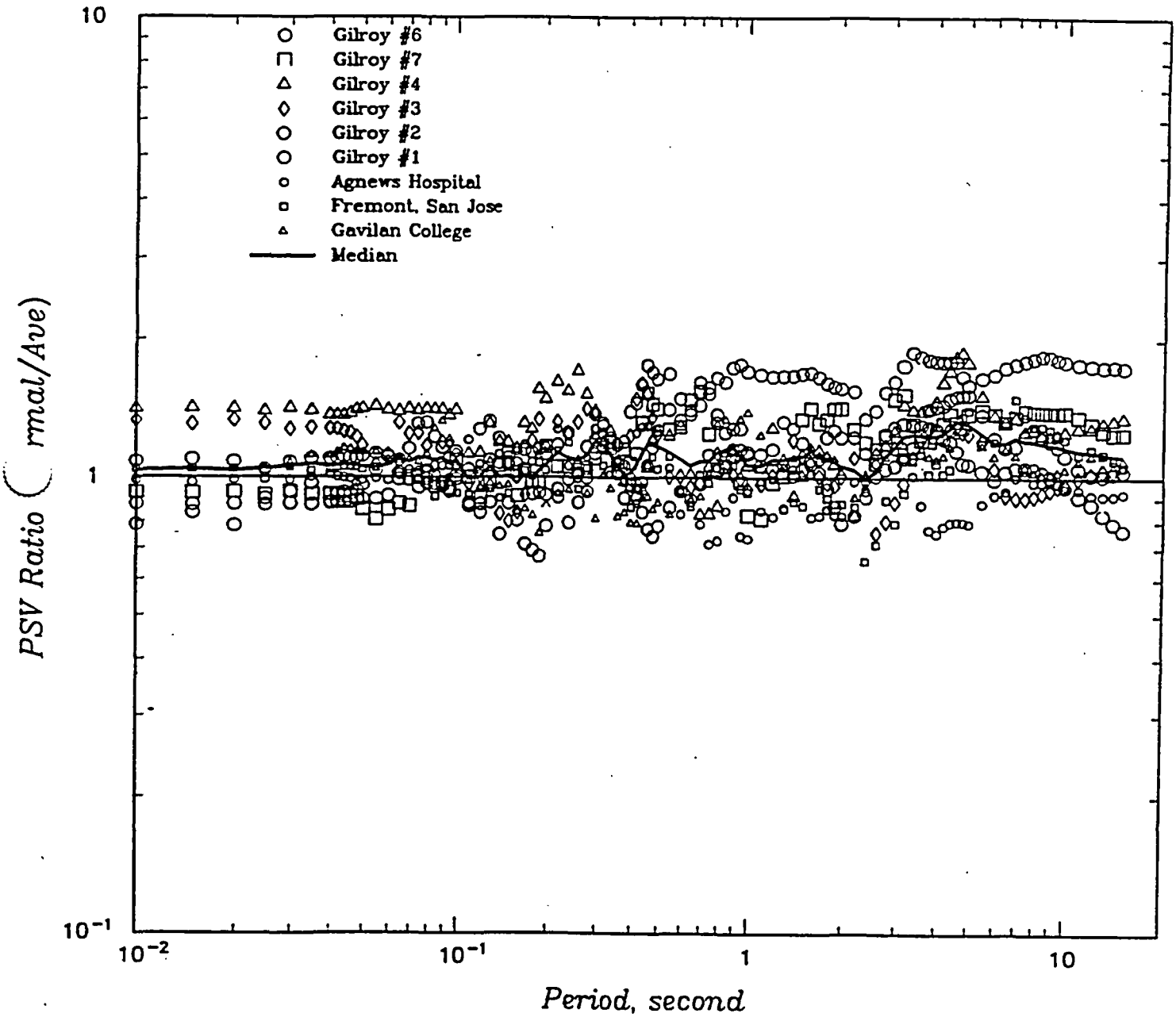

Morgan Hill, 1984; Distance to Fault Greater Than 10 KM

Figure E-5

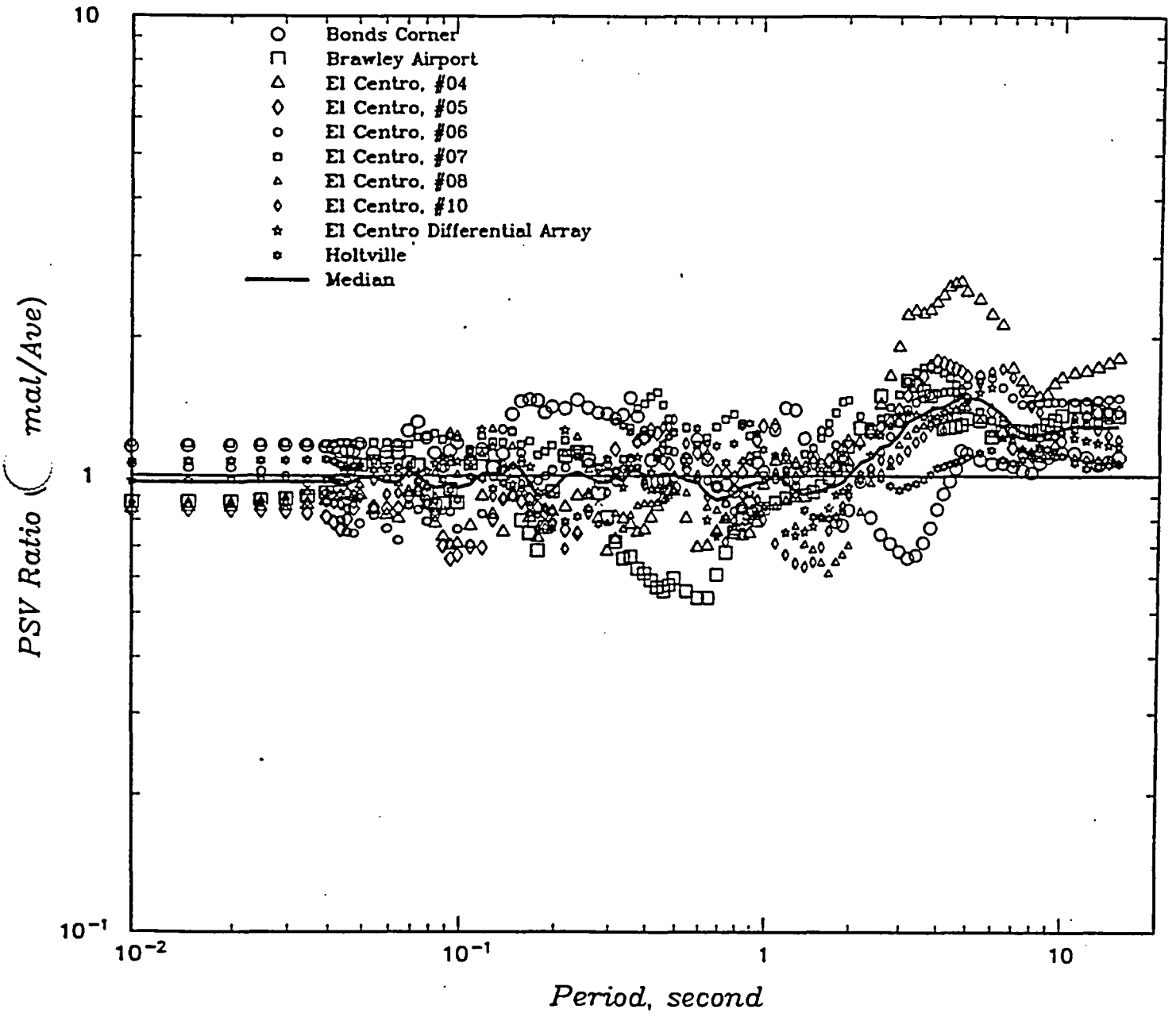

Imperial Valley, 1979; Distance to Fault Less Than 10 KM

Figure E-6

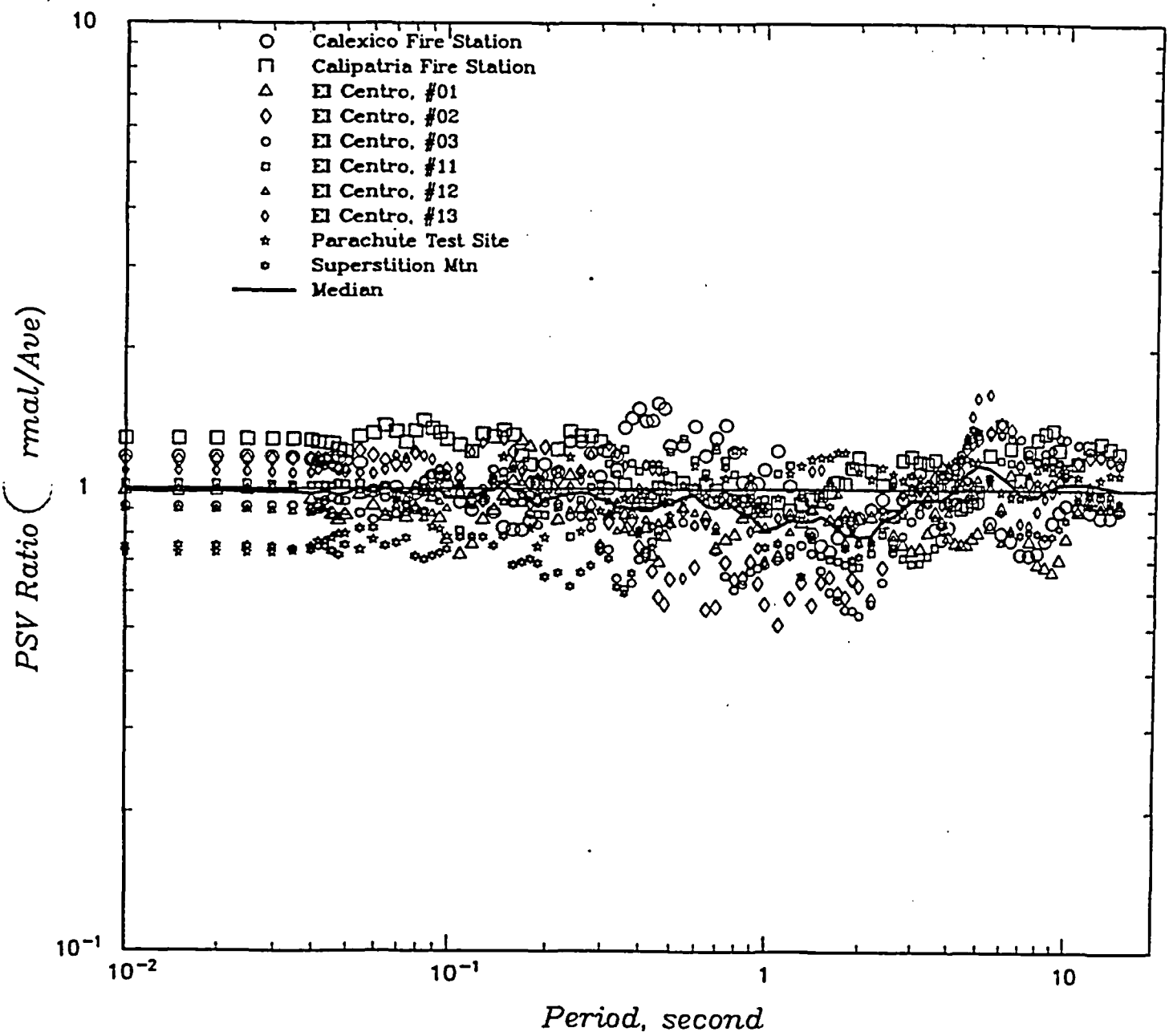

Imperial Valley, 1979; Distance To Fault Greater Than 10 KM

Figure E-7

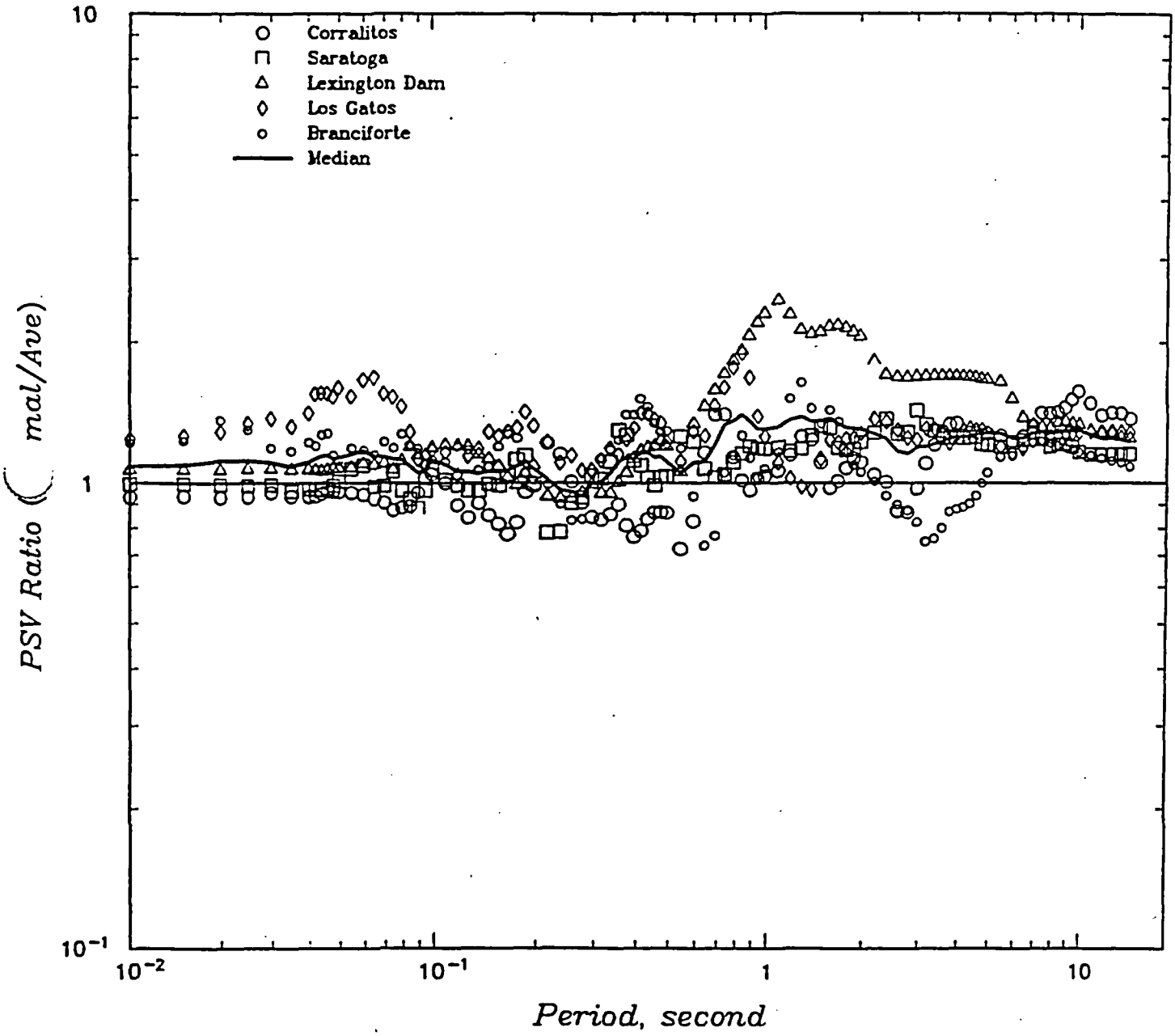

Loma Prieta, 1989; Distance To Fault Less Than 10 KM

Figure E-8

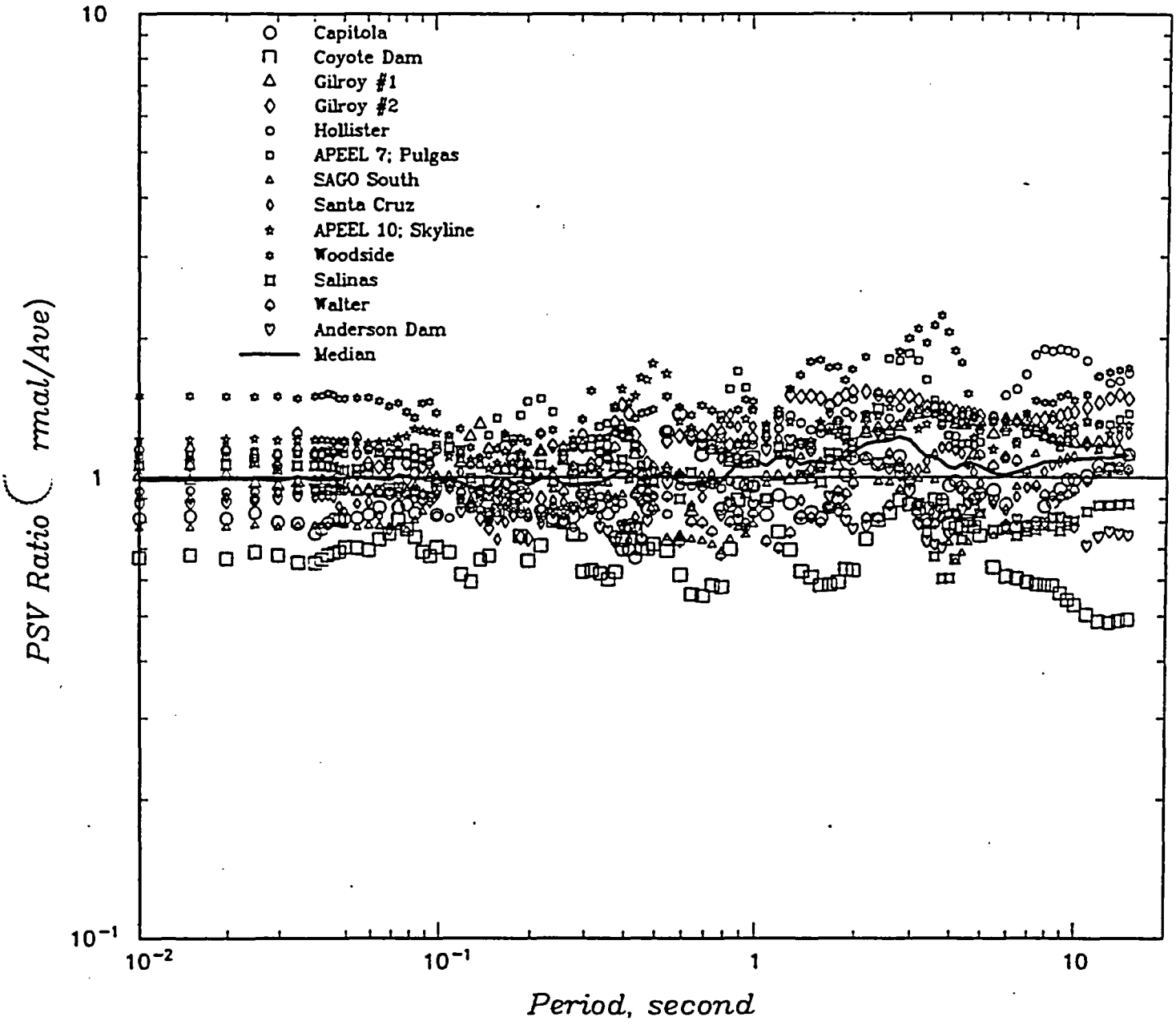

Loma Prieta. 1989; Distance to Fault Greater Than 10 KM

Figure E-9

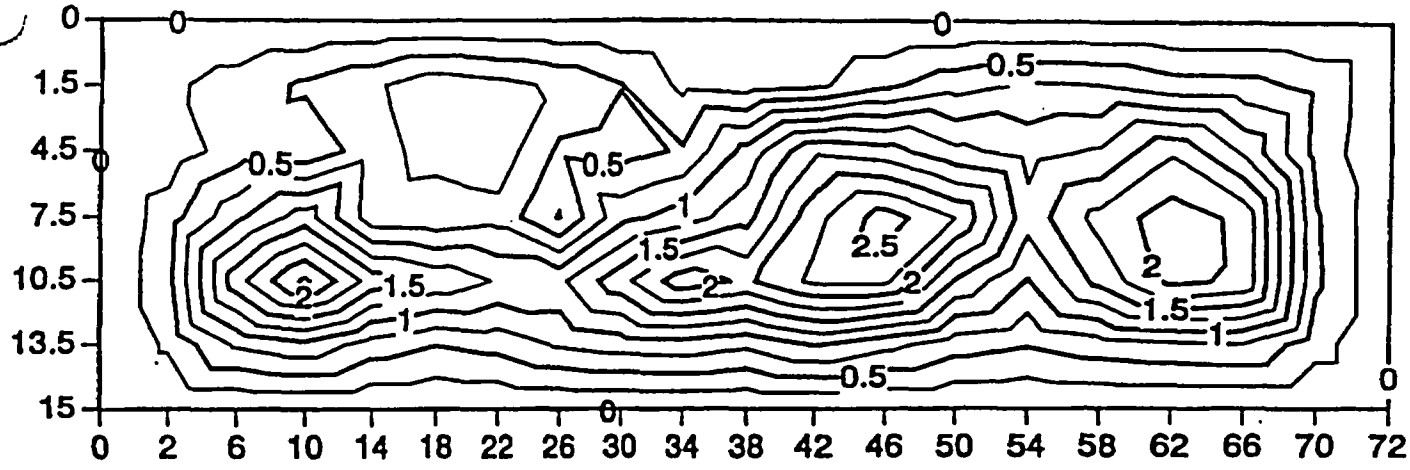

Relative slip

Figure E-10

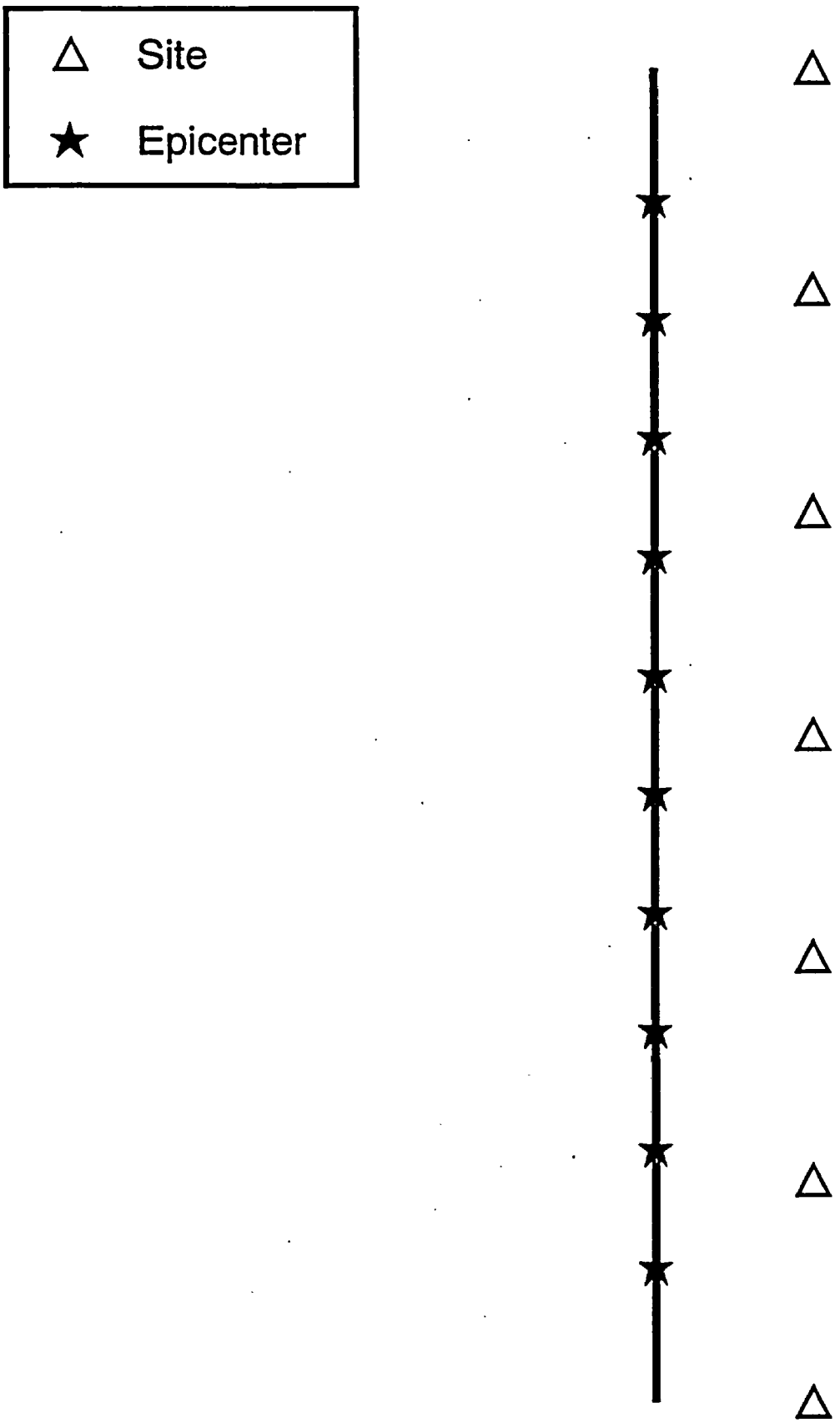

Figure E-11

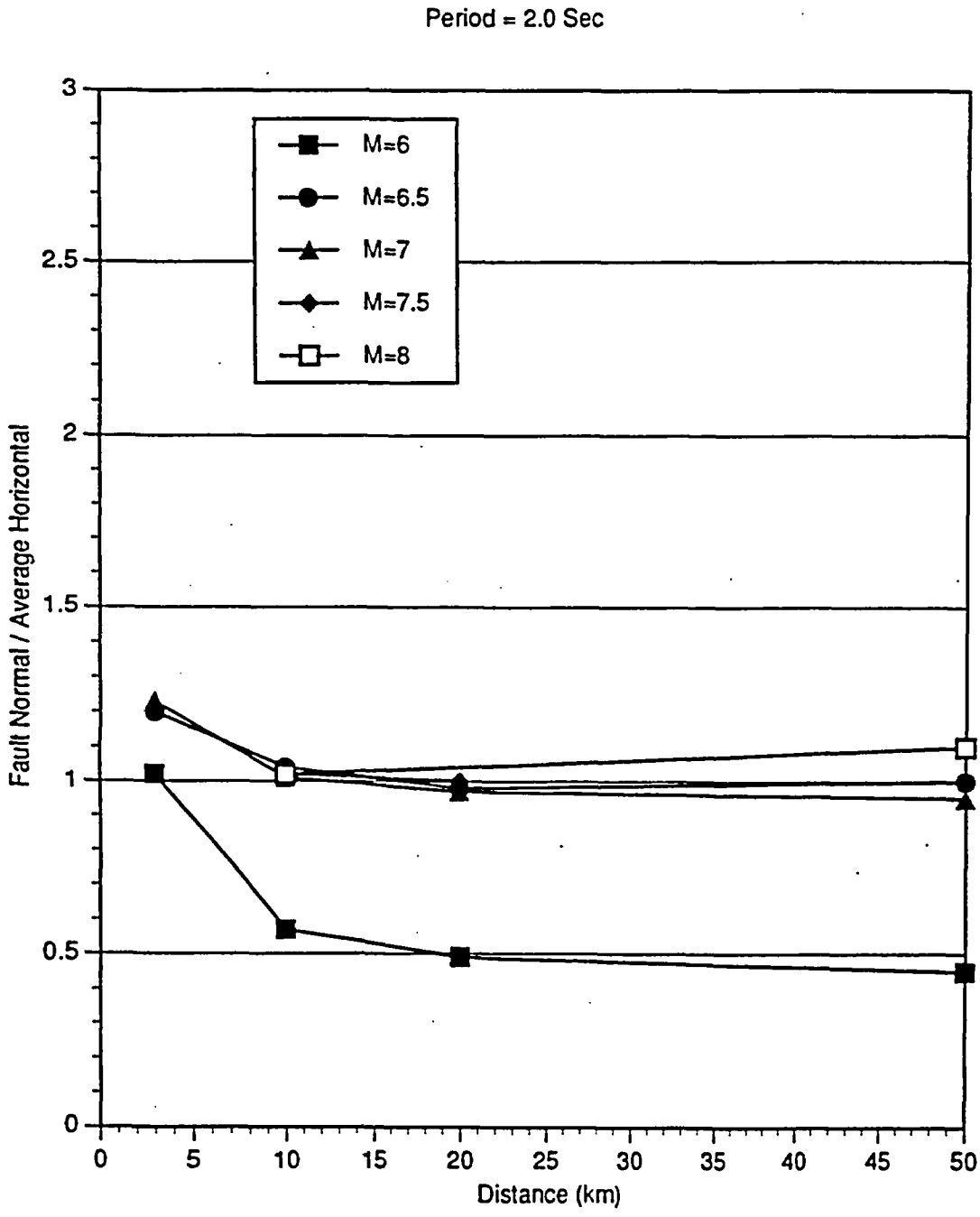
Period = 2.0 Sec
M=6
M=6.5
M=7
M=7.5
M=8
Fault Normal / Average Horizontal
Distance (km)
0
0.5
1
1.5
2
2.5
3
0
5
10
15
20
25
30
35
40
45
50

Figure E-12

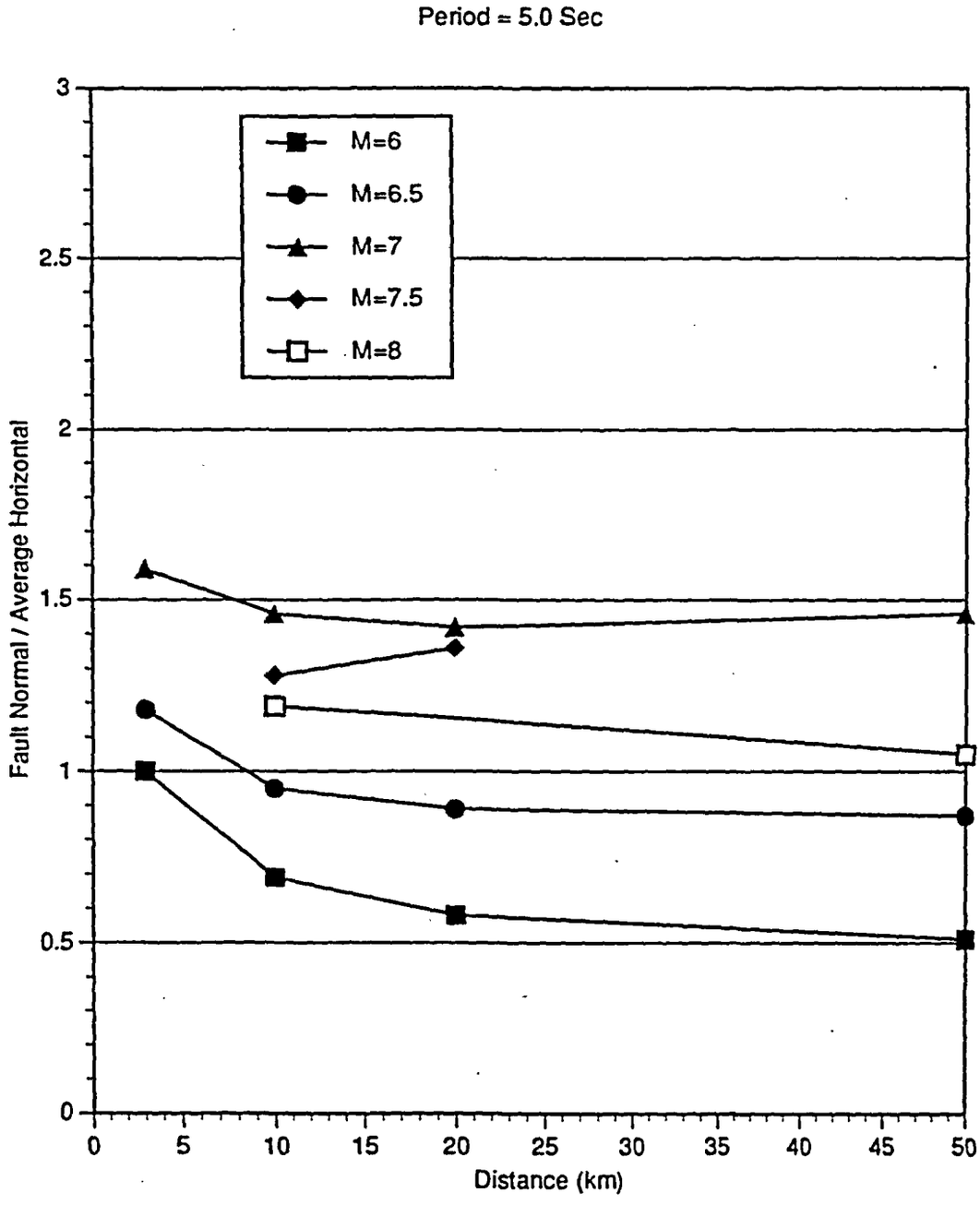
Period = 5.0 Sec
M=6
M=6.5
M=7
M=7.5
M=8
Fault Normal / Average Horizontal
Distance (km)
0
0.5
1
1.5
2
2.5
3
0
5
10
15
20
25
30
35
40
45
50

Figure E-13

GEOMATRIX

APPENDIX F

SECTION 3.1 SUBDUCTION ZONE EARTHQUAKE GROUND MOTIONS AND APPENDIX C NUMERICAL SIMULATION OF STRONG GROUND MOTION USING THE STOCHASTIC GROUND MOTION MODEL FOR SUBDUCTION EARTHQUAKES, BOTH ABSTRACTED FROM GEOMATRIX (1993)

Section 3.1 from Geomatrix (1993)

3.1 SUBDUCTION ZONE EARTHQUAKE GROUND MOTIONS

3.1.1 Background and Approach

Three recent studies have focused on estimation of ground motions from Cascadia subduction zone earthquakes. Youngs and others (1988) developed attenuation relationships for peak acceleration on rock and soil sites and response spectra on rock sites by analyzing empirical strong motion data and the results of numerical modeling studies. These relationships were used to estimate ground motions at the Satsop Nuclear Power Plant Site (Washington Public Power Supply System, 1988). More recently, Crouse (1991) presented attenuation relationships for soil site motions based on empirical strong ground motions. Crouse's relationship for peak ground acceleration provides ground motion estimates that are consistent with the soil site relationships developed by Youngs and others (1988) for large magnitude events. Cohee and others (1991) presented ground motion estimates for a magnitude M 8 earthquake occurring on the Cascadia subduction zone based on numerical modeling techniques. Cohee and others (1991) point out that attenuation relationships based on their modeling results do not agree with the empirical model of Youngs and others (1988) and suggest that the discrepancy may be due to the regression technique used by Youngs and others (1988), as suggested by Fukashima and Tanaka (1990).

The ground motion analysis presented below represents an update of the relationships presented by Youngs and others (1988). The strong motion database used by Youngs and others (1988) was updated to include additional data reported by Crouse (1991) as well as recent strong motion recordings, including those from the 1992 Cape Mendocino earthquake sequence. We analyzed these data using regression techniques that address the issues raised by Fukashima and Tanaka (1990). In addition, we performed numerical ground motion simulation studies using updated techniques to provide guidance in formulating the regression models and to provide direct estimates of site ground motions.

3.1.2 Empirical Ground Motion Analyses

3.1.2.1 Strong Motion Database

The data set collected and analyzed in this study is listed in Appendix B. Part of this data set is identical to the data set used in the previous study of the Cascadia subduction zone by Youngs and others (1988). Additional data include: Japanese data collected by Crouse (1990); Alaskan subduction zone data collected by the National Center for Earthquake Engineering Research; data recorded during the 1989 Acapulco earthquake (Anderson and others, 1989); and data from the 1992 Petrolia earthquake mainshock (CDMG, 1992).

Source parameters of these earthquakes (epicenter location, focal depth, magnitude, and fault plane solution) were compiled from published special studies or the Harvard centroid moment tensor solution. Harvard's solution was used only for seismic moment, M_o, and fault plane solution. Moment magnitude, M, is defined by $log_{10} M_o = 1.5 M + 16.1$ (Hanks and Kanamori, 1979). If no special study was found for an event, then earthquake location and magnitude given in the International Seismological Center or National Earthquake Information Center catalogs were used. If seismic moment was not reported, then the surface wave magnitude, M_S, was used, assuming that it is equivalent to moment magnitude in the magnitude range of 6 to 7.5 (Hanks and Kanamori, 1979). If only body wave magnitude, m_b was reported, then m_b values in the range of 5 to 6 were converted to M_S using the relationship $M_S = 1.8 m_b - 4.3$ proposed by Wyss and Habermann (1982) and the resulting value taken to be equivalent to moment magnitude.

We characterized source-to-site distance, R, in terms of the closest distance to the ruptured surface, which is normally inferred from the distribution of aftershocks occurring within the first few days after the mainshock. If the ruptured surface has not been defined for an event, then the hypocentral distance was used as source-to-site distance.

The recording stations were classified into three groups: rock, shallow stiff soil (depth to rock less than 20 m), and deep soil sites (depth to rock deeper than 20 m). These classification were based on published information on site conditions listed in the various data sources. The data used in the analysis were restricted to free-field recordings from magnitude 5.0 and greater events. For this analysis, free-field recordings are considered recordings obtained at

the basement or the first floor of a building of less than four stories. In addition, data were excluded if the quality of the recorded acceleration time history was poor or if a portion of the main shaking was not recorded.

We classified the selected data into six groups according to the recording site conditions and the type of subduction zone earthquake: interface-soil, interface-stiff soil, interface-rock, intraslab-soil, intraslab-stiff soil, and intraslab-rock. Previous analyses (e.g., Youngs and others, 1988) have indicated significant differences in ground motions from the two types of subduction zone earthquakes and differences in the peak accelerations recorded on difference site conditions. The differentiation between interface and intraslab events was done on the basis of the faulting mechanism, when reported, or on the basis of the focal depth, with events below a depth of 50 km considered to be intraslab events. The number of ground motion data from various subduction zones is tabulated in the following table.

	Interface			Intraslab		
	Rock	Shallow Soil	Deep Rock	Rock	Shallow Soil	Deep Soil
Alaska	17	2	3	0	0	1
Cascadia	2	4	8	0	0	3
Chile	8	6	22	4	6	5
Japan	0	41	110	0	12	41
Mexico	62	9	50	4	0	12
Peru	0	5	1	0	8	0
Solomons	2	2	5	1	1	23
Total	91	69	199	9	27	85

Figure 3-1 shows the magnitude-distance scattergram of the strong motion data set collected for analysis. Figures 3-2a and 3-2b show the geometric mean of the horizontal peak ground acceleration versus distance for interface and intraslab earthquakes, respectively. The largest group of data is the soil data for interface events. A large portion of the rock data are from the three Mexican subduction zone earthquakes recorded at the Guerrero Array. The 1992

Petrolia earthquake mainshock was also included as an interface event. Following the discussion in Youngs and others (1988), we characterize the horizontal ground motion parameters as the geometrical mean of the two horizontal components.

3.1.2.2 Analysis of Peak Horizontal Acceleration Data

Attenuation relationships for subduction zone earthquakes were evaluated by performing regression analyses on the empirical data. Because each of the six groups does not have sufficient data to render stable estimates of the regression parameters by itself, except for the interface soil data, we performed a joint regression analysis. The constants determined from the analyses include the attenuation relationship coefficients for the selected reference group and parameters representing the perturbations of the other five groups from the reference attenuation relationship. In the following analyses, a set of indicator variables were used to identify data from each group: Z_t indicates source type and is set to zero for interface events and one for intraslab events; Z_s indicates deep soil conditions and is set to one for deep soil sites and zero otherwise; Z_f indicates shallow stiff soil sites and is one for shallow stiff soil sites and zero otherwise; Z_r is one for rock and zero otherwise.

Base-Case Analysis. The basic regression model follows the form used previously by Youngs and others (1988):

$$\begin{aligned}(\ln a_{max})_{ij} &= C_1^* + C_2 M_i + C_3^* \ln[R_{ij} + e^{C_4^* - \frac{C_2}{C_3^*} M_i}] + C_5 Z_t + C_9 H_i + C_{10} Z_f + \eta_i + \epsilon_{ij}, \\ C_1^* &= C_1 + C_8 Z_r, \\ C_3^* &= C_3 + C_6 Z_r, \\ C_4^* &= C_4 + C_7 Z_r\end{aligned} \quad (3\text{-}1)$$

where i is the earthquake index, j is the recording station index, a_{max} (in units of g) is the geometrical mean of the two horizontal peak ground accelerations, M is the moment magnitude, R is the source-to-site distance (in kilometers), H is focal depth (in kilometers), and the C_k, $k=1, 10$, are unknown coefficients. The terms H and Z_f are additions to the Youngs and others (1988) model.

The error term is partitioned into an inter-event component, η_i representing the earthquake-to-earthquake variability of ground motions, and an intra-event component, ϵ_{ij} representing within earthquake variability of ground motions. The regression coefficients and the error terms η_i and ϵ_{ij} were obtained by *random effects* regression. This technique has been shown by Brillinger and Preisler (1985) and Joyner and Boore (1993) to be equivalent to the two-stage regression technique advocated for subduction zone data by Fukashima and Tanaka (1990), and thus should address the issue raised by Cohee and others (1991) concerning the adequacy of the regression model. The specific regression algorithm used is that described in Abrahamson and Youngs (1992). In Equation (3-1), the η_i and ϵ_{ij} are assumed to be independent normally distributed variates with variances τ^2 and σ^2, respectively.

Figure 3-3 shows the residuals resulting from the fit of Equation (3-1) to the peak acceleration data shown on Figures 3-2a and 3-2b. The residuals indicate that a reasonable fit is achieved over the full magnitude and distance range of the data.

Figure 3-4 compares the fitted relationships for magnitude M 8 interface earthquakes with recorded rock and deep soil data. Previously published attenuation relationships for subduction zone earthquakes are also shown. As indicated on the figure, the results of this study are very similar to the Youngs and others (1988) model and are consistent with the results obtained by Crouse (1991) for soil sites. The model developed by Fukashima and Tanaka (1990) does not appear to fit the large-magnitude subduction zone earthquake data well.

Equation (3-1) included effects of near-field magnitude saturation, source type, depth effect, and site conditions. The significance of these effects were examined individually.

Near-field Magnitude Saturation. A decrease in the dependence of peak acceleration on earthquake magnitude as the source is approached has been reported by several investigations of crustal earthquake strong ground motions (e.g., Campbell, 1981, 1989; Sadigh and others, 1986, 1989). Crouse (1991) also found a similar effect in his evaluation of peak soil site

motions from subduction zone earthquakes. Accordingly, the regression model defined by Equation (3-1) assumes that ground motions are independent of magnitude at zero distance.

To test the hypothesis of near field magnitude saturation, the term $-C_2/C^*_3$ in Equation (3-1) was replaced by $B^* = B_1 + B_2 Z_r$. The resulting coefficients indicate slight under-saturation of peak accelerations on soil ($C_2 + C_3 B^* = 0.26$) and slight over-saturation of peak accelerations on rock ($C_2 + C_3 B^* = -0.05$). We tested the statistical significance of these results using the likelihood ratio test (Seber and Wild, 1989). Application of the test to the regression results indicates that we can not reject the null hypothesis of $B^* = -C_2/C^*_3$. However, because of the limited near-field data, the true form of the attenuation relationship at distances less than about 30 km is not well constrained.

Effect of Source Type and Depth. Previous investigations have found that depth or source type have an effect on the level of peak ground acceleration. Crouse and others (1988) found that peak accelerations on soil sites increased with increasing focal depth of the subduction zone earthquake. This result was confirmed by the updated analysis of Crouse (1991). Youngs and others (1988) found that the effect of depth could be represented by systematic difference in the peak accelerations produced by interface and intraslab earthquakes. Intraslab earthquakes, which occur deeper, produce larger ground motions than interface earthquakes of similar magnitude. Youngs and others (1988) found that the separation of subduction zone earthquakes into the two groups accounted for the depth dependence in their data set.

Both the effect of depth and the effect of source type were examined with the expanded data set collected for this study. We find that the effect of source depth is statistically significant (at the 5 percent significance level) both for the interface earthquake data and for the intraslab earthquake data. The presence of a systematic difference between intraslab and interface earthquakes was also found to be statistically significant, with and without inclusion of a term to account for source depth. Therefore, both effects are retained in the model.

Because the amount of intraslab data is too limited to warrant an independent regression analysis, the effect of source difference is represented by a simple constant scaling factor in the attenuation model. We examined the validity of this model by computing the residuals for intraslab data based on an attenuation relationship fit to interface data only. Inspection of the residuals, shown on Figure 3-5, indicates no significant trend with magnitude or distance.

Effect of Site Conditions. Consistent with previous analyses, we find that ground motions on soil sites are systematically higher than on rock sites for both soil classifications. This effect is examined in greater detail below.

Dependence of Variance on Earthquake Magnitude. Youngs and others (1988) found that the scatter of peak acceleration data about the median attenuation relationship decreased with increasing magnitude. This effect has been reported in previous studies of crustal earthquakes (e.g., Sadigh, 1983; Sadigh and others, 1986, 1989; Abrahamson, 1988). Youngs and others (1993) conducted a rigorous examination of California strong motion data using the random effects regression model and concluded that both inter-event and intra-event components of ground motion variability are magnitude dependent. The need for such magnitude dependence in the subduction zone data set was investigated by fitting linear relationships of the form $\tau = V_1 + V_2 M$ and $\sigma = V_3 + V_4 M$ to the variance terms of Equation (3-1). We found that, using the likelihood ratio test, the null hypothesis that $V_2 = V_4 = 0$ can be rejected at the 1 percent significance level. We also found that the variance in the updated data set is larger than previously reported by Youngs and others (1988).

Soil/Rock Amplification. The base-case analysis indicates amplification of soil motions over rock motions at all distances. The upper left-hand plot on Figure 3-6 shows soil to rock amplification ratios predicted by the base-case model, hereafter referred to as Model 1. The fitted relationship results in increasing amplification with increasing rock acceleration level. This is inconsistent with the amplification ratios observed in studies of crustal events (e.g., Seed and Idriss, 1982). This upward trend is a result of the relatively low rock peak

accelerations predicted by Model 1 at small distances. It is noted that only a limited number of rock data were recorded at small distances, and that a large portion of their values are smaller than 0.2 g. Thus the data do not provide a strong constraint on the near-field soil/rock amplification ratios. Numerical simulations of soil and rock peak ground accelerations were used to study the anticipated shape of soil/rock amplification in the near field in order to provide guidance in constructing attenuation relationships.

Numerical Simulation of Soil/Rock Amplification. We simulated peak ground accelerations using the numerical ground motion modeling methodology presented in Appendix C. Ground motions were simulated for both crustal earthquakes and subduction zone earthquakes. Crustal earthquakes were examined because the empirical data from crustal earthquakes have been studied to a greater extent, and the soil/rock amplification as a function of rock acceleration level is generally understood. Thus, comparisons between the empirical and modeling estimates for crustal earthquakes provide a check on the applicability of the modeling results for subduction zone earthquakes.

Using the numerical ground motion simulation model outlined in Appendix C, we simulated ground motions for events of magnitude M 5.5 to 7.5 using properties for western North American earthquakes and crustal rocks. Because the intent of the exercise was to examine soil/rock ratios, point source approximations were used in the crustal earthquake simulations. Ground motion predictions were made for a rock site and three soil sites with soil thickness of 20, 120, and 500 ft. The 20-ft thickness of soil is representative of a shallow stiff soil site in our site classification, and the 500-ft soil profile is considered representative of a typical deep soil site. Soil site motions were computed using a one-dimensional wave propagation model coupled with an equivalent-linear representation of the nonlinear behavior of soils (Silva, 1991). Figure 3-7 shows the soil properties used in the ground motion simulations. These soil properties are considered representative of typical alluvial soils. The soil properties at the recording stations represented in the strong motion database are expected to be generally similar, although there is insufficient information to verify this assumption. We

expect that the general trends deduced from these analysis will be consistent with those that would be computed from a reasonable range of soil properties.

Figure 3-8 shows the variation of simulated peak accelerations as a function of magnitude and distance for rock sites and the three soil profiles. The results show a reduction in the scaling of ground motions with earthquake magnitude in the near field as the depth of the soil profile increases. Figure 3-9 shows the soil/rock amplification as a function of rock peak acceleration computed from the simulation results shown on Figure 3-8. It is noted that the computed amplification ratios are independent of magnitude. The predicted amplification for the shallow soil profile (20 ft) supports the use of a constant factor to approximate the amplification effect of stiff soil in the range of observed rock peak accelerations (Equation 3-1). For the other two soil profiles, the natural log of the soil/rock amplification ratios can be approximated by the relations $(15.6/(a^r_{max}+1.0))^{1/2} -- 3.3445$ for 500 ft of soil, and $(15.6/(a^r_{max}+1.0))^{1/2} -- 2.6343$ for 120 ft of soil, where a^r_{max} represents peak acceleration on rock in g's. Although the available site descriptions for the data in the subduction zone strong motion data set are not sufficient to allow detailed categorization of recorded data by the soil thickness, it is judged that the 500-ft-deep profile is more typical the soil thickness one would find under recording stations located on alluvial sites.

Also shown on Figure 3-9 is the soil/rock amplification ratio derived from the empirical strong motion data by Silva and others (1993). These results are based on western North American strong motion data recorded at rock sites and soil sites with a range of soil depth. The empirical results are generally consistent with the results of the simulations, indicating that the numerical modeling method produces reasonable results for both soil and rock motions.

The soil/rock amplification ratios for large subduction zone earthquakes were evaluated by simulating ground motions on soil and rock sites using the finite-fault simulation model presented in Appendix C together with the rupture characteristics of the 1985 M 8 Michoacan earthquake. Figure 3-10 shows the resulting soil/rock peak acceleration values and

amplification factors. Also shown on the figure is the approximate soil amplification curve for the 500-ft profile from the point source simulations. The trends shown on Figures 3-9 and 3-10 are very similar.

Imposition of Soil/Rock Amplification Functions in Fit to Empirical Data. The numerical modeling results shown on Figures 3-9 and 3-10 were used to constrain the form of the attenuation relationship fit to the empirical data. Three additional attenuation forms were developed. The results of fits of these relationships to the empirical data are shown on Figures 3-11a through 3-11f, and the fitted coefficients are listed in Table 3-1. The basis for the model development is as follows.

Model 2

The results of the above numerical simulations suggest the following regression model:

$$\ln(a_{max})_{ij} = \ln(a^r_{max})_{ij} + Z_s \left[\left[\frac{C_5}{(a^r_{max})_{ij}+1.0} \right]^{a_1} - \left[\frac{C_5}{a_2+1.0} \right]^{a_1} \right] + C_6 Z_f + \eta_i + \epsilon_{ij}, \quad (3\text{-}2)$$

$$\ln(a^r_{max})_{ij} = C_1 + C_2 M_i + C_3 \ln[R_{ij} + e^{C_4 - \frac{C_3}{C_3} M_i}] + C_7 H_i + C_8 Z_t$$

In this functional form, soil peak acceleration is amplified when input rock peak acceleration is less than an acceleration of a_2 g. Initial analyses show that coefficients a_1, a_2, and C_5 are strongly coupled and cannot be simultaneously resolved from the data, and they are nearly de-coupled from the rest of the regression coefficients (i.e., coefficients for the rock peak acceleration relationship). We also performed regression with a_1 fixed at 0.5 and the results again indicate strong correlation between a_2 and C_5. The result of this analysis predicts an increase of amplification factor with increasing rock motion, which is contradictory to the trend indicated by numerical simulations and empirical observations of crustal earthquakes. Therefore, in the subsequent regression procedure, a_1 and a_2 were fixed at the values $a_1 = 0.5$ and $a_2 = 0.4$, compatible with those given by the numerical simulations. The regression

results for other coefficients (except C_5) are not expected to be strongly affected by changes of the assumed values of a_1 and a_2.

Comparison of Model 2 with Model 1 (Figure 3-11) indicates the imposed soil-rock relationship has little effect on the predicted rock peak acceleration at distances greater than 50 km. At distances less than 30 km, interface rock peak acceleration is only slightly higher than the peak acceleration of Model 1, but the soil peak acceleration is much lower than the values of Model 1. This suggests the rock data controls the location of the median soil relationship at small distances. The resulting soil/rock amplification factor is in agreement with the results of the simulations as a result of lowering the predicted peak accelerations on soil at small distances.

Model 3

It is noted that numerically simulated soil/rock amplification is one near a peak acceleration of 0.4 g, which is close to the soil peak acceleration value predicted by Model 1 at R = 10 km. Thus, in Model 3, soil and rock peak accelerations are forced to converge when approaching R = 0 km. Convergence ensures that the more numerous soil data will control the location of the near source rock prediction. The Model 3 relationships form is

$$\begin{aligned} \ln(a_{max})_{ij} &= C_1^* + C_2 M_i + C_3^* \ln[R_{ij} + e^{C_4^* - \frac{C_2}{C_3^*} M_i}] + C_5 Z_f + C_8 Z_t + C_9 H_i + \eta_i + \epsilon_{ij}, \\ C_1^* &= C_1 + C_3 C_4 - C_3^* C_4^*, \\ C_3^* &= C_3 + C_6 Z_s, \\ C_4^* &= C_4 + C_7 Z_s \end{aligned} \qquad (3\text{-}3)$$

Model 3 is identical to Model 1 except there is one less unknown coefficient due to the constraint of soil-rock convergence at R = 0. This model, like Model 2, does not alter the rock predictions at large distances, but the predicted peak acceleration at short distance is considerably higher than the previous two models. It is also noted that soil peak acceleration predicted by this model is quite different from that of Model 1 at all distances and this model over-predicts the soil peak acceleration at distance greater than 200 km. The latter leads to

the rapid increase in predicted amplification factor at low rock peak acceleration. It was thought that imposing both magnitude saturation and soil-rock convergence at the same time is probably too restrictive. Therefore, we relaxed the assumption of magnitude saturation in the next model.

Model 4

In Model 4, magnitude saturation is not enforced but soil-rock convergence is still imposed. As a result, magnitude scaling at far-field (the 2nd term in the model) is allowed to be different between soil and rock attenuation equations. The resulting attenuation form is

$$\begin{aligned} \ln(a_{max})_{ij} &= C_1^* + C_2 M_i + C_3^* \ln[R_{ij} + e^{C_4^* + C_5^* M_i}] + C_6 Z_f + C_{10} Z_t + C_{11} H_i + \eta_i + \epsilon_{ij}, \\ C_1^* &= C_1 + C_3 C_4 - C_3^* C_4^* + (C_3 C_5 - C_3^* C_5^*) M_i, \\ C_3^* &= C_3 + C_7 Z_s, \\ C_5^* &= C_5 + C_9 Z_s \end{aligned} \qquad (3\text{-}4)$$

With relaxation of imposed magnitude saturation, a better fit to soil peak acceleration at large distances is achieved (Figure 3-11) and the soil/rock amplification factor is still in good agreement with Models 2 and 3. Although magnitude saturation was not assumed in this model, the regression results indicate both rock and soil peak accelerations approach saturation at small distances for large magnitude events.

The comparisons shown on Figure 3-11 indicate that all four models fit the data equally well. No significant differences in the fitted error terms or the intraslab/interface and depth terms were found between the four models. Therefore, all four models were used to predict ground motions for the Trojan site.

3.1.2.3 Analysis of Spectral Velocity Data For Rock Sites

Because only limited digitized recordings obtained on rock sites were available, primarily from the Guerrero array data, attenuation relationships of the 5 percent damped horizontal response spectral velocities, *Sv*, (in cm/sec) on rock from interface event were developed

using the procedures employed by Sadigh (1983). These involve developing relationships for the ratio Sv/a_{max} (cm/sec/g) as a function of magnitude and distance and then applying these relationships to attenuation relationships for peak acceleration.

Forty-four spectral ratios at 12 natural periods from 0.04 sec to 3.0 sec were formed by taking the ratio of the geometric mean of Sv to the geometric mean of peak acceleration recorded at distance less than 120 km. As two examples, spectral ratios at periods of 0.1 and 1 seconds are shown in Figure 3-12. In the magnitude band of $M = 7.8$ to 8.2, the 1985 Michoacan earthquake ($M = 8.0$) and the 1985 Chilean earthquake ($M = 7.9$) are the only two events that contribute to the data set; in the $M = 6.8$ to 7.2 range, the data set is dominated by the 1989 Acapulco earthquake ($M = 7.0$).

Examination of the available data set indicates that Sv/a_{max} is dependent on source-to-site distance and on earthquake magnitude at long periods. Both magnitude and distance dependencies are thus included in the regression relationship. The attenuation relationship for any one period is:

$$\ln [Sv/a_{max}]_{ij} = B_1 + B_2 (B_4 - M_i)^{B_5} + B_3 \ln [R_{ij} + e^{\alpha_1 + \alpha_2 M_i}]. \qquad (3\text{-}5)$$

The second term accounts for the magnitude scaling of ground motions, and the last term for the observed distance dependence, where α_1 and α_2 are constants whose values are set equal to the coefficients C_4 and C_5 of the peak acceleration attenuation relationships. The remaining variables have the same meanings as those used in the peak acceleration regression model. In conducting the regression, B_4 was fixed at 10 to provide for a monotonic dependence on magnitude over the magnitude range of interest to the study, and B_5 was fixed at 3 representing an average of the values obtained at long periods where the data exhibit significant magnitude effect on Sv/a_{max}. Applying these constraints, we found that parameters B_2 and B_3 vary linearly with the log of natural period, and thus the attenuation relationship may be rewritten for all 12 vibration periods as:

where T_k is the k-th period, $k = 1, 12$; and δ_{lk} is the Kronecker delta. With this model, we performed the regression analysis for all 12 periods simultaneously. Values of α_1 and α_2 from

$$
\begin{aligned}
\ln\,[Sv/a_{max}]_{ijk} &= (B_1)_k + (B_2)_k(10.0-M_i)^3 + (B_3)_k \ln[R_{ij}+e^{\alpha_1+\alpha_2 M_i}] + \eta_i + \epsilon_{ij}\ , \\
(B_1)_k &= A_l \delta_{lk}\ ,\ l=1,12\ , \\
(B_2)_k &= A_{13} - A_{14}\ln[T_k]\ , \\
(B_3)_k &= A_{15} - A_{16}\ln[T_k]\ ,
\end{aligned}
\qquad (3\text{-}6)
$$

the four peak acceleration attenuation relationships were used. Estimated values of A_k, $k = 1$, 16 are listed in Table 3-2 and values of B_1, B_2, and B_3 are plotted as a function of period on Figure 3-13. The small estimated values of B_2 at short periods (<0.1 sec) agree with the typically observed weaker dependence on magnitude of short-period motions compared to long-period motions.

3.1.2.4 Ground Motion Variability

Table 3-1 lists the parameters for estimation for the variance of peak ground acceleration as a function of earthquake magnitude. These values indicate that the total standard error of the natural log of peak acceleration for a magnitude M 8 earthquake is 0.65. Standard errors for spectral accelerations were computed for the 12 periods individually using the coefficients listed in Table 3-2 to define the median attenuation relationships. Figure 3-14 shows the resulting computations for events in two magnitude intervals, 7.5 ± 0.2 and 8 ± 0.2. The resulting estimates are somewhat lower than the values obtained for peak acceleration (shown on Figure 3-14 at a period of 0.02 seconds). Examination of the analysis results indicates that the inter-event components of the standard errors were nearly zero for most periods. This result is likely due to the limited number of earthquakes represented in the spectral ordinate data set. Therefore, we increased the total standard errors for the spectral ordinates account for an inter-event component of variance estimated from the peak acceleration data. The resulting relationships are shown on Figure 3-14.

3.1.3 Numerical Simulation of Interface Ground Motions

Numerical simulations of large interface earthquakes were performed using the stochastic ground motion model (Hanks and McGuire, 1981; Boore, 1983, 1986; Silva, 1991), which has been extended to represent finite source dimensions by Silva and others (1990) and Silva and Stark (1992). Appendix C summarizes the simulation methodology and presents a validation of the simulation model using ground motions recorded during the 1985 Chile and Mexico subduction zone earthquakes of magnitude M ~8.

3.1.3.1 Simulation Model Parameters

Figure 3-16 shows the geometry of the interface used in the simulations. Based on the geometry of the interface defined in Section 2.1, the preferred idealization of the plate interface was a plane dipping at 12° with a width of 70 km lying at 115 km from the Trojan site (30 km offshore). The alternative geometry was a plane dipping at 12° with a width of 100 km lying at 85 km from the Trojan site (at the coastline). We computed ground motions for the Trojan plant site and for two sites lying 25 km north and south of the plant site, and the results for the three sites were combined to provide the ground motion estimates. Table 3-3 presents the simulation parameters used in the base-case analysis for a magnitude M 8.5 earthquake occurring on a 70-km-wide interface, the uncertainty in the base-case parameters used to evaluate the parametric uncertainty, and alternative parameters used in sensitivity analyses. The basis for the selection of these parameters and the sensitivity of the computed motions to parameter variations is as follows.

The base-case slip distribution is the slip model for the 1985 Michoacan, Mexico earthquake developed by Mendez and Anderson (1991). For larger events we scaled this slip distribution upward to match the rupture area and seismic moment. The simulations were performed using a magnitude 6.4 subevent size. We generated simulated slip distributions for use in the forward modeling for the Cascadia events. The slip distribution of the 1985 M 8 Michoacan earthquake developed by Mendez and Anderson (1991) was used as a starting model. The two-dimensional wavenumber spectrum of this slip distribution was computed and the amplitude spectrum used for all simulations. Simulated slip distributions were then generated

by applying a random phase to the amplitude spectrum and then performing an inverse two-dimensional transform. The resulting process produces slip models that are consistent with the Michoacan subduction earthquake, but with asperities at variable locations. Large slips near the rupture boundaries were suppressed by applying cosine tapers to the simulated slip model. We generated thirty random slip models with this process and used them in the ground motion simulations. Slip distributions for larger magnitudes were generated by repeating the Michoacan slip model to fill out the larger rupture area and then applying the randomization process. Figures 3-17a and 3-17b show examples of simulated slip distributions for magnitude 8 and 8.5 events, respectively.

The nucleation point of rupture was assumed to occur randomly within an area lying between 50 percent and 90 percent of the downdip dimension of the fault and between 10 percent and 90 percent of the along-strike dimension. The base-case analysis assumed that the nucleation point occurred in the center of this area, directly opposite the site.

We modeled wave propagation of individual ray paths using a simple whole space travel path model of 1/R for the first 100 km, becoming $1/R^{½}$ at larger distances. As a sensitivity study, we replaced the simple body wave geometric attenuation model with the formulation developed by Ou and Herrmann (1990) that accounts for the effects of direct and critically reflected waves on geometric attenuation and duration of motions. The crustal velocity structure used was that proposed by Cohee and others (1991).

Anelastic attenuation and scattering of motions along the travel path was modeled using a frequency-dependent quality factor, $Q(f)$. The base-case values used the Q model determined for the Michoacan region by Humphrey and Anderson (1993). We performed sensitivity analyses using the Q model parameters determined by Singh and Herrmann (1983) for the Pacific Northwest and the general Q model used by Boore (1986) for simulation of ground motions in western North America. Uncertainty in the parameters of the Q model were set at values representative of the variability in estimating the model parameters from recorded data.

Amplification of waves by the crust was modeled using the crustal velocity structure of the region proposed by Cohee and others (1991). As a sensitivity study, we used the average crustal amplification factors for western North American crust developed by Boore (1986). Near surface attenuation resulting from absorption and scattering of waves in the shallow crust was modeled by the κ model of Anderson and Hough (1984). The average value of κ for western North American rock sites is approximately 0.04 seconds (Silva and Darragh, 1992). However, to reflect the fact that the Trojan site is underlain by basalt, which may be somewhat harder than the rock typically encountered at western North American recording stations, the base-case value of κ was set to 0.02 seconds. Sensitivity analyses were performed using a κ value of 0.04 seconds. We set the uncertainty in κ to the variability observed for stations that recorded the 1989 Loma Prieta earthquake (Schneider and others, 1993).

Figure 3-18 shows the sensitivity of the base-case computations for a magnitude M 8.5 event to the alternative parameter values. As indicated by the results shown, the largest effect results from use of the alternative Q models, both of which produce significantly lower short-period motion than obtained using the base-case model. Because we used the base-case Q model to calibrate the model through estimation of the strong motion data from Mexico and Chile, it was used in the simulations for the Cascadia margin. The alternative Q models are representative of the crust inland from the continental margin, and thus may not be applicable to the particular ray path being modeled.

The results shown on Figure 3-18 also indicate that the ground motions are sensitive to the assumption of the site κ. It is expected that the appropriate value for the Trojan site lies between 0.02 seconds and 0.04 seconds, and results for both values were used to estimate the site ground motions. Most of the remaining parameter sensitivity analyses indicate only minor effects on the result. Use of typical western North American crustal amplification factors would lead to somewhat larger short period motions. However, these amplification factors are for crust with relatively large κ values and low Q found in California. Given that only

the high Q model was used in the final simulations, the crustal amplifications were computed using only the crustal velocity structure proposed by Cohee and others (1991).

3.1.3.2 Simulation Results

Ground motions simulations were performed for magnitude M 8 and 8.5 earthquakes using the 70-km interface width and for magnitude M 9 earthquakes using the 100-km width. We performed the simulations using modeling parameters drawn from the parametric distributions defined in Table 3-3. Fifty simulations were made for each magnitude and the response spectra were computed at three sites located equal-distant from the rupture and spaced 25 km apart along strike near the midpoint of the fault rupture. The results of the 150 simulations were then used to compute median (mean log) peak spectral motions and the uncertainty in the ground motion estimates resulting from parametric uncertainty.

Figure 3-19 shows the resulting median spectra for the three events. Considering that the minimum distance to rupture for the M 9 event is 30 km less than for the M 8 and 8.5 events, the simulations indicate a tendency for ground motion saturation at very large earthquakes.

Figure 3-20 shows the parametric uncertainty computed for the magnitude M 8.5 simulations. Also indicated on the figure is the parametric uncertainty due solely to the randomization of the fault slip. As indicated by the results shown on the figure, the slip randomization represents the major portion of the parametric uncertainty at long periods. At short periods, other factors control the parametric uncertainty. As indicated by the results of the sensitivity analyses shown on Figure 3-18, the parameters contributing to the short-period parametric uncertainty are likely to be uncertainty in κ and Q. The total uncertainty in the simulation ground motion estimation is obtained by combining the parametric uncertainty with the modeling uncertainty shown in Appendix C, assuming that the two components of variance are independent. The resulting total standard error is about 0.5 for the natural log of peak acceleration, slightly lower than the values obtained from the analysis of empirical data.

We combined the results of the simulations for the various maximum magnitudes and distances using Equations (3-7) and (3-8) to obtain median and 84th-percentile response spectra for the interface SME. Because the details of the wave propagation characteristics of the rocks at the Trojan site are not known, equal weight was given to simulations using κ values of 0.02 and 0.04 seconds. We used the results of the sensitivity studies shown on Figure 3-18 to extend the simulation results to κ values of 0.04 seconds and a rupture width of 100 km for all three magnitudes. The resulting median and 84th-percentile response spectra are compared to the results from the empirical models on Figure 3-21. The results of the two approaches agree fairly well in at periods less than about 0.8 seconds. The large deviation between the two models at long periods is to be expected given the large modeling bias reported for long period motions in Appendix C.

TABLE 3-1

ESTIMATED PARAMETERS FOR PGA

	Model 1	Model 2	Model 3	Model 4
C_1	-0.6686600	-0.1216200	0.2418400	-0.9580800
C_2	1.4381000	1.4430000	1.4142000	0.9265600
C_3	-2.3291000	-2.5230000	-2.5526000	-1.7926000
C_4	0.0926130	0.5300600	0.5777600	0.1238200
C_5	0.3642700	20.1770000	0.4188200	0.5212900
C_6	2.3217000	0.5053600	0.2333100	0.4396500
C_7	-0.4312400	0.0059403	-0.2101700	-1.3477000
C_8	1.1230000	0.3830800	0.3846100	0.5906900
C_9	0.0064767		0.0060722	0.1076300
C_{10}	0.4596900			0.3520400
C_{11}				0.0070316
V_1	0.8259700	1.0337000	1.1106000	0.7265400
V_2	-0.0633540	-0.0917710	-0.1018400	-0.0500770
V_3	1.4201000	1.4046000	1.2870000	1.3856000
V_4	-0.1075500	-0.1053500	-0.0878380	-0.1025300

TABLE 3-2

ESTIMATED PARAMETERS FOR SPECTRAL ORDINATES ON ROCK FROM INTERFACE EVENT

A (Period)	Model 1	Model 2	Model 3	Model 4
A_1 (0.0400 Sec)	3.7412	3.3987	3.3616	2.854
A_2 (0.0667 Sec)	3.8531	3.6585	3.6486	3.3477
A_3 (0.1000 Sec)	4.0018	3.9245	3.9362	3.7994
A_4 (0.2000 Sec)	3.9912	4.1146	4.1633	4.307
A_5 (0.2860 Sec)	3.7983	4.0249	4.0927	4.3807
A_6 (0.4000 Sec)	3.6039	3.9279	4.0136	4.4378
A_7 (0.6667 Sec)	3.1848	3.6567	3.7696	4.4006
A_8 (0.8000 Sec)	2.8752	3.3999	3.5225	4.2272
A_9 (1.0000 Sec)	2.5905	3.1798	3.3143	4.1094
A_{10} (1.5000 Sec)	1.9608	2.666	2.8219	3.779
A_{11} (2.0000 Sec)	1.4548	2.2447	2.4162	3.4918
A_{12} (3.0000 Sec)	0.5347	1.4448	1.6385	2.8822
A_{13}	-0.0049	-0.0060	-0.0064	-0.0085
A_{14}	0.0018	0.0021	0.0023	0.0034
A_{15}	0.4312	0.3396	0.3189	0.1876
A_{16}	-0.2341	-0.1902	-0.1828	-0.1186

TABLE 3-3

MODEL PARAMETERS USED IN NUMERICAL SIMULATIONS OF CASCADIA EVENTS

Parameter	Base-Case Value	Uncertainty	Sensitivity
Slip Distribution	Michoacan	Randomized (see text)	-
Nucleation Point	Midpoint	Randomized (see text)	North and south ends of rupture
Wave Propagation	1/R 0<R<100 km $1/R^{1/2}$ R>100 km	None	Ou and Herrmann (1990)
Q model ($Q = Q_0 f^{\eta}$)	$Q = 273f^{0.66}$	sigma $\ln(Q_0) = 0.2$ sigma $\eta = 0.05$	$Q = 180f^{0.3}$ (Singh and Herrman, 1983) $Q = 150f^{0.6}$ (WNA)
Crustal Structure	Cohee and others (1991)	None	WNA average amplification (Boore, 1986)
Site κ	0.02 sec	sigma $\ln(\kappa) = 0.3$	$\kappa = 0.04$ sec

REFERENCES

Abrahamson, N.A., 1988, Statistical properties of peak ground accelerations recorded by the SMART1 array: Bulletin of the Seismological Society of America, v. 78, p. 26-41.

Abrahamson, N.A., and Youngs, R.R., 1992, A stable algorithm for regression analysis using the random effects model: Bulletin of the Seismological Society of America, v. 82, p. 505-510.

Anderson, J.G., and Hough, S.E., 1984, A model for the fourier amplitude spectrum of acceleration at high frequencies: Bulletin of the Seismological Society of America, v. 74, p. 1969-1993.

Anderson, J.G., Quaas, R., Castro, R., Singh, S.K., Velasco, J.M., Almora, D., Mena, E., Vasquez, R., Castro, G., Perez, C., Lopez, B., and Mejia, R., 1989, Accelerograms from the Guerrero, Mexico, strong motion array for the April 25, 1989 earthquake (M_S = 6.9), a preliminary report: Report GAA-6, Seismological Laboratory, University of Nevada at Reno, Reno Nevada, and Instituto de Ingenieria, Universidad Nacional Autonoma de Mexico, Mexico City.

Boore, D.M., 1983, Stochastic simulation of high-frequency ground motions based on seismological models of the radiated spectra: Bulletin of the Seismological Society of America, v. 73, p. 1865-1894.

Boore, D.M., 1986, Short period P- and S-wave radiation from large earthquakes: Implications for spectral scaling relations: Bulletin of the Seismological Society of America, v. 76, p. 43-64.

Brillinger, D.R., and Preisler, H.K., 1985, Further analysis of the Joyner-Boore attenuation data: Bulletin of the Seismological Society of America, v. 75, p. 611-614.

Campbell, K.W., 1981, Near-source attenuation of peak horizontal acceleration: Bulletin of the Seismological Society of America, v. 71, p. 2039-2070.

Campbell, K.W., 1989, Empirical prediction of near-source ground motion for the Diablo Canyon Power Plant Site, San Luis Obispo County, California: U.S. Geological Survey Open-File Report 89-484.

California Division of Mines and Geology (CDMG), 1992, Processed CSMIP strong-motion data from the Cape Mendocino/Petrolia earthquake of April 25, 1992: Release No. 1, Office of Strong Motion Studies Report No. OSMS 92-12.

Cohee, B.P., Somerville, P.G., and Abrahamson, N.A., 1991, Simulated ground motions for hypothesized M_W = 8 subduction earthquakes in Washington and Oregon: Bulletin of the Seismological Society of America, v. 81, p. 28-56.

Crouse, C.B., 1990, Ground-motion attenuation equations for earthquakes on the Cascadia subduction zone: Report to U.S. Geological Survey and Electric Power Research Institute, May.

Crouse, C.B., 1991, Ground-motion attenuation equations for earthquakes on the Cascadia subduction zone: Earthquake Spectra, v.7, p. 201-236.

Crouse, C.B., Vyas, Y.K., and Schell, B.A., 1988, Ground motions from subduction-zone earthquakes: Bulletin of the Seismological Society of America, v. 78, p. 1-25.

Fukashima Y., and Tanaka, T., 1990, A new attenuation relationship for peak horizontal acceleration of strong ground motion in Japan: Bulletin of the Seismological Society of America, v. 80, p. 757-783.

Geomatrix Consultants, 1993, Seismic margin earthquake for the Trojan Nuclear Power Plant, Ranier, Oregon: Report prepared for Portland General Electric, Trojan Nuclear Plant, Ranier, Oregon, April.

Hanks, T.C., and Kanamori, H., 1979, A moment magnitude scale: Journal of Geophysical Research, v. 84, p. 2348-2350.

Hanks, T.C., and McGuire, R.K., 1981, The character of high frequency strong ground motion: Bulletin of the Seismological Society of America, v. 71, p. 2071-2095.

Humphrey, J.R., and Anderson, J.G., 1993, Shear-wave attenuation and site response in Guerrero, submitted to the Bulletin of the Seismological Society of America.

Joyner, W.B., and Boore, D.M., 1993, Methods for regression analysis of strong-motion data: Bulletin of the Seismological Society of America, v. 83, p. 469-487.

Mendez, A.J., and Anderson, J.G., 1991, The temporal and spatial evolution of the 19 September 1985 Michoacan earthquake as inferred from near-source ground motion records: Bulletin of the Seismological Society of America, v. 81, p. 844-861.

Ou, G.-B., and Herrmann, R.B., 1990, A statistical model for ground motion produced by earthquakes at local and regional distances: Bulletin of the Seismological Society of America, v. 80, p. 1397-1417.

Sadigh, K., 1983, Considerations in the development of site-specific spectra: Proceedings of Conference XXII; Site-Specific Effects of Soil and Rock on Ground Motions and the Implications for Earthquake Resistant Design: U.S. Geological Survey Open-File Report 83-845, p. 423-458.

Sadigh, K., Chang, C.-Y., Makdisi, F., and Egan, J.A., 1989, Attenuation relationships for horizontal peak ground acceleration and response spectral acceleration for rock sites: Seismological Research Letters, v. 60 p. 19.

Sadigh, K., Egan, J.A., and Youngs, R.R., 1986, Specification of ground motion for seismic design of long period structures (abs.): Earthquake Notes, v. 57, n. 1, p. 13.

Schneider, J., Silva, W.P., and Stark, C., 1993, Source, path, and site ground motion model for the 1989 Loma Prieta earthquake: Earthquake Spectra, in press.

Seber, G.A.F., and Wild, C.J., 1989, Nonlinear Regression: John Wiley and Sons, New York.

Seed, H.B., and Idriss, I.M., 1982, Ground motions and soil liquefaction during earthquakes: Earthquake Engineering Research Institute Monograph Series, v. 5, 134 p.

Silva, W.J., 1991, Global characteristics and site geometry: Proceedings NSF/EPRI Workshop on Dynamic Soil Properties and Site Characterization, Electric Power Research Institute Research Project NP-7337.

Silva, W.J., Darragh, R.B., and Wong, I.G., 1990, Engineering characterization of earthquake strong ground motions with application to the Pacific Northwest, *in* Hays, W.W., (ed.), Proceedings of the Third NEHRP Workshop on Earthquake Hazards in the Puget Sound/Portland Region: U.S. Geological Survey Open-File Report.

Silva, W.J., and Darragh, R.B., 1992, Engineering characterization of strong ground motion recorded at rock sites: Report prepared for the Electric Power Research Institute, EPRI RP 2556-48.

Silva, W.J., and Stark, C.L., 1992, Source, path, and site ground motion model for the 1989 M 6.9 Loma Prieta earthquake, Research Report prepared for the California Division of Mines and Geology.

Silva, W.J., Youngs, R.R., and Schneider, J.F., 1993, Observations of pervasive nonlinear soil response at deep, firm soil sites: Seismological Research Letters, v. 64, n. 1, p. 28.

Singh, S., and Herrmann, R.B., 1983, Regionalization of crustal coda Q in the continental United States: Journal of Geophysical Research, v. 88, p. 527-538.

Washington Public Power Supply System (WPPSS), 1988, Cascadia Subduction Zone, an evaluation of the earthquake potential and implications to WNP-3: Washington Public Power Supply System Response to U.S. NRC Questions 230.1 and 230.2.

Wyss, M., and Habermann, R.E., 1982, Conversion of m_b to M_s for estimating the recurrence time of large earthquakes: Bulletin of the Seismological Society of America, v. 72, no. 5, p. 1651-1662.

Youngs, R.R., Abrahamson, N.A., Makdisi, F., and Sadigh, K., 1993, Magnitude-dependent variance of peak ground acceleration: Paper submitted to the Bulletin of the Seismological Society of America.

Youngs, R.R., Day, S.M., and Stevens, J.P., 1988, Near field motions on rock for large subduction zone earthquakes, *in* Earthquake Engineering and Soil Dynamics II - Recent Advances in Ground Motion Evaluation: ASCE Geotechnical Special Publication 20, p. 445-462.

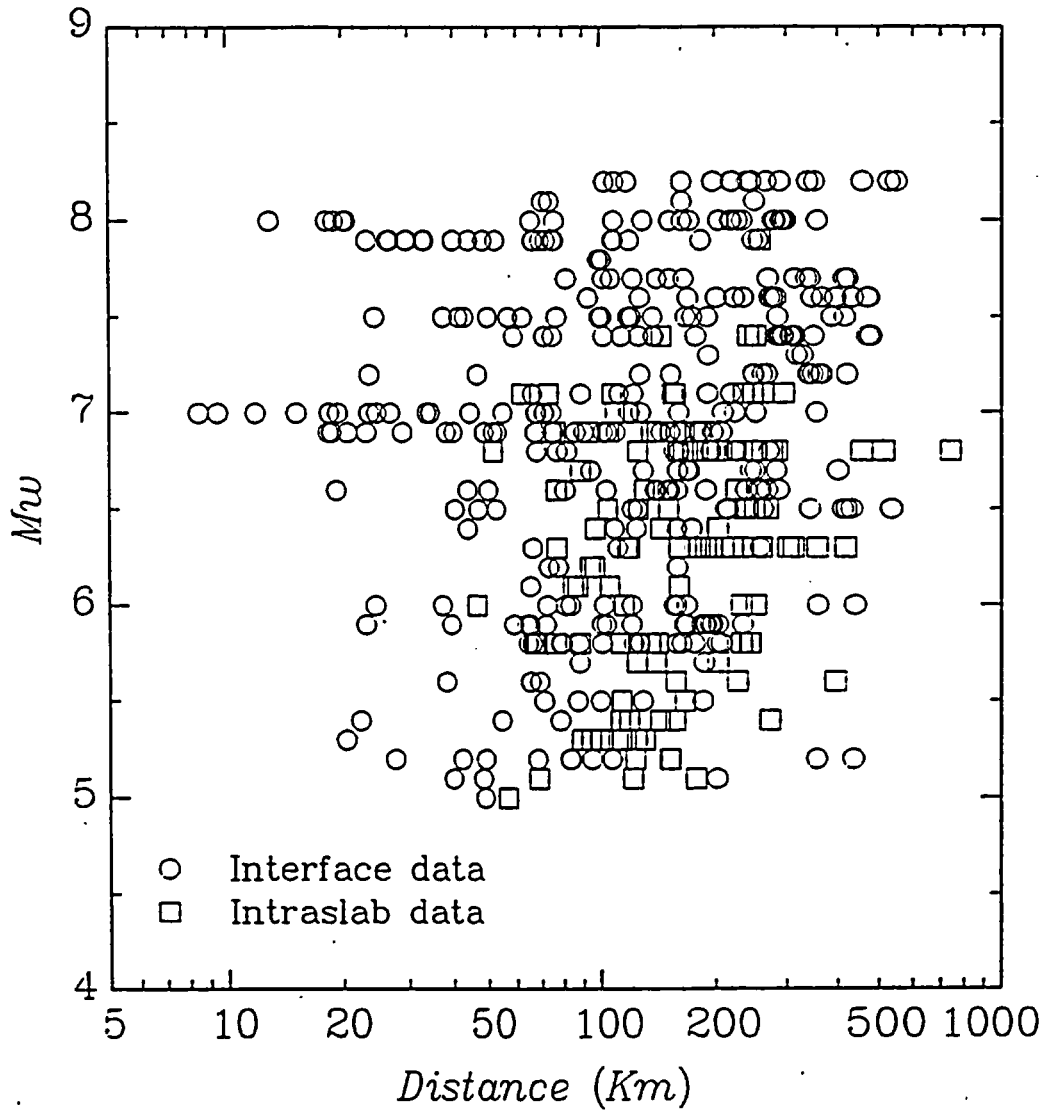

Figure 3-1 Distribution of strong motion data used in regression analysis of peak horizontal acceleration data.

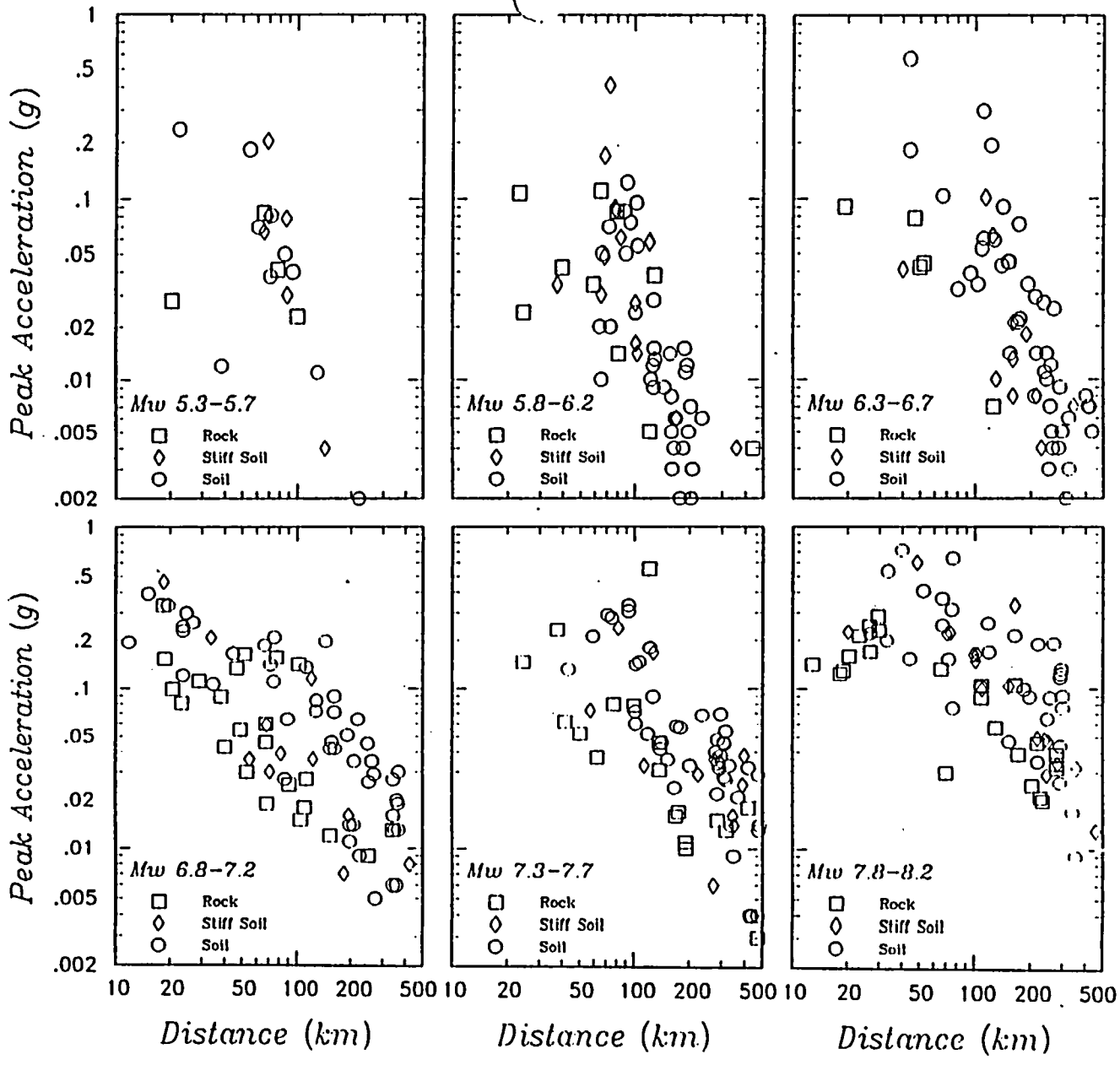

Figure 3-2a Recorded peak horizonal accelerations on rock, stiff soil, and soil sites for magnitude 5.3 to 8.0 interface earthquakes. Shown is the geometrical mean of the horizontal components.

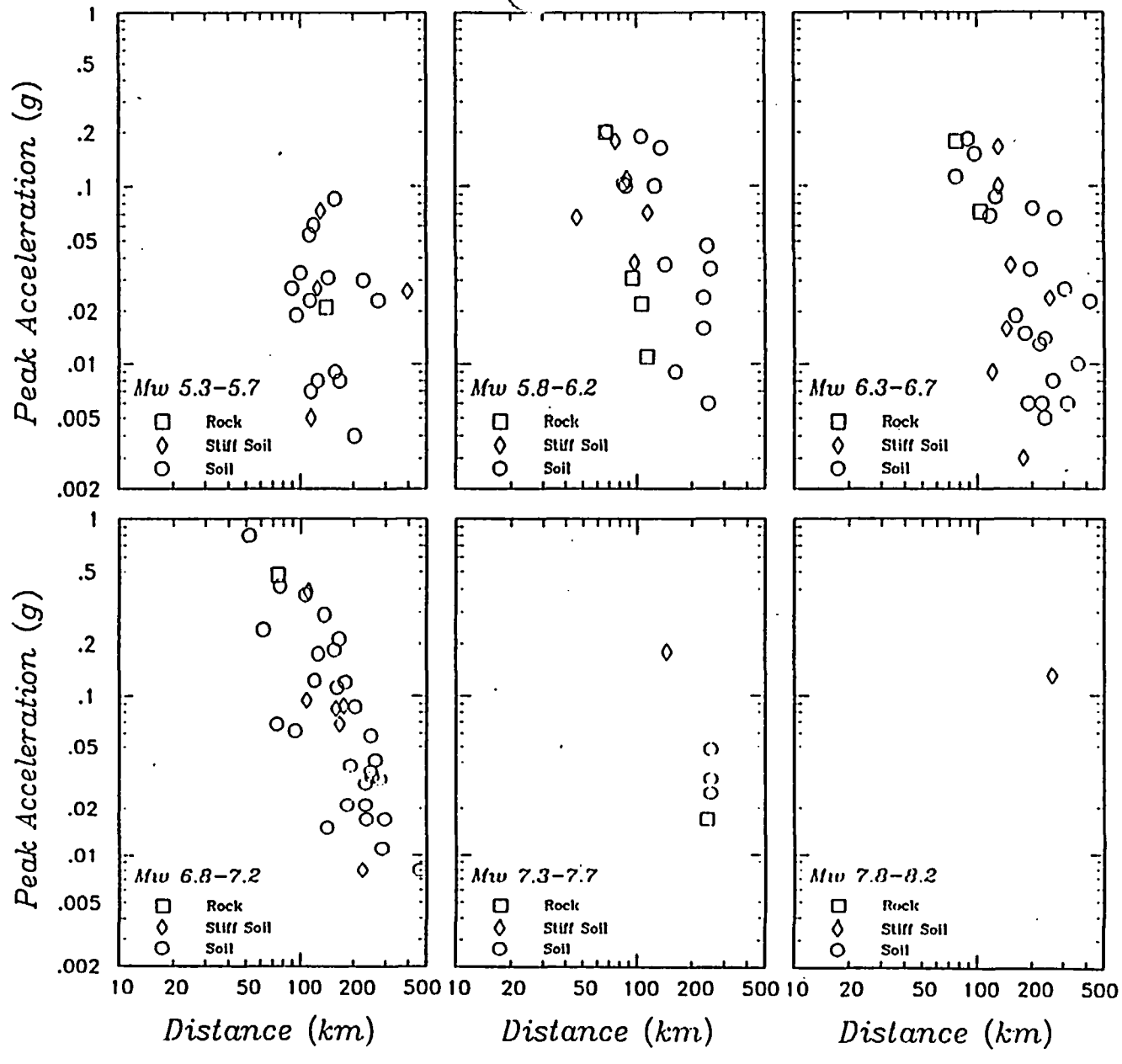

Figure 3-2b Recorded peak horizonal accelerations on rock, stiff soil, and soil sites for magnitude 5.3 to 8.0 intraslab earthquakes. Shown is the geometrical mean of the horizontal components.

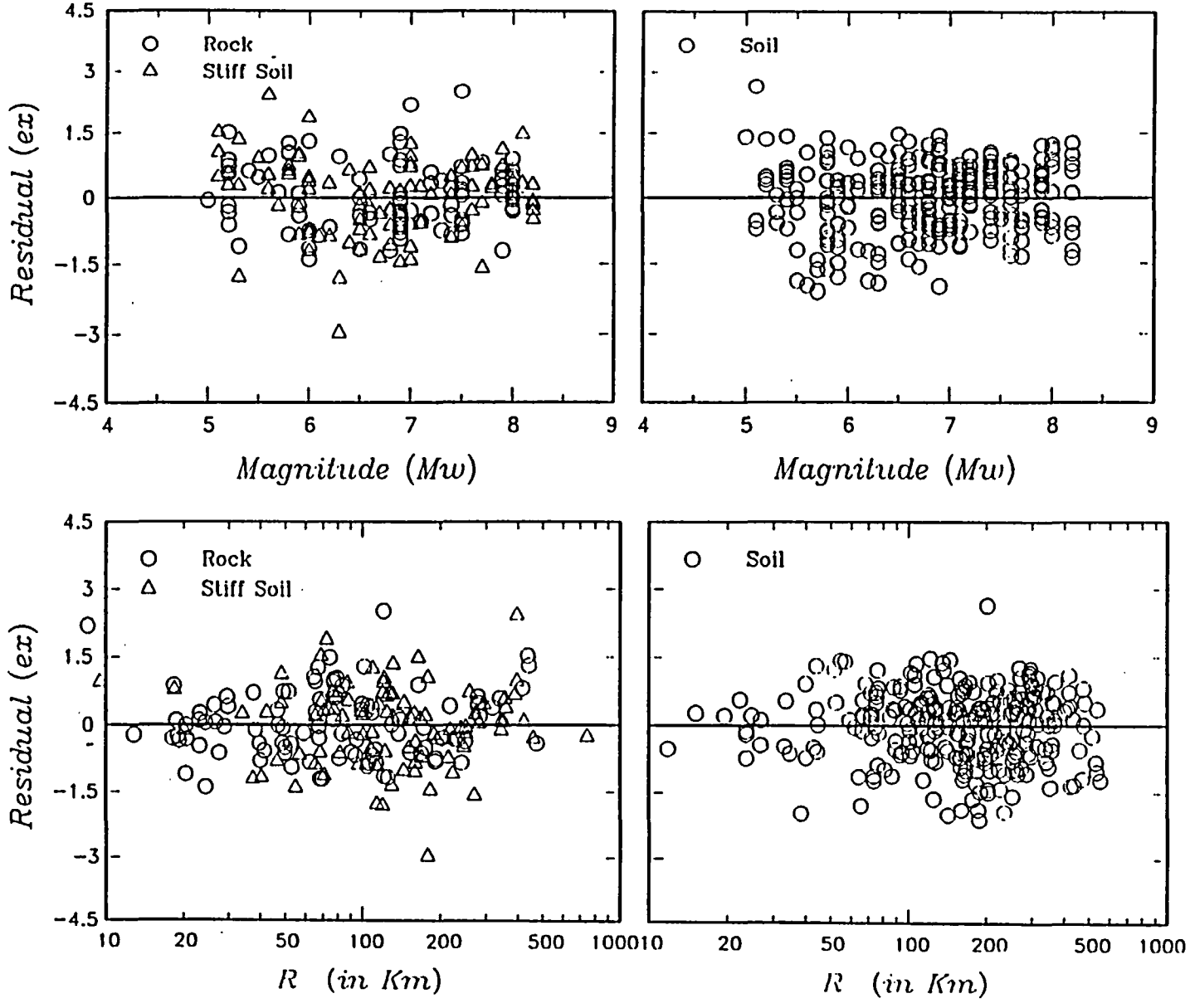

Figure 3-3 Residuals plotted against magnitude and distance for fit of Equation (3-1) to peak acceleration data.

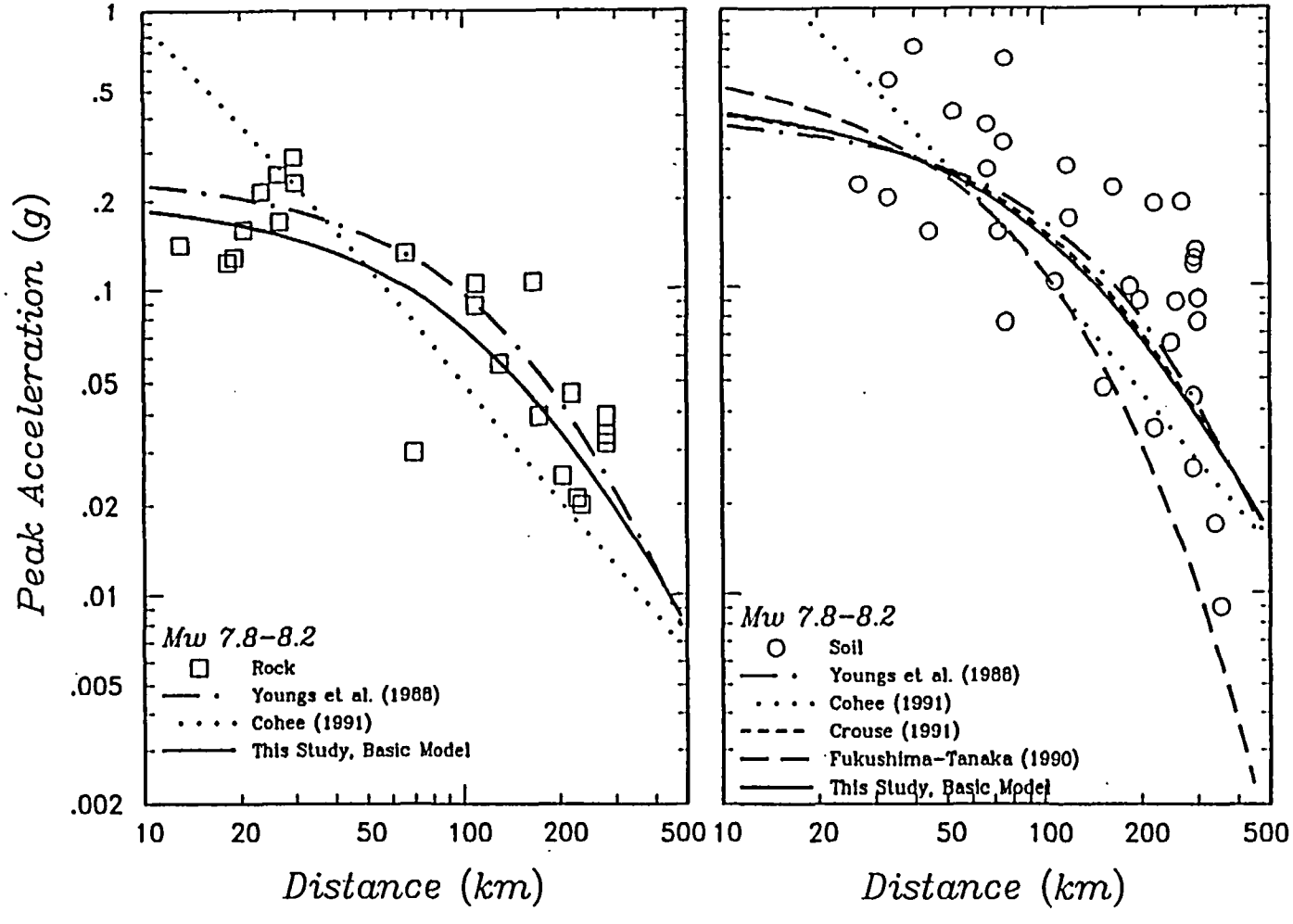

Figure 3-4 Comparison of fit of Equation (3-1) to magnitude M 8 interface earthquake rock and soil data with previous attenuation relationships.

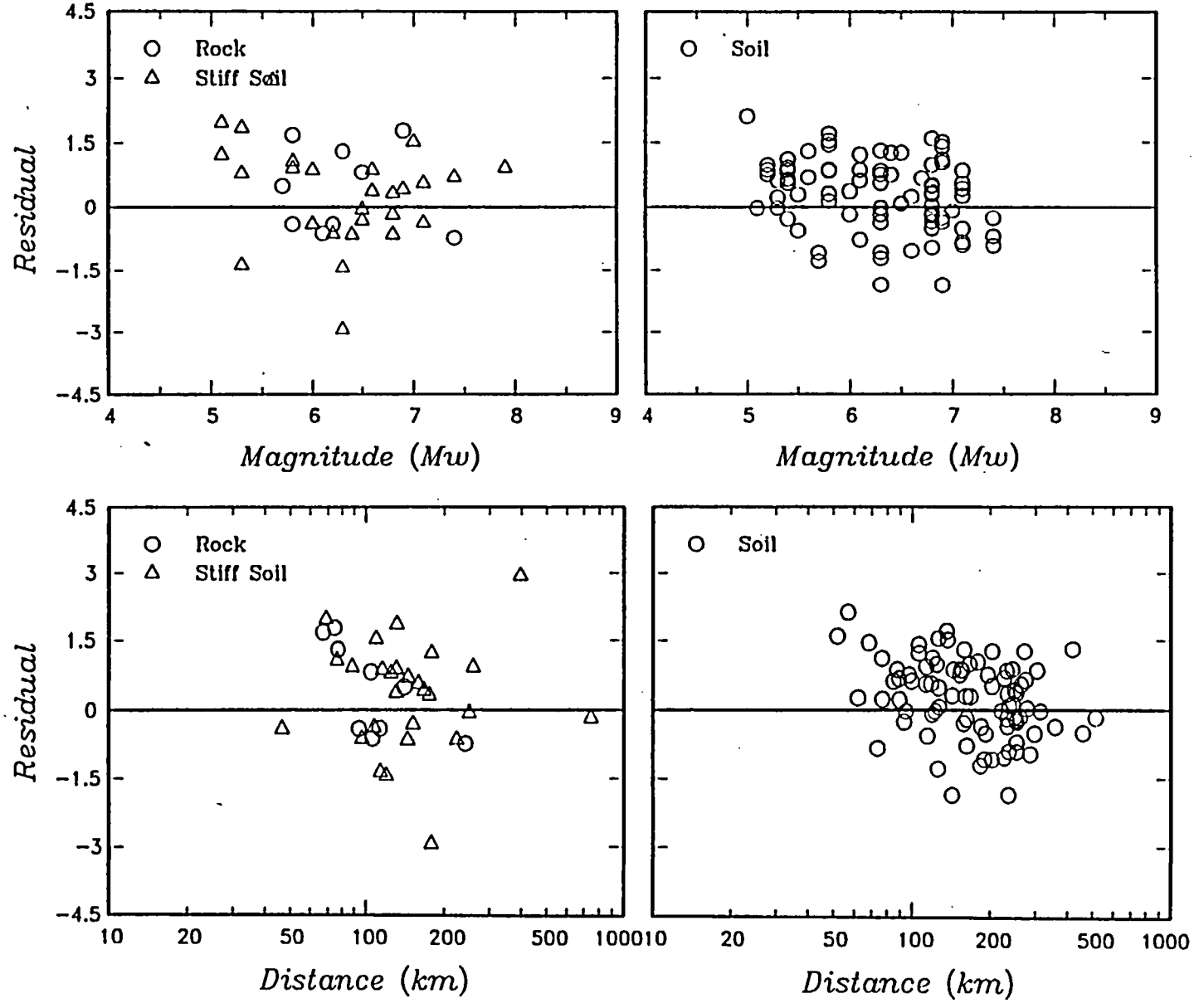

Figure 3-5 Residuals of intraslab data about attenuation relationship estimated from interface data alone.

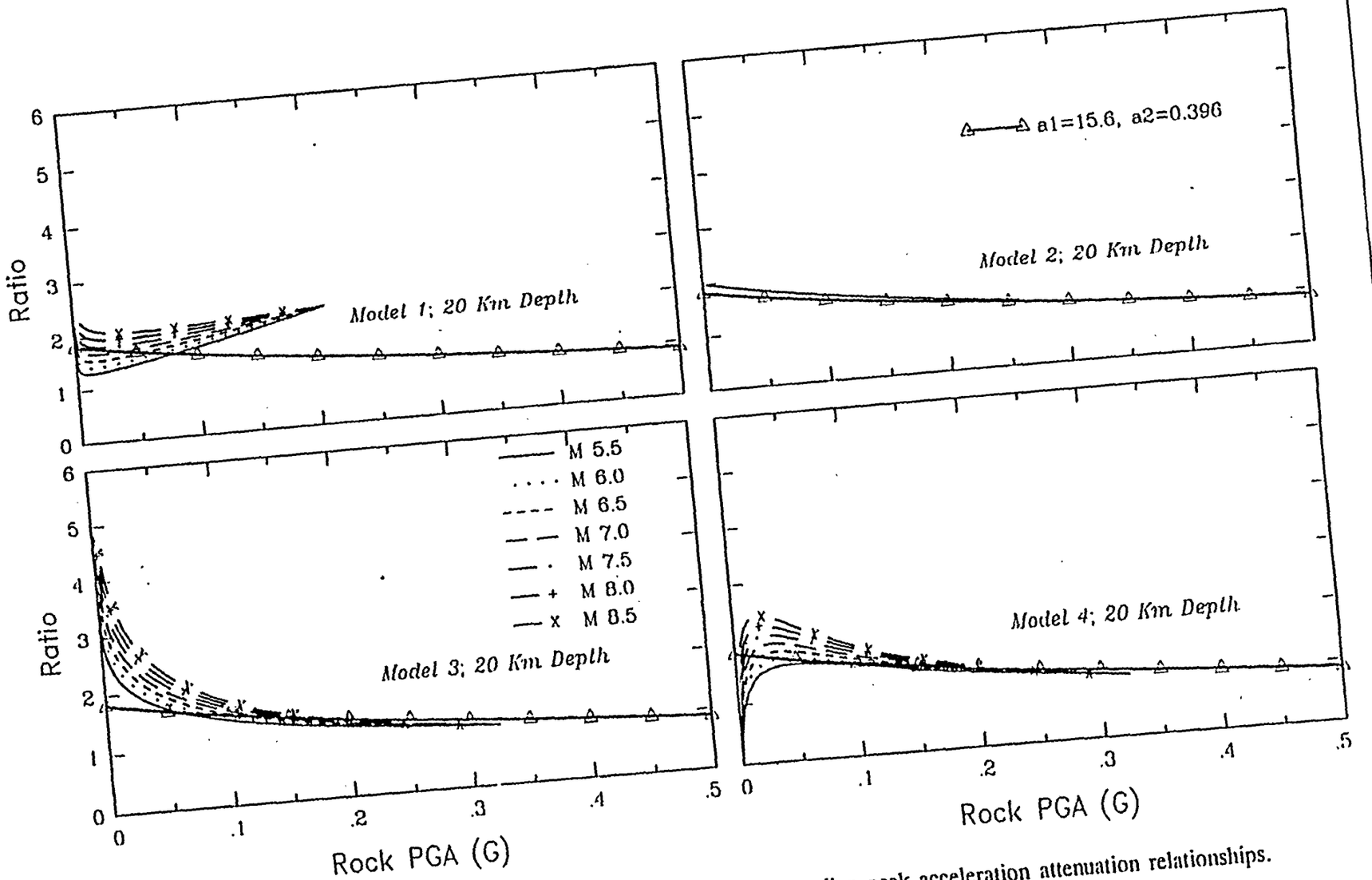

Figure 3-6 Soil/Rock amplification ratios based on the predicted median peak acceleration attenuation relationships. Triangles are the ratios from numerical modeling predictions shown on Figure 3-8.

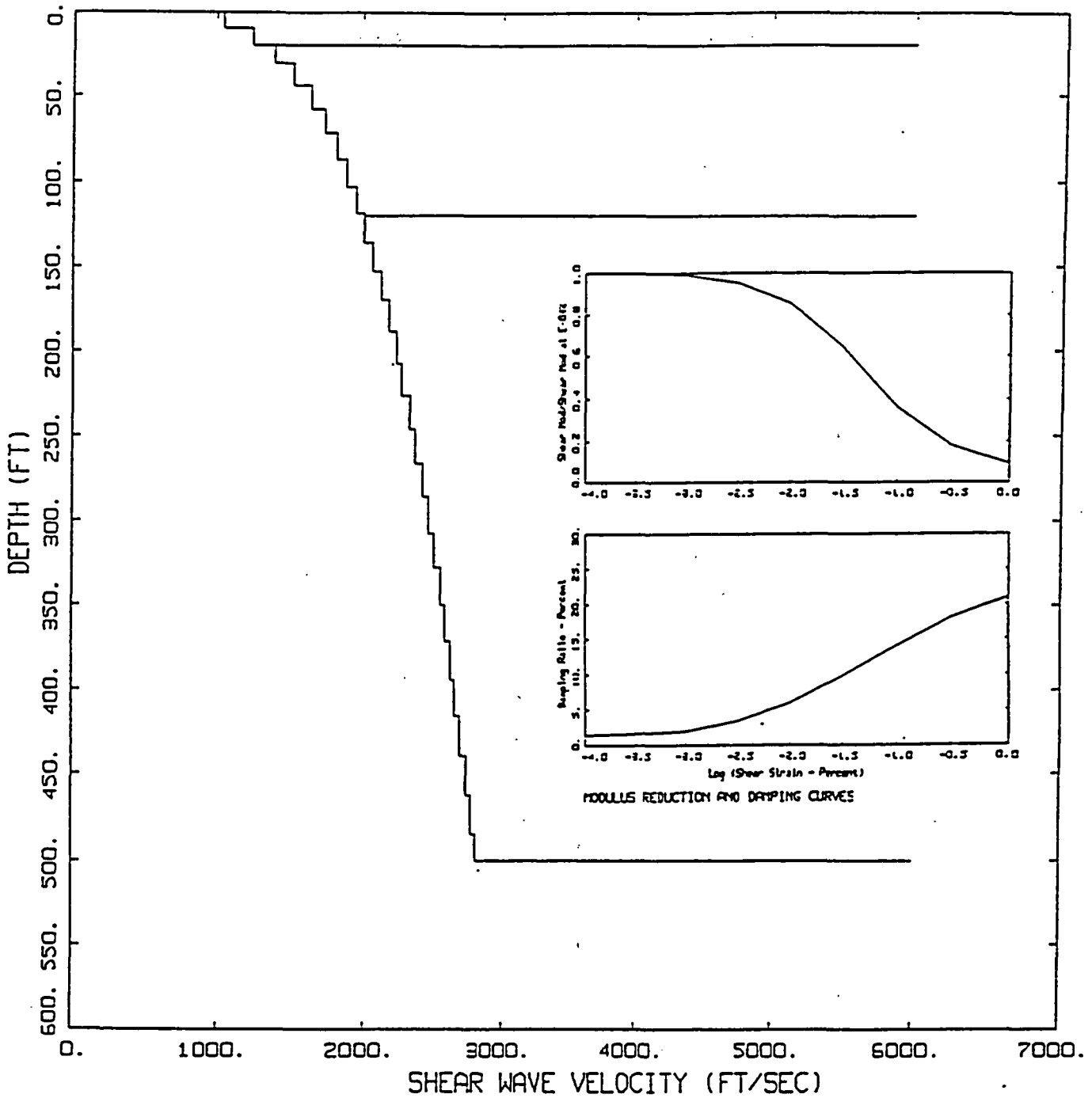

SHEAR WAVE VELOCITY PROFILE

Figure 3-7 Soil properties used in ground motion simulations.

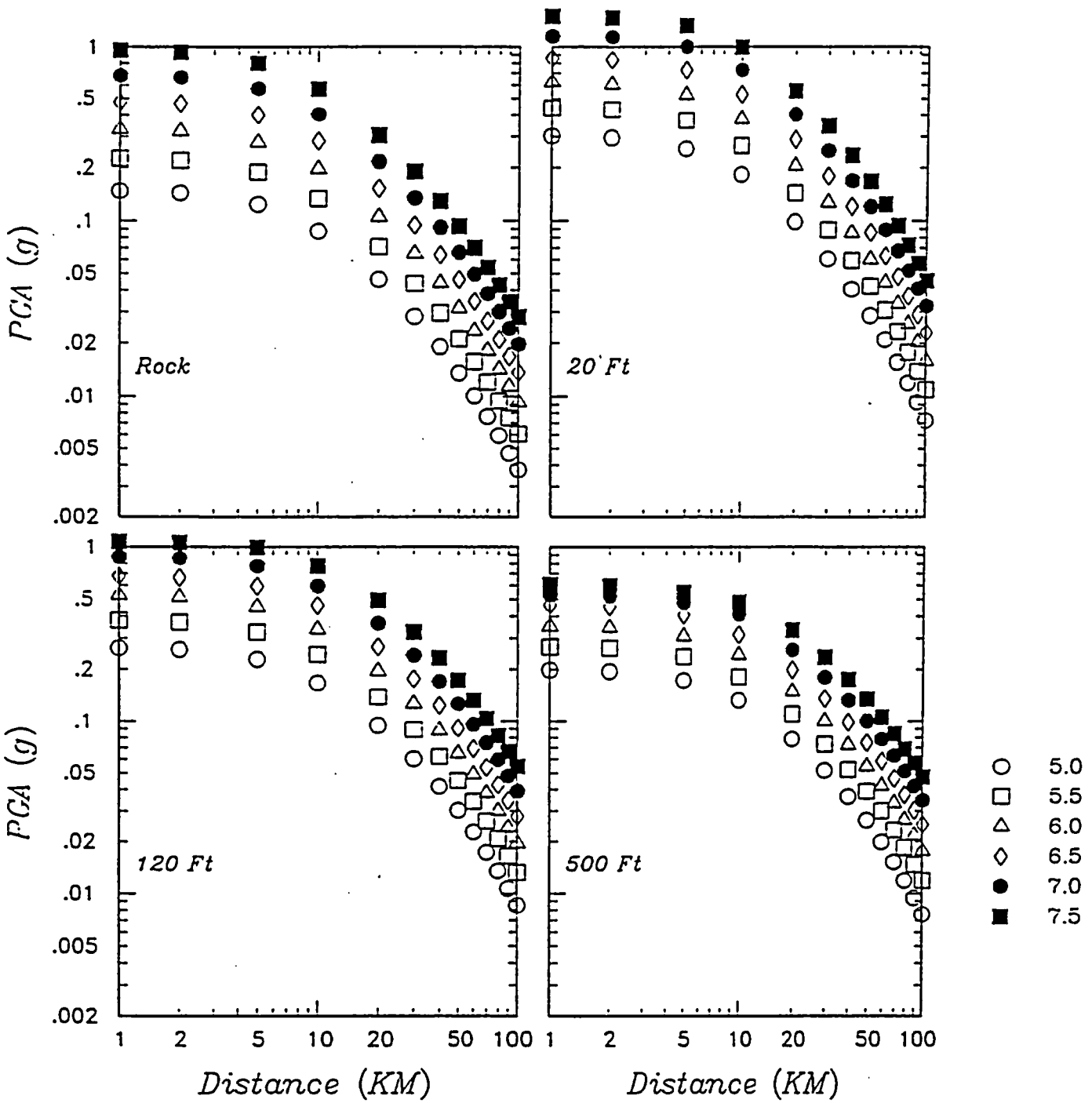

Figure 3-8 Predicted peak horizontal accelerations of magnitude 5.0 to 7.5 earthquakes based on point-source simulation model of Appendix C.

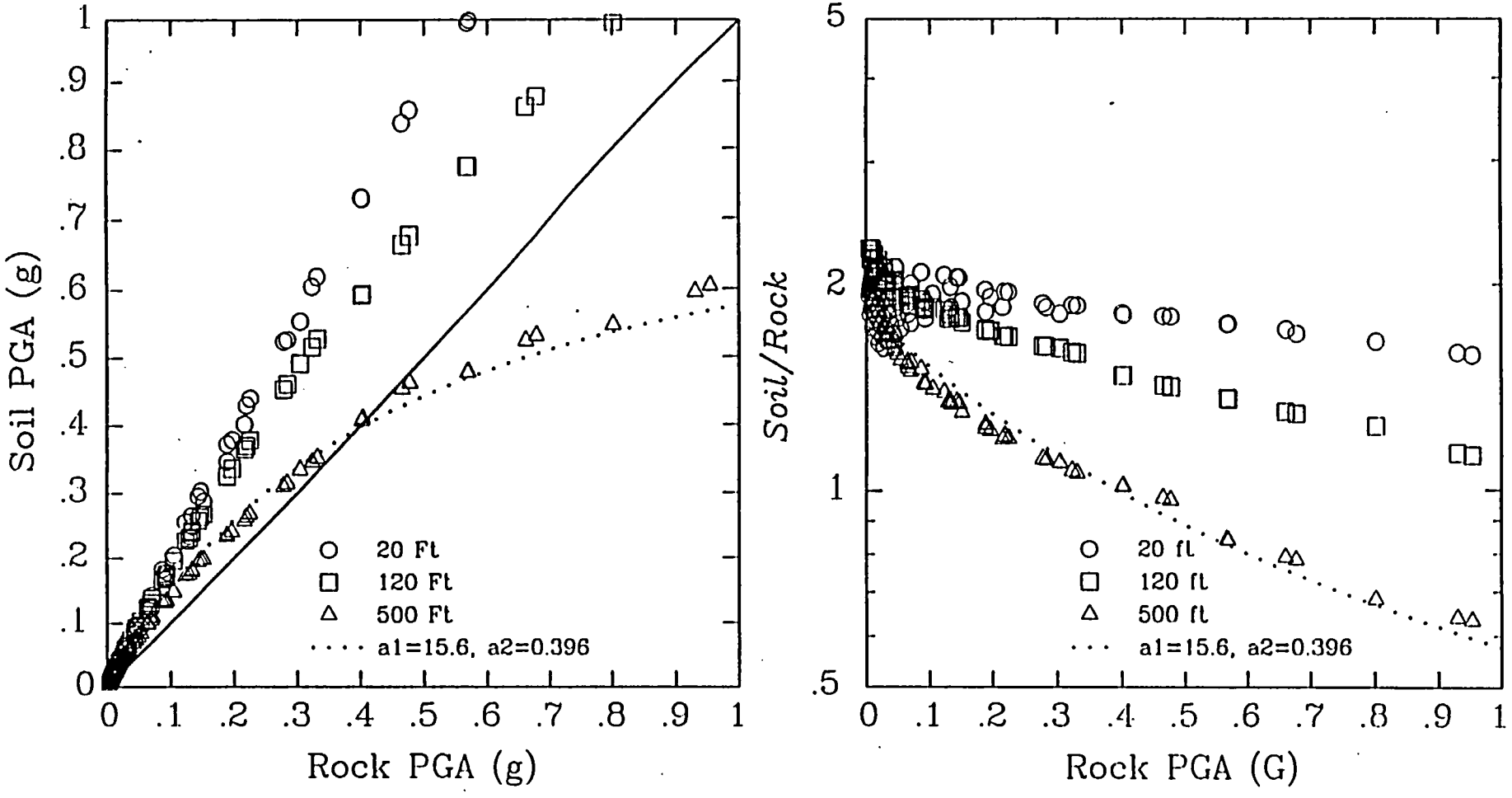

Figure 3-9 Left hand plot - predicted soil peak acceleration vs. predicted rock peak acceleration. Right hand plot - amplification factor vs. rock peak acceleration. Dotted lines are computed from the fit of amplification function in Model 2 to the 500 ft values shown in this figure. Data are from the BLWN-RVT simulations shown in Figure 8.

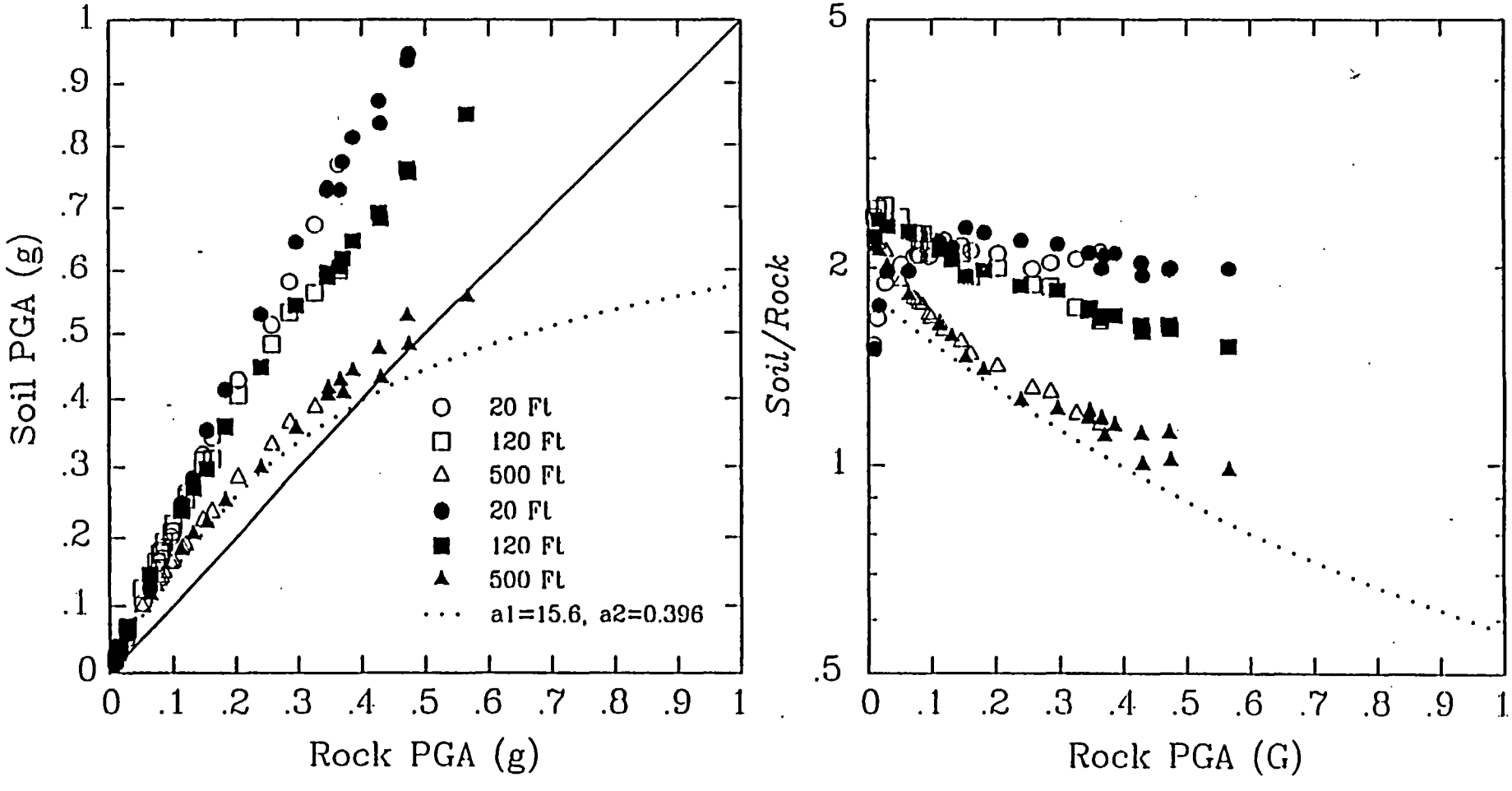

Figure 3-10 Left hand plot - simulated soil peak accelerations vs. rock peak accelerations for a M 8 subduction zone earthquake. Right hand plot - amplification factor vs. rock peak acceleration based on finite-fault simulations shown in (a). Dotted curves are results for point source model from Figure 3-9.

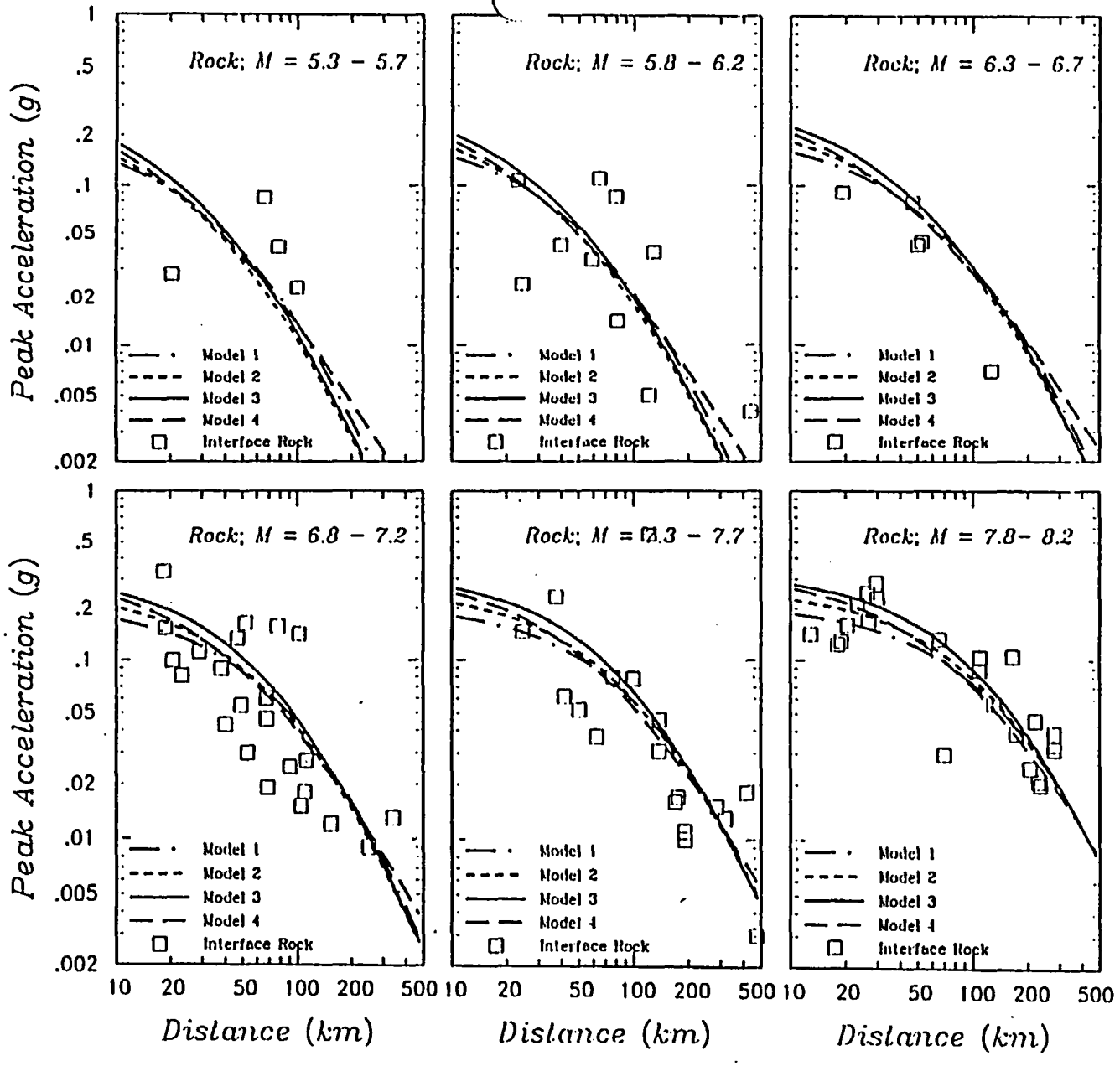

Figure 3-11a Comparison of the predicted median peak accelerations for Models 1, 2 3 and 4 for interface rock motions.

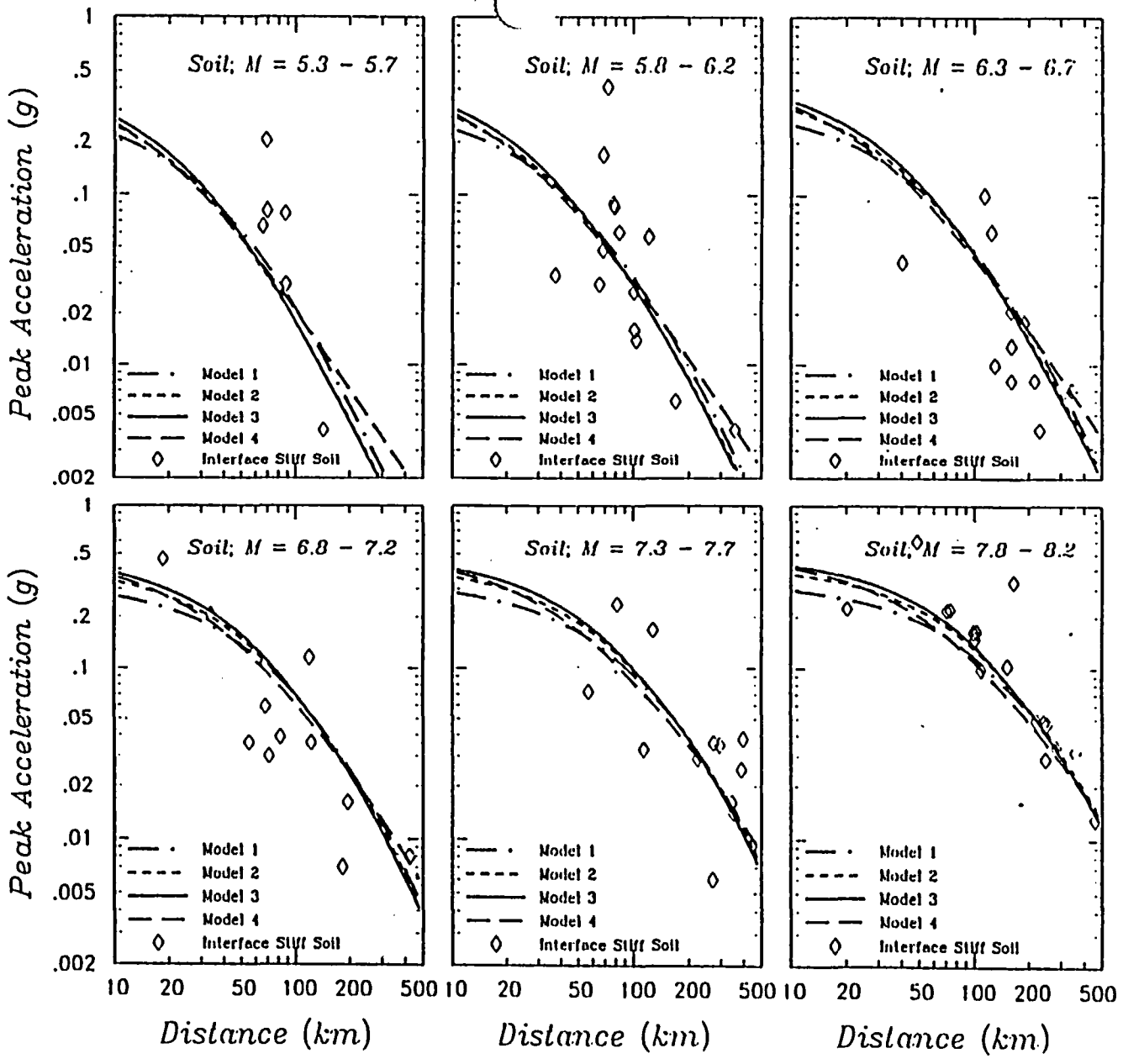

Figure 3-11b Comparison of the predicted median peak accelerations for Models 1, 2 3 and 4 for interface shallow stiff soil motions.

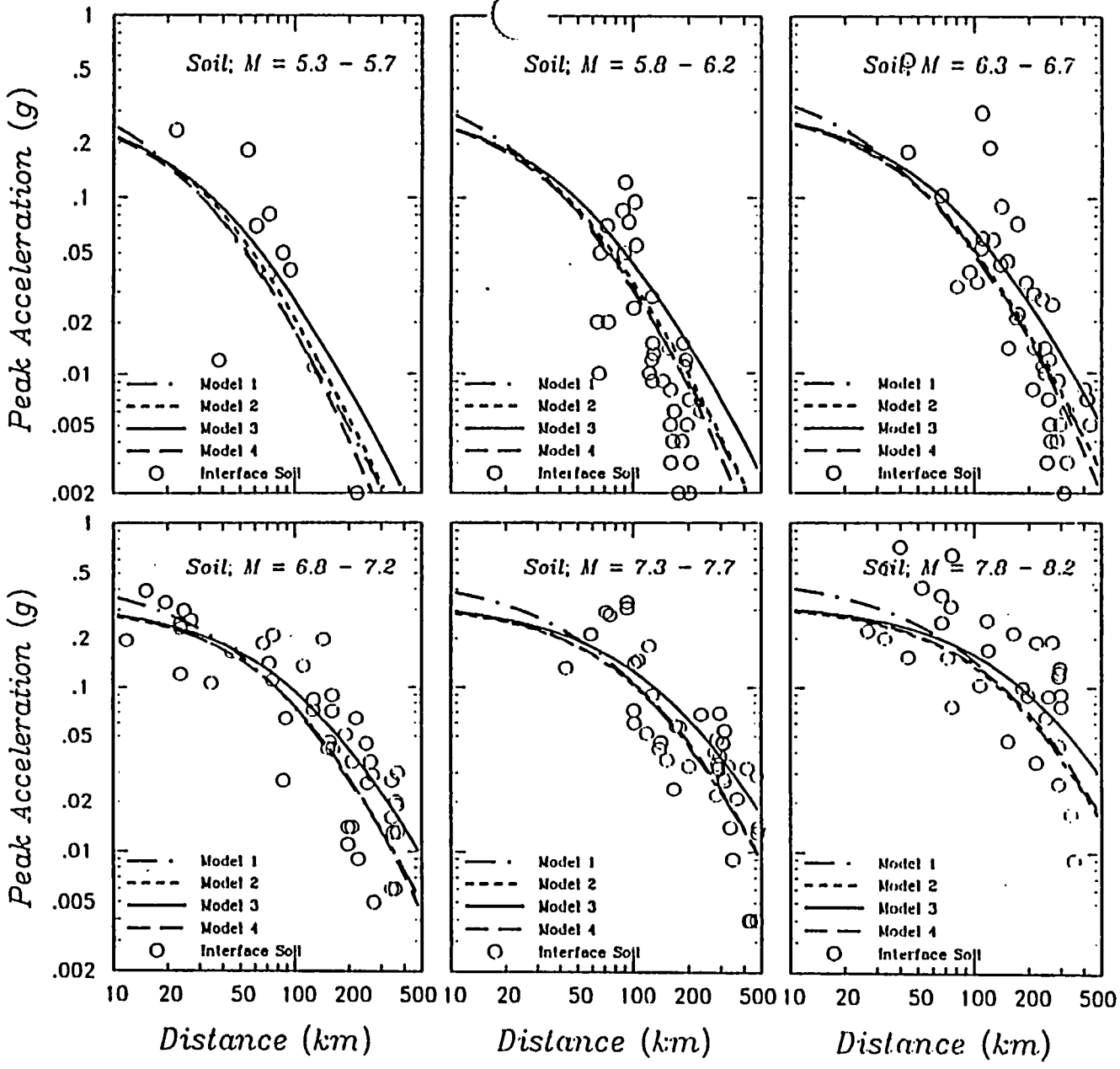

Figure 3-11c Comparison of the predicted median peak accelerations for Models 1, 2 3 and 4 for interface deep soil motions.

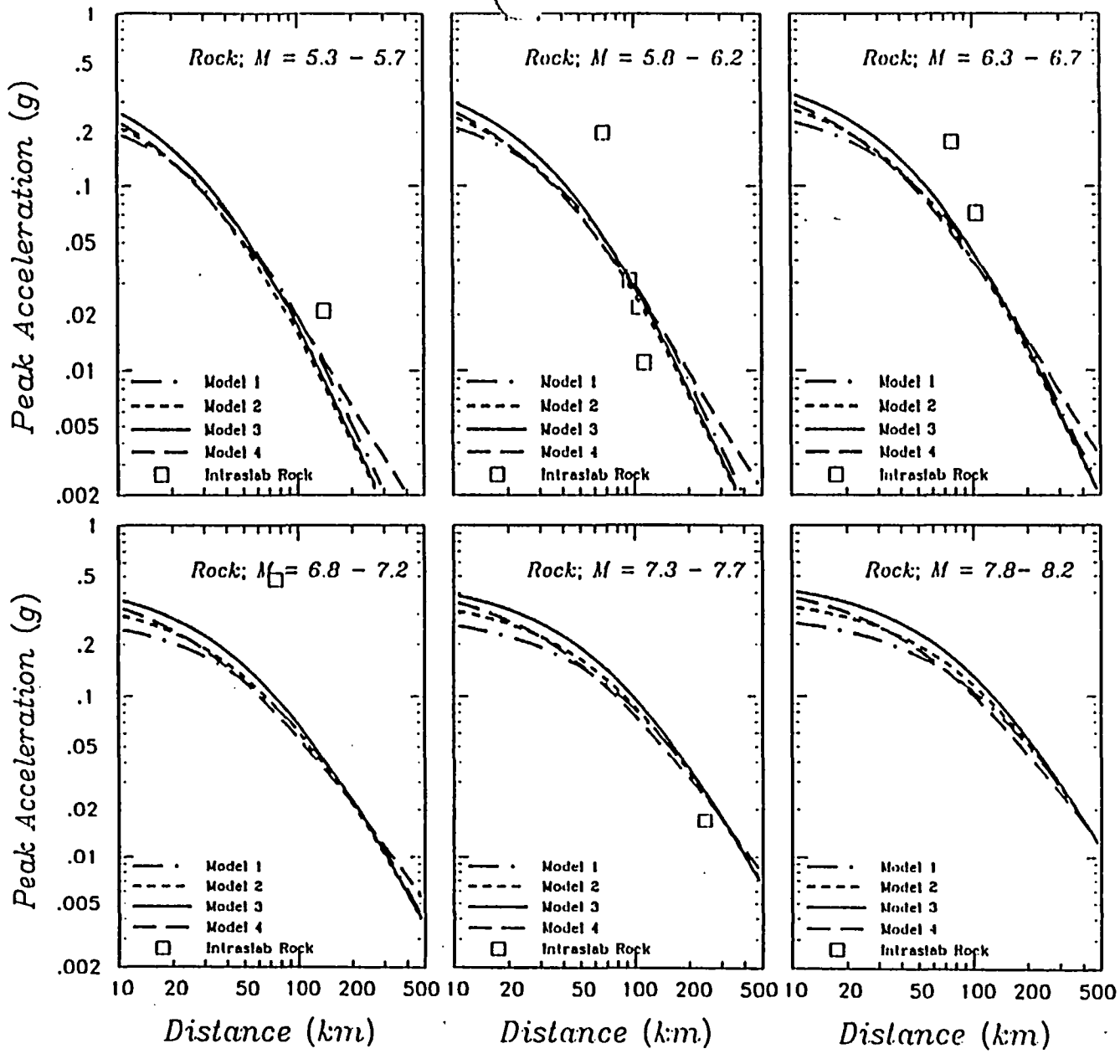

Figure 3-11d Comparison of the predicted median peak accelerations for Models 1, 2 3 and 4 for intraslab rock motions.

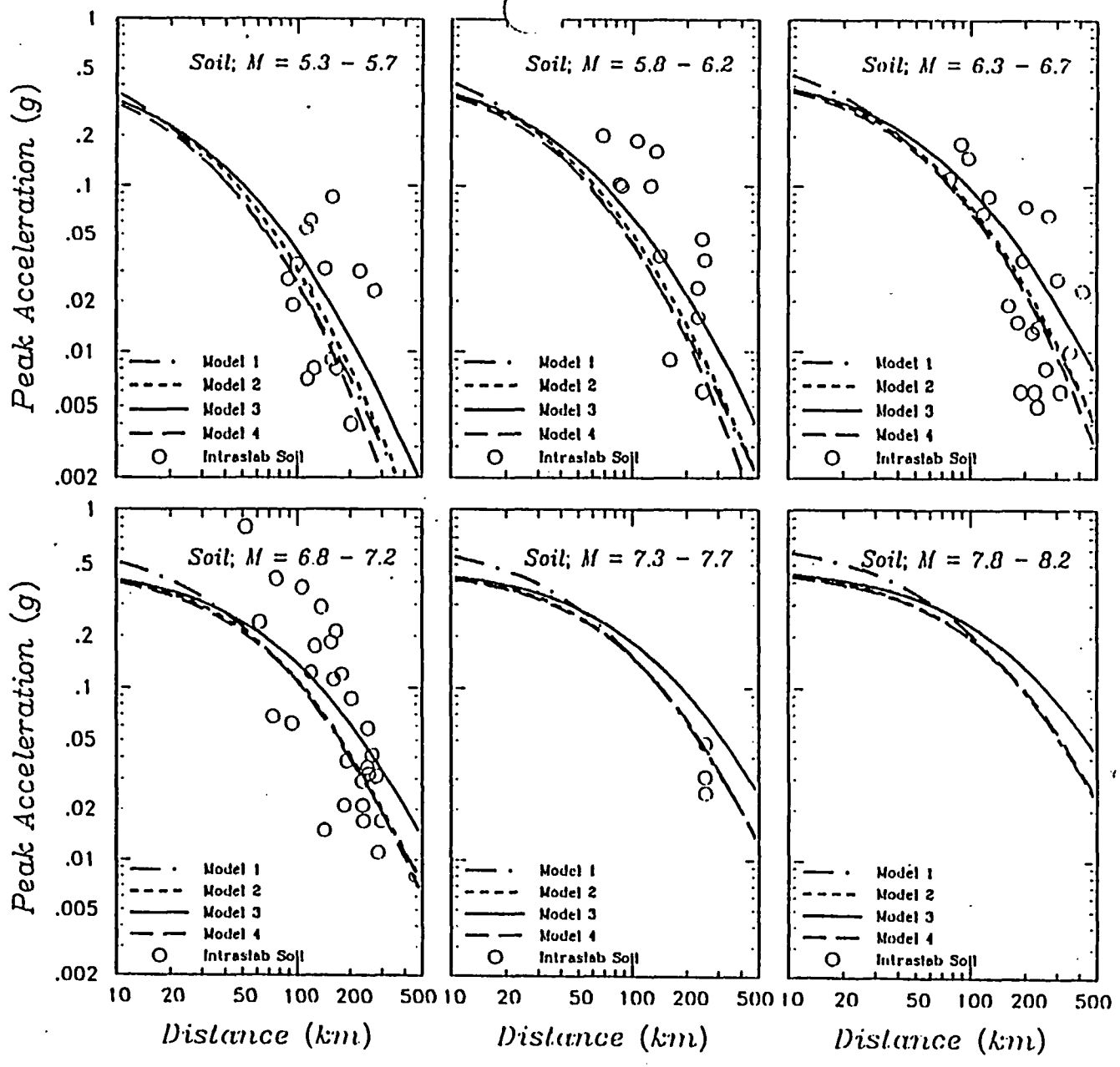

Figure 3-11e Comparison of the predicted median peak accelerations for Models 1, 2 3 and 4 for intraslab shallow stiff soil motions.

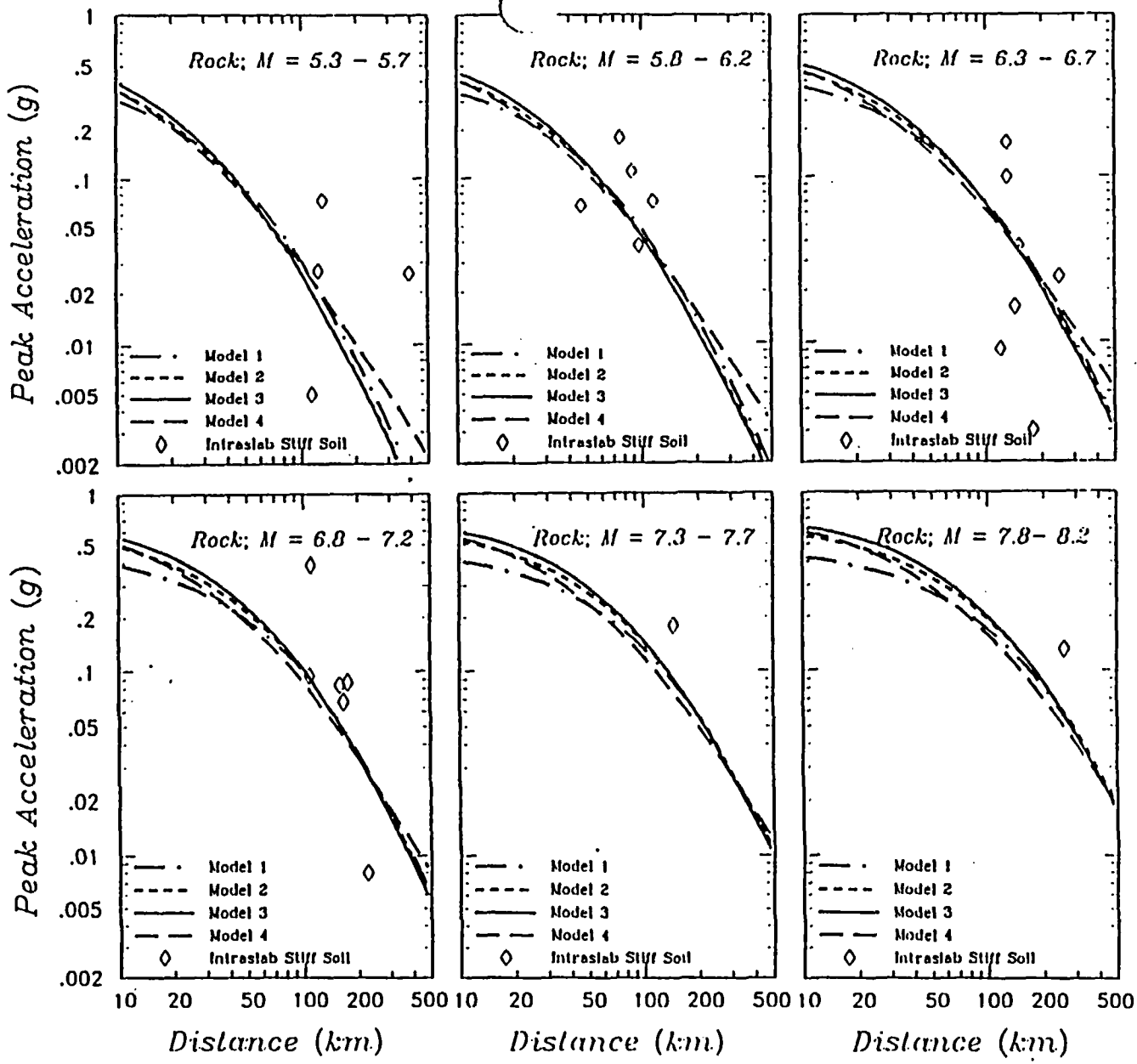

Figure 3-11f Comparison of the predicted median peak accelerations for Models 1, 2 3 and 4 for intraslab deep soil motions.

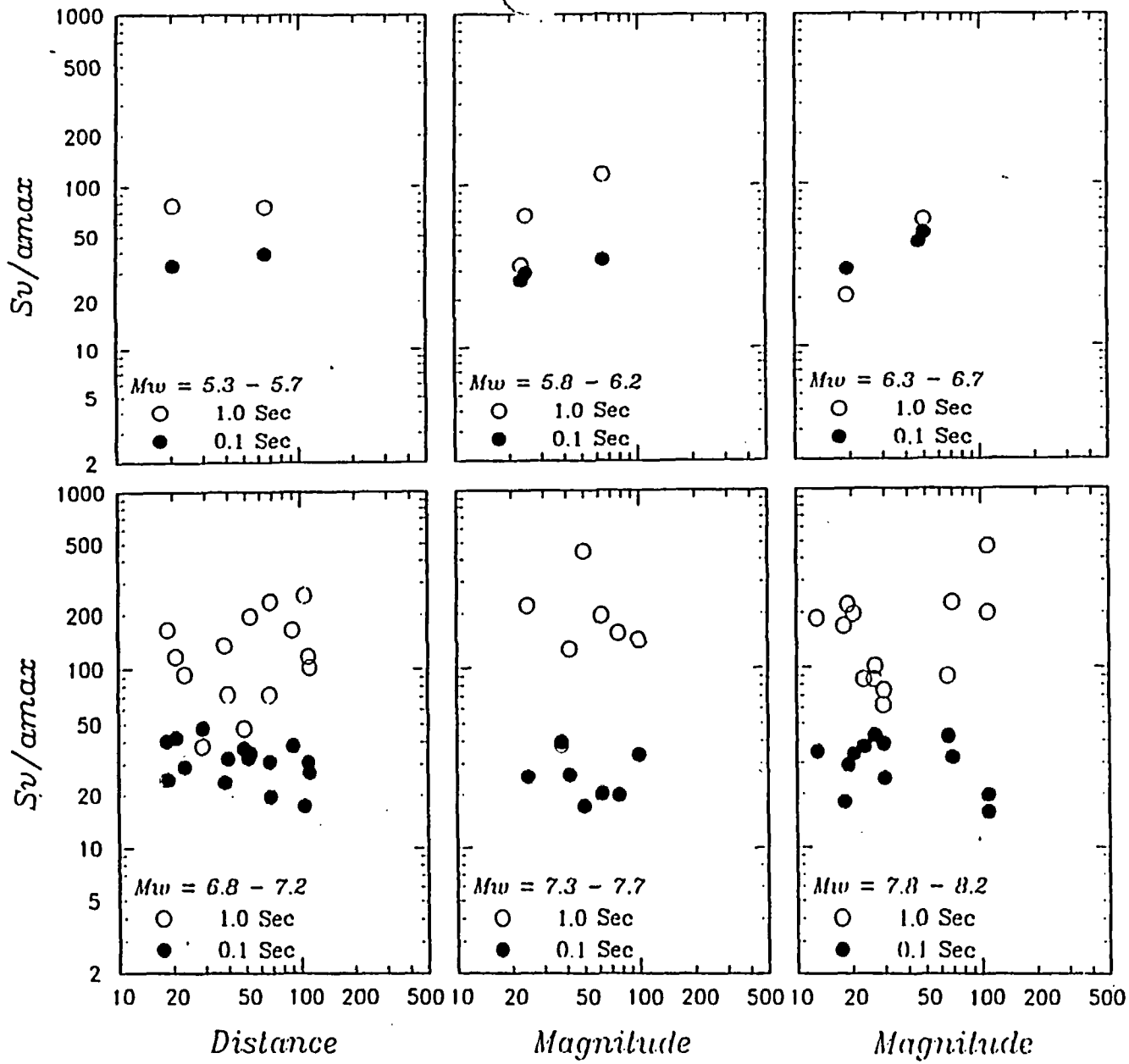

Figure 3-12 Ratio Sv/a_{max} on rock from interface event for 1.0 and 0.1 sec periods.

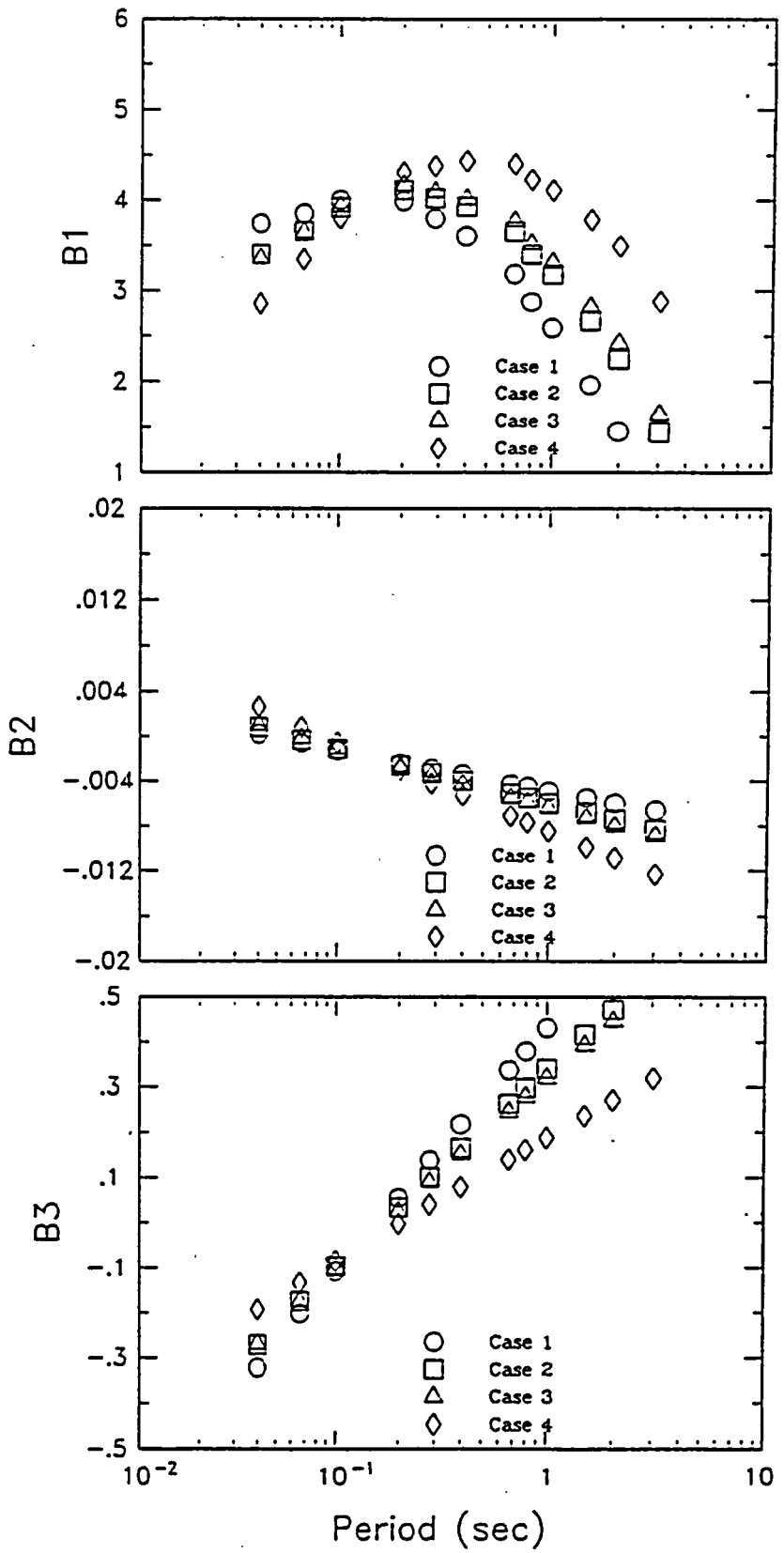

Figure 3-13 Estimated values of B_1, B_2, and B_3 for the Sv/a_{max} relation.

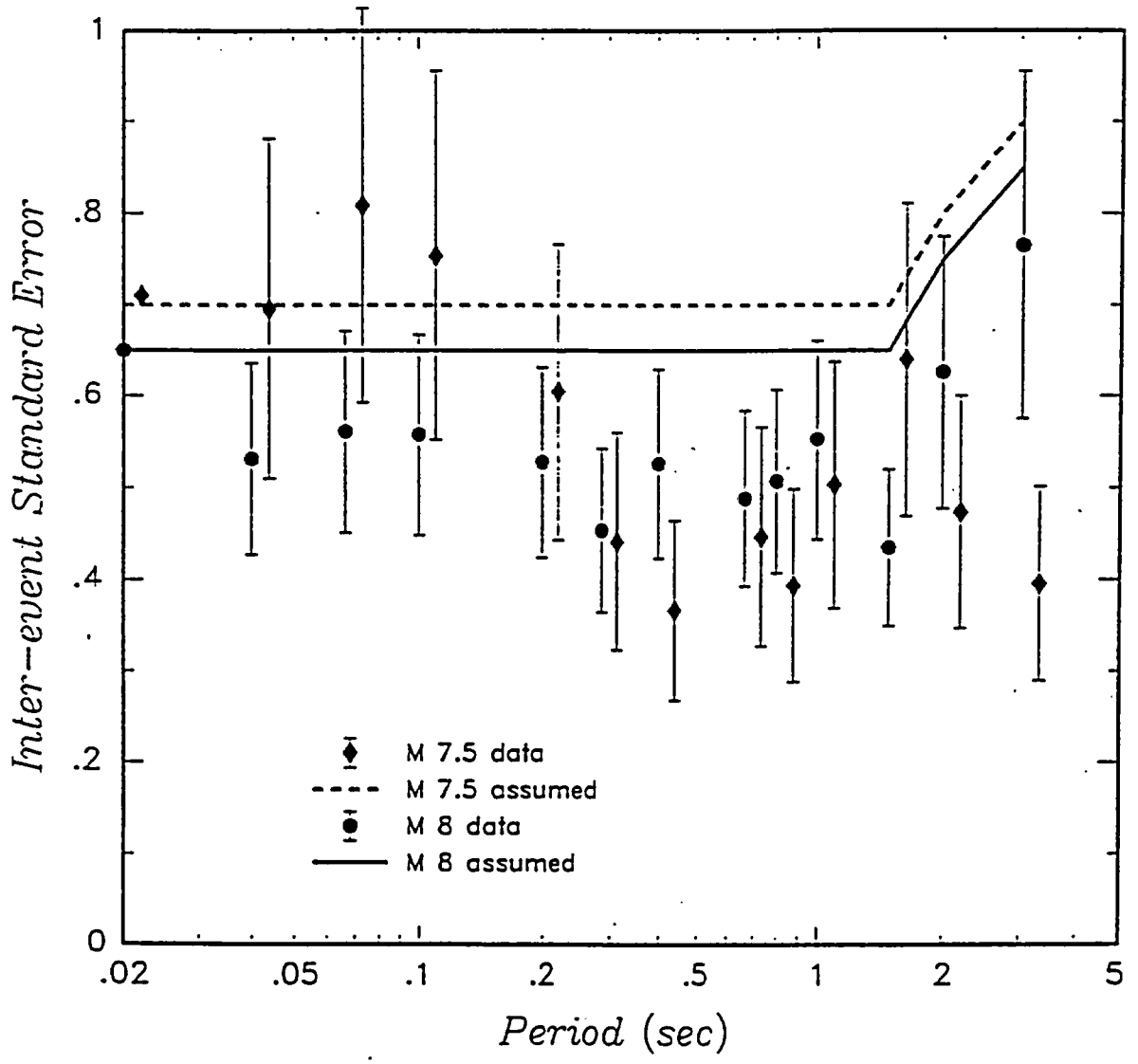

Figure 3-14 Standard error as a function of period and magnitude used to compute 84th-percentile ground motions. Points with error bars show estimated computed from response spectral ordinates for magnitude 7.5$\pm$0.2 and magnitude 8$\pm$0.2 events. Curves show selected relationships.

Appendix C from Geomatrix (1993)

NUMERICAL SIMULATION OF STRONG GROUND MOTION USING THE STOCHASTIC GROUND MOTION MODEL FOR SUBDUCTION EARTHQUAKES

INTRODUCTION

The estimation of strong ground motion, particularly at close distances to large magnitude earthquakes is a difficult task. Until recently, only empirical approaches could be reliably used to specify median values and to provide estimates of uncertainty. Early numerical methods were notoriously cumbersome and highly dependent upon a large number of poorly characterized parameters. As a result, ground motion predictions based on these numerical modeling techniques suffered from generally poor and unquantified reliability. Due to computational limitations, results based on these methods were generally non site-specific such that the effects of the shallow crustal properties as well as soil profiles were not directly modeled. In addition, as a result of being highly sensitive to poorly known parameters as well as having large computational demands, the uncertainties of predicted motions due to parameter uncertainties and possible model bias were left largely unquantified.

Recently however, a new ground motion model has been introduced that characterizes strong ground motions as stochastic in time, with a Fourier amplitude spectrum specified by a fundamentally simple and deterministic seismological model of the source, path, and site (Hanks and McGuire, 1981; Boore, 1983, 1986; Silva, 1991). An essential and significant aspect of the new model is that, while being extremely simple, it also provides estimates of strong ground motions with remarkable accuracy. Additional, but important, side benefits arising from the model's simplicity are the natural separation of source, path, and site effects and the accompanying computational efficiency. As a result, an accurate appraisal of the effects of uncertainties in source, path, and site parameters as well as any model bias can be readily quantified.

POINT SOURCE GROUND MOTION MODEL

The stochastic ground motion model (sometimes referred to as the Band-Limited-White-Noise or BLWN model), in which the energy is distributed randomly over the duration of the source, has proven remarkably effective in correlating with a wide range of ground motion observations. Time-domain measures such as peak acceleration and peak particle velocity, Wood-Anderson magnitude, and short-period P- and S-wave amplitudes as well as frequency-domain measures such as relative velocity response and Fourier amplitude spectra, have been predicted with reasonable accuracy (Hanks and McGuire, 1981; Boore, 1983, 1986; Boore and Atkinson, 1987; Silva and Lee, 1987; Toro and McGuire, 1987; Silva and Darragh, 1992). The ground motion model employed here uses an ω-square Brune source model (Brune, 1970; 1971) with a single corner frequency and a constant stress drop (Boore, 1983; Atkinson, 1984) (Figure C-1).

The acceleration spectral density a(f), where f is frequency, is given by

$$a(f) = C \frac{f^2}{1+ (f / f_c)^2} \frac{M_0}{R} P(f) A(f) e^{-\frac{\pi f R}{\beta_0 Q(f)}} \qquad \text{(C-1)}$$

where

M_o	=	Seismic moment
R	=	Distance to the equivalent point source
β_o	=	Shear-wave velocity at the source
Q(f)	=	$Q_0 f^{\eta}$, frequency-dependent quality factor model where Q_0 and η are model parameters
A(f)	=	Near-surface amplification factors
P(f)	=	High-frequency truncation filter
f_c	=	Source corner frequency and
C	=	$(1/\rho_o\beta_o^3)$ x (2) x (0.55) x ($1/\sqrt{2}$) x π.

C is a constant which contains source-region density ρ_s and shear-wave velocity terms and accounts for the free-surface effect (factor of 2), the source radiation pattern averaged over a sphere (0.55) (Boore, 1986), and the partition of energy into two horizontal components ($1/\sqrt{2}$).

Source scaling is provided by specifying two independent parameters, the seismic moment (M_o) and the stress drop ($\Delta\sigma$) (Figure C-1). The seismic moment is related to magnitude through the definition of moment magnitude M by the relation

$$\log M_0 = 1.5\ M + 16.1 \qquad \text{(Hanks and Kanamori, 1979)} \qquad \text{(C-2)}$$

The stress drop $\Delta\sigma$ relates the corner frequency f_c to M_0 through the relation

$$f_c = \beta_s\ (\Delta\sigma/8.44\ M_o)^{1/3} \qquad \text{(Brune, 1970; 1971)} \qquad \text{(C-3)}$$

The spectral shape of the single-corner-frequency ω-square source model is then described by the two free parameters M_o and $\Delta\sigma$. The corner frequency increases with the shear-wave velocity and with increasing stress drop, both of which may be region dependent.

In order to compute peak time-domain values, i.e., peak acceleration, peak particle velocity, and peak oscillator response, random vibration theory (RVT) is used to relate RMS calculations to peak value estimates (Boore, 1983; Boore and Joyner, 1984).

POINT SOURCE MODEL PARAMETERS

In a half-space model, the near-surface amplification factors, $A(f)$, account for the increase in amplitude as the seismic energy travels through lower-velocity crustal materials near the surface (Figure C-1) (Boore, 1986; Silva and Darragh, 1992). These factors depend on average crustal and near-surface shear-wave velocity and density.

The P(f) filter models the observation that acceleration spectral density appears to fall off rapidly beyond some region-dependent maximum frequency. This observed phenomenon truncates the high-frequency portion of the spectrum and is responsible for the band-limited nature of the stochastic model. This spectral fall-off has been attributed to near-site attenuation (Hanks, 1982; Anderson and Hough, 1984) or to source processes (Papageorgiou and Aki, 1983) or perhaps to both effects. Hanks (1982) termed the phrase f_{max} to describe this site-dependent corner frequency. In the Anderson and Hough (1984) attenuation model, which is adopted in this study, the form of the P(f) filter is taken as

$$P(f) = e^{-\pi\kappa(0)f} \qquad \text{(C-4)}$$

$\kappa(0)$ is a site- and distance-dependent parameter (here taken at r=0) that represents the effect of intrinsic attenuation on the seismic waves as they propagate through the crust from source to receiver (Figure C-1). Kappa depends on epicentral distance (r) and on both the shear-wave velocity (β_R) and quality factor (Q_s) averaged over a depth of H beneath the receiver or site. At zero epicentral distance, κ is given by

$$\kappa(0) = \frac{H}{\overline{\beta_R}\ \overline{Q_s}} \qquad \text{(C-5)}$$

The value of $\kappa(0)$ is attributed to attenuation in the very shallow crust directly beneath the site (Hough and Anderson, 1988). Silva and Darragh (1992) suggest that the predominant kappa effects extend from the surface down to several hundred meters and possibly as deep as 1 to 2 km. The intrinsic attenuation along this part of the path is thought to be frequency-independent, but site-dependent (Hough et al., 1988). Kappa has been determined for several rock and soil sites representative of western North America (WNA) (Anderson and Hough, 1984; Anderson et al., 1986). For an average WNA rock site, a value between 0.02 and 0.06 sec is appropriate (Boore, 1986; Silva and Darragh, 1992). For eastern North America, a

stable continental interior with generally older and stronger crustal rocks, average kappa values range from about 0.004 sec to about 0.01 sec (Silva and Darragh, 1992).

The crustal anelastic attenuation from the source to just below the site is modeled with the frequency-dependent quality factors $Q(f)$. Geometrical attenuation is taken as $1/R$ (or $1/\sqrt{R}$ for distances greater than about 100 km). In order to accommodate the effects of direct and supercritically-reflected waves in a crustal structure, this simple geometrical attenuation can be replaced by a formulation due to Ou and Herrmann (1990). With this technique, the geometrical attenuation and duration for direct plus post-critical reflections may be computed in a manner appropriate to the BLWN-RVT model.

The Fourier amplitude spectrum, $a(f)$, models direct shear waves in a homogeneous half-space (with effects of a velocity gradient through the $A(f)$ transfer function). For vertically heterogenous layered structures, the plane-wave propagators of Silva (1976) are used to propagate SH or P-SV motion through the layered structure.

To model an average horizontal component, the computed Fourier amplitude spectrum (Equation C-1) is input as outcrop motion at the top of the source layer using the SH propagators. Normal incidence is assumed and the crust is taken as elastic with damping accommodated in the $Q(f)$ and kappa factors.

For fixed magnitude (moment) and distance, specific source, path, and site parameters are stress drop ($\Delta\sigma$), crustal damping ($Q(f)$), crustal shear-wave velocity profile, and kappa (κ). These represent the point-source ground-motion parameters for a rock site.

FINITE SOURCE MODEL GROUND MOTION MODEL

In the near-source region of large earthquakes, aspects of a finite source including rupture propagation, directivity, and source-receiver geometry can be significant and may be incorporated into strong ground motion predictions. To accommodate these effects, a

methodology that combines the aspects of finite-earthquake-source modeling techniques (Hartzell, 1978) with the BLWN-RVT point-source ground motion model has been developed to produce response spectra as well as time histories appropriate for engineering design (Silva et al., 1990; Silva and Stark, 1992). The approach is very similar to the empirical Green function methodology introduced by Hartzell (1978) and Irikura (1983). In this case however, the stochastic point source is substituted for the empirical Green function and peak amplitudes; PGA, PGV, and response spectra (when time histories are not produced) are estimated using random process theory. Use of the stochastic point source as a Green function is motivated by its demonstrated success in modeling ground motions in general and particularly strong ground motions (Boore, 1983, 1986; Silva and Stark, 1992) and the desire to have a model that is truly site and region specific. The model can accommodate a region specific Q(f), Green function sources of arbitrary moment or stress drop, and site specific kappa values. The necessity of regional and site specific recordings or the modification of possibly inappropriate empirical Green functions is eliminated.

For the finite-source characterization, a rectangular fault is discretized to provide the locations of NS subfaults of moment M_0^s. The empirical relationship

$$M = 4.02 + \log A \quad \text{(Wells and Coppersmith, 1993)} \tag{C-6}$$

is used to assign areas to both the target earthquake (if its rupture surface is not fixed) as well as to the subfaults. The subevent magnitude M^s is generally taken in the range of 5.0-6.5 depending upon the size of the target event. The value of NS is determined as the ratio of the target event area to the subfault area. To constrain the proper moment, the total number of events summed (N) is given by the ratio of the target event moment to the subevent moment. The subevent rise time is determined by the equation

$$\log \tau_s = 0.33 \log M_0^s - 8.62 \tag{C-7}$$

which results from a fit to the M_0 - rise time data listed in Heaton (1990). Slip on each subfault continues for a time τ_s times N/NS which is the modeled or target event rise time. Heterogeneity of the earthquake source process is modeled by randomizing the location of the sub-events within each subfault (Hartzell, 1978) as well as the subevent rise time. The stress drop of the stochastic point-source Green function is taken as

$$\Delta\sigma = \frac{7}{16}\left(\frac{M_e}{R_e^3}\right) \qquad \text{(C-8)}$$

where R_e is the equivalent circular radius of the rectangular sub-event.

Different values of slip are assigned to each subfault as relative weights so that asperities or non-uniform slip can be incorporated into the methodology. The rupture velocity is taken as depth independent at a value of 0.8 times the shear-wave velocity generally at the half-depth of the slip surface. A random component (20%) is added to the rupture velocity. The radiation pattern is computed for each subfault, a random component added, and the RMS applied to the motions computed at the site.

The ground-motion time history at the receiver is computed by summing the contributions from each subfault associated with the closest Green function, transforming to the frequency domain, and convolving with the Green function spectrum (Equation C-1). The locations of the Green functions are generally taken at center of each subfault for small subfaults or at a maximum separation of about 5-10 km for large subfaults. As a final step, the individual contributions associated with each Green function are summed in the frequency domain multiplied by the RMS radiation pattern, and the resultant power spectrum at the site is computed. The appropriate duration used in the RVT computations for PGA, PGV, and oscillator response is computed by transforming the summed Fourier spectrum into the time domain and computing the 5-75% Arias intensity (Ou and Herrmann, 1990).

As with the point-source model, crustal response effects are accommodated through the amplification factor (A(f)) or by using vertically propagating shear waves through a vertically heterogenous crustal structure. Propagation path damping, through the Q(f) model, is incorporated from each fault element to the site. Near-surface crustal damping is incorporated through the kappa operator (Equation C-1). To model crustal propagation path effects, the method of Ou and Herrmann (1990) can be applied from each subfault to the site.

Time histories may be computed in the process as well by simply adding a phase spectrum appropriate to the subevent earthquake. The phase spectrum can be extracted from a recording made at close distance to an earthquake of a size comparable to that of the subevent (generally M 5.0-6.5). Interestingly, the phase spectrum need not be from a recording in the region of interest. A recording in WNA can effectively be used to simulate motions appropriate to ENA (Silva et al., 1989). Transforming the Fourier spectrum computed at the site into the time domain results in a computed time history which includes all of the aspects of rupture propagation, source finiteness, as well as propagation path and site effects.

For fixed fault size, mechanism, and moment, the specific source parameters for the finite fault are slip distribution, location of nucleation point, and site azimuth. Variability in these parameters may be thought of as replacing the variability in stress drop associated with the point source model. The propagation path and site parameters remain identical for both source models.

EFFECTS OF SURFICIAL SOILS

The effects of a soil column upon strong ground motion have been well documented and studied analytically for many years. Wood (1908) and Reid (1910), using apparent intensity of shaking and distribution of damage from the 1906 San Francisco earthquake, gave evidence that the severity of shaking can be substantially affected by the local geology and soil conditions. Gutenberg (1957) developed amplification factors representing different site geology by examining recordings of microseisms and earthquakes from instruments located

on various types of ground. More recently, Borcherdt and Gibbs (1976), Seed et al. (1969), Wiggins (1964), Idriss and Seed (1968), Berrill (1977), Joyner et al. (1976), Duke and Mal (1978), Silva (1991), and Silva and Stark (1992) have shown that during small and large earthquakes, the surface soil motion can differ in significant and predictable ways from that on adjacent rock outcrops. In addition, other investigators have utilized explosion data either independently or in conjunction with earthquake data to examine site response characteristics (Murphy et al., 1971; Rogers et al., 1984; and Hays et al., 1979). Recent work using horizontal as well as vertical arrays of instruments have demonstrated the general consistency of the site response for seismic events of different sizes, distances, and azimuths (Tucker and King, 1984; Benites et al., 1985).

Results of these and other studies have demonstrated, in a general sense, the adequacy of assuming plane-wave propagation in modeling one-dimensional site response for engineering purposes. The simple model then represents a useful analytical tool to approximate site effects on strong ground motion.

To model soil response, an RVT-based equivalent-linear approach is used by propagating either the point- or finite-source outcrop power spectral density through a one-dimensional soil column. RVT is used to predict peak time domain values of shear-strain based upon the shear-strain power spectrum. In this sense, the procedure is analogous to the program SHAKE (Schnabel et al., 1972) except that peak shear strains in SHAKE are measured in the time domain. The purely frequency domain approach obviates a time domain control motion and, perhaps just as significantly, eliminates the need for a suite of analyses based on different input motions. This arises because each time domain analysis may be viewed as one realization of a random process. In this case, several realizations of the random process must be sampled to have a statistically stable estimate of site response. The realizations are usually performed by employing different control motions with approximately the same level of peak acceleration. In the frequency- domain approach, the estimates of peak shear strain as well as oscillator response are, as a result of the RVT, fundamentally probabilistic in nature.

Stable estimates of site response can then be rapidly computed permitting statistically significant estimates of uncertainties based on parametric variations.

The parameters that influence computed response include the shear-wave velocity profile and the strain dependencies of both the shear modulus and shear-wave damping.

FINITE SOURCE MODEL UNCERTAINTIES

An important aspect of any numerical modeling approach is a proper statistical estimate of uncertainty. Modeling uncertainty is basically a goodness-of-fit test using given model parameter values. The combination of parametric uncertainty (the variation in computed response due to a variation in parameters) and modeling uncertainty represents the total uncertainty in the ground motion prediction.

A quantitative assessment of the modeling uncertainty (Abrahamson et al., 1990) associated with both the finite-fault RVT numerical predictions has been computed for the 1985 Michoacan, Mexico and 1985 Valpariso, Chile earthquakes. For the Michoacan earthquake, strong ground motions recorded at 14 rock sites in the epicentral distance range of 20-400 km were modeled using the stochastic finite-fault RVT model (Silva and Stark, 1992). For the Valpariso, Chile earthquake 6 rock sites were modeled.

MICHOACAN, MEXICO SIMULATIONS

Source Model

Figure C-2 shows a map of central Mexico along with epicenters and aftershock zones of large earthquakes which occurred in the region since 1951. The aftershock zone of the September 19, 1985 earthquake is outlined in long dashed lines with PGA values recorded at the Guerrero acceleragraph array are shown in parenthesis. The slip model used in the Michoacan simulations is taken from Mendez and Anderson (1991) and approximates the aftershock zone shown in Figure C-2. This model is preferred over the slip distribution of

Mendoza and Hartzel (1989) because it more closely matches the area outlined by the aftershocks. The Mendez and Anderson (1991) slip model is 80 km wide and 180 km long with a seismic moment of 1.4 x 10^{28} dyne-cm (M 8.03) and is shown in Figure C-3. Magnitude 6.2 (2.6 x 10^{25} dyne-cm) subevents are used on subfaults with lengths and widths of 15 and 10 km resulting in 12 elements along strike and 8 along dip. The total number of events summed is given by the moment ratio of the target event (1.4 x 10^{28} dyne-cm) to the subevent moment (2.6 x 10^{25} dyne-cm) or about 538. Since 96 subfaults are used to cover the slip surface, each element is taken to rupture for a duration of 3.6 seconds; six times the subevent rise time of 0.6 sec (Equation C-7).

Path Model

Geometrical attenuation is taken as 1/R for subfault to site distances less than 100 km and 1/SQRT(R) otherwise. The Q(f) model was determined by Humphrey and Anderson (1993) by inverting strong motion data recorded at the Guerrero array from about 30 earthquakes. The model is given by 273 $f^{0.66}$. The crustal velocity model, used only to compute vertical propagating shear-wave amplification assuming an average source depth of 15 km, is taken from Somerville et al. (1991).

Site Model

Fourteen rock sites of the Guerrero array covering the rupture surface-to-site distance range of about 15 to 250 km are modeled. Kappa values are available for all of the sites as well as amplification factors for several of the sites from independent studies (Silva and Darragh, 1993; Humphrey and Anderson, 1993). Table C-1 lists the site names, labels, and kappa values and also indicates which sites have frequency dependent site factors. The kappa values determined by Silva and Darragh (1993) are based on template fits to response spectral shapes for several earthquakes while the kappa values and site factors determined by Humphrey and Anderson (1993) are a result of fits to Fourier amplitude spectra using 30 earthquakes. Figure C-4 shows the Humphrey and Anderson site terms available for the modeled sites which are plotted over the bandwidths considered reliable for each site. Only those site terms with three or more recordings (and not including the Michoacan main shock) are used. The site terms

represent unmodeled site amplifications and deamplification due to crustal heterogeneities and perhaps topographic effects. The values are near 1 on average and can vary by factors of 5 or more with frequency.

Michoacan Modeling Uncertainty

Comparisons of 5% damped spectral acceleration computed for the 1985 M 8.03 Michoacan main shock to the log average of the two horizontal components computed from the recordings are shown in Figure C-5. Included in the simulations are the site specific kappa values (Table C-1) as well as the site factors of Humphrey and Anderson (1993) (Figure C-4). For most of the sites, there is good agreement between recorded motions and computed motions from PGA values at 0.02 sec out to 10-20 sec. At the closest sites: CMP, VIL, UNI, and ZIH model predictions generally exceed recorded motions. While for the more distant sites, the agreement is closer. Overall the model predicts the recorded motions very well considering its simplicity in that no computationally intensive wave propagation calculations were performed and a simple theoretical single-corner-frequency constant-stress-drop set of Green functions were used.

To provide a quantative measure of the uncertainties in the ground-motion predictions, a simple goodness-of-fit was performed at each spectral period. The difference of the logarithms of the observed average 5%-damped acceleration response spectra and the predicted response spectra were calculated at each period, squared, and summed over the total number of sites (14 sites). Dividing the resultant by the number of sites (assuming zero bias) results in an estimate of the model variance or uncertainty (Abrahamson et al., 1990). Figure C-6 shows the computed standard error (σ_{ln}) verses frequency from 0.01 Hz to 50 Hz as well as the computed model bias (Abrahamson et al., 1990). Over the frequency range of interest, 1-30 Hz, the uncertainty is quite low, with an average about 0.35-0.40, indicating an accurate prediction of the recorded motions. For frequencies below about 0.5 Hz, the uncertainty rises sharply to an average level of about 0.75. The increase in uncertainty at low frequencies is the result of a general overprediction of the ground motions and is reflected in the negative bias values. In general however, the simple model gives an accurate prediction

of the recorded motions over a surprisingly wide bandwidth and shows zero bias (90% confidence limits) from 50-0.5 Hz.

To examine the effect of modeling direct plus post-critically reflected waves from each subfault to the site, the method of Ou and Herrmann (1990) was incorporated into the methodology. The results are shown in Figure C-7 for response spectra and Figure C-8 for the uncertainty and bias using the same model parameters. Interestingly, the improvement in fit is most significant at low frequencies (about 0.1-0.5 Hz) with a slight reduction in uncertainty at high frequencies. For frequencies above 0.5 Hz, this result is very good news for strong ground motion prediction since it suggests that an accurate and detailed crustal model does not significantly improve the accuracy of the simulated motions. Apparently, over this frequency range, the recorded strong ground motions are largely stochastic in nature and random source processes as well as non-uniform vertical and lateral variations in crustal properties results in significant departures from detailed deterministic model predictions. Simply using 1/R (1/SQRT(R) for R>100 km) works about as well as detailed wave propagation modeling, relaxes the dependence on an accurate crustal model as well as the possibility of inaccurate motions if the crustal model is incorrect, and is a lot easier and more cost effective to implement.

To examine the effects of site specific kappa values as well as the 6 site functions, two additional analyses were performed. Model uncertainties were computed for simulations using site specific kappa values only (no site factors) as well as using simply an average kappa value of 0.042 sec (mean of the site specific values), again with no site factors. The results are shown in Figure C-9. Eliminating the site factors only, retaining site specific kappa terms, results in a dramatic increase in uncertainty for frequencies above about 2-3 Hz to an average value of about 0.5, an increase of over 60%. Replacing the site dependent kappa values with a constant of 0.042 sec further increases the uncertainty but for frequencies exceeding about 4 Hz. Interesting, although the site terms are considered stable and reliable for frequencies below 2-3 Hz they offer no apparent reduction in uncertainty and only slightly improve the bias estimates at low frequencies (Figure C-9).

In terms of model predictions, these results indicate that for rock sites with kappa values in the range sampled be (0.02 to about 0.10 sec with a mean of 0.042 sec) knowledge of site kappa can reduce uncertainty by a significant amount for frequencies above about 4 Hz. Additionally, assuming the contributions to the site terms at high frequencies are due to local shallow velocity profiles, it may be possible to further improve the accuracy of model predictions at rock sites with knowledge of the velocity profile.

In computing the final model uncertainty and bias estimates both the Michoacan, Mexico and Valpariso, Chile modeling results will be combined. For the Michoacan computations, only site specific kappa values will be included. The site factors are not included in computing the modeling uncertainty since neither an appropriate site factor is not available for the site under study nor is site amplification treated in the parametric variations.

VALPARISO, CHILE SIMULATIONS

Source Model

For the March 3, 1985 Valpariso, Chile earthquake, little is known about the details of the slip model. Fewer free field strong motion sites are available and the site characteristics are much less well known than is the case for the Michoacan, Mexico earthquake. Somerville et al. (1991) have derived a slip model by perturbing the teleseismic model of Houston (1987) to improve the fit to the strong motion data. That slip model is adopted for use here and is shown in Figure C-10 along with the sites used in the modeling exercise. The rupture surface is 80 km wide and 210 km long with a seismic moment of 1.0 x 10^{28} dyne-cm (M 7.93) (Somerville et al., 1991). As with the Michoacan modeling, M 6.2 subevents are used with lengths and widths of 15 km and 10 km respectively. This results in 14 elements along strike and 8 along dip. The total number of events summed is 1.0 x 10^{28} dyne-cm/2.6 x 10^{25} dyne-cm or about 385. There are a total of 112 subfaults (8 x 14), each element then ruptures for a duration of 1.8 sec; 3 times the subevent rise time of 0.6 sec.

Path Model

Geometrical attenuation is taken as 1/R (1/SQRT(R) for R>100 km) for subfault to site distances. Results from the Michoacan modeling, as well as modeling of the 1987 Loma Prieta earthquake, (Silva and Stark, 1992) suggested that this simple approach provided as good a fit to recorded strong ground motions at intermediate to high frequencies (>0.5 Hz) as approaches which incorporate detailed wave propagation models. In this case these results are significant since the crustal structure is poorly known in this region.

To include crustal amplification, the near-surface amplification factors (A(f); Boore, 1986) discussed earlier are used. These factors are appropriate for a generic western North America or tectonically active crustal province. The WNA factors are shown in Figure C-11 compared to those computed for the Michoachan earthquake moldeling. The WNA amplification factors are higher at high frequencies reflecting the large near-surface velocity gradient typical of soft-rock crustal areas (Boore, 1986).

In addition to the crustal structure, the appropriate crustal damping model (Q(f)) is also poorly constrained. As a result, the Michoacan Q(f) model (273 $f^{0.66}$) is adopted. To be consistent with treating crustal damping in parametric variations, the Q(f) model should be varied to minimize the modeling uncertainty. However, since the slip model is likely poorly constrained as well, it makes little sense compensating the misfit by varying the Q(f) model.

Site Model

Six rock sites are modeled (Figure C-10) since very little is known about the site specific profiles at the soil sites. Site specific kappa values were determined using templates of response spectral shapes (Silva and Darragh, 1993) and are listed on Table 2.

Valpariso Modeling Uncertainty

Computed 5% damped acceleration response spectra for the six rock sites are shown in Figure C-12 compared to recorded motions. At high to intermediate frequencies (50 Hz-1Hz), the match is good, again considering the simplicity of the model and, in this case, poorly

constrained slip distribution as well as crustal damping model. Figure C-13 shows the resulting modeling uncertainty and bias estimates. The low frequency range is probably limited to about 0.25 Hz since the accelerographs have film recorders. In general, the uncertainty is quite low above about 0.7 Hz and extremely low at high frequencies (above 10 Hz). The bias estimates are essentially zero (90% confidence limits) above about 0.7 Hz. Of significance, any departure of the bias estimates from zero is negative indicating an overprediction. As a result, one can then reasonably use the bias estimates to correct the model uncertainty.

TOTAL MODELING UNCERTAINTY

Combining the simulations for both the Michoacan, Mexico and Valpariso, Chile earthquakes results in the total modeling uncertainty. Both the uncertainty and bias estimates are shown in Figure C-14. The total modeling uncertainty is quite low, generally below about 0.5 for frequencies above about 1 Hz with a small peak near 1 Hz. Above 0.6 Hz, the bias correction is essentially zero and is reflected in the near zero bias estimates above about 0.5-0.6 Hz. Over this frequency range (0.5-50 Hz), the simple model using a Brune omega-square point-source as a Green function coupled with 1/R and 1/SQRT (R) geometrical attenuation provides accurate predictions of strong ground motions from large subduction earthquakes.

REFERENCES

Abrahamson, N.A., Somerville, P.G., and Cornell, C.A. (1990). "Uncertainty in numerical strong motion predictions." *Proceedings of the Fourth U.S. National Conference on Earthquake Engineering*, Palm Springs, California, 1, 407-416.

Anderson, J.G., Bodin, P., Brune, J.N., Prince, J., Singh, S.K., Quaas, R., and Onate, M. (1986). "Strong ground motion from the Michoacan, Mexico, earthquake." *Science,* 223, 1043-1049.

Anderson, J.G., and Hough, S.E. (1984). "A model for the shape of the Fourier amplitude spectrum of acceleration at high frequencies." *Bulletin of the Seismological Society of America,* 74, 1969-1993.

Atkinson, G.M. (1984). "Attenuation of strong ground motion in Canada from a random vibrations approach." *Bulletin of the Seismological Society of America,* 74(5), 2629-2653.

Benites, R., Silva, W.J., and Tucker, B. (1985). "Measurements of ground response to weak motion in La Molina Valley, Lima, Peru. Correlation with strong ground motion." *Earthquake Notes, Eastern Section, Bulletin of the Seismological Society of America*, 55(1).

Berrill, J.B. (1977). "Site effects during the San Fernando, California, earthquake." *Proceedings of the Sixth World Conference on Earthquake Engineering,* India, 432-438.

Boore, D.M. (1983). "Stochastic simulation of high-frequency ground motions based on seismological models of the radiated spectra." *Bulletin of the Seismological Society of America,* 73, 1865-1894.

Boore, D.M. (1986). "Short-period P- and S-wave radiation from large earthquakes: implications for spectral scaling relations." *Bulletin of the Seismological Society of America,* 76(1), 43-64.

Boore, D.M., and Atkinson, G.M. (1987). "Stochastic prediction of ground motion and spectral response parameters at hard-rock sites in eastern North America." *Bulletin of the Seismological Society of America,* 77(2), 440-467.

Boore, D.M., and Joyner, W.B. (1984). "A note on the use of random vibration theory to predict peak amplitudes of transient signals." *Bulletin of the Seismological Society of America,* 74, 2035-2039.

Borcherdt, R.D., and Gibbs, J.F. (1976). "Effects of local geologic conditions in the San Francisco Bay region on ground motions and the intensities of the 1906 earthquake." *Bulletin of the Seismological Society of America,* 66, 467-500.

Brune, J.N. (1970). "Tectonic stress and the spectra of seismic shear waves from earthquakes." *Journal of Geophysical Research,* 75, 4997-5009.

Brune, J.N. (1971). "Correction." *Journal of Geophysical Research*, 76, 5002.

Duke, C.M., and Mal, A.K. (1978). "Site and source effects on earthquake ground motion." *University of California at Los Angeles Engineering Report* 7890.

Gutenberg, B. (1957). "Effects of ground on earthquake motion." *Bulletin of the Seismological Society of America*, 47, 221-250.

Hanks, T.C. (1982). "f_{max}." *Bulletin of the Seismological Society of America,* 72, 1867-1879.

Hanks, T.C., and Kanamori, H. (1979). "A moment magnitude scale." *Journal of Geophysical Research*, 84, 2348-2350.

Hanks, T.C., and McGuire, R.K. (1981). "The character of high-frequency strong ground motion." *Bulletin of the Seismological Society of America*, 71, 2071-2095.

Hartzell, S.H. (1978). "Earthquake aftershocks as Green's functions." *Geophysical Research Letters*, 5, 1-4.

Hays, W.W., Rogers, A.M., and King, K.W. (1979). "Empirical data about local ground response." *Proceedings of the Second U.S. National Conference on Earthquake Engineering*, Earthquake Engineering Research Institute, 223-232.

Heaton, T.H. (1990). "Evidence for and implications of self-healing pulses of slip in earthquake rupture." *Physical Earth Planetary International*, 64, 1-20.

Hough, S.E., and Anderson, J.G. (1988). "High-frequency spectra observed at Anza, California: Implications for Q structure." *Bulletin of the Seismological Society of America*, 78, 692-707.

Hough, S.E., Anderson, J.G., Brune, J., Vernon III, F., Berger, J., Fletcher, J., Haar, L., Hanks, T., and Baker, L. (1988). "Attenuation near Anza, California." *Bulletin of the Seismological Society of America*, 78(2), 672-691.

Houston, H. (1987). "Source characteristics of large earthquakes at short periods." Ph.D. Thesis, California Institute of Technology, Pasadena.

Humphrey, J.R., and Anderson, J.G. (1993). "Shear-wave attenuation and site response in Guerrero." Submitted to *Bulletin of the Seismological Society of America.*

Idriss, I.M., and Seed, H.B. (1968). "Seismic response of horizontal soil layers." *Proceedings of the American Society of Civil Engineers, Journal of Soil Mechanics and Foundations Division*, 94, 1003-1031.

Irikura, K. (1983). "Semi-empirical estimation of strong ground motions during large earthquakes." *Bulletin of the Disaster Prevention Research Institute*, Kyoto Univ., 33, 63-104.

Joyner, W.B., Warrick, R.E., and Oliver III, A.A. (1976). "Analysis of seismograms from a downhole array in sediments near San Francisco Bay." *Bulletin of the Seismological Society of America*, 66, 937-958.

Mendez, A.J., and Anderson, J.G. (1991). "The temporal and spatial evolution of the 19 September 1985 Michoacan earthquake as inferred from near-source ground-motion records." *Bulletin of the Seismological Society of America*, 81(3), 844-861.

Mendoza, C., and Hartzell, S.H. (1989). "Slip distribution of the 19 September 1985 Michoacan, Mexico, earthquake: near-source and teleseismic constraints." *Bulletin of the Seismological Society of America*, 79, 655-669.

Murphy, J.R., Davis, A.H., and Weaver, N.L. (1971). "Amplification of seismic body waves by low-velocity surface layers." *Bulletin of the Seismological Society of America*, 61, 109-145.

Ou, G.B., and Herrmann, R.B. (1990). "A statistical model for ground motion produced by earthquakes at local and regional distances." *Bulletin of the Seismological Society of America*, 80, 1397-1417.

Papageorgiou, A.S., and Aki, K. (1983). "A specific barrier model for the quantitative description of inhomogeneous faulting and the prediction of strong ground motion. I. Description of the model." *Bulletin of the Seismological Society of America*, 73, 693-722.

Reid, H.F. (1910). "The California earthquake of April 18, 1906." *The Mechanics of the Earthquake,* Carnegie Institute of Washington, 87, 21.

Rogers, A.M., Borcherdt, R.D., Covington, P.A., and Perkins, D.M. (1984). "A comparative ground response study near Los Angeles using recordings of Nevada nuclear tests and the 1971 San Fernando earthquake." *Bulletin of the Seismological Society of America*, 74, 1925-1949.

Schnabel, P.B., Lysmer, J., and Seed, H.B. (1972). "SHAKE: A computer program for earthquake response analysis of horizontally layered sites." Earthquake Engineering Research Center, University of California at Berkeley, EERC 72-12.

Seed, H.B., Idriss, I.M., and Kiefer, F.W. (1969). "Characteristics of rock motions during earthquakes." *Journal of Soil Mechanics and Foundations Division*, American Society of Civil Engineers, ASCE, 95(SM5).

Silva, W.J. (1976). "Body waves in a layered anelastic solid." *Bulletin of the Seismological Society of America*, 66(5), 1539-1554.

Silva, W.J. (1991). "Global characteristics and site geometry." *Proceedings: NSF/EPRI Workshop on Dynamic Soil Properties and Site Characterization*, Electric Power Research Institute, EPRI NP-7337.

Silva, W.J., and Darragh, R.B. (1993). "Engineering characterization of strong ground motion recorded at rock sites." Draft Final Report Submitted to Electric Power Research Institute, EPRI RP 2556-48.

Silva, W.J., Darragh, R.B., Green, R.K., and Turcotte, F.T. (1989). "Estimated ground motions for a New Madrid event." U.S. Army Engineers Waterways Experiment Station, Washington DC, Misc. Paper GL-89-17.

Silva, W.J., Darragh, R.B., and Wong, I.G. (1990). "Engineering characterization of earthquake strong ground motions with applications to the Pacific Northwest." in Hays, W.W., ed., *Proceedings of the Third NEHRP Workshop on Earthquake Hazards in the Puget Sound/Portland Region*, U.S. Geological Survey Open-File Report.

Silva, W.J., and Lee, K. (1987). "*WES RASCAL* code for synthesizing earthquake ground motions." State-of-the-Art for Assessing Earthquake Hazards in the United States, Report 24, U.S. Army Engineers Waterways Experiment Station, Misc. Paper S-73-1.

Silva, W.J., and Stark, C.L. (1992). "Source, path, and site ground motion model for the 1989 M 6.9 Loma Prieta earthquake." California Division of Mines and Geology draft final report.

Somerville, P., Sen, M. and Cohee, B. (1991). "Simulation of strong ground motions recorded during the 1985 Michoacan, Mexico, and Valparaiso, Chile, earthquakes." *Bulletin of the Seismological Society of America*, 81(1), 1-27.

Toro, G.R., and McGuire, R.K. (1987). "An investigation into earthquake ground motion characteristics in eastern North America." *Bulletin of the Seismological Society of America*, 77, 468-489.

Tucker, B.E., and King, J.L. (1984). "Dependence of sediment-filled valley response on the input amplitude and the valley properties." *Bulletin of the Seismological Society of America*, 74, 153-165.

Wells, D.L., and Coppersmith, K.J. (1993). "Updated empirical relationships among magnitude, rupture length, rupture area, and surface displacement." Submitted to *Bulletin of the Seismological Society of America.*

Wiggins, J.H. (1964). "Effects of site conditions on earthquake intensity." *Journal of Structural Division, Proceedings*, American Society of Civil Engineering, ASCE 90(2), Part I.

Wood, H.O. (1908). "Distribution of apparent intensity in San Francisco, in the California earthquake of April 18, 1906." *Report of the State Earthquake Investigation Commission*, Wash., D.C.: Carnegie Institute, 1, 220-245.

TABLE C-1

MICHOACAN MODELING
SITES AND KAPPA VALUES

Name	Label	Kappa(sec)	Site Function
Caleto de Campos	CMP	0.045[1]	
La Villita	VIL	0.100[1]	
La Union	UNI	0.045[1]	
Zihuatanejo	ZIH	0.050[1]	
Papanoa	PPN	0.020[1]	*
El Suchil	SUC	0.040[2]	
Atoyac	ATO	0.028[2]	
El Paraiso	PAR	0.024[2]	*
El Cayaco	CAY	0.036[2]	*
Coyuca	CYC	0.036[2]	
Teacalco	TEA	0.049[2]	*
El Ocotito	OTT	0.027[2]	*
Cerro de Piedro	CDP	0.038	*
Las Mesas	MES	0.021[2]	

[1] From Silva and Darragh, (1993)
[2] From Humphrey and Anderson (1993)

TABLE C-2

VALPARISO MODELING
SITES AND KAPPA VALUES

Name	Label	Kappa (sec)
Valpariso UTFSM	VALU	0.040[1]
Zapallar	ZAP	0.020[1]
Papudo	PAP	0.020[1]
Los Vilos	LVI	0.060[1]
Pichilemu	PIC	0.040[1]
Constitucion	CNS	0.040[1]

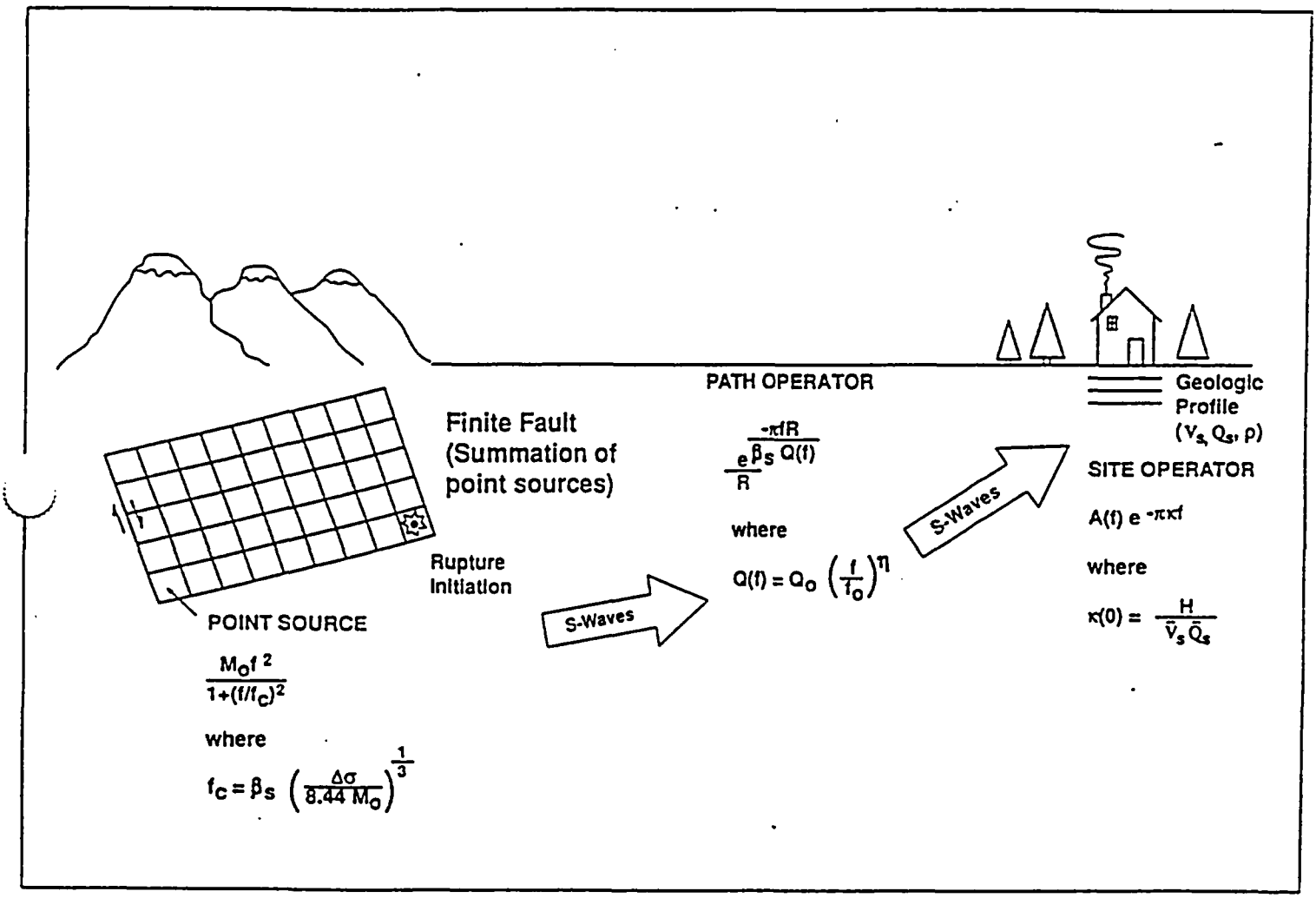

Figure C-1 Schematic of ground motion model.

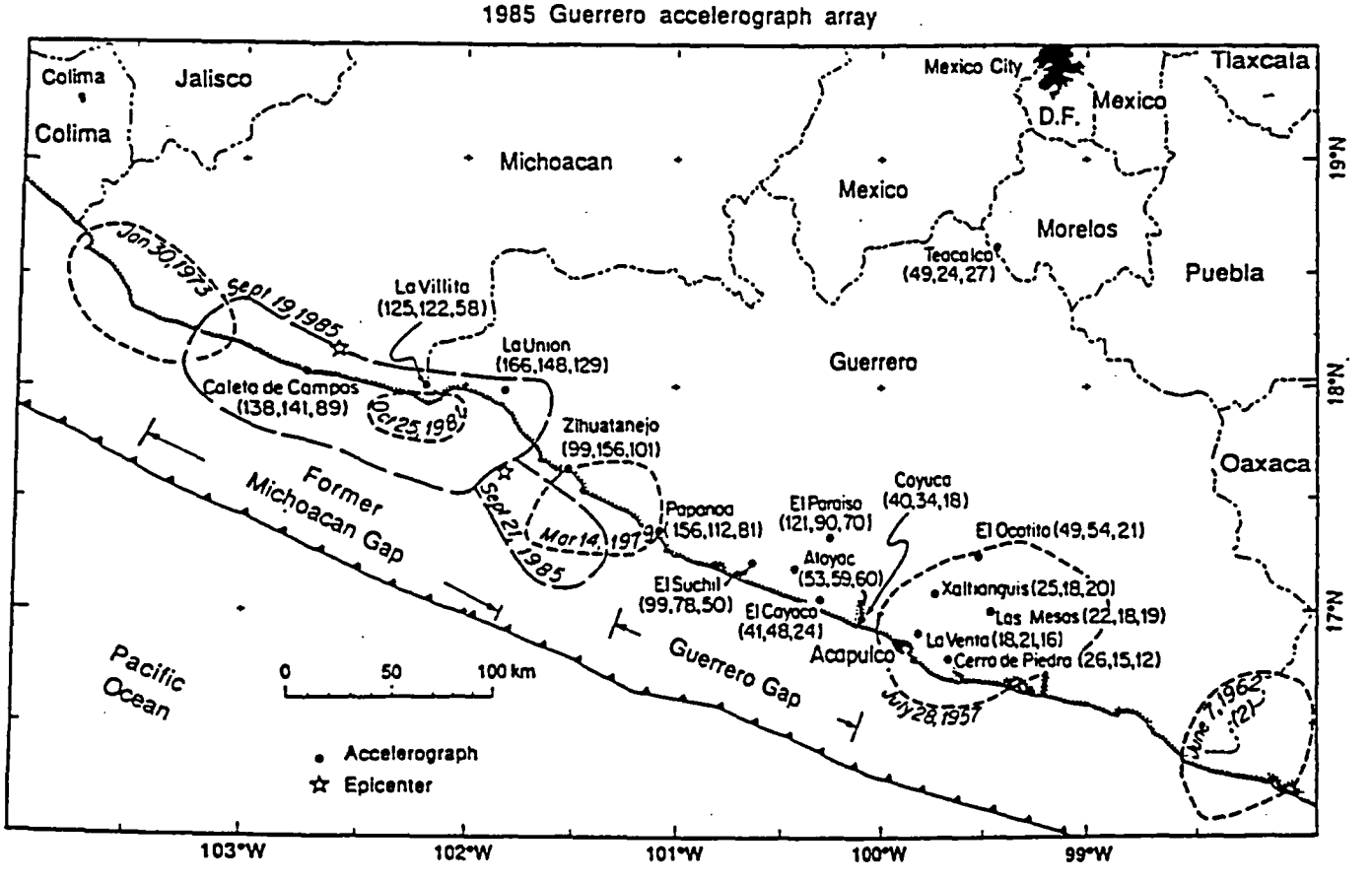

Figure C-2 Map of coastal Mexico, epicenters and aftershock zones of 1985 events, and locations of strong motion stations in Guerrero array on September 19, 1985. Short dashed lines show limits of aftershocks of large earthquakes in this region since 1951. Peak accelerations (cm/sec^2) are given for each station for the north, east, and vertical components, respectively, in parentheses (Source: Anderson et al., 1986).

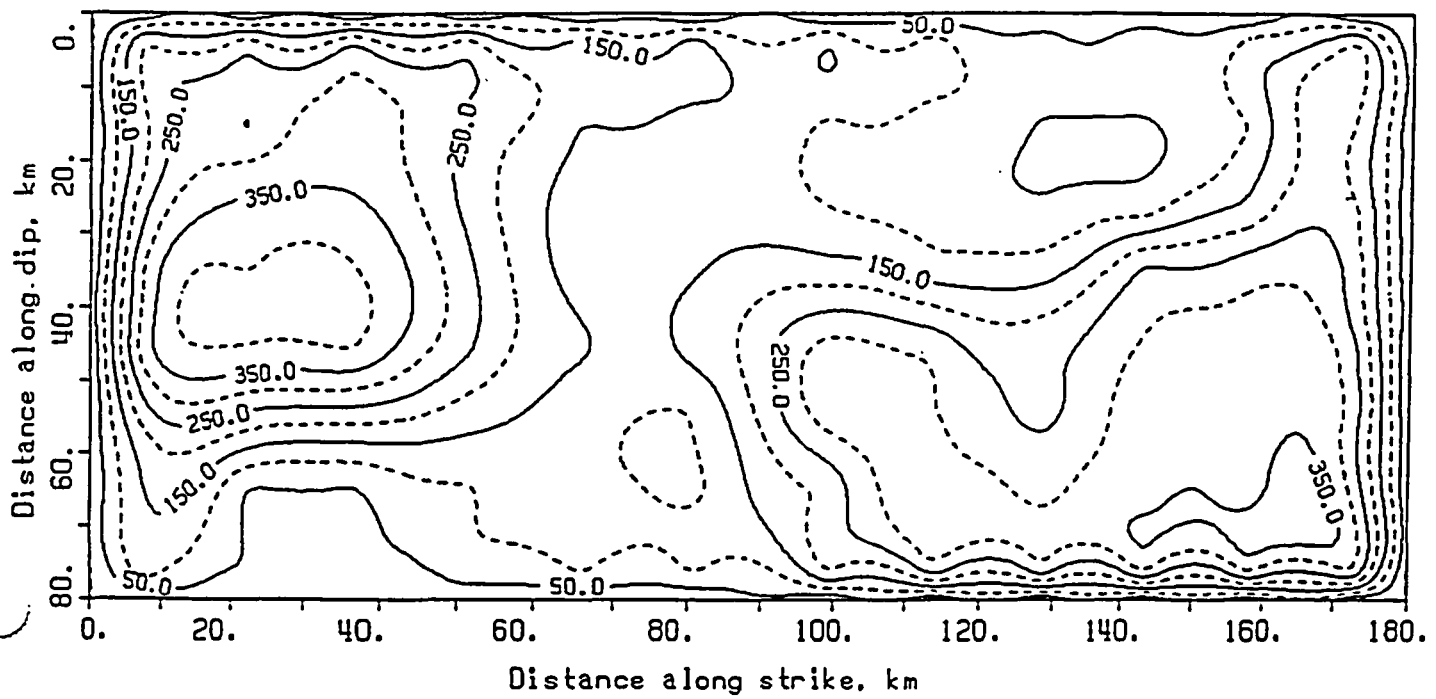

Figure C-3 Slip model of the September 19, 1985, M 8.03 Michoacan, Mexico, earthquake (Source: Mendez and Anderson, 1991)

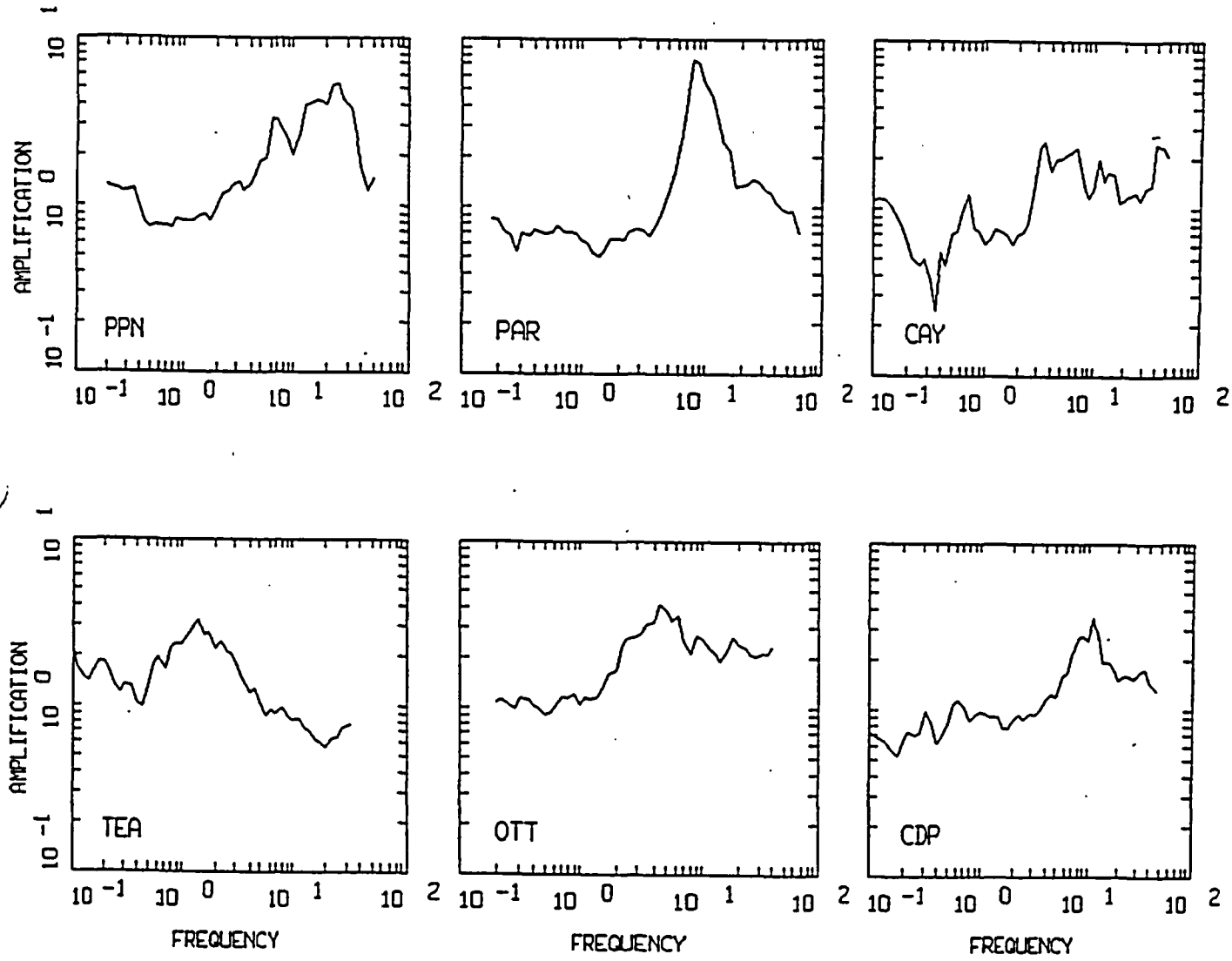

Figure C-4 Site amplification factors available for six of the fourteen sites of the Guerrero accelerograph array which were modeled (see Table C-1 for site names and Figure C-2 for site locations).

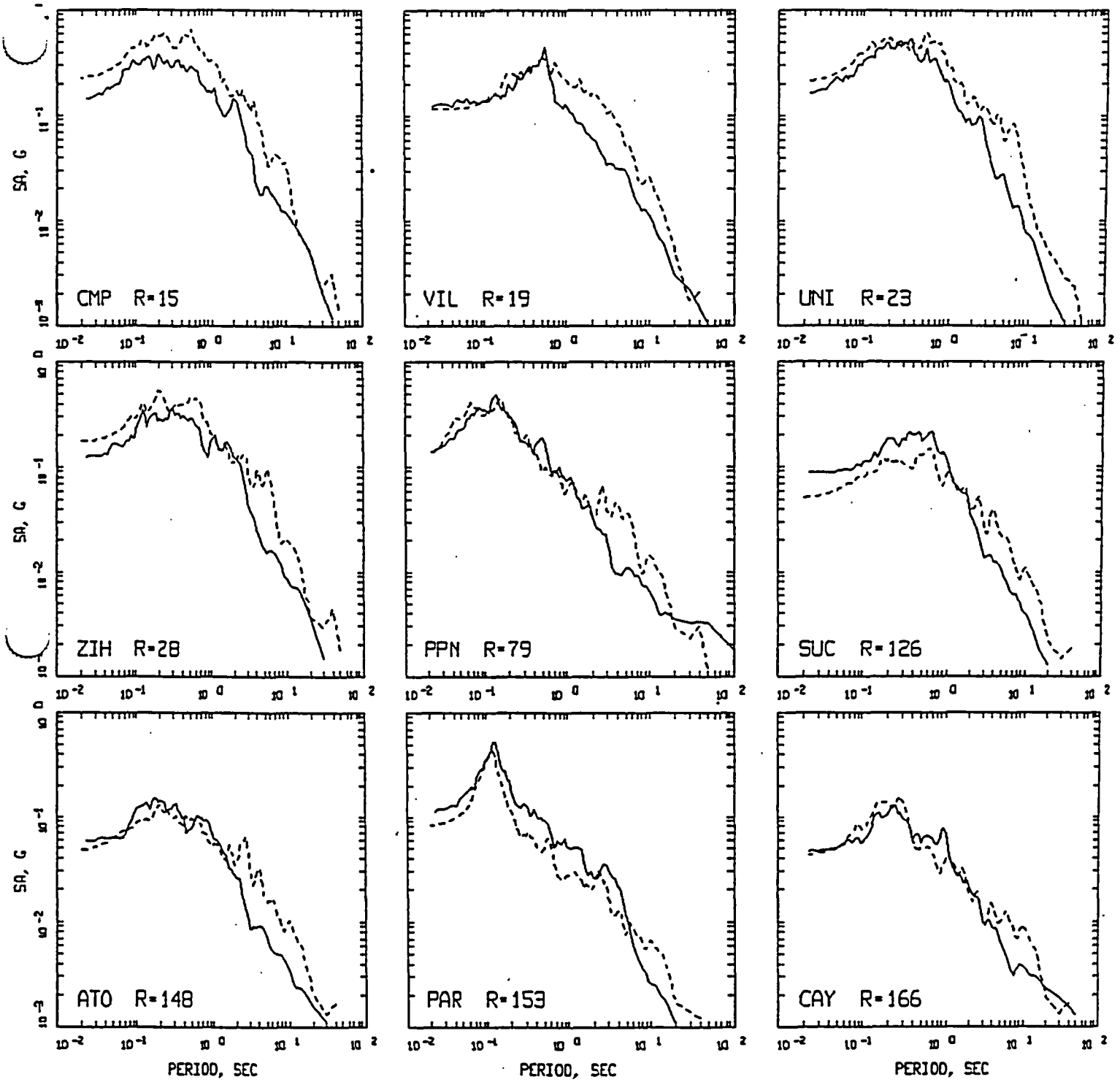

Figure C-5 Comparison of 5% damped acceleration response spectra computed for the Michoacan, Mexico, earthquake (dashed lines) to average of the two horizontal components computed from the recorded motions (solid lines) at fourteen rock sites.

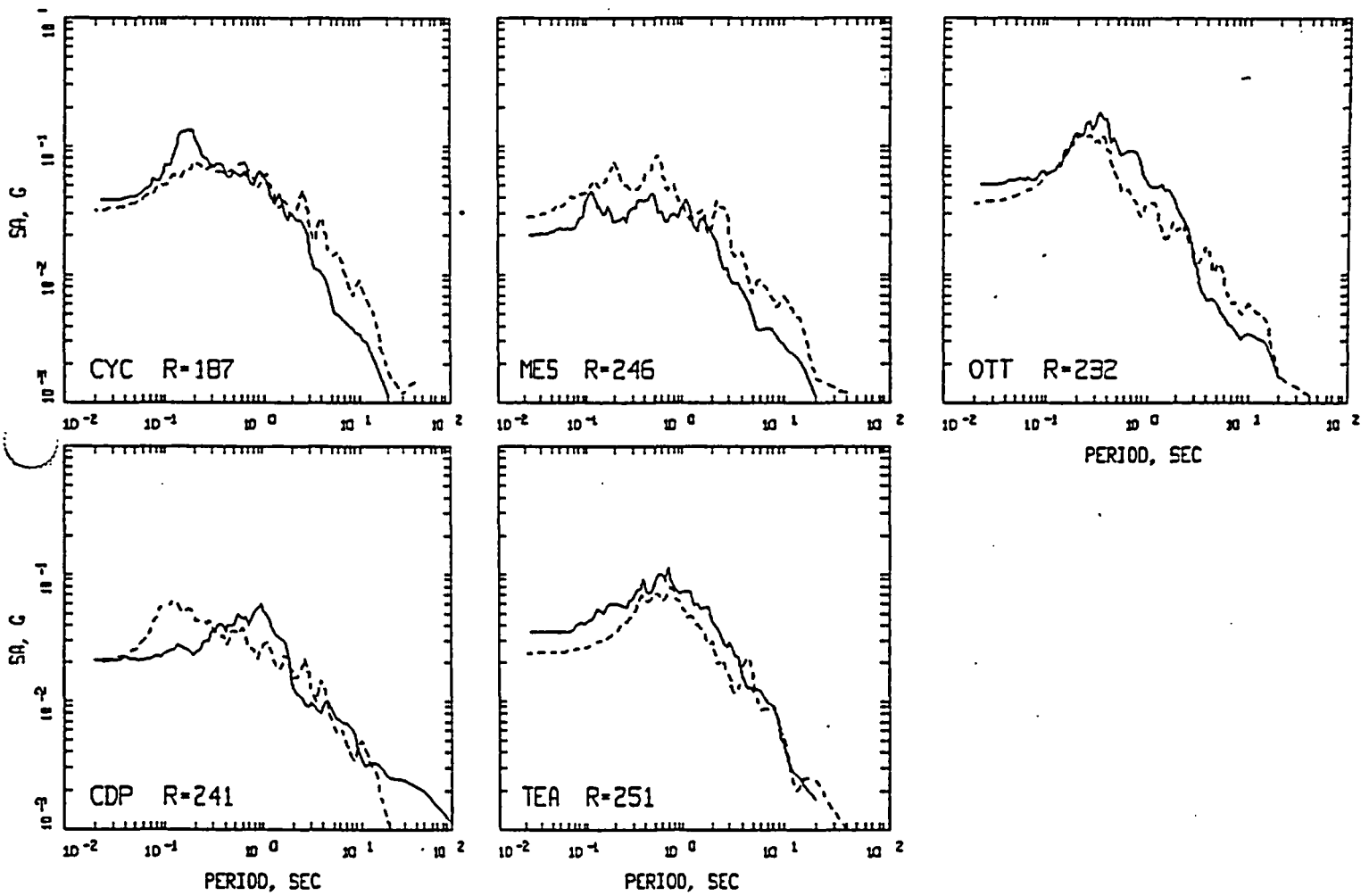

Figure C-5 (Continued).

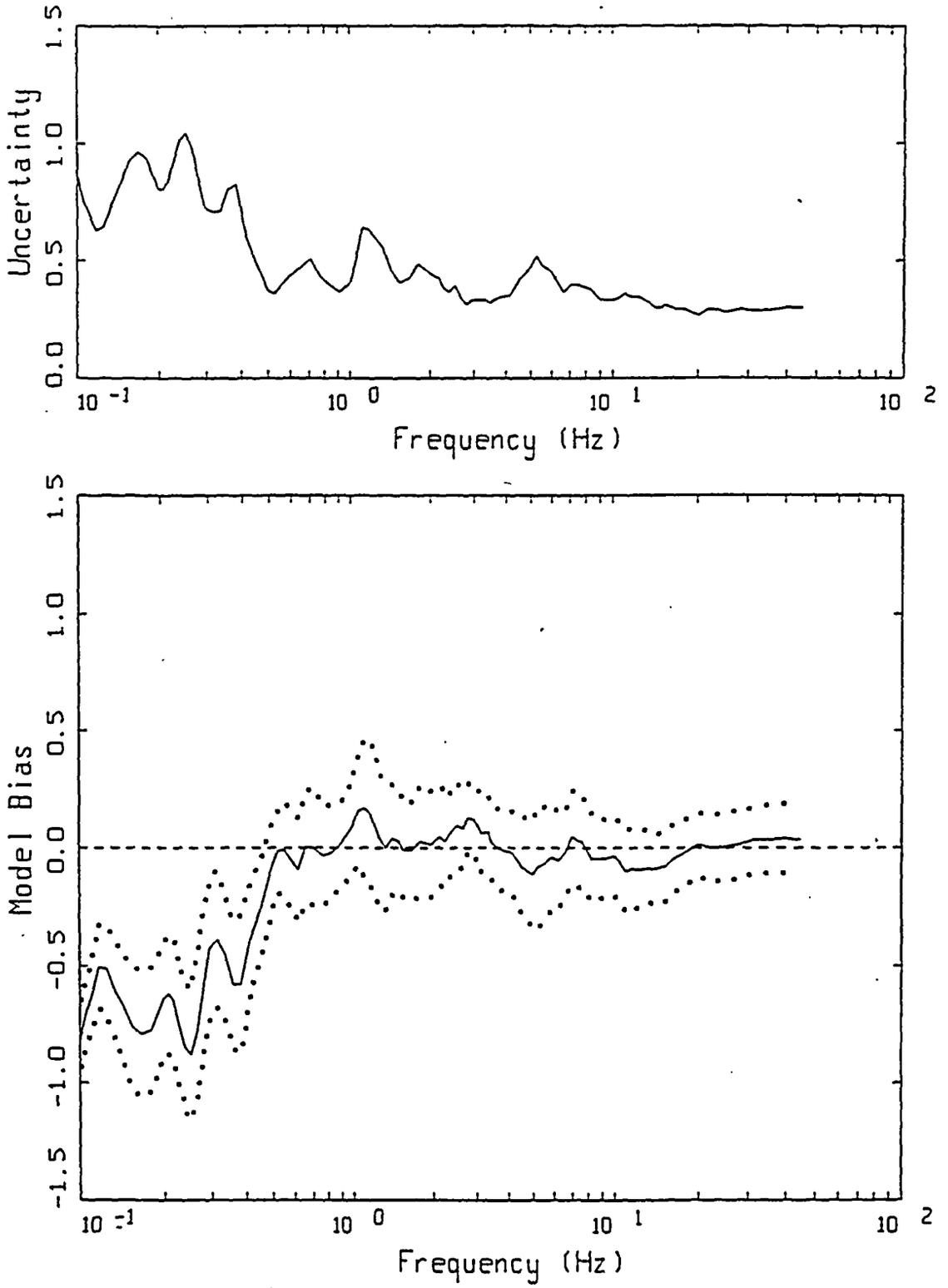

Figure C-6 Modeling uncertainty (σ_{ln}) (upper) and model bias with 90% confidence limits (lower) computed for the Michoacan, Mexico, earthquake.

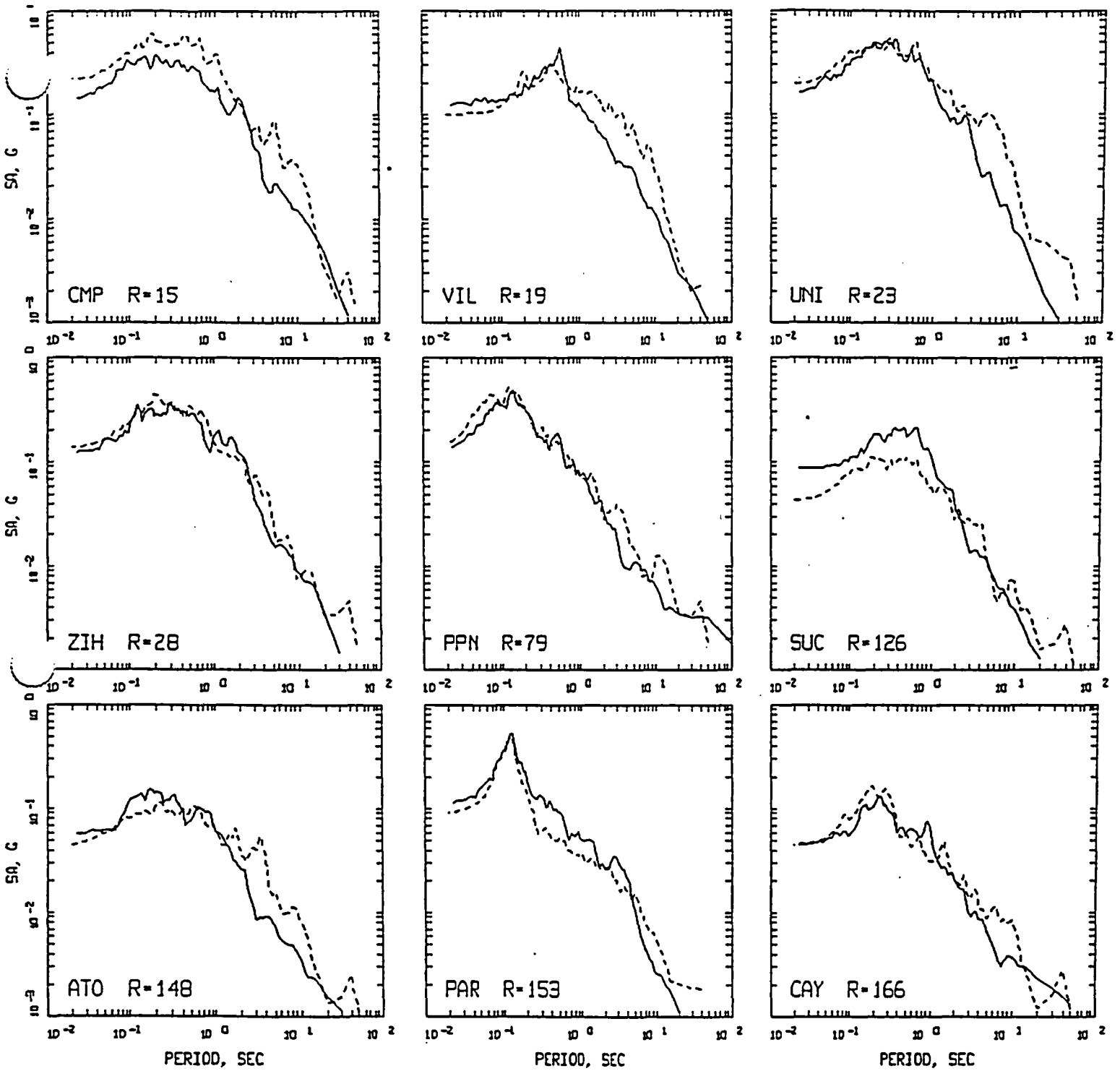

Figure C-7 Comparison of 5% damped acceleration response spectra computed for the Michoacan, Mexico, earthquake (dashed lines) modeling the effects of direct waves plus post-critically reflected waves to average of the two horizontal components computed from the recorded motions (solid lines) at fourteen rock sites.

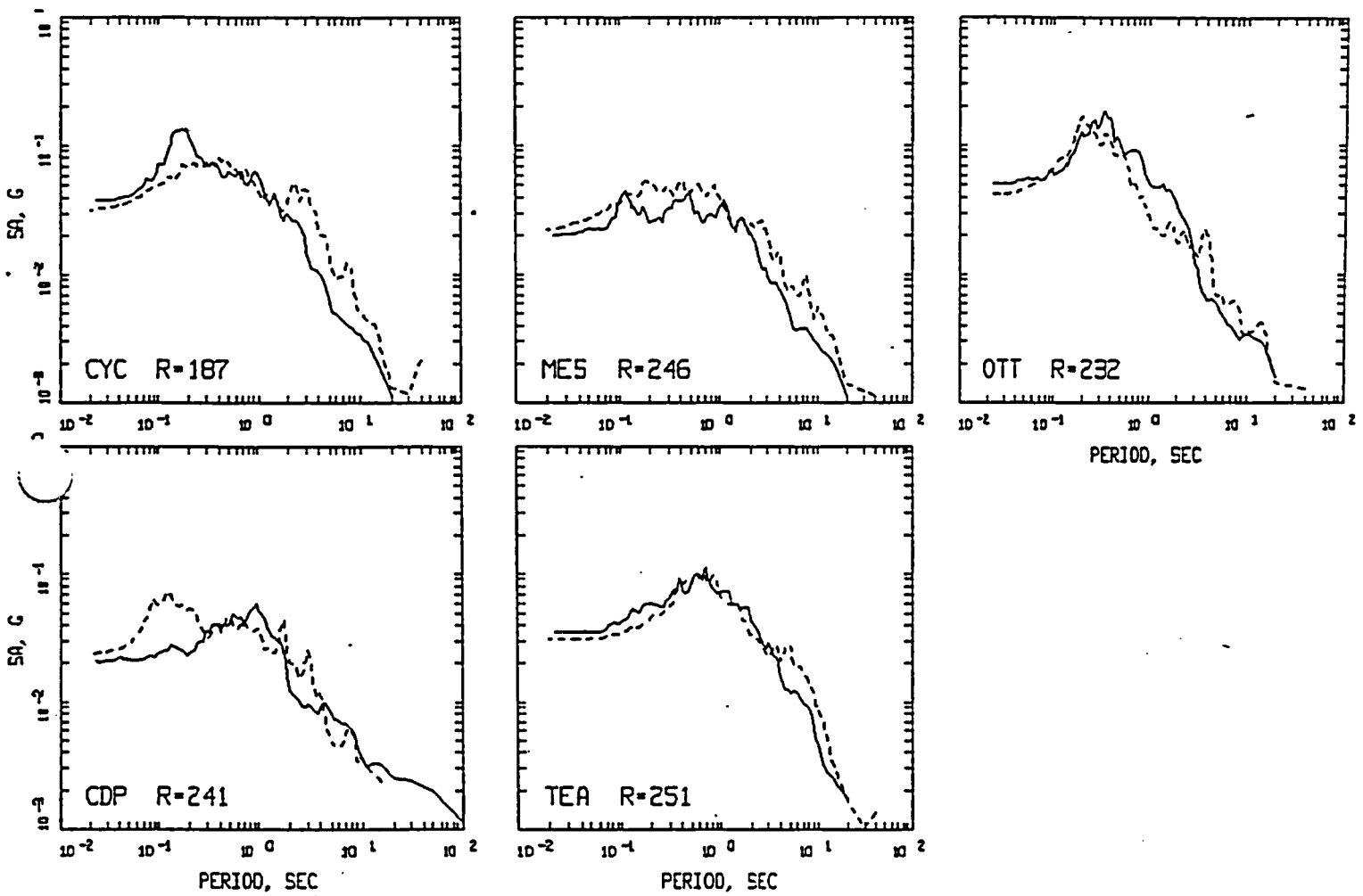

Figure C-7 (Continued).

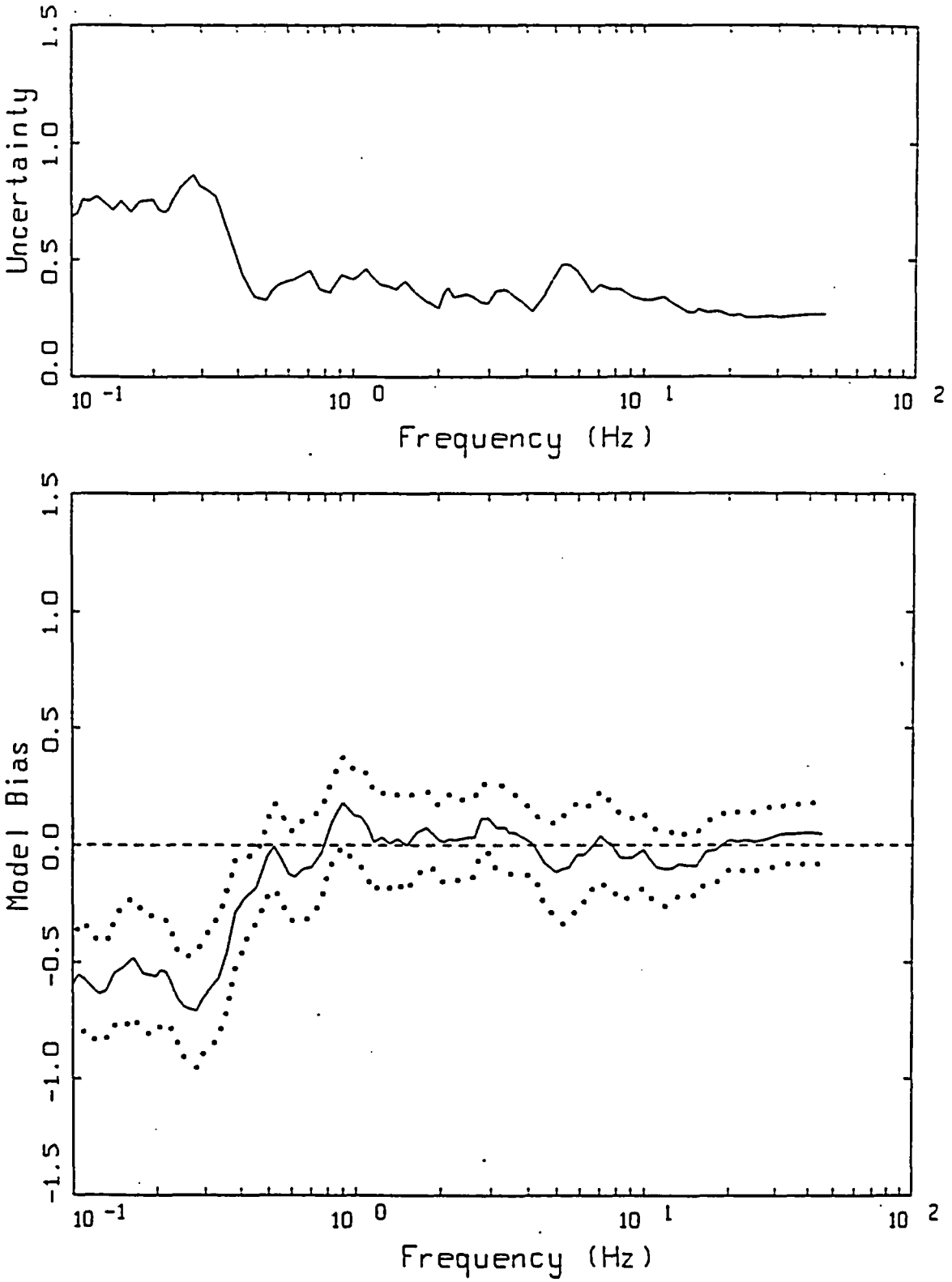

Figure C-8 Modeling uncertainty (σ_{ln}) (upper) and model bias with 90% confidence limits (lower) computed for the Michoacan, Mexico, earthquake. Model predictions include the effects of direct waves plus post-critical reflections.

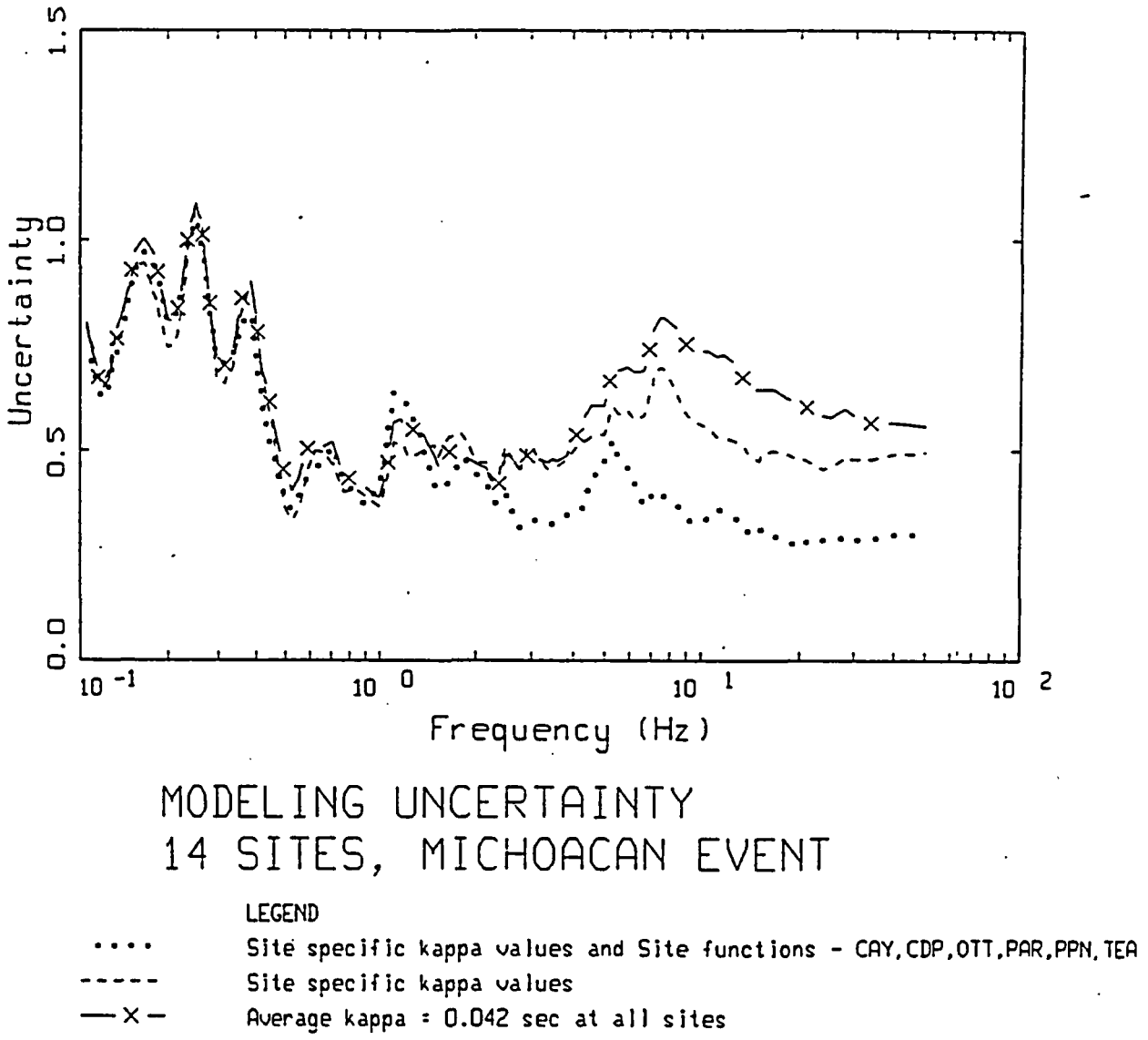

Figure C-9 Comparison of modeling uncertainty computed using site functions and site specific kappa values (dotted line, same as Figure C-6), without site functions but retaining site specific kappa values (dashed line), without site functions and with a constant average kappa value of 0.042 sec (crosses).

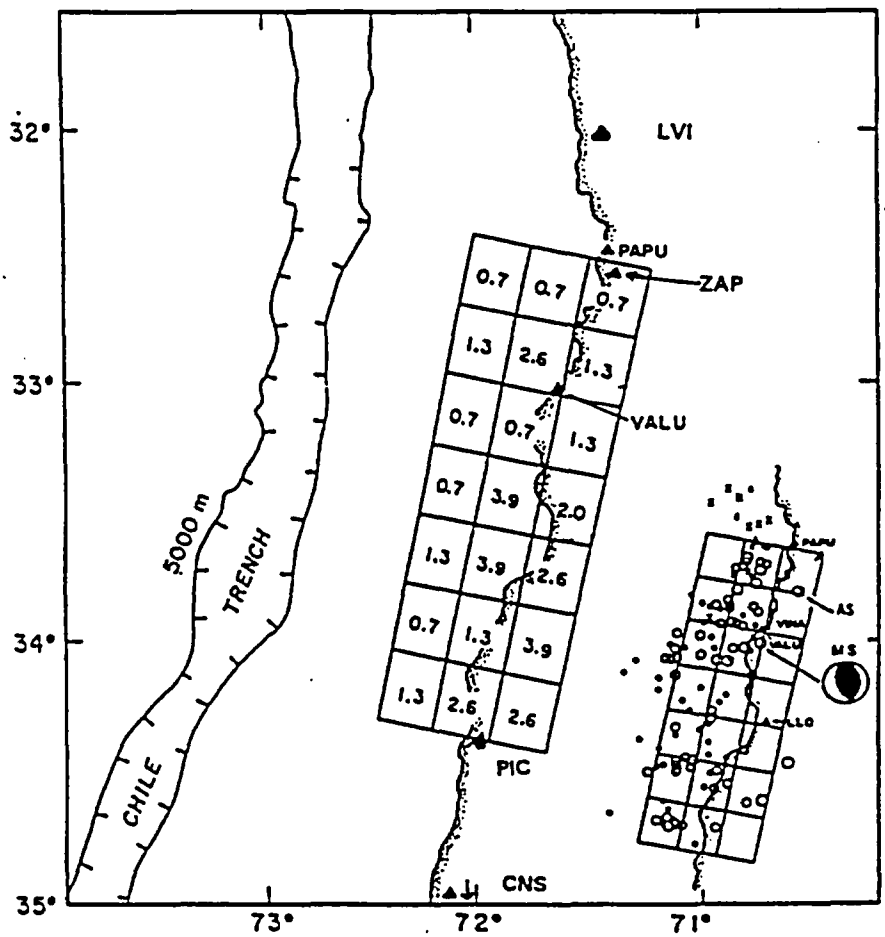

Figure C-10 Slip model (Somerville et al., 1990) and station locations for the March 3, 1985, Valpariso M 7.93 earthquake.

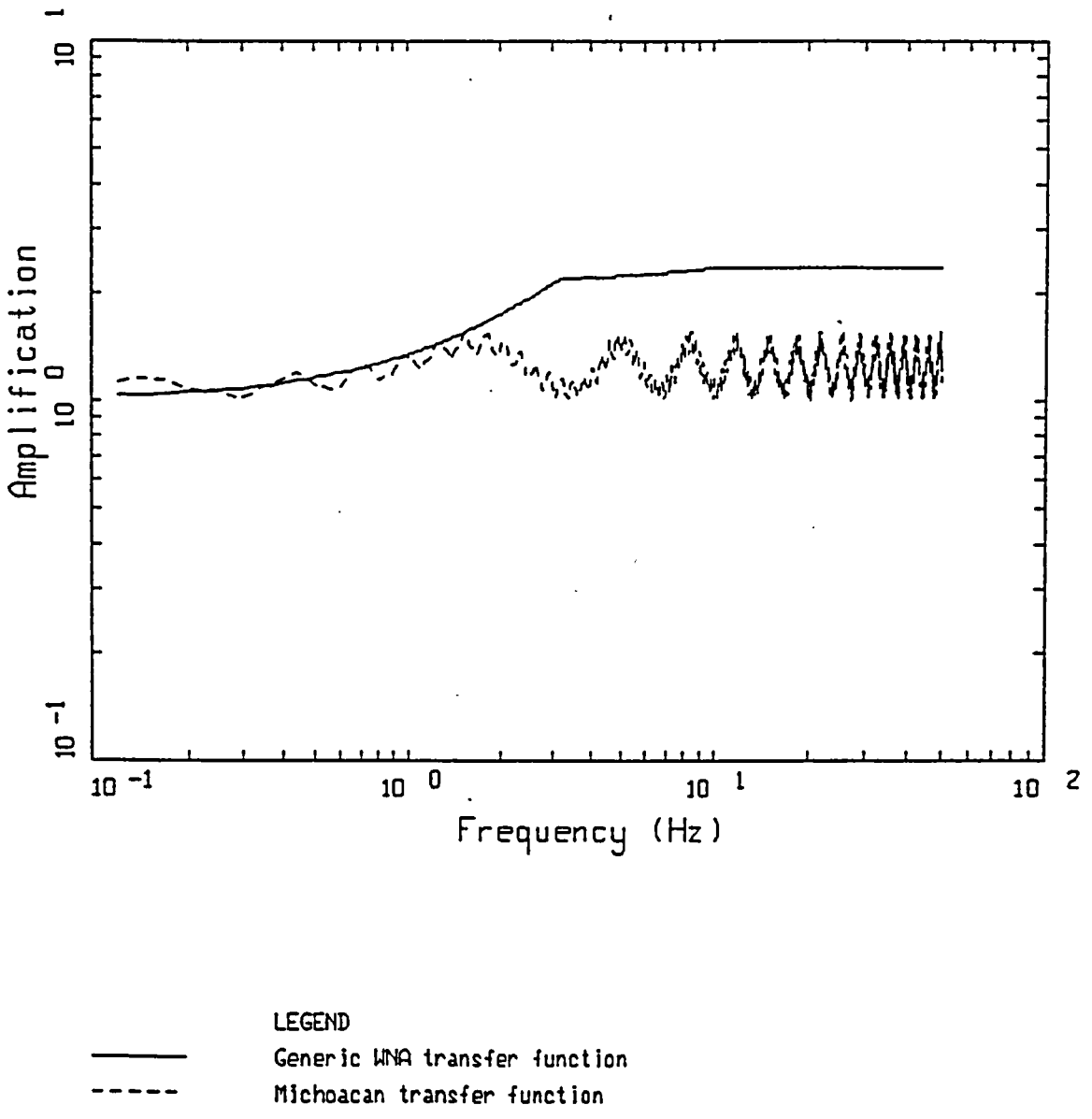

Figure C-11 Comparison of crustal amplification for generic western North America (Boore, 1986) with that computed for the crustal structure of the Guerrero array.

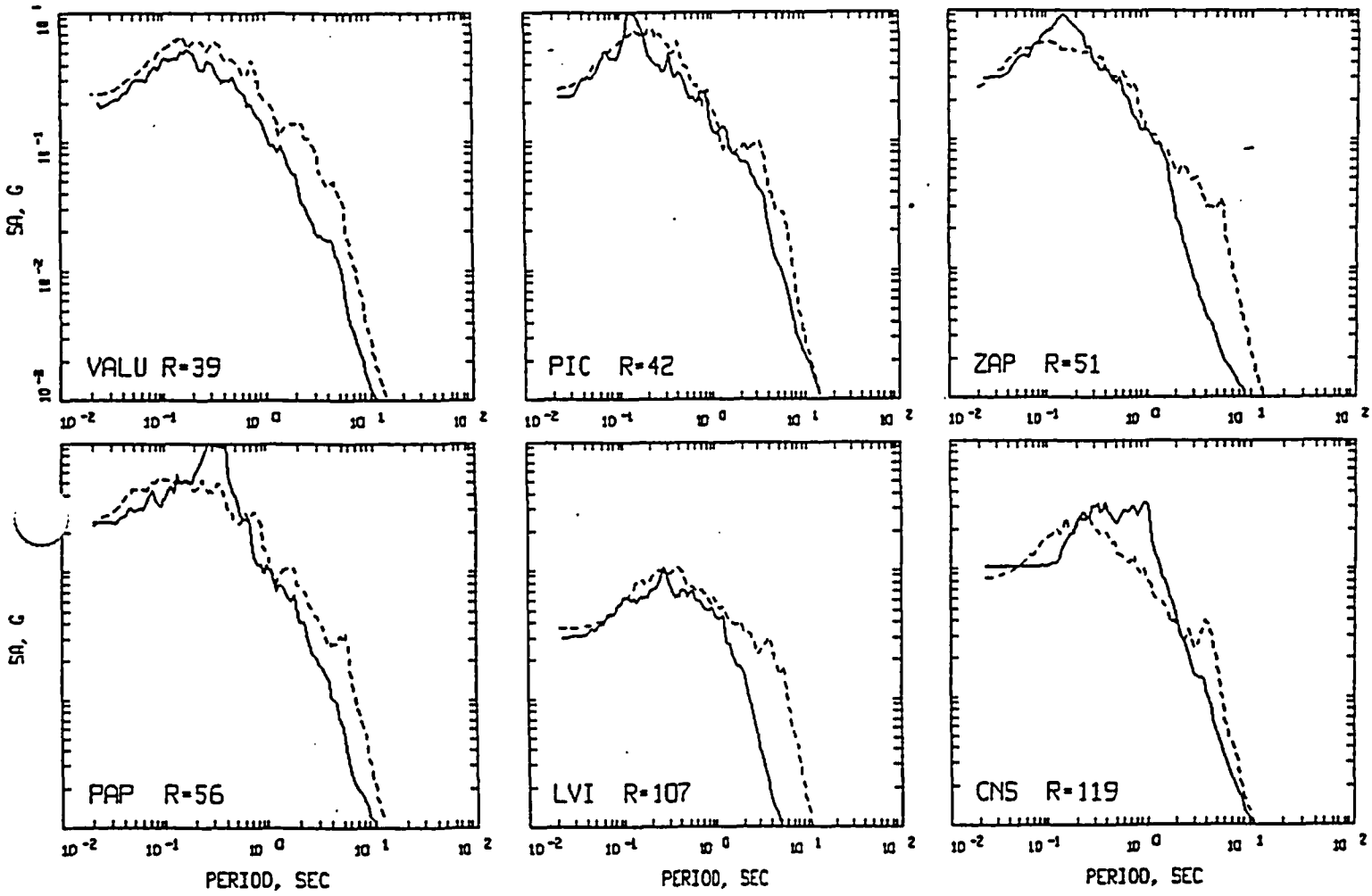

Figure C-12 Comparison of 5% damped acceleration response spectra computed for the Valpariso, Chile, earthquake (dashed lines) to average of the two horizontal components computed from the recorded motions (solid lines) at six rock sites.

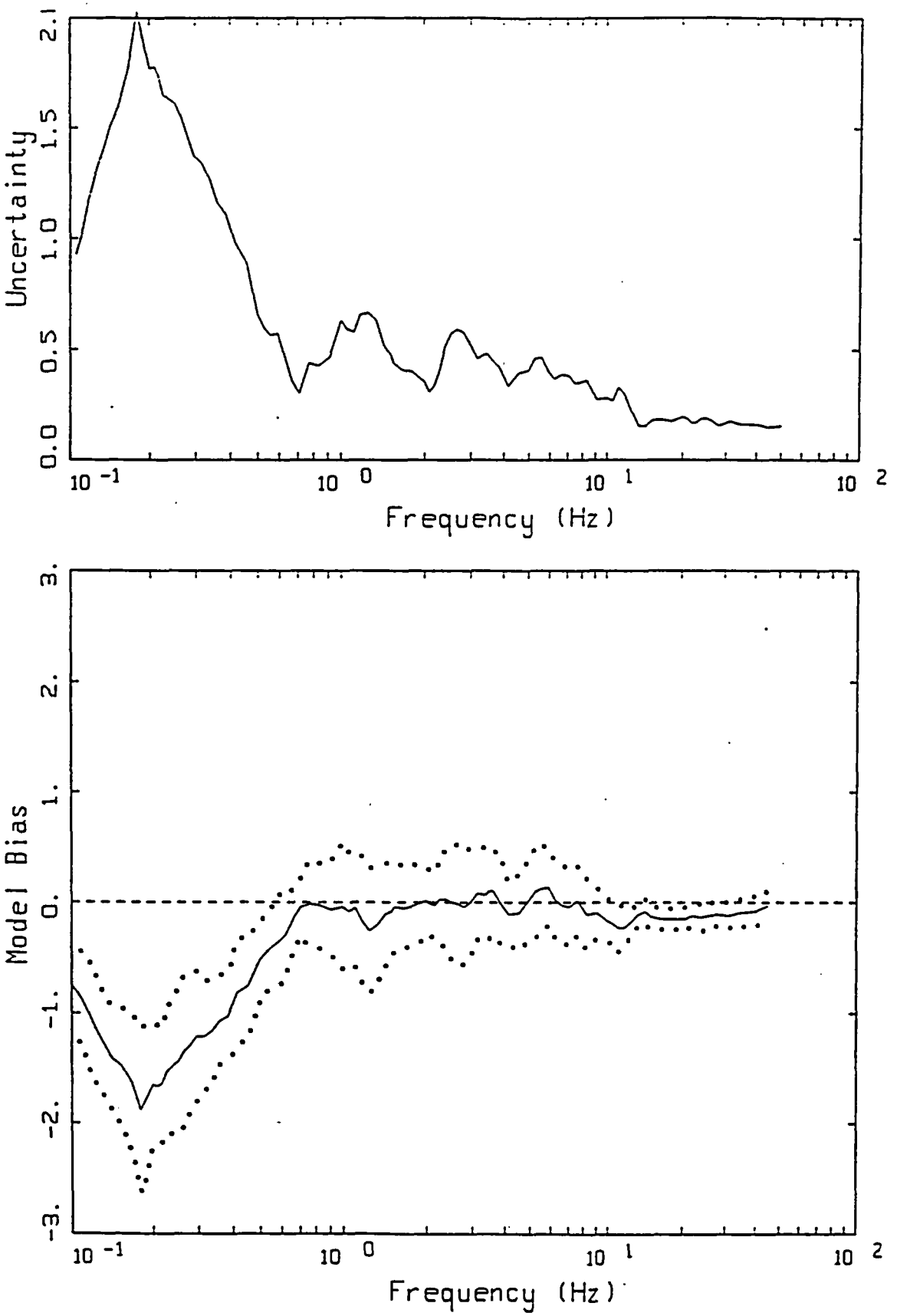

Figure C-13 Modeling uncertainty (σ_{in}) (upper) and model bias with 90% confidence limits (lower) computed for the Valpariso, Chile, earthquake.

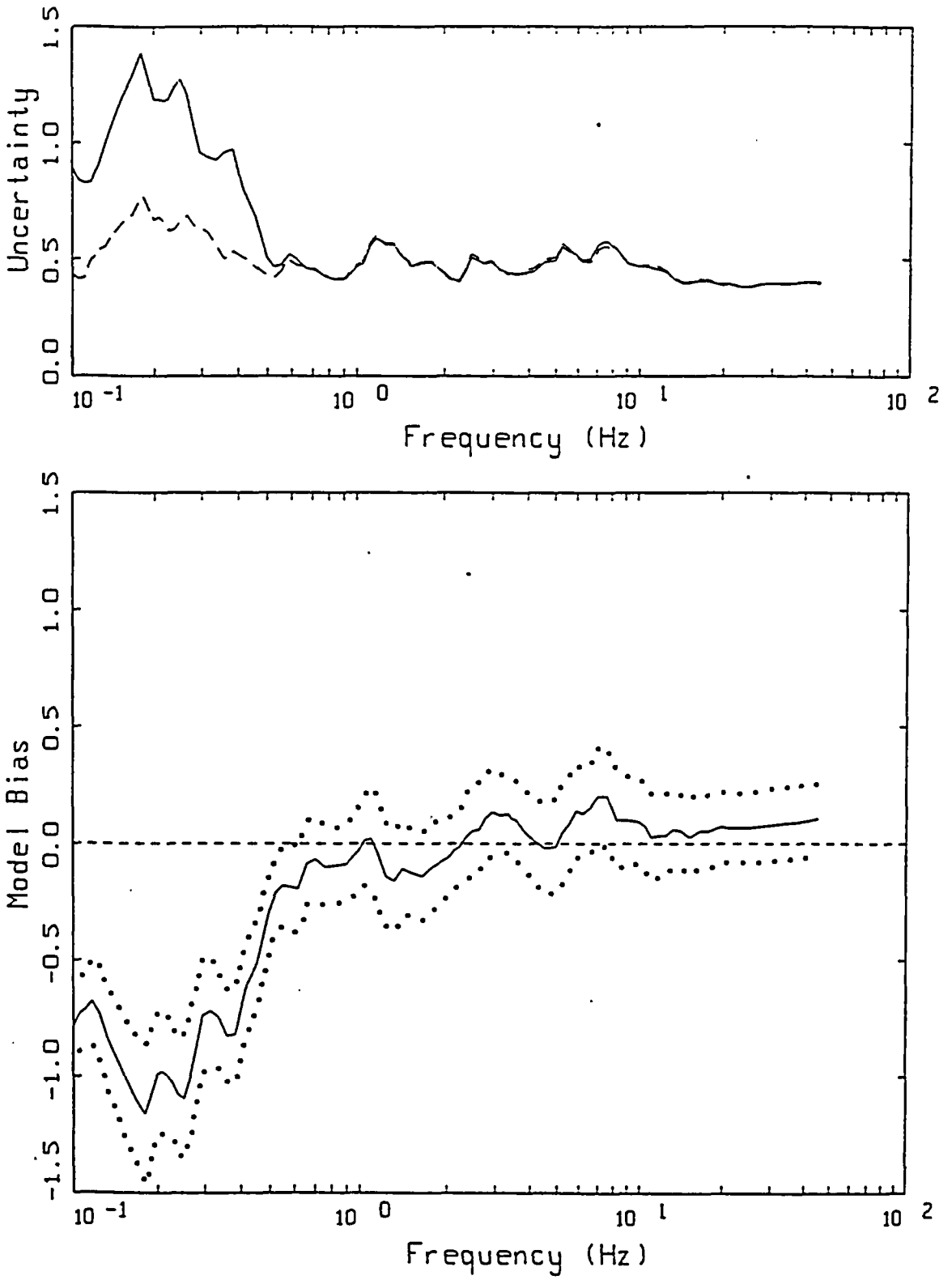

Figure C-14 Modeling uncertainty (solid lines) and bias corrected modeling uncertainty (dashed lines) (both σ_{ln}) (upper) and model bias with 90% confidence limits (lower) computed for both the Michoacan, Mexico, and Valpariso, Chile, earthquakes.

GEOMATRIX

APPENDIX G

PRELIMINARY EVALUATION OF BASIN EFFECT

APPENDIX G

PRELIMINARY EVALUATION OF BASIN EFFECT

In a previous study, Vidale and Helmberger (1988) showed that variations in the attenuation of long period ground motions in Los Angeles could be explained by large scale two-dimensional sedimentary basins using finite-difference calculations. The peak ground velocity at the center of a basin was up to a factor of 2 larger than the peak ground velocity at the edge of a basin (or rock outcrop) for similar closest distances.

This section describes a preliminary analysis of the significance of large basins on the ground motion at the Humboldt Bay Crossing site. The intent is not to determine the basin effect, but rather to determine if the basin effect is likely to significantly increase the ground motion at the bridge site.

G.1 METHODOLOGY

Synthetic seismograms are computed using 2-D ray tracing based on the method of Cerveny (1985). The computer programs were provided by Robert Hermann. Since this is a ray method, it does not explicitly include surface waves, but is fast compared to finite-difference methods. Up to five multiple reflections within each layer are included in the calculation. Both the SH and P-SV motions are computed.

For this analysis, we compare the ground motion computed for the 2-D structure with the ground motion computed for 1-D structure where the 1-D structure is taken as the 1-D model under the Bridge site. By comparing the 2-D response to the 1-D response, we can determine if the use of 1-D site response will significantly underestimate the ground motions. This will tell us if the 2-D structure is likely to focus the energy toward the site and thus indicate that the site response is likely to be anomalously large. Since this project is primarily concerned with long period response, the ground motion is characterized by the peak ground velocity.

G.2 RESULTS

A review of the two-dimensional structure was made by examining geologic cross-sections at the bridge sites. In this analysis, the direction that produces the maximum basin dip is used because it is expected to produce the largest 2-D effects.

For the Eureka bridges, the most prominent 2-D structure is along section A-A' (see Figure G-1). There are several small basins with thicknesses of about 1 km.

The cross-section along A-A' for the Eureka bridge is shown in Figure G-2. For the analysis, this structure was simplified to the structure shown in Figure G-3. The projected location of the Eureka Bridges is at the center of the deepest part of the basin. The S-wave velocities in m/s are shown in the figure. The ground velocities were computed at the locations shown by

the triangles using hypocenters on the Fresh-Water fault with a focal depth of 5 km (shown by the star).

The ratios of the average 2-D to 1-D peak velocities are listed above each triangle. For the Eureka Bridge, we find that the 2-D structure slightly amplifies the ground motion at the site. The ratio of the 2-D to 1-D peak velocity is 1.1 at the projected bridge site. This 10% increase is not significant in comparison to the accuracy of the method.

The impedance contrasts for the Eureka structure are smaller than for the Los Angeles basin. Therefore, it is reasonable to expect that the basin effect would be less in Eureka than in the Los Angeles basin.

We conclude that the 2-D basin effects at the Eureka bridges are not likely to produce significant anomalously large motions at the bridge sites.

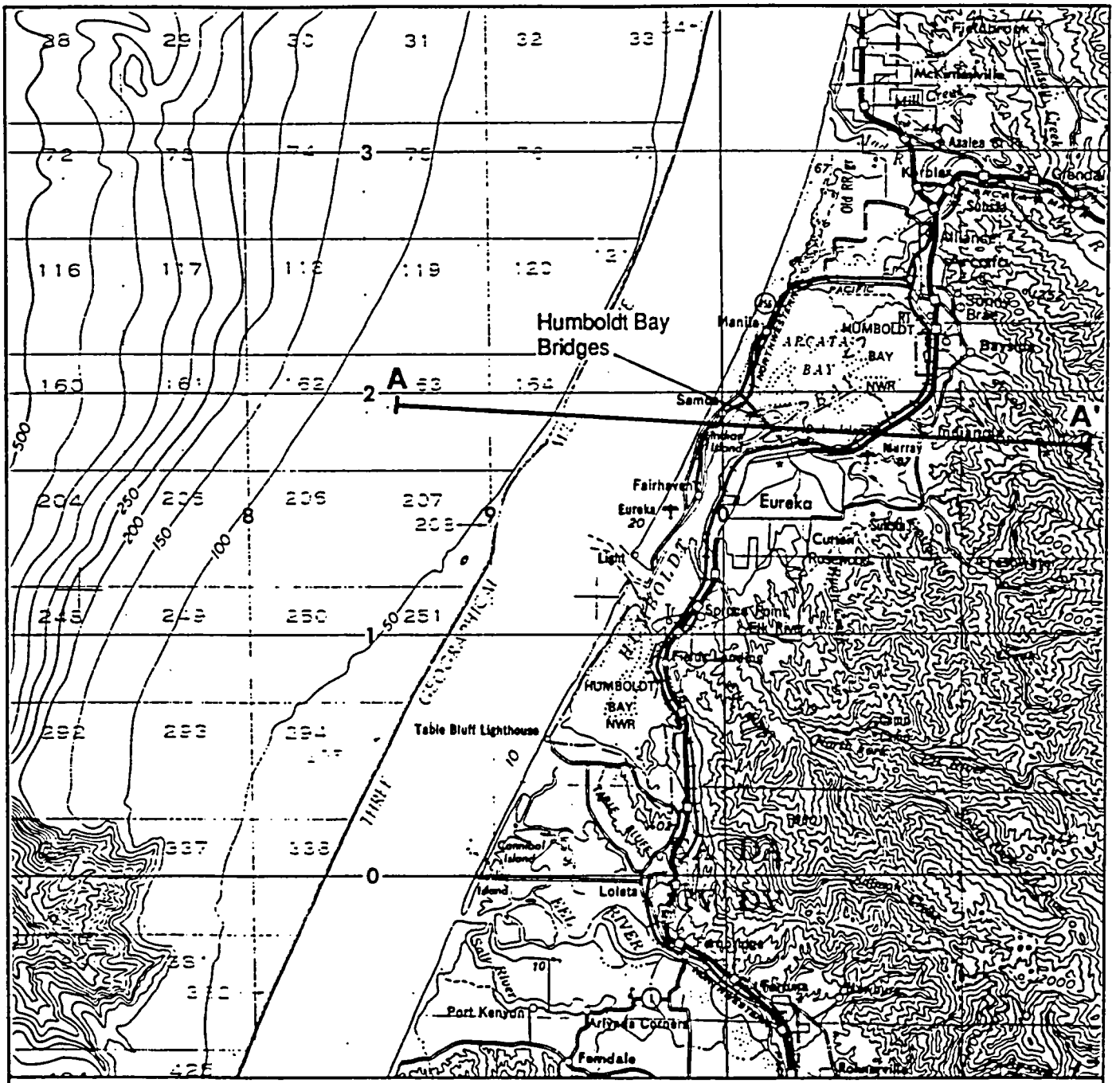

GEOMATRIX	LOCATION OF GEOLOGIC CROSS SECTION A-A' Seismic Ground Motion Studies for Humboldt Bay Bridges Humboldt County, California	Figure G-1 Project No. 2016G

GEOMATRIX

GEOLOGIC CROSS SECTION A-A'
Seismic Ground Motion Studies for Humboldt Bay Bridges
Humboldt County, California

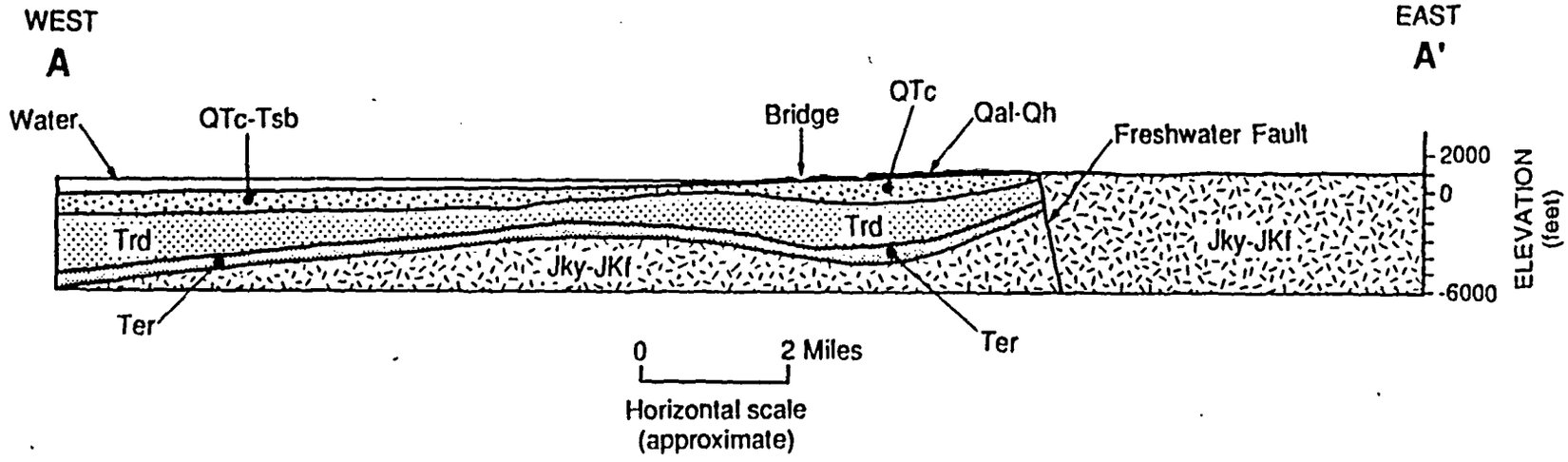

EXPLANATION

Formation and Description

JKf – Franciscan Formation; sandstone, shale, and chert

JKy – Yager Formation; indurated mudstone, shale, graywacke, and conglomerate

Ter – Eel River Formation; mudstone, siltstone, and sandstone

Trd – Rio Dell Formation; massive mudstone and thin sandstone layers

Tsb – Scotia Bluff Sandstone; massive, friable, fine-grained sandstone

QTc – Carlotta Formation; conglomerate, sandstone, and claystone

Qh – Hookton Formation; gravel, sand, and silt

Qal – Recent alluvium; gravel, sand, silt, clay, and bay mud

Sources: Ogle, B. A., 1953; Evenson, R. E.,1959; Strand, R. G., 1962; and Schymiczek, H. and Suchsland, R., 1987.

Figure G-2

Project No. 2016G

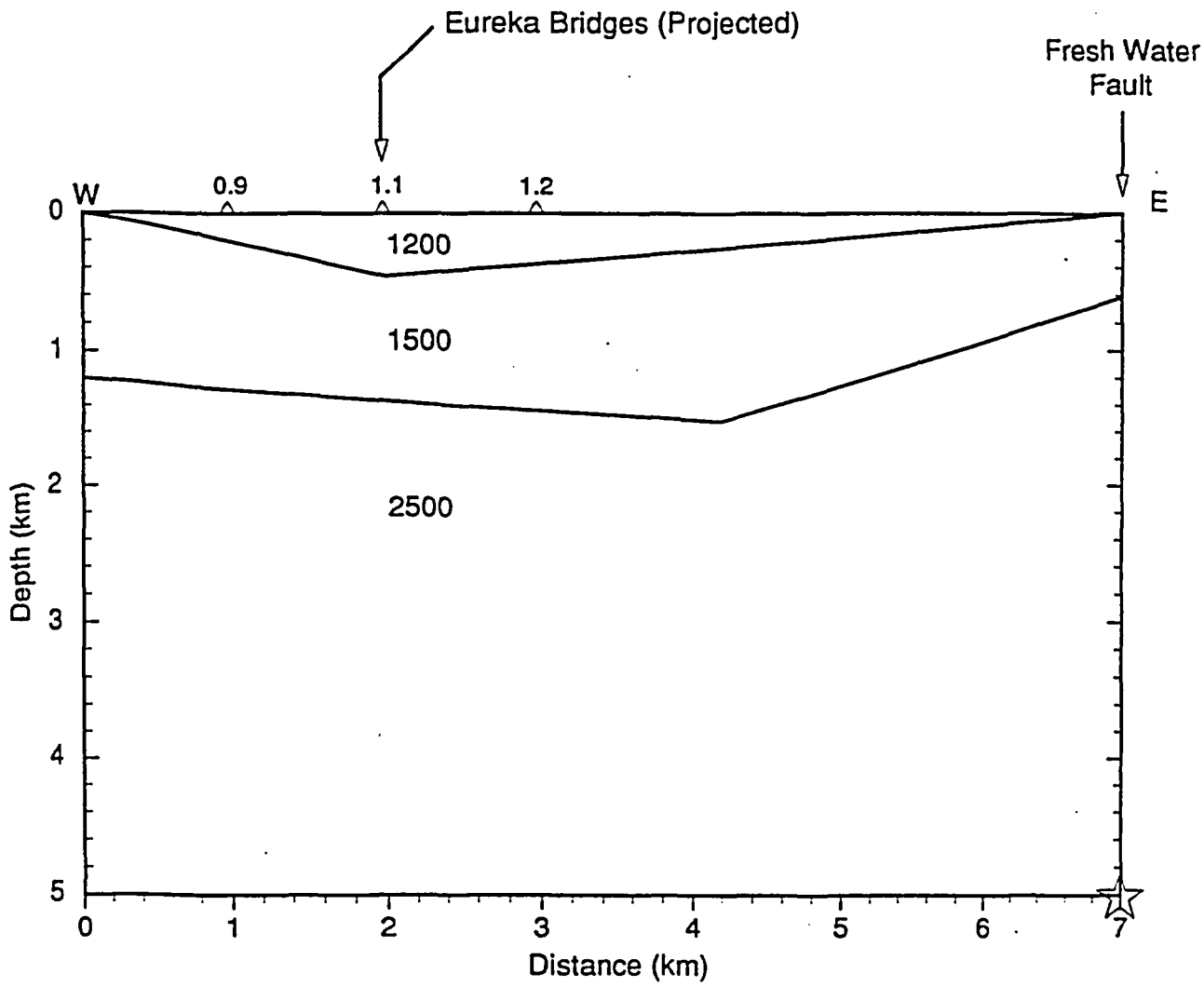

GEOMATRIX

SIMPLIFIED GEOLOGIC CROSS-SECTION USED IN ANALYSIS OF BASIN EFFECT
Seismic Ground Motion Studies for Humboldt Bay Bridges
Humboldt County, California

Figure
G-3

Project No.
2016G